Les dynamismes éruptifs et mécanismes associés en contexte basaltique : étude du Piton de la Fournaise, île de La Réunion, France

Simon Thivet

UNIVERSITE CLERMONT AUVERGNE

Collegium des Sciences Fondamentales

ECOLE DOCTORALE DES SCIENCES FONDAMENTALES

Thèse de doctorat

Présentée en vue de l'obtention du grade de

DOCTEUR D'UNIVERSITE

Spécialité : Volcanologie

Par

Simon Thivet

Titulaire du Master Recherche Magmas et Volcans

Les dynamismes éruptifs et mécanismes associés en contexte basaltique : étude du Piton de la Fournaise, île de La Réunion, France

Soutenue le 29 Novembre 2019

Devant le jury composé de :

Patrick Bachèlery	LMV, Université Clermont Auvergne	Président du jury
Rosa Anna Corsaro	INGV di Catania	Rapporteure
Michel Pichavant	ISTO, Université d'Orléans	Rapporteur
Margherita Polacci	University of Manchester	Examinatrice
Hélène Balcone-Boissard	ISTeP, Université Sorbonne Paris Cité	Examinatrice
Georges Boudon	IPGP, Université de Paris	Examinateur
Lucia Gurioli	LMV, Université Clermont Auvergne	Directrice de thèse
Andrea Di Muro	IPGP-OVPF, Université de Paris	Codirecteur de thèse

Laboratoire Magmas et Volcans

Université Clermont Auvergne

Campus Universitaire des Cézeaux

6 Avenue Blaise Pascal

TSA 60026 – CS 60026

63178 AUBIERE Cedex

Résumé

Les éruptions basaltiques sont de plus en plus étudiées au sein de nombreux volcans. Cependant, les processus pré- et syn-éruptifs gouvernant ces éruptions ne sont pas entièrement compris. Dans le but de caractériser et comprendre l'ensemble des mécanismes opérant depuis le système magmatique superficiel jusqu'à la surface, cette thèse est principalement axée sur l'étude des produits éruptifs du Piton de la Fournaise (île de la Réunion, France), qui est l'un des volcans les plus actifs au monde. Des analyses texturales et géochimiques sur les pyroclastes et les laves sont conjointement réalisées dans le but d'identifier des paramètres clés pouvant être reliés à des processus magmatiques majeurs, à des dynamiques éruptives et à des mécanismes de fragmentation. Lorsque cela est pertinent, ces interprétations sont intégrées à des données de surveillance pré- et syn-éruptives acquises au sol ou par télédétection.

Le premier objectif de cette étude intégrée est de mieux comprendre les mécanismes à l'origine des surpressions magmatiques et des dynamiques éruptives lors des éruptions récentes du Piton de la Fournaise. Au cours de l'éruption de Juin 2014, les déclenchements éruptifs ainsi que les transitions syn-éruptives d'un régime hawaiien vers un régime strombolien relativement faible, associés à une diminution du flux lavique, ont été liés à une vésiculation et à une surpression pré-éruptive du magma qui furent indirectement mises en évidence par l'émission de pyroclastes de type *golden pumice* (pyroclastes très vésiculés et vitreux). Au contraire, l'éruption de Juillet 2015 (émission de *golden pumice* relativement rare) a été déclenchée par un apport magmatique superficiel qui a pu être identifié au sein des signatures texturales et géochimiques des produits éruptifs.

Un an plus tard, une autre éruption de courte durée s'est produite en Septembre 2016, produisant beaucoup de pyroclastes de type *golden pumice*. Cependant, cette éruption dominée par des fontaines de lave, se comporta de manière atypique et fut associée à une augmentation du flux lavique et d'une émission inhabituelle de cendres lors du dernier jour de l'activité éruptive. Le deuxième objectif de la thèse est donc d'améliorer nos connaissances sur la transition d'une activité hawaiienne (associée à l'émission de pyroclastes de type *golden pumice* et *fluidal scoria*) vers une activité plus explosive associée à l'émission de scories et de cendres relativement denses et riches en cristaux, de type *transitional* et *opaque*. Les analyses texturales et chimiques des produits éruptifs confirment l'hypothèse selon laquelle ces scories et cendres

denses sont issues du refroidissement et du dégazage à pression ambiante du magma initialement vésiculé et peu cristallisé. Il est donc possible de former un bouchon faiblement perméable, provoquant des impulsions magmatiques pressurisées à faible profondeur et une activité explosive transitoire sous l'influence et la remontée tardive d'un magma relativement peu dégazé.

Il est communément admis que l'activité effusive représente la majorité du volume magmatique émis au sein des volcans boucliers basaltiques. Cependant, l'éruption de Septembre 2016 a montré que les éruptions basaltiques peuvent parfois produire des aléas liés à des émissions de cendres non-négligeables. Par conséquent, le troisième but de la thèse est de rassembler une série d'échantillons correspondant aux principales éruptions historiques et récentes des volcans du Piton de la Fournaise et du Karthala (île de Ngazidja, Comores). L'étude de ces différents dépôts cendreux révèle des caractéristiques texturales très différentes suggérant différents processus de fragmentation, à savoir la fragmentation ductile, la fragmentation fragile (provoqué par la cristallisation syn-éruptive du magma juvénile), des interactions entre le magma et des fluides externes, des vitesses de remontée magmatiques élevées ou encore la fragmentation par cisaillement pendant l'effondrement de calderas.

Toutes ces connaissances exposent de nombreux processus magmatiques et de fragmentation qui mettent en évidence la complexité des mécanismes à l'origine de telles éruptions basaltiques. Ces travaux de thèse ne représentent qu'une partie des possibilités de recherche sur les éruptions basaltiques. Dans le futur, de nombreuses études de laboratoire supplémentaires et de surveillance de l'activité en temps-réel pourront être réalisées pour encore mieux comprendre et mieux prévoir l'évolution de l'activité éruptive en surface qui peut présenter des risques inattendus pour les populations environnantes.

Abstract

Basaltic eruptions are increasingly studied in a lot of active volcanoes around the world. Yet, their pre- and syn-eruptive processes are not fully understood. In order to characterize and understand the set of mechanisms occurring from the shallow magmatic system to the surface, this thesis is focused on the study of the eruptive products of Piton de la Fournaise volcano (La Réunion Island, France), which is one of the most active volcano in the world. Integrated textural and chemical analysis on tephra and lava are performed to identify some key parameters which can be related to major magmatic processes, eruptive dynamics and fragmentation processes. When it is available and relevant, these interpretations are integrated with pre- and syn-eruptive monitoring measurements acquired by ground-based and remote sensing observation systems.

The first objective of this integrated study is to gain insight on the magmatic overpressure, conduit and eruptive dynamics during basaltic dyke eruptions. During the June 2014 eruption, eruptive triggers and syn-eruptive transitions from Hawaiian-style to mild Strombolian-style activities, associated with a decreasing of the lava flux, have been related to a second boiling mechanism and a pre-eruptive pressurization which was indirectly evidenced by golden pumice emission (highly vesicular and glassy tephra). On the contrary, the July 2015 eruption (relatively scarce golden pumice emission) was triggered by a shallow magmatic input that was tracked in the textural and chemical features of the eruptive products.

On year later, another short-lived eruption occurred on September 2016, which emitted a lot of golden pumice. However, this eruption, dominated by Hawaiian fountaining, behaved atypically with an increase in lava flux associated with uncommon ash emission the last day of the eruptive activity. Thus, the second objective of the thesis is to improve our comprehension on the transition from Hawaiian-style (associated with golden pumice and fluidal scoria) to more explosive activities (associated with dense, crystal-rich opaque scoria and ash emission). The integrated study on this eruption supports the hypothesis that the opaque scoria and ash were inherited from the sub-surface cooling and degassing of the golden pumice material. This suggests the formation of a low-permeable plug, which modulated overpressure pulses at shallow levels and transient explosive activity under the late input of a relatively undegassed and ascending magma.

It is commonly accepted that effusive activity represents the main emitted magmatic volume in basaltic shield volcanoes. However, the September 2016 eruption reminded us that basaltic eruptions can sometime produce hazards related to ash-dominated events. Therefore, the third purpose of the thesis is to bring together a comprehensive sampling of tephra from major historical and recent eruptions at Piton de la Fournaise and Karthala (Ngazidja Island, Comoros) volcanoes. The study of these different deposits reveals very different textural characteristics reflecting different fragmentation processes, as ductile fragmentation, brittle fragmentation (triggered by syn-eruptive crystallization of the juvenile magma), interactions between magma and external fluids, high magma ascent velocities and shear-induced fragmentation mechanisms during caldera collapse events.

All these insights expose a lot of different magmatic and fragmentation processes which highlight the complexity of the mechanisms driving such basaltic eruptions. This thesis only represent a part of the research possibilities on basaltic eruptions. In the future, many additional laboratory studies and real-time monitoring of the eruptive activity can be performed in order to even better understand and better predict the change in eruptive activity than can represent unexpected threats to the environing populations.

Remerciements

Au cours de l'ensemble de mon cursus universitaire m'ayant amené au doctorat, j'ai eu la chance et le privilège de rencontrer, de travailler et de partager des moments avec de nombreuses personnes que je souhaite remercier.

Je voudrais tout d'abord remercier la personne à qui je dois le plus sur l'aboutissement de mes travaux et mon épanouissement dans le monde de la recherche, ma directrice de thèse **Lucia Gurioli**, qui m'a accompagné et supporté tout au long de cette thèse mais aussi pendant mon stage de recherche en Master 2. Un grand merci à mon codirecteur **Andrea Di Muro**, qui m'a permis d'élargir mes connaissances et qui a apporté une réflexion essentielle à mes travaux. Pendant ces trois années de thèse, j'ai eu le privilège d'étudier des choses fascinantes et dans des conditions inespérées. Au-delà de votre gentillesse et de votre accueil en toutes circonstances, j'aimerai souligner votre professionnalisme et votre intérêt que vous m'avez tous les deux porté. Ces trois années de thèse sous votre direction ont été assurément la période la plus enrichissante de ma jeune carrière et je vous en remercie profondément.

Je voudrais apporter une attention particulière à l'ensemble des membres du jury, **Patrick Bachèlery**, **Rosa Anna Corsaro**, **Michel Pichavant**, **Margherita Polacci**, **Hélène Balcone-Boissard** et **Georges Boudon**, qui ont accepté d'examiner et juger mes travaux de thèse. Je suis très reconnaissant de votre présence et de l'échange très intéressant que nous avons pu avoir à la suite de ma soutenance.

Merci beaucoup à l'ensemble des membres du Laboratoire Magmas et Volcans pour votre accueil, votre gentillesse et votre bonne humeur. Un merci tout particulier à **Andrew Harris**, **Julia Eychenne**, **Oryaëlle Magdalena Chevrel**, **Mathieu Gouhier**, **Ivan Vlastélic**, **Benjamin Van Wyk de Vries**, **Federica Schiavi**, **Etienne Médard** et **Pierre-Jean Gauthier** pour vos encouragements et vos conseils scientifiques très précieux. J'aimerais aussi remercier **Claire Fonquernie**, **Mhammed Benbakkar**, **Jean-Marc Hénot**, **Sylvaine Jouhannel**, **Krzysztof Suchorski** et **Christophe Constantin** pour vos conseils techniques et votre aide sur l'avancement des différentes analyses que j'ai pu réaliser ou utiliser au cours de mes travaux de thèse. Je remercie également l'ensemble du personnel administratif et plus particulièrement

Audrey Chazal, **Céline Lavet**, **Nathalie Elaydi**, **Isabelle Roche**, **Valérie Guesneau** et **Cécile Sergère** pour leur gentillesse et leur efficacité.

Je remercie l'ensemble des membres de l'Observatoire Volcanologique du Karthala ainsi que de l'Observatoire Volcanologique du Piton de la Fournaise pour leur accueil chaleureux, notamment **Allan Derrien**, **Nicole Richter**, **Guillaume Boudoire**, **Aline Peltier**, **Patrice Boissier**, **Valérie Ferrazzini**, **Christophe Brunet**, **Gian Luciano Garavaglia** et **Philippe Kowalski** avec qui j'ai passé des moments très enrichissants et très agréables.

J'ai aussi réussi à m'épanouir dans le milieu de la recherche grâce à mes proches et mes amis. Merci pour la distribution considérable de tranches. J'ai une mention spéciale pour mes collègues de bureau et amis doctorants **Alexis Droïde**, **Damien Bagarre** et **Nathan Fantôme**. Vous avez eu en effet le mérite de me supporter pendant ces trois années de sérieux mais aussi de fissures. Une grosse pensée aux anciens, notamment à la paire de **Valentin** et à **Swetha Brown Sugar**. Pour votre bonne humeur et simplicité, merci à tous les étudiants, thésards et post-docs que j'ai pu côtoyer pendant ces trois années au Laboratoire Magmas Volcans mais aussi ailleurs.

Enfin, un grand merci aux membres de la Tranche, notamment **Berthof** et **Dobter** sans oublier tous les cantalous bien sûr, avec qui j'ai pu passer d'excellents moments riches en tranches et fissures notamment au Sanki et au Mayor.

Table des matières

CHAPITRE I

INTRODUCTION GENERALE

1. Contexte

La volcanologie et les processus magmatiques au sens large, comprend l'ensemble des mécanismes physico-chimiques opérant depuis la fusion partielle de la roche en profondeur, l'évolution des magmas à travers la croûte jusqu'à leur éruption et dispersion au sein de l'atmosphère ou de l'hydrosphère. L'activité volcanique se manifeste sur l'ensemble de la surface de la croûte terrestre par l'émission de produits magmatiques très variés et au sein d'édifices volcaniques relativement diversifiés (Rogers 2015 et références incluses).

Cette thèse est consacrée à l'étude de l'activité volcanique en domaine basaltique, impliquant des magmas relativement peu évolués, peu visqueux et de haute température. Sur l'ensemble des systèmes planétaires telluriques connus, le volcanisme basaltique est le plus répandu. Sur Terre, on retrouve des volcans basaltiques actifs dans tous les contextes géodynamiques (Walker 1993). Il est donc important de comprendre l'ensemble des processus magmatiques opérant dans de tels systèmes. De par leurs caractéristiques physico-chimiques, les magmas basaltiques sont généralement liés à des activités relativement faibles en termes d'explosivité, produisant des volumes laviques relativement élevés par rapport aux produits explosifs appelés pyroclastes ou téphras (Stix 2015 et références incluses).

Néanmoins, en observant continuellement l'activité volcanique mais aussi et en étudiant les dépôts d'éruptions passées, une gamme d'activité éruptive relativement grande est souvent observée sur la plupart de ces volcans (Houghton 2015 et références incluses), impliquant des aléas et des risques associés non-négligeables. En considérant cette variabilité, un des enjeux majeurs de la volcanologie moderne est de prévoir et comprendre l'évolution des processus pré- et syn-éruptifs grâce à la surveillance en temps réel de l'activité volcanique ainsi qu'à l'étude des produits éruptifs (laves et pyroclastes) en laboratoire.

2. Connaissances générales sur les éruptions basaltiques

2.1. Les paramètres majeurs contrôlant les styles éruptifs

La variabilité des styles éruptifs au sein des systèmes basaltiques est un fait naturel relativement étudié et surveillé grâce à une multitude de techniques. Les éruptions basaltiques forment généralement des coulées de laves (ex. Harris et al. 2007, 2017 ; Harris et Rowland 2015 ; Staudacher et al. 2016), souvent associées à des activités plus ou moins explosives (ex. Taddeucci et al. 2015 ; Houghton et al. 2016 ; Polacci et al. 2019). Le style éruptif des éruptions basaltiques est majoritairement contrôlé par (i) la quantité initiale des éléments volatils dissous dans le magma ainsi que leur exsolution lors de la remontée de celui-ci vers la surface (Gonnerman et Manga 2012), et par (ii) la viscosité du magma (McBurney et Murase 1984 ; Parfitt 2004).

2.1.1. Le rôle des éléments volatils

Initialement et en profondeur, les magmas basaltiques peuvent contenir quelques pourcents de H_2O, avec des teneurs relativement plus faibles en CO_2, S et en halogènes (ex. Sato 1978 ; Mangan et al. 1993 ; Taddeucci et al. 2015, Di Muro et al. 2016). Chacun de ces éléments volatils se comporte différemment lors de la décompression et s'exsolve du magma à des pressions différentes pour former des bulles pouvant rester ou non au sein du magma. La nucléation et la croissance des bulles dans les magmas est donc un processus fondamental s'opérant lors de leur remontée vers la surface. Généralement, le terme de bulle est employé au sein d'un magma liquide et le terme de vésicule est employé au sein d'une roche solide.

Grâce à des modèles expérimentaux, deux mécanismes de nucléation des magmas ont été mis en évidence : la nucléation homogène et la nucléation hétérogène (ex. Massol et Koyaguchi 2005 ; Cashman and Scheu 2015 ; Shea 2017 ; Fig. 1.1). Dans le cas de la nucléation homogène, c'est-à-dire une nucléation sans l'aide d'énergie d'interface avec un solide, une

sursaturation relativement élevée des éléments volatils dissous dans le magma (d'environ 150 MPa) est nécessaire pour nucléer des bulles (Mangan et al. 2004). Au contraire, dans le cas de la nucléation hétérogène, les bulles nucléent à partir de solides (cristaux ou roches encaissantes), ne nécessitant pas de sursaturation élevée. D'après des tests sur ces théories, il apparait que la nucléation hétérogène est le processus dominant dans les systèmes magmatiques, et plus particulièrement dans les systèmes basaltiques, la nucléation homogène donnant des résultats irréalistes en termes de profondeur de stockage magmatique et de taux de décompression (Shea et al. 2017). Les bulles se formerait donc majoritairement à partir de cristaux préexistant (nanométriques à centimétriques) ou à partir des parois des réservoirs et des conduits magmatiques.

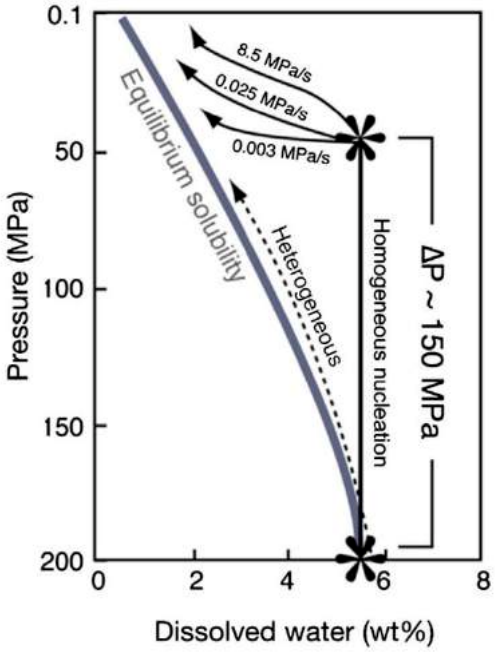

Figure 1.1 *– Quantité de H_2O dissoute dans le magma en fonction de la pression pour différents taux de décompression. La nucléation hétérogène (ligne noire pointillée) permet d'exsolver beaucoup plus tôt les volatils (notamment H_2O) par rapport à la nucléation homogène (ligne noire pleine). Figure modifiée à partir de Cashman et Scheu (2015).*

En reprenant les différentes espèces volatiles présentes initialement dans les magmas basaltiques, le CO_2 est communément la première espèce volatile à s'exsolver : pour des magmas typiques du Piton de la Fournaise, et à partir de 700 MPa, le CO_2 commence à

s'exsolver à des taux relativement constants en fonction du taux de décompression, jusqu'à la surface (Di Muro et al. 2016). De cette façon, les magmas superficiels (< 100 MPa) ont perdu la quasi-totalité du CO_2 initialement présent en profondeur. Au contraire, le dégazage de H_2O et de S s'opère de manière pseudo-exponentielle et augmente à des pressions relativement superficielles (< 100 MPa). H_2O étant le gaz le plus concentré et exsolvant relativement tardivement, il est le volatil magmatique contrôlant majoritairement l'explosivité des magmas en surface (Sparks 1997). En prenant en compte l'ensemble des comportements de chacun de ces volatils en fonction de la pression, la mesure de leur concentration en surface, avant et pendant les éruptions peut renseigner sur l'origine et l'arrivée de nouveaux magmas plus ou moins profonds et plus ou moins dégazés (Fig. 1.2).

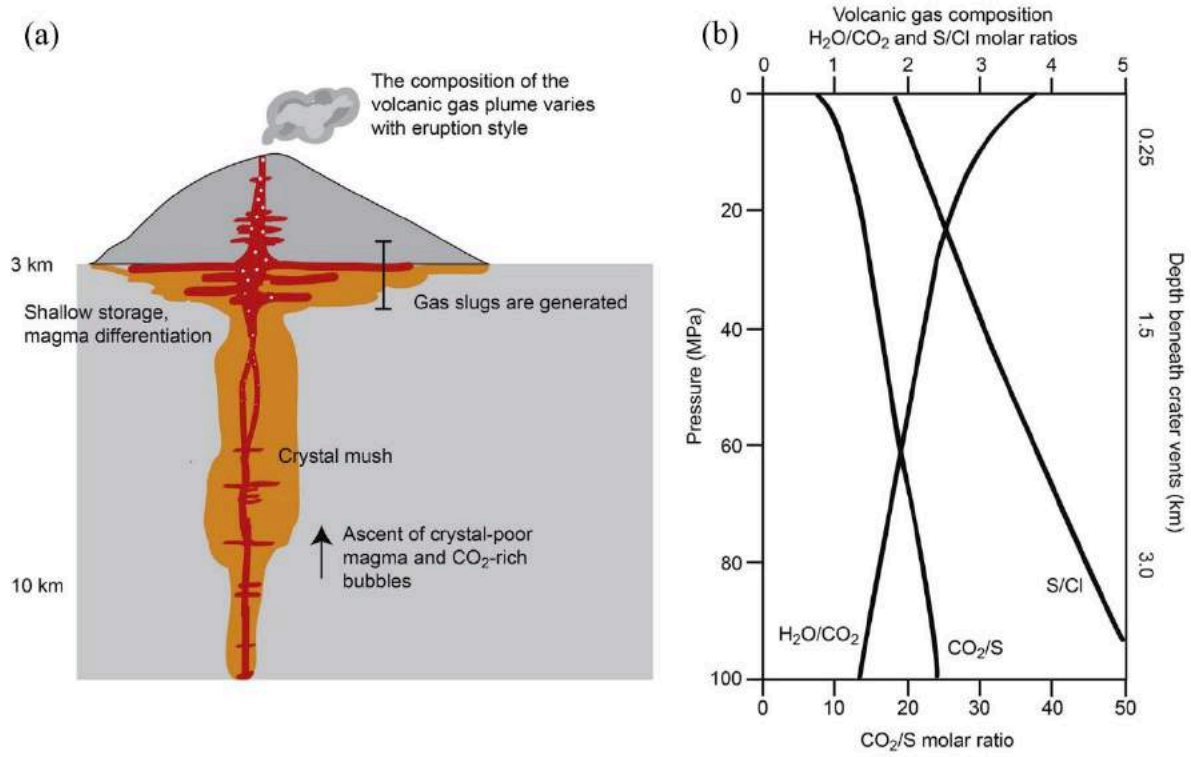

Figure 1.2 *– (a) Coupe interprétative montrant l'ascension de magmas basaltiques à travers un édifice volcanique, appliqué au Stromboli (Italie). (b) Evolution de la composition des gaz volcaniques en fonction de la pression. Figure modifiée à partir de Taddeucci et al. (2015).*

2.1.2. Le rôle de la viscosité

La viscosité du magma ($Pa.s^{-1}$) est le second paramètre principal qui contrôle le style éruptif et la fragmentation du magma (Gonnerman et Manga 2003 ; Fig. 1.3). Ce paramètre peut être défini par la résistance à l'écoulement du fluide magmatique (comprenant liquide, bulles et cristaux). La viscosité du magma est principalement contrôlée par la composition et la température du liquide magmatique (Giordano et al. 2008) ainsi que par la teneur en cristaux (Maron et Pierce 1959 ; Mader et al. 2013) et en bulles (Llewellin et Manga 2005 ; Truby et al. 2014) du magma. Les magmas basaltiques font partie des magmas les moins visqueux ayant des teneurs en SiO_2 relativement faibles (de 45 à 52 pds%), associées à des températures relativement élevées (> 1050°C). Cependant, la teneur en cristaux et en bulles sont des paramètres très variables qui peuvent notamment augmenter la viscosité et le potentiel d'explosivité de ces magmas. De plus, la formation de cristaux peut être engendrée soit par (i) une baisse de température (cristallisation en dessous de la limite chimique et thermique du liquidus ; Fenner 1929 ; Cashman 1993), ou par (ii) dégazage des espèces volatiles (de manière pseudo-isothermique ; Applegarth et al. 2012, 2013). Il est donc important de quantifier l'ensemble de ces paramètres magmatiques pouvant potentiellement contrôler le style éruptif en surface et mettre en évidence certains processus magmatiques pré- et syn-éruptifs.

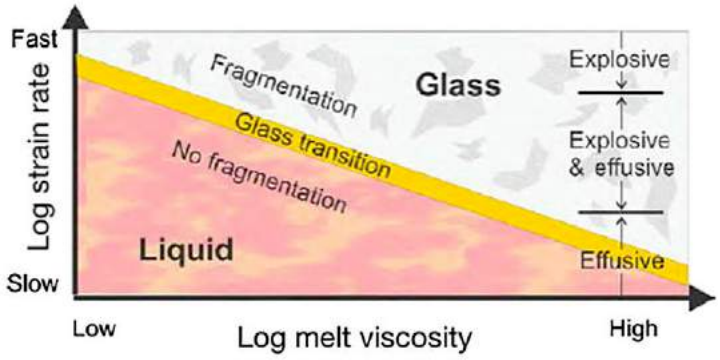

Figure 1.3 *– Illustration théorique de l'effet de la viscosité ainsi que du taux de déformation lors de la remontée du magma sur le style éruptif en surface (figure modifiée à partir de Gonnerman et Manga 2003). Pour de faibles taux de déformations et de faibles viscosités, le magma réagit comme un liquide et aucune fragmentation fragile ne se produit. Au contraire, des taux de déformations élevés associés à des viscosités élevées entrainent généralement une fragmentation fragile et un style éruptif relativement explosif.*

2.2. L'importance des conditions magmatiques initiales au sein des réservoirs superficiels

Le moment et la façon dont les magmas se propagent vers la surface sont fortement contrôlés par les conditions dans lesquelles ces magmas sont préalablement stockées au sein de l'édifice volcanique (ex. Tait et al ; 1989 ; Parfitt et al. 1993 ; Marsh 1989, 2015). Chaque édifice et système magmatiques possèdent leurs propres caractéristiques, en termes de profondeur, de taille et de forme (ex. Walker 1993 ; Marsh 2015 ; Michon et al. 2015 ; Peltier et al. 2015 ; Cassidy et al. 2018). L'ensemble du système magmatique du Piton de la Fournaise est plus particulièrement introduit au sein du **chapitre II** et des comparaisons avec des systèmes basaltiques tels que ceux du Kilauea (Hawaï) ou encore de l'Etna (Italie) sont brièvement établies au cours de cette thèse.

Néanmoins, certains paramètres généraux sont observés sur la majorité des systèmes volcaniques connus et apparaissent comme étant des paramètres répandus à l'origine des déclenchements des éruptions et de leurs évolutions (Fig. 1.4). Tout d'abord, la composition chimique et la teneur en volatils des magmas ainsi que leur différenciation et cristallisation (par refroidissement ou par dégazage) sont des facteurs majeurs contrôlant la stabilité des magmas au sein des réservoirs plus ou moins superficiels (ex. Bachmann et Bergantz 2006 ; Marsh 2015 et références incluses ; Cashman et al. 2017 et références incluses). La mesure de ces paramètres grâce à des approches et des techniques analytiques appropriées permettent de tracer d'éventuels déséquilibres géochimiques provoquées par exemple par des processus de mélanges magmatiques, par le fractionnement de certaines phases minérales ou encore par l'exsolution de certaines espèces gazeuses (Cassidy et al. 2018 et références incluses). Ces processus magmatiques peuvent provoquer l'accumulation de cristaux, la formation de poches riches en bulles de gaz ainsi que des zones magmatiques pauvres en cristaux et riches en volatils dissouts (Cashman et al. 2017 et références incluses ; Cassidy et al. 2018 et références incluses). Ces derniers auteurs suggèrent aussi que les propriétés telles que la porosité, la perméabilité, la température, la viscosité et la pression interne du magma peuvent être impactées, reliant indirectement les mécanismes pré-éruptifs aux processus syn-éruptifs et aux dynamismes éruptifs en surface.

En outre, les précurseurs des éruptions, notamment basaltiques, sont directement liés aux processus volcano-tectoniques pré-éruptifs et se traduisent généralement par une sismicité

relativement élevée au niveau de la chambre magmatique et du conduit en train de se former, un dégazage diffus pré-éruptif anormal avec une augmentation des concentrations de SO_2, H_2S ou encore de CO_2, et une inflation du sol plus ou moins importante (ex. Aiuppa et al. 2010 ; Bell et Kilburn ; Belousov et al. 2015 ; Peltier et al. 2016 ; Gurioli et al. 2018).

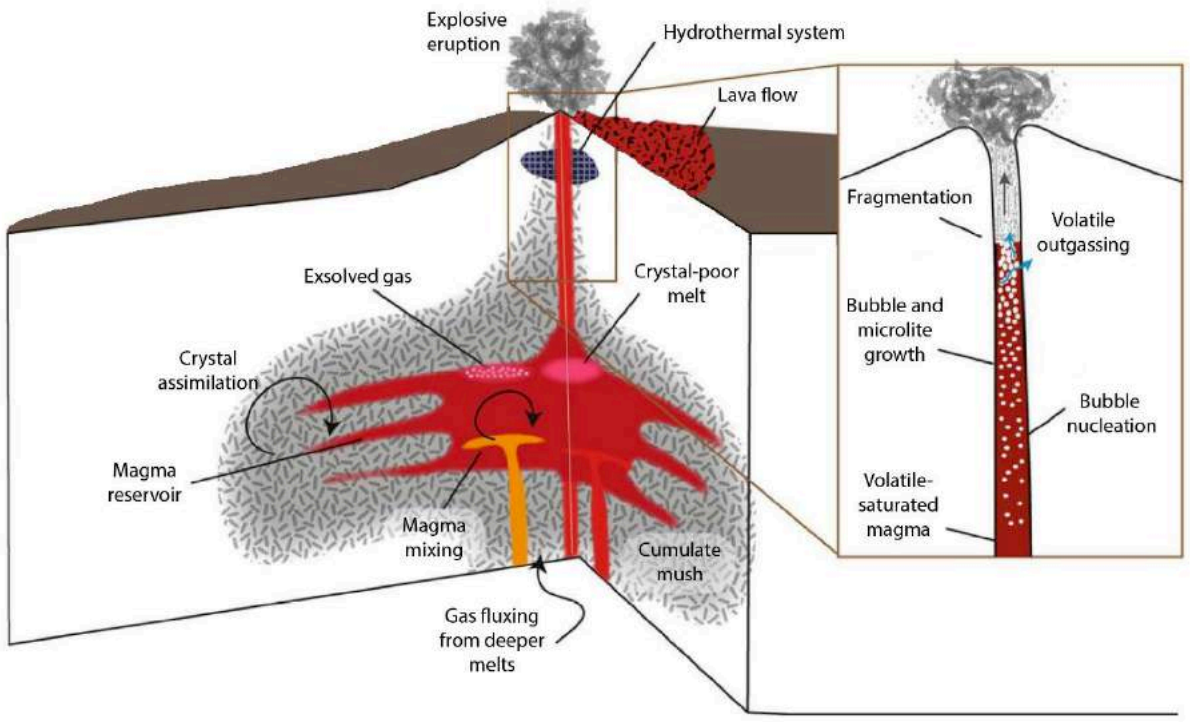

Figure 1.4 *– Schéma illustrant la gamme de processus pouvant déclencher des éruptions et affecter le style éruptif en surface (figure modifiée à partir de Cassidy et al. 2018).*

2.2. Dynamiques d'ascension et fragmentation du magma

Lorsque des magmas préalablement stockées à des niveaux plus ou moins superficiels se propagent vers la surface, différents types d'écoulements au sein des conduits ont été modélisés et observés (ex. Wallis 1969 ; Jaupart et Vergniolle 1988, 1989 ; Gonnerman et Manga 2012). Dans le cas de magmas basaltiques relativement peu visqueux, une ségrégation partielle entre les bulles et le liquide est généralement observée (Taddeucci et al. 2015 et références incluses). Cette ségrégation est principalement fonction du flux magmatique (pouvant jouer sur le taux de déformation du magma lui-même au sein du conduit éruptif ; Fig. 1.3), de la quantité de volatils exsolvés, de la viscosité du magma et de la géométrie du conduit

éruptif (James et al. 2004). L'exsolution des bulles ainsi que leur croissance et leur éventuelle coalescence lors de la décompression, facilitent et accélèrent la vitesse de remontée de ces bulles par rapport à la phase liquide (augmentation de la flottabilité). Au contraire, la perte des espèces volatiles dissoutes, la cristallisation ainsi que le refroidissement potentiel de la phase liquide peut freiner légèrement la vitesse d'ascension des bulles (augmentation de la viscosité du magma).

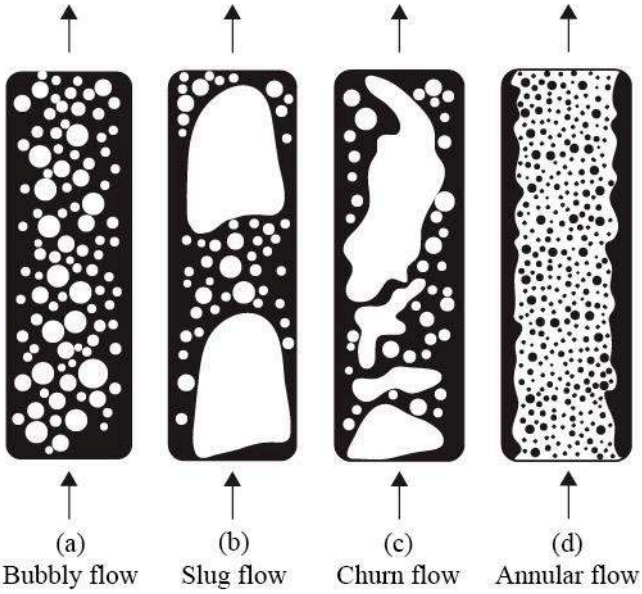

Figure 1.5 *– Les grands types de régime d'écoulement dans les conduits éruptifs basaltiques, reproduits par modélisation analogique (figure modifiée d'après Houghton et Gonnerman 2008 et Gonnerman et Manga 2012). La phase gazeuse est représentée en blanc et la phase liquide en noire. (a) Ecoulement plus ou moins homogène et riche en bulles isolées dans un liquide magmatique, de type bubbly. (b) Ecoulement composé de grosses bulles ascendantes et intermittentes, de type slug. (c) Ecoulement légèrement plus riche en gaz et plus chaotique que le précédent, comportant une multitude de bulles ascendantes irrégulières, de type churn. (d) Ecoulement de type annulaire, composé d'un flux de gaz central plus ou moins constant.*

De cette façon, différents écoulements peuvent se former au sein des conduits volcaniques (ex. Parfitt 2004 ; Houghton et Gonnerman 2008 ; Gonnerman et Manga 2012 et références incluses ; Fig. 1.5), façonnant différents styles explosifs en surface (ex. Sparks 1978 ; Houghton et al. 2004 ; Taddeucci et al. 2015 et références incluses ; Fig. 1.6). La Figure 1.5 schématise et résume les modèles extrêmes d'écoulement dans les conduits basaltiques

superficiels. Des transitions syn-éruptives d'un type d'écoulement à un autre sont fréquentes et résultent souvent à un changement de style éruptif en surface. Les processus magmatiques à l'origine de ces changements sont donc des paramètres clés pour la compréhension et l'anticipation de certains événements explosifs.

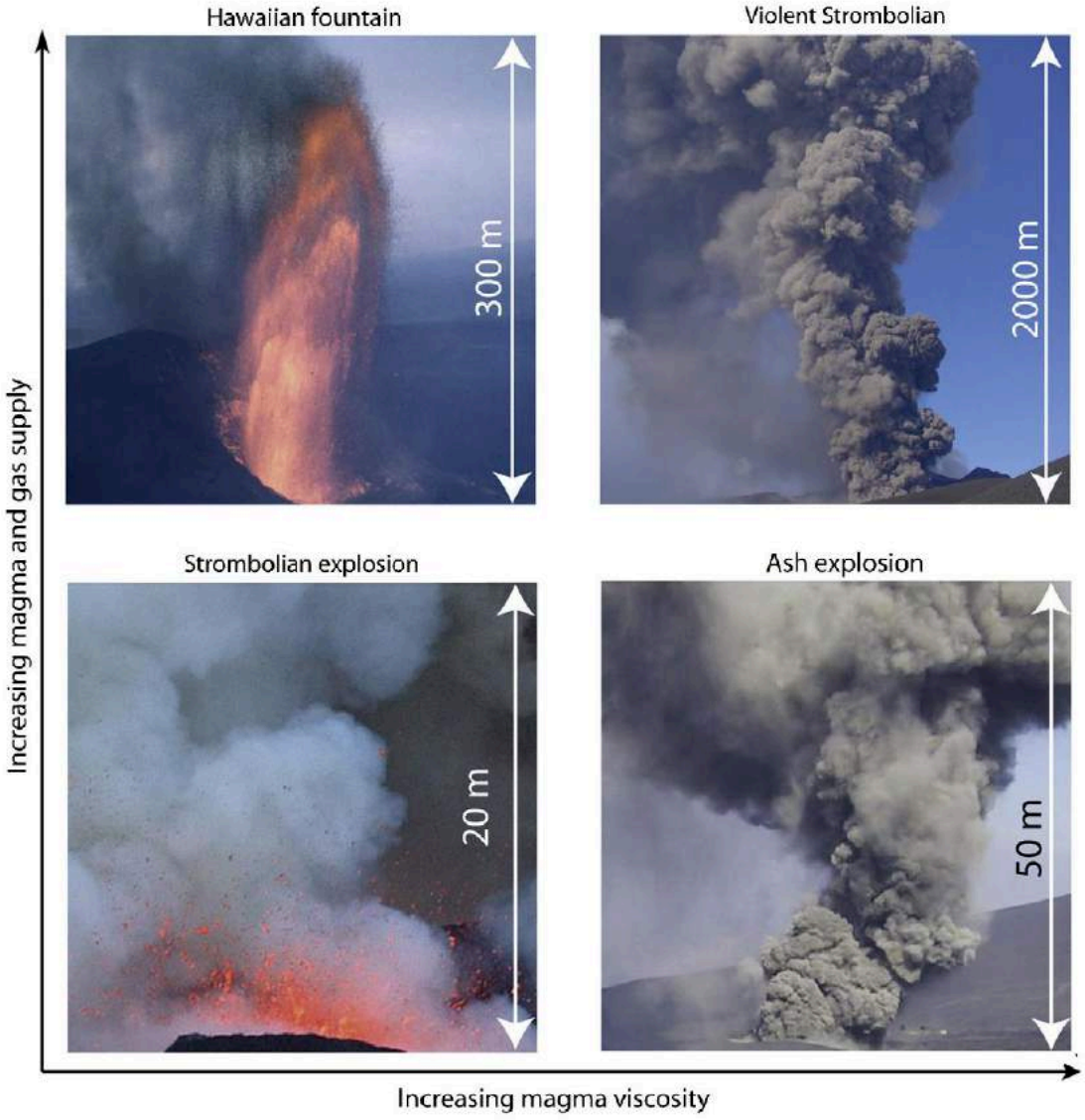

Figure 1.6 *– Photos représentative d'activités hawaïennes, stromboliennes et variations associées. Toutes les photos ont été prises à l'Etna, excepté celle d'en haut à gauche représentant une activité soutenue de fontaine de lave au Kilauea (Hawaï). Figure modifiée d'après Taddeucci et al. (2015). Les éruptions sont grossièrement classées en fonction de l'alimentation en magma et en gaz ainsi qu'en fonction de la viscosité du magma.*

La Figure 1.6 représente des activités explosives typiques de magmas basaltiques et exprime les différents types de fragmentation du magma associées. Les activités explosives de type hawaïen (fontaines de lave) et strombolien (explosions intermittentes) sont généralement les plus communes en domaine basaltique avec néanmoins des variations associées impliquant des activités relativement plus explosives. Récemment, Houghton et al. (2016) a mis en place une classification entre éruptions de type hawaïen et de type strombolien, notamment en fonction de la masse des produits éruptifs émis de la durée des explosions/éruptions (Fig. 1.7).

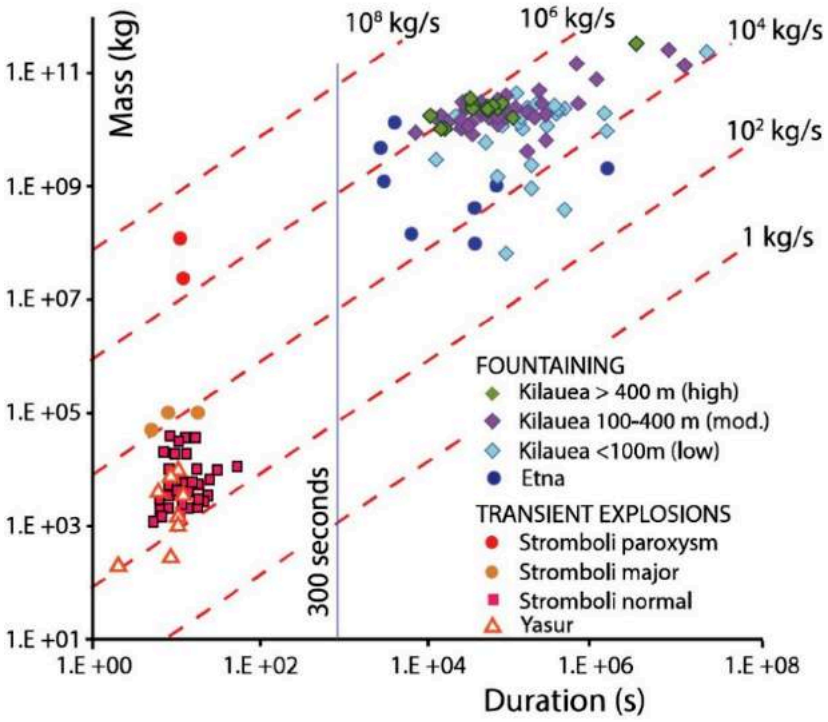

Figure 1.7 *– Masse des produits éruptifs émis en fonction de la durée des activités éruptives (dérivées d'observations directes ou d'analyses d'images) au Yasur (Vanuatu), Stromboli (Italie), à l'Etna (Italie) et au Kilauea (Hawaï). D'après Houghton et al. (2016).*

La classification de Houghton et al. (2016) met notamment en avant des flux massiques plus importants pour les activités hawaïennes (généralement entre 10^4 et 10^6 kg.s^{-1}) par rapport aux activités stromboliennes (généralement entre 10^2 et 10^4 kg.s^{-1}), sans compter les éruptions stromboliennes paroxysmales au Stromboli pouvant atteindre des flux relativement élevés similaires à ceux observés lors d'activité hawaïennes soutenues (entre 10^6 et 10^8 kg.s^{-1}). Cette classification, basée sur des observations géophysiques (durées et masses éjectées), contraste

de manière significative avec la classification de Walker (1973), basée sur la dispersion des dépôts, utilisé comme proxy pour contraindre le flux massique et l'intensité des éruptions. Selon cette approche, les éruptions hawaïennes sont considérées comme moins explosives que les activités stromboliennes. Or, les observations géophysiques apportées par Houghton et al. (2016 et références incluses) concernant les éruptions hawaïennes et stromboliennes permettent aujourd'hui de dépasser les limites de la classification de Walker (1973) pour de telles éruptions, et montrent que dans la plupart des cas, les éruptions stromboliennes typiques ont une intensité plus faible en terme de flux massique, que les éruptions hawaïennes.

2.2.1. Dégazage actif

Le premier modèle d'écoulement, de type *bubbly*, est caractérisé par un flux ascendant de magma composé d'une multitude de petites bulles de gaz isolées, dispersées aléatoirement au sein du liquide (Fig. 1.5a). Aucune interaction dynamique, tel que la coalescence n'est observée. Ce type d'écoulement engendré par un apport de gaz généralement faible résulte majoritairement à un dégazage actif en surface et/ou l'émission de coulée de lave sans fragmentation du magma. Selon certains modèles (Parfitt et Wilson 1995), une densité de bulles relativement élevée, elle-même causée par une nucléation élevée, pourrait cependant former une activité de fontaine de lave en surface (fragmentation ductile par rapide accélération), ou encore, dans le cas d'un magma visqueux une activité relativement plus explosive (Cashman et Scheu 2015 ; Fig. 1.3).

2.2.2. Eruptions stromboliennes

Le deuxième type d'écoulement, de type *slug* est caractérisé par la formation de grosses bulles (Fig. 1.5b). A partir d'un certain apport gazeux (plus fort que pour le précèdent type d'écoulement), la densité des bulles initialement présentes, n'est plus distribuée de manière uniforme et la tension de surface des bulles n'est plus suffisante provoquant la coalescence de

ces dernières, formant des bulles de gaz de tailles comparables au diamètre du conduit éruptif. Selon différents modèles, ces bulles se forment soit par l'effondrement d'une mousse magmatique initialement présente dans le réservoir magmatique (Jaupart et Vergniolle 1988, 1989), soit dynamiquement lors de l'ascension du magma vers la surface (Parfitt et Wilson 1995). Ces bulles ont des vitesses de remontée relativement élevées par rapport à la phase liquide, induisant la formation d'un liquide magmatique appauvri en volatils.

Les bulles sous pression ainsi formées par ce type d'écoulement explosent au contact d'une surface libre entre le magma et l'air (ex. Blackburn et al. 1976 ; Chouet et al. 2003 ; Harris et Ripepe 2007). Néanmoins, plusieurs types d'explosions stromboliennes peuvent se produire (Fig. 1.6), en fonction de la durée de l'explosion, de la taille et la vitesse d'ascension des bulles (ex. Vergniolle et al. 1996 ; Vergniolle et Brandeis 1996 ; Ripepe et al. 2001 ; Taddeucci et al. 2012 ; Pioli et al. 2014 ; Taddeucci et al. 2015), mais aussi en fonction de la viscosité du magma (ex. Jha et al. 2011 ; Pioli et al. 2014 ; Cashman et Scheu 2015 ; Capponi et al. 2016), ainsi que de la forme et de la disposition du système magmatique superficiel (ex. Jaupart et Vergniolle 1989 ; Burton et al. 2007 ; Patrick et al. 2007). Ainsi les explosions stromboliennes peuvent former une large gamme de pyroclastes (Fig. 1.6), allant des bombes (diamètre intermédiaire supérieur à 64 mm), des lapilli (entre 64 et 2 mm) jusqu'aux cendres (inférieur à 2 mm). Généralement, la durée des explosions stromboliennes est comprise entre quelques secondes à une minute, ne produisant pas plus de 10^5 kg de téphra, excepté certains paroxysmes (observés à Stromboli) pouvant produire jusqu'à 10^9 kg de téphra (Fig. 1.7).

Lorsque que le flux de gaz est légèrement supérieur à celui observé au sein d'un écoulement de type *slug*, les bulles peuvent se fragmenter et coalescer de nouveau pour donner un troisième type d'écoulement appelé *churn* (Fig. 1.5c), dans lequel la forme des bulles sont relativement irrégulières. De plus, ce type d'écoulement est plus turbulent et chaotique que l'écoulement de type *slug* (Cantelli et al. 2006 ; Houghton et Gonnerman 2008) où les bulles peuvent atteindre la surface de fragmentation plus fréquemment et plus rapidement, se rapprochant d'une activité explosive soutenue (Taddeucci et al. 2015).

2.2.3. Eruptions hawaïennes

En augmentant considérablement le flux de gaz par rapport à un écoulement de type *slug* ou *churn*, un écoulement laminaire est obtenu, où la phase gazeuse représente la majeure partie de l'écoulement au sein du conduit magmatique (Fig. 1.5d). La phase gazeuse, qui peut inclure des fragments liquides, occupe la partie centrale du conduit qui est entouré par une fine couche annulaire de magma plaqué contre les parois. Ce type d'écoulement implique un flux de gaz ascendant plus ou moins constant et la vitesse d'ascension de la phase gazeuse (potentiellement formée par l'effondrement d'une couche riche en bulles dans le réservoir magmatique) est un ordre de grandeur supérieure à celle de la phase liquide (Jaupart et Vergniolle 1988, 1989). Dans le cas d'un magma pauvre en cristaux et peu visqueux, ce type d'écoulement mène à une activité soutenue de fontaine de lave en surface (Houghton et al. 2016), caractérisé par un flux important et plus ou moins constant de magma et de gaz (Fig. 1.6). Cela se traduit par des durées d'activités relativement plus longues par rapport à une activité strombolienne, allant de plusieurs minutes ou heures à plusieurs mois, produisant jusqu'à 10^{11} kg de téphras (Fig. 1.7). Ce type d'activité produit généralement des bombes, lapilli et cendres grossières parfois associées à des cheveux de Pelé (particules de cendre allongées lors de leur trajectoire post-fragmentation). De façon similaire aux autres types d'écoulement, la viscosité du magma va aussi contrôler l'explosivité en surface et l'intensité de la fragmentation du magma (de type ductile si le magma est majoritairement liquide, ou de type fragile si le magma est composé majoritairement de cristaux).

2.2.4. Variabilité des styles éruptifs

La variabilité des éruptions basaltiques en termes de durée, de flux, et d'intensité de fragmentation est un phénomène relativement étudié. Même si certaines éruptions basaltiques sont relativement faibles en termes d'intensité, elles peuvent constituer une menace pour la population touristique qui s'approche habituellement de ces sites éruptifs, comme par exemple à l'Etna (Italie), au Stromboli (Italie), au Kilauea (Hawaï), ou encore au Piton de la Fournaise (France). De plus, les explosions dominées par l'émission de cendres peuvent potentiellement

avoir des impacts plus importants sur les populations et environnement locaux par rapport aux éruptions moins intenses (ex. Blong 1984, 1996 ; Barsotti et al. 2010; Scollo et al. 2013; Morin et al. 2016 ; Brown et al. 2017 ; Papale 2017).

Malgré que certains processus sont encore mal compris, beaucoup d'études ont montré que la proportion entre des magmas relativement visqueux (riches en microcristaux et pauvres en gaz) et des magmas peu visqueux (pauvres en microcristaux et riches en gaz) peut potentiellement moduler la transition entre des styles éruptifs très différents (ex. Lautze et Houghton 2005 ; Gurioli et al. 2014 ; Del Bello et al. 2015 ; Leduc et al. 2015 ; Capponi et al; 2016 ; Fig. 1.4). En effet, les éruptions basaltiques peuvent changer de comportement pendant un même évènement éruptif. Par exemple, l'activité éruptive peut passer de strombolienne à une activité de fontaine de lave (Polacci et al. 2006), ou inversement (Gurioli et al. 2018). Une activité de fontaine de lave peut rapidement évoluer à une activité strombolienne plus ou moins violente, de faibles explosions stromboliennes peuvent devenir plus violentes (Pioli et al. 2008 ; Cimarelli et al. 2010), jusqu'à des dynamiques pliniennes (ex. Houghton et al. 2004 ; Sable et al. 2006 ; Constantini et al. 2010 ; Pompilio et al. 2017 ; Moitra et al. 2018). Ce dernier cas est notamment possible à cause d'une augmentation de la quantité de microcristaux dans le magma provoquant l'augmentation (de plus de deux ordres de grandeur) de la viscosité de celui-ci (Cimarelli et al. 2011).

3. Problématiques principales

Cette thèse est focalisée sur le volcan du Piton de la Fournaise (île de La Réunion, France) qui est un des volcans boucliers les plus actifs au monde produisant actuellement deux éruptions par an en moyenne (Staudacher et al. 2016 ; Peltier 2018). De plus, la relative facilité d'accès aux sites éruptifs ainsi que la densité des différents réseaux de surveillance établis par l'Observatoire Volcanologique du Piton de la Fournaise (OVPF) en font un volcan idéal pour l'étude des différents processus magmatiques opérant au sein de son système magmatique jusqu'à la surface.

A travers la caractérisation de nombreux produits effusifs et explosifs en termes de texture et de chimie, ainsi qu'à l'intégration de données de surveillance acquises sur des périodes clés, les objectifs des travaux présentés dans cette thèse sont multiples. (i) Il s'agit tout d'abord de quantifier et comprendre les processus pré-éruptifs et déclencheurs opérant au sein du système magmatique superficiel. Pour cela l'étude des produits éruptifs (émis sur la période 2014-2016) a permis d'identifier certains d'entre eux. (ii) Le second objectif est d'évaluer les impacts des processus pré-éruptifs préalablement identifiés, sur les processus syn-éruptifs s'opérant lors de la remontée du magma ainsi que sur l'activité volcanique en surface. Ces deux premiers objectifs sont fondamentaux pour comprendre l'évolution des magmas émis et en quoi ils contrôlent le changement du type d'activité en surface, notamment du passage syn-éruptif d'une activité hawaïenne produisant des fontaines de lave, à une activité strombolienne relativement faible et plus sporadique (éruptions de Juin 2014 et Juillet 2015) ou encore à une activité légèrement plus explosive pouvant produire une quantité de cendre non-négligeable (éruption de Septembre 2016). (iii) Enfin, le dernier objectif principal de cette thèse est d'identifier un ensemble d'évènements explosifs majeurs plus ou moins récents (dont un au sein du volcan bouclier du Karthala, île de Ngazidja, Comores) et de comprendre les origines de la formation relativement importante des cendres basaltiques, lors d'éruptions paroxysmales.

Ces études sont focalisées sur des objets naturels spécifiques mais l'ensemble des mécanismes mis en évidence peuvent être largement projetés sur d'autres systèmes basaltiques similaires au Piton de la Fournaise et au Karthala.

4. Plan de thèse

Après ce chapitre d'introduction (**chapitre I**), ce manuscrit est divisé en six autres chapitres principaux, abordant progressivement les différents points clés des travaux réalisés pendant cette thèse :

- Le **chapitre II** présente les objets géologiques actifs ciblés : le volcan du Piton de la Fournaise sur lequel ces travaux de thèse se sont majoritairement focalisés et celui du Karthala sur lequel des dépôts cendreux spécifiques ont été étudiés. Le contexte géodynamique, géologique et structural, ainsi que l'histoire éruptive connue de ces deux volcans basaltiques actifs de l'Océan Indien, sont abordés. La revue de ces différentes caractéristiques révèle certaines similarités mais aussi différences notables entre ces deux volcans. Le fonctionnement du système magmatique actuel du Piton de la Fournaise vient particulièrement compléter l'introduction générale établie au sein du **chapitre I**.

- Le **chapitre III** expose l'approche de travail utilisée dans le cadre de ces travaux de thèse. Il est aussi consacré aux différentes méthodes et techniques analytiques utilisées afin de répondre aux différentes questions scientifiques posées. L'approche multidisciplinaire choisie est particulièrement mise en avant, avec notamment la présentation des techniques d'échantillonnage, d'analyses texturales et géochimiques ainsi que de l'utilisation des données de surveillance acquises sur le terrain ou par télédétection.

- Le **chapitre IV** met en avant les résultats obtenus à partir de l'étude texturale et géochimique des produits éruptifs émis sur la période 2014-2015 au Piton de la Fournaise. Cette période est reconnue au sein de ce volcan comme étant le début d'un nouveau cycle éruptif impliquant progressivement des magmas de moins en moins différenciés. Ces résultats sont intégrés à des données géophysiques et de pétrologie expérimentale. Ce chapitre permet de quantifier un certain nombre de paramètres pré- et syn-éruptifs opérant au sein d'un tel système magmatique. En outre, cette étude a permis de caractériser la transition syn-éruptive d'un dynamisme soutenu de type hawaïen vers un dynamisme discontinu et relativement faible de type strombolien.

- Le **chapitre V** présente l'étude intégrée de l'éruption de Septembre 2016 au Piton de la Fournaise. Au contraire des éruptions étudiées lors du précédent chapitre, une transition syn-éruptive d'un dynamisme soutenu de type hawaïen vers un dynamisme transitoire et relativement explosif a été observé et des quantités de cendres non-négligeables ont été

produites. Cette étude met en évidence l'évolution du dégazage et de la fragmentation du magma émis lors de cette éruption afin de déterminer l'ensemble des différents mécanismes magmatiques intervenant dans ce changement rapide de dynamismes éruptifs.

- Le **chapitre VI** est focalisé sur un ensemble d'échantillons pyroclastiques récoltés à la fois au Piton de la Fournaise et au Karthala. L'étude réalisée au sein du chapitre précèdent a permis de montrer un mécanisme spécifique à la production de cendres dans un contexte basaltique. Afin d'étendre l'étude des mécanismes de fragmentation en domaine basaltique, une large gamme d'échantillons a été récoltée et analysée. La variabilité des cendres présentes au sein de ces volcans reflète l'existence de nombreux mécanismes de fragmentation dont les impacts peuvent être relativement importants.

- Enfin, le **chapitre VII** résume la totalité des conclusions apportées par ces travaux de thèse. Les processus magmatiques pré- et syn-éruptifs ainsi que les mécanismes de fragmentation du magma lors d'activités éruptives variées sont compilés afin d'exposer l'ensemble des implications scientifiques utiles à la compréhension des systèmes magmatiques du Piton de la Fournaise, du Karthala et plus largement des volcans basaltiques. Enfin, les perspectives de travail, en vue d'une amélioration des données et d'un approfondissement du raisonnement, sont énoncées.

CHAPITRE II

OBJETS D'ETUDE : LE PITON DE LA FOURNAISE (ILE DE LA REUNION, FRANCE) ET LE KARTHALA (ILE DE NGAZIDJA, UNION DES COMORES)

1. Le Piton de la Fournaise : un volcan laboratoire

Cette première partie décrit les aspects généraux concernant le volcan du Piton de la Fournaise (La Réunion, France), sur lequel cette thèse est majoritairement focalisée. Le contexte géodynamique et l'origine du volcanisme de cette zone sont brièvement abordés. La géologie et les structures majeures du volcan sont décrites pour ensuite se focaliser sur les connaissances du système magmatique profond et superficiel, dont le fonctionnement, intimement lié aux dynamismes éruptifs en surface, est étudié et discuté au cours de cette thèse. Enfin, une brève description des dépôts et des éruptions étudiés est réalisée.

1.1. Contexte géodynamique et origine du volcanisme de l'île de La Réunion

La Réunion est une île volcanique située dans l'Océan Indien, à l'extrémité Sud de l'archipel des Mascareignes et à environ 800 km à l'Est de l'île de Madagascar (Fig. 2.1). Malgré une étude remettant en cause l'existence d'une anomalie mantellique majeure dans cette zone (Sheth 2005), l'origine du volcanisme intra-plaque de La Réunion est aujourd'hui unanimement attribuée à la présence d'un point chaud mantellique générant des basaltes d'îles océaniques (OIB pour *Ocean Island Basalts*). Basés sur des évidences géodynamiques (ex. Courtillot et al. 1986 ; Duncan et al. 1989, 1990 ; Richards et al. 1989 ; Vandamme et al. 1990) et géochimiques (ex. Fisk et al. 1988, 1989 ; Graham et al. 1990), de nombreuses études ont prouvé que l'existence du volcanisme de La Réunion est lié à une anomalie thermique ponctuelle au sein du manteau terrestre. Cette même anomalie fut à l'origine de la mise en place des plateaux basaltiques du Deccan, il y a près de 65 Ma. A la faveur du mouvement vers le Nord de la plaque indienne, le panache mantellique, relativement stable et peu mobile par rapport aux mouvements crustaux, a progressivement formé les rides volcaniques des Laquedives, des Maldives et de Chagos (de 60 Ma à 48 Ma) ainsi que l'ensemble du plateau des Mascareignes (autour de 35 Ma), l'île Maurice (7 à 1 Ma) et enfin l'île de La Réunion (< 5 Ma). Le décalage apparent entre l'alignement Laquedives-Maldives-Chagos et celui des

Mascareignes (Fig. 2.1) est attribué au mouvement divergent de la dorsale médio-océanique indienne (Duncan et al. 1990).

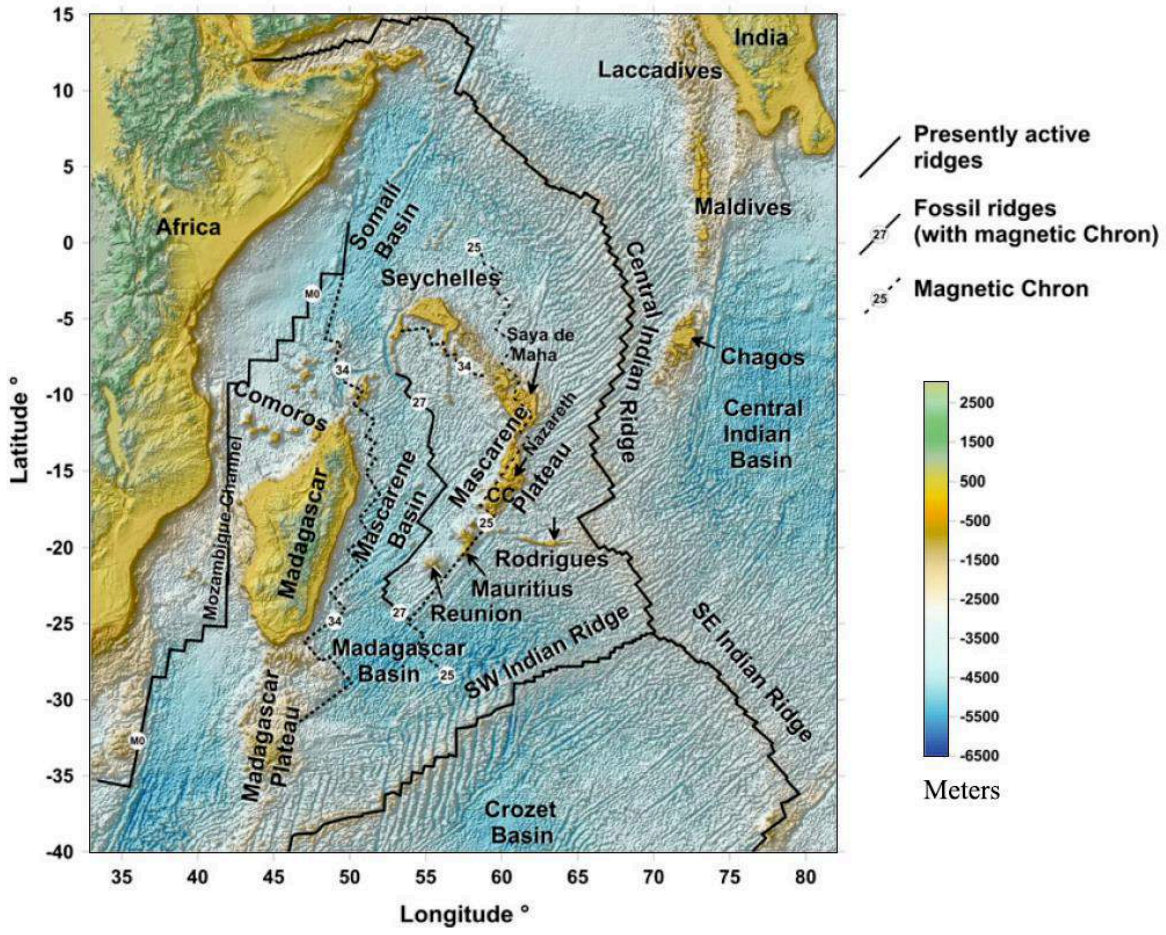

Figure 2.1 *– Contexte géodynamique de l'île de La Réunion et de l'archipel des Comores, montrant les masses continentales africaine, malgache et indienne ainsi que les différentes structures océaniques de la partie Ouest de l'Océan Indien. Figure modifiée à partir de Lénat et al. (2009).*

L'île de La Réunion est donc l'édifice émergé le plus récent lié à l'activité du point chaud. L'ensemble de l'édifice réunionnais repose sur une portion de croute océanique profonde de 4 km (Lénat et Labazuy 1990), âgée d'environ 67 Ma et large d'environ 350 km délimitée par deux failles transformantes majeures au NO et SE ainsi que par une paléo-dorsale au SO (Fig. 2.2). La base de l'édifice au niveau de la croute océanique possède un diamètre d'environ 220 km et seulement 3 à 4 % du volume total de l'édifice est émergé (De Voogd et al. 1999 ; Catry 2011). Contrairement à d'autres édifices volcaniques de point chaud, notamment ceux de l'île d'Hawaï (Watts et al. 1985 ; Sleep 1990), plusieurs études sismiques

ont mis en évidence l'absence d'une importante flexure lithosphérique sous l'île de La Réunion (Charvis et al. 1999 ; Gallard et al. 1999 ; Fontaine et al. 2015). En parallèle, ces mêmes études montrent la présence d'un sous-plaquage magmatique à l'interface entre le manteau et la croute. De plus, une anomalie bathymétrique positive est clairement visible sur la portion de croute décrite précédemment (Fig. 2.2), dont la profondeur est anormalement faible (4 km de profondeur) par rapport à la croute océanique environnante (5 km de profondeur).

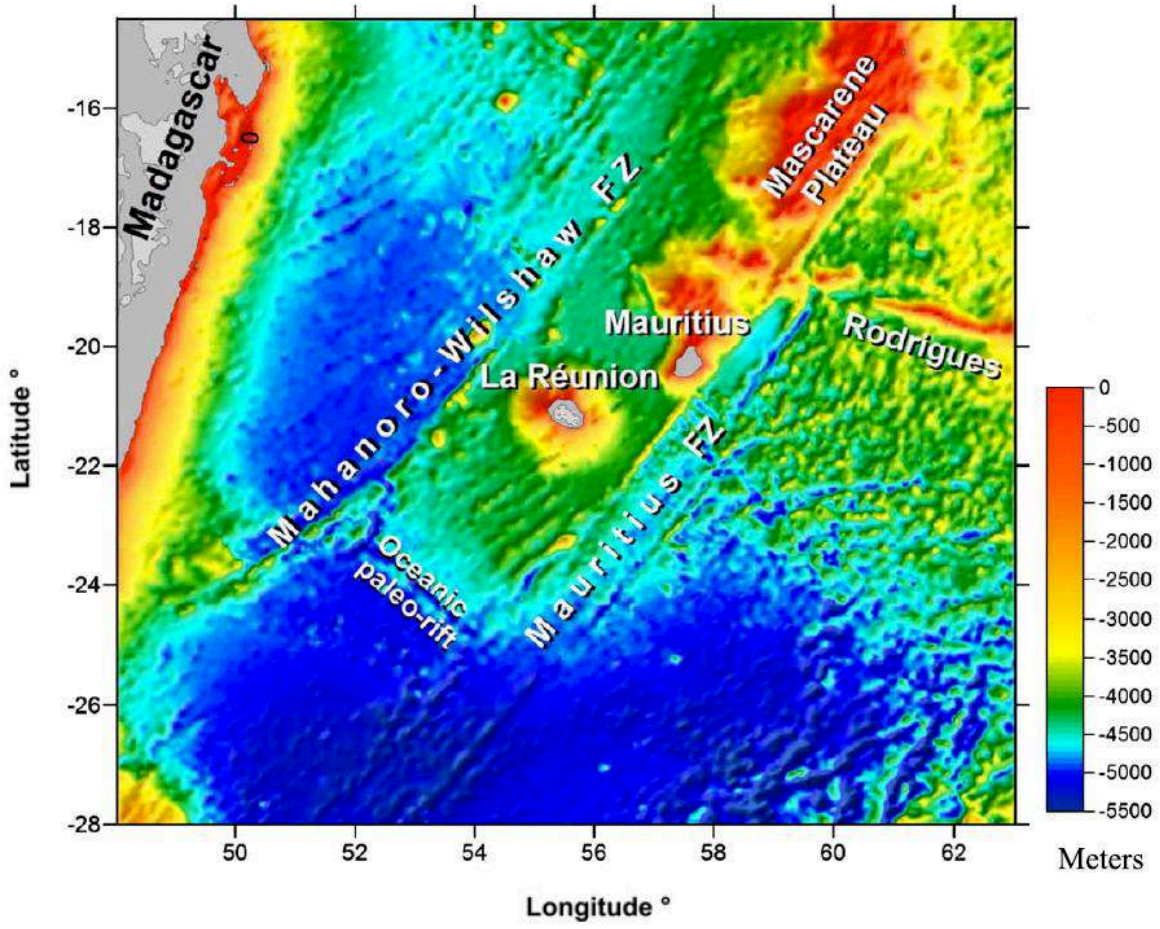

Figure 2.2 *– Carte bathymétrique centré sur l'île de La Réunion montrant les structures tectoniques locales (FZ : zone de fracture) jouant un rôle sur la profondeur de la croûte océanique. Figure modifiée à partir de Lénat (2016b).*

L'utilisation de modèles théoriques et analogiques ont permis de visualiser en détail la structure du manteau lithosphérique et de mettre en évidence une canalisation du panache mantellique dans la zone délimitée par les structures crustales préexistantes (Fig. 2.2) autour de l'île de La Réunion (Lénat et al. 2009). D'après des données gravimétriques (Bonneville et al. 1988) et sismiques (Barruol et Fontaine 2013), la position actuelle du point chaud de La

Réunion se situerait respectivement entre 300 km au SO de l'île et 200 km au Nord de l'île. A partir d'arguments géochimiques et isotopiques, l'origine relativement profonde et peu dégazée (panache primaire) de la racine mantellique du panache de La Réunion est privilégiée (Courtillot et al. 2003 ; Graham et al. 1990 ; Staudacher et al. 1990). Le panache mantellique échantillonnerait donc une portion de manteau commune aux sources des OIB sans évidences majeures de sources liées au manteau supérieur appauvri, tels que les basaltes de rides médio-océaniques (MORB pour *Middle Oceanic Ridge Basalts*), ni de processus de recyclage avec des plaques subductées (Vlastélic et al. 2006). Récemment, et d'après des arguments isotopiques, Peters et al. (2018) suggèrent que les magmas de La Réunion sont partiellement issus d'une source primitive mantellique relativement ancienne et différenciée, offrant un aperçu sur des hétérogénéités potentielles au sein du manteau terrestre.

1.2. Contexte géologique et structural de l'île de La Réunion et du Piton de la Fournaise

La morphologie actuelle de l'île de La Réunion, d'une forme elliptique dans la direction NO-SE avec une largeur de 50 km et une longueur de 70 km, résulte chronologiquement de l'édification de plusieurs massifs volcaniques (Bachèlery 1981, 1999). Le Piton des Neiges (3069 m), occupant le deux tiers NO de l'île, et le Piton de La Fournaise (2632 m) au SE de l'île constituent les deux massifs volcaniques actuellement visibles sur l'édifice réunionnais (Fig. 2.3a). Plusieurs campagnes géophysiques associant données magnétiques et gravimétriques révèlent la présence d'un ancien massif appelé La Montagne à l'extrémité NO de l'île et confirment l'existence du complexe intrusif du volcan des Alizés sous l'extrémité Est de l'île (ex. Malengreau et al. 1999 ; Gailler et al. 2009 ; Gaillet et Lénat 2010, 2012). La Montagne (de 2,2 à 1.8 Ma), le massif du Piton des Neiges (de 1.2 Ma à 12 ka) et celui du Piton de la Fournaise (actif depuis 530 ka) montrent des âges progressivement plus récent du NO vers le SE (ex. Gillot et al. 1994 ; Bret et al. 2003 ; Salvany et al. 2012). Le complexe hypo-volcanique des Alizés est quant à lui antérieur à l'activité du Piton de la Fournaise (Lénat et al. 2012). L'évolution des différentes formations principales de La Réunion est synthétisée dans la figure 2.3b. De nombreuses évidences, notamment des dépôts sous-marins de turbidites, des

structures d'avalanches de débris et de glissements (Figs. 2.3c, 2.4a), démontrent que l'ensemble des massifs constituant de l'île, sujets à un climat tropical, ont été érodés par des évènements gravitaires et d'instabilité de flancs plus ou moins importants (ex. Lénat et al. 2001 ; Oehler et al. 2004, 2008 ; Babonneau et al. 2016).

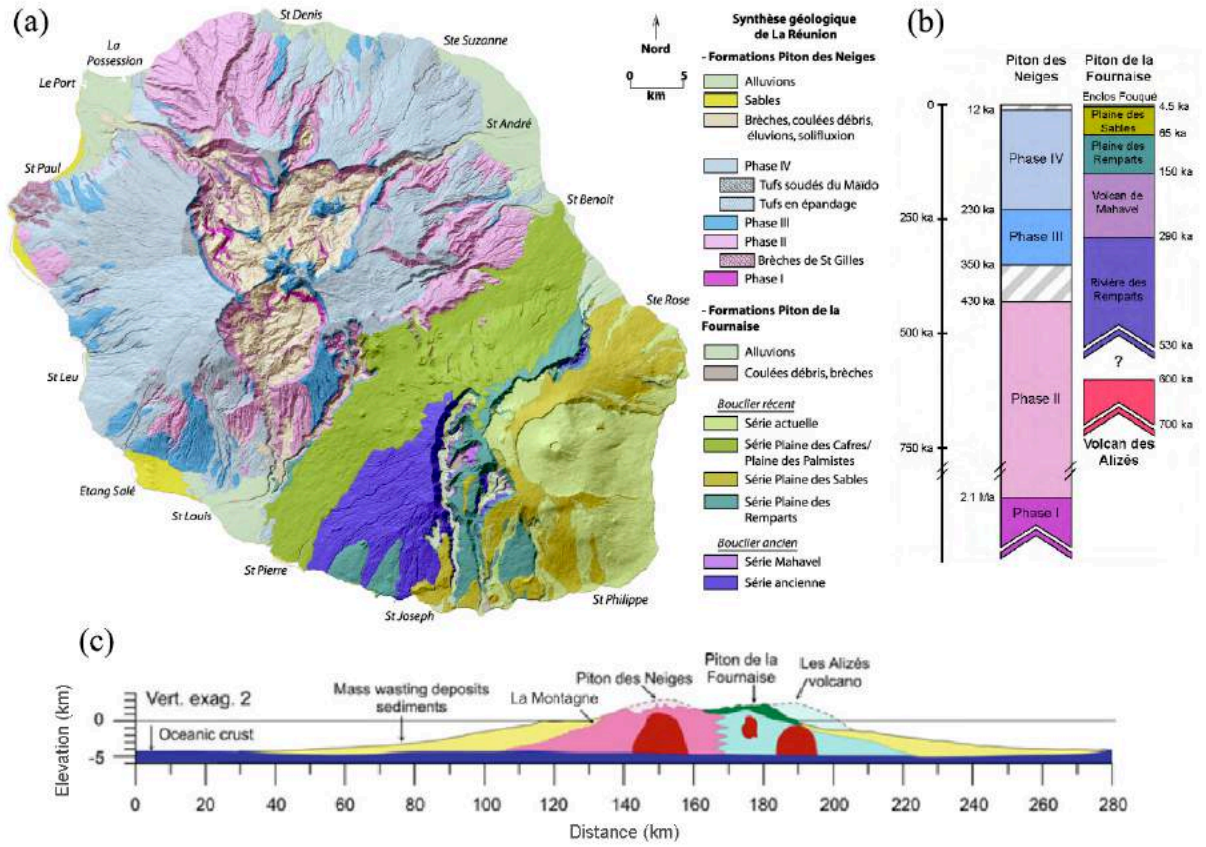

Figure 2.3 *– (a) Synthèse géologique de l'île de La Réunion compilée par Fèvre (2005) avec au NO le massif du Piton des Neiges et au SE celui du Piton de la Fournaise. (b) Logs géochronologiques du Piton des Neiges ainsi que du Piton de la Fournaise et des Alizés, d'après Welsch (2000), Smietana (2001) et Fèvre (2005). (c) Coupe géologique simplifiée NO-SE montrant les différents massifs volcaniques ainsi que l'accumulation des sédiments sur les flancs sous-marins de l'île de La Réunion. Figure modifiée à partir de Lénat et al. (2016c).*

En ce qui concerne le Piton de la Fournaise, qui est actuellement le seul volcan bouclier relativement actif de l'île de La Réunion, plusieurs phases évolutives et structures majeures ont été identifiées (ex. Gillot and Nativel 1989 ; Bachèlery 1981, 1999 ; Bachèlery and Mairine 1990). Les roches les plus anciennes du massif affleurent au niveau des dépressions

topographiques, notamment dans la vallée de la rivière des remparts (Figs. 2.3a, 2.4a). Entre 150 et 40 ka, le centre d'émission volcanique, initialement situé au niveau de la Plaine des

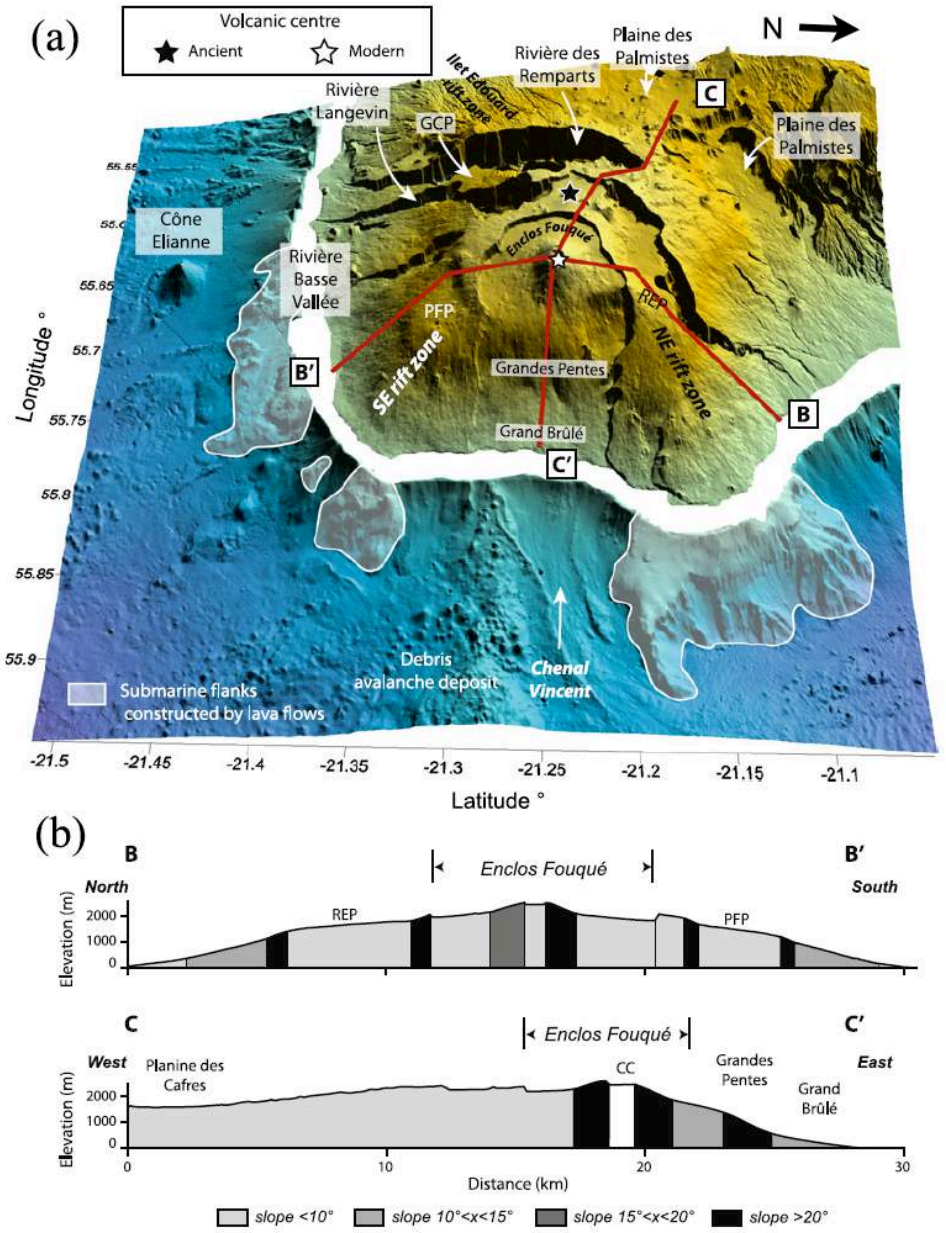

Figure 2.4 *– (a) Morphologie du Piton de la Fournaise montrant les différentes structures d'effondrement sur la partie immergée de l'édifice ainsi que les structures d'érosions sous-marines (PFP : plateau du Piton de Fourche ; REP : plateau de la rivière de l'E ; GCP : plateau de Grand Coude). L'ancien centre volcanique (étoile noire) est situé au niveau de la Plaine des Sables, ancienne caldera du Piton de la Fournaise. L'actuel centre volcanique (étoile blanche) est situé au niveau du cône sommital au sein de l'Enclos Fouqué, caldera principale du Piton de la Fournaise actuel. (b) Deux coupes topographiques correspondant aux lignes rouges tracées dans (a) et montrant les différentes pentes du volcan (CC : cône central). Figure modifiée à partir de Michon et al. (2016a).*

Sables actuelle, migre vers l'Est (Bachèlery and Mairine, 1990), pour progressivement former l'actuel Piton de la Fournaise (Fig. 2.4a). De nombreuses études mettent en évidence et débattent de l'origine des mécanismes des différentes structures d'effondrements visibles au sein du Piton de la Fournaise (ex. Bachèlery 1981 ; Lénat et al. 1989a ; Labazuy 1996 ; Merle et Lénat 2003 ; Oelher et al. 2004, 2008 ; Michon et Saint-Ange 2008).

L'Enclos Fouqué représente la principale structure volcano-tectonique du Piton de la Fournaise actuel (Figs. 2.4 et 2.5). Cette structure en forme de fer à cheval est composée de plusieurs lobes, correspondant à une dépression de 100 à 250 m de profondeur, mesurant environ 13 km de long en axe E-O et de 6 à 8 km de large en axe N-S. Elle a tout d'abord été interprétée comme étant le résultat d'un grand glissement de flanc (Labazuy 1996). Des études plus récentes (Merle et Lénat 2003 ; Michon et Saint-Ange 2008) suggèrent que la partie orientale de l'Enclos est le résultat d'un glissement de terrain global vers l'Est provoquant ensuite la déformation et le glissement latéral d'un ancien système hydrothermal situé sous les cratères sommitaux du volcan, ainsi que l'effondrement vertical de la partie supérieure occidentale (Fig. 2.5).

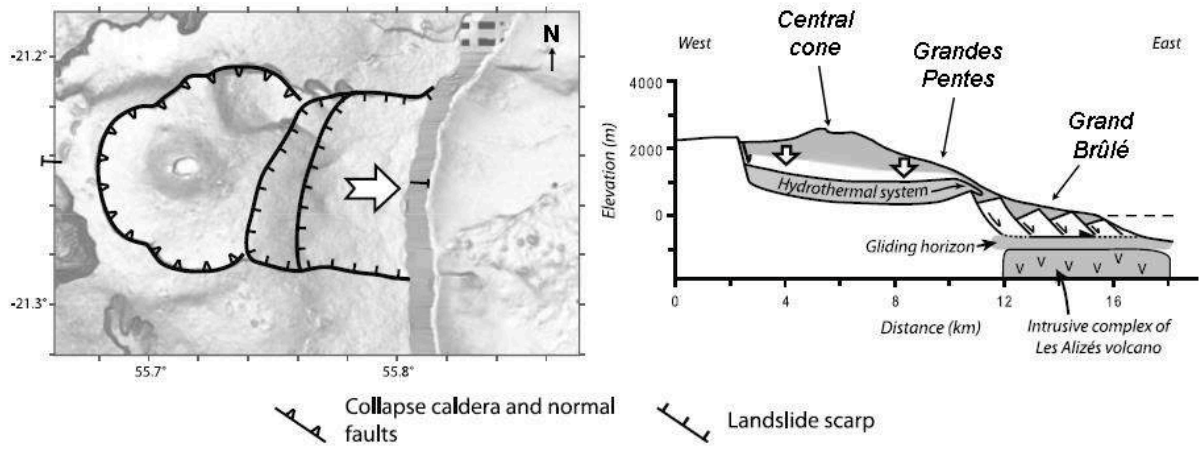

***Figure 2.5** – Interprétation simplifiée de la formation de l'ensemble de l'Enclos Fouqué ainsi que la formation des zones des Grandes Pentes et du Grand Brûlé, d'après Merle et Lénat (2003). Figure modifiée à partir de Michon et Saint-Ange (2008).*

L'identification d'une succession de plusieurs dépôts explosifs et hydrothermaux partiellement liés à la mise en place de cette structure majeure (cendres de Bellecombe, dans la partie orientale de la Plaine des Sables ; cf. **chapitre VI**) suggère d'une part que la formation de la caldera s'est effectuée en plusieurs étapes et d'autre part que la déstabilisation et la remobilisation d'un système hydrothermal et/ou magmatique étaient bien impliquées dans ces

effondrements (Ort et al. 2016). La datation de la mise en place de ces dépôts, interprétée comme étant contemporaine à la formation de l'Enclos Fouqué, suggère des âges allant d'environ 4800 à 2300 BP pour l'ensemble des cendres de Bellecombe (Bachèlery 1981 ; Morandi et al. 2016).

La plupart des produits éruptifs affleurant à l'intérieur de la caldera de l'Enclos Fouqué ont été émis après les cendres de Bellecombe (Morandi et al. 2016) à l'exception notable de certaines zones du cône central (ou terminal ou encore sommital) du volcan (Figs. 2.4, 2.5 et 2.6). L'évolution de la structure et de la morphologie de la zone sommitale du cône est surtout contrôlée par l'alternance d'effondrements caldériques liés à des vidanges magmatiques majeures, comme lors de l'éruption d'Avril 2007 (cf. **chapitre VI**), et d'épisodes de remplissage progressif par des coulées de lave (Villeneuve et Bachèlery 2006 ; Michon et al. 2007, 2009, 2013 ; Peltier et al. 2009b ; Staudacher et al. 2009 ; Staudacher 2010 ; Lénat et al. 2012 ; Fontaine et al. 2014 ; Lénat 2016a). Aujourd'hui, le cône sommital est composé de deux cratères d'effondrement de formes elliptiques (Fig. 2.6). Le plus petit est nommé cratère Bory et situé sur la partie occidentale du sommet (environ 400 m de long en axe N-S et 350 m de large en axe E-O). Sa limite Est est tronquée par le second et plus grand cratère nommé Dolomieu et situé sur la majeure partie orientale du sommet (environ 1100 m de long en axe E-O et 800 m de large en axe N-S).

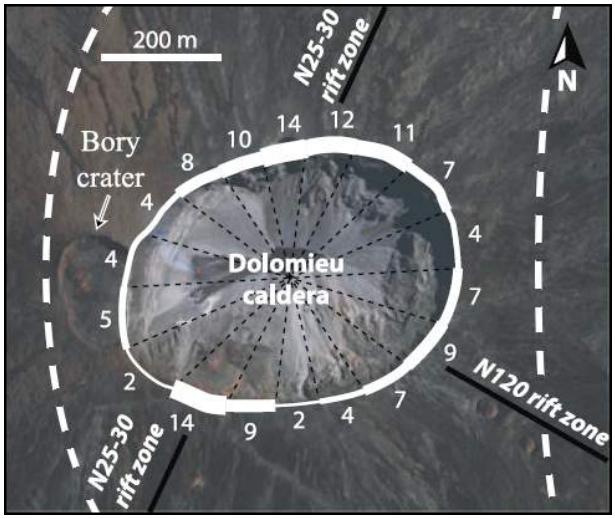

Figure 2.6 *– Distribution radiale du nombre de dykes observables au sein des falaises internes du cratère Dolomieu. L'épaisseur du trait blanc entourant la limite de la caldera est proportionnelle à la densité de population des dykes observés. Les traits noirs représentent les rift-zones identifiées par Michon et al. (2009) et la zone délimitée par les traits pointillés représente les rift-zones N10 et N170 identifiées par Bachèlery (1981). Figure modifiée d'après Michon et al. (2016b).*

Plusieurs études suggèrent différentes zones préférentielles d'intrusions et extrusions magmatiques (ou *rift-zones*). En se basant sur l'orientation des fissures éruptives autour du cône central du Piton de la Fournaise, Bachèlery (1981) identifie deux *rift-zones* relativement larges et orientées N10 et N170 à partir des cratères sommitaux (Fig. 2.6). En se focalisant sur l'activité récente (entre 1981 et 2006), Michon et al. (2009) identifient deux *rift-zones* sommitales orientées N25-30 et N120. En parallèle, Michon et al. (2016b) montrent que ces deux *rift-zones* correspondent aussi aux endroits où les dykes (ou conduits magmatiques) apparaissent les plus nombreux sur les parois de la caldera sommitale (Fig. 2.6). Enfin, basé sur le comptage morphométrique des différents cônes de scories présents à la surface du massif du Piton de la Fournaise, Bonali et al. (2011) suggèrent une multitude de *rift-zones* rayonnant autour des cratères sommitaux, dont certaines s'étendent en dehors de la caldera de l'Enclos Fouqué (*rift-zones* externes).

1.3. Connaissances sur le système magmatique actuel du Piton de la Fournaise

De nombreuses études sismiques, géodésiques et géochimiques ont permis la conception et une visualisation plus ou moins précise du système magmatique actuel au sein de l'édifice du Piton de la Fournaise.

Depuis les années 1980, de nombreuses données de polarisation spontanée, de résistivité électrique et de magnétisme ont été acquises lors de campagnes géophysiques. Dans l'analyse de ces données, Malengreau et al. (1994) et Gailler et Lénat (2012) identifient notamment une zone conductrice et peu magnétique anormalement peu profonde sous les cratères sommitaux du volcan à environ 2 km au-dessus du niveau de la mer (quelques centaines de mètres sous la surface du sommet du Piton de la Fournaise). Ces auteurs interprètent cette zone centrale et peu profonde comme faisant partie d'un système magmatique et/ou hydrothermal actif (Fig. 2.7), ce qui est cohérent avec la présence d'anomalies thermiques et de fumerolles au sein du cratère Dolomieu (Staudacher 2010). Suite à l'effondrement caldérique sommital du cratère Dolomieu lors de l'éruption d'Avril 2007, Peltier et al. (2012) déduisent d'après l'observation des parois de l'effondrement que le système hydrothermal est confiné à une profondeur supérieure à 350

m. De plus, des données gravimétriques (Gailler et al. 2009) suggèrent que l'ensemble du cône central est constitué de roches relativement peu denses (téphras et laves vésiculées) et fracturées. En s'éloignant du cône central, ces mêmes auteurs mettent en évidence la présence d'épaisses coulées de laves relativement denses sur la partie Ouest de l'Enclos Fouqué et de la Plaine des Sables (Fig. 2.7). Ces auteurs identifient aussi la présence d'objets relativement denses sous la Plaine des Sables et sous le niveau de la mer, considérés comme étant les témoins d'un ou plusieurs anciens systèmes magmatiques successifs lorsque l'activité du Piton de la Fournaise était focalisée plus à l'Ouest (Bachèlery et Mairine 1990).

En parallèle, des études sismiques révèlent différentes zones de sismicité préférentielle. Lors de l'éruption de 1998, des évènements volcano-tectoniques (VT) liés à la remontée du magma vers la surface ont était identifiés jusqu'à 5 km sous le niveau de la mer (Aki et Ferrazzini 2000 ; Battaglia et al. 2005b) et suggèrent que le magma de cette éruption a directement migré vers la surface à partir d'une zone de stockage magmatique dont la partie supérieure est située vers 5 km en dessous du niveau de la mer et légèrement décalée à l'Ouest par rapport au cône central du volcan (Fig. 2.7). Ces résultats sont cohérents avec les données de télédétection radar dont les modèles évoquent une source éruptive profonde de 5 à 7 km de profondeur (Sigmundson et al. 1999 ; Fukushima et al. 2005) et avec un dégazage diffus en CO_2 préférentiellement observé sur le flanc Ouest du volcan (Boudoire et al. 2017, 2018). Une deuxième zone, sismiquement plus active, se situe sous les cratères sommitaux et entre le niveau de la mer et la surface du volcan. Cette zone sismique est généralement active pendant mais aussi entre les périodes éruptives et reflète une zone de transfert et de stockage magmatique entre un réservoir superficiel situé au niveau de la mer (Fig. 2.7) et la surface (Battaglia et al 2005b ; Massin et al. 2011). La fréquence des VT enregistrés dans cette zone superficielle en fait la zone sismique la plus active du Piton de la Fournaise. Enfin, une troisième zone sismique moins active a aussi été identifiée à l'Est du cône central, au niveau des Grandes Pentes et entre 0 et 5 km sous le niveau de la mer. Cette faible sismicité, notamment en termes de fréquence, est considérée comme étant causé par la tendance de l'édifice à glisser dans la direction de son flanc libre à l'Est (Lénat et al. 2012 ; Froger et al. 2015).

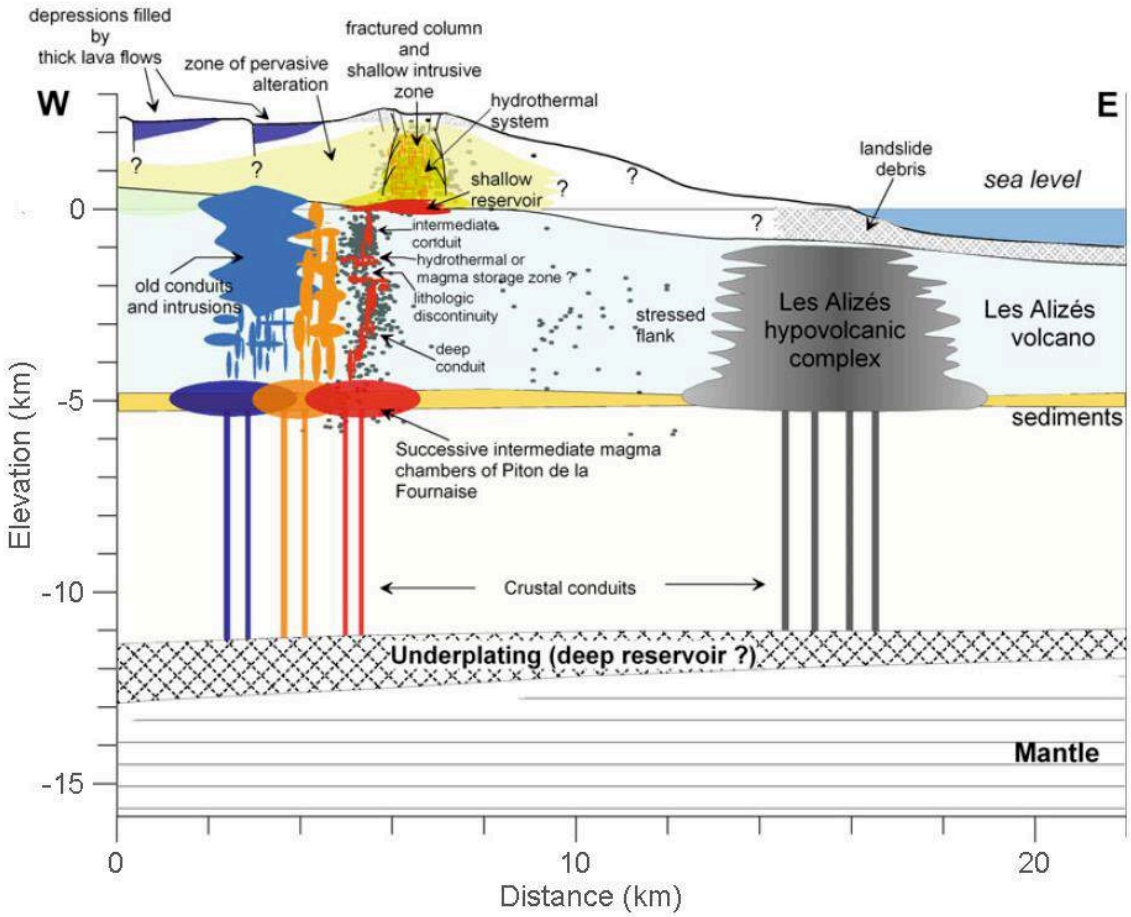

Figure 2.7 *– Coupe géologique O-E interprétant les structures majeures du Piton de la Fournaise basée sur des études géodésiques et sismiques. Figure modifiée à partir de Lénat et al. (2012).*

D'autres études ont permis de caractériser plus finement la géométrie des structures présentes dans le système magmatique superficiel du Piton de la Fournaise (de la surface jusqu'à environ 3 km sous le niveau de la mer). Basés sur des arguments sismiques et de déformations, Lénat et Bachèlery (1990) sont les premiers auteurs à proposer l'existence d'une multitude de poches de magma entre 2 et 0 km d'altitude, liées aux éruptions sommitales et proximales au cône central (Fig. 2.8). Parallèlement, Peltier et al. (2008) interprètent à partir de données géodésiques, la présence d'un réservoir magmatique au niveau de la mer et sous le cône central (Fig. 2.8). Enfin, plusieurs études de tomographie sismique (Nercessian et al. 1996 ; Prôno et al. 2009) ont permis de mettre en évidence une zone relativement grande dans laquelle les ondes sismiques (Vp et Vs) se propagent à de faibles vitesses, suggérant une zone majeure de stockage magmatique entre 0 et 2 km sous le niveau de la mer (Fig. 2.8).

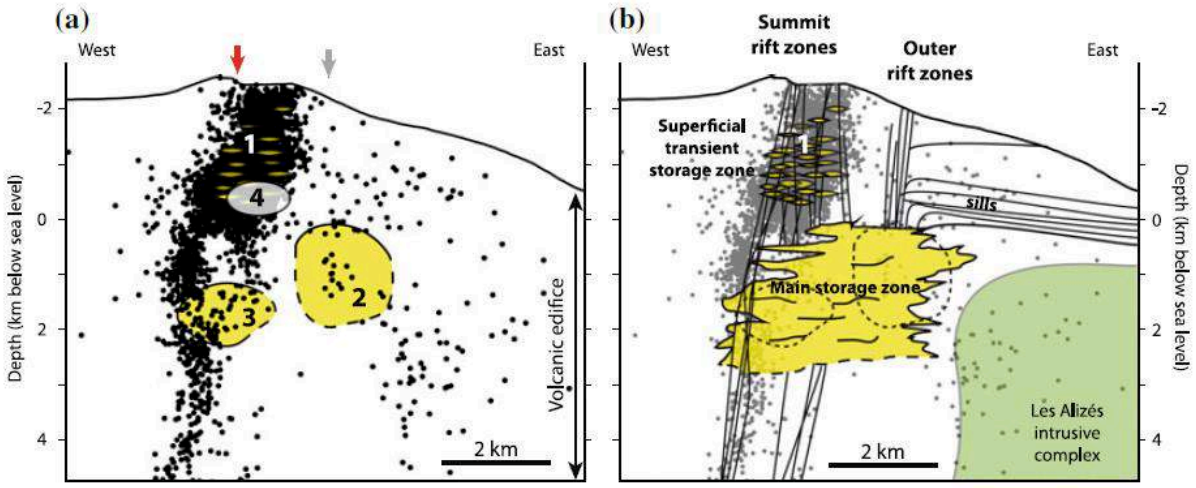

Figure 2.8 *– (a) Evènements sismiques liés aux éruptions sommitales et proximales entre 1998 et 2000 (points noirs). 1 : source des séismes volcano-tectoniques (VT) et des déformations liés aux éruptions sommitales et proximales (Lénat et Bachèlery 1990) ; 2 et 3 : zones de faible vitesse sismique (Nercessian et al. 1996 ; Prôno et al. 2009 respectivement) ; 4 : source des déformations lors de la période Mai 2004-Decembre 2005 (Peltier et al. 2008). (b) Interprétation de la structure actuelle du système magmatique superficiel du Piton de la Fournaise, d'après les données présentées dans (a). Figure modifiée à partir de Michon et al. (2016b).*

L'ensemble des études focalisées sur le système magmatique du Piton de la Fournaise montrent donc l'importance des différentes zones de stockage magmatique ainsi que des vecteurs de transferts, tels que les dykes et sills, entre ces zones et vers la surface (Figs 2.7 et 2.8). De nombreuses études géochimiques permettent aujourd'hui d'intégrer un modèle de l'évolution géochimique des magmas à travers l'ensemble du système magmatique du Piton de la Fournaise. En effet, à partir d'arguments isotopiques (Vlastélic et al. 2005 ; Sigmarsson et al. 2005), d'études d'inclusions fluides et vitreuses (ex. Bureau et al. 1998a, 1998b ; Famin et al. 2009) et d'analyses sur les éléments majeurs, traces et isotopiques (ex. Albarède et al. 1997 ; Boudoire et al. 2018, 2019), un modèle conceptuel de stockage et de transport de magma, en accord avec les études structurales précédemment décrites, a pu être établi (Fig. 2.9). Les magmas parentaux de type basaltes transitionnels (intermédiaire entre des compositions alcalines et tholéitiques) du Piton de la Fournaise actuel sont stockés dans le réservoir profond (Figs. 2.7, 2.9a) à la base de l'édifice réunionnais (> 5 km sous le niveau de la mer). Ludden

(1978) et plus récemment Villemant et al. (2009) ont estimé la composition moyenne de ces magmas parentaux. Par modélisation géochimique, cette dernière étude suggère un magma parental moyen d'une température d'environ 1300 °C, dont la composition est représentée dans la figure 2.9b. Ces magmas parentaux peuvent parfois migrer directement du réservoir profond vers la surface. Dans ce cas, les magmas subissent une différenciation contrôlée par le fractionnement du plagioclase, du clinopyroxène et plus rarement de l'olivine au cours de leurs ascensions produisant des laves appelées anormales (Fig. 2.9). Ce type de laves est rarement observé au sein de l'Enclos Fouqué comme par exemple pendant l'éruption formant le cratère Hudson en 1998 (Boivin et Bachèlery 2009). Ce type de lave est surtout extrudé à l'Ouest de l'Enclos Fouqué (Pichavant et al. 2016 ; Boudoire 2018, 2019) formant par exemple les cônes excentriques du Piton Haüy et du Piton Chisny (cf. **chapitre VI**). Cependant, la majeure partie du magma parental est transféré épisodiquement vers la zone de stockage superficielle au niveau de la mer et vers les petites poches magmatiques situées au-dessus du niveau de la mer (Fig. 2.9a). Entre ces recharges épisodiques, le réservoir superficiel principal se différencie par fractionnement simultanée de clinopyroxène, de plagioclase et d'olivine générant des basaltes cotectiques (SSB pour *Steady State Basalts*) dans la partie supérieure (ex. Ludden 1978 ; Bachèlery 1981 ; Famin et al. 2009) et des basaltes picritiques dans la partie inférieure du réservoir, présentant une large gamme de composition en MgO contrôlée par leur teneur variable (de 10 à 40 vol%) en xénocristaux d'olivine (Salaün et al. 2010). L'étude de la saturation du H_2O et du CO_2 au sein d'inclusions vitreuses suggèrent une pression maximum d'environ 50 MPa pour les niveaux de stockages des SSB (Di Muro et al. 2014, 2016). Lors de leur ascension vers la surface, ces magmas cristallisent des microcristaux de plagioclase, clinopyroxène et plus rarement de l'olivine (**cf. chapitres IV et V**). Enfin, un groupe de lave, appelé évolué ou différencié (par fractionnement du plagioclase, du clinopyroxène et de l'olivine), dont la présence est très rare dans l'activité récente du Piton de la Fournaise (Vlastélic et al. 2011), est majoritairement attribué à l'activité ancienne du volcan (Albarède et al. 1997) ou du complexe hypo-volcanique des Alizées (Smietana 2011).

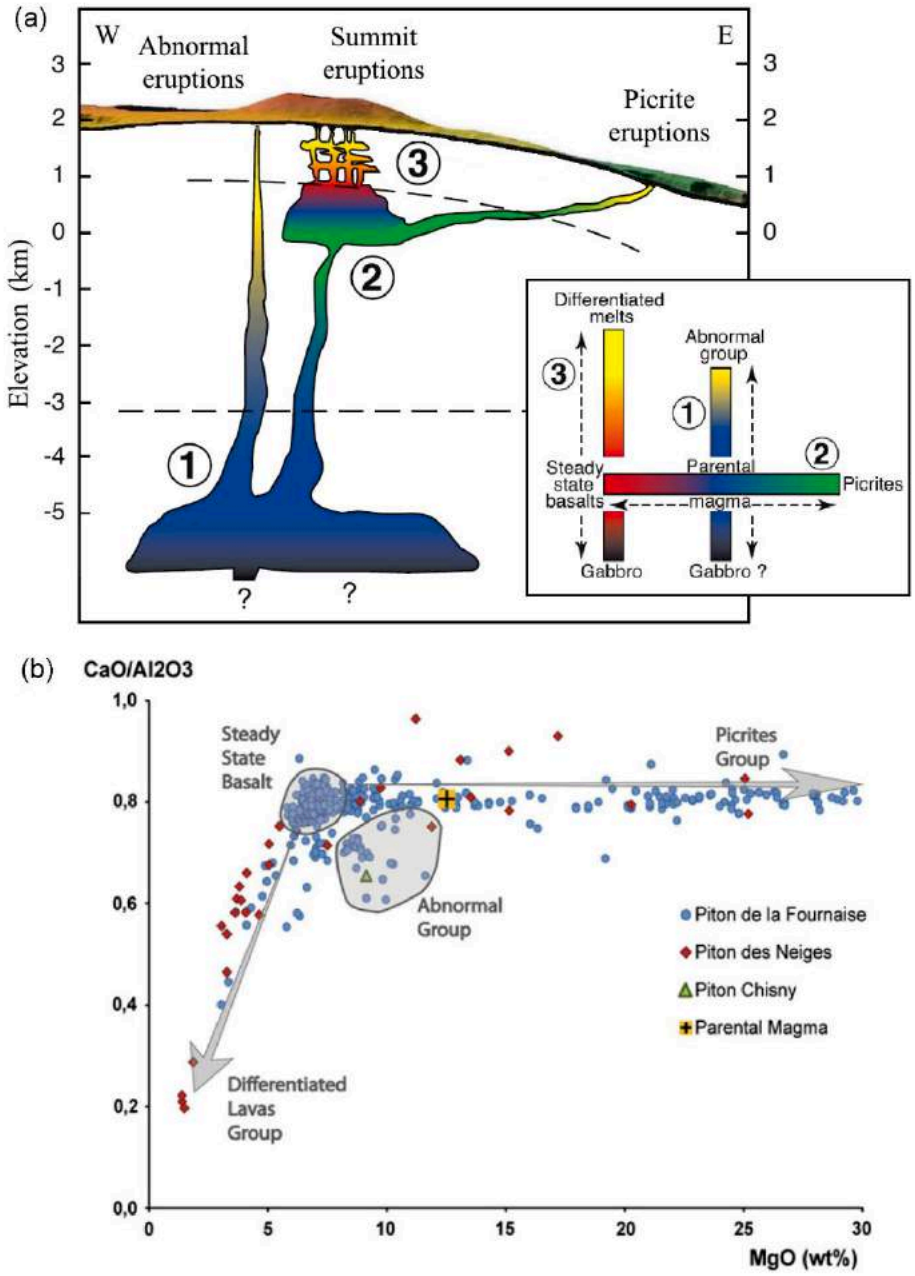

Figure 2.9 *– (a) Modèle conceptuel de l'évolution géochimique des magmas du Piton de la Fournaise. Figure modifiée d'après Famin et al. (2009). Un réservoir profond accueille le magma parental (en bleu). Ligne 1 : fractionnement du plagioclase et du clinopyroxène lors de la remontée directe du magma vers la surface, donnant des produits appelés anormaux (en jaune). Des gabbros peuvent éventuellement se former en profondeur (en noir). Ligne 2 : après un transfert magmatique vers un réservoir superficiel, le magma parental se différencie pour produire des picrites (en vert) par fractionnement et accumulation d'olivine et pour produire des basaltes cotectiques (SSB) par fractionnement du clinopyroxène, du plagioclase et de l'olivine dans la partie supérieure du réservoir (en rouge). Ligne 3 : Fractionnement*

superficiel du plagioclase, clinopyroxène et de l'olivine au sein des SSB formant des liquides basaltiques différenciés (en jaune) et des cumulats gabbroïques (en noir). (b) Compositions (CaO/Al_2O_3 vs. MgO wt%) des différents magmas cités précédemment d'après une compilation de données établie par Pichavant et al. (2016). Cette espace graphique représentant à la fois la teneur en MgO (contrôlé par le fractionnement de l'olivine), CaO et Al_2O_3 (contrôlé par le fractionnement du plagioclase et du clinopyroxène) représente un bon proxy de différentiation des magmas basaltiques du Piton de la Fournaise.

Certaines poches de magma superficielles peuvent être déconnectées du complexe de stockage superficiel principal et évoluer plus longtemps et individuellement par fractionnement de plagioclase et de clinopyroxène, produisant des petites éruptions différenciées comme en Juin 2014 (Gurioli et al. 2018 ; cf. **chapitre IV** et **Annexe 2**). Les SSB et les basaltes riches en olivine sont stockés à des niveaux relativement superficiels. Ils ont donc tendances à provoquer des éruptions sommitales et proximales au cône central. Certains magmas peuvent être aussi transférés de façon latérale donnant lieu à des éruptions dites distales (Longpré et al. 2007 ; Peltier et al. 2008).

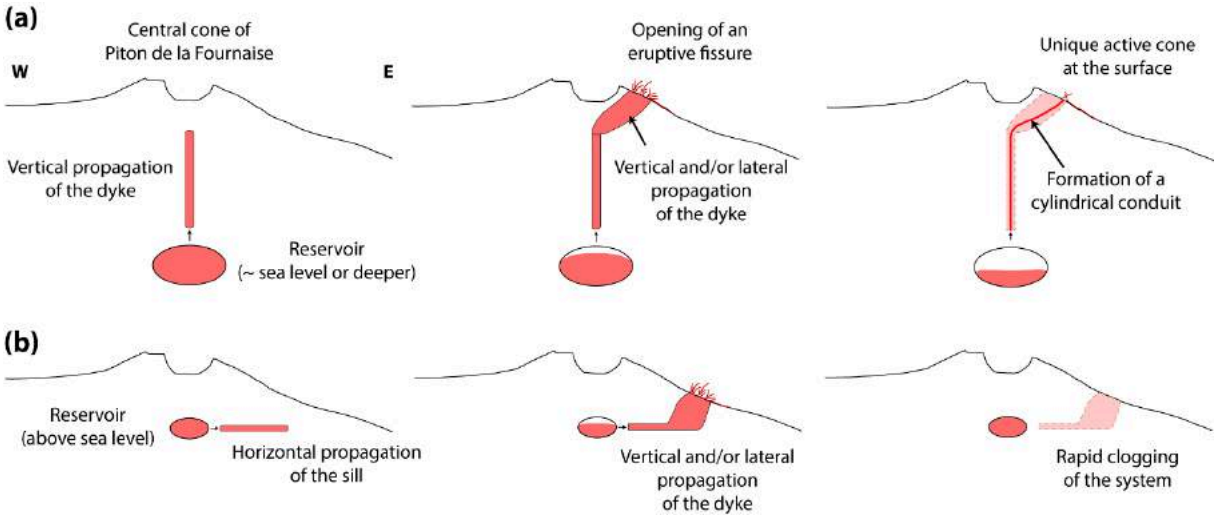

Figure 2.10 *– (a) Modèle de transfert et de mise en place du magma en surface proposé par Peltier et al. (2005) et Fukushima et al. (2010). (b) Modèle de transfert et de mise en place du magma en surface lors de l'éruption de Mai 2016 proposé par Smittarello et al. (2018).*

La majeure partie de l'activité volcanique du Piton de la Fournaise se traduit donc par l'injection épisodique de magmas basaltiques plus ou moins différenciés à travers l'édifice grâce à des conduits formés lors de la propagation du magma vers la surface. La source et la

localisation à la surface des différentes éruptions, préférentiellement localisées au sein des *rift-zones* décrites précédemment, sont donc généralement différentes et dépendent aussi des changements du champ de contraintes local de l'édifice (Peltier et al. 2012). Bien que l'activité explosive sommitale (cf. **chapitre VI**), parfois associée à des effondrements (trois cas répertoriés en près de 40 ans de surveillance), représente les risques majeurs au Piton de la Fournaise (Michon et al. 2013), le type d'activité lié à ces processus magmatiques est majoritairement effusif associé à des activités hawaïennes et stromboliennes (cf. **chapitres IV et V**).

L'évolution pré- et syn-éruptive de la sismicité et des déformations montrent que la propagation des conduits éruptifs jusqu'à la surface peuvent se faire de différentes manières selon la profondeur, la localisation et la pression interne des réservoirs magmatiques impliqués dans les éruptions sommitales et proximales au cône sommital. De manière générale, Peltier et al. (2005) et Fukushima et al. (2010) suggèrent que la propagation du magma vers la surface s'effectue d'abord verticalement (à une vitesse d'environ 2 à 3 $m.s^{-1}$) à partir de réservoirs magmatiques se situant aux alentours du niveau de la mer. La propagation verticale des dykes serait contrôlée par l'importante flottabilité des magmas riches en gaz (activité sismique importante). A des niveaux relativement superficiels, la propagation des dykes, guidée par des fractures préexistantes (activité sismique relativement faible), peut continuer d'évoluer de façon verticale ou se propager façon latérale à des vitesses plus faibles (< 1 $m.s^{-1}$) jusqu'à l'éruption du magma en surface (Fig. 2.10a). L'évolution latérale et horizontale des dykes serait cohérente avec des magmas atteignant leur niveau de flottabilité neutre par rapport aux roches encaissantes. Fukushima et al. (2010) montrent aussi que l'influence de la surpression initiale des réservoirs magmatiques peut jouer sur la géométrie des conduits éruptifs (Fig. 2.10a). Ainsi, lorsqu'une éruption liée à une unique source magmatique se déclenche, le dyke se propageant de façon verticale ou latérale provoque l'ouverture d'une ou plusieurs fissures alignées (ex. éruption de Septembre 2016, cf. **chapitre V**) ou en-échelon (ex. éruption de Juillet 2015, cf. **chapitre IV**). Il est souvent observé qu'au fur et à mesure de l'extrusion du magma en surface, la surpression ainsi que le flux de magma diminuent (Coppola et al. 2017). Cette baisse de flux magmatique au sein du dyke favorise son rétrécissement en un conduit plus ou moins cylindrique (taille d'environ 1 m de diamètre) formant généralement une unique source d'émission en surface (ex. éruption de Septembre 2016, cf. **chapitre V**). Plus récemment, Smittarello et al. (2019) suggèrent que certaines éruptions dont les sources se situent légèrement au-dessus du niveau de la mer, peuvent être alimentées par des sills se propageant latéralement

(ex. éruption de Mai 2016). Ces sills seraient ensuite reliés aux fissures éruptives par des dykes sub-verticaux sur les flancs ou à la base du cône central du volcan (Fig. 2.10b).

1.4. Histoire éruptive du Piton de la Fournaise

1.4.1 Eruptions préhistoriques et historiques majeures étudiées, avant la création de l'Observatoire Volcanologique du Piton de la Fournaise (OVPF)

Grâce à l'investigation et l'étude des anciens dépôts au sein du Piton de la Fournaise, plusieurs études montrent l'évolution du type d'activité volcanique qu'a pu avoir le volcan au cours de son histoire récente. Des campagnes de forage et d'excavation ont permis la caractérisation et la datation des plusieurs éruptions majeures ayant eu lieu il y a moins de 5000 ans (Morandi et al. 2016). Dans cette période, et avant la création de l'Observatoire Volcanologique du Piton de la Fournaise (OVPF) à la fin du 20ème siècle, quatre différents dépôts correspondant à plusieurs éruptions majeures ont été choisies dans le but de caractériser plus en détail ces derniers afin de mieux contraindre les mécanismes éruptifs associés (cf. **chapitre VI**).

Chronologiquement, les premier dépôts ciblés sont les téphras de Bellecombe, qui représentent les produits éruptifs de l'activité explosive la plus violente du Piton de la Fournaise dans la période étudiée (Morandi et al. 2016 ; Ort et al. 2016). Ces dépôts sont relativement dispersés au sein du massif du Piton de la Fournaise. D'après ces auteurs, ces dépôts sont issus d'une série d'évènements phréatiques et/ou phréatomagmatiques liés au remaniement de plusieurs anciens systèmes hydrothermaux pendant la formation épisodique de l'Enclos Fouqué (Fig. 2.5). Comme précisé précédemment, leurs datations donnent des âges compris entre 4745 ± 130 et 2320 ± 90 BP (Morandi et al. 2016). L'étude de cette série d'évènements explosifs est focalisée sur certaines couches échantillonnées sur le site dit de la Petite Carrière, où affleurent des dépôts relativement proximaux à la source d'émission (Ort et al. 2016).

Les deuxièmes dépôts étudiés sont les Téphras Noirs que l'on retrouve sur la majeure partie occidentale de la Plaine des Sables (Principe et al. 2016). Ces téphras ont été les derniers

à être émis sur la zone du Piton Chisny et sont datés entre 1447 à 1628 AD (Morandi et al. 2016). Le Piton Chisny est un édifice d'environ 150 m de proéminence et situé à l'Ouest de l'Enclos Fouqué au sein de la Plaine des Sables et fait partie d'un ensemble de cônes adventifs (ou excentriques), situés hors de la caldera centrale actuelle du Piton de la Fournaise (Valer 2016). Ces cônes font tout de même partie du massif du Piton de la Fournaise et se concentrent majoritairement au niveau de la Plaine des Sables et des *rift-zones* extérieures à l'Enclos Fouqué (Fig. 2.4a). Ils sont généralement formés par une alimentation magmatique relativement profonde provenant directement du système magmatique profond (Villeneuve et Bachèlery 2006), qui est légèrement décalé à l'Ouest par rapport au cône sommital du Piton de la Fournaise (Michon et al. 2015) et donc géographiquement proche de la Plaine des Sables (Figs. 2.7 et 2.9). Comme précisé précédemment, ces magmas profonds produisent des produits éruptifs dits anormaux (Fig. 2.9), typiquement associées à des activités hawaiienne (Valer et 2016). Aujourd'hui, leur occurrence est relativement faible par rapport aux éruptions de SSB au sein de l'Enclos Fouqué. Le Piton Chisny est un des rares cônes adventifs à être polygénique, c'est-à-dire d'avoir produits plusieurs éruptions au cours de sa formation (Michon et al. 2015 ; Morandi et al. 2016). Ses dépôts les plus récents mais aussi les plus importants en termes de volume (Téphras Noirs) ont été échantillonnés dans une zone proximale à la source d'émission au Nord du Piton Chisny. Ils représentent l'activité hawaïenne la plus énergétique de la période historique du Piton de la Fournaise.

Les troisièmes dépôts étudiés sont ceux issus de l'éruption sommitale de 1860. Des écrits historiques (Hugoulin 1860 ; Maillard 1862 ; Lacroix 1936) décrivent l'évolution de la zone centrale du Piton de la Fournaise et démontrent l'ampleur de cette éruption. En effet, suite au débordement puis à la vidange d'un ancien lac de lave actif situé dans un ancien cratère sommital appelé Cratère Brûlant et situé sur la partie orientale du cône sommital (Janvier et Février 1860), plusieurs fissures éruptives se sont ouvertes sur le flanc du cône (Février et Mars 1860). La vidange des conduits et réservoirs sommitaux aurait provoqué l'arrivée brutale d'un volume d'eau hydrothermale et/ou météoritique dans ce système partiellement vidangé et encore chaud (Bachèlery 1981, 1999 ; Michon et al. 2013) induisant des explosions phréatiques et/ou phréatomagmatiques sommitales le 19 Mars 1860. Le cratère Brûlant a ainsi été partiellement démantelé et élargi d'environ 300 m. Cette série d'explosions d'environ une journée furent associées à la formation d'un panache de cendre important. Des blocs et lapilli ont recouvert environ la moitié Nord de l'Enclos Fouqué alors que les retombées de cendres ont été recensées jusqu'à l'extrémité Sud de l'île de La Réunion ainsi qu'à plusieurs dizaines

de kilomètres à l'Est au large de l'île (Lacroix 1936 ; Bachèlery 1999 ; Villeneuve et Bachèlery 2006). Une étude récente (Michon et al. 2013) documente les dépôts sommitaux relativement bien conservés de cette éruption, échantillonnés à l'Ouest du cratère Bory. Dans cette thèse, l'étude de ces dépôts est focalisée sur certaines couches cendreuses.

Enfin, les derniers dépôts étudiés sont ceux reliés à l'activité volcano-tectonique de Septembre 1936. Une activité plus ou moins continue entre 1931 et 1936 engendra lors du mois de Septembre 1936 un effondrement partiel de la caldera sommitale du Dolomieu (Lénat et al. 2016a). Les dépôts associés à cette activité d'effondrement ont aussi été vraisemblablement liés à une activité éruptive hawaïenne locale synchrone.

1.4.2. Résumé de l'activité récente et des éruptions étudiées depuis la création de l'OVPF

La création de l'OVPF date de 1979, suite à l'éruption de Mars et Avril 1977 qui forma une série de fissure au Nord et en dehors de l'Enclos Fouqué (Bachèlery 1981). Ces fissures alimentèrent deux coulées de lave. Une d'entre elles atteignit le village de Piton Sainte-Rose et détruisit une partie du village. L'une des missions principales de l'OVPF est donc d'établir une surveillance continue de l'activité du Piton de la Fournaise et de l'évolution des aléas volcaniques associés. Depuis la création de l'OVPF, deux autres éruptions se produisirent hors de l'Enclos Fouqué, la première en 1986 au Sud du massif, la seconde en 1998 sur la bordure Nord de caldera.

Depuis cette phase éruptive de 1998, toute l'activité volcanique du Piton de la Fournaise est focalisée à l'intérieure de l'Enclos Fouqué avec l'occurrence d'une éruption tous les neufs mois en moyenne (Roult et al. 2012), correspondant à $32{,}7.10^6$ m^3 de magma émis en moyenne chaque année (Staudacher et al. 2016). Cette fréquence éruptive et ce volume de magma émis relativement élevés font du Piton de la Fournaise un des volcans les plus actifs sur Terre actuellement.

Après une période de repos de six années et un regain d'activité depuis 1998, Bachèlery (1999) et Villeneuve et Bachèlery (2006) avertissent que l'extrusion de grandes quantité de

magmas et donc la vidange d'un ou plusieurs réservoirs magmatiques, sont étroitement liées aux changements majeurs de la morphologie des cratères sommitaux. Peu de temps après, une éruption majeure se produit en 2007, formant tout d'abord trois phases éruptives distinctes au sein de l'Enclos Fouqué (Staudacher et al. 2009). La première eut lieu entre le 18 et le 19 Février sur la zone sommitale (environ 34 h d'activité). La seconde apparue le 30 Mars, à environ 1900 m d'altitude et au SE de la base du cône central (environ 10 h d'activité). Ces deux phases éruptives correspondent à la vidange de petites poches magmatiques relativement superficielles (Albert et al. 2019). Malgré des durées très courtes de ces deux éruptions, l'activité sismique restera relativement intense (Michon et al. 2011) et deux nouvelles fissures éruptives distales se forment le 2 Avril à une altitude d'environ 600 m, proche de la limite Sud de l'Enclos Fouqué. Rapidement, une seule fissure reste active (formant le Piton Tremblet), au sein de laquelle se forment des fontaines de lave atteignant des hauteurs allant de 100 à 150 m (Staudacher et al. 2009). Le pic en intensité de l'éruption est enregistré le 6 Avril, avec des débits laviques atteignant au moins 200 $m^3.s^{-1}$ et avec des hauteurs de fontaines de près de 200 m (Michon et al. 2007, 2011). Cette intensité exceptionnellement élevée provoque une vidange brutale du réservoir magmatique (qui a cependant débutée dès le début de l'éruption) situé sous le cône sommital à environ 2 km sous la surface (Peltier et al. 2008). Dès le 5 Avril, un premier effondrement sommital est enregistré par les stations sismiques et géodésiques. Un effondrement majeur se produit quelques heures après, modifiant considérablement la morphologie de la zone sommitale. Cet effondrement est associé à l'émission de cendres (cf. **chapitre VI**) se dispersant au sein de l'Enclos Fouqué (Staudacher et al. 2009 ; Michon et al. 2011, 2013). Par la suite, de nombreux, mais plus petits effondrements successifs se sont produit jusqu'au 15 Avril (Fontaine et al. 2014) produisant une dépression de 340 m de profondeur et d'un volume total d'environ 96.10^6 m^3 (Urai et al. 2007). En parallèle, la localisation relativement basse de la source éruptive ainsi que des débits laviques très élevés permettent aux coulées massives d'atteindre l'Océan Indien rapidement (Michon et al. 2011). Au niveau du littoral, les laves forment une plateforme émergée d'environ 5.10^5 m^2 (Saint-Ange 2009). La lave rentrant en contact avec l'eau, des explosions hydro-volcaniques se produisent et dispersent une quantité de cendres non-négligeable aux alentours (cf. **Chapitre VI**). Le magma émis a d'abord été relativement pauvre en phénocristaux d'olivine (< 5 vol%) puis s'en est rapidement enrichi (jusqu'à 30 vol%) vers la fin de l'éruption, montrant des compostions picritiques (Staudacher et al. 2009 ; Di Muro et al. 2014). Le volume total de magma émis a été estimé entre 170.10^6 m^3 (Saint-Ange 2009) et 210.10^6 m^3 (Staudacher et al. 2009). Grâce à des données interférométriques, Froger et al. (2015) mettent en évidence un glissement du flanc du

volcan vers l'Est contemporain et postérieur à l'éruption. Pour ces auteurs, il est probable que le magma alimentant les fissures éruptives de Mars et Avril 2007 fut injecté dans des discontinuités préexistantes facilitant ainsi le glissement (déplacement horizontal de 0,3 m entre Avril 2007 et Avril 2008) d'une majeure partie du flanc Est du volcan vers l'Océan Indien.

Cette éruption a été l'un des événements historiques les plus intenses et volumineux du Piton de la Fournaise et a été suivie par un ensemble d'éruptions de faibles volumes et d'intrusions peu profondes entre 2008 et 2011. Ces évènements, notamment l'éruption de 2007, ont considérablement drainé le système magmatique superficiel du volcan (Di Muro et al. 2014, 2016) et ont été suivis par une phase de repos longue de 41 mois, entre 2011 et 2014 (Peltier et al. 2016). Un nouveau cycle éruptif (Vlastélic et al. 2018) a ensuite débuté par l'éruption de Juin 2014 (Gurioli et al. 2018), suivi par quatre autres éruptions sur la période 2014-2015 (cf. **chapitre IV**). En corrélant la fréquence éruptive du Piton de la Fournaise depuis près de 80 ans avec des mesures géochimiques et isotopiques, Vlastélic et al. (2018) montrent que l'activité éruptive du volcan fluctue selon des cycles de pauses et d'activités éruptives et suggèrent que ces cycles seraient directement liées aux variations temporelles du taux de fusion de la source mantellique. L'ensemble des éruptions de 2014-2015 reflètent le début d'une phase majeure de remplissage, par un magma profond et relativement peu différencié, du système magmatique superficiel du Piton de la Fournaise (Coppola et al. 2017).

Ainsi, l'extrusion de magmas relativement peu différenciés pendant l'éruption d'Août-Octobre 2015, associée à une activité sismique profonde et superficielle ainsi qu'une inflation du volcan plus ou moins constante depuis le début de l'année 2015 (Peltier et al. 2016, 2018) montrent que le système magmatique superficiel, initialement rajeuni par la remontée de magmas plus profonds, est relativement actif depuis 2014, alimentant près de 13 éruptions sur la période 2014-2018, sur lesquelles cette thèse s'est partiellement focalisée (**cf. chapitres IV, V et VI**).

1.5. Conclusions sur les principales caractéristiques du Piton de la Fournaise et contextualisation des éruptions étudiées

En conclusion, le Piton de la Fournaise est un volcan relativement bien étudié et dont les structures volcano-tectoniques ainsi que l'évolution géochimique des magmas sont bien contraintes (Fig. 2.11). L'étude des dépôts anciens ainsi que l'observation des éruptions historiques et récentes suggèrent que ce volcan produit majoritairement des éruptions hawaïennes et stromboliennes, associées à l'émission de laves (cf. **chapitres IV et V**). Cependant, la complexité de l'évolution du système magmatique du Piton de la Fournaise ainsi que de sa structure superficielle, peut causer des aléas volcaniques différents et plus importants en termes d'intensité, volume et dispersion. Ces aléas sont liés à des événements paroxysmaux pouvant émettre une quantité de produits éruptifs, notamment de cendres, non-négligeable (cf. **chapitre VI**).

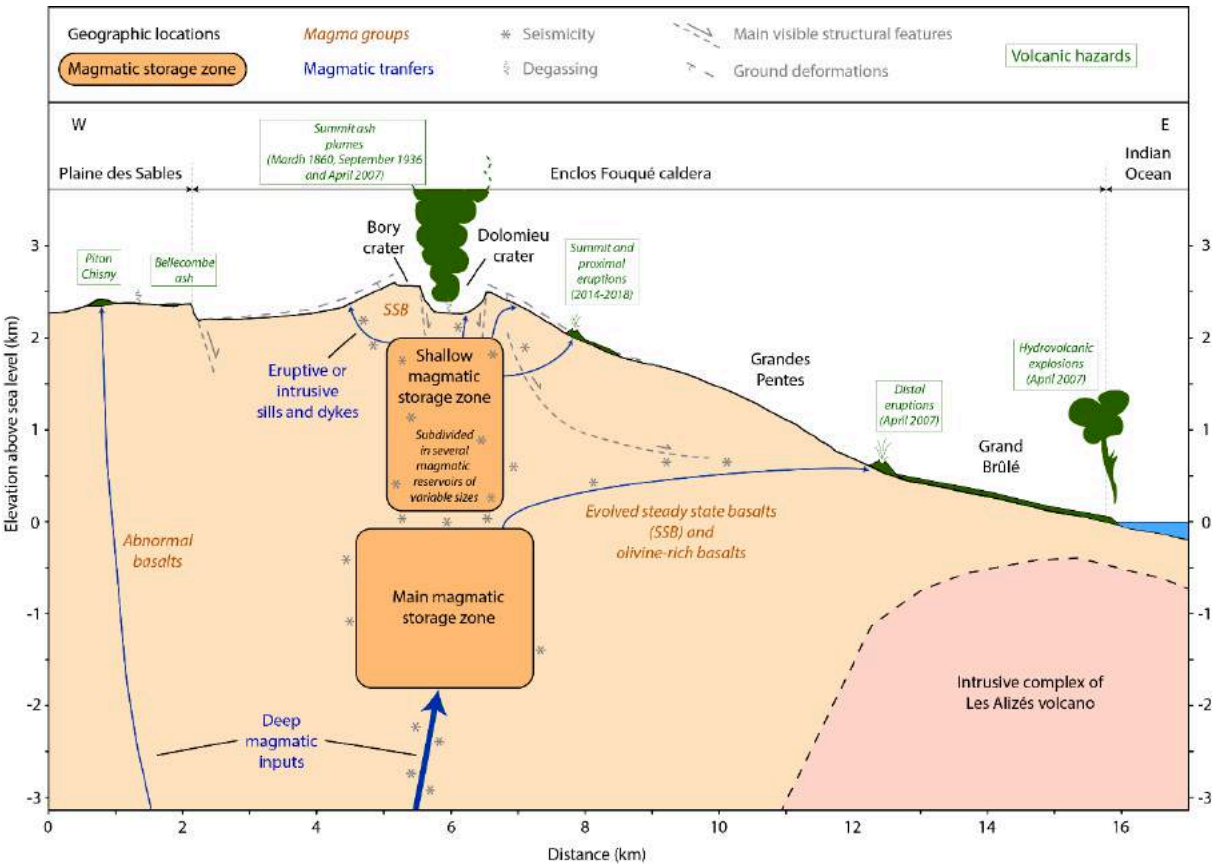

Figure 2.11 *– Coupe géologique O-E simplifiée du Piton de la Fournaise, associée aux principales structures volcano-tectoniques et aux éruptions étudiées dans cette thèse. La sismicité, la déformation du sol, ainsi que le dégazage du sol, constamment mesurés par l'OVPF, ont aussi été matérialisés.*

Aujourd'hui, l'activité de surveillance constante du volcan de la part de l'OVPF et de ses partenaires (Harris et al. 2017), permettent d'anticiper plus ou moins à court termes sur l'activité éruptive du volcan et d'acquérir une multitude de données sur l'évolution de son comportement. De plus, un échantillonnage systématique (syn- et post-éruptif) des produits émis (laves et téphras) est réalisé pour chaque éruption. Cette thèse est consacrée à l'échantillonnage des produits éruptifs de certaines éruptions clés (Fig. 2.11) et de leurs analyses en laboratoire (cf. **chapitre III**) dans le but de comprendre les processus magmatiques pré- et syn-éruptifs contrôlant l'évolution texturale et géochimiques des échantillons ainsi que l'évolution de l'activité éruptive en surface (cf. **chapitres IV, V et VI**).

2. Le Karthala : un volcan relativement méconnu

Cette seconde partie décrit brièvement les aspects généraux concernant le volcan du Karthala (île de Ngazidja, Union des Comores), sur lequel cette thèse consacre une étude sur des dépôts cendreux émis lors de deux éruptions en 2005 (cf. **chapitre VI**). Comme dans la première partie de ce chapitre, le contexte géodynamique et l'origine du volcanisme de cette zone est brièvement abordé. Par la suite, la géologie, les structures majeures ainsi que l'activité récente du volcan sont décrites.

2.1. Contexte géodynamique et origine du volcanisme de l'archipel des Comores

L'archipel des Comores est un ensemble de quatre îles volcaniques situées dans la partie Nord du canal du Mozambique et alignées dans une direction WNW-ESE (Fig. 2.1). Ces quatre îles sont d'Ouest en Est, Ngazidja (ou Grande Comore), Mohéli, Anjouan et Mayotte (Fig. 2.12a). Ces îles reposent sur un fond océanique d'environ 3 km de profondeur (Michon 2016). L'origine du volcanisme comorien est débattue entre deux principales théories. La première met en cause la présence d'un panache mantellique profond, comme pour le volcanisme de la Réunion (Emerick et Duncan 1982 ; Emerick 1985). Selon cette hypothèse, l'anomalie mantellique serait aussi à l'origine de la formation du plateau des Seychelles (Fig. 2.1). Cependant, certaines incohérences géodynamiques entre les Seychelles et les Comores amènent d'autres études plus récentes à émettre une différente théorie (Nougier et al. 1986 ; Courtillot et al. 2003 ; Michon 2016). Selon ces derniers auteurs, le volcanisme de l'ensemble des Comores serait plutôt lié à une déformation lithosphérique sous-jacente et à la réactivation de failles lithosphériques contrôlant la propagation du magma selon l'alignement des édifices volcaniques au sein du canal du Mozambique. Selon le modèle de Courtillot et al. (2003), les déformations lithosphériques liées aux structures volcano-tectoniques du rift Est africain pourraient provoquer des perturbations asthénosphériques et ainsi former une anomalie mantellique superficielle (panache tertiaire) au niveau du canal du Mozambique.

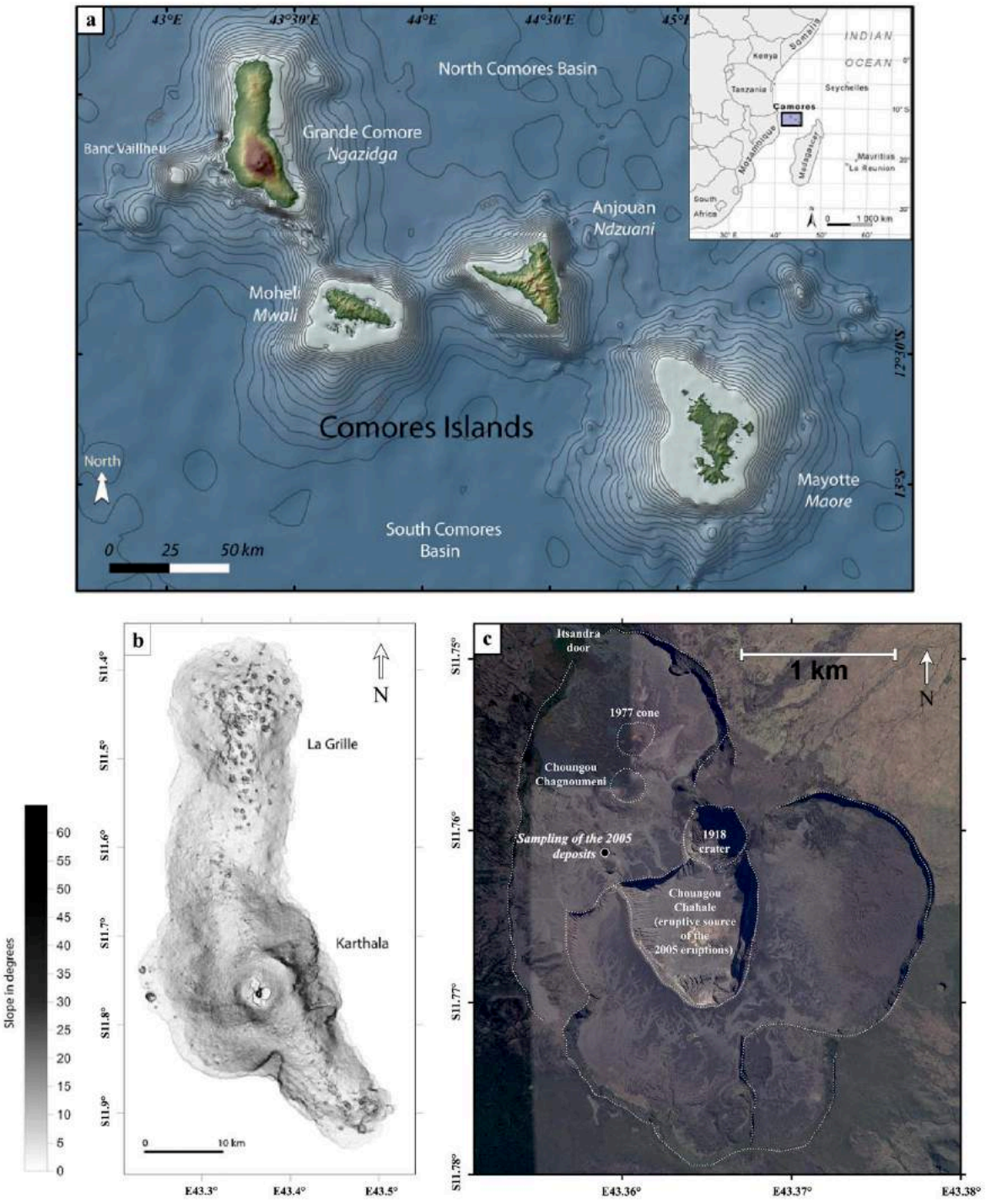

Figure 2.12 *– (a) Situation géographique et bathymétrique de l'archipel des Comores, d'après Bachèlery et al. 2016. (b) Carte des pentes de l'île de la de Ngazidja mettant en évidence les différentes structures de l'île avec les massifs de la Grille sur le tiers Nord et le Karthala sur les deux tiers Sud, d'après Bachèlery et al. 2016. (c) Photo satellite de la zone sommitale du Karthala composée du plusieurs calderas, cratères et cônes emboités. L'échantillonnage des cendres fines des éruptions de 2005 est localisé au NO du cratère Choungou-Chahalé.*

L'ensemble de ce volcanisme s'est développé sur une croûte dont la nature fait aussi objet de débats. En effet, la présence d'enclaves gréseuses au sein des laves comorienne suggèrerait que la croute sous-jacente serait de nature continentale et impliquerait que le volcanisme se serait implanté sur un microcontinent immergé (Flower et Strong 1969). Cependant, grâce à des données magnétiques, Coffin et Rabinowitz (1987) confirment la présence d'une croûte océanique dans cette zone. De plus, Leclaire et al. (1989) avancent des arguments sédimentaires et tectoniques pour expliquer la déposition de dépôt détritiques continentaux, parfois massifs (comme sur l'île d'Anjouan ; Debeuf 2004), sur cette croûte océanique.

Michon (2016) montre que le volcanisme des Comores débuta tout d'abord au niveau de l'île de Mayotte il y a près de 20 Ma pour ensuite former de manière quasi-simultanée les îles d'Anjouan, de Mohéli et de Ngazidja il y a environ 10 Ma. Cet auteur remarque aussi l'érosion progressive des édifices volcaniques constituants l'archipel, depuis l'Ouest vers l'Est. Cependant, l'observation récente d'une activité volcanique sous-marine à l'Est au large de l'île de Mayotte (ex. Lemoine et al. submitted) montre que le volcanisme est potentiellement actif même sur la partie orientale de l'archipel. Les magmas récents issus du volcanisme comorien sont majoritairement alcalins et des analyses des éléments traces ainsi que des analyses isotopiques suggèrent que ces magmas sont issus de sources mantelliques relativement superficielles et dégazées associées à une signature lithosphérique plus ou moins présente (Nougier et al. 1986 ; Debeuf 2004 ; Class et al. 2005 ; Bachèlery et Hémond 2016).

2.2. Contexte géologique et structural de l'île de Ngazidja et du Karthala

L'île de Ngazidja est la plus occidentale et septentrionale de l'archipel. Sa forme caractéristique (allongée dans la direction N-S sur sa partie Nord, puis allongée dans la direction NO-SE sur sa partie SE) reflète la présence de deux massifs majeurs (Figs. 2.12b, 2.13), avec au Nord le volcan de La Grille (1087 m) et au Sud le volcan du Karthala (2361 m). Des prospections géologiques, qui ont mené à la constitution de la carte géologique de l'île de Ngazidja (Bachèlery et Coudray 1993), ont identifié un troisième ancien massif à l'extrémité

SE, nommé M'Badjini, dont l'appartenance au massif du Karthala est incertaine (Bachèlery et al. 2016).

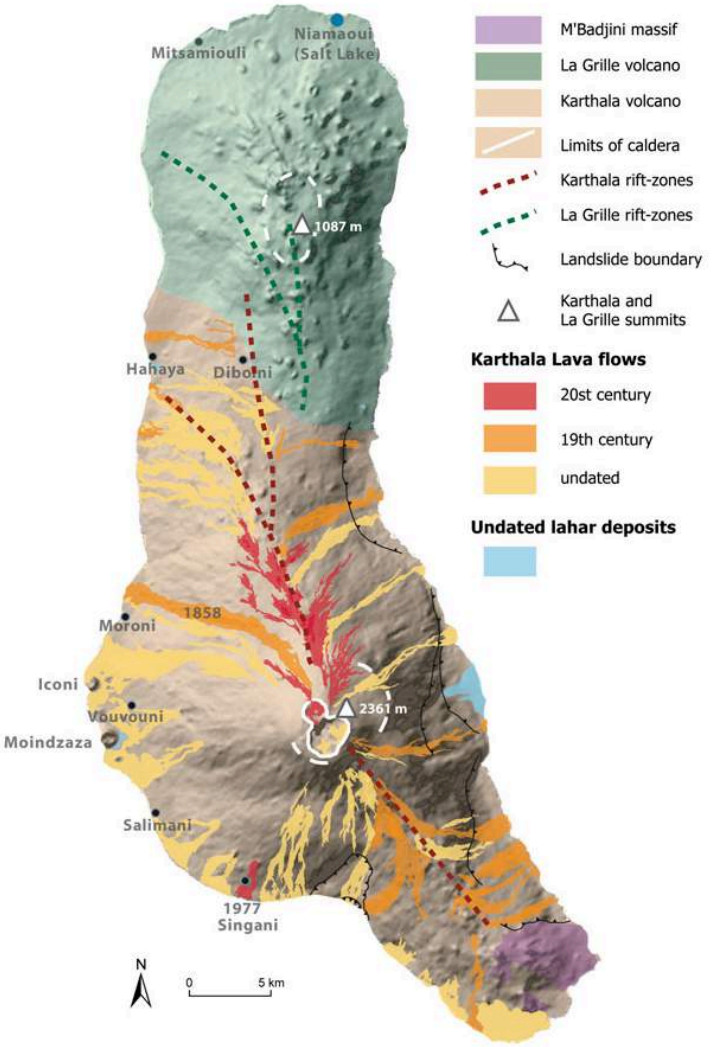

Figure 2.13 *– Carte géologique simplifiée de l'île de Ngazidja, d'après Bachèlery et al. (2016).*

Actuellement, le volcan bouclier du Karthala est le seul volcan actif émergé du canal du Mozambique. Il est majoritairement constitué de basaltes alcalins (Bachèlery et Hémond 2016). Sur les flancs Sud et Est du Karthala, plusieurs zones de forme concave et dont les pentes sont relativement élevées ont été interprétées comme les traces de grands glissement de terrains (Bachèlery et Coudray 1993). Sur sa zone sommitale, le Karthala est constitué d'un complexe caldérique de forme elliptique d'environ 3,5 km de long et de 2,8 km de large (Fig. 2.12c). La zone centrale est occupée par un *pit-crater* nommé Choungou-Chahalé, source éruptive de la plupart des éruptions sommitales récentes du Karthala (cf. **chapitre VI**), à l'exception de

l'éruption de Janvier 2007 qui eut lieu légèrement plus au Nord au sein du *pit-crater* Choungou-Chagnoumeni (Bachèlery et al. 2016). La présence de structures d'effondrements de différentes tailles au sommet du volcan (Poppe 2012) ainsi que la détection de crises sismiques pré-éruptives relativement superficielles (Smietana 2007) suggèrent qu'un ou plusieurs réservoirs magmatiques superficiels se sont mis en place sous les cratères sommitaux du volcan et entre la surface et le niveau de la mer (Fig. 2.14). Ces cratères sommitaux se situent à la jonction de deux *rift-zones* bien définies et orientées respectivement N-S sur la partie Nord, et NO-SE sur la partie SE du Karthala (Fig. 2.13). Depuis sa source en profondeur, le magma est possiblement stocké et différencié dans plusieurs niveaux crustaux. Les phénocristaux observés dans les produits éruptifs du Karthala, qui reflètent la dernière phase de fractionnement des magmas (Class et Goldstein 1997 ; Claude-Ivanaj et al. 1998), sont majoritairement des olivines, des clinopyroxène avec plus rarement des plagioclases dans certaines roches relativement anciennes au sein du massif de M'Badjini, mais aussi plus récentes au sein de certaines laves sommitales (Bachèlery et Hémond 2016).

En l'absence significative de datations absolues des produits éruptifs du Karthala, Bachèlery et Coudray (1993) ont établi une chronologie relative de ces différents produits basée sur l'état de conservation, l'altération et le niveau de végétation recouvrant ces roches. Ces auteurs proposent trois unités majeures. Premièrement, l'ancien Karthala est composé des plus anciennes formations dont les roches sont complétement altérées. Cette unité affleure uniquement sur le flanc Est du volcan et au niveau du massif de M'Badjini. Deuxièmement, le Karthala récent recouvre une majorité de la surface actuelle du volcan et dont les roches sont peu altérées. Enfin, le Karthala actuel représente les produits éruptifs les plus récents datant du 19ème siècle à aujourd'hui (Fig. 2.13).

2.3. Connaissances générales sur l'histoire éruptive du Karthala et comparaison avec le Piton de la Fournaise

D'après les observations des habitants de l'île de Ngazidja, le Karthala est rentré au moins 15 fois en éruption au cours du 20ème siècle (Bachèlery et al. 2016). Avec la collaboration du l'OVPF, l'Observatoire Volcanologique du Karthala (OVK) fut créé en 1988. Malgré des

moyens techniques et humains inférieurs à l'OVPF (Morin et al. 2016), l'OVK surveille l'activité du volcan entre et pendant les éruptions. Depuis sa création, cinq éruptions sommitales ont eu lieu en 1991, 2005 (deux éruptions), 2006 et 2007. L'éruption du 11 Juillet 1991 était de nature phréatique et sans émission de magma alors que les éruptions d'Avril et de Novembre-Décembre 2005 ont été répertoriées comme étant de nature phréatomagmatiques (Bachèlery et al. 2016). Les deux éruptions de Mai-Juin 2006 et du 13 janvier 2007 ont été purement magmatiques. Ces cinq éruptions se sont toutes produites au sein du Choungou-Chahalé à l'exception de celle du 13 Janvier 2007 qui se manifesta au sein du *pit-crater* Choungou-Chagnoumeni et dont les laves comblèrent le cratère (Bachèlery et al. 2016). Les cendres relativement fines des dépôts des deux éruptions de 2005 ont pu être échantillonnées pour être ensuite analysées et comparées aux diverses cendres étudiées du Piton de la Fournaise (cf. **chapitre VI**).

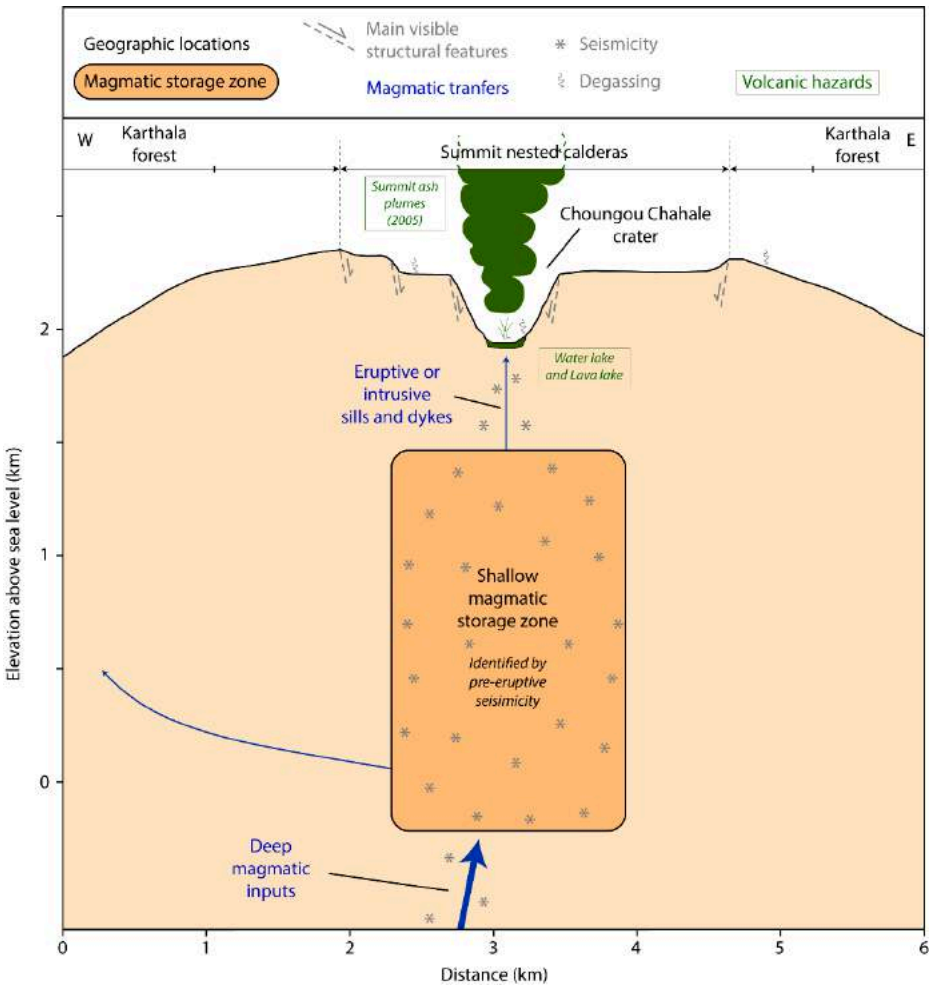

Figure 2.14 *- Coupe géologique O-E simplifiée du Karthala, associée aux principales structures volcano-tectoniques sommitales connues et aux éruptions étudiées dans cette thèse. La sismicité (mesurée par l'OVK) ainsi que le dégazage du sol, ont aussi été matérialisés.*

Malgré des intérêts scientifiques moins marquées concernant le Karthala du fait de son activité éruptive moins importante et son accès relativement difficile par rapport à d'autres volcans basaltiques comme ceux du Kilauea (Hawaï), de l'Etna (Italie) ou encore du Piton de la Fournaise (France), des similarités entre ces volcans apparaissent. En effet, le volcan bouclier du Karthala possède des structures similaires au Piton de la Fournaise et au Kilauea avec un complexe caldérique sommital d'où rayonnent des *rift-zones*. De plus, la pétrologie et la géochimie des laves du Karthala en termes de cristaux et d'éléments majeurs est relativement similaire à celles du Piton de la Fournaise. Comme décrit précédemment, l'activité éruptive du Karthala n'est pas aussi fréquente que celle du Piton de la Fournaise. Cette activité éruptive se traduit parfois par des éruptions distales ou sommitales de type hawaïen et/ou strombolien mais plus récemment par des éruptions sommitales relativement explosives dues notamment à l'interaction avec un système hydrothermal relativement actif. Il est donc intéressant de comparer les types d'activités volcaniques qui peuvent se manifester sur ces deux volcans. L'émission relativement importante de cendres lors des deux éruptions de 2005 au Karthala, non-observé au sein de l'activité récente du Piton de la Fournaise est donc l'opportunité d'étudier en détail ces dépôts pour analyser, comparer et comprendre l'ensemble des aléas volcaniques pouvant se produire sur ce type de volcan bouclier.

CHAPITRE III

APPROCHE ET METHODOLOGIES

1. Approche et objectifs

L'objectif principal de cette thèse est de caractériser plusieurs types de produits basaltiques représentant un maximum de style éruptifs différents. En intégrant ces caractérisations à un ensemble de connaissances sur les systèmes magmatiques et sur les éruptions concernées, le but final est de comprendre quels sont les mécanismes à l'origine des éruptions et de l'évolution des styles éruptifs observés au sein de volcans basaltiques de point chaud comme ceux du Piton de la Fournaise et du Karthala.

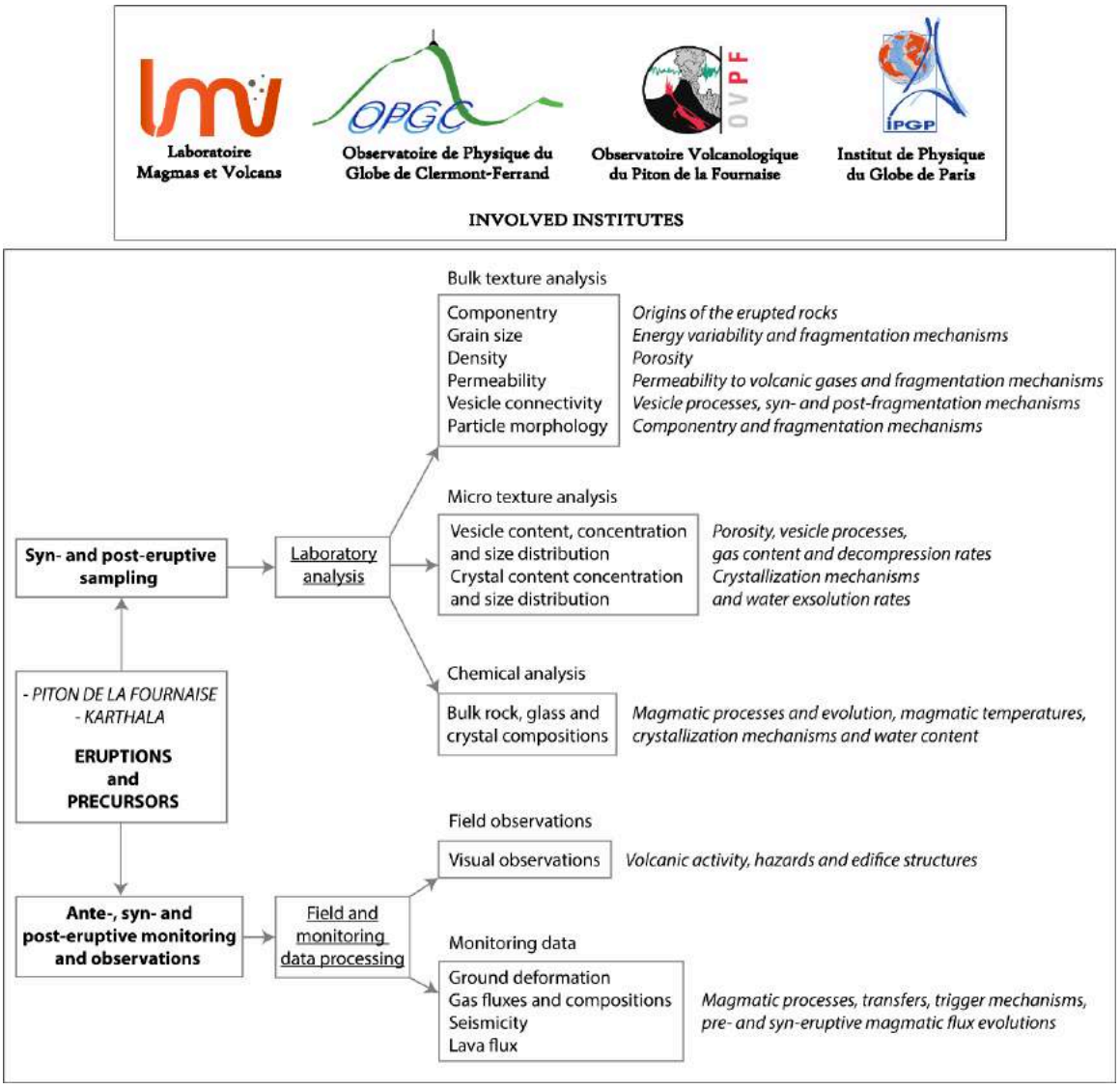

Figure 3.1 *– Schéma montrant l'approche de travail idéale, ainsi que les méthodes appliquées et les objectifs de recherche associés pour l'étude d'une ou plusieurs éruptions. Selon les cas d'étude et la disponibilité des données, certaines méthodes sont privilégiées.*

La figure 3.1 résume l'approche de travail adopté afin de comprendre l'ensemble des mécanismes magmatiques et/ou tectoniques associés à l'émission des différents produits éruptifs étudiés. A partir d'un échantillonnage des produits éruptifs sur le terrain, de nombreuses analyses de laboratoire, liant mesures texturales et géochimiques, ont été réalisées au Laboratoire Magmas et Volcans (LMV) afin de lier les différentes caractéristiques des échantillons à des processus pré-, syn- ou post-éruptifs (Gurioli et al. 2016 ; cf. **Annexe 1**). En complément, certaines données de surveillance associées aux éruptions étudiées regroupant des observations de terrain, des mesures de la déformation du sol, du dégazage, de la sismicité ou encore du flux magmatique, peuvent être prises en compte dans le but d'intégrer les informations texturales et géochimiques des échantillons dans des modèles éruptifs plus complets prenant en compte l'évolution de nombreux paramètres.

2. Echantillonnages des produits éruptifs

2.1. Echantillonnages manuels

Pour chaque éruption se produisant au Piton de la Fournaise, un échantillonnage systématique est réalisé par les membres de l'OVPF et de DynVolc (Gurioli et al. 2016 ; Harris et al. 2017). DynVolc (pour *Dynamics of Volcanoes*) qui est un des services d'observation de l'Observatoire de Physique du Globe de Clermont-Ferrand (OPGC), répertorie une base de données (DynVolc 2017) sur les produits éruptifs de plusieurs volcans et plus particulièrement du Piton de la Fournaise en termes d'études de terrain, mesures texturales et analyses géochimiques. Grâce au réseau de surveillance de l'OVPF et des données d'imagerie, de géodésie, de sismicité, chaque début d'éruption peut être situé dans le temps et dans l'espace. De plus, la nature et l'évolution de chaque éruption, en termes d'intensité, volume et géométrie, sont suivies en temps réel.

Grâce à ce suivi ainsi qu'à une réponse rapide de l'OVPF, un échantillonnage des produits est généralement effectué dans les heures suivant le début de chaque éruption. Selon les conditions d'accès aux sites éruptifs, aux conditions météorologiques particulièrement changeantes dans cette zone et à la durée des éruptions, les échantillonnages syn-éruptifs peuvent être parfois difficiles à entreprendre. Cependant, sur une grande majorité d'éruptions, de nombreux échantillons sont recueillis pendant l'éruption. L'échantillonnage des laves est réalisé avec un bâton en acier galvanisé (Fig. 3.2a) permettant de limiter des contaminations chimiques éventuelles pour les éléments chimiques majeurs (Harris et al. 2017). Cette procédure est réalisée au plus proche de la source d'émission de la lave dans le but de conserver les informations texturales et géochimiques primaires des échantillons laviques, qui peuvent être altérées par des processus de surface au sein de l'écoulement. Dans certains cas, les échantillonnages ont pu être réalisés à différentes distances du point d'émission pour quantifier ces effets de surfaces sur les coulées de lave (cf. **chapitre IV** et **Annexe 4**). Les projections de grande taille (lapilli et bombes) sont également échantillonnées à la main dès leur retombées au sol tout en respectant des conditions raisonnables de sécurité. Les laves et téphras ainsi échantillonnées sont immédiatement trempés dans l'eau (Fig. 3.2b) permettant leur

solidification rapide afin qu'ils n'enregistrent aucunes informations post-éruptives qui ne sont pas liées aux processus magmatiques pré- et syn-éruptifs.

Si l'accès au site éruptif est difficile ou que les conditions météorologiques ne permettent pas un échantillonnage syn-éruptif direct, des échantillonnages complémentaires peuvent être réalisés après chaque éruption, notamment pour accéder à des zones de dépôts relativement proximales et stratégiques (Fig. 3.2c). Sur des téphras de petite taille (petits lapilli et cendres), les trempes naturelles sont relativement rapides (Xu et Zang 2002 ; Porritt et al. 2012) et suffisent généralement à conserver les conditions primaires des échantillons. Cette particularité est plus particulièrement discutée au sein du **chapitre V**.

Figure 3.2 *– (a) Echantillonnage syn-éruptif d'une coulée de lave, proche de sa source d'émission, lors de l'éruption de Juillet 2015. (b) Echantillonnage syn-éruptif de bombes et lapilli incandescents récupérés peu après leur émission proche de l'évent, lors de l'éruption de Avril-Mai 2018. Une trempe est ensuite effectuée dans l'eau à la fois pour les laves et les téphras. (c) Echantillonnage post-éruptif de lapilli et petites bombes, après l'éruption de Juin 2014 (Gurioli et al. 2018).*

En ce qui concerne le Karthala, les échantillonnages des produits éruptifs sont beaucoup moins fréquents du fait de la fréquence éruptive du volcan et de son accessibilité qui sont relativement faibles par rapport au Piton de la Fournaise. Néanmoins, une mission de terrain a permis d'échantillonner des dépôts sommitaux et cendreux issus des deux éruptions de 2005 qui ont montré des dynamismes éruptifs relativement différents de ceux observé récemment au Piton de la Fournaise (cf. **chapitre VI**).

2.2 Mise en place de l'ASHER

Au cours de cette thèse, une procédure d'échantillonnage syn-éruptif de cendres a été développé à partir de l'ASHER (pour *ASH collector and sizER*) qui est un instrument de terrain acquis au sein du projet ANR STRAP (Synergie Transdisciplinaire pour Répondre aux Aléas liés aux Panaches volcaniques). Cet instrument autonome (Fig. 3.3) est constitué d'une unité principale ainsi qu'une barrière optique. L'unité principale est composée d'un collecteur cylindrique recueillant les cendres. Une balance mesurant la masse de cendres accumulées (entre 0 et 5 kg avec une précision de 1 g) et un capteur à ultrasons mesurant l'épaisseur de cendres collectées (jusqu'à 1 m d'épaisseur avec une résolution de 1 mm), sont directement installés sur le collecteur permettant de mesurer le taux d'accumulation des particules. La barrière optique est composée d'un émetteur laser (longueur d'onde de 365 nm) et d'un récepteur. Ce système détecte les particules lorsqu'elles traversent le faisceau laser (d'une largeur de 30 mm et d'une épaisseur d'1 mm) sous forme de pics d'obscurcissement. D'une manière similaire à un disdromètre (Fréret-Lorgeril 2019), ces pics d'obscurcissement sont utilisés pour mesurer la taille des particules mais aussi leurs vitesses verticales. La taille résulte directement de l'amplitude de l'obscuration (proportionnel à la taille des particules traversant le faisceau) alors que (ii) la vitesse est dérivée du délai de l'obscuration. Ainsi, les particules allant de 4 mm à 90 µm de diamètre peuvent être analysées en termes de taille et de vitesse de sédimentation.

Tous ces paramètres sont mesurés par l'ASHER toutes les 30 secondes sur l'ensemble du temps d'acquisition. Grâce à un système dédié, l'instrument fournit donc en temps réel la distribution de la taille des particules, leurs vitesses verticales, ainsi que le taux d'accumulation en termes d'épaisseur et de masse. Un récepteur GPS assure la synchronisation des données et la localisation précise de l'échantillonnage. L'ASHER a été déployé lors de l'éruption d'Avril-Mai 2018 pour tester la faisabilité de cette procédure instrumentale de terrain pour la première fois au Piton de la Fournaise (cf. **chapitre VI**).

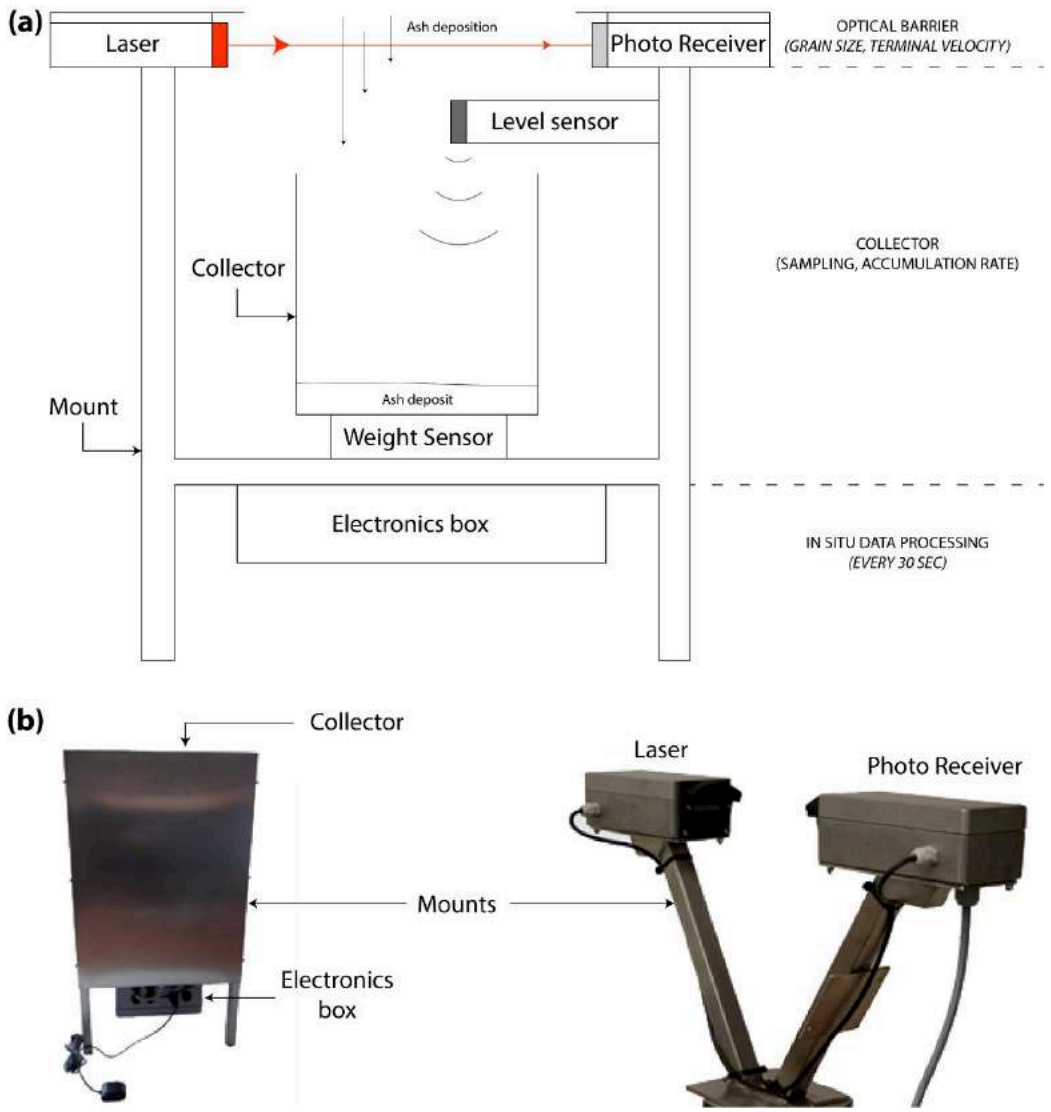

Figure 3.3 *– (a) Schéma simplifié du fonctionnement de l'ASHER. (b) Photos de l'ASHER, montrant à gauche l'unité principale composé du collecteur de cendres, des capteurs de niveau et de masse (à l'intérieur de la monture en aluminium) ainsi de la console électronique (sous la monture) et à droite la barrière optique composé d'un émetteur laser et d'un récepteur.*

3. Analyses des échantillons rocheux en laboratoire

Les échantillons récoltés (laves et pyroclastes) sont d'abord triés, numérotés et décrits d'après les conditions d'échantillonnage. Ils sont ensuite envoyés au LMV pour effectuer des analyses complémentaires. L'ensemble des mesures de laboratoire sur les échantillons sont décrites dans cette partie et sont détaillées de manière chronologique, c'est-à-dire en suivant l'ordre de la procédure analytique adopté dans ces travaux de thèse. Dès la réception des échantillons au laboratoire, ils sont systématiquement placés dans une étuve à environ 80 °C pour y être séchés.

3.1. Mesures des paramètres macroscopiques et apparents

3.1.1. Mesure de la taille des grains

Mesure directe et tamisage manuel

En se focalisant sur la taille des pyroclastes une classification a été établie (Schmid 1981), décrivant les fragments dont la longueur intermédiaire est supérieure à 64 mm comme des bombes (forme arrondie) ou des blocs (forme anguleuse). Entre 64 mm et 2 mm, les fragments sont nommés lapilli. Enfin les pyroclastes, dont la taille moyenne est inférieure à 2 mm, sont appelés cendres.

Pour chaque éruption étudiée, la mesure de la taille des pyroclastes a systématiquement été effectuée. Sur une sélection de fragments intacts (bombes et lapilli) qui vont être analysés par la suite, la longueur maximum, minimum et l'axe intermédiaire ont été mesurés.

Sur des dépôts totaux représentatifs de l'activité éruptive étudiée, la mesure de la distribution de la taille des particules (PSD pour *Particle Size Distribution*) a été mesurée par tamisage manuel (cf. **chapitres V et VI**). Chaque tamis est composé d'une maille (ou ouverture)

quadrillée déterminant la taille minimale des fragments (axe intermédiaire) restant au sein du tamis. Chacun des tamis utilisés possèdent des mailles différentes et sont classés selon une gamme de taille en échelle Φ (Wentworth 1922 ; Krumbein 1934, 1938) censée être une échelle logarithmique pratique pour visualiser et analyser statistiquement la distribution granulométrique d'un dépôt sur une large gamme de tailles de particules, où $\Phi = -\log_2 d$ (d représente le diamètre intermédiaire des particules en mm). La gamme de maille des tamis utilisés pour ce genre de mesure sont généralement espacé de ½ ou ¼ Φ en partant de -6 Φ (64 mm) jusqu'à 5 Φ (32 µm). Cette procédure manuelle a donc permis de mesurer la PSD des dépôts sans altérer la taille des différents fragments qui peuvent être très vésiculés et donc fragiles.

Mesure par diffraction laser

Pour les dépôts relativement fins (< 32 µm), les PSDs ont été mesurées par diffraction laser (cf. **chapitre VI**) grâce à l'utilisation du granulomètre à diffraction laser Mastersizer 3000 de Malvern (Fig. 3.4). Après un nettoyage complet de l'instrument et une fois l'échantillon de cendres dispersé de façon homogène dans de l'eau distillé, le mélange est introduit dans l'unité principale. Les particules en suspension diffractent la lumière émise par un laser (de longueur d'onde de 632.8 nm). L'analyse de la figure de diffraction de cette lumière permet de retrouver la PSD de l'échantillon (Eshel et al. 2004). L'interprétation se fait grâce à la théorie de Fraunhofer (pour des particules opaques et de tailles supérieures à 10 fois la longueur d'onde du laser) et de Mie (toutes tailles de particules). En intégrant l'indice de réfraction du dispersant pour la longueur d'onde du laser utilisé (1,330), ainsi que l'indice de réfraction (de 1,560 à 1,590) et d'absorption (de 0,000 à 0010) des particules analysées dans les modèles de diffusion utilisés (l'utilisation des deux théories dans les calculs donne des résultats très similaires), les PSD des cendres sont recalculées (la taille des particules calculée est le diamètre des particules sphériques diffusant de manière équivalente).

Figure 3.4 *– Schéma simplifié du fonctionnement du granulomètre Mastersizer 3000 de Malvern utilisant la dispersion de l'échantillon par voie humide.*

Enfin, pour des dépôts dont les particules sont à la fois grandes (bombes et lapilli) et petites (cendres fines < 32 mm) les données de tamisage manuel et de diffraction laser sont additionnées et corrigées pour former des PSD totales (cf. **chapitre VI**).

3.1.2. Analyse des composants

Chaque fragment et dépôt étudiés ont ensuite été analysés en termes de composants. Une première classification (White et Houghton 2006) consiste à identifier les fragments juvéniles (appartenant au magma de l'éruption étudiée), non-juvéniles (fragments lithiques n'appartenant pas au magma de l'éruption étudiée) et composites (fragments composés d'un mélange des deux pôles précédents). Les critères d'identification sont généralement macroscopiques, où les fragments juvéniles sont issus d'un magma frais et relativement peu altéré (ex. ponces, scories, matériel juvénile recyclé par une ou plusieurs explosions de l'éruption étudiée) et où les fragments non-juvéniles sont issus des roches encaissantes de la source éruptive (ex. blocs de laves anciennes, roches intrusives, matériel recyclé provenant d'une éruption antérieure).

Toujours basé sur des critères macroscopiques, une seconde classification a ensuite été réalisée sur les fragments juvéniles et non-juvéniles. Pour les fragments juvéniles, plusieurs types de téphras peuvent être identifiés en se basant sur leur aspect général, leur forme et leur couleur (cf. **chapitres IV, V et VI**). De la même façon plusieurs types de fragments non-juvéniles peuvent être identifiés (cf. **chapitre VI**). L'utilisation d'un microscope optique et d'une loupe binoculaire a permis de travailler sur des fractions granulométriques jusqu'à l'échelle millimétrique.

Pour l'analyse des fractions granulométriques relativement petites à l'échelle micrométrique, le Microscope Electronique à Balayage (MEB) JEOL JSM-5910 LV a été utilisé. La préparation la plus utilisée pour l'utilisation du MEB est basée sur la construction de plots (25 mm de diamètre), où l'échantillon est enrobé dans de la résine époxy et poli progressivement jusqu'au ¼ de micron, puis métallisé au carbone. Les particules sont disposées aléatoirement au sein du plot et sur une surface adhérente pour éviter un tri artificiel des particules par densité au sein de la résine. L'échantillon est inséré dans la chambre du MEB où un vide de quelques mbar est mis en place. La zone source du MEB émet un faisceau d'électrons qui est ensuite canalisé et focalisé dans la colonne du MEB et balaye la surface de l'échantillon (la tension d'accélération utilisée est de 15 kV). L'analyse de l'énergie (EDS pour *Energy Dispersive Spectroscopy*) des électrons rétrodiffusés (BSE pour *Back Scattered Electron*) permet une imagerie de la texture de l'intérieur des cendres sur la section polie de la préparation (Reed 2005 et références incluses). L'image créée à partir de ce signal offre un contraste directement lié à la composition chimique de l'échantillon analysé : les zones claires sur les images BSE contiennent plus d'éléments lourds par rapport aux zones sombres. La texture des cendres peut être ensuite directement liée à un des composants de l'échantillon total. L'analyse d'au moins 200 particules par échantillon est nécessaire pour statistiquement atteindre une représentativité satisfaisante par rapport à l'échantillon étudié.

3.1.3. Mesure de la densité d'enveloppe et de la porosité

De par la taille et le nombre d'échantillon à analyser, les densités d'enveloppe ont été mesurées par différentes méthodes décrites successivement dans cette sous-partie. Pour des

fragments relativement grands deux différentes méthodes ont été utilisées (cf. **chapitres IV et V**). Dans certains cas, les échantillonnons trop volumineux pour ce type d'analyse (> 10 cm) ont été sciés. Enfin, une troisième procédure a été utilisée pour mesurer la densité des particules de cendres. (cf. **chapitre V**).

Pycnométrie à eau pour les lapilli, bombes et fragments de laves

Une première méthode a tout d'abord été utilisée reprenant la procédure analytique de Houghton et Wison (1989) et de Shea et al. (2010). Cette technique basé sur la poussée d'Archimède permet de calculer la densité d'enveloppe ($\rho_{enveloppe}$) d'un échantillon en mesurant sa masse dans l'air (m_{air}) et dans l'eau (m_{eau}) grâce à l'équation suivante :

$$\rho_{enveloppe} = \frac{m_{air}}{m_{air} - m_{eau}}$$

Afin d'imperméabiliser l'échantillon mesuré lors des pesées dans l'eau, l'application d'un parafilm autour de celui-ci est nécessaire. Cette masse ($m_{parafilm}$), potentiellement négligeable par rapport à la masse de l'échantillon, est néanmoins considérée dans le calcul de densité :

$$\rho_{enveloppe} = \frac{m_{air}}{m_{air} - m_{eau} + m_{parafilm}}$$

De cette façon, les densités des échantillons sont calculées et converties en masses volumiques ($kg.m^{-3}$). Dans le cas où les échantillons sont moins denses que l'eau, une cage solide est utilisée pour les immerger totalement. Sur une série de cinq mesures répétées, une reproductibilité relativement bonne est atteinte (écart-type maximum de ± 40 $kg.m^{-3}$ 1σ).

Utilisation du Geopyc 1360 de Micromeritics pour les lapilli et fragments de laves

En parallèle, l'utilisation du pycnomètre Geopyc 1360 de Micromeritics (Fig. 3.5a), a permis de mesurer les densités d'enveloppe de petites bombes et de lapilli (Kawabata et al.

2015). L'instrument est composé de plusieurs chambres cylindriques de diamètres connus (de 12 à 50 mm) selon la taille des échantillons. Le principe de l'instrument est de mesurer le volume interne de la chambre cylindrique utilisée dans laquelle sont insérés par étape un milieu solide et l'échantillon. Ce milieu solide, appelé DryFlo, est composé de petites sphères rigides (< 1 mm) présentant un haut degré de fluidité et permettant l'enrobage total de l'échantillon possédant des surfaces plus ou moins irrégulières. Si l'échantillon possède des pores inférieures à 1 mm, il est nécessaire d'imperméabiliser les échantillons avec du parafilm dont le volume est négligeable par rapport au volume d'enveloppe de l'échantillon. Après avoir choisi une chambre dont le diamètre est adéquat pour accueillir l'échantillon voulu, une première étape de calibration sans DryFlo ni échantillon mesure la position initiale du piston avec un volume interne nul (Fig. 3.5b). La force exercée sur le piston est reproductible et pré-calibrée pour chaque taille de chambre. Une deuxième étape consiste à introduire uniquement un montant suffisant de DryFlo pour potentiellement enrober la totalité de l'échantillon voulu. La position du piston est de nouveau mesurée par l'instrument (position A dans la Fig. 3.5b) pour établir une ligne de base uniquement avec le DryFlo. La troisième étape consiste à ajouter l'échantillon dans la chambre contenant le DryFlo. Un processus de rotation intermittent de la chambre lors du compactage de l'assemblage par le piston permet au DryFlo d'enrober uniformément l'échantillon, idéalement positionné au centre de l'assemblage. La position du piston est de nouveau mesurée par l'instrument (position B dans la Fig. 3.5b). A chaque étape, cinq cycles de mesures sont effectués pour obtenir des résultats moyennés et une reproductibilité relativement bonne (écart-type maximum de ± 30 $kg.m^{-3}$ 1σ). Le volume d'enveloppe ($V_{enveloppe}$) de l'échantillon est directement déduit de la différence des volumes cylindriques mesurés entre les étapes 2 et 3 :

$$V_{enveloppe} = \pi r^2 X$$

r étant le rayon de la chambre cylindrique et X la différence de position du piston entre les étapes 2 et 3 (Fig. 3.5b). Cette procédure instrumentale est rapidement décrite dans le **chapitre IV** introduisant un facteur de conversion v (égal à $\pi.r^2$), simplifiant l'équation ci- dessus, v étant directement dépendant de la valeur du rayon de la chambre cylindrique utilisée. La densité d'enveloppe ($\rho_{enveloppe}$) des échantillons est directement calculée en divisant la masse de l'échantillon (m_{air}) par le volume d'enveloppe mesuré ($V_{enveloppe}$) et convertie par la suite en masse volumique ($kg.m^{-3}$).

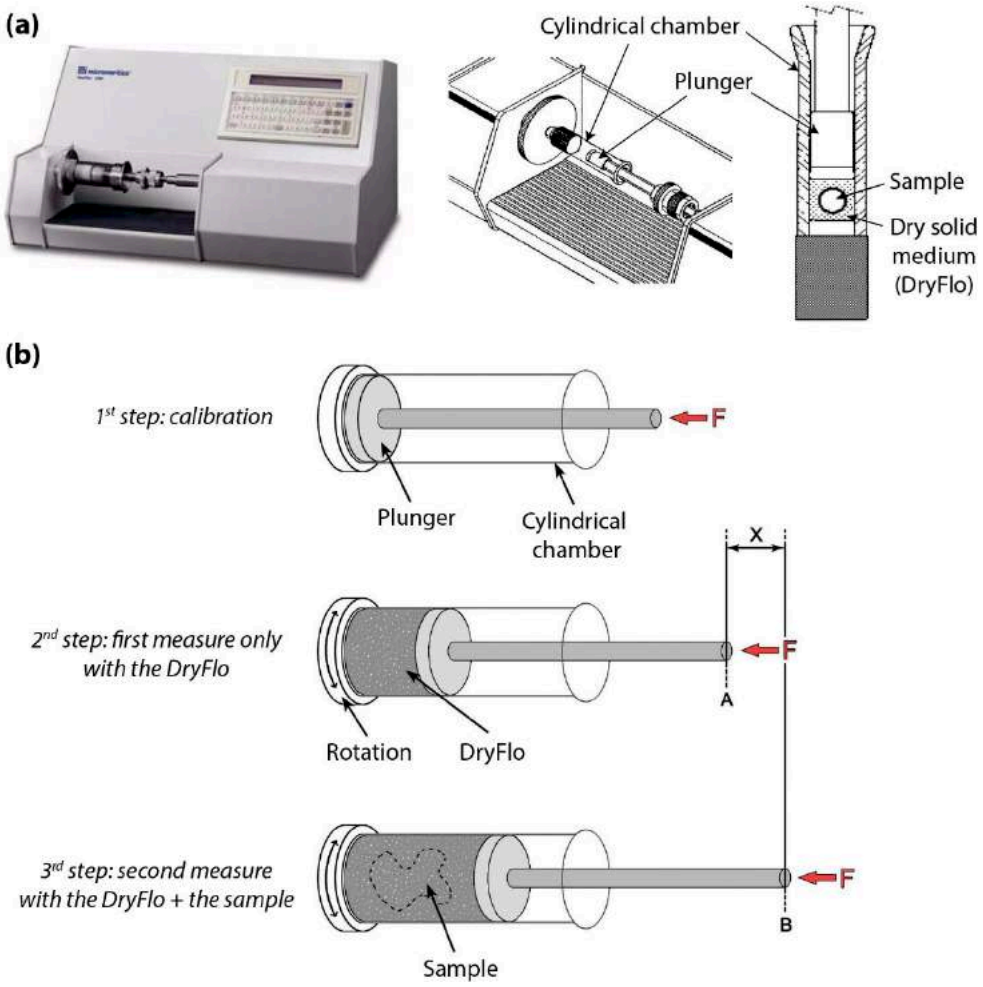

Figure 3.5 *– (a) Schéma montrant les principales caractéristiques instrumentales du GeoPyc 1365 de Micromeritics. (b) Schéma montrant les étapes de mesures réalisées pour calculer la densité d'enveloppe des échantillons. F représente la force de consolidation constante pour la suite de mesures, appliquée sur le piston.*

Les mesures de densité effectués lors de ces travaux de thèse montrent que les résultats issus des deux méthodes décrites précédemment et utilisées pour mésuser la densité de fragments de laves, bombes et lapilli, sont relativement similaires et que les erreurs de mesure engendrées par ces techniques analytiques sont négligeables par rapport à la variation de densité naturelle des échantillons mesurés (cf. **chapitre IV**).

Pycnométrie à eau pour les cendres

Les deux méthodes de mesure de densité précédemment décrites ne s'appliquent uniquement que pour des échantillons de tailles moyennes supérieures à environ 1 cm. Par conséquent une troisième méthode de pycnométrie a été utilisée pour les échantillons relativement petits, notamment les cendres (cf. **chapitre V**). Cette méthode reprend le principe utilisée par la pycnométrie à eau pour les gros échantillons. Cependant, le protocole expérimental a été adapté pour la mesure de petites particules et décrit par Eychenne (2012), Eychenne et Le Pennec (2012) et Fréret-Lorgeril (2019). Ce protocole consiste à mesurer la masse de plusieurs particules de cendres dans l'air et dans l'eau. La densité d'enveloppe ainsi obtenue est la moyenne de la densité de l'ensemble des particules mesurées. Pour des particules de cendres, la tension de surface de l'eau est considérée comme suffisamment élevée pour empêcher l'eau de rentrer dans les vésicules potentiellement présentes dans les cendres. Le pycnomètre utilisé est une fiole en verre dont le bouchon est doté d'un trait de jauge renseignant le volume précis de l'intérieur de la fiole. Cette précision expérimentale, ainsi que l'utilisation d'une balance de haute précision (jusqu'à 10^{-3} g), sont nécessaires au calcul de pycnométrie à eau car les masses utilisées pour ces mesures sont relativement faibles.

Mesure de la densité de la roche totale et calcul de la porosité

Dans le but de déterminer le taux de porosité à partir de la densité d'enveloppe des échantillons, la densité squelettique ou densité de roche totale (ρ_{dense}) des échantillons doit être connue. ρ_{dense} correspond à la densité des produits éruptifs sans prendre en compte la porosité et dépend de la composition du liquide magmatique et des cristaux que composent le magma. En considérant qu'une éruption émet un magma chimiquement homogène, les mesures de ρ_{dense} sont similaires et moyennées sur deux échantillons juvéniles, représentatifs chaque l'éruption étudiée (cf. **chapitres IV et V**). Le volume solide de chaque poudre ainsi obtenue est ensuite mesuré grâce au pycnomètre à hélium Accupyc II 1340 de Micromeritics (Fig. 3.6). L'utilisation de l'hélium est relativement bien adaptée pour ce type de mesure car ce gaz inerte

peut s'infiltrer dans les aspérités les plus petites, pour ne mesurer que le volume solide de la poudre.

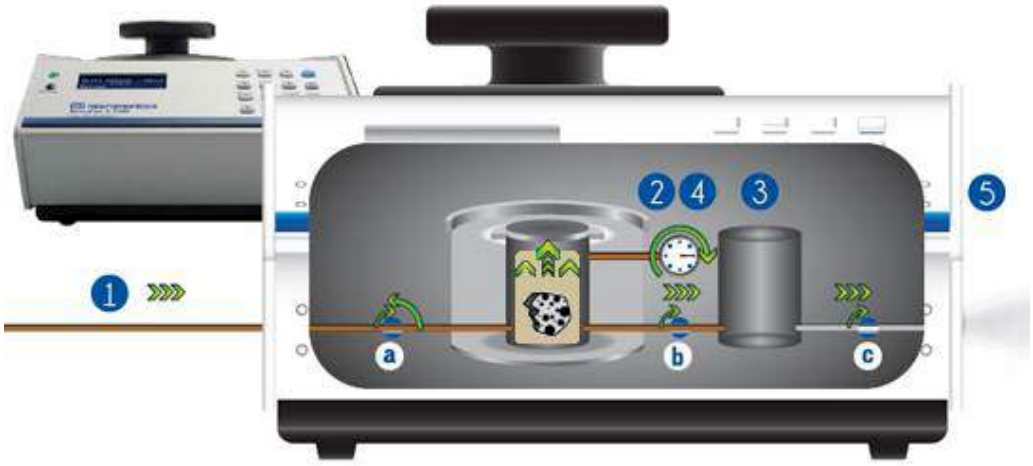

Figure 3.6 *– Schéma montrant le fonctionnement de l'AccuPyc II 1340 de Micromeritics. Voir le texte ci-dessus pour la procédure expérimentale.*

Après avoir calibré le pycnomètre avec des objets de volumes connus et introduit l'échantillon dans une chambre étanche et appropriée (volumes internes de 350, 100, 35 ou 10 cm^3), une première valve (a) s'ouvre et l'hélium s'écoule dans la chambre où se trouve l'échantillon (étape 1 dans la Fig. 3.6). Une fois l'équilibre de pression atteint, la valve (a) se referme puis la pression du gaz (P_1) et la température (T_1) sont mesurées (étape 2 dans la Fig. 3.6). Ensuite, la deuxième valve (b) s'ouvre laissant la quantité d'hélium utilisée dans la première chambre, circuler dans la seconde, de volume connu V_2 (étape 3 dans la Fig. 3.6). La pression (P_2) et la température (T_2) sont une nouvelle fois mesurées (étape 4 dans la Fig. 3.6). La pression est ensuite évacuée de l'instrument (étape 5 dans la Fig. 3.6). Dans le cas de l'hélium, la loi des gaz parfaits est applicable et pour un volume molaire équivalent (pas de perte de gaz entre les deux chambres), cette loi donne :

$$\frac{P_2 V_2}{P_1 V_1} = \frac{T_2}{T_1}$$

où V_1 est le volume de la chambre de l'échantillon ($V_{chamber}$) moins le volume solide de l'échantillon (V_{dense}). L'instrument mesure et calcule directement le V_{dense} de cette façon (m^3):

$$V_{dense} = V_{chamber} - \frac{P_2 V_2 T_1}{T_2 P_1}$$

Les mesures sur V_{dense} sont reproductibles jusqu'à 10^{-8} m^{-3}. En divisant la masse de l'échantillon par V_{dense}, ρ_{dense} est ainsi obtenue ($kg.m^{-3}$). Grâce à la relation donnée par Houghton et Wilson (1989), la porosité (P) des échantillons est ainsi calculé (vol%) :

$$P = \frac{100\ (\rho_{dense} - \rho_{enveloppe})}{\rho_{dense}}$$

3.1.4. Mesure de la connectivité des vésicules

L'utilisation de cette procédure instrumentale permet aussi de mesurer le taux de connectivité entre les vésicules d'un échantillon intact non-broyé (Colombier et al. 2017a, 2017b). Le volume d'hélium va ainsi remplir les vésicules connectées de l'échantillon, sans remplir les vésicules isolées. Formenti et Druitt (2003) établie la relation suivante, permettant de calculer le taux de la porosité interconnectée (P_c) :

$$P_c = 1 - \frac{V_{dense}}{V_{enveloppe}}$$

Le degré de connexion des vésicules (c) est obtenu en normalisant P_c à la porosité totale P (vol%) :

$$c = \frac{100\ P_c}{P}$$

3.1.5. Mesure de la perméabilité à l'air

La perméabilité à l'air d'une sélection d'échantillon de plusieurs éruptions (cf. **chapitres V et VI**) a été mesurée en suivant la procédure expérimentale de Colombier et al. (2017a) et Gurioli et al. (2018). La perméabilité représente la capacité d'un matériau à laisser passer un fluide sous un gradient de pression. Les échantillons doivent avoir une taille moyenne supérieure à environ 2 cm (lapilli et bombes) pour la préparation exigée pour ce type de mesure.

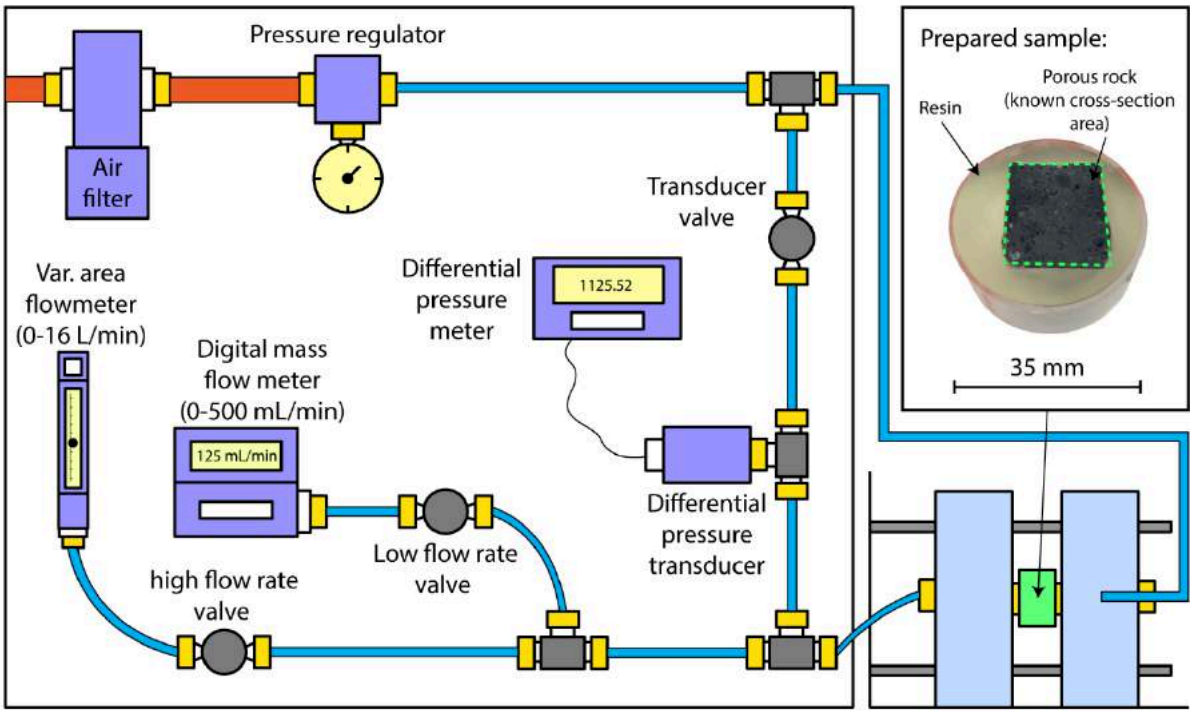

Figure 3.7 *– Schéma montrant le fonctionnement du perméamètre basé sur les plans de Takeuchi et al. (2008), ainsi que l'aspect final d'un échantillon prêt à être analysé.*

Les fragments sélectionnés (porosité et connectivité des vésicules préalablement mesurées) sont tout d'abord coupés en prismes rectangulaires ce qui permet de connaitre de manière précise les longueurs, aires et volume de chaque échantillon, nécessaires au calcul de perméabilité. Les côtés de chaque prisme, (sans les deux extrémités) sont ensuite recouverts d'une fine pellicule de résine visqueuse époxy. Chaque prisme sont intégralement enveloppés de parafilm, de façon à ce qui la fine pellicule de résine époxy préalablement déposée à la surface des côtés de chaque échantillon adhère parfaitement au parafilm sans que cette résine ne rentre dans les pores de l'échantillon. Les échantillons sont enfin enrobés de résine époxy dans des moules en les disposant de telle façon que leurs extrémités ne soit pas en contact direct avec la résine remplissant les moules. Le but final de cette préparation est d'avoir des échantillons de forme prismatique rectangulaire, enrobés de résine, tout en préservant leurs structures internes et leurs extrémités (Fig. 3.7). Les échantillons préparés sont placés dans un porte-échantillon directement relié au perméamètre construit au LMV (Fig. 3.7) selon le système expérimental mis en place par Takeuchi et al. (2008). Une fois l'échantillon branché de façon imperméable au circuit d'air de l'instrument, plusieurs mesures de débit d'air ($L.min^{-1}$) et de pression différentielle (Pa) sont réalisées pour différentes pressions d'air initiales. La

pression d'air initiale est directement paramétrée grâce à un régulateur de pression. La pression différentielle (différence entre la pression d'arrivée avant le passage dans l'échantillon et la pression de retour après le passage dans l'échantillon) est mesurée par un manomètre différentiel entre 0 et 200000 Pa. Le débit d'air final est mesuré par deux débitmètres, l'un mesurant des faibles débits relativement précisément de 0 à 0,5 $L.min^{-1}$, l'autre mesurant des débits plus élevés allant de 0 à 16 $L.min^{-1}$. La pression d'air est évacuée au niveau des débitmètres. La corrélation entre le débit d'air et la pression différentielle permet de résoudre l'équation de Darcy-Forchheimer pour un fluide compressible (Rust et Cashman 2004 ; Yokoyama et Takeuchi 2009 ; Bai et al. 2010). Cette équation est applicable pour mesurer la perméabilité d'un échantillon poreux grâce à l'inertie d'un fluide (dans notre cas l'air) :

$$\frac{{P_2}^2 - {P_1}^2}{2\,P_0\,L} = \frac{\mu_{gas}}{k_1} q + \frac{\rho_{gas}}{k_2} q^2$$

où k_1 (m^2) est la perméabilité visqueuse (ou darcienne), k_2 (m^2) est la perméabilité inertielle (ou non-darcienne), q est le débit volumétrique d'air par l'aire de la coupe transversale de l'échantillon ($m.s^{-1}$), P_0 (~101325 Pa = 1 atm) est la pression à laquelle est mesurée le débit d'air est mesuré, P_2 et P_1 sont respectivement les pressions d'entrée (Pa) et de sortie (~101325 Pa = 1 atm) de l'échantillon, L est la longueur de l'échantillon (m), ρ_{gas} et μ_{gas} sont respectivement la densité (1,2041 $kg.m^{-3}$ pour une température ambiante de 20 °C) et la viscosité (1,81 10^{-5} Pa.s) de l'air. En recalculant q (utilisant le débit d'air et l'aire de la coupe transversale de l'échantillon), k_1 et k_2 sont obtenus à partir du meilleur fit polynomial du deuxième ordre.

Dans le cas de l'utilisation de l'air et dans la gamme de débits utilisés, les effets d'inertie sont négligeables par rapport aux effets visqueux. La perméabilité visqueuse (ou darcienne) est donc le paramètre retenu pour ce genre de mesure (Bai et al. 2010).

3.1.6. Analyse de la morphologie des cendres

L'analyseur optique Morphologi G3 de Malvern (Fig. 3.8a) a été utilisé (cf. **chapitres V et VI**) dans le but de mesurer et de quantifier la morphologie des particules de cendres (Leibrandt et Le Pennec 2015 ; Fréret-Lorgeril 2019). Cet instrument permet d'analyser un grand nombre de particules dans un temps de mesure relativement court, en termes de taille, de forme et de transparence.

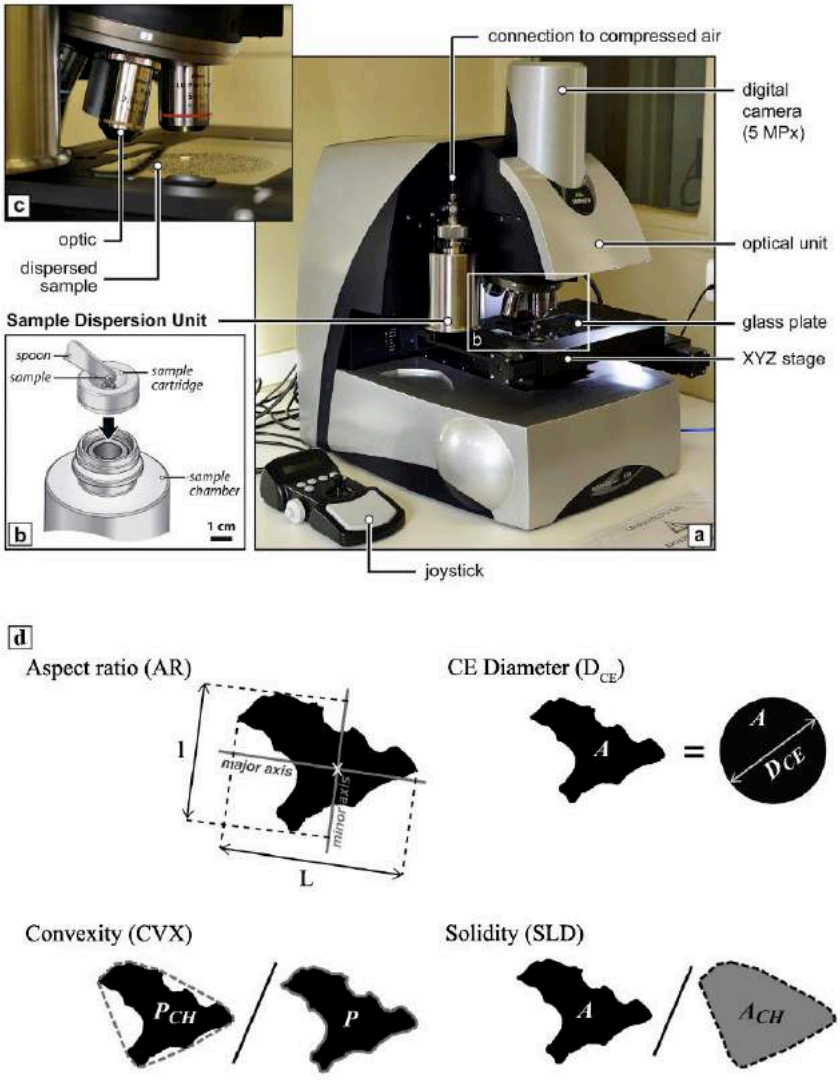

Figure 3.8 *– Schéma du fonctionnement du Morphologi G3 de Malvern. (a) Vue d'ensemble de l'instrument et de ses principales caractéristiques. (b) Optiques de l'instrument. (c) Schéma de la procédure de dispersion de l'échantillon cendreux. (d) Principales caractéristiques morphométriques d'une particule mesurées dans ce travail de thèse. Figure modifiée d'après Leibrandt et Le Pennec (2015).*

Chaque analyse est focalisée sur une seule classe granulométrique déterminée par tamisage manuel ¼ Φ. Les classes granulométriques sont généralement choisie par rapport à la représentativité de l'échantillon total, c'est-à-dire en choisissant la classe granulométrique la plus massique et volumineuse du dépôt total. Dans un souci de compatibilité, les résultats sur la morphologie des cendres sont comparés sur des classes granulométriques similaires car la morphologie d'un même dépôt de cendre varie potentiellement selon la taille des grains. Une fois la classe granulométrique choisie et isolée du dépôt total, les particules de cendres sont parfois lavées à l'eau ou à l'éthanol et en utilisant des ondes ultrasons, pour supprimer d'éventuelles microparticules ou dépôts secondaires pouvant modifier la forme primaires des particules. Dans le cas où l'échantillon est composé de plusieurs composants, les particules sont triées pour potentiellement analyser l'échantillon composant par composant. Après séchage et homogénéisation, une partie de l'échantillon est introduit dans l'unité de dispersion de l'instrument (Fig. 3.8b) dans des proportions variables selon la taille des grains, grâce à des cuillères dont les volumes sont standardisés (de 1 à 19 mm^3). La quantité de particules introduite dans l'unité est ensuite dispersée au sein d'une chambre de la forme d'une cloche par un flux d'air dont la pression et la durée sont paramétrées selon la taille des grains. Les cendres se dispersent et sédimentent sur une plaque de verre. Idéalement, les cendres sédimentent individuellement sur la plaque.

Une illumination diascopique (par le bas) des particules permet à un ensemble de six optiques (× 1, × 2,5, × 5, × 10, × 20 et × 50) et une caméra digitale de capturer la projection en deux dimensions (APASH) de chaque particule. La plaque où sont déposées les particules est montée sur une platine motorisée permettant le mouvement de la plaque en trois dimensions (Fig. 3.8c). Ainsi, à chaque mouvement horizontal de la plaque, l'instrument acquiert une image et repère de façon programmée les contours des particules (seuil défini par l'utilisateur). Le logiciel de traitement d'image associé assemble automatiquement les particules coupées entre plusieurs prises d'images. La ou les optiques utilisées dépendent de la taille des particules, et une mise au point multiple sur chaque prise d'image (mouvement vertical de la plaque) permet une mesure relativement précise de la morphologie des particules. L'étendu de l'analyse sur plaque de verre est initialement choisie selon une estimation du nombre de particules présentes. Statistiquement, et grâce à des tests empiriques, une mesure peut être considérée robuste à partir d'environ 1000 particules.

La résolution de la caméra digitale (5 Mpx) ainsi que l'utilisation d'optiques adéquates permettent une erreur analytique relativement faible. Un traitement manuel des données brutes

est cependant nécessaire pour filtrer et supprimer les particules potentiellement mal dispersées (agglomérats), floues (mise au point) ou encore mal recomposées par le logiciel.

Les paramètres de tailles et de formes sont automatiquement calculés par l'instrument (Fig. 3.8d). Outre la mesure de la longueur (L) et la largeur (l) des particules, permettant de calculer leur élongation (AR pour *aspect ratio*, qui est égal à l/L), le diamètre équivalent à un cercle de la particule est systématiquement calculé : ce diamètre (µm) est égal au diamètre du disque dont l'aire est équivalente à la particule mesurée. La mesure directe du périmètre (P) et de l'aire (A) de chaque particule, ainsi que le périmètre et l'aire de leur enveloppe convexe (P_{CH} et A_{CH} respectivement), permettent aussi de définir les paramètres de convexité (CVX) et de solidité (SLD) selon ces formules :

$$CVX = \frac{P_{CH}}{P} \quad et \quad SLD = \frac{A}{A_{CH}}$$

où la CVX et SLD sont des valeurs sans dimensions comprises entre 0 et 1, et représentent respectivement la rugosité texturale (à petite échelle) et la rugosité morphologique (à l'échelle de la particule). Leibrandt et Le Pennec (2015) ainsi que Liu et al. (2015) résument l'ensemble des paramètres de forme existant dans la littérature.

Les cristaux libres et les cendres purement vitreuses peuvent être aussi identifiés grâce au taux de lumière que ce type de particules laisse passer lors de l'analyse, contrairement aux particules opaques microcristallines qui ne laissent passer aucun rayonnement lumineux (cf. **chapitre VI**).

3.2. Mesures des textures microscopiques internes

Une fois les mesures des paramètres apparents effectuées, une sélection d'échantillon est réalisée pour l'analyse microscopique des vésicules et des cristaux présents au sein des produits éruptifs. Pour chaque éruption étudiée, cette sélection comprend au moins un échantillon de chaque composant juvénile préalablement identifié dans les produits éruptifs. Des lames minces et des plots sont ensuite réalisés sur l'ensemble des échantillons sélectionnés pour les microanalyses. L'objectif est de quantifier et caractériser la distribution de la taille des

vésicules et des cristaux, ainsi que la densité du nombre de vésicules (N_V) et de cristaux (N_C) pour chaque échantillon.

3.2.1. Préparation des échantillons et acquisition des images

Pour l'étude des produits éruptifs de grande et taille (fragments de lave, bombes et gros lapilli), des lames minces polies et métallisées au carbone sont réalisées (dimensions latérales de 30 × 45 mm et de 30 µm d'épaisseur de roche). Les échantillons friables et poreux sont préalablement enrobés de résine époxy. Pour l'étude de cendres, des plots sont réalisés et métallisés dans lesquels les particules de cendres, dont la taille de grain est au préalable choisie selon la PSD du dépôt, sont enrobés et polies dans de la résine époxy. L'objectif de ce type d'analyse est de quantifier l'ensemble des vésicules et des cristaux présents dans l'échantillon, en partant des plus gros objets, visibles à l'œil nu au sein de la mince, jusqu'au plus petits, non-visibles à l'œil nu, nécessitant une imagerie plus fine au MEB.

Pour ce faire, et pour chaque échantillon, la lame mince (pour les plus gros échantillons) est tout d'abord scannée et numérisée en lumière naturelle ainsi qu'en lumière polarisée, en utilisant des feuilles polarisantes disposées perpendiculairement et de part et d'autre de la lame mince scannée. La numérisation en lumière polarisée permet d'identifier clairement les phénocristaux potentiellement visibles au sein de la lame mince. Cette étape permet d'obtenir un premier niveau de grossissement et d'identifier les plus grosses vésicules et les plus gros cristaux présents dans l'échantillon étudié. Une multitude d'images BSE sont ensuite acquises au MEB. Le choix des différents grandissements est directement lié aux gammes de taille des vésicules et des cristaux. De façon générale, deux grossissements à × 25 et × 100 suffisent à obtenir une résolution d'image satisfaisante pour caractériser les plus petits objets présents au sein des échantillons. Shea et al. (2010) montre qu'un grandissement de × 100 est suffisant pour imager des objets de diamètre équivalent à 5 µm, sans générer d'erreur analytique significative. La figure 3.9 représente la stratégie d'imagerie adoptée pour chaque échantillon analysé. Dans un souci de représentativité, plus le grossissement est fort, plus le nombre d'image prises en compte est élevé pour avoir suffisamment de vésicules et de cristaux mesurés. De manière empirique, environ 1000 objets (vésicules ou cristaux) mesurés suffisent à représenter

correctement et statistiquement la porosité ou la cristallinité de l'échantillon (Cabré Brullas 2015). Pour l'analyse texturale des cendres, des images MEB sont acquises particules par particules jusqu'à atteindre le nombre d'objets suffisant pour que la mesure soit statistiquement représentative de la texture réelle de l'échantillon analysée.

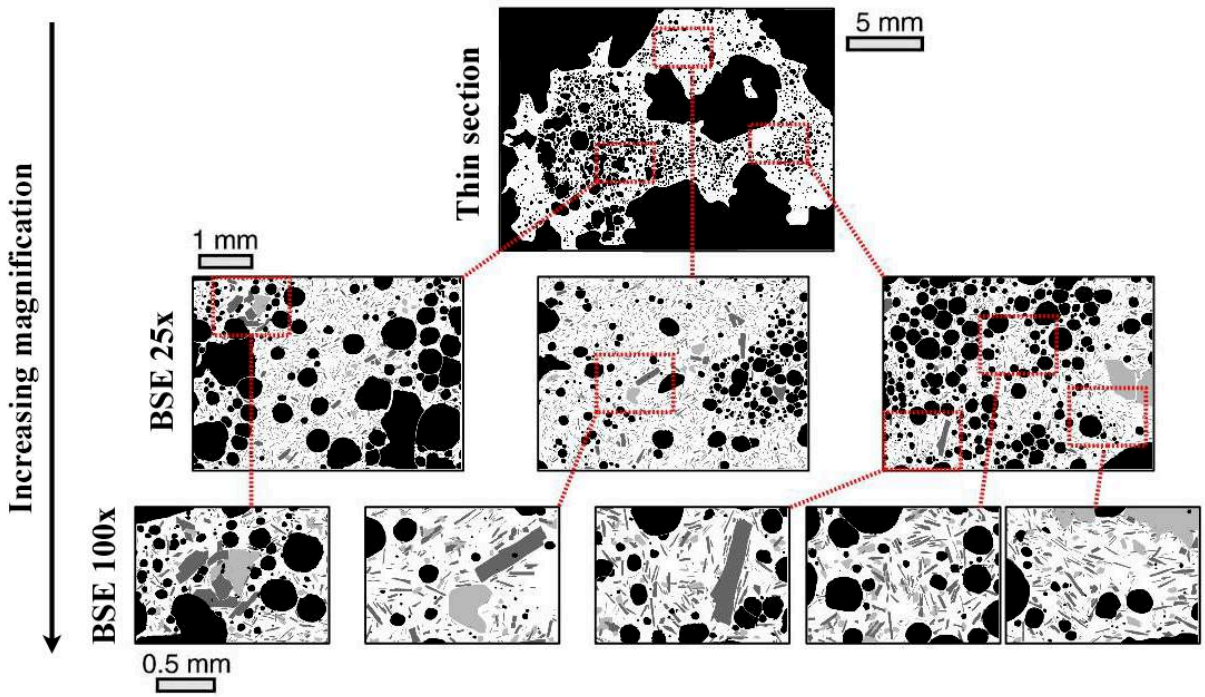

Figure 3.9 *– Procédure d'analyse texturale (vésicules et cristaux) sur des échantillons de type bombes, lapilli ou fragments de lave, permettant le mesure intégrée des plus grands (lame mince) mais aussi des plus petits (images MEB x25 et x100) objets (vésicules et cristaux). Les images sont issues de la binarisation d'un ensemble d'images optiques (lame mince) et d'images BSE (MEB) d'un échantillon (lapilli) issu de l'éruption de Juillet 2015 au Piton de la Fournaise.*

3.2.2. Traitement des images

Une fois que les images optiques et électroniques de chaque échantillon ont été acquises, une binarisation des images est nécessaire afin de faciliter l'analyse texturale et de clairement identifier et classifier chaque type d'objets présents dans les images. Généralement ce traitement d'image est réalisé sous le logiciel Adobe Photoshop, où le verre magmatique est représenté en blanc, les vésicules en noirs et les différents types de cristaux en différents niveaux de gris (Figs. 3.9 et 3.10).

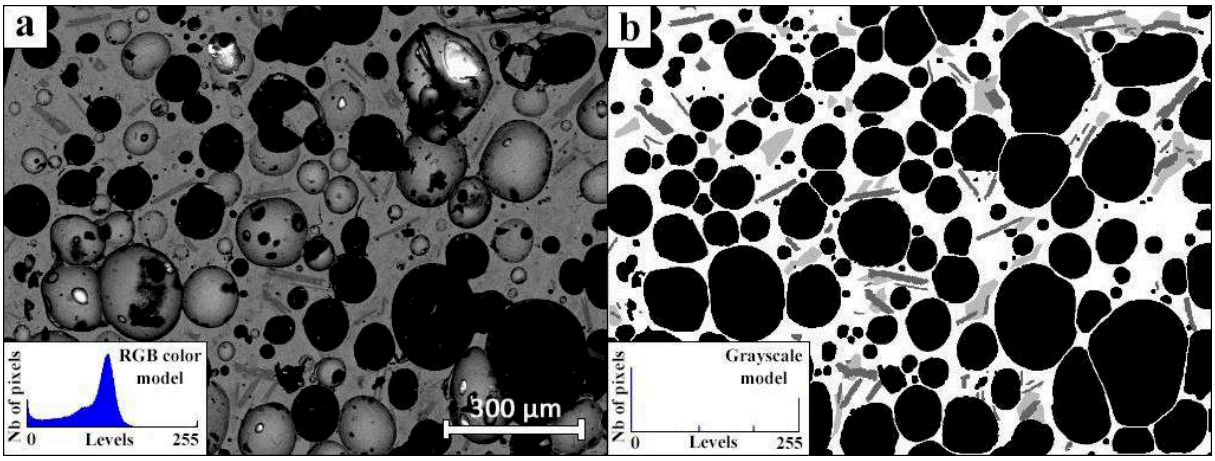

Figure 3.10 *– Exemple de processus de binarisation. (a) Image BSE brute. (b) Image transformée en échelle de gris ou chaque niveau de gris représente un type de texture (verre magmatique en blanc, vésicules en noir, plagioclases en gris foncé, clinopyroxènes en gris clair).*

3.2.3. Caractérisation de la porosité avec le programme FOAMS

Le programme FOAMS (*Fast Objects Analysis and Measurement System*) est un programme Matlab qui permet la caractérisation complète de la texture des vésicules des échantillons (Shea et al 2010). A partir d'images préalablement binarisées en niveaux de gris, ce programme mesure et caractérise l'ensemble des objets identifiés sur ces images (vésicules et cristaux). Pour ce faire, les images binarisées ainsi que leurs facteurs d'échelle associés

($px.mm^{-1}$) sont tout d'abord importées dans le programme. La taille minimum désirée des objets mesurés est ensuite précisé dans le but de supprimer le bruit potentiel associé aux processus de binarisation. Cette taille minimum choisie est généralement de 5 pixels (équivalent à un objet de 6 µm de diamètre sur une image BSE acquise à un grandissement × 100) pour permettre au programme de mesurer les plus petites vésicules et plus petits cristaux (généralement plus grands que ce seuil de mesure) tout en s'affranchissant du bruit potentiel des images.

Le programme va ensuite compter et mesurer les caractéristiques de chaque type d'objet préalablement déterminé selon leur niveau de gris. Les différents grandissements d'images sont ensuite intégrés. L'un des principaux atouts de ce programme est d'ensuite à appliquer des schémas de conversions stéréologiques (en trois dimensions) aux vésicules mesurées sur une section à deux dimensions en considérant des vésicules sphériques à partir des paramètres introduit par Underwood (1972) et des équations de Sahagian et Proussevitch (1998). La porosité totale de chaque échantillon, la distribution de la taille des vésicules (VSD pour *Vesicle Size Distribution*), ainsi que la densité du nombre de vésicules par mm^{-3} (N_V) sont calculées à partir des densités du nombre de vésicules par unité de surface (mm^{-2}) pour les différentes tailles de vésicule observées. Selon que la croissance des bulles a lieu avant, pendant ou après la formation des phases cristallines et notamment des phénocristaux, une correction sur la valeur de N_V est effectuée pour d'affranchir du volume de ces phénocristaux, qui se forment potentiellement avant la remontée du magma vers la surface. En considérant que les vésicules observées se sont formées lors de la remontée du magma, la valeur de N_V peut être indirectement liée au taux de décompression du magma lors de sa remontée (cf. **chapitres IV et V**) en utilisant le modèle de Toramaru (2006).

Un dernier paramètre directement lié à la porosité est le ratio entre le volume de vésicule et le volume de liquide des échantillons (V_G/V_L) est calculé (Gardner et al. 1996). Ce rapport est corrigé du taux de phénocristaux éventuellement présent dans les échantillons, pour ne prendre qu'en compte le volume des vésicules et le volume du liquide magmatique.

3.2.4. Caractérisation de la cristallinité avec la base de données CSDslice et le programme CSDcorrections

La même procédure analytique que pour les vésicules est appliquée pour l'analyse texturale des cristaux. Cependant le programme FOAMS ne permet pas la conversion stéréologique des surfaces des cristaux (deux dimensions), en volume (trois dimensions), car ils ne sont pas forme sphérique. La détermination précise des trois dimensions (petit, moyen et grand axes) des différents types de cristaux est donc nécessaire. A partir des données brutes analytiques de FOAMS, le petit axe et grand axe des cristaux (en deux dimensions) sont dans un premier temps recueillis. La base de données nommée CSDslice et établie par Morgan et Jerram (2006) regroupe un ensemble de plus de 700 types de cristaux de formes connues et sur lesquels une série de sections aléatoires ont été réalisées. De façon empirique, le ratio petit axe sur grand axe est alors corrélé à l'ensemble de la base de données CSDslice (Fig. 3.11). La meilleure correspondance empirique est choisie et retenue lorsque le coefficient de détermination R^2 est supérieur à 0,80.

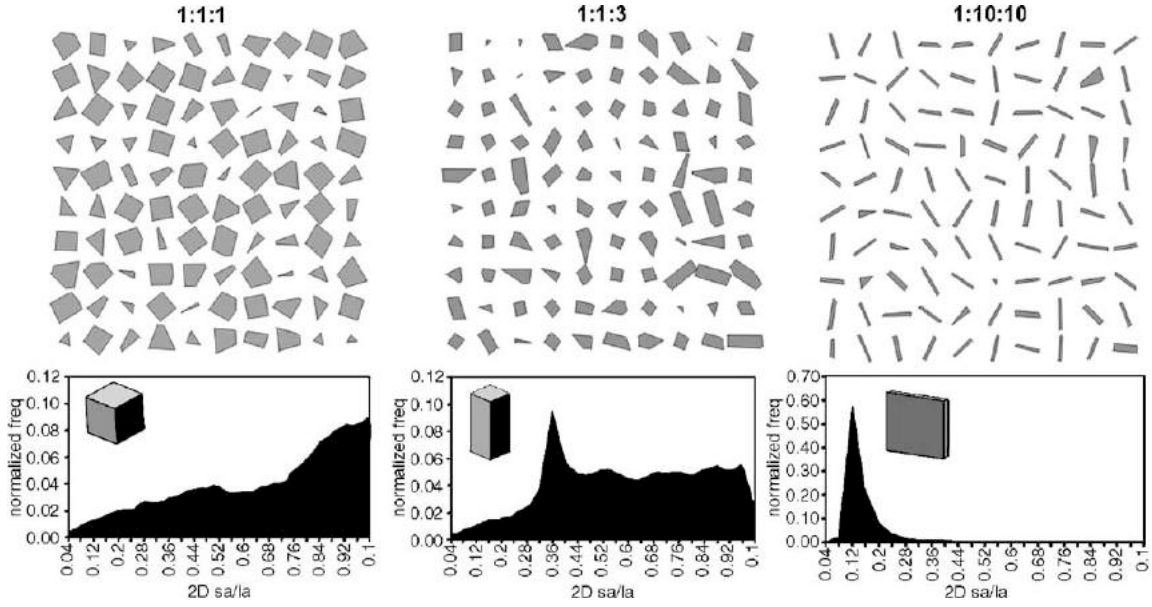

Figure 3.11 *– Sections aléatoires à travers trois formes en trois dimensions connues associées à leurs courbes de forme (fréquence normalisée vs. Ratio petit axe : grand axe des données en deux dimensions). Ces données en deux dimensions peuvent être corrélées à une base de données établie par Morgan et Jerram (2006) pour ainsi retrouver la forme en trois dimensions des cristaux étudiés notée x : y : z (petit : intermédiaire : grand axe).*

De façon similaire au programme FOAMS, le logiciel CSD corrections (Higgins 2000) convertit des unités de surface en volume en utilisant des lois de probabilité d'intersection, appropriées à des formes non-sphériques et de dimensions connues : les données brutes mesurées par FOAMS concernant les densités du nombre de cristaux par mm^{-2} pour les différentes tailles de cristaux observées, sont introduites dans le logiciel CSDcorrections. La circularité apparente des cristaux peut aussi être ajustée. De cette façon, la cristallinité de chaque échantillon, la distribution de la taille des cristaux (CSD pour *Crystal Size Distribution*) ainsi que la densité du nombre de cristaux par mm^{-3} (N_C) sont calculées. De façon similaire au paramètre N_V pour les vésicules, la valeur de N_C pour les microlites se formant lors de la décompression du magma peut être liée au taux d'exsolution d'H_2O lors de la remontée du magma vers la surface (cf. **chapitres IV et V**) en utilisant le modèle de Toramaru et al. (2008).

3.3. Analyses géochimiques

3.3.1 Analyse de la composition des roches totales par ICP-AES

Pour chaque éruption étudiée, la composition chimique en éléments majeurs des produits éruptifs est tout d'abord mesurée en choisissant des fragments de lave ou pyroclastes de grande taille. Idéalement, plusieurs types de composant ainsi que des produits éruptifs émis à différentes dates sont choisis pour identifier d'éventuelles variations chimiques temporelles. Chaque échantillon est réduit en poudre à l'aide d'un concasseur puis d'un mortier. La poudre obtenue est ensuite mélangée à une poudre de métaborate de lithium ($LiBO_2$), placée dans un creuset en graphite et fondues dans un four à induction à 1050 °C pendant environ cinq minutes. Un verre homogène est ainsi produit et dissous rapidement dans une solution aqueuse et d'acide nitrique (HNO_3) puis dilué 2000 fois. La perte au feu des poudres lors de la fusion est quantifiée en deux étapes de chauffage à 110 et 1000 °C. La solution finale est finalement analysée par Spectrométrie à Plasma à Couplage Inductif (ICP-AES pour *Inductively Coupled Plasma Optical Emission Spectroscopy*) avec le spectromètre Ultima-C Jobin Yvon de Horiba (Gurioli et al. 2018). La solution est introduite dans le spectromètre et évaporée dans une chambre de nébulisation puis ionisée dans un plasma d'argon à très haute température. Les atomes de la

solution sont ainsi excités et les électrons de ces atomes émettent des photons lorsqu'ils repassent à l'état fondamental. Cette lumière, émise dans des longueurs d'onde caractéristiques des éléments présents dans l'échantillon, est analysée et comparée à différents étalons de composition connue. Cette technique d'analyse est suffisamment précise pour les éléments majeurs dont les concentrations sont suffisamment élevées dans les échantillons mesurés.

3.3.2. Analyse des verres et des cristaux par microsonde électronique

Des analyses ponctuelles sur les verres magmatiques et les cristaux sont effectuées grâce à la microsonde électronique (EPMA pour *Electron Probe Micro-Analyzer*) SX100 de Cameca en utilisant une tension d'accélération de 15 kV et un courant de 4 à 8 nA. Un faisceau de 5 à 10 µm de diamètre a été utilisé pour l'analyse des verres alors qu'un faisceau focalisé d'un µm a été utilisé pour l'analyse des cristaux (Gurioli et al. 2018). De façon analogique au MEB, les échantillons analysés (lames minces et plots) sont polis et métallisés au carbone. L'EPMA analyse l'émission des rayons X produite par l'interaction des électrons incidents et les éléments constituant l'échantillon. Ces rayons X, dont la longueur d'onde est caractéristique des atomes présents dans l'échantillon, sont analysés par quatre spectromètres à dispersion de longueur d'onde (WDS pour *Wavelength Dispersion Spectrometer*).

3.3.3. Identification des phases minérales par diffractométrie de rayons X (XRD)

Afin d'identifier certaines phases minérales présentes dans les échantillons de cendres (cf. **chapitre VI**) réduits en poudre, des analyses de diffractométrie de rayons X (XRD pour *X-ray diffraction*) ont été réalisées grâce au diffractomètre Panalytical Empyrean, exploité à 43 kV et 38 mA et avec utilisant le rayonnement K-alpha d'une anode en cuivre. Les phases minérales sont ensuite identifiées à l'aide des bases de données ICSD (*Inorganic Crystal Structure Database*) et COD (*Crystallography Open Database*).

3.3.3. Utilisation de données expérimentales

En parallèle des mesures géochimiques effectuées sur les échantillons naturels, des données sur des mesures expérimentales effectuées par Brugier (2016) ont été exploitées (cf. **chapitre IV**). L'ensemble de ces données se présentent en deux séries d'expériences de refroidissement à partir d'une température de 1225 °C et reprenant la composition chimique du magma de Novembre 2009 au Piton de la Fournaise. La première série d'expériences est réalisée à 50 MPa (pression de saturation de H_2O et de CO_2 enregistrée au sein des inclusions vitreuses dans les olivines au Piton de la Fournaise, Di Muro et al. 2014, 2016) avec des teneurs en H_2O dissoutes variant de 0.5 à 1.6 pds%. Ces conditions sont censées représenter les conditions magmatiques au sein du réservoir superficiel principal du Piton de la Fournaise. La seconde série d'expériences est réalisée à pression atmosphérique et dans des conditions anhydres, censées représenter les conditions magmatiques en sub-surface de produits éruptifs dégazés.

La composition des liquides et des phases cristallines à différents pas de températures sont ainsi comparées aux compostions des échantillons naturels et permettent la mise en place de deux géothermomètres basés sur la composition en MgO des liquides magmatiques, à 50 MPa et dans des conditions atmosphériques dégazées (cf. **chapitre IV**).

4. Utilisation des données de surveillance

Dans le cadre de cette thèse et pour l'étude des éruptions actuelles au Piton de la Fournaise (cf. **chapitre IV et V**), des données de surveillance ont été utilisées pour quantifier et comprendre les différents mécanismes pré-éruptifs à l'origine des éruptions. Ces données géophysiques (sismicité et déformation du sol) et géochimiques (compositions et concentration des gaz) sont principalement acquises par le réseau de surveillance de l'OVPF (Peltier et al. 2016 ; 2018). En parallèle, des mesures des flux magmatiques par télédétection sont aussi utilisées.

4.1. Données acquises par l'OVPF : sismicité, déformation du sol et dégazage

Le réseau de surveillance de l'OVPF et constitué d'une multitude de stations (environ 100 instruments déployés sur 35 sites) permettant l'acquisition de données sur l'activité du Piton de la Fournaise en continu. La sismicité est enregistrée de façon permanente et la nature de chaque évènement sismique est déterminée (ex. séisme volcano-tectonique VT, profond, effondrement). La mesure des VT permet plus particulièrement d'identifier des périodes sismiquement actives liées à des activités magmatiques plus ou moins superficielles (Battaglia et al. 2016).

La déformation du sol est mesurée par un réseau de stations GPS (mais aussi par des inclinomètres et extensomètres). Le déplacement relatif entre deux stations GPS permet de mesurer la déformation du sol au niveau du sommet et à la base du volcan. De façon similaire à la sismicité, des périodes d'inflation ou de déflation du sol sont ainsi identifiées et peuvent être reliées à des activités magmatiques plus ou moins profondes (Peltier et al. 2016 ; Staudacher et Peltier 2016).

Enfin, un réseau géochimique permanent effectue des mesures de SO_2, H_2S et CO_2 au sein des fumerolles présentes au somment du Piton de la Fournaise (Galle et al. 2010 ; Peltier et al. 2016 ; Harris et al. 2017). La concentration de CO_2 dans le sol est aussi mesurée en champs lointain (Boudoire et al. 2017, 2018). Ces espèces chimiques gazeuses s'exsolvent de la phase

liquide du magma a des pressions différentes. La mesure de leurs concentrations à la surface peut ainsi apporter des informations sur les transferts magmatiques à travers l'édifice.

De façon générale, l'analyse de ces données ont permis une amélioration de la compréhension des processus déclencheurs pré-éruptifs et des mécanismes syn-éruptifs. En outre, l'ensemble des éruptions au Piton de la Fournaise ont été anticipées à moyen ou court terme, grâce à l'interprétation et la corrélation de l'ensemble de ces données de surveillance.

4.2. Données sur le flux magmatique par télédétection

Le flux magmatique (TADR pour *Time-Averaged Discharge Rate,* ou VFR pour *Volume Flow Rate*) des éruptions est un élément relativement important pour mieux caractériser les dynamismes éruptifs et de mieux comprendre les processus magmatiques associés (Harris et al. 2007). Afin de quantifier l'évolution des TADR de chaque éruption au Piton de la Fournaise, deux jeux de données issus de systèmes de télédétection différents ont été utilisés, se basant sur la mesure de la radiation infrarouge par télédétection du magma émis à la surface du volcan.

Tout d'abord les TADR mesurés et calculés par le système MIROVA (Coppola et al. 2009, 2015, 2017; Coppola et Cigolini, 2013) ont utilisés pour caractériser l'évolution de l'intensité des éruptions de 2014, 2015 (cf. **chapitre IV**) et Septembre 2016 (cf. **chapitre V**). Ce système d'observation utilise les données MODIS (*MODerate resolution Imaging Spectroradiometers*) de deux satellites défilants (Terra et Aqua) permettant l'acquisition de données sur une position terrestre fixe toute les six heures. Des données de VFR acquise par le système HOTVOLC (Gouhier et al. 2012, 2016) ont été aussi utilisées concernant l'éruption de Septembre 2016. Ce système d'observation utilise des données SEVIRI (*Spinning Enhanced Visible and InfraRed Imager*) du satellite géostationnaire Meteosat, permettant l'acquisition des données sur un point terrestre fixe toutes les 30 minutes.

CHAPITRE IV

DYNAMIQUES PRE- ET SYN-ERUPTIVES LORS D'ACTIVITES HAWAIIENNES ET STROMBOLIENNES SUR LA PERIODE 2014-2015

1. Présentation générale

Le premier ensemble de résultats présentés dans cette thèse concernent la période relativement active de 2014-2015 au Piton de la Fournaise. En effet, cette période représente le début d'un nouveau cycle d'activité sur ce volcan, après plus de trois ans d'inactivité. L'étude texturale et géochimique des produits éruptifs des éruptions de Juin 2014, Février 2015, Mai 2015 et Juillet 2015, ainsi que l'intégration de ces éléments à des données de surveillance, a permis de quantifier un certain nombre de processus magmatiques à l'origine de la réactivation du système magmatique et d'apporter certaines réponses sur l'évolution des styles éruptifs en surface. Cette approche est partiellement basée sur des procédures analytiques présentées dans le **chapitre III** ainsi que dans Gurioli et al. (2016) au sein de l'ouvrage de L'Observatoire de Physique du Globe de Clermont-Ferrand (OPGC), *Des Volcans aux Nuages* (cf. **Annexe 1**).

Chronologiquement, une première étude s'est focalisée sur la courte éruption de Juin 2014, qui fut la première activité éruptive au Piton de la Fournaise après plus de 3 ans de repos. Les données et les interprétations issues de ce travail collaboratif, faisant parti des données traitées pendant cette thèse, sont présentées dans Gurioli et al. (2018). Cette étude est publiée au sein du journal *Solid Earth* (cf. **Annexe 2**).

Ce chapitre, majoritairement focalisé sur l'éruption de Juillet 2015, développe la suite logique de l'étude présentée par Gurioli et al. (2018). La section suivante est présentée en anglais et correspond à un article soumis au journal *Contribution to Mineralogy and Petrology*.

2. Quantification des processus pré- et syn-éruptifs lors de l'éruption de Juillet 2015

Basaltic dyke eruptions at Piton de La Fournaise: quantification of magmatic overpressure, conduit and eruptive dynamics

Simon Thivet[(1)], Lucia Gurioli[(1)], Andrea Di Muro[(2)]

[1] Laboratoire Magmas et Volcans, Université Clermont Auvergne - CNRS - IRD, OPGC, Campus Universitaire des Cézeaux, 6 Avenue Blaise Pascal, 63178 Aubière Cedex, France

[2] Institut de Physique du Globe (IPGP), Sorbonne Paris-Cité, CNRS UMR-7154, Université Paris Diderot, Observatoire Volcanologique du Piton de la Fournaise (OVPF), Bourg Murat, France

Article and revision submitted to *Contribution to Mineralogy and Petrology*

Acknowledgments

We thank A. J. L. Harris and G. Boudoire for the syn-eruptive sampling of the July 2015 products, J-L. Devidal and J-M. Hénot for their precious support in using the EPMA and the SEM, M. Benbakkar for the bulk rock analysis. Thanks to M.D. Higgins, and L. Pioli with whom we had constructive discussions. This paper was greatly improved by the review of the anonymous reviewer and the editor. We thank the STRAP project funded by the Agence Nationale de la Recherche (ANR-14-CE03-0004-04). This research was financed by the French Government Laboratory of Excellence initiative, the Région Auvergne and the European Regional Development Fund.

Supplementary material (labelled Tables S in the manuscript) are available at:

http://lmv.uca.fr/thivet-simon-2/

Key-words

Basalt; Degassing; Hawaiian-style activity; Piton de la Fournaise; Strombolian-style activity; Triggers.

Abstract

Small-volume and proximal-summit eruptions, sometimes with only little precursors, are common at Piton de la Fournaise (La Reunion Island, France). Their eruptive style ranges from Hawaiian to Strombolian but their eruptive mechanisms are still not completely understood. To gain insight, we combined syn-eruptive field work, textural, geochemical and geophysical measurements on the short-lived eruption of July 2015 and we compared it with the 2014 eruption, which opened the ongoing eruptive cycle at Piton de la Fournaise. Crystal-poor and moderately vesicular components were predominant at the beginning of the eruptions, during the lava flux peak and the Hawaiian-style activity. Their abundance decreased with time in favour of less vesiculated and crystal-rich components during the decrease of the lava flux and the Strombolian-style activity. Physical, textural and chemical characterization of the pyroclasts, as well as thermometry calculations, permit to relate the different texture and chemical features of the eruptive products with the pre- and syn-eruptive processes. Geophysical precursors detected several weeks before the July 2015 eruption, as well as some evidences of magmatic reheating recorded in bulk and crystal compositions highlight that the July 2015 magma results from a pre-eruptive mixing between more and less differentiated magmas. We finally deduced that the observed syn-eruptive textural variations are related to the same batch of magma undergoing different cooling and degassing dynamics.

2.1. Introduction

2.1.1. Context

Basaltic systems exhibit a wide range of magmatic eruption styles, from effusive eruptions generating lava flows (e.g. Harris et al. 2007, 2017; Staudacher et al. 2016), Hawaiian and/or Strombolian-style activities (e.g. Head and Wilson et al. 1987, 1989; Jaupart and Vergniolle 1988, 1989; Parfitt and Wilson 1995; Parfitt, 2004; Stovall et al. 2011, 2012; Houghton et al. 2016), up to more violent explosions (e.g. Houghton and Gonnermann 2008; Morandi et al. 2016; Ort et al. 2016). Eruptive styles are controlled primarily by syn-eruptive

magma ascent dynamics within volcanic conduit systems (e.g. Sparks 1978; Vergniolle and Jaupart 1990; Houghton et al. 2004; Gonnermann and Manga 2012; Applegarth et al. 2013; Pioli et al. 2012, 2017; Pering et al. 2017) and pre-eruptive magmatic conditions of the reservoirs (e.g. Sparks and Huppert 1984; Anderson 1995; Corsaro and Pompilio 2004; Roeder et al. 2006; Gurioli et al. 2018). These dynamics are strongly dependent on the physicochemical properties of the magma, like its temperature, pressure, volatiles content and chemical composition (e.g. Tait et al. 1989; Di Muro et al. 2014, 2015, 2016; La Spina et al. 2015; Mollo et al. 2015; Rae et al. 2016).

Petrographic and textural measurements on basaltic products can provide critical information regarding the pre-eruptive storage and magma ascent conditions (e.g. Kuo and Kirkpatrick 1982; Polacci et al. 2006, 2012; Di Muro et al. 2014, 2015 ; Pioli et al. 2014; Gurioli et al. 2015, 2018). However, post-fragmentation effects can obliterate the primary signature of the magma, especially during high intensity lava fountain activities (e.g. Mangan and Cashman 1996; Stovall et al. 2011, 2012; Parcheta et al. 2013; Moitra et al. 2013, 2018; Kawabata et al. 2015; Lindoo et al. 2016, 2017). Piton de la Fournaise (PdF) is one of the most active volcanoes in the world in term of eruption frequency but it frequently exhibits low intensity Hawaiian to Strombolian-style activities, allowing efficient and fast natural quenching of the eruptive products that are not significantly modified by post-fragmentation expansion phenomena. Recently, Gurioli et al. (2018) have proved that the textural features of the pyroclast products from the mild recent activity of PdF are representative of the fragmentation conditions and thus can provide information related to (i) the shallow reservoirs which feed the eruptions and (ii) track the degassing history of the ascending magmas. These latter authors also provided a complete dataset of the June 2014 eruption that marked the beginning of a new and still ongoing eruptive cycle at PdF after a long quiescence period.

2.1.2. Objectives

In this work we combine macroscopic analysis (componentry), bulk texture measurements (density, porosity and vesicle connectivity), microscopic texture measurements (Vesicle Size Distribution, VSD and Crystal Size Distribution, CSD), and petro-chemical

analysis (bulk rock, glass and crystal compositions) on lava and tephra, of the July 2015 eruption at PdF. We also completed the textural dataset of Gurioli et al. (2018), adding the CSD of the June 2014 eruptive products. In parallel, these data are integrated with componentry measurements acquired on the June 2014, February and May 2015 eruptions of PdF, also with already published bulk rock analyses, experimental data (cooling experiments) and geophysical insights acquired on the June 2014-July 2015 period (ground deformations, magma output rates and seismic spectrograms).

Based on the specific case of the 2014-2015 eruptive period at PdF, the main objectives of this work are focused on (i) the general processes driving a magmatic system reactivation and on (ii) the mechanisms controlling the eruptive styles. More specifically, we wanted to check (iii) if the processes operating at the origin of the magmatic overpressures triggering such eruptions were different on the entire period of June 2014-July 2015, and (iv) if the textural signature of the emitted products reveal similar or different ascent mechanism and degassing histories in the eruptive dyke.

2.2. Geological background

2.2.1. The shallow magma storage system of PdF

With the exception of three eruptions that occurred during the twentieth century, the recent volcanic activity of PdF is confined within the Enclos Fouqué caldera which corresponds to the most recent big caldera of the volcano (Bachèlery 1981). This caldera is a poly-lobed depression, 100 to 250 m depth, in the centre of which the cone of PdF is built (Fig. 4.1a). According to the seismic data acquired by the Observatoire Volcanologique du Piton de La Fournaise (OVPF) monitored by the Institut de Physique du Globe de Paris (IPGP), the magmatic system feeding the central activity at PdF, extends vertically in the crust between the volcano top (2.6 km above the sea level) and 7 km below the sea level (Battaglia et al. 2005; Peltier et al. 2015; Lengliné et al. 2016). Geophysical data suggest that the main shallow magmatic storage system is located close to the sea level below the central cone (Peltier et al.

2008; Prôno et al. 2009). Based on surface deformations, Peltier et al. (2008) interpreted the summit or proximal eruptions (located close to the central cone of PdF), with low volume and short time lag between initiation of the dyke propagation and the beginning of the eruption, as the drain of small and shallow (above sea level) volumes located beneath the volcano summit. Geochemical and barometric data (Di Muro et al. 2014, 2015) as well as geodetic data (Peltier et al. 2016) support the existence of a multitude of shallow crustal reservoirs, which represent an active storage unit below the central cone.

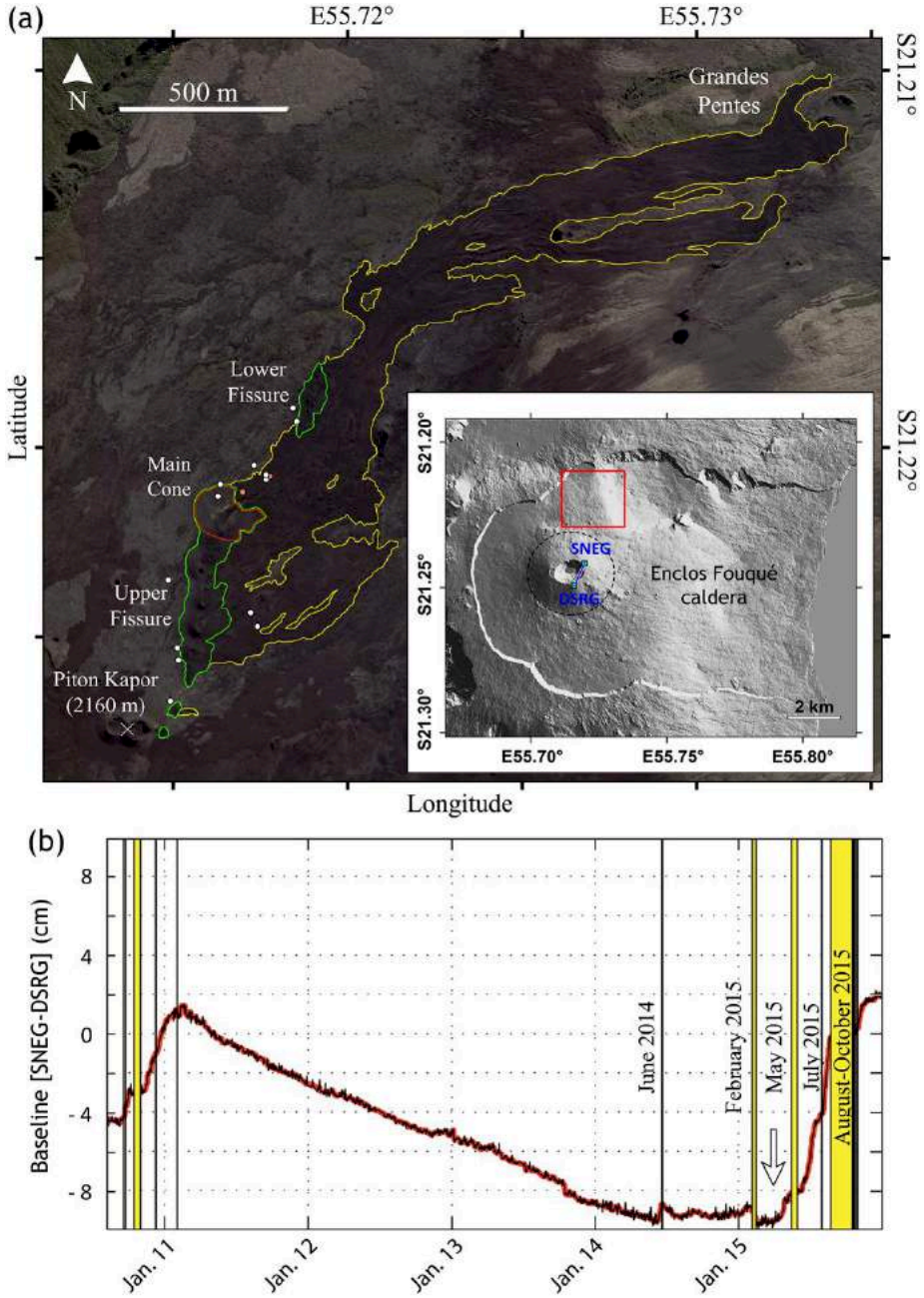

Figure 4.1 *– (a) Digital elevation model (DEM) of PdF and map of the July 2015 eruption. The yellow line shows the outline of the lava flow, the green ones represent both upper and lower eruptive fissures and the red line outline the main cone. White dots represent the*

different pyroclast sampling sites, red ones show the lava sampling sites. Blue squares and line on the DEM show the summit GNSS baseline [SNEG-DSRG]. Dashed black line represent the central cone of PdF. (b) Summit [SNEG-DSRG] baseline evolution from late 2010 to late 2015 reflecting ground deformation (modified from Gurioli et al. 2018). Eruptive and intrusive activities are materialized by the yellow periods. The vertical arrow represent the main phase of deep seismicity (Peltier et al. 2016). The rapid and strong variations linked to dike injections preceding eruptions have been removed.

2.2.2. The 2014-2015 eruptions: the beginning of a new eruptive cycle

Recent activity at PdF produces on average one eruption every nine months (Roult et al. 2012) but cycles of frequent eruptive activity alternate with phases of quiescence lasting up to six years (Peltier et al. 2008). The April 2007 major caldera-forming eruption represents one of the most intense and voluminous events of the historical activity of PdF (Staudacher et al. 2009). This large eruption was followed by a set of small-volume eruptions and shallow intrusions between 2008 and 2011, followed by a 41 months long resting phase, between 2011 and 2014 (Fig. 4.1b; Peltier et al. 2016). Sudden and quite weak precursors of a new unrest were detected in June 2014: after 11 days of weak inflation, a new short-lived eruption started the 20 June 2014 (Gurioli et al. 2018). This event marked the beginning of a new, and still ongoing, cycle of activity at PdF that produced five eruptions in the 2014-2015 period.

With the remarkable exception of the complex, long lasting and large August-October 2015 event (emitted volume of 45.2 10^6 m^3; Coppola et al. 2017), the eruptions of the 2014-2015 period had relatively simple patterns of rapid exponential decay in magma output rates or TADR (time-averaged lava discharge rates; Harris et al. 2007) and emplaced relatively small volumes of lava (all < 10 10^6 m^3 and often < 2 10^6 m^3). Indeed, the first four eruptions of the 2014-2015 period, share similar characteristics in terms of duration, eruption pattern and total extruded volume (0.3 10^6 ± 0.1 for June 2014, 0.8 10^6 ± 0.3 for February 2015, 6.5 10^6 ± 2.3 for May 2015 and 1.6 10^6 ± 0.6 m^3 for July 2015; Coppola et al. 2017).

Bulk rock composition changed during the 2014-2015 eruptions, suggesting an initial differentiation trend followed by a progressive mixing of the resident, evolved magma with a

primitive magma batch, whose volumetric contribution further increased during the large August 2015 eruption (Coppola et al. 2017). The 2014-2015 set of eruptions has thus been interpreted as the result of a major phase of refilling and rejuvenation of the shallow PdF plumbing system, which had been substantially drained away in the caldera forming 2007 eruption (Di Muro et al. 2014; Peltier et al. 2016). The June 2014 (evolved magma) and the July 2015 (hybrid magma) events are the focus of this research.

2.2.3. Chronology and field sampling of the July 2015 eruption

Since mid-April 2015, several precursors were observed (Peltier et al. 2016): deep seismicity was detected below the central cone, associated with a change in the composition of the intra-caldera gas emissions (CO_2 and H_2S enrichment in the summit fumaroles) and an increase of the summit ground inflation (4 cm along the summit GNSS baseline, three months before the eruption; Fig. 4.1b). According to the OVPF activity bulletin of July 2015 (ISSN 2610-5101; http://www.ipgp.fr/fr/ovpf/bulletin-dactivite-mois-de-juillet-2015), the July 2015 eruption started on the 31 July at 5:20 a.m. (all time cited in this paper are in UTC) after an intensification in the shallow volcano-tectonic (VT) seismicity located below the volcano central cone (seismicity peaks on the 7, 13, 28 and 31 of July). This eruption was thus preceded by a set of unambiguous precursors and a longer lasting phase of pre-eruptive inflation with respect to the smaller and sudden inflation recorded only 11 days before the June 2014 eruption (Gurioli et al. 2018) as well as relatively weak inflation preceding the February and May 2015 eruptions (Peltier et al. 2016; Fig. 4.1b).

Following the OVPF activity bulletins and field observations, the July 2015 eruption occurred along two en-echelon eruptive fissures (upper and lower fissures), corresponding to the same dyke, which extended from the NE of the 1998 Piton Kapor cone towards the NNE (Fig. 4.1a). This eruption was located in the N10 rift zone defined by Bachèlery (1981). Lava fountains at the beginning of the eruption were followed by mild Strombolian explosions towards the end of the eruption, which formed a set of pyroclastic cones aligned along the eruptive fissures and fed several lava flows (Fig. 4.2), some of them spreading out to the North of the Grandes Pentes area (Fig. 4.1a). On the basis of the thermal emission measured by the

MODIS sensor (Moderate Resolution Imaging Spectroradiometer, MIROVA monitoring system, Coppola et al. 2016), the maximum TADR was estimated at 22 ± 8 m^3 s^{-1} during the first hours of the eruption and then declined exponentially towards the end of the eruptive activity. In comparison, the TADR of the June 2014 eruption followed a comparable temporal trend but its maximum output rate was three times lower than that of July 2015. From the night between the 31 July and 1 August, the tremor intensity and TADR started to decrease, mirroring a rapid decline in the magmatic activity and the closure of some eruptive vents. After several hours of intensity seismic fluctuation, corresponding to gas piston events, the tremor disappeared the 2 August at around 7:30 am after 50 hours of activity.

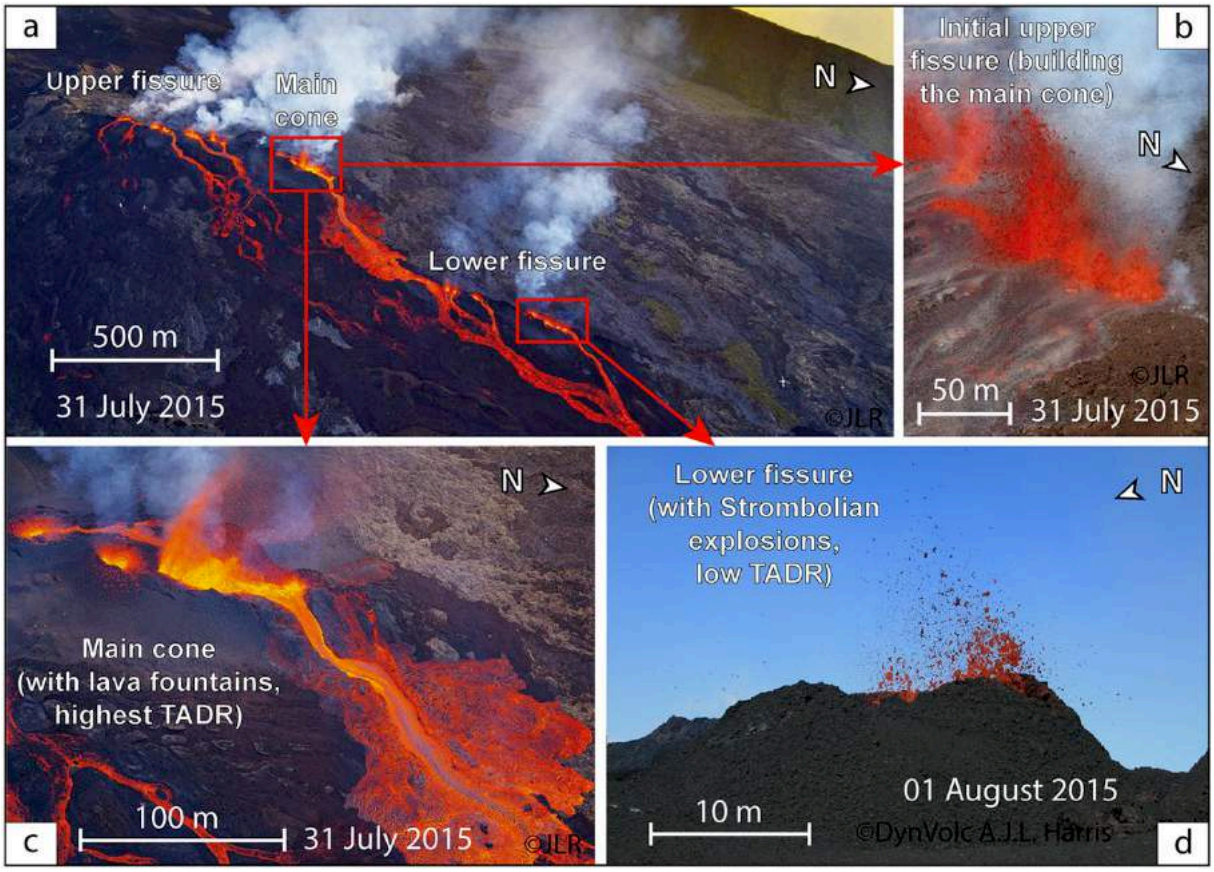

Figure 4.2 *– Pictures of the different eruptive activity during the July 2015 eruption. (a) Aerial picture of the whole eruption site (Journal de La Réunion, JLR 2015-08-01, picture by Hervé Douris). (b) Aerial picture of the initial upper fissure at the very beginning of eruption (JLR, 2015-08-01, picture by Guillaume Cazarré). (c) Aerial picture of the main cone (JLR 2015-08-01, picture by Hervé Douris). The most intense lava fountains can reach several tens of meters in height during the maximum TADR. (d) The TADR is rapidly decreasing and the Hawaiian activity turns in Strombolian-style activity with the burst of large bubbles (picture by A. J. L. Harris).*

The two eruptive fissures did not produce the same activity during the eruption. (i) The upper fissure was active all along the eruption and the main part of the activity was concentrated in this area, especially in the northernmost cone (which grew progressively during the eruption and is described as the main cone of the eruption, Figs. 4.1a and 4.2) of this eruptive fissure. (ii) The lower fissure (towards the NNE; Figs. 4.1a, 4.2a and 4.2d) began to form few hours after the upper one, during the maximum TADR and its activity stopped about one or two hours before that of the upper fissure. Nevertheless, the transition between Hawaiian and Strombolian-style activity observed during the eruption was widespread and happened quite suddenly at the same time along both fissures (Fig. 4.2).

Thanks to the rapid scientific response of the OVPF and the DynVolc teams (Harris et al. 2017), as well as relatively good weather conditions, detailed syn-eruptive sampling and characterisation of eruptive dynamics were performed. The juvenile samples were collected close to different active zones and at different times to constrain the eruptive dynamics both in space and time (Fig. 4.1b and Table S4.1). The first sampling site was the main cone of the eruption, at the NNE extremity of the upper fissure (Figs. 4.1b and 4.2). The sampling of this site was done a few hours after the beginning of the eruption, when Hawaiian fountaining was still intense and during the maximum TADR phase. The second sampling site was the other part of the upper fissure, which was active throughout the entire eruption. Sampling was done during the second part of the eruption and the mild Strombolian-style activity, when TADR was declining. Finally, the third and last sampling site was the lower fissure, which opened just after the upper one and its sampling was performed during the second part of the eruption as well. These three sampling sites permitted to document the change in eruptive style and the decline in eruption intensity (from Hawaiian to Strombolian-styles). Lava samples were directly taken from the active lava flows (mainly the one emitted from the main cone) and gently quenched in water. It is important to note that most of the lava samples were sampled in the same way and near their point of emission (Harris et al. 2017). Hereafter these lava samples will be called typical lava sample.

2.3. Laboratory Methods

After the eruption, all the samples were brought to the Laboratoire Magmas et Volcans (LMV) at Clermont-Ferrand, France, to be analysed and then stored at the OVPF and LMV repositories. A full description of the routine measurements reported below, as well as the raw data presented in this paper, are available in the DynVolc database (2017) and the supplementary material of this paper.

2.3.1. Componentry

Considering that each sampling was done randomly (with no clasts selection), the samples are representative of the type of the activity at that moment, without any sample biasing. Specimen selection can be done afterwards in the laboratory. Following the nomenclature of White and Houghton (2006) clasts were subdivided into three broad components: juvenile, non-juvenile and composite fragments. Based on the Gurioli et al. (2018) nomenclature, juvenile fragments are then classified based on their macroscopic characteristics (surface typology, shape and colour).

2.3.2. Bulk texture

Density and Helium (He) vesicle connectivity measurements were performed on 208 samples (lapilli, bombs and lava fragments). Density measurements were carried out on all samples in the range of 1.5 to 12 cm (for the major axis). Two different methods were used for these density measurements (Table S4.2). (i) First, the density was measured using the water-immersion technique based on the Archimedes principle described by Houghton and Wilson (1989) and Shea et al. (2010). This technique is the most used, and allows us to compare a wide range of data with a good reproducibility of ± 40 kg m^{-3} (1σ) on five repeated measurements.

(ii) Another method was performed using a density analyser (Micromeritics Geopyc 1360). As already briefly presented by Kawabata et al. (2015), the instrument measures object volume and density of particles with different sizes and shapes. The envelope volume of a sample is determined by the difference in how far the plunger is driven (by a stepping motor) into a cylinder (of known diameter) containing a fine grained medium (C_1) and after the sample addition (C_2). These steps of the motor are counted and used to calculate the sample envelope volume (V): V (cm^3) = [(C_2-C_1)v]. When a calibration test is made with a sample of known volume V, the equation is solved for v (cm^3 mm^{-1}) which is the conversion factor of the raw measurement. This parameter is introduced in order to account for the consolidation of the medium around the sample surface and the friction of the plunger movement. The envelope density of the sample corresponds to its mass divided by its envelope volume V. The medium used is called DryFlow and composed of small rigid spheres (< 1 mm) with a high degree of fluidity that permits to completely coat the samples. Thus, samples with large vesicles need to be wrapped with thin laboratory parafilm (which does not affect the overall density) to avoid the medium penetrating in the pores of the specimen. These density measurements lead to reproducible data with a maximum standard deviation of ± 30 kg m^{-3} (1σ) on five repeated measurements. For the sake of accuracy, several samples were analysed using the two methods described above and the data correlate relatively well (Table S4.2). Moreover, the errors of these measurements are insignificant in comparison with the variability of natural porosity in the samples (Gurioli et al. 2015). The porosity of the samples was then calculated based on Houghton and Wilson (1989) using a vesicle-free rock density of 2884 ± 35 kg m^{-3} (1σ). This parameter was determined by powdering four samples and by measuring their masses and volumes using the Micromeritics Accupyc 1340 Helium pycnometer (maximum standard deviation of ± 3.10^{-8} m^3, 1σ, on five repeated measurements for the volume measurements). The Accupyc pycnometer was also used to determine the skeletal volumes of the samples in order to calculate the He vesicle connectivity for each clast (Table S4.2), using the Formenti and Druitt (2003) and Colombier et al. (2017) methods.

2.3.3. Microscopic texture

Based on the density distribution and the variability of the clasts, seven pyroclasts and four lava samples, covering the texture evolution in time and space of the July 2015 eruption, have been selected (Table S4.3). In order to perform a detailed comparison with the products of the June 2014 eruption, we extended the original dataset of Gurioli et al. (2018) by adding the CSD data of eight samples (seven pyroclasts and one lava fragment) of that eruption. Multiple magnification images were taken in order to quantify all the petrographic characteristics of both pyroclasts and lava samples from the micron (25x and 100x Scanning Electron Microscopy imagery, SEM) to the centimetre scales (thin section scans). The digitization of these thin sections was both performed under natural and polarized light, using polarized foils. For 25x and 100x magnifications, the SEM JEOL JSM-5910 LV of LMV was used to acquire Back-Scattered Electron (BSE) images with an acceleration voltage of 15 kV.

All these images were then transformed and binarized in grayscale to allow Matlab program FOAMS (version 1.0.5; Shea et al. 2010) to acquire 2D raw data of all the selected objects (vesicles and crystals) and calculate 3D textural characteristics of the samples, based on the whole sets of images. Both for vesicles and crystals, the minimum object measured was five pixels (equivalent to 6 µm at the maximum magnification 100x we used with the SEM). VSD and vesicle number density (N_V) were measured with FOAM (Shea et al. 2010) counting a total of 48528 vesicles measured for both the July 2015 and June 2014 eruptions. Vesicle to melt ratio (V_G/V_L) was calculated following Gardner et al. (1996). This ratio represent the vesicle volume divided by the matrix volume. N_V and V_G/V_L parameters are corrected for the phenocryst content.

Based on 38441 plagioclase and 9610 clinopyroxenes 2D measurements, 3D crystal habits (x:y:z) were determined using CSDslice database (version 4; Morgan and Jerram, 2006): the best fit dimensions are 1:4:10 (tabular shape) for plagioclase crystals and 1:1.5:2.4 (rectangular prism shape) for clinopyroxene crystals. Then CSDcorrections software (version 1.6; Higgins 2000) was used to calculate the CSD, crystal content and crystal number density (N_C) of the samples. Based on SEM image observations, the circularity of the crystals is fixed at 0.1 and 0.3 for plagioclase and clinopyroxene, respectively (on a scale of 0 to 1). Olivines and oxides are too rare in the eruptive products of 2014 and 2015 to be statistically measured. As the raw data of crystals from FOAMS are obtained from several nested image

magnifications, normalized size frequency data from FOAMS is the most appropriate input to use within the CSDcorrections software. This frequency data calculated from FOAM (N_A, number per unit of area) were used in the frequency data input section of the CSDcorrections software. Calculations are corrected for the vesicle content. Moreover, FOAM size frequency raw data are based on the crystal equivalent diameters, whereas CSDcorrections input does not use this shape parameter. Thus, the best input measurement to use is the major axis of the crystal ellipse combined with the phase abundance correction measured with FOAM and corrected for the porosity. This procedure is a requirement to correct stereological conversion of 2D crystal size measurement to 3D CSDs by combining the FOAM program ouput with the CSDcorrections software. Based on the work of Cashman (1988), Marsh (1988) and Higgins (2006), one CSD slope theoretically defines a specific crystal population, which form during a single step of nucleation and growth. Slope changes permit to identify different crystal populations (the steeper the slope, the lower the residence time assuming a constant growth, or inversely the steeper the slope, the lower the growth rate assuming a constant residence time). In our dataset, the slope change was defined by the intercept of the best fitting lines of the different crystal populations. All the textural parameters described in this section, as well as the crystal nucleation density (N^0), which is the CSD value at x (crystal lenght) = 0, are reported in the Table S4.3.

2.3.4. Chemical analysis

Bulk rock analyses (ICP-AES) discussed in this study have been already published (Coppola et al. 2017; Gurioli et al. 2018) and were performed on several quenched pyroclasts and lavas (Table S4.4). We compare these data with our new micro-analyses of July 2015 glasses and crystals (Table S4.4). They were carried out for major elements by using the Cameca SX100 Electron Probe Micro-Analyser (EPMA). EPMA analysis of June 2014 products have been already published in Gurioli et al. (2018). Counting times were 10 seconds for each element, with an acceleration voltage of 15 kV and a current intensity of 8 nA. A 10 µm beam and a focused beam were used for the glass and crystal analysis respectively. Maximum errors (2σ; wt%) for each oxides are ± 0.87 for SiO_2, ± 0.15 for TiO_2, ± 0.36 for

Al_2O_3, ± 0.67 for FeO, ± 0.17 for MnO, ± 0.37 for MgO, ± 0.32 for CaO, ± 0.31 for Na_2O, ± 0.04 for K_2O and ± 0.16 for P_2O_5.

We also estimated the equilibrium of each mineral phase with bulk rock and glass compositions (Table S4.4). For the plagioclase (plg), we used the plagioclase/liquid equilibrium constant of Putirka (2008) calibrated for melts whose temperature exceeds 1050 °C: $K_D(An - Ab) = (X^{plg}_{Ab} X^{liq}_{AlO_{1.5}} X^{liq}_{CaO})/(X^{plg}_{An} X^{liq}_{NaO_{0.5}} X^{liq}_{SiO_2}) = 0.27 \pm 0.11$, where X is the molar fraction of the corresponding oxides or albite/anorthite content within plg and melt. For the clinopyroxene (cpx), we used the Mg-Fe coefficient distribution $K_D(Mg - Fe) = (X^{cpx}_{FeO} X^{liq}_{MgO})/(X^{liq}_{FeO} X^{cpx}_{MgO}) = 0.28 \pm 0.05$ at equilibrium (Putirka 2008; Brugier 2016). Similarly for the olivines, we used the Mg-Fe distribution coefficient $K_D(Mg - Fe) = (X^{ol}_{FeO} X^{liq}_{MgO})/(X^{liq}_{FeO} X^{ol}_{MgO})$ from Roeder and Emslie (1970; K_D = 0.30 at equilibrium), Fisk et al. (1988; K_D = 0.306 at equilibrium) and Putirka (2008; K_D = 0.30 ± 0.03 at equilibrium). An average Fe^{3+}/Fe_{total} ratio of 0.18, calibrated for La Réunion Island basaltic melts (Pichavant et al. 2016), was used to calculate FeO content of the liquid phase.

2.3.5. Geo-thermometry setup and H_2O content estimations

Recently, Brugier (2016) studied experimentally the evolution of phase equilibria and phase compositions during the cooling of November 2009 mafic magma in the temperature range 1200-1100 °C. Two sets of experiments were performed (i) at 50 MPa with 0.5 to 1.6 dissolved H_2O content in the melt, that is at the H_2O-CO_2 saturation pressure typically recorded by olivine hosted melt inclusions at PdF (Di Muro et al. 2014, 2016), and (ii) at atmospheric and dry conditions. (i) Hydrous experimental data of Brugier (2016) acquired at 50 MPa and controlled redox conditions (between NNO and NNO-1.7) are fitted to define a first hydrous MgO-thermometer (black line in Fig. 4.3): $T\ (°C) = 943.7 + 27.5\ MgO^{liq}$ (R^2 = 0.83). (ii) Experimental data of Brugier (2016) acquired at atmospheric and controlled redox conditions (NNO and NNO-0.5) are fitted to define a second MgO-thermometer for sub-surface dry magmatic conditions (blue line in Fig. 4.3): $T\ (°C) = 1041.7 + 17.7\ MgO^{liq}$ (R^2 = 0.75). Then

we are able to compare these newly calibrated thermometers with already published ones (Fig. 4.3).

H_2O content within the natural melts of July 2015 eruption are also estimated using the plagioclase-melt hygrometer of Lange et al. (2009).

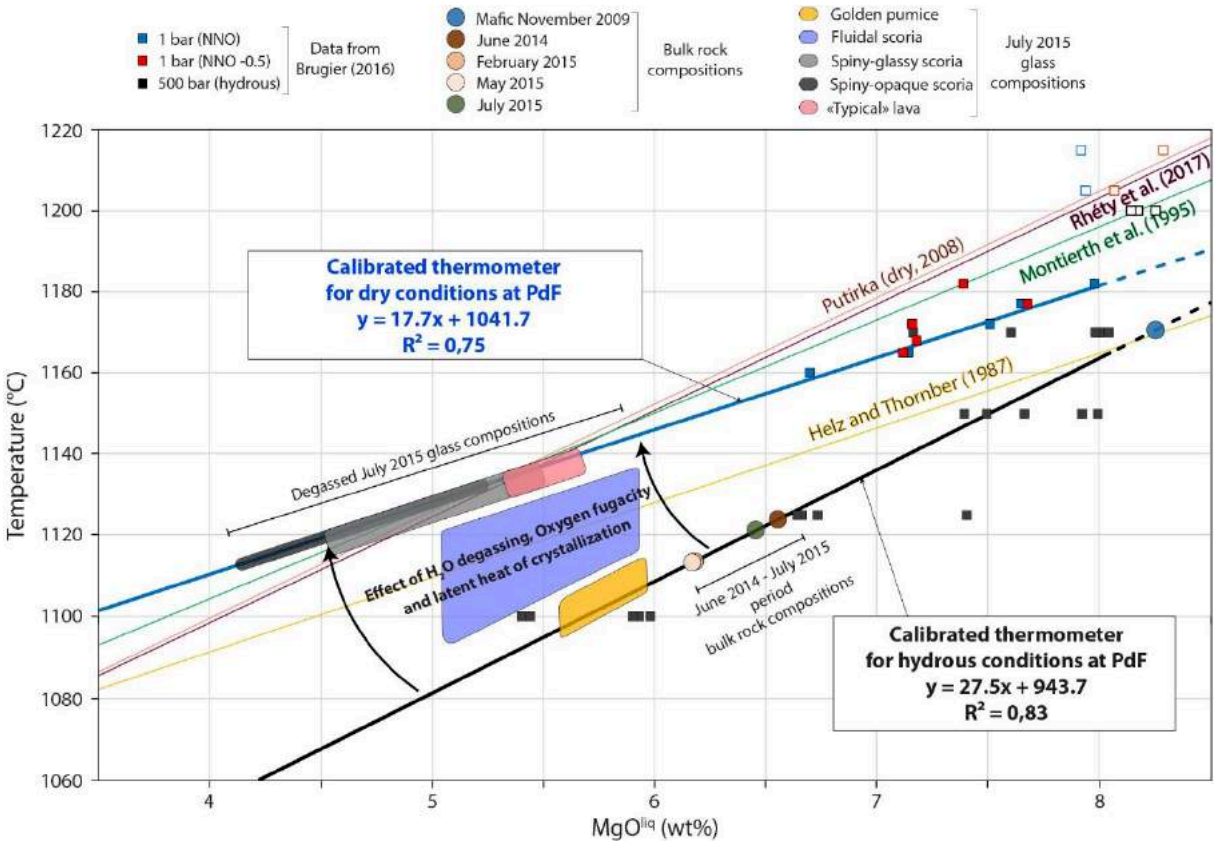

Figure 4.3 *– Temperature vs. MgO content in basaltic melts. The different lines show the MgO-thermometers of Helz and Thornber (1987), Montierth et al. (1995), Putirka (2008) and Rhéty et al. (2017) as well as the two new calibrated ones for pre-eruptive (hydrous, 50 MPa) and syn-eruptive melts (dry, 1 atm), from the Brugier (2016) data. Experiments that suffer of iron loss as well as those exceed a temperature of 1200 °C are excluded (empty circles and squares). These latter are not crystallizing olivine yet, which control the MgO content of melt. Rhety et al. (2017) propose another calibration based on the composition of PdF glasses measured at 1 bar under oxidizing conditions by Villeneuve et al. (2008). Interestingly, Rhety's calibration is almost identical to the Putirka's recalibration of the original equation of Helz and Thornber (1987). Rhety's and our new dry MgO-thermometer converge at a temperature of around 1140°C (MgO 5.5 wt%), while Rhety's calibration produces slighlty higher T estimates with respect to our new dry one for magnesian melts. In conclusion,*

Brugier (2016) data confirm the influence of melt oxidation on the calibration of MgO-thermometer, as this parameter influences directly the crystallisation and the composition of mafic phases like olivine, which exert a first order control on melt composition. Nevertheless, the convergence of experimentally defined glass thermometer at lower temperature permits to confidently apply this method to the range of evolved glass compositions studied here.

2.4. Results

2.4.1. Componentry

The July 2015 products consist of juvenile fractions which represent the primary magma involved in these eruptions (lavas and pyroclasts). Based on the classification of Gurioli et al. (2018), the July 2015 tephra samples were divided into four types of juvenile pyroclasts: (i) golden pumice, (ii) fluidal scoria, (iii) spiny-glassy scoria and (iv) spiny-opaque scoria. As described by these latter authors, golden pumice are characterized by very smooth, shiny and brown/yellow surfaces. Fluidal scoria are characterized by smooth and shiny dark surfaces. Spiny-glassy scoria show shiny but rough and spiny surfaces. Spiny-opaque clasts are characterized by dark matt and spiny surfaces.

Figure 4.4 represents the componentry measurements performed on the first four eruptions of the 2014-2015 period, as well as their associated TADR (Coppola et al. 2017). The time distribution of the different eruptive components is not constant in time and evolved in parallel with changes in TADR. Samples of the initial phase of these four eruptions show that the pyroclasts emitted during this initial intense phase were mostly fluidal clasts. Only one golden pumice was collected during the initial intense phase of the July 2015 eruption. The scarcity in golden pumice during the three eruptions occurring in 2015 contrasts with the June 2014 eruption, which emitted a significant amount of golden pumice during the maximum TADR (Fig. 4.4a). Additionally, samples collected in the declining phases of these four eruptions (with relatively low TADR and mild Strombolian-style activity) mostly consist of spiny scoria (both spiny-glassy and spiny-opaque).

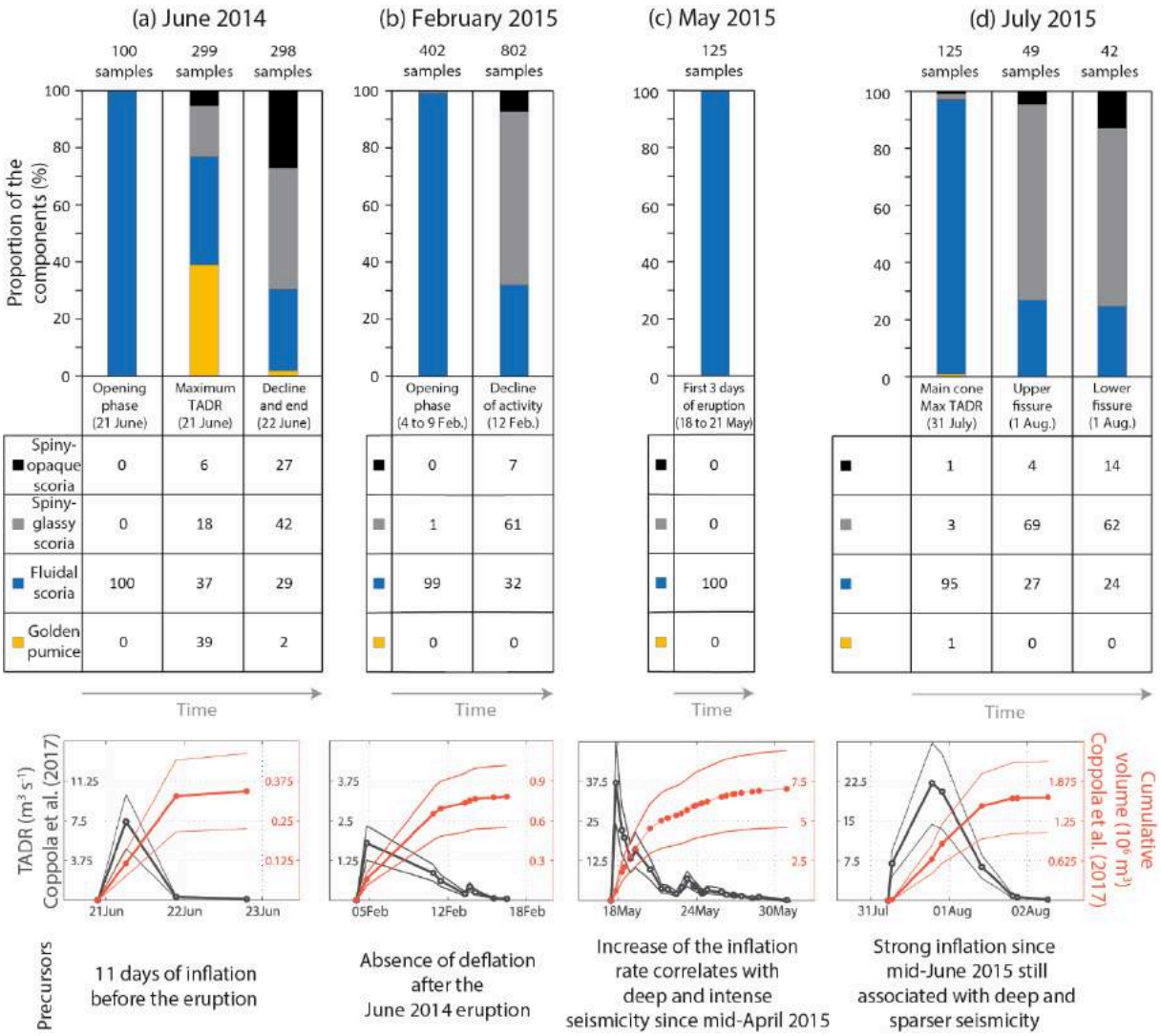

Figure 4.4 *– Componentry of the eruptive products sampled during the (a) June 2014, (b) February, (c) May and (d) July 2015 eruptions. Associated time-series of MODIS-derived TADR and cumulative emitted volume of the different eruptions are shown in black and red curves respectively, modified from Coppola et al. (2017). Uncertainties are represented by thin lines.*

2.4.2. Bulk texture

The textural components are marked by distinct porosity distributions and textures (Fig. 4.5a). Focusing on the July 2015 dataset, the densities of the spiny clasts (both glassy and

opaque) vary from 700 to 1900 kg m^{-3} with an average of 1300 kg m^{-3}, while the densities of the fluidal clasts vary from 500 to 1600 kg m^{-3} with an average of 800 kg m^{-3}. Only one golden pumice sample has a density of 600 kg m^{-3}. The magma emitted during the maximum TADR is quite porous, while the magma erupted during the decrease in TADR is denser. Typical lava fragments sampled close to the main vent have a density range between 1200 and 1600 kg m^{-3} close to that of spiny clasts. However, two lava fragments sampled within the channel, around 100 m from the emission point record extreme density values (500 kg m^{-3} for the vesicle-rich lava sample and 2100 kg m^{-3} for the dense one). The dense fragment was collected from the channel margin, while the vesicle-rich one was collected within the channel plug, therefore not representative any more of the vent conditions.

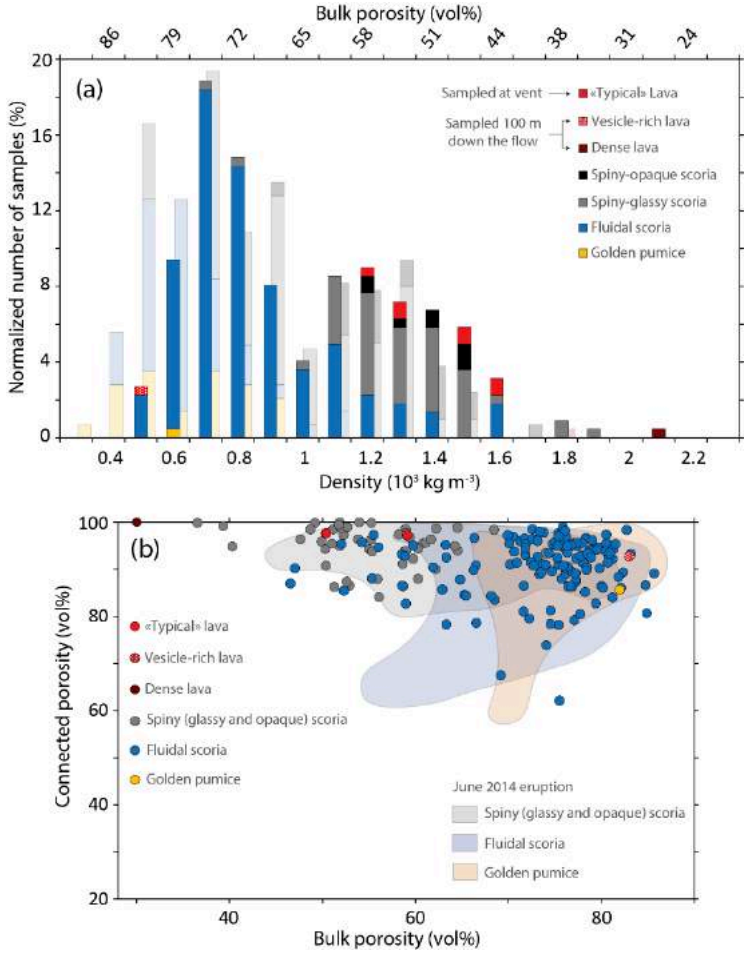

Figure 4.5 *– (a) Density distribution histogram for the June 2014 (from Gurioli et al. 2018) and July 2015 samples. (b) Connected porosity measured with He for the June 2014 (from Gurioli et al. 2018) and July 2015 samples. The connected porosity is normalized to the total porosity. Fields in the background are datasets from the June 2014 eruption (Gurioli et al. 2018).*

Vesicle He connectivity measurements (Fig. 4.5b) show that the content in isolated vesicles increases in porous clasts with bulk porosity > 60 vol%. The July 2015 fluidal clasts and golden pumice have variable content of isolated vesicles up to 40 vol%. In contrast, spiny clasts and lavas have less or no isolated vesicles (from 0 to 15 vol%).

2.4.3. Micro texture

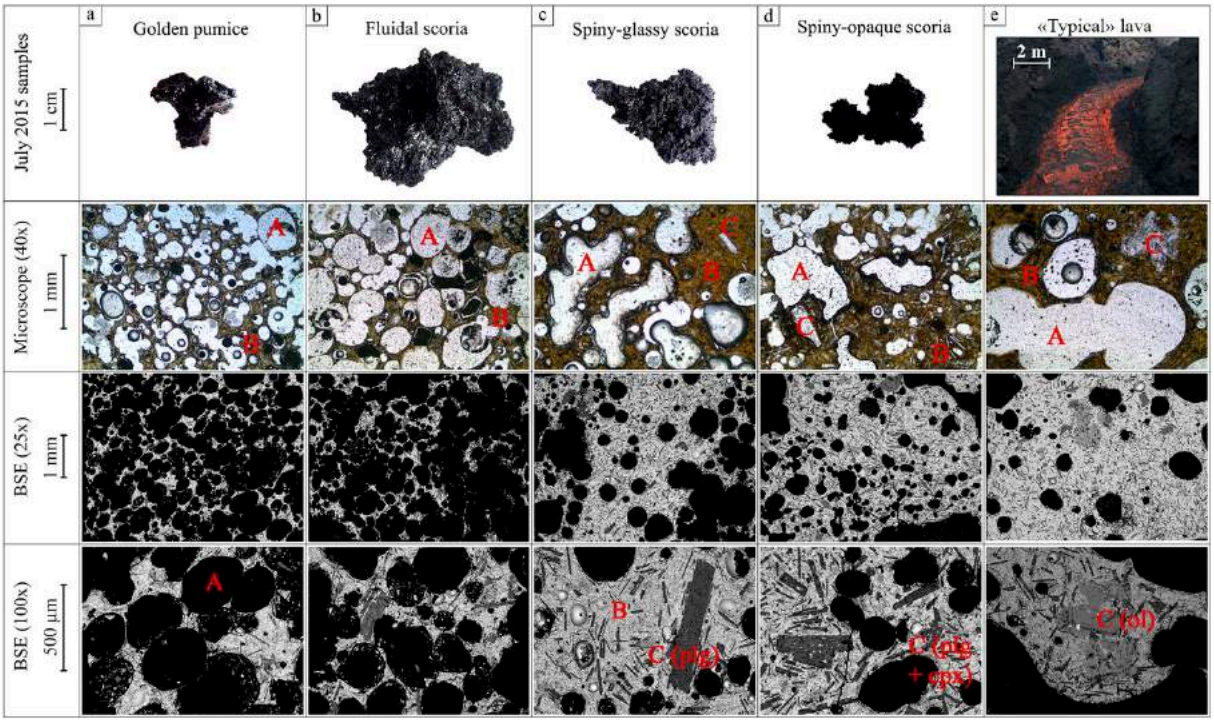

Figure 4.6 *– General texture of the different July 2015 quenched samples: (a) golden pumice, (b) fluidal scoria, (c) spiny-glassy-scoria, (d) spiny-opaque scoria and (e) typical lava (sampled near the main vent). A is for vesicles, B for matrix (glass and microlites), C for micro-phenocrysts, plg for plagioclase, cpx for clinopyroxene and ol for olivine.*

Figure 4.6 represents an overview of the textures of the different pyroclasts and lavas from July 2015 eruption. General and qualitative information are provided here, being quantitatively detailed in the sections hereafter. (i) Golden pumice clasts (Fig. 4.6a) are highly porous and crystal-poor. Thin sections and SEM images show a very low micro-crystallinity, and micro-phenocrysts (called mesocrysts by Gurioli et al. 2018) are very scarce in these samples. Vesicles are rounded. (ii) Fluidal scoria samples (Fig. 4.6b) have variable but still high

porosities and contain slightly more microlites than the golden clasts, and scarce micro-phenocrysts. Vesicles are rounded. (iii) Spiny-glassy scoria (Fig. 4.6c) have lower porosities than the two previous components and a few big irregular coalesced vesicles occur. Microlites are more abundant and larger, and micro-phenocrysts are still scarce. (iv) Spiny-opaque scoria (Fig. 4.6d) porosities are quite similar or even lower than in the spiny-glassy scoria with several big coalesced vesicles. Their crystal contents are clearly higher than in the other types of pyroclasts, but still with low micro-phenocryst contents. (v) Typical lavas (Fig. 4.6e) are dense with intermediate crystal content and show a similar micro-phenocrysts content as in the pyroclasts. The lavas sampled down the flow (not shown in Fig. 4.6), namely the dense one from the shear-zone and the vesicle-rich one from the plug, have extreme values of porosities and the dense lava contains a larger amount of microlites than the vesicle-rich lava.

2.4.3.1. Vesicle characteristics and Size Distributions

Figure 4.7a shows the VSD as a function of the total volume that the vesicles represent in the measured samples. The 2015 golden pumice VSD shows a single population of vesicles, ranging from 20 µm to 2.5 mm in diameter, with vesicles of 0.4 mm representing the main mode. A similar distribution is found in the four fluidal scoria pyroclasts that contain also a few big rounded vesicles, up to 4 mm in diameter. Both VSDs of spiny-glassy and spiny-opaque scoria show a bimodal distribution. The main population of this latter distribution corresponds to small vesicles whose main size mode coincides approximately with that of the previous clast types (0.4 and 0.2 mm for the spiny-glassy and spiny-opaque samples respectively). However, the volume of this population is about half than the one found in the fluidal and golden clasts. The second population corresponds to large vesicles with irregular contours whose size ranges between 1.5 and 6 mm in diameter. The VSDs of lavas have asymmetric distribution with a main mode of large vesicles at 1 mm in diameter and isolated peaks of large vesicles up to 6 mm. The VSD of the dense lava sample has an asymmetric distribution skewed toward large vesicles and a very low total vesicle volume fraction. In contrast, the VSD of the vesicle-rich lava sample is characterized by a unimodal population of small vesicles with a mode at 0.6 mm.

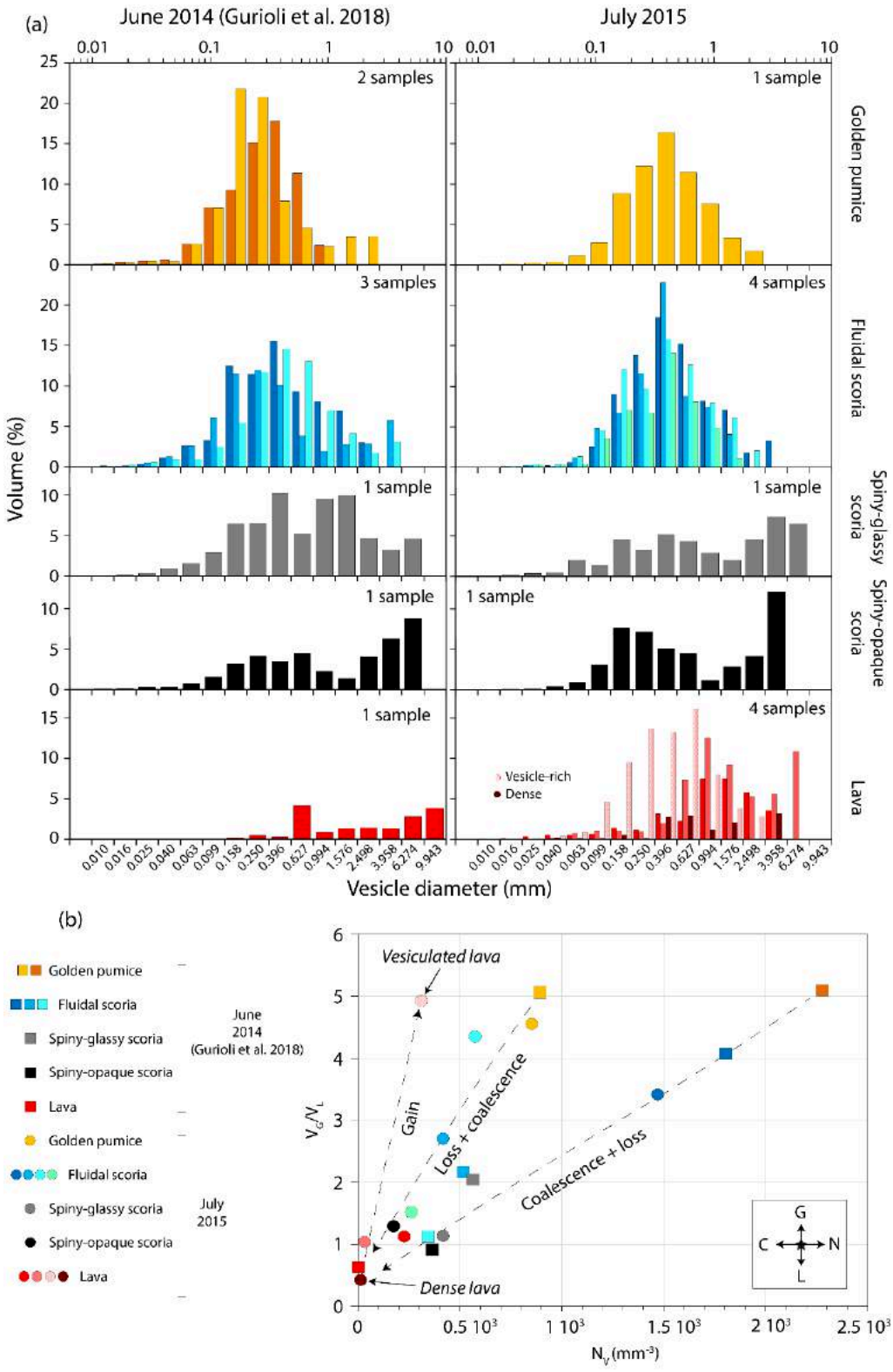

Figure 4.7 *– (a) Vesicle Size Distributions (VSD) of the June 2014 (Gurioli et al. 2018) and July 2015 selected samples. (b) Vesicle to melt ratio (V_G/V_L) vs. vesicle density number (N_V). The different trends reflecting different mechanisms are represented by the arrows: N for bubble nucleation, G for bubble growth, C for bubble coalescence and L for bubble loss.*

Both vesicle density numbers and vesicle to melt ratios progressively decrease from the golden and fluidal clasts to the spiny clasts and lavas, except the vesicle-rich lava (Fig. 4.7b). V_G/V_L of the 2015 dataset decrease from the golden pumice (4.6), to the fluidal scoria (between 1.5 and 4.4) and to the spiny scoria (1.2). The V_G/V_L ratio of typical lavas are closed to 1, with the exception of the vesicle-rich (4.9) and dense (0.4) fragments. July 2015 N_V values decrease from golden pumice and fluidal scoria (between 2.6 10^2 and 1.5 10^3 mm^{-3}) to spiny scoria (between 1.7 10^2 and 4.1 10^2 mm^{-3}). N_V for lava samples are lower than 2.2 10^4 cm^{-3}.

2.4.3.2. Mineral assemblage and Crystal Size Distributions

The July 2015 pyroclasts and lavas contain plagioclase (plg), clinopyroxene (cpx) and scarce olivine (ol) in order of decreasing abundance and size (Fig. 4.6). Micro-phenocrysts occur as isolated or clusters of several euhedral crystals of plg, cpx and scarce ol. Little resorption/dissolution textures are observed within the 2015 micro-phenocrysts of ol (cf. 100x BSE image of the typical lava sample on Fig. 4.6e). Evidences of crystal resorption have not been found in the other phases (plg and cpx) of the July 2015 magma. Microlite texture is similar for both eruptions, with isolated crystals and aggregates of several crystals, in which plg microlites crosscut cpx grains, ol being scarce and isolated in the glass matrix (subsequent micro-crystallization of ol).

The limit between the microlite and micro-phenocryst populations on plg and cpx (Fig. 4.8a) is mostly dependent on the maximum length of the microlite population that evolves from a component to another. Ol crystals, smaller in size than plg and cpx, were too scarce for statistical analysis. The maximum length of the 2015 plg microlites (equivalent to the 3D crystal length) increases from golden pumice (0.5 mm) to fluidal and spiny-glassy scoria (0.9 mm) to lava (1.1 mm) and spiny-opaque scoria (1.2 mm); the maximum length of the cpx microlites increase from golden pumice (0.1 mm) to spiny-glassy scoria (0.4 mm) to lava (0.6 mm) and fluidal and spiny-opaque (0.7 mm). As stressed in the introduction, we also performed CSD analysis on some June 2014 eruptive products, that was not presented in Gurioli et al. (2018) and the maximum length evolution of the June 2014 microlites also show the same trend.

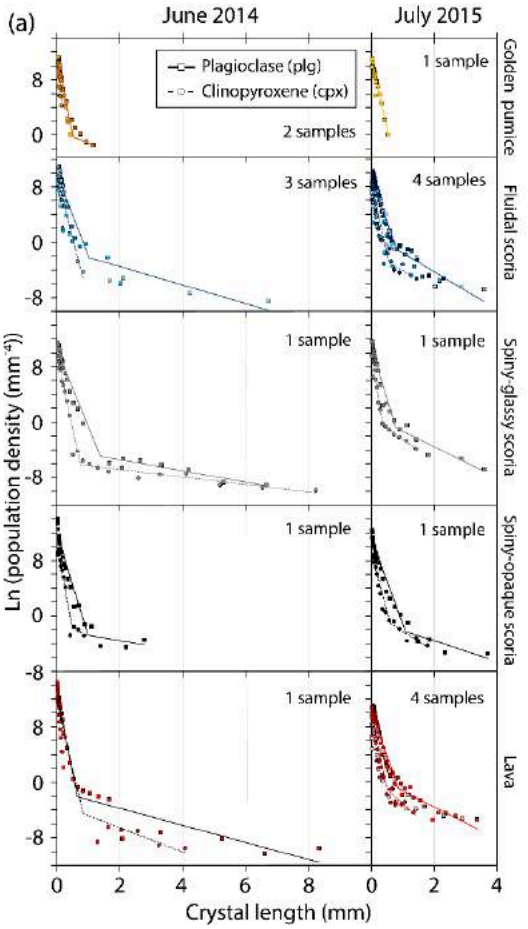

(b)

Sample type		Sample	$Cryst_{tot}$ (vol%)	Plg_{micro} (vol%)	$Plg_{\mu\text{-pheno}}$ (vol%)	Cpx_{micro} (vol%)	$Cpx_{\mu\text{-pheno}}$ (vol%)
June 2014	Golden	Reu141118_3_4	8	6	0	2	0
		Reu141118_3_8	9	6	1	2	0
	Fluidal	Reu140624_3_8	22	17	1	4	0
		Reu140624_9_8	16	11	1	4	0
		Reu140624_13b	18	12	1	5	0
	Spiny-glassy	Reu140624_3_13	50	31	1	14	4
	Spiny-opaque	Reu140624_3_5	51	32	2	17	0
	Lava	Reu140624_12	100	62	4	32	2
July 2015	Golden	Reu150731_7_3	11	10	0	1	0
	Fluidal	Reu150731_7_2	14	12	1	1	0
		Reu150803_1_1	19	13	1	5	0
		Reu150803_2	16	11	0	5	0
		Reu150803_4_2	15	11	1	3	0
	Spiny-glassy	Reu150731_7_4	29	18	2	7	2
	Spiny-opaque	Reu150801_3	48	31	2	12	3
	Lava	Reu150731_2a	35	23	1	11	0
		Reu150731_5_1	31	21	2	7	1
		Reu150801_4a (dense)	32	21	1	10	0
		Reu150801_4b (gas-rich)	17	12	1	3	1

Figure 4.8 *– (a) Crystal Size Distributions (CSD) of the June 2014 and July 2015 selected samples. (b) Crystal content of the June 2014 and July 2015 selected samples.*

July 2015 crystal content varies significantly in the different components (Fig. 4.8b), while their CSDs change only little (Fig. 4.8a). (i) In the golden pumice, few microlites formed mostly by plg (10 vol%) and scarce cpx (1 vol%) were observed (plg/cpx microlites volume ratio of 10). Total crystal content of golden pumice is the lowest of all the components with only 11 vol% of microlites with very scarce micro-phenocrysts (< 1 vol%). (ii) Fluidal scoria contain a slightly higher content of microlites (13 to 18 vol% with an average plg/cpx of 5) and their content in micro-phenocrysts remain very low (around 1 vol%). (iii) Spiny-glassy and spiny-opaque have higher content in microlites (25 and 43 vol% respectively with an average plg/cpx of 3) and micro-phenocrysts are slightly more abundant (4 and 5 vol% respectively). (iv) Microlite content from typical lava fragments (excluding the vesicle-rich and dense one) range from 28 to 34 vol% (average plg/cpx of 3) with 1 to 3 vol% of micro-phenocrysts. Maximum size of micro-phenocrysts is the same for all the components (no more than 4 mm),

except for the golden pumice in which big crystals are not incorporated. CSD of the June 2014 products show that these products incorporated bigger micro-phenocrysts of plg and cpx (up to 8 mm) than the July 2015 magma.

2.4.4. Bulk rock, glass, crystal and experimental analyses

2.4.4.1. Crystal compositions

We identify three different groups of crystals with distinct compositions and sizes: (i) the phenocrysts, (ii) the micro-phenocrysts and (iii) the microlites. Phenocrysts (larger than 1 cm and interpreted as antecrysts in June 2014; Gurioli et al. 2018) have not been observed in July 2015.

In July 2015 products, micro-phenocrysts of plagioclase (An_{73-85}) are more calcic than the microlites (An_{63-69}). A compositional gap is observed between the two populations (Fig. 4.9a). Some of the July 2015 micro-phenocrysts of plg are reversely zoned (from An_{75} in the cores to An_{80} in the rims, see c_1-r_1 and c_2-r_2 couples in Fig. 4.9a and Table S4.4). This reverse zoning has been only observed on plg micro-phenocrysts

Cpx crystals of July 2015 (both microlites and micro-phenocrysts) straddle between augite and diopside compositions within a narrow range of composition ($En_{48-40}Fs_{9-14}Wo_{42-46}$; Table S4.4). The populations of cpx microlite and micro-phenocryst can be distinguished for their TiO_2 content and the percentage of the tetrahedral sites occupied by Al (Fig. 4.9b), called Al(z). Micro-phenocrysts have low TiO_2 content and Al(z) (between 0.7 and 1.5 of TiO_2 wt%; between 3 and 7% for Al(z)), while microlites exhibit the highest values (between 1.5 and 4 of TiO_2 wt%; between 7 and 17% for Al(z)). A change in the slope of the increasing trend of Al(z) and TiO_2 content is observed. This trend was already observed in the other PdF products and attributed to the effect of enhanced plg crystallization (Al-rich) on the melt composition (Boivin and Bachèlery 2009; Di Muro et al. 2015).

Ol crystals of July 2015 are unzoned and homogeneous in composition, which correspond to Fo_{78-80} for micro-phenocrysts and Fo_{76-77} for microlites (Fig. 4.9c and Table S4.4).

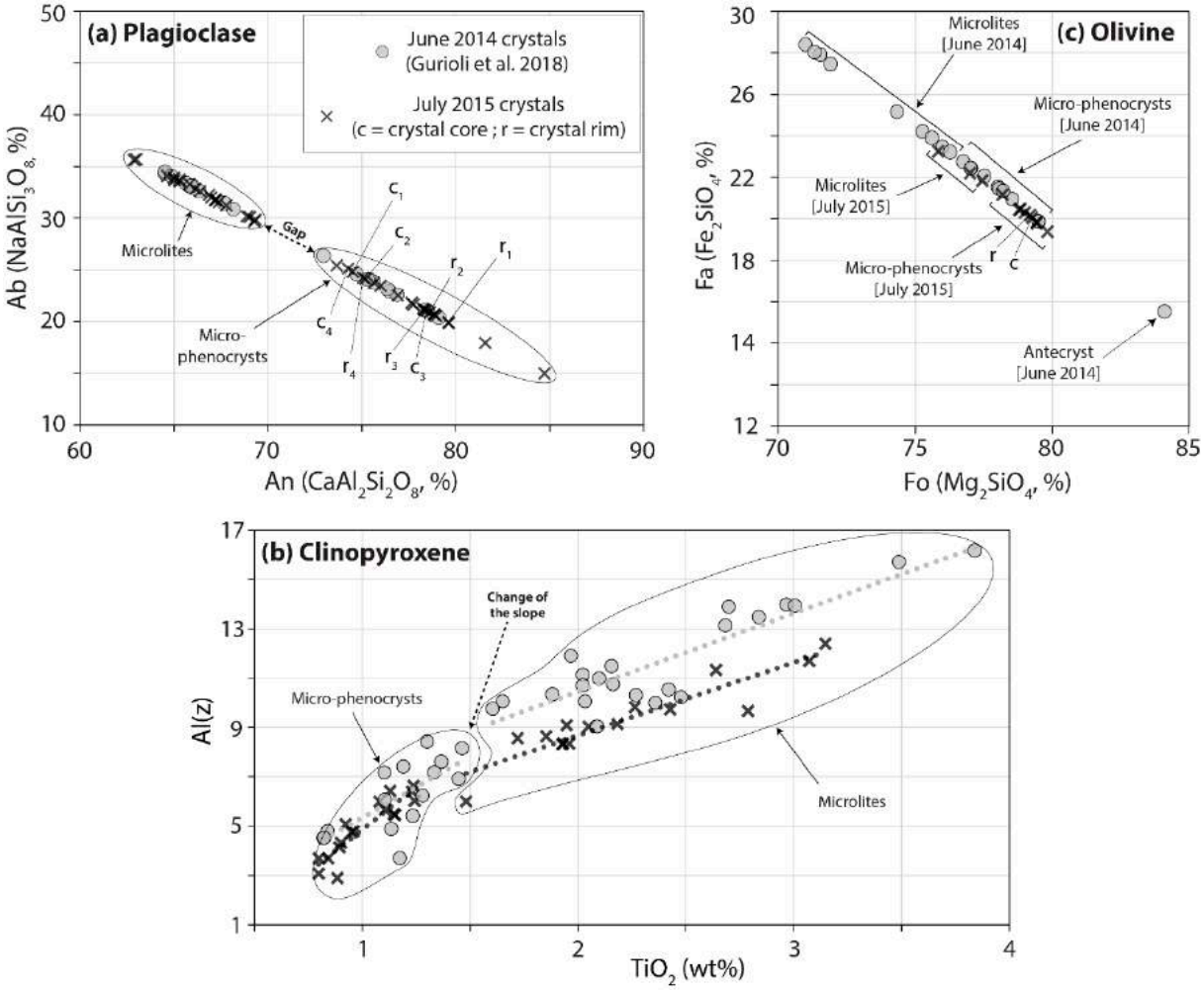

Figure 4.9 *– Crystal compositions of (a) plagioclases (albite vs. anorthite), (b) clinopyroxenes (Al(z) vs. TiO_2) and (c) olivines (fayalite vs. forsterite) for the June 2014 (grey dots, Gurioli et al. 2018) and July 2015 eruptions (black crosses). Each c and r represent a couple of core and rim compositions on a same crystal.*

2.4.4.2. Bulk rock and glass analyses

Magmas emitted by PdF between June 2014 and July 2015 are aphyric transitional basalts (MgO: 6.1-7.1 wt%; K_2O: 0.7-0.8 wt%; CaO/Al_2O_3: 0.7-0.8; red box in Fig. 4.10a; Table

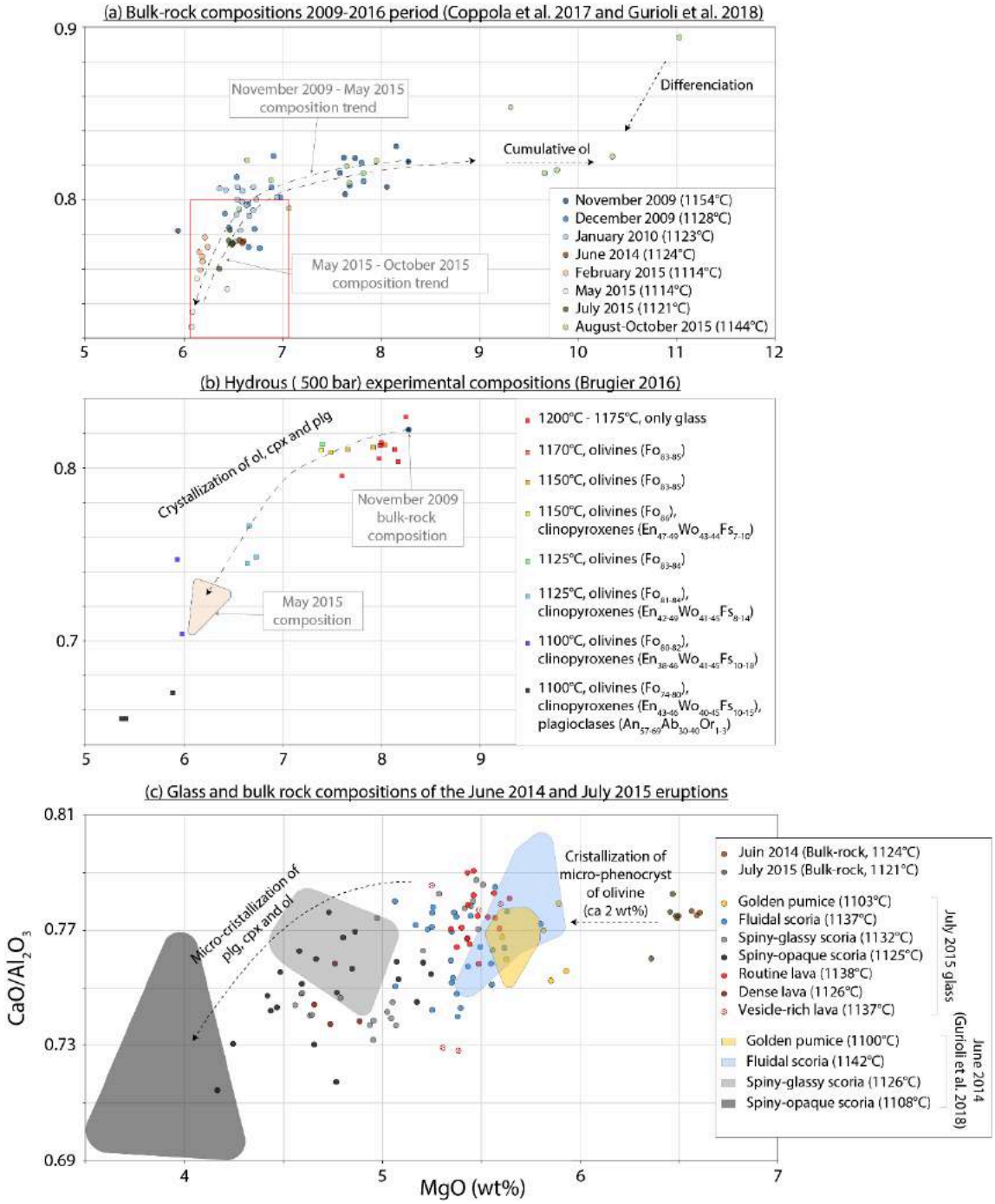

Figure 4.10 *– (a) Bulk rock compositions of the different eruptions that occurred between November 2009 and August-October 2015 (CaO/Al_2O_3 vs. MgO). The red box represent the composition range of the typical aphyric transitional basalts of PdF. (b) Glass compositions (CaO/Al_2O_3 vs. MgO) from hydrous experiments of Brugier (2016). Experiments were performed from the November 2009 melt composition and by progressively cooling from 1200°C until 1100°C with a constant pressure of 50 MPa and controlled redox conditions. The experimental temperatures and the different present phases with their compositions are also reported. (c) Bulk-rock and glass compositions (CaO/Al_2O_3 vs. MgO) of the June 2014 (Gurioli et al. 2018) and July 2015 samples.*

S4.4). In the frame of the 2014-2015 sequence of eruptions, the products of June 2014, February and May 2015 events were evolved basalts. Hydrous experimental compositions performed by Brugier (2016) show a marked decrease in CaO/Al_2O_3 at T < 1150°C (ol crystallization above this temperature, with the occurrence of ol, cpx then plg below this temperature) and reproduce relatively well the natural bulk rock compositions from December 2009 to May 2015 by decreasing temperature from 1200 to 1100 °C (Fig. 4.10b). A reverse trend is then observed since the July 2015 eruption with a progressive increase of the CaO/Al2O3 and MgO content until the August-October 2015 magmas (Fig. 4.10a; Copolla et al. 2017).

Focusing on the July 2015 products, the golden pumice glass has an average CaO/Al_2O_3 ratio of 0.76 (close to that of the bulk rock) and an average MgO content of 5.8 wt% (slightly lower than the bulk rock). This difference can be explained by the occurrence of a small amount of micro-phenocrysts of ol (ca. 2 wt%) within the bulk rock. MgO content (controlled by the micro-crystallization of ol) and CaO/Al_2O_3 ratio (controlled by the micro-crystallization of plg and cpx) of interstitial glasses decrease from the golden, to the fluidal, to the spiny clasts (Fig. 4.10c; Table S4.4). Microlite-rich spiny opaque clasts have the most evolved interstitial glasses (from 4.2 to 5.3 wt% in MgO and from 0.71 to 0.78 for CaO/Al_2O_3). Matrix in lavas have similar compositions to the fluidal scoria. The July 2015 tephra glass compositions mimic those found in the June 2014 eruption (Gurioli et al. 2018).

2.4.4.3. Phase equilibria

Plg microlites observed in the July 2015 products are in equilibrium with their matrix (K_D = 0.29 on average), and most of the plg micro-phenocrysts (included the reversely zoned plg) are in equilibrium with the hybrid bulk rock (average K_D = 0.22). Plg micro-phenocryst of July 2015 with relatively high anorthite (> An_{82}) might be considered as antecrysts because they do not fulfil the equilibrium conditions with the bulk rock (like the high Fo olivine in the June 2014 magma). The cpx micro-phenocrysts are in equilibrium (K_D = 0.24 on average) with the bulk rock as well as the microlites with their matrix (K_D = 0.28 on average). Both ol microlites and micro-phenocrysts are in equilibrium with their surrounding glass (K_D = 0.28 on average) and bulk rock (K_D = 0.28 on average), respectively.

2.4.6. Temperature and H_2O content

Regarding the progressive increasing microlites content of the different eruptive component (from golden pumice to fluidal scoria to spiny) and the progressive increasing of K_2O content (incompatible element) from the bulk rock (0.74 wt% on average), to the golden pumice (0.89 wt% on average), to fluidal scoria and lava (0.96 wt% on average), to spiny scoria (1.07 wt% on average), we suggest that (i) bulk-rock represent the microlite-free and pre-eruptive conditions end-member, (ii) whereas the fluidal, lava and spiny components represent the microlite-rich and syn-eruptive conditions end-member, with golden pumice representing the beginning of the crystallization of the melt during the ascent of the magma and the transition between the pre and syn-eruptive conditions. Using the newly calibrated hydrous thermometer to constrain pre-eruptive conditions (Fig. 4.3), we calculated temperatures from 1171 °C for the November 2009 most mafic bulk magma composition to 1114 °C for the February and May 2015 bulk magma compositions. Calculated June 2014 and July 2015 bulk magma temperatures are 1124 and 1121 °C respectively. The average temperature of the golden pumice component, which is thought to also correspond to pre-eruptive melt conditions, is 1103 ± 4 °C. These bulk magma and golden pumice temperatures are fully consistent with the temperature of crystallization of ol and cpx in equilibrium within the hydrous experiments of Brugier (2016). Temperatures of the other component (fluidal scoria, spiny scoria and lavas), which we considered as mainly degassed, are calculated using the newly calibrated dry thermometer (Fig. 4.3). Average temperature range from 1137 ± 6 °C for fluidal scoria and typical lavas to 1128 ± 6 and 1127 ± 9 °C for spiny-glassy and spiny-opaque respectively (July 2015 eruption). Calculated temperatures of the vesicle-rich lava (plug of the lava flow) and dense lava (margin of the lava flow) are respectively 1138 ± 3 °C and 1126 ± 2 °C.

H_2O calculations were performed on plg crystals and melts on equilibrium (Table S4.4). (i) Equilibrium between plg micro-phenocrysts and bulk rock compositions lead to relatively high H_2O content of 1.1 ± 0.3 wt% (using pre-eruptive parameters of 1121 °C and 50 MPa) which are consistent with the dissolved H_2O content in Brugier (2016) 50 MPa experiments (0.5 to 1.6 wt%) and with PdF pre-eruptive conditions (Di Muro et al. 2014, 2016). (ii) Golden pumice water content can be estimated using the equilibrium between plg microlites and surrounding glass compositions. With this assumption, H_2O content values between 0.8 ± 0.3 wt% have been found using pre-eruptive parameters (1103 °C and 50 MPa). The H_2O contents

of the other eruptive components (fluidal scoria, spiny scoria and lavas) are estimated using the equilibrium between plg microlites and surrounding glass compositions, with syn-eruptive and atmospheric conditions. It leads to an average H_2O of 0.4 ± 0.3 wt%.

2.5. Discussion

2.5.1. Componentry evolution with magma output rates and eruptive dynamics

As stressed in the introduction, the textural and chemical features of the juvenile samples collected during the different eruptions, are representative of the magma at fragmentation. The exception is represented by the spiny-opaque fragments which are interpreted as recycled, composite juvenile products (Gurioli et al. 2018). We also assume that the sampling procedure is statistically representative of the on-going eruptive activity at the time of the sampling. Therefore we can infer some important conclusions.

The chronological evolution of the componentry of the material emitted during the first four eruptions of the 2014-2015 period, mirrors the progressive TADR decrease (Fig. 4.4) and the eruptive dynamics evolution (Fig. 4.2). (i) Vesicular fluidal scoria (800 kg m^{-3}; Fig. 4.5a) is preferentially emitted at the beginning of the eruptions, correlated with the TADR peaks and with mild lava fountains (Hawaiian-style activity; Figs. 4.2a, 4.2b and 4.2c). (ii) Denser spiny scoria (1300 kg m^{-3}; Fig. 4.5a) emissions preferentially occur afterwards and at the end of these eruptions, correlated with the TADR decrease and a Strombolian-style activity; Fig. 4.2d). Thus, the vesicle content within the eruptive products decreases with the decreasing of TADR, eruptive intensity and time.

The four components (Fig. 4.6) are not systematically ubiquitous in the studied eruption products (Fig. 4.4). The vesicular golden pumice (800 kg m^{-3}) are in fact only present in the June 2014 eruption and just one single fragment has been found in the July 2015 deposits. These golden pumice occurred during the TADR peak at the beginning of the eruptions. During the June 2014 eruption, a 100% crystallized and dense (1800 kg m^{-3}) lava was extruded as well. Gurioli et al. (2018) interpreted these features as derived from a second boiling mechanism

which segregated the exsolved gas (golden pumice) and the crystals (lava) within the shallow reservoir and triggered the eruption. Therefore, the highly vesicular golden pumice occurrence is not necessarily linked with the eruptive intensity, as the June 2014 eruption was relatively low in terms of TADR and emitted volume compared to the other eruptions (Fig. 4.4). On the other side, the fact that these end-member products (vesicular and crystal-free golden pumice vs. dense and crystal-full lava) are no longer observed in the following eruptions of February, May and July 2015 eruptions, evidence the occurrence of different trigger mechanisms than the June 2014 eruption as well as different cooling conditions of the shallow reservoirs.

2.5.2. Pre-eruptive shallow magmatic reservoir conditions

Natural and experimental melt compositions (Figs. 4.10a and 4.10b) coupled with micro-phenocrysts sizes (Fig. 4.8a), contents (Fig. 4.8b) and compositions (Fig. 4.9) of juvenile fragments are the main direct measurements to gain information on the pre-eruptive conditions of the eruptions. First, experimental melt composition evolution from Brugier (2016) support the idea of Coppola et al. (2017) and Gurioli et al. (2018) that the June 2014 magma, as well as the February and May 2015 magmas, are chronologically inherited from the differentiation of the November 2009 parental magma (Fig. 4.10b). However, Coppola et al. (2017) highlight the fact that the MgO content and CaO/Al_2O_3 ratio of the July 2015 bulk rock composition (6.44 wt% and 0.77 respectively) is slightly higher, than those of the May 2015 one (6.18 wt% and 0.74; Fig. 4.10a). Therefore, these authors interpret the July 2015 bulk rock composition as representative of a hybrid magma resulting from a process of magmatic rejuvenation of the shallow system of PdF. Again, these observations suggest that the June 2014 and the July 2015 eruptions were triggered by different pre-eruptive conditions.

Two crystal populations are clearly visible on the CSD performed on the eruptive products of both June 2014 and July 2015 eruptions (Fig. 4.8a). The first crystal population of relatively small size (< 1.2 mm) and high slope represents the microlite population and will be discussed in the section hereafter. The second crystal population represents the micro-phenocrysts, with lower CSD slopes and larger sizes, and may give us some indications of the pre-eruptive processes. The following observations suggest that the July 2015 magma exhibited

a partial pre-eruptive rejuvenation. (i) Some of the July 2015 plg micro-phenocrysts record reverse zoning (Fig. 4.9a) and (ii) rare plg micro-phenocrysts has been measured with a very high anorthite content (An_{85}; Fig. 4.9a) that may be inherited from a new relatively low differentiated magmatic input. (iii) The incapability of the hydrous experiments to reproduce calcic plg composition may also suggest that they result from a magma hybridisation process, which was not experienced by the experiments. (iv) Slightly higher forsterite contents of the July 2015 ol micro-phenocrysts are observed compared to those of June 2014 (Fig. 4.9c) and (v) rare resorbed features are observed on the July 2015 ol micro-phenocrysts (Fig. 4.6e), which is consistent with the input of a relatively hot mafic magma into a dominantly cold differentiated magma. Finally, (vi) we suggest that the surprisingly high temperature range measured in the July 2015 lava matrix actually records the pre-eruptive hybridisation processes. Again, all these results are coherent with the idea of Coppola et al. (2017) that suggest that the July 2015 magma is the result of a mixing between 65-75 % of a differentiated magma and 25-35 % of less differentiated magma. Moreover, the cooling hydrous experiments of Brugier (2016) confirm that the natural evolved basalts emitted between December 2009 and May 2015 are formed by progressive cooling and crystallization of a former magma recharge occurred in November 2009 (Fig. 4.10b). CSDs also suggest that the June 2014 micro-phenocrysts are larger (up to 8 mm) than the July 2015 one (4 mm), which is in agreement with a more mature and relatively crystal-richer shallow reservoir for the June 2014 eruption.

On the other hand, the new hydrous MgO-thermometer, calibrated for pre-eruptive magmatic conditions (50 MPa and dissolved H_2O from 0.5 to 1.6 wt% within experimental samples; black line in Fig. 4.3) leads to relatively low pre-eruptive temperatures of 1103 (golden pumice) to 1121 °C (bulk rock) for July 2015, mostly because the H_2O content dissolved in the pre-eruptive magmas tends to decrease the magma temperature. Moreover, H_2O calculations with the plg micro-phenocrysts/bulk rock equilibrium lead to relatively high H_2O content in the natural samples (0.8 to 1.5 wt% ± 0.3, 1.1 wt% on average) that show that the micro-phenocrysts form under undegassed (saturated) and pressurized conditions, by cooling-driven crystallization.

2.5.3. Syn-eruptive conduit processes

Micro-texture as VSD (Fig. 4.7a), microlite sizes (Fig. 4.8a), contents (Fig. 4.8b) and compositions (Fig. 4.9), as well as glass compositions (Fig. 4.10c) are the most relevant parameters that we can measure from the eruptive products to track the syn-eruptive conduit processes.

First, VSDs show an initial unimodal vesicle population within the golden pumice and fluidal scoria (Fig. 4.7a), which represent bubble nucleation and growth mostly within the eruptive dyke during the initial phases of both June 2014 and July 2015 eruptions, when the TADR were still relatively high and coupled with Hawaiian-style activity. Concerning the June 2014 golden pumice, bubble nucleation also occur before the eruption as Gurioli et al. (2018) interpreted this highly vesiculated component as the product of a pre-eruptive second boiling mechanism. Then, the VSDs within the spiny-scoria and typical lavas are characterized by two different modes. These latter modes represent an episode of bubble nucleation and growth (for the small size vesicles, occurring in the golden pumice and fluidal scoria as well) followed in time by the formation of large vesicles (up to 1 cm in diameter) by coalescence. This coalescence phase is probably enhanced by slow ascent of the magma in the conduit, coinciding with low TADR and Strombolian-style dominantly effusive activity. Moreover, we observe within the pyroclasts two positive correlation trends between N_V and V_G/V_L, with distinct slopes (Fig. 4.7b). These two trends are mostly explained by bubble coalescence together with gas loss. Bubble coalescence within the collected samples is also highlighted by the He vesicle connectivity measurements (Fig. 4.5b) where vesicles of the spiny scoria and lavas are more connected (0 to 15 vol% of isolated vesicles) than in the golden pumice and fluidal scoria (0 to 40 vol% of isolated vesicles). All these observations explain the transition between an initial closed degassing system dominated by relatively high TADR and high magma ascent rates (golden pumice and fluidal scoria occurrence) with an open system degassing dominated by relatively low TADR and low magma ascent rates (spiny scoria occurrence). This interpretation is also coherent with the decrease of N_v from golden to spiny fragments that should reflect a decrease of the decompression rate (Toramaru 2006; Table S4.3): considering all the vesicles of each erupted component and assuming that they form in the conduit (which may not be accurate for the June 2014 golden pumice), the model permits to calculate maximum decompression rates at the beginning of the eruptions during Hawaiian-style activities (0.08

MPa s^{-1} for the July 2015 golden pumice), whereas lower decompression rates are calculated for latter Strombolian-style activities (between of 0.03 and 0.05 MPa s^{-1} for spiny-glassy scoria of the July 2015 and June 2014 eruptions respectively). These decompression rates are typically similar than those estimated in basaltic eruptions with dyke radius around 1 m (Shea 2017).

The presence of isolated vesicles in golden pumice and fluidal scoria suggest also that these erupted products are naturally quenched in a relatively hot surface environment (lava fountaining thermal environment) whereas the spiny scoria are quenched in a colder environment (colder Strombolian explosions environment) where brittle mechanisms may occur (rock cracking that connect the vesicles).

Similarly to decompression rate meter of Toramaru (2006), we applied the N_C water exsolution rate meter of Toramaru et al. (2008; Table S4.3). Calculated water exsolution rates are decreasing from the golden pumice (2.1 and 2.2 10^{-4} wt% s^{-1} for the July 2014 and June 2015 eruptions respectively) to spiny-glassy scoria (2.8 and 5.8 10^{-4} wt% s^{-1} for the July 2015 and June 2014 eruptions respectively) and typical lavas (3.7 10^{-4} wt% s^{-1} for the July 2015 eruption). On the other hand, and thanks to pre-eruptive seismic spectrograms (Aki and Ferrazzini 2000; Battaglia et al. 2005; Peltier et al. 2005; Roult et al. 2012), we can estimate an average initial magma residence time within the dyke of 40 min and 55 min for the June 2014 and July 2015 eruptions respectively (Fig. 4.11). Thus total exsolved H_2O contents from the melt are increasing from the Hawaiian (between 0.5 and 0.7 wt% for the both eruptions) to the Strombolian products (between 0.9 and 1.4 wt% for spiny-glassy scoria of the June 2014 and July 2015 eruptions respectively) and typical lavas (1.2 wt% for the July 2015 eruption).

The microlites population (which is volumetrically dominant) is identifiable in the CSD thanks to its higher slope and smaller size (Fig. 4.8a). These microlites are in equilibrium with their surrounding matrix, with relatively low anorthite content for plg (An_{63-69}; Fig. 4.9a), high Al(z) and TiO_2 content for cpx (> 8 and > 1.5 wt% respectively; Fig. 4.9b) and low forsterite content for ol (Fo_{71-77}; Fig. 4.9c). Eruptive temperature estimated by using the dry MgO-thermometer (blue line in Fig. 4.3) leads to syn-eruptive temperatures between 1116 and 1139 °C for July 2015 depending on the components. Most of these syn-eruptive temperatures are higher than the pre-eruptive temperature estimations because this calibration is based on totally degassed melts and because latent heat of crystallization due to the micro-crystallization may also play a role. However, we hypothesize that the higher temperature range measured in the lava matrix actually reflects the pre-eruptive hybridisation processes. H_2O content calculations with plg microlites/matrix equilibrium leads to variable but lower H_2O content (between 0.1

and 0.8 wt% of H_2O, 0.4 wt% on average) compared to the pre-eruptive conditions. This support the hypothesis that plg and cpx microlites form under variable and partially degassed and sub-surface conditions, by degassing-driven crystallization within the dyke. We also suggest that ol microlites form by cooling-driven crystallization under relatively low melt temperatures (< 1130 °C) and under atmospheric conditions. Moreover, the maximum lengths (as well as width, which is not measured by the CSD) of microlites and crystal number density (Table S4.3) globally increase with decreasing vesicularity, which is coherent with a progressive increase of the residence time of the magma in the eruptive dyke.

When a magma is decompressed and is migrating toward the surface, degassing models (Lesne et al. 2011; Di Muro et al. 2016; Shea 2017) suggest that basaltic melts start their main exsolving and heterogeneous nucleation phase around 1 km below the surface. For magmatic reservoir deeper than 1 km, bubble nucleation and associated degassing-driven crystallization (Applegarth et al. 2013) may not start at the very beginning of the magma ascent towards the surface. For the June 2014 and July 2015 cases, this crystallization delay may be represented by the compositional gap between the micro-phenocrysts and the microlites (Fig. 4.9).

Finally, the crystal nucleation densities N^0 are quite stable for each eruption, except for the spiny-opaque components where they drastically increase for plg. This support the idea that the spiny-opaque scoria are juvenile but recycled products because plg microlites may form within the eruptive vents after the fragmentation. Their low vesicle content and evidences of bubble coalescence (irregular contours associated with low N_V and V_G/V_L) also highlight subsurface degassing that may occur during a recycling mechanism. Concerning lava samples, we were able to evidence bubble segregation mechanism within the lava flow, highlighted by the sharp increase in the V_G/V_L ratio from the typical and dense samples to the vesiculated one (Fig. 4.8), corresponding to vesicle gain because of the bubble nucleation and/or segregation at the surface.

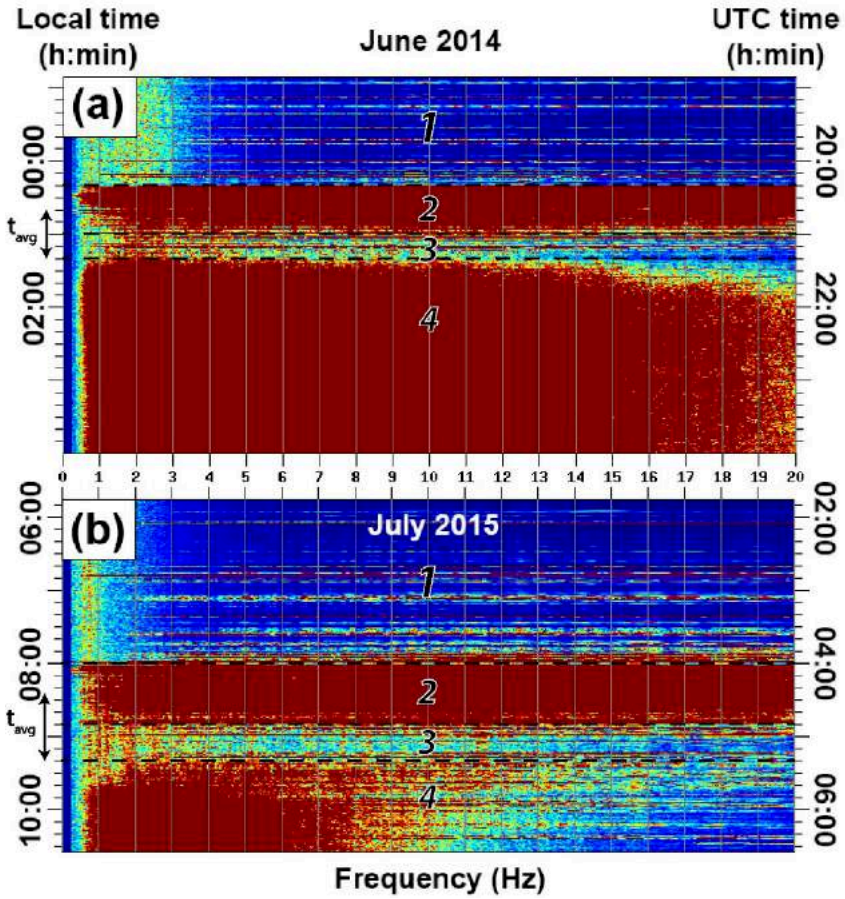

Figure 4.11 - *Seismic spectrograms (frequency vs. time) for the June 2014 (a) and July 2015 (b) eruptions. The four different seismic phases are reported on each spectrogram from 1 to 4, as well as the suggested average residence times of the magma (t_{avg}) within the eruptive dyke at the beginning of the eruptions. Phase 1 is characterized by an acceleration of the seismicity with a relatively small number of Volcano-Tectonic earthquakes (VT). Phase 2 is called the swarm phase and characterized by numerous overlapping VT events with larger magnitude than in the previous phase (interpreted as the brittle dyke propagation). Phase 3 correspond to a seismically low intensity sequence with small number of VT events (interpreted as the aseismic magmatic transfer). Phase 4 (beginning of the tremor) correspond in our case to the beginning of the eruptions at the surface. We suggest here a minimum residence time in the dyke (t_{min}) corresponding only to the duration of low intensity seismic phase (30 and 20 min for the June 2014 and July 2015 eruptions respectively) and a maximum residence time (t_{max}) corresponding to the low intensity sequence with the seismic swarm duration (80 and 60 min for the June 2014 and July 2015 eruptions respectively), because we speculate that the magma transfer may began during the dyke fracking and not only at the beginning of the low intense seismic sequence.*

2.5.4. Implications on the eruptive styles and comparison with other basaltic systems

Pre-and syn-eruptive processes, controlling the volatile and crystal contents of the magma which govern the magma viscosity (Giordano and Dingwell 2003) and fragmentation mechanisms (Edmonds and Wallace 2017), are dependent on the geometry of the magmatic systems and magma paths towards the surface that are more or less different from one volcano to another (Michon et al. 2015; Peltier et al. 2015). At PdF, pre-eruptive magmas contain a moderate content in dissolved water (up to 1.4 wt%; Di Muro et al. 2014, 2016) and are generally stored within multiple and relatively shallow levels, between a few hundred (multitude of small magma pockets) up to 3 km (main reservoir) bellow the summit craters (Peltier et al. 2008, 2015, 2016). In contrast, pre-eruptive Kilauea magmas have slightly lower water content (less than 1 wt%; Gerlach 1986; Wallace and Anderson 1998) and are stored within two main reservoirs located between 2 and 3 km below the summit caldera (Edmonds et al. 2013; Peltier et al. 2015). At Etna, pre-eruptive magmas are stored within multiple levels spanning a wider range of depth (from 1 to 10 km deep) than PdF and Kilauea (Patanè et al. 2008; Aloisi et al. 2011; Bonaccorso et al. 2013; Peltier et al. 2015), and contain relatively high water content (up to 2.3 wt%; Métrich and Rutherford 1998; Giordano and Dingwell 2003).

During the June 2014-July 2015 period at PdF, we support that the efficient syn-eruptive degassing, the moderate micro-crystallization, the relatively low volume of erupted magmas and the lack of an important continuous re-filling of fresh, volatile-rich magma do not allow the formation of sustained and energetic lava fountains. In contrast at Kilauea, although a relatively low content of dissolved water in the melt, major basaltic eruptions, implying relatively large magmatic supplies and volumes, are generally associated with relatively high decompression rates, low syn-eruptive degassing and low degassing-driven crystallization, generating sustained and intense lava fountains (e.g. Head and Wilson 1987, 1989; Mangan and Cashman 1996; Parfitt 2004; Stovall et al. 2011, 2012; Parcheta et al. 2013; Holt et al. 2019). At Etna, petrological and geochemical investigations suggest that the initial volatile-rich magmas associated with relatively efficient degassing processes towards the surface can sometimes lead to crystal-rich and viscous magmas near the fragmentation level (Métrich and Rutherford 1998), generating violent Strombolian activities (Polacci et al. 2019). On this volcano, syn-eruptive transitions between Hawaiian-style and more violent activities have also

been largely documented, but contrary to PdF, these transitions were mainly from Strombolian-style to Hawaiian-style activity (e.g. Polacci et al. 2006; Sable et al. 2006; Corsaro et al. 2017; Pompilio et al. 2017; Edwards et al. 2018). According to these latter authors, this evolution is marked by the same textural signatures of the emitted products as in our study, where the degassed Strombolian products are more crystalline and less vesiculated than their Hawaiian counterparts. In the early 2000, the volcanic system of Etna was fed by a magmatic system progressively more degassed whose volatile exsolution caused bubble coalescence and the formation of slugs that burst into the typical Strombolian explosions, fragmenting a melt having experienced prolonged residence at depth (Polacci et al. 2006). The transition to fire fountain activity occurred when coalescence became so efficient to produce a foam of gas bubbles that eventually collapsed, rose in the conduit as a gas core surrounded by a moderately vesiculated liquid annulus, and erupted explosively as vigorous jets of gas and liquid magma (Polacci et al. 2006; Andronico and Corsaro 2011; Alparone et al. 2012). Alternatively, Houghton et al. (2004), Sable et al. (2006) and Pompilio et al. (2017), suggest that the transition between weak intracrater Strombolian activity and paroxysmal phases with several km-high sustained columns, could be related to different proportions, within the conduit, between high (microlite-rich) and low (microlite-poor and gas rich) viscosity magma portions. In both cases the contrasting textures of the pyroclasts are not genetically related to each other. In our case at PdF, we suggest that the eruptive dynamics evolution is controlled by distinct processes with respect of those described in these latter papers, at least in eruptions in which moderate Hawaiian-style activity precedes Strombolian-style activity (Fig. 4.12). In these cases, the textural variation is related to the same batch of magma undergoing different cooling and degassing histories.

2.6. Conclusions on the eruptive models and fragmentation implications

From all the observations and interpretations brought by this multi-disciplinary work, we are able (i) to reconstruct the pre-eruptive conditions of the PdF shallow magmatic system for the June 2014-July 2015 period, (ii) to quantify the implications for the syn-eruptive processes within the eruptive dykes and (iii) to correlate the previous points with the eruptive dynamics and emitted products (Figs. 4.12a and 4.12b).

The reactivation of the shallow plumbing system of PdF in June 2014, followed by the beginning of its rejuvenation since early 2015 imply several changes in the shallow magmatic reservoirs at PdF. The June 2014 evolved magma was reactivated by internal magmatic processes. This reactivation was triggered by a second boiling and a gas/crystal segregation (golden pumice vs. crystallized lava) within the magmatic volume that increase the internal overpressure of this reservoir at the origin of the eruption (Gurioli et al. 2018). This is consistent with low intensity precursors and weak inflation rate preceding the eruption (Peltier et al. 2016). On the other hand the July 2015 eruption (with probably the February and May 2015 ones) erupt a less mechanically stratified magma (scarce golden pumice and absence of fully-crystallized end-member) inherited from a mixing between a differentiated magma and a less differentiated one. This new magmatic input of pristine magma is consistent with a relatively strong summit ground inflation preceding this eruption (Peltier et al. 2016).

Pre-eruptive reservoir conditions are more or less impacting the syn-eruptive processes that occur within the eruptive dykes. In June 2014, the pre-eruptive gas segregation accumulated a foam, which probably provoked an annular dominated flow within the dyke (Jaupart and Vergniolle 1998, 1989; Vergniolle and Jaupart 1990). However, Hawaiian-style activity is also observed without significant golden pumice emission, as in the July 2015 eruption. Less continuous conduit gas flow as churn flow (Houghton and Gonnerman 2008), associated with a high bubble nucleation rate can also produce mild lava fountains and might occur during the fluidal scoria emission. Finally, we suggest that discontinuous slug flow (open system degassing) are the most relevant flow regime for Strombolian phases at the end of the PdF eruptions.

Estimated initial residence time durations within the eruptive dyke, thanks to the seismic spectrograms, are coherent with shallow reservoir depths estimated between 1.3 and 1.7 km below the volcano top by Peltier et al. (2016). Estimated decompression rates from 0.08 (annular and churn flows) to 0.03 MPa s^{-1} (slug flows) and are also coherent with melt inclusion saturation pressure measured by Di Muro et al. (2014 and 2016). According to the Gonnerman and Manga (2012) model (Fig. 4.12c), these decompression rates, which can be related to corresponding TADR are in agreement with theoretical Hawaiian-style activity assuming typical basaltic viscosities (Villeneuve et al. 2008; Rhéty et al. 2017; Kolzenburg et al. 2018) and with estimated vertical migration of dyke by Peltier et al. (2005) of about 2 to 3 m s^{-1} (assuming a pressure gradient of around 42 MPa km^{-1}). Increasing the residence time within the dyke (equivalent to a decreasing of the ascent velocity and to a decreasing TADR), associated

with an increase of the viscosity because of the increasing microlite content is also consistent with Strombolian-style activity associated with effusive emission.

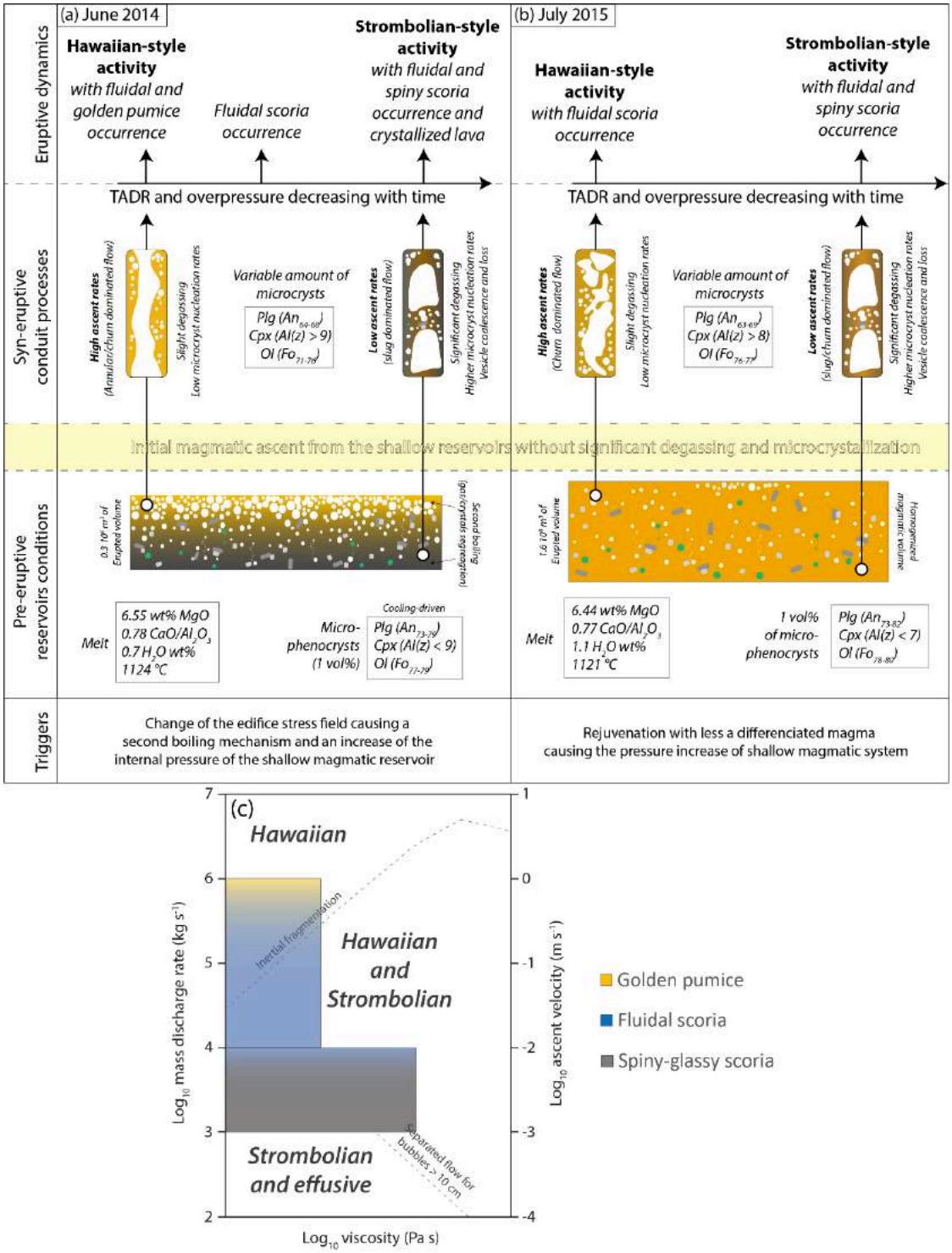

Figure 4.12 *– Comparison of the eruptive models of (a) the June 2014 and (b) the July 2015 eruptions. The shades of yellow represent a microlite-free matrix whereas the shades of grey represent a microlite-rich matrix. (c) Eruptive dynamics with associated products integrated in the Gonnerman and Manga (2012) model, considering basaltic viscosities, magma mass discharge rates and ascent velocities.*

New thermometers are also calibrated in this paper considering pre-eruptive and syn-eruptive conditions that helps (i) understanding the effect of pressure and dissolved gas on the magma temperature evolution before and during an eruption, and (ii) discriminating cooling-driven crystallization from degassing-driven crystallization. Focusing on the pre-eruptive (micro-phenocryst population) and syn-eruptive (microlite population) crystals, it appears that these two populations are very distinct both in terms of CSD and compositions. Further interesting research, (i) as determine the delay between the cooling-driven and degassing-driven crystallizations, and (ii) quantify the residence time of the magma within the dyke for each eruptive styles (based on the CSD theory) should be the new objectives of such research, as this parameters can involve important implications in terms of volatile content and viscosity at the fragmentation levels.

3. Perspectives

3.1. Quantification du temps de résidence du magma au sein du conduit éruptif ainsi que des taux de croissance et de nucléation des microcristaux

Comme souligné dans le **chapitre I** et dans la conclusion de la section précédente, les volatiles dissous et exsolvés, ainsi que la cristallinité des magmas, jouent un rôle majeur sur la viscosité de celui-ci et donc aussi sur les mécanismes de fragmentation qui contrôlent les styles éruptifs. En ce qui concerne l'ensemble de données acquises au sein de ce chapitre, il peut être intéressant d'effectuer davantage de quantifications sur les processus syn-éruptifs et, plus spécifiquement, de mieux comprendre la dynamique de la cristallisation syn-éruptive. En se basant sur les données de CSD, nous pouvons théoriquement estimer les taux de croissance des microcristaux de plagioclase et de clinopyroxène, à partir de cette loi $G = -\frac{1}{\alpha t}$ (ex. Cashman 1988 ; Marsh 1988 ; Higgins 2006 ; Bain et al. 2018), où G représente le taux de croissance des cristaux ($mm.s^{-1}$), α est la pente moyenne de la CSD (mm^{-1}) et t est le temps de résidence de la population de cristaux (s).

Grâce à l'estimation du temps de résidence du magma initial dans le conduit éruptif (respectivement 40 et 55 min pour les éruptions de Juin 2014 et Juillet 2014 ; Fig. 4.11), le taux de croissance des cristaux de plagioclase et de clinopyroxène peuvent être estimés en considérant les pyroclastes émis lors des phases initiales de ces éruptions, en l'occurrence les scories de type *fluidal* (Fig. 4.4). Le taux de nucléation (J en $mm^{-3}.s^{-1}$) des cristaux peuvent être également estimés grâce à la relation $J = N_0G$, où N_0 représente la densité de nucléation (mm^{-4}) qui est théoriquement la valeur de la CSD à x = 0 (Higgins 2000, 2006).

Suite à ces calculs, les valeurs de G sont comprises entre $2{,}4.10^{-5}$ (Juillet 2015) et $3{,}5.10^{-5}$ $mm.s^{-1}$ (Juin 2014) pour le plagioclase et entre $1{,}5.10^{-5}$ (Juillet 2015) et $2{,}3.10^{-5}$ $mm.s^{-1}$ (Juin 2014) pour le clinopyroxène. Les valeurs de J sont comprises entre 0,6 (Juillet 2015) et 2,1 $mm^3.s^{-1}$ (Juin 2014) pour le plagioclase et entre 0,3 (Juillet 2015) et 1,4 $mm^3.s^{-1}$ (Juin 2014) pour le clinopyroxène. Les valeurs de G et J sont systématiquement plus élevés pour le plagioclase que pour le clinopyroxène, ce qui est cohérent avec les teneurs mesurées. Avec des

conditions expérimentales similaires, Burkhard (2002, 2005) suggère des valeurs de G aussi similaires pour ces phases.

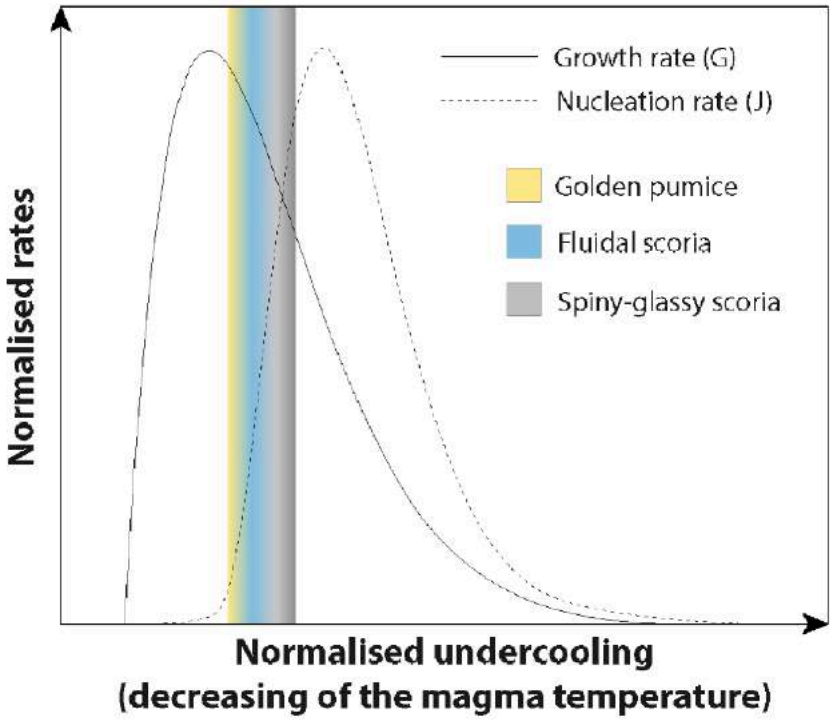

Figure 4.13 *– Interprétation schématique de l'évolution des taux de nucléation et de croissance en fonction de la surfusion (figure modifié à partir de Higgins 2006).*

En admettant que la valeur de G reste constante pendant toute la durée des deux éruptions, le temps de résidence du magma dans le conduit peut être estimé pour les autres composants émis, c'est-à-dire, pour les pyroclastes de type *golden pumice* et de type *spiny-glassy scoria*. Le résultat principal de cette approche est que le temps de résidence des *golden pumice* est dans tous les cas deux fois inférieur aux *fluidal scoria*, ce qui est cohérent avec l'interprétation initialement établie. Cependant, les temps de résidence des scories de type *spiny-glassy* et des laves contrastent avec l'interprétation initiale qui suggère une augmentation progressive du temps de résidence dans le conduit éruptif. En effet, le temps de résidence calculé pour les scories de type *spiny-glassy* (45 min) est inférieur à celui des scories de type *fluidal* (55 min). Le temps de résidence calculé pour les laves (54 min) est similaire à celui des scories de type *fluidal* (valeurs estimées à partir des taux de croissance des plg de l'éruption de Juillet 2015).

Cette incohérence reflète très probablement la limite de cette approche qui admet un taux de croissance G constant sur l'ensemble de l'éruption. Or, les taux de nucléation G et de croissance J sont variables (Fig. 4.13) et dépendent principalement de la teneur en H_2O dans le magma, de la vitesse de refroidissement de celui (Burkhard 2002, 2005) et de la surfusion (Higgins 2006 ; Arzilli et al. 2016 ; Bain et al. 2018) qui représente la différence entre la température du magma et la température du liquidus des différentes phases.

L'évolution de la texture du magma au cours de sa remontée (dégazage et cristallisation) peut induire une évolution de la température et de la teneur en H_2O, ayant pour conséquence des modifications significatives du taux de croissance G et du taux de nucléation J des microlites. Ainsi, la Figure 4.13 montre de manière schématique, comment la surfusion joue sur ces paramètres. Compte tenu de ces évolutions, les temps de résidence du magma calculés au sein des conduits éruptifs (en considérant une valeur de G constante) ne sont pas exacts et représentent des valeurs extrêmes. Le taux de croissance des cristaux est plus particulièrement développé au sein du **Chapitre V**.

3.2. Contribution des données texturales et géochimiques pour un modèle de viscosité et la modélisation de coulées de lave

L'intégration des données texturales et géochimiques, notamment des températures magmatiques, des teneurs en cristaux et en vésicules, ainsi que des densités squelettiques des échantillons de laves fraîchement récoltés sur le terrain, peuvent aider aux calculs de viscosité. Cette viscosité est en effet calculée suivant la procédure de Chevrel et al. (2018 et références incluses). Dans ce contexte, une étude publiée dans *Annals of Geophysics* (Harris et al. 2018) présente une validation d'une réponse aux crises effusives au Piton de la Fournaise (exemple de l'éruption d'Avril 2018), afin de mieux anticiper l'évolution de la direction et de la vélocité des coulées de lave (cf. **Annexe 3**).

Enfin, l'observation syn-éruptive de la coulée de Juillet 2015 et les données texturales et géochimiques mesurées en laboratoire sur les échantillons laviques correspondants, ont permis de mettre en évidence la mise en place d'un mécanisme de cisaillement au sein de la

coulée de lave favorisant l'écoulement. Cette étude (cf. **Annexe 4**) a été soumise au sein de la revue *Geology*.

CHAPITRE V

EVOLUTION D'UNE ACTIVITE HAWAIENNE VERS UNE ACTIVITE TRANSITOIRE PLUS EXPLOSIVE : ETUDE DE CAS SUR L'ERUPTION DE SEPTEMBRE 2016

1. Présentation générale

Après avoir décrit un certain nombre d'observations et mis en place des quantifications sur les processus pré- et syn-éruptifs concernant la période éruptive 2014-2015 caractérisée par des activités hawaïennes et stromboliennes relativement peu explosives (cf. **chapitre IV**), la deuxième étude majeure de cette thèse est focalisée sur l'éruption de Septembre 2016. A la différence des éruptions de 2014 et de 2015, cette éruption fut caractérisée par une activité relativement plus intense et transitoire, produisant une quantité de cendres plus élevées par rapport aux précédentes éruptions étudiées au sein du chapitre précédent.

L'enjeu de cette étude est de caractériser et comprendre les processus magmatiques et les mécanismes de fragmentation associés qui sont responsables du changement du style éruptif, d'une activité hawaïenne vers une activité transitoire plus explosive. La suite de ce chapitre, présenté en anglais, correspond à un article soumis au journal *Geochemistry, Geophysics, Geosystems*.

2. Les processus syn-éruptifs à l'origine du changement de style éruptif lors de l'éruption de Septembre 2016

Evidence of plug pressurization enhancing magma fragmentation during the September 2016 basaltic eruption at Piton de la Fournaise (La Réunion Island, France)

Simon Thivet[(1)], Lucia Gurioli[(1)], Andrea Di Muro[(2)], Allan Derrien[(2)], Valérie Ferrazzini[(2)], Mathieu Gouhier[(1)], Diego Coppola[(3)], Bo Galle[(4)], Santiago Arellano[(4)]

[1] Laboratoire Magmas et Volcans, Université Clermont Auvergne - CNRS - IRD, OPGC, Campus Universitaire des Cézeaux, 6 Avenue Blaise Pascal, 63178 Aubière Cedex, France

[2] Institut de Physique du Globe (IPGP), Sorbonne Paris-Cité, CNRS UMR-7154, Université Paris Diderot, Observatoire Volcanologique du Piton de la Fournaise (OVPF), Bourg Murat, France

[3] Dipartimento di Scienze della Terra, Università di Torino, Via Valperga Caluso 35, 10125 Turin, Italy

[4] Chalmers University of Technology, Department of Space, Earth and Environment, SE-41296 Gothenburg, Sweden

Article and revision submitted to *Geochemistry, Geophysics, and Geosystems*

Acknowledgments

We thank J-L. Devidal and J-M. Hénot for their valuable help for the use of the EPMA and the SEM, M. Benbakkar for the bulk rock analysis, measured at ICP-AES at the LMV. We also thank all the staff of the OVPF with whom we had constructive discussions. We finally thank Giuseppe La Spina and an anonymous reviewer for their constructive and helpful comments. This research was financed by ClerVolc, the French Government Laboratory of Excellence initiative.

Supplementary material (labelled Figure S and Tables S in the manuscript) are available at

http://lmv.uca.fr/thivet-simon-2/

Key-words

Ash; Basaltic; Fragmentation; Hawaiian-style activity; Piton de la Fournaise; Plug; Transient explosions.

Abstract

In September 2016, Piton de la Fournaise volcano, well-known for its effusive and Hawaiian fountaining activity, produced, at the end of the eruption, an unusual phase of pulsating ash and bomb emission. Integration of geophysical data, with textural and petrological analysis of the samples, allowed us to constrain the main factors that controlled this sudden shift in activity, potentially dangerous for the tourist population that usually approach these "gentle" eruptive sites. Volcanic tremor, lava discharge rates, fountain heights and SO_2 emission changed rapidly during the eruption. Grain size and componentry of the tephra beds evolved from unimodal all along the sequence to bimodal on the last day of the activity, reflecting the contribution of both Hawaiian fountaining at the main vent (vent A) and transient explosive activity at the second vent (vent B). Hawaiian fountaining produced highly vesicular and almost microlite-free tephra (golden pumice and fluidal scoria) while transient explosive activity emitted denser and crystal-rich tephra (transitional and opaque scoria) sometimes mingled with vesicular fragments. Permeability measurements on lapilli and bomb-sized samples reveal that golden and fluidal components were more gas-permeable than the transitional and opaque ones, while textural and chemical analyses of the ash support the hypothesis that the transitional and opaque components were inherited from the crystallization of the initial golden pumice and fluidal scoria related magma at the surface. We thus suggest that the vent B accumulated a plug of degassed, cooled and low-permeable magma, which modulated overpressure pulses under the late input of ascending magma.

2.1. Introduction

Nowadays, active volcanoes are increasingly monitored and studied with a panel of multidisciplinary techniques. Focusing on basaltic volcanism and the associated volcanic hazards, ash-dominated explosions can potentially have large and unexpected impacts on the local populations and environments, compared to low explosive eruptions (e.g. Barsotti et al. 2010; Scollo et al. 2013; Brown et al. 2017). Even if these ash and bomb explosions can be relatively small and mild, they can pose a threat to the tourist population that usually approach

these “gentle” eruptive sites (e.g. at Etna, Hawaii, Stromboli, Piton de La Fournaise, Masaya; see also Blong 1984, 1996; Papale 2016; Morin et al. 2016). Thus, it is critical to characterize, quantify and understand what control the transition from mild to more violent eruptive phases (e.g. Houghton et al. 2004; Sable et al. 2006; Andronico et al. 2009; Di Traglia et al. 2009; Cimarelli et al. 2010; Corsaro et al. 2017) and what control the magmatic processes occurring before and during an explosive event (e.g. Villemant et al. 2009; Di Muro et al. 2014, 2015, 2016; Arzilli et al. 2015, 2019a; Edwards et al. 2018; Gurioli et al. 2018). Many studies proved that textural quantification, in terms of vesicle and crystal contents and size distributions of basaltic erupted products like bombs (e.g. Rosseel et al. 2007; Gurioli et al. 2014; Leduc et al. 2015; Gurioli et al. 2018; Jones et al. 2018), lapilli (e.g. Walker and Croasdale 1971; Sparks 1978; Marsh 1988; Houghton and Wilson 1989; Toramaru et al. 1989; Mangan and Cashman 1996; Lautze and Houghton 2005; Polacci et al. 2006; 2009; Costantini et al. 2010; Stovall et al. 2011; Carey et al. 2012; Parcheta et al. 2013; Gurioli et al. 2018; Holt et al. 2019) and more recently ash (e.g. Taddeucci et al. 2002, 2004; Cioni et al. 2008; 2014; D’Oriano et al. 2011a, 2014; Porrit et al. 2012; Lautze et al. 2013 ; Liu et al. 2015; Cannata et al. 2019) are fundamental to achieve this goal. Since the 2000’s, new approaches have been developed by combining textural measurements on basaltic tephra with field data (e.g. Andronico et al. 2014; Romero et al. 2018; Edwards and Pioli 2019), petrological and geochemical analysis (e.g. Taddeucci et al. 2002, 2004; Polacci et al. 2006; Bai et al. 2011; Pioli et al. 2014; Di Muro et al. 2014, 2015; Pompilio et al. 2017; Gurioli et al. 2018), as well as geophysical insights (e.g. Burton et al. 2007; Patrick et al. 2007; Andronico et al. 2008, 2013, 2014; Gurioli et al. 2008, 2013, 2014; Miwa et al. 2009; Polacci et al. 2009; Colo’ et al. 2010; Landi et al. 2011; Pistolesi et al. 2011; Miwa and Toramaru 2013; Leduc et al. 2015). Several of these studies have already shown that relative proportions between low-viscous (crystal-poor), high-viscous (crystal-rich) as well as volatile-poor and volatile-rich magmas within different levels of the magmatic conduits can potentially modulate the transition between ash-free and ash-rich eruptions. Following these approaches we focused on the main factors that control the shift in activity from Hawaiian fountaining events to transient bomb and ash explosions during the September 2016 eruption at Piton de la Fournaise (PdF) volcano (La Réunion Island, France).

2.2. Geological setting

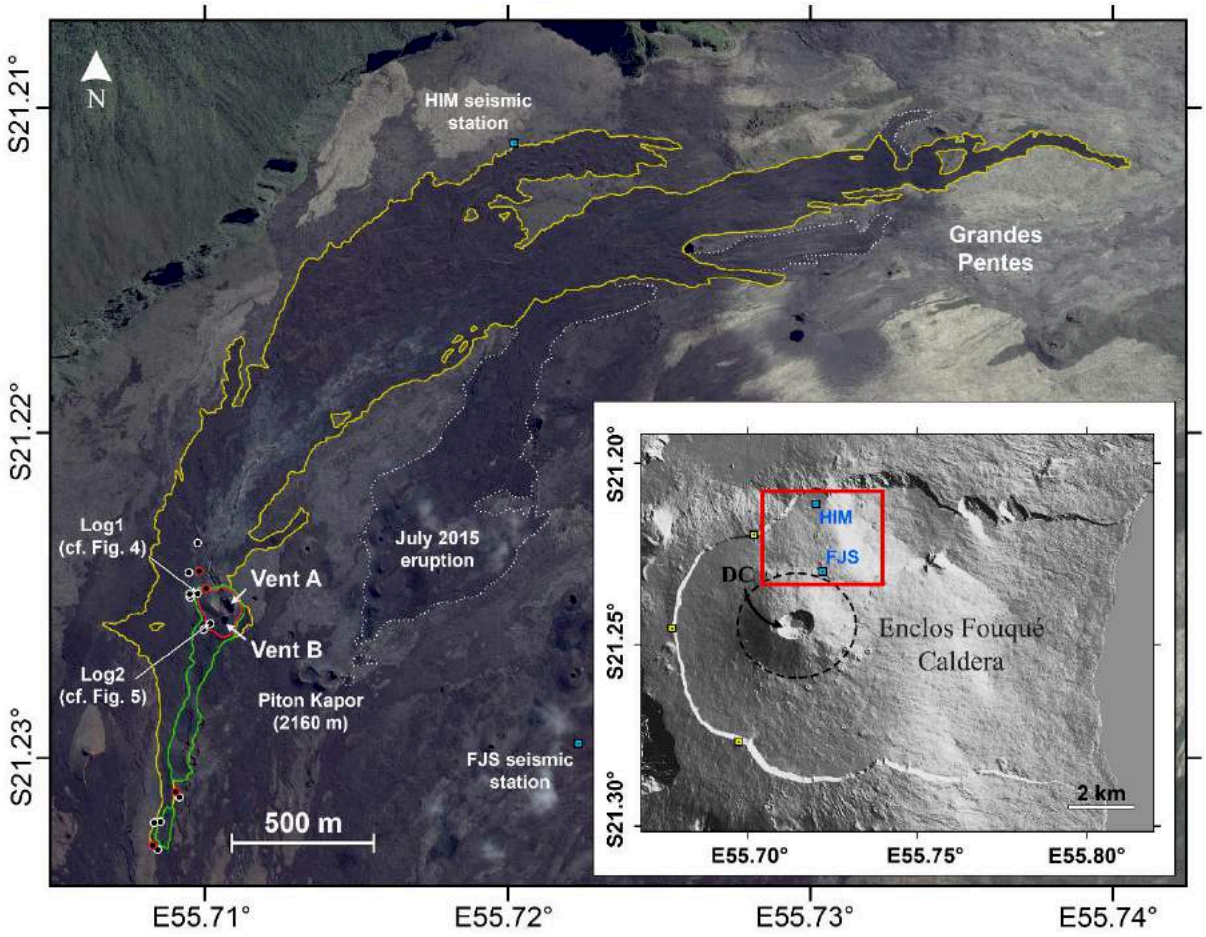

Figure 5.1 *– Map of the September 2016 eruption with associated DEM of PdF. DC: Dolomieu caldera. The black dashed line represents the central cone of PdF. Blue and yellow squares are the location of the seismic and NOVAC stations respectively. White and red dots represent the different tephra and lava sampling sites respectively. The yellow, green and red lines represent respectively the outline of the lava flows, the eruptive fissure system and main active cone edifice with the vent A and vent B.*

PdF is one of the most active basaltic volcanoes on Earth (Staudacher et al. 2016; Peltier et al. 2018). On this volcano, investigations on prehistoric and historic deposits show that large volume explosive events can occur inside or outside the Enclos Fouqué caldera (e.g. Michon et al. 2013; Ort et al. 2016; Morandi et al. 2016), which is the most recent and main caldera of the volcano (Fig. 5.1). More recent activity has also been well-documented by Staudacher et al. (2016) and Peltier et al. (2018) especially between 1998 and 2013. This period was relatively

active with an emitted magma volume of 32.6×10^6 m^3 per year on average. Since 1998, all the eruptions occurred within the Enclos Fouqué caldera, with variable durations (hours to months) and variable output rates (Roult et al. 2012; Coppola et al. 2017). These eruptions were mostly typical basaltic fissure eruptions with a few exceptions like the summit ash emission linked with the collapse of the Dolomieu summit caldera (Fig. 5.1) during the April 2007 eruption (e.g. Staudacher et al. 2009, 2016; Peltier et al. 2009; Michon et al. 2013) which involved more magma than any other eruption at PdF since at least 200 years. Since, the eruptive regime at PdF has been mainly effusive, coupled with more or less intense Hawaiian-style and weak Strombolian-style activity (e.g. Harris et al. 2017; Gurioli et al. 2018; Peltier et al. 2018). Weak Strombolian-style activity at PdF is mainly characterized by short and sporadic bubble bursts that only form coarse lapilli, bombs and spatters with scarce ash emission (DynVolc 2017; Gurioli et al. 2018), while Hawaiian-style fragmentation is characterized by moderate sustained lava fountains, following the classification of Houghton et al. (2016), and usually produce lapilli and coarse ash sometimes with Pele's hairs (e.g. Villemant et al. 2009; Di Muro et al. 2014, 2015; Gurioli et al. 2018).

More recently, the 11-18 September 2016 eruption produced a different and unexpected behavior. While typical Hawaiian fountaining dominated the entire eruption, ash and bombs were produced the last day of the eruptive activity. Although this ash formation has been relatively weak compare to big explosive and plume forming events (e.g. the more violent Strombolian events of 1759, 1791, 1860 and 1961 eruptions, Michon et al. 2013), this kind of discreet ash plumes are very unusual in the recent activity of PdF. Similarly to the Hibert et al. (2015) approach to the January 2010 eruption at PdF (that was without ash emissions), the purpose of this study was to gather and organize all the useful datasets to trace the complex degassing and fragmentation history of the September 2016 eruption and above all, understand the formation of this uncommon ash, which represent an unexpected hazard that could potentially occur during the next eruptions at Piton de la Fournaise and other basaltic systems.

2.3. Methods

2.3.1. Field observations, samplings and monitoring networks

The September 2016 eruption lasted seven days, from the 11 to the 18. Field sampling was jointly realized by the Observatoire Volcanologique du Piton de la Fournaise (OVPF, La Réunion, France) and by the DynVolc teams (from the Observatoire de Physique du Globe de Clermont-Ferrand, OPGC, and from the Laboratoire Magmas et Volcans, LMV). Since the first day of activity, several samples were collected during the eruption, especially on the southern and upper tip of the fracture system. Other samplings were done on the 16 of September, still during the volcanic activity (Table S5.1). Syn-eruptive tephra sampling was performed by hand and a galvanized steel pipe was used to sample the molten lava near the source of emission. Then, these samples were gently quenched in water. Other samples were collected a few days after the end of eruption to be able to access very proximal and strategic deposits in order to reconstruct the entire sequence of the eruption (Fig. 5.1). The purpose of the sampling was to identify all the different components of the emitted tephra during the eruption, to quantify their respective proportions, while preserving the most primitive signature of the juvenile magma (Gurioli et al. 2015; Harris et al. 2017; Gurioli et al. 2018). These different samples were carefully numbered, sorted (Table S5.1) and sent to the LMV, in Clermont-Ferrand (France), to be analyzed in terms of textural, petrological and geochemical analyses. The raw data used in this study are available in the DynVolc database (2017) as well as in the supplementary material of this article.

Data from the field monitoring network of the OVPF were compiled to constrain the volcano dynamics before and during the eruption. The evolution of all the monitoring measurements listed hereafter (volcanic tremor, lava discharge rate, ash emission and SO_2 flux) could be compared in order to quantify the evolution of the eruptive dynamics (Hibert et al. 2015). Ground-based (webcam situated 1100 m from the active vents, and cameras) and aerial photos (drone) taken during the eruption, permitted to continuously follow the eruptive activity (depending on the weather conditions). The volcanic tremor is usually generated by the movement of magmatic fluids and this signal is continuously recorded by the seismic stations of the OVPF. In this study, tremor data from Crater Himiltrude (HIM) and Piton Faujas (FJS)

seismic stations (broad-band three-components stations; Battaglia et al. 2016; white squares on Fig. 5.1) and filtered on five different frequency bands (from 0.5 to 32 Hz) are shown. Pre- and syn-eruptive deformation was monitored on three different Global Navigation Satellite System (GNSS) baselines (Peltier et al. 2018). In order to quantify the lava discharge rate of the eruption, we combined in this study two different datasets from two near real-time remote sensing systems: (i) the HOTVOLC observing system (Gouhier et al. 2012, 2016), using data from the Spinning Enhanced Visible and InfraRed Imager, onboard the geostationary platform Meteosat (MSG-SEVIRI) and (ii) the MIROVA observing system (Coppola et al. 2009, 2015, 2017; Coppola and Cigolini 2013), using the sun-synchronous orbit of two satellites (Terra and Aqua) which embed the Moderate Resolution Imaging Spectroradiometers (MODIS). From the HOTVOLC system, we were able to collect thermal data every 15 min and to generate high temporal resolution time series of the lava Volume Flow Rate (VFR), obtained from IR satellite data. Also, the MIROVA system collected thermal data every six hours to deduce a time series of the Time-Averaged Discharge Rate (TADR). Hereafter, VFR and TADR are described as lava flux. From webcam images analysis (one image every two minutes), HOTVOLC-derived lava flux dataset was filtered and discarded in case of significant low-altitude cloud cover, which can possibly disturb these space-based IR measurements. In order to be compared with MIROVA-derived lava flux, we applied a moving average on seven points (~ two hours) for the entire HOTVOLC-derived lava flux dataset. Using the HOTVOLC system, we were also able to qualitatively monitor the presence or the absence of both ash plumes and SO_2 emission (Guehenneux et al. 2015). In parallel, SO_2 flux measurements were quantitatively estimated by the Network for Observation of Volcanic and Atmospheric Change (NOVAC, Galle et al. 2010), based on three ground-based ultraviolet absorption spectroscopy station arranged around the Enclos Fouqué caldera (yellow squares on Fig. 5.1). These measurements, taken with a typical rate of one gas flux value every 10 min, led to a single averaged SO_2 flux value each day during the monitoring period, as well as to daily statistics of gas plume direction and altitude.

2.3.2. Grain size and componentry

Grain size analysis were performed following the procedure of Gurioli et al. (2018), on samples within two log sections (eight different layers in total) representing the entire sequence emplaced during the September 2016 eruption. Samples were dried in the oven at 90 °C during a minimum duration of 24 hours. To avoid bias in the grain size data, sieving was realized manually because the main part of the deposit was highly vesicular and fragile. Componentry was carried out in two steps. First, following the nomenclature of White and Houghton (2006), to distinguish juvenile, non-juvenile and composite clasts. Then, all these clasts were classified into different juvenile components depending on their colors, surface and shapes (e.g. Stovall et al. 2012; Pompilio et al. 2017; Gurioli et al. 2018) within the bomb- and lapilli-size fractions as well as the coarse ash particles (> 500 µm in diameter).

2.3.3. Bulk texture analysis (porosity, Helium connectivity and air permeability)

Bulk texture analysis were performed on a selection of different clasts. Envelope density and helium vesicle connectivity were measured on 108 samples from the September 2016 eruption, following the procedure presented within the **Chapter IV**. Density measurements were realized using the Micromeritics Geopyc 1360 envelope density analyzer and both helium vesicle connectivity and Dense Rock Equivalent (DRE) measurements were performed using the Micromeritics Accupyc 1340 Helium pycnometer (Formenti and Druitt 2003; Kawabata et al. 2015; Colombier et al. 2017b). Density measurements allow us to calculate porosity of each pyroclasts, while helium vesicle connectivity measures the percentage of connected and isolated vesicles within each sample.

Ash density measurements were performed using water pycnometry following the procedure of Eychenne and Le Pennec (2012). Three different density measurements were carried out on each ash component. Ash componentry was first determined using basic macroscopic observations with binoculars while Scanning Electron Microscope (SEM, JEOL JSM-5910 LV, acceleration voltage of 15 kV) was used to acquire Back-Scattered Electron

(BSE) images on the different ash components. The grain size used for the water pycnometry was between 0.5 ϕ (710 µm) and 1 ϕ (500 µm) for all the components. A balance (precision of 10^{-3} g) was used, as well as high precision pycnometers and distilled water. Envelope density of the each ash component can be confidently determined supposing that the water do not enter the sample pores due to the relatively high water surface tension. The particles were weighed after each measurement, to confirm that the water did not enter. At least 100 ash particles of the same component were used for each measurement. Thus, the calculated density and porosity value is the average of all the ash particles of that size, measured for each component.

Air permeability measurements were carried out on 64 samples (of known density and helium vesicle connectivity values) from different eruptions of PdF, 21 of which belong to the September 2016 eruption. The others are from recent Hawaiian/Strombolian-style activities between June 2014 and January 2017 (DynVolc 2017) and also from historical and intense activities of Piton Chisny black tephra fall (Hawaiian fountaining activity; Morandi et al. 2016; Principe et al. 2016; Colombier et al. 2017b) and from the 1860 eruption (phreatomagmatic activity; Michon et al. 2013). This large range of samples from different eruptive dynamics allowed us to compare the permeability characteristics of different type of pyroclasts, both within the September 2016 eruption and with a larger set of samples. Following the procedure of Colombier et al. (2017a) and Gurioli et al. (2018), the clasts were cut into rectangular prisms (to know precise sample cross-sectional area which is required to calculate the permeability) and dried, before being imperviously wrapped with laboratory parafilm. The samples were then coated with resin. Then sample extremities were cut again to ensure to be resin-free and allow the air flow to pass through the sample. Some of the samples were destroyed during the preparation which was sometimes difficult to perform due to the fragility of the samples. The prepared samples were then placed within the sample holder of the home-made permeameter (cf. **Chapter III**) following the instrumental processing of Takeuchi et al. (2008). The permeameter has a large broad measurements range, which allows to measure the permeability from 10^{-17} to 10^{-9} m^2. Two different flow meters of different measurement ranges (0-500 and 0-16000 mL min^{-1}) as well as a differential pressure meter (0-200000 Pa) are used to measure the air flow and the pressure drop across the sample, in order to solve the Forchheimer equation and deduce the Darcian (viscous) permeability k_1 of the measured samples (Rust and Cashman 2004; Bai et al. 2010).

2.3.4. Ash morphology

For each ash component, the method developed by Leibrandt and Le Pennec (2015) was used to characterize their projected 2D morphology. Optimized morphometry of volcanic ash can yields crucial information on fragmentation processes during explosive activity (e.g. Heiken 1974; Sheridan and Marshall, 1983; Wohletz, 1983; Büttner et al. 1999; Taddeucci et al. 2002; Riley et al. 2003; Maria and Carey 2007; Lautze et al. 2012; Dellino et al. 2012; Liu et al. 2015; Schmith et al. 2017; Nurfiani and Bouvet de Maisonneuve 2018). Several series of Apparent Projected Shape of Ash (APASH) on a very high number of ash particles were carried out using the automatized morpho-grainsizer Morphologi G3 of Malvern, able to disperse the ash sample on a glass slide and measure both the size and the morphology of the particles. APASH can be represented by roughness parameters as the solidity (SLD) and the convexity (CVX), which represent morphological (particle scale) and textural (smaller scale) roughness of the particles respectively (Liu et al. 2015), as well as shape parameters like the aspect ratio (AR). These three parameters were used to compare the different morphology characteristics of the ash and are defined using simple relations summarized by Leibrandt and Le Pennec (2015): $SLD = A/A_{CH}$, $CVX = P_{CH}/P$ and $AR = W_b/L_b$ where A is the particle area (μm^2), A_{CH} is the convex-hull area that is the area contain in the convex-hull perimeter (μm^2), P is the particle perimeter (μm), P_{CH} the convex-hull perimeter that is the smallest convex polygon that contains all the pixels of the particle (μm), W_b the minor axis and L_b the major axis of the particle. SLD, CVX and AR values are thus dimensionless values between 0 and 1. This way, we measured the ash particles morphologies on the 0.5-1 ϕ (710-500 μm) grainsize fraction for each ash component. The raw data were filtered in case of artificial particle agglomerates. Statistical analysis on these morphology data were also performed using boxplot representation.

2.3.5. Chemical analysis

Glass and crystals in-situ measurements for major elements were carried out on the ash fraction and following the same procedure adapted in the **Chapter IV**, using a Cameca SX100 electron microprobe, with a 15 kV acceleration voltage and a focused spot size (1 μm) for

crystals and a spot diameter of 10 µm for the glass. Bulk rock compositions on the September 2016 products were performed by ICP-AES (Horiba Jobin-Yvon Ultima C spectrometer) analysis following the same procedure adapted by Gurioli et al. (2018), both on coarse (bombs and lapilli) and fine (ash) samples. All these analysis and associated errors are provided in the supplementary material.

2.3.6. Micro-texture analysis

Petrographic observations and micro-texture analysis were performed using optical microscope and SEM imagery (BSE) on selected bomb and ash samples. Vesicle size distribution (VSD), vesicle number density (N_V) and vesicle to melt ratio (V_G/V_L) were measured following the Shea et al. (2010a) and **Chapter IV** procedures. In these calculations, the volume of melt is considered as micro-phenocryst-free and bubble-free. Crystal size distribution (CSD) and crystal number density (N_C) were measured following the Higgins (2000, 2002, 2006) and **Chapter IV** procedures. For these micro-textural quantification, 15 ash particles (0.5-1 ϕ grainsize fraction) were used on average for each component in order to statistically acquire enough textural data (based on the vesicle and crystal quantity to count). Both for vesicles and crystals, the minimum object size measured was 2 pixels (equivalent to 3 µm for the most common used magnification 90x with the SEM). Based on our analyses and using the crystals shape database of Morgan and Jerram (2006), average crystal habits (x:y:z) for plagioclase (plg), clinopyroxene (cpx) , olivine (ol) and oxides (ox) are respectively 1:3.2:10, 1:1.3:2, 1:1.4:1.4 and 1:1:1.

2.4. Results

2.4.1. The September 2016 eruption

2.4.1.1. Eruptive precursors

The September 2016 eruption is the seventh eruption at PdF since its reactivation in 2014 (after more than three years of rest, Gurioli et al. 2018), and the second of 2016 (after the May 2016 eruption). Mid-term precursors were represented by a short seismic crisis associated with slight ground inflation around 50 days before the eruption (Peltier et al. 2018). Then, after one month of quiescence with no significant ground deformation, SO_2 emissions from the summit craters began to slightly increase from the 27 of August. Shallow seismic activity located below the central cone suddenly increase the 10 of September (20 volcano-tectonics earthquakes, VT), just few hours before the beginning of the eruption. On the 11, an intense seismic swarm (489 VT) started at 3:35 (all time cited in this paper are in UTC, LT = UTC+4 hours) and the eruption began at 4:35, which was confirmed by the thermal anomaly detected by the HOTVOLC system at 04:45. During the eruptive activity which ended shortly after midnight of 18 of September, summit, basal and distant GPS baselines did not record significant ground deformation.

2.4.1.2. Eruptive phenomenology, volcanic tremor, lava flux, and SO_2 emissions

High (4-8 and 8-32 Hz) and low (0.5-1 Hz) frequency bands of the volcanic tremor have relatively low intensities during the eruption, except at the beginning of the eruption (when the signal was relatively high) and for some short-lived anomalies. The anomalies in the very high (8-32 Hz) frequency band reflect very local disturbance near the FJS seismic station when the lava flow path was very close to the station (Fig. 5.1). The intermediate (1-2 and 2-4 Hz) frequency bands have relatively high intensities that broadly correlate with the evolution of the

eruption intensity, the lava flux (both from HOTVOLC and MIROVA datasets) and the SO_2 emissions (Fig. 5.2). The tremor (2-4 Hz) level reached its highest level very soon at the beginning of the eruption which was synchronous to the opening of several vents aligned on a 900 meters long fissure, where sustained lava fountains (height of about 40 m) were observed. The associated lava flux (between 30 and 50 m^3 s^{-1}) and SO_2 emissions (2500 tons d^{-1}) were also the highest recorded within the eruption. Then, the volcanic tremor, lava flux (around 10 m^3 s^{-1}) and SO2 emissions (down to 200 tons d^{-1}) rapidly decreased and slightly fluctuated at low levels until the 13 of September, at 12:00. This decrease in intensity was linked with the progressive closure of the southern part of the fissure, with still active Hawaiian fountaining within the Northern tip of the fissure (12 of September). From the 13, only two closely spaced vents remained active until the end of the eruption. We named them vent A and vent B (Fig. 5.1). Between the 13, at 12:00 and the 16, at 00:00 the tremor slightly increased and reached intermediate and stable levels, with peaks reflecting short-lived (few minutes) but intense fountaining activity in the main cone A (up to four times the average fountain height equivalent to a maximum of 150 m high, e.g. on the 14, at 18:00 and on the 15, at 12:00). These short-lived but relatively intense phases were immediately followed by sudden edifice collapses coupled with lava overflow, which briefly increased the IR signal recorded by the HOTVOLC system (around 25 m^3 s^{-1}). During the whole day of the 16, we observed a slight decrease in the intensity of the tremor, without significant changes of the lava flux and SO_2 emissions. In the meantime, visual observations confirmed that lava fountains remained active on the vent A while only a very slight degassing was observed on the vent B. Then, a progressive increase in the tremor intensity was observed during the whole day of the 17, which correlated with the lava flux (between 20 and 40 m^3 s^{-1}) and SO_2 emissions (around 600 tons d^{-1}) increase. This changes in terms of the geophysical signals were also visible on the field as the eruptive activity within the vent B reactivated, which was characterized by bomb- and ash-dominated transient explosions, while Hawaiian fountaining (fountain heights around 30 meters) was still active within the vent A. The eruption suddenly stopped the 18 of September around midnight.

The cumulative volume estimated with HOTVOLC data is 6.5×10^6 m^3, while estimated cumulative volume with the MIROVA data is 6.1×10^6 m^3. These estimations are relatively coherent with the total erupted volume of 5.9×10^6 and 6.8×10^6 m^3 calculated by photogrammetry (Peltier et al. 2018) and InSAR (Hrysiewicz personal communication) respectively. This total emitted volume and the duration of the eruption can be considered as intermediate values regarding the recent eruptions at PdF (Peltier et al. 2018).

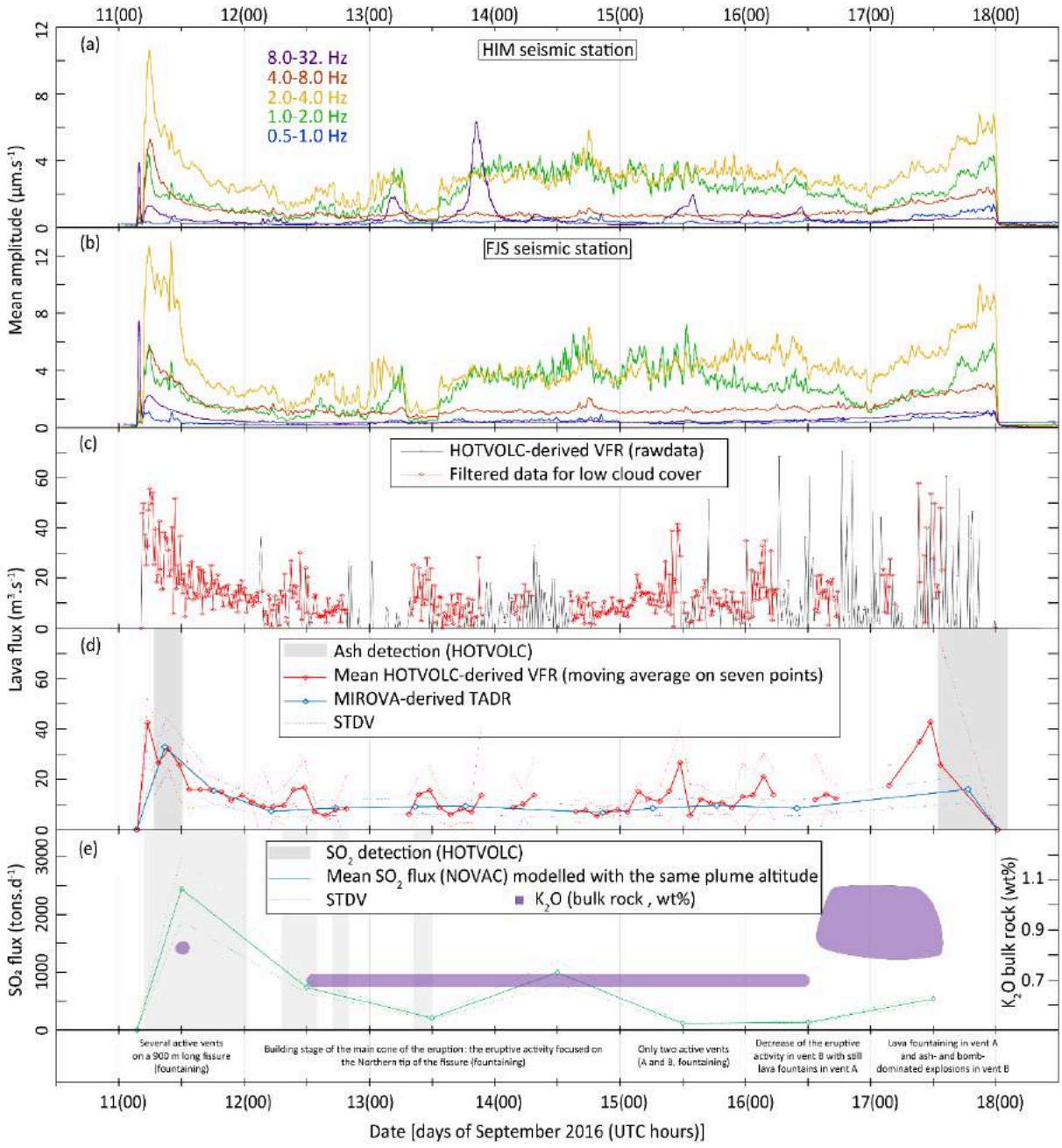

Figure 5.2 *– (a) and (b) Evolution of the volcanic tremor measured by the HIM and FJS seismic stations respectively. (c) And (d) represent the evolution of the lava fluxes by the HOTVOLC system (raw data, filtered data, average) and the MIROVA system. Periods with ash detected by HOTVOLC are displayed in grey areas. (e) Evolution of the SO_2 flux measured by the NOVAC stations. Periods with SO_2 detected by HOTVOLC are displayed in grey areas.*

The associated lava flow expanded to the N-NE until the Grandes Pentes area and cover a small part of the July 2015 lava flow (Fig. 5.1). Note that periods with ash detected by the HOTVOLC system are also displayed in grey areas in Figure 5.2d and correspond to the beginning and end of the eruption. Ash detected at the beginning may correspond to typical fountain-fed plumes during the initial high magmatic flux. Ash plumes during the last day of activity were well observed by satellite and ground-based field observations. Actually, these ash plumes and bomb emission were produced by sporadic pulses, well observed every 10-20 sec on average. The maximum plume height was estimated around 300-400 m above the source and was slightly higher than the northern caldera wall of the Enclos Fouqué caldera. Thus some of the eruptive products probably impacted the tourist and local population situated outside the caldera. This sudden change of activity associated with the increase of the fragmentation intensity and ballistics projections is also likely to be a source of hazards for those approaching the eruptive sites, especially considering that this type of eruptive phenomenon is difficult to anticipate.

2.4.1.3. Stratigraphy and componentry

The detailed sampling of the pyroclastic deposits located near the main active cone (delimited in red in Fig. 5.1), allowed us to identify the different layers emplaced during the entire eruption. Log 1 corresponds to a sampling site situated 100 m to the NE from the vent A (Figs. 5.1 and 5.3) and encompasses the whole sequence of the vent A activity, which was active during the entire eruption (Hawaiian fountaining). It also includes the ash deposit from vent B that was emplaced on the 17 of September (based on field observations and wind direction). The first sequence is formed by a clast-supported, 40 cm thick, reversely graded bed of golden pumice and scarce fluidal fragments (crystal-poor sideromelane, following the Gurioli et al. 2018 nomenclature). The particle size distributions (PSD) of this first sequence (base, middle and top, histograms 1 to 3 in Fig. 5.3) are asymmetric and are mostly comprised between lapilli and coarse ash, with a mode between -3 and -2.5 ϕ. Histograms 1 and 2 are bimodal with a coarse mode (histograms 1 and 2) between -5.5 and -4 ϕ (bomb). The reverse gradation is marked by an increase in the amount of bombs up to 15 cm in diameter. Big bombs were not sampled due to their large size and thus they do not appear in the PSDs. This first sequence is

overlain by a clast-supported, 30 cm thick, normally graded bed with similar components and PSD to that of the previous beds (histogram 4, Fig. 5.3). All these pyroclasts were deposited during the first six days of the eruption (from the 11 to the 16 of September), forming a 70 cm thick bed.

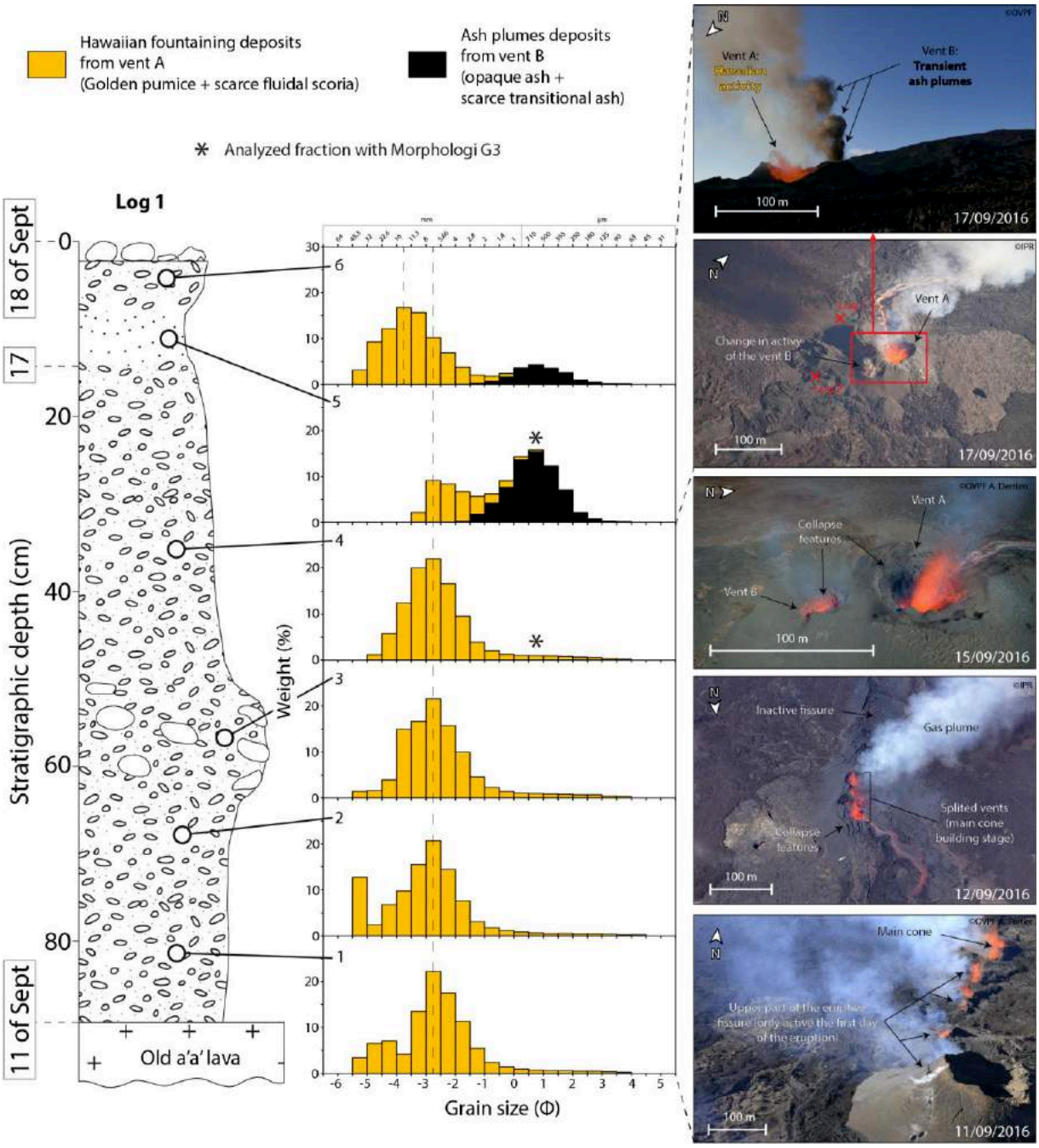

Figure 5.3 *– Stratigraphic log of the main section (log 1), with corresponding grain size, componentry and eruptive activity of the different sampled tephra beds.*

During the seventh and last day of the activity, the previous sequence was overlain by two 5 cm thick finer bed (histograms 5 and 6, Fig. 5.3) coming from both vents. The PSDs of the two ash-rich beds are bimodal and comprises a first coarse-grained population, with a mode between -3 and -2.5 ϕ (for layer 5, Fig. 5.4) and between -4 and -3.5 ϕ (for layer 6), composed by golden pumice and scarce fluidal scoria, emitted by the vent A. The fine-grained population, formed by dense opaque (tachylite-like) and scarce transitional (crystal-rich sideromelane-like) components, is symmetric and comprised between -2 and 4.5 ϕ, the mode being systematically between 0.5 and 1 ϕ (histograms 5 and 6, Fig. 5.4). These relatively fine deposits are overlain by scattered golden pumice, fluidal scoria and rare opaque, dense bombs, coming from the very last activity of both vents.

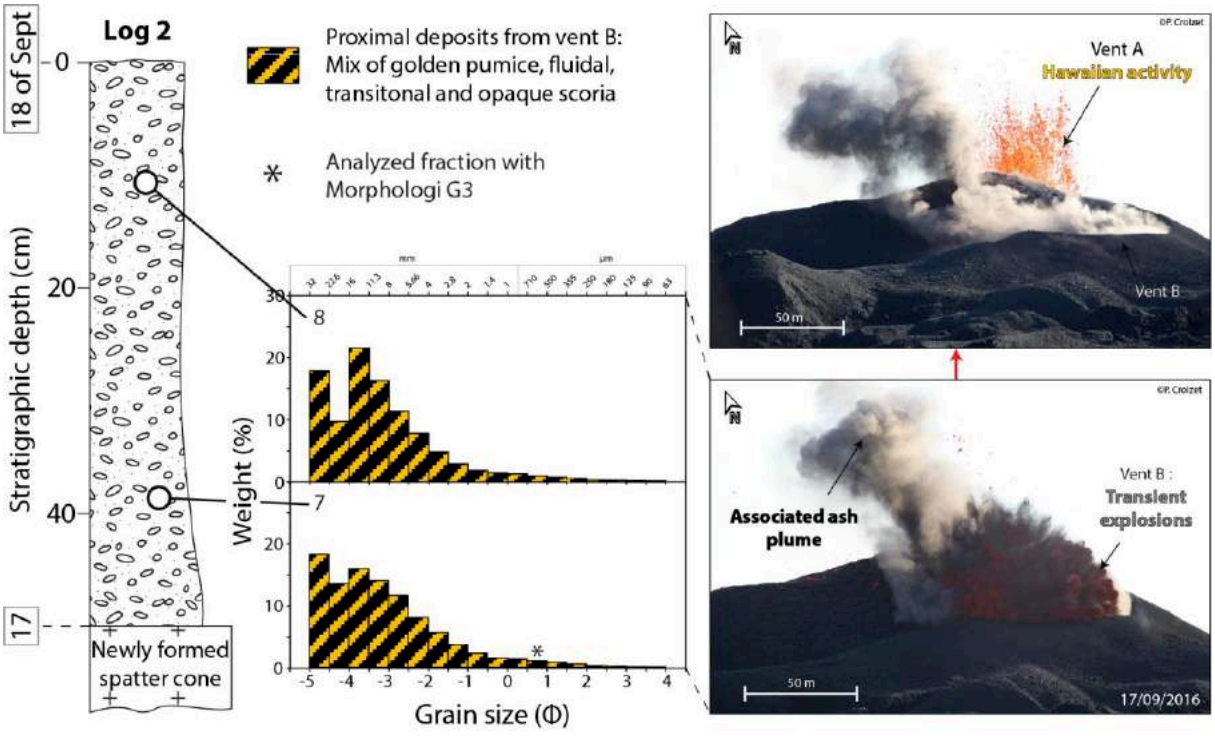

Figure 5.4 *– Stratigraphic log of the proximal vent B section (log 2), with corresponding grain size, componentry and eruptive activity of the different sampled tephra beds.*

The log 2 (Fig. 5.4) is situated 70 m, WSW from the vent B and is representative (still based on field observations and wind direction) of the proximal deposits from the vent B during the last day of the eruption. At this site, deposits are 50 cm thick (two bulk samples were collected, at the base and at the top of the deposits) and are composed of coarse golden pumice,

fluidal, transitional, opaque and scarce mingled scoria fragments. In both sampled beds (histograms 7 and 8 in Fig. 5.4), PSDs are unimodal, very asymmetric, skewed to relatively coarse grainsize (because of the proximity of the sampling to the vent) with a mode between -5 and -4.5 ϕ and between -4 and -3.5 ϕ for the layers 8 and 9 respectively. In comparison to layers 5, 6, and 7 (log 1), the fine fraction of these proximal deposit is mainly composed of transitional ash associated with scarce opaque ash. Opaque ash were mainly transported by the transient ash plumes and were deposited further North, within the log 1 (Fig. 5.3). Transitional ash particles are abundant in the proximal sampling site of the vent B (log 2) and have a metallic aspect because of the condensate deposition (Vlastélic et al. 2016, Fig. 5.5b). Transitional ash particles are scarce in distal sampling site (log 1) and have a glassy aspect without condensate deposition (Fig. 5.5b). Note that, during the last of the eruption, the vent B activity oscillated between (i) slight degassing around the crater rim to (ii) transient emissions of incandescent (golden and transitional material) as well as dark (opaque material) bombs, and (iii) transient emission of dark ash within discrete plumes (mainly opaque ash). The opaque ash plumes seemed to be emitted from the crater boundaries while the bombs were emitted during larger explosions on the entire surface of the crater.

Based on their macroscopic characteristics, different components have been identified in the pyroclastic deposits, both during the syn-eruptive sampling and during the laboratory analysis (Fig. 5.5). All the emitted products were juvenile. The Hawaiian fountaining produced only (i) golden pumice and scarce fluidal scoria all along the eruption. Golden pumice are characterized by highly vesicular, smooth and yellowish glassy surface. Fluidal scoria are slightly denser and darker, still with a finely vesiculated glass. During the last day of the eruption, the vent B also produced some Hawaiian products coupled with (ii) transitional (dark color with more or less fluidal shape) and (iii) opaque scoria (relatively dense with a dark and opaque surface aspect). These transitional and opaque scoria have similar macroscopic characteristics as the spiny-glassy and spiny-opaque scoria already described by Gurioli et al. (2018) and in **Chapter IV** during the 2014-2015 eruptions at PdF. However, we named them differently since we evidenced that these eruptive material show different micro-textural features and thus different magmatic mechanisms. It is important to note all the different juvenile components emitted by the vent B during the transient explosions are sometimes mingled together both at macroscopic and microscopic scale (Figs. 5.5a and 5.5b), the golden, fluidal or transitional components being always on the sample surfaces of the opaque ones, as a coating and/or as an infiltration within small cracks. The amount of mingled clasts is relatively

small compared to the non-mingled ones. Also note that the golden pumice abundance all along the eruption is peculiar and unusual compare to previous eruptions at PdF in which the eruptive products collected or observed were mainly fluidal scoria (DynVolc 2017; Gurioli et al. 2018; **Chapter IV**). This eruption produced a relatively high amount of ash, especially the last day of activity, compared to the other eruptions of the current eruptive cycle at PdF (DynVolc 2017).

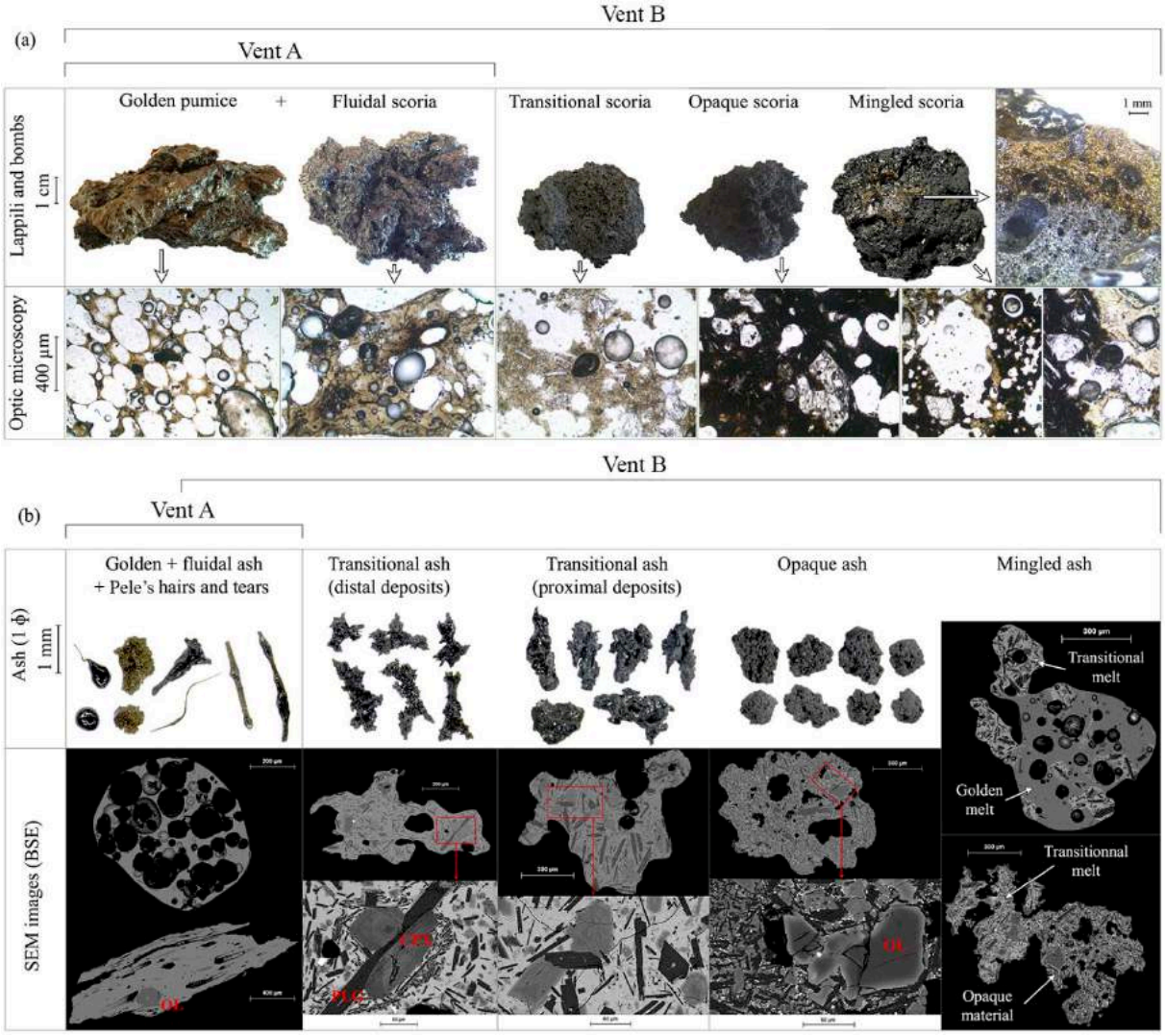

Figure 5.5 *– (a) Bomb-sized tephra componentry of the eruption, with corresponding thin section images with natural light. (b) Ash componentry, with corresponding BSE images.*

The different ash components (Fig. 5.5b) are genetically linked to the coarser material (Fig. 5.5a) produced by the eruption. Hawaiian fountaining produced golden and fluidal ash coupled with some Pele's hairs and tears. Pulsating activity from the vent B produced both transitional (brownish or grey color) and opaque ash (dark color). Quantitative chemical

analysis, petrographic observations and textural measurements are described later in this paper but SEM images in Figure 5.5b provide an overview of the general texture of the different components. Micro-phenocrysts of olivine (ol) are observed in all the different pyroclast components and lavas, in different proportion depending on the time of the eruption (from 0 to 12 vol%) and these crystals are the biggest observed together with very scarce clinopyroxene (cpx) micro-phenocrysts (< 1 vol%). Micro-phenocrysts of plagioclase (plg) are not observed. Golden and fluidal particles are highly vesicular with rounded vesicles and are poorly crystallized with very scarce and relatively small plg microlites and almost inexistent small cpx microlites. Transitional particles are less vesicular with both rounded and irregular-shaped vesicles and are more crystallized with small and slightly bigger microlites of plg and oscillatory zoned cpx microlites. This latter zoning has already been observed in other eruptions of PdF (DynVolc 2017) and may be attributed to variable crystal growth kinetic mechanisms under low pressure conditions (Burkhard 2005). Opaque particles have relatively low vesicle content with irregular-shaped vesicles and are fully crystallized with both small and slightly bigger microlites of plg, in respect to the other components, and oscillatory zoned cpx as in the transitional component, associated with microlite of ol and micron-sized Fe-Ti oxides. These small oxides are also sometimes observed within the transitional component. The abundance of these Fe-Ti oxides is unusually high with respect to typical PdF products (DynVolc 2017).

2.4.2. Bulk texture of the bomb, lapilli and ash size fractions

Envelope density and bulk porosity (Fig. 5.6a) as well as Helium vesicle connectivity (Fig. 5.6b) measurements were performed on coarse fragments both from the vent A (all along the eruption) and the vent B (last day of the eruption, Table S5.2). Three fragments of lava, sampled near the vent A were measured as well. Golden pumice and fluidal scoria are the most porous eruptive components, their density ranging between 0.3×10^3 and 1.5×10^3 kg m^{-3} (mode between 1.0×10^3 and 1.1×10^3 kg m^{-3}). No significant difference in porosity is observed between the golden pumice from the vent A and from the vent B. Transitional scoria densities range between 0.9×10^3 and 1.5×10^3 kg m^{-3} (mode at 1.0×10^3 kg m^{-3}) and opaque scoria densities are slightly higher, between 1.2×10^3 and 1.8×10^3 kg m^{-3} (mode at 1.2×10^3 kg m^{-3}). The three lava samples have been measured at 1.1, 1.2 and 1.4×10^3 kg.m^{-3}. Bulk porosity

(Fig. 5.6) was derived from the density using the measured DRE of 2.88×10^3 kg m^{-3}. Water pycnometry performed on ash size fractions (between 0.5 and 1 ϕ) lead to average porosities of 36, 14 and 7 vol% for the golden/fluidal, transitional and opaque ash respectively.

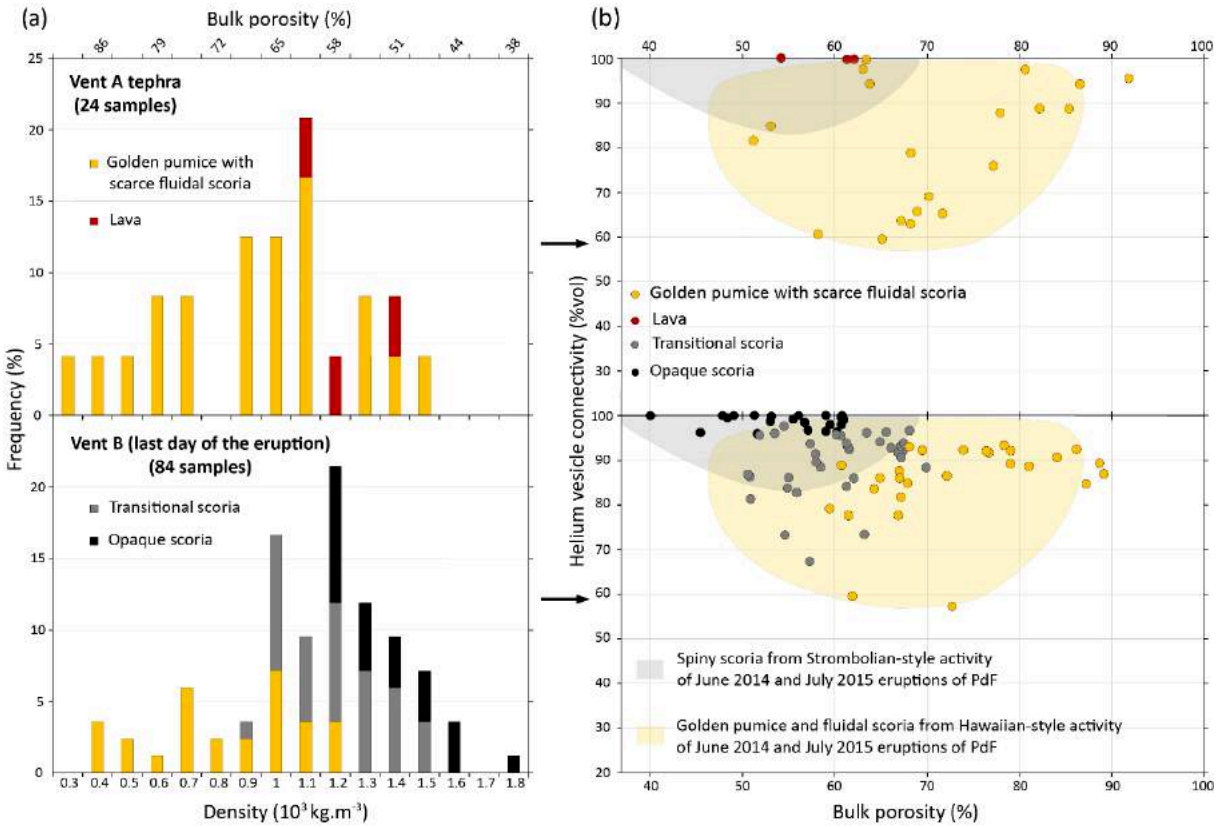

Figure 5.6 *– (a) Density and porosity measurements, displayed in histograms and normalized to the total number of samples for the vent A and the vent B. (b) Helium vesicle connectivity measurements vs. porosity.*

Vesicle connectivity measurements are characterized by different trends for each identified component. The connectivity represents the percentage of vesicle volume interconnected. Golden pumice and fluidal scoria show the highest fraction of isolated vesicles, connectivity ranging between 57 and 100 vol% (81 vol% on average). On the other hand, transitional scoria vesicles are slightly more connected, connectivity ranging between 67 and 97 vol% (89 vol% on average), as well as opaque scoria vesicles which are almost all connected (between 96 and 100 vol%, 98 vol% on average). Three lava samples were measured and they show 100 vol% of vesicle connectivity. Helium vesicle connectivity from the June 2014 and July 2015 eruptions are also shown (Gurioli et al. 2018; **Chapter IV**) and are relatively coherent

with the September 2016 data. Vesicle connectivity data performed on the transitional scoria show intermediate values, reflecting the transition between low vesicle connectivity within the golden pumice (emitted during Hawaiian fountaining) and high vesicle connectivity within opaque scoria for the September 2016 eruption and spiny scoria for the 2014-2015 pyroclasts (emitted during Strombolian-style or more explosive activity).

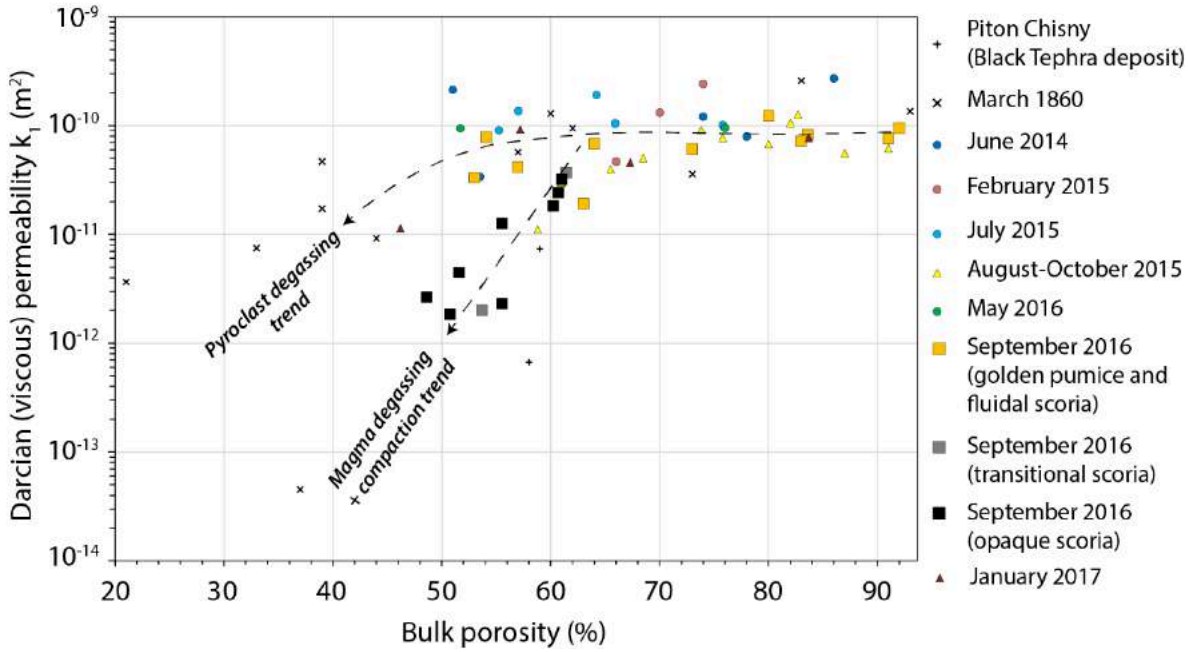

Figure 5.7 *– Darcian permeability (k_1) vs. porosity of several samples from different eruptions of PdF.*

Concerning the tephra permeability (Fig. 5.7), most of the recent products analyzed (June 2014 and after) show a sub-horizontal trend with porosity between 50 to 92 vol% and Darcian (viscous) permeability k_1 ranging between 10^{-11} and 10^{-9} m^2. Concerning the September 2016 eruption, the Hawaiian fountaining products are part of this trend while the transitional and opaque scoria follow another trend with a decrease of k_1 (between 10^{-12} and 10^{-10} m^2) coupled with the decrease in porosity. Permeability measurements were also carried out on some products from the high explosive event of the 1860 phreatomagmatic eruption (Michon et al. 2013) and on some deposits of the energetic lava fountaining produced by the last Piton Chisny eruptive activity at PdF (Morandi et al. 2016; Principe et al. 2016). The measurements show a large range of permeability and porosity on these samples, especially for the 1860 products which are very dense (down to 20 vol% of porosity) and relatively impermeable (down to 3×10^{-14} m^2).

2.4.3. Ash morphometric measurements (APASH)

Morphometric measurements on each ash component (0.5-1 ϕ grainsize fraction) were carried out and APASH data are represented on Figure 5.8. Solidity (morphological roughness, SLD) vs. convexity (particle roughness, CVX) plot are represented and display all the particle shapes for each component sample (Table S5.3). Each component have between 1056 and 1510 analyzed and filtered particles. This relatively high amount of particles (> 1000) is needed to be statistically representative of the emitted ash particles. These data show that each ash component has its own APASH signature. Golden/fluidal ash (yellow dots in Fig. 5.8a) has a very large range of different ash shapes: the particles can be perfectly smooth and rounded particles (round droplets of vesicular melt, with SLD and CVX = 1), or can be relatively irregular, whose shape is reminiscent of vesicle walls (with SLD and CVX down to 0.55 and 0.60 respectively). A wide range of different particle shapes is observed between these two end-members and are basically formed by vesicular and glassy fragments. Pele's hairs and tears (red dots in Fig. 5.8a), which are part of the same deposits of the golden/fluidal ash, have even more difference in shapes. These particles have approximately the same range in CVX (small scale roughness, between 0.60 and 1) as the golden/fluidal ash, but they have a wider range in SLD (particle scale roughness, between 0.25 and 1) reflecting particle elongation and deformation. Particles with transitional APASH features (Fig. 5.8b, SLD between 0.50 and 1, CVX between 0.60 and 1) look similar to the golden/fluidal ash components but without the hairs and tears component, and have a slightly more spiny shape. Parameters measured in distal transitional ash samples (transported within ash plumes, log 1; purple dots in Fig. 5.8b) and proximal transitional ash samples (log 2; green dots in Fig. 5.8b) span a very similar range, with only a few differences which can be attributed to the condensate deposition observed on the proximal samples, whose effect is to slightly smooth the particle shape. Finally, opaque APASH is significantly different from that of the other components (Fig. 5.8c), with a narrow range of both SLD (0.75 to little bit less than 1) and CVX (0.85 and little bit less than 1 as well). These values reflect a relatively high degree of roundness but with a high amount of small scale irregularities. Rounded particles with SLD and CVX at 1 (like found in the golden/fluidal and transitional components) are not observed any more within the opaque ash. Statistical analysis represented in boxplots (Fig. 5.8d) highlights that both SLD and CVX increase from the golden/fluidal ash + hairs/tears, to transitional ash, to opaque ash, in terms of median value (red lines) as well as 25th and 75th percentile (blue boxes which englobe the half of each dataset).

Also note that the boxplot whiskers (which represent approximately the 2.7 σ boundaries of each dataset), as well as the outliers (data outside 2.7 σ represented by the red crosses) are progressively closer to the median from the golden/fluidal ash and hairs/tears particles, to transitional ash, to opaque ash. Aspect ratio (AR) of each component is also represented and show that particles are progressively more elongated from the opaque, to the transitional, until the golden/fluidal and Pele's hairs and tears components.

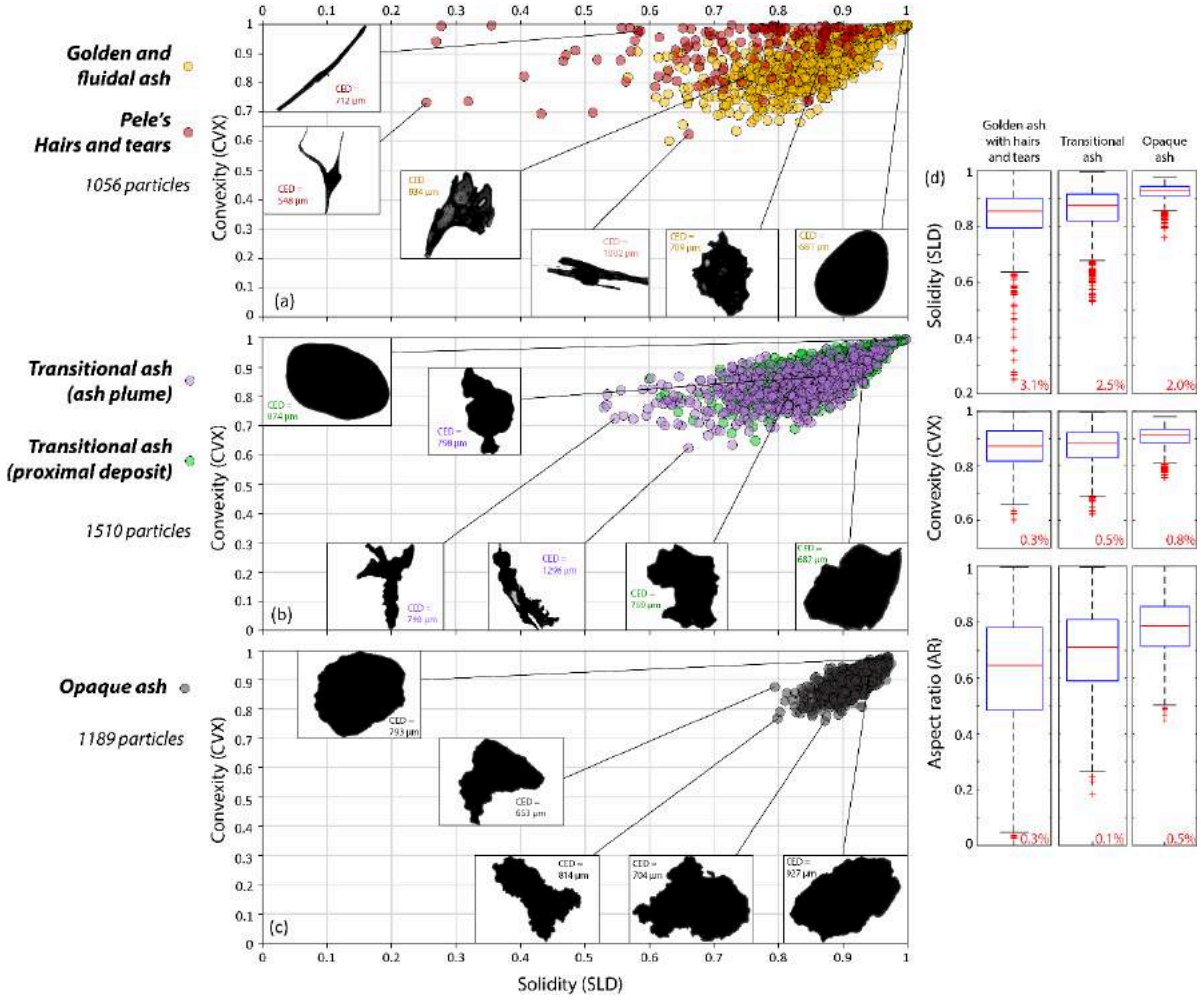

Figure 5.8 *– Morphometric (APASH, solidity vs. convexity) dataset of each ash component at 0.5-1 ϕ grain size fraction. (a) Golden/fluidal ash with Pele's hairs and tears, (b) transitional ash and (c) opaque ash. (d) Statistical analysis of each component dataset on boxplots for solidity, convexity and aspect ratio of the particles. Middle red lines represent the median, blue boxes represent all the particles between the 25th and 75th percentiles (englobes 50% of the dataset), boxplot whicker boundaries represent 2.7 σ of the data, and red crosses represent each ash particles outside this boundary (outliers).*

2.4.4. Chemical analysis of the bomb, lapilli and ash size fractions

2.4.4.1. Bulk rock and glass compositions

Major and minor element analysis of bulk rocks and glasses (Table S5.4) were performed in order to constrain potential pre- and syn-eruptive variations of the magmatic composition. Bulk rock analyses were performed on all the different pyroclastic components, including a lava fragment.

The comparison between the August-October 2015 bulk rock compositions with the May and September 2016 ones (Fig. 5.9) reveals several notable facts. (i) It shows that the magma erupted in August-October 2015 was first relatively differentiated and olivine-free (around 0.8 in CaO/Al_2O_3, 6.5 wt% in MgO and 0.7 wt% in K_2O) but then become progressively more mafic and olivine-rich towards the end of the eruption (up to 0.9 in CaO/Al_2O_3, 11.0 wt% in MgO and down to 0.6 K_2O wt%). (ii) Then, the May 2016 eruption emitted an olivine-rich magma (0.8 in CaO/Al_2O_3 and 9.1 wt% in MgO) and exhibit a wide range in K_2O (from 0.6 to 1.1 wt%). (iii) Focusing on the September 2016 eruption, the magma emitted was first relatively differentiated (0.8 in CaO/Al_2O_3) and K_2O-poor (0.8 wt% in K_2O, without ol phenocrysts 6.5 wt% in MgO).

Similarly to some recent eruptions at PdF, the magma of the September 2016 eruption is progressively olivine-bearing (cf. the trends of increasing amount of ol in Fig. 5.9). The high variability in MgO is attributed to the variable abundance of the ol micro-phenocrysts that increase towards the end of the eruption: considering (i) an average MgO content in the golden pumice liquid of 6.5 wt%, (ii) an average MgO content in the ol phenocryst of 43.3 wt% and (iii) a MgO content in the bulk rock compositions ranging between 6.5 and 11.1 wt% (cf. sections here after for these values, Table S5.4), we were able to estimate by mass balance the ol phenocrysts content (X_{ol}) between 0 vol% (11 September sample without ol) and 12 vol% (17 September, most ol-rich sample). Moreover, since the 16 of September, we observed the occurrence of K_2O-richer magmas (mostly fresh golden pumice and lava) whose compositions range between 0.8 and 1.1 wt% in K_2O (compositions in between the K_2O-poor magmas of August-October 2015 and the K_2O-rich May 2016 end-member). It is important to note that the two opaque scoria fragments analyzed have the same composition of the initial K_2O-poor

golden pumice. On the other hand, the analyzed transitional and opaque ash particles have K_2O-rich compositions.

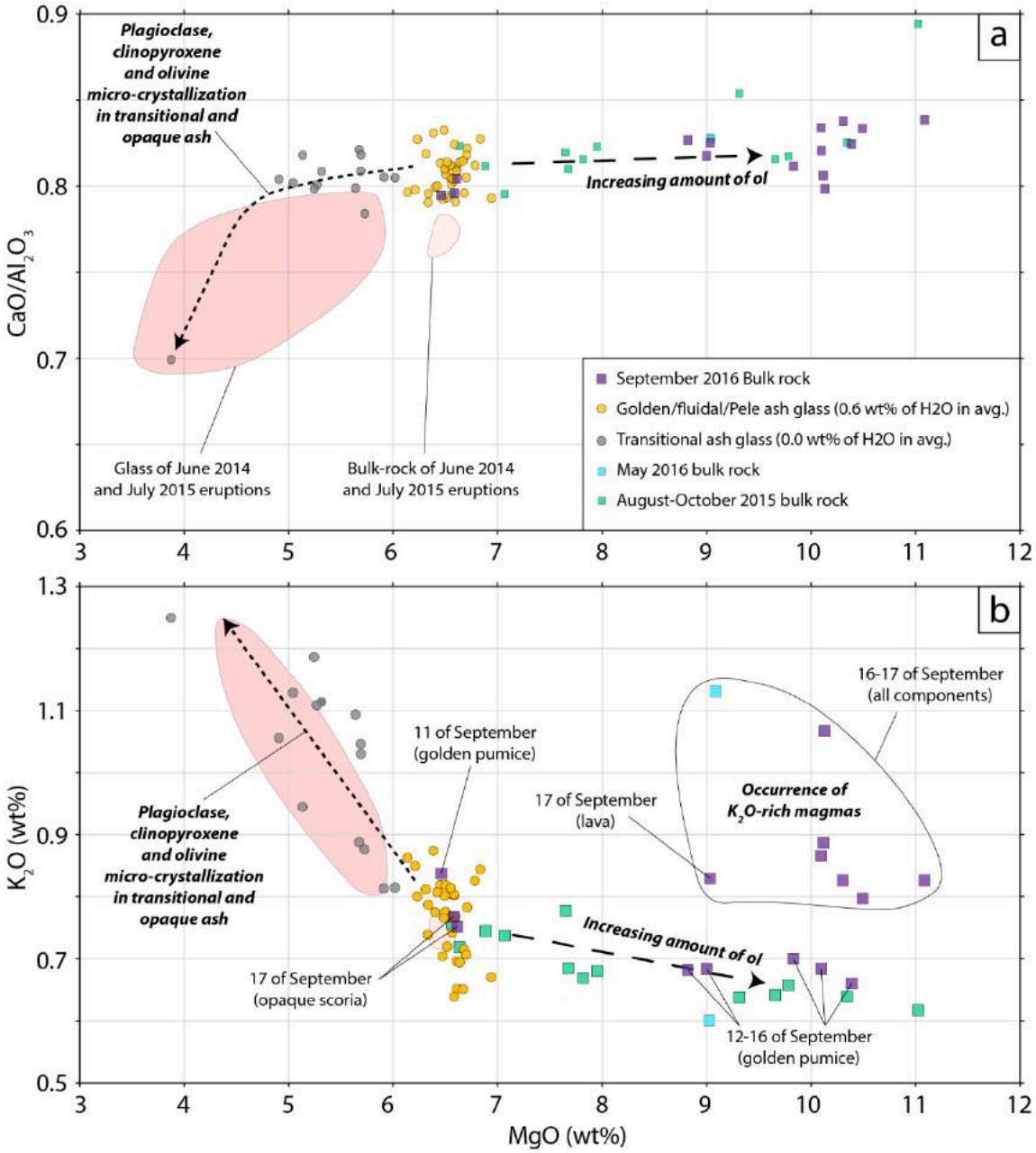

Figure 5.9 *– Bulk rock and in-situ glass compositions (MgO vs. CaO/Al_2O_3) of the eruptive products.*

Because the eruption produced a large amount of ash compared to the other recent eruptive fissure at PdF (DynVolc 2017), we mostly focused on the ash particles to perform the glass composition measurements, petrology analysis and the micro-texture characterization.

Moreover, we suggest that the ash can conserve the more pristine signature of the fragmentation processes because of the relatively fast natural quenching in air (Xu and Zang 2002; Potuzak et al. 2008; Porritt et al. 2012; D'Oriano et al. 2014; Di Muro et al. 2015; Pompilio et al. 2017) compared to the large lapilli and the inner parts of the bomb-sized tephra. The golden/fluidal glass compositions (Fig. 5.9) range between 6.14 and 6.94 wt% in MgO, between 0.79 and 0.83 in CaO/Al_2O_3 and between 0.64 and 0.87 wt% in K_2O. Considering the analytical uncertainties (Table S5.4), they thus encompass the ol-free bulk-rock compositions, and this is consistent with a crystal-poor matrix. Transitional glass is characterized by a wider range of composition reflecting different degrees of crystallization of relatively Na-rich plg, cpx and relatively Fe-rich ol (between 3.88 and 6.47 wt% MgO, between 0.70 and 0.83 in CaO/Al_2O_3 and between 0.70 and 1.25 wt% in K_2O), with a relatively similar compositional trend as observed for the 2014-2015 matrix. No glass has been observed in the opaque component.

2.4.4.2. Mineral assemblage and compositions in the ash particles

The different mineral phases present in the eruptive products are plg, cpx, Fe-Ti oxides and ol in order of abundance, without considering the increase of ol micro-phenocrysts towards the end of the eruption. On the basis of the crystal size, shape and compositions, we identify four distinct crystal populations within the September 2016 eruptive products that are listed in order of appearance within the erupted magma.

(i) First, the compositions of the euhedral ol micro-phenocrysts range between Fo_{78-84}. Mg-Fe distribution coefficients (K_D) between these ol and bulk rock composition are on average 0.24, which show that most of these ol are too rich in Mg considering our bulk rock composition (equilibrium reach at $K_D = 0.30 \pm 0.03$, Putirka 2008). In order to calculate the FeO content of the cumulative ol-free bulk rock composition (6.46 wt% in MgO and 10.16 wt% in FeO), we used an average Fe^{3+}/Fe_{total} ratio of 0.18 for La Réunion island basaltic melts (Pichavant et al. 2016). We thus conclude that most of these ol micro-phenocrysts originate from cumulative processes (22 analysed crystals with Fo > 80) and only a few crystals are in equilibrium with the pre-eruptive/bulk rock melt (six analysed crystals with Fo_{78-80}). The ol micro-phenocrysts content varies from 0 (beginning of the eruption) to 12 vol% (end of the eruption) within each

eruptive component and these crystals are the largest observed in the September 2016 products (up to 600 µm in length and 400 µm in width). Scarce ol-free micro-phenocrysts are observed in the ash produced by the vent B the last day of the eruption in grain size fraction lower than 2 ϕ.

(ii) The second crystal population is represented by the euhedral micro-phenocrysts in equilibrium with the bulk rock composition, namely the scarce ol micro-phenocrysts (Fo_{78-80}) described previously associated with very scarce cpx micro-phenocrysts (only one agglomerate of three cpx crystals observed within the golden/fluidal component, with around 500 µm in length and 300 µm in width for each crystal). These crystals represent < 1 vol% in all the eruptive components. The cpx crystals in equilibrium (K_D of 0.25 on average, equilibrium reach at 0.28 ± 0.08, Putirka 2008) have a composition range of Wo_{44-46} En_{45-47} Fs_{9-10}.

(iii) The third crystal population (field 1 in Fig. 5.10a), is represented by the microlites (plg and cpx) of the golden component (> 0.05 and > 0.02 mm for plg and cpx respectively) as well as the cores of the slightly bigger microlites of the transitional and opaque components (plg and cpx). Their compositions range between $An_{65-71}Ab_{28-34}Or_1$ for the plg and $Wo_{35-46}En_{41-52}Fs_{12-14}$ for the cpx. Their occurrence depend on the components (Figs. 5.5 and 5.10a).

(iv) The fourth and last crystal population to form (field 2 in Fig. 5.10a) is represented by the small microlites (< 0.05 and < 0.02 mm for plg and cpx respectively) of plg, cpx, oxides and ol (with some rims of bigger crystals) that form within the transitional and opaque components (Fig. 5). Their compositions ($An_{56-64}Ab_{34-41}Or_{1-3}$ for plg, $Wo_{37-44}En_{39-49}Fs_{12-17}$ for cpx and $Fo_{69-78}Fa_{21-30}$ for ol) are the richest in Na for the plg and the richest in Fe for the cpx and ol. The micron-sized oxides observed in the opaque component are rich in Fe and Ti. As well as the latter microlite population, their occurrence depend on the components (Figs. 5.5 and 5.10a).

Both population of microlites (small and large plg and cpx of all the components) are in equilibrium with their surrounding glass: K_D = 0.25 on average for plg, using the plg-melt equilibrium constant of Putirka (2008) calibrated for melts whose temperature exceeds 1050°C (An-Ab K_D = 0.27 ± 0.11 at equilibrium), K_D = 0.30 on average for cpx (equilibrium reached at K_D = 0.28 ± 0.08). K_D for ol microlites cannot be calculated because these crystals only occurred in the opaque component which lack interstitial glass, which suggest that ol microlites, with the micro-ox, are the latest phases to crystallize.

2.4.4.3. Magma temperature and H_2O content estimations

We then used the two MgO-thermometers of **Chapter IV** calibrated (experimental data) for (i) undegassed and pre-eruptive conditions (using bulk rock and golden pumice glass compositions, T (°C) = 27.5 MgO^{liq} + 943.7) and for (ii) degassed and syn-eruptive eruptive conditions (using transitional glass compositions, T (°C) = 17.7 MgO^{liq} + 1041.7). Ol-free bulk rock composition (6.46 wt% of MgO) which represent the initial magma composition, leads to a calculated magma temperature of 1121 °C. In parallel, the golden pumice component (which do not have significant microlite and thus do not exert micro-crystallization yet) whose glass composition is similar to that of the bulk rock, (6.55 wt% of MgO on average) lead to melt temperatures between 1112 and 1134 °C (1124 °C on average). Using the Lange et al. (2009) hygrometer based on the plg-melt equilibrium (An-Ab $K_D = 0.27 \pm 0.11$ at equilibrium; Putirka 2008), we can estimate the dissolved H_2O content of the magma. We used both plg microlite compositions and glass compositions that are in equilibrium, in order to estimate the dissolved H_2O content within the eruptive products, which leads to calculated H_2O content between 0.3 and 0.7 wt% (0.6 wt% on average) for the golden pumice. On the other hand, the estimated transitional melt temperatures range between 1110 °C and 1148 °C and dissolved H_2O contents range between 0.0 and 0.2 wt% (0.05 wt% on average).

2.4.5. Crystal contents and Size Distributions

CSDs were measured on the ash particles in order to study crystals that did not form due to post-fragmentation cooling, but which likely nucleated and grew by degassing during the magma ascent toward the surface and cooling at very shallow levels. Micro-phenocrysts could not be taken in account in these textural measurements because they were too scarce both in the ash particles and as free crystals. We only focus on the two microlite populations previously described that are representative of the syn-eruptive crystallization of the magma.

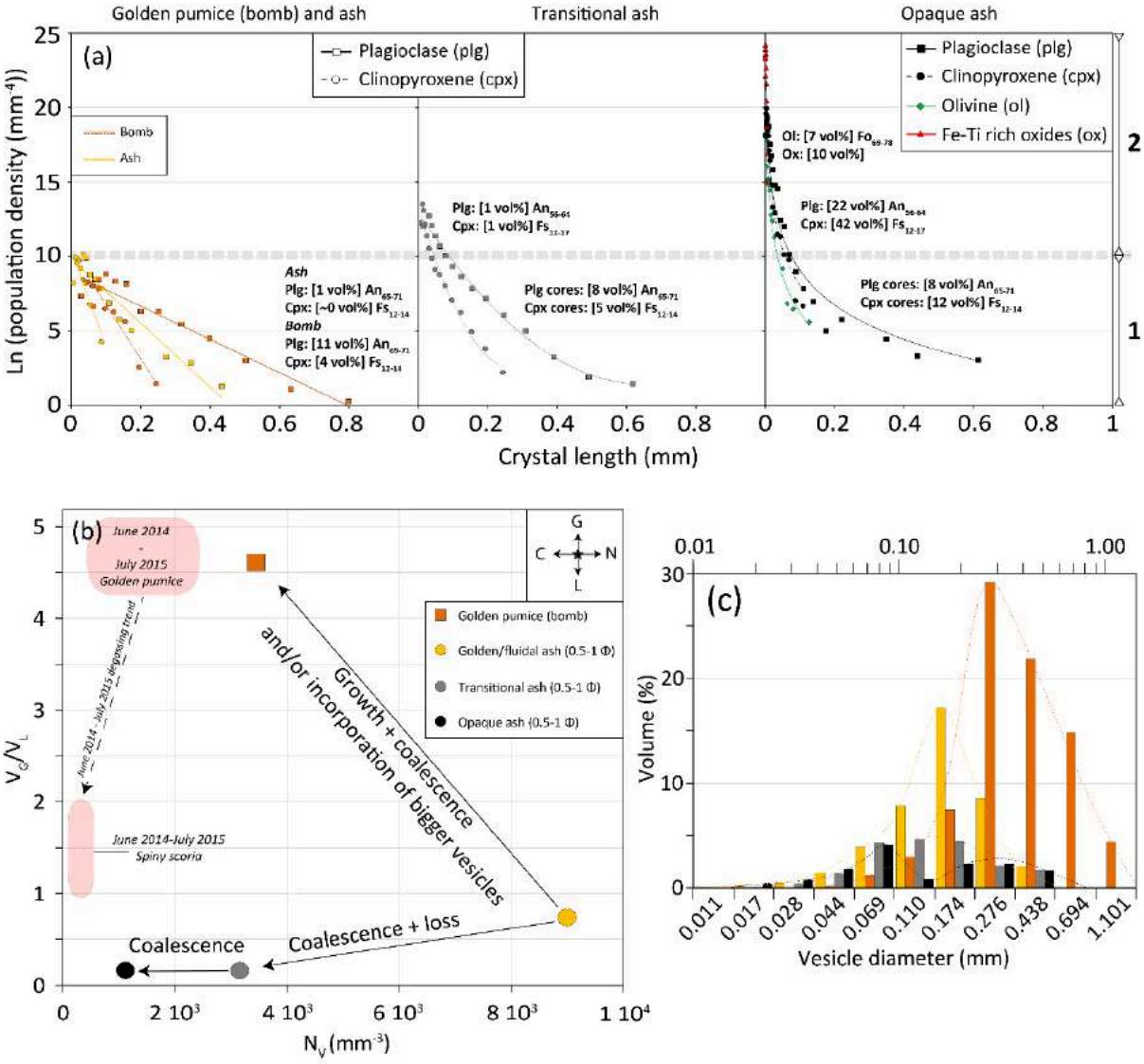

Figure 5.10 *– (a) CSDs of the different components with associated crystal contents and compositions. Field 1: Golden microlites + inherited big microlites (> 0.05 mm) of the transitional and opaque components. Field 2: Small microlites (< 0.05 mm) of the transitional and opaque components + ol and ox microlites of the opaque component. (b) N_V vs. V_G/V_L of the different components. G: bubble growth; N: bubble nucleation; L: gas loss; C: bubble coalescence. (c) VSDs of the different components.*

The golden/fluidal ash is almost crystal free (Fig. 5.10a) with only 1 vol% (all the crystal contents are corrected for porosity and micro-phenocryst content) of small microlites of plg (< 0.5 mm in length) and very scarce small microlite of cpx (< 0.1 mm in length). In parallel, the crystal content of the golden pumice (bomb-sized) is higher (15 vol%) with 11 vol% of small

microlites of plg (< 0.8 mm in length) and 4 vol% of small microlites of cpx (< 0.3 mm in length) which confirmed that coarse clasts can contain post-fragmentation crystallization. Golden/fluidal ash CSDs of plg and cpx show linear trends (CSD slopes of -21.49 and -65.14 mm^{-1} respectively), with relatively low nucleation densities N^0 ($e^{9.84}$ and $e^{10.47}$ mm^{-4} for plg and cpx respectively; these values are the population densities at crystal length = 0) and low number density of crystals N_C (1.1×10^3 and 4.0×10^2 mm^{-3} for plg and cpx respectively, Table S5.5). Golden pumice CSDs show similar characteristics as the golden/fluidal ash, except that their linear CSD slopes are slightly gentler, reflecting longer crystallization time (Fig 5.10a). For the next components, we only focused on the ash fraction.

The crystal content of the transitional ash component (Fig. 5.10a) is higher than in the golden ash (17 vol%) with 9 vol% of plg and 6 vol% of cpx, with also higher nucleation densities N^0 (around ln(13) mm^{-4}) and higher crystal number density N_C (1.2×10^4 and 2.4×10^3 mm^{-3} for plg and cpx respectively). Crystal lengths are slightly higher than in the golden ash ones (< 0.6 and < 0.4 mm for plg and cpx respectively). The bigger microlites are also wider (Fig. 5.5b) but this parameter does not appear in the CSD measurements as CSD plots only show the crystal lengths. These wider crystals are nevertheless distinguishable in the CSD as they are characterized by the same range of population densities as the golden/fluidal ash microlites (< ln(10) mm^{-4}). On the other hand, small microlites (< 0.05 and < 0.02 mm in length for plg and cpx respectively) show more sodic An_{56-64} and ferric Fs_{12-17} compositions, associated with higher population densities than the golden microlites and the transitional big microlites (> ln(10) mm^{-4}). It is also important to note that the CSD slopes of the transitional component are not linear as the golden ones but slightly curved with relatively steep slopes for small microlites and relatively gentle slopes for the largest crystals compare to the golden/fluidal ash linear CSD (Fig. 5.10a).

The opaque ash component is 100 vol% crystallized with 54 vol% of cpx, 30 vol% of plg, 10 vol% of Fe-Ti micron-sized oxides and 7 vol% of ol on average (optical microscopy observations confirmed that bomb-sized opaque scoria are also 100 vol% crystallized, Fig. 5.5a). Crystal number densities are the highest of the three different eruptive components (1.6×10^6, 1.5×10^6, 9.0×10^4 and 5.4×10^7 mm^{-3} for plg, cpx, ol and oxides respectively). Crystal length are approximately the same as the previous components (< 0.5 and < 0.2 mm for plg and cpx respectively), but some plg and cpx crystals are wider than the ones of the golden component. We observed the same plg and cpx crystals populations as in the transitional CSDs (small and larger microlites with the same composition evolution). However, the occurrence of

micron-sized oxides (< 0.01 mm in diameter) and Fo_{69-78} ol (< 0.2 mm in length) contrast with the absence of these late crystallized phases within the golden and transitional components. Moreover, the ol micro-phenocrysts are often normally zoned in the opaque component (Fo_{79-84} on the cores and down to Fo_{72} on the rims); this normal zoning is only observed within the opaque component. As in the transitional component, the CSD slopes of the opaque component are not linear but slightly curved with relatively steep slopes for small microlites and relatively gentle slopes for the largest crystals compare to the golden/fluidal ash linear CSD (Fig. 5.10a).

2.4.6. Vesicle content and Size Distributions

The golden pumice/fluidal scoria component is relatively porous (Fig. 5.6a) with an average of 72 vol% of vesicles (from 48 to 89 vol%). Water pycnometry measurements on the golden/fluidal/Pele ash (0.5-1 ϕ) lead to a much lower average vesicularity of 36 vol% (from 35 to 38 vol%, Table S5.2). Vesicles are rounded and elongated in the Pele's hairs and tears, but they do not show evidence of coalescence. For different particle size of a same component, a large difference is observed in porosity. We thus performed micro-texture analysis (Table S5.5) on one golden pumice thin section from a 10 cm large bomb emitted by the vent A, in order to quantify the differences between coarse and fine material (as in the previous section for the crystal analysis). In spite of the difference in vesicularity, the N_v values of the ash and the golden bomb are both up to 10^3 mm^{-3}. The VSD (Fig. 5.10c) of the golden ash show only one population of vesicles, from a few microns to 0.4 mm in diameter, with a mode around 0.2 mm in diameter (V_G/V_L of 0.7 and N_V of 9.0×10^3 mm^{-3}). Concerning the golden pumice textural analysis, we also found one population of vesicles but it is skewed towards bigger size, from around 40 µm to 1.1 mm in diameter, with a mode around 0.3 mm in diameter (V_G/V_L of 4.6 and N_V of 3.4×10^3 mm^{-3}). Note that the porosity estimated for the ash fraction with the micro-texture counting the vesicles (42 vol%), is quite coherent with the water pycnometry measurement (36 vol%).

Transitional scoria is less porous than the latter component (Fig. 5.6a) with an average value of 61 vol% (from 47 to 68 vol%). Water pycnometry measurements on the transitional ash (0.5-1 ϕ) lead to an average vesicularity of only 14 vol% (from 11 to 16 vol%). Transitional

ash has a low V_G/V_L ratio of 0.2 and a N_V of 3.2×10^3 mm^{-3} (Fig. 5.10b), reflecting bubble coalescence and loss from the golden ash. Its VSD show a unimodal population (Fig. 5.10c) with relatively low vesicle volume (porosity of 13 vol% coherent with the water pycnometry measurements). Vesicle sizes range from around 20 µm to 0.4 mm, with a mode around 0.1 mm. Vesicles can be ever rounded or irregular-shaped.

Opaque component represent the more degassed and crystallized component with an average value of porosity of 54 vol% (from 38 to 58 vol%) concerning the lapilli- and bomb-sized pyroclasts (Fig. 5.6a) and 7 vol% (from 7 to 8 vol%) for the ash fraction. This ash component has a very low V_G/V_L ratio of 0.2 and a N_V of 1.1×10^3 mm^{-3} (Fig. 5.10b), reflecting further bubble coalescence with respect to the transitional ash. The VSD show very low vesicle volume (porosity of 10 vol% coherent with the water pycnometry measurements) from around 20 µm to 0.4 mm in vesicle diameter (Fig. 5.10c). Two potential modes are observed, the first one at 70 µm, which is slightly lower than the modes of the golden/fluidal and transitional ash (which might reflects gas loss) and the second one around 0.3 mm which is higher than the other ash components and is represented by irregular-shaped vesicles which might reflects coalescence.

Comparing the V_G/V_L and N_V values of the September 2016 eruption with those measured for the June 2014 and July 2015 eruptions (Gurioli et al. 2018; **Chapter IV**), slightly different trends appear. This comparison show that the vesicles are more abundant in the September 2016 golden pumice than in the June 2014 and July 2015 ones, in term of N_V, which highlight a slightly higher nucleation rate for the September 2016 golden pumice.

2.5. Discussion

2.5.1. Eruptive trigger

One of the main challenges of typical dyke eruptions at PdF, as the September 2016 one, is to characterize their precursors to understand their triggers mechanisms and anticipate their starting and evolution. This eruption was preceded by several mid-terms precursors as the slight

increase in the ground gas emission, the change of gas compositions within the summit fumarole and the increase in the seismicity (Peltier et al. 2018). However, and similarly to the short-lasting eruptions of June 2014 and May 2016, slight ground inflation was detected just shortly before the eruption. For the June 2014 eruption, this relatively late ground inflation was interpreted by Gurioli et al. (2018) as the pre-eruptive second boiling process that trigger the eruption a few days later, but not evidence of a new input of magma was found. Instead, clear evidences of rejuvenation were found during the long lasting and voluminous eruption of August-October 2015 that lasted almost two months and was characterized by different ground inflation trends (Coppola et al. 2017; Peltier et al. 2018). The first question is: where the 2016 eruption is placed between these two end-member behaviors?

The September 2016 lava flux evolution is quite similar to that measured during typical eruptions of PdF (Hibert et al. 2010 for the January 2010 eruption; Coppola et al. 2017 for the 2014-2015 eruptions) with nevertheless a few important and notable characteristics. The absolute values of these measured lava flux are higher than those observed during the small eruptions of the 2014-2015 period documented by Coppola et al. (2017), namely the June 2014 (maximum lava flux around 7 m^3 s^{-1}), February 2015 (maximum lava flux around 2 m^3 s^{-1}), May 2015 (maximum lava flux around 35 m^3 s^{-1}) and July 2015 (maximum lava flux around 22 m^3 s^{-1}) eruptions. However, the September 2016 lava flux values are comparable to that measured during the August-October 2015 eruption. Similarly to this later eruption, we also observed a late increase in the lava flux for the September 2016 eruption (Coppola et al. 2017). However for the August-October 2015 eruption, this late increase in lava flux was correlated with a deep recharge of the magmatic system and the emission of relatively pristine magmas (high MgO and CaO/Al_2O_3 content) without ash emission**,** while during the September 2016 eruption the late increase in lava flux was correlated to the change in activity style with ash and bomb emission but without the emission of pristine magmas. Indeed, the bulk rock chemical evolution since 2014 at PdF suggests that the rejuvenation of the shallow plumbing system began to be evidenced with the July and August-October 2015 eruptions (Coppola et al. 2017). However, the September 2016 erupted magma is not as pristine as the August-October ones, but was quite differentiated (Fig. 5.9a). The lack of deep input is also supported by the relatively low SO_2 emissions. Thanks to the conversion lava flux-SO_2 flux established in a previous study (equation 5 in Hibert et al. 2015), we can estimate the SO_2 flux considering a given lava flux and the porosity of the magma at the fragmentation level. Using the initial lava flux peak (between 30 and 50 m^3 s^{-1}, Fig. 5.2d) and the golden pumice porosity (between 60 and 70 vol%,

Fig. 5.6a), the estimated SO_2 flux is very coherent with the measured one of 2500 tons d^{-1} (Fig. 5.2e) only if we considered a pre-eruptive degassed magma condition (that contrast with a primitive gas-rich magma). A similar reasoning is also applicable on the entire eruption, thus involving a relatively degassed magma, even during the increase of the lava flux at the end of the eruption (Figs 5.2d and 5.2e). Moreover, no textural and chemical features evidence any pre-eruptive magmatic inputs. In summary, we state that the magma emitted during the September 2016 eruption is not compatible with the contribution of a relatively deep and gas-rich magma and is rather coherent with a partial degassed shallow magma. The ubiquity of golden pumice in the eruptive deposits, similarly to the beginning of the June 2014 eruption, suggest that this differentiated magma experienced significant pre-eruptive bubble nucleation to erupt: we suggest that the first phase of the eruption associated with the emission of chemically differentiated golden pumice and typical decreasing lava flux trend until the 13 of September (Fig. 5.2d) was triggered by similar pre-eruptive second boiling mechanism as the June 2014 eruption (Gurioli et al. 2018).

2.5.2. Eruptive-style evolution

Since the 16 of September and towards the end of the eruption, the magma became enriched in K_2O (Figs. 5.2e and 5.9b). This reflects the emission of a different magma, with respect to the first days of the activity, which have intermediate compositions ranging between the initial differentiated magma (11 of September) and the May 2016 K_2O-rich magma (Fig. 5.9). The occurrence of this K_2O-rich magma during the September 2016 eruption could be eventually linked with the tremor and lava flux fluctuations since the 16 (Figs. 5.2a, 5.2b and 5.2d) and the progressive increase of these signal intensities during the 17 of September. The slight decrease of the volcanic tremor (Figs. 5.2a and 5.2b) can be linked to the significant decrease of the activity in the vent B, while the vent A remained relatively active. We thus suggest that both sub-surface eruptive conduit and scoria cone edifice geometry evolutions induced changes in the observed activity at the surface (Pioli et al., 2017). During the 17, the activity increased in terms of volcanic tremor, lava flux (between 15 m^3 s^{-1} and 40 m^3 s^{-1}; Fig. 5.2d) and both bomb and ash emissions from the vent B (Fig. 5.4) whereas the vent A remained active with typical Hawaiian-style activity (Fig. 5.3). Although this increase of intensity

(associated with the presence of the K_2O-rich magma) probably helped the resumption of the activity, it cannot be the only explanation of the unusual high degree of fragmentation produced at vent B, as we already observed the same relative intensity at the beginning of the eruption, but without significant pulsating ash emission. The second and main question of this study is: what are the mechanisms linked with this eruptive-style change?

2.5.2.1. Golden and fluidal scoria/ash ubiquity representative of a not completely degassed magma associated with open-vent Hawaiian fountaining activity

The presence of Hawaiian fountaining all along the eruption (vent A), mainly produced golden pumice with scarce fluidal scoria. We suggest that the golden pumice represent the fragmented material which stay the longest within the central part of the lava fountain, as already documented in strong Hawaiian-style activity (e.g. Stovall et al. 2011, 2012; Parcheta et al. 2013) and in the relatively mild Hawaiian-style activity of PdF (Gurioli et al. 2018). Theoretically, the difference in porosity can be explained mostly by post-fragmentation bubble expansion (V_G/V_L of 4.6 and N_V of 3.4×10^3 mm^{-3}) that occur in coarse clasts (Fig. 5.10b), compared to ash particles (V_G/V_L of 0.7 and N_V of 9.0×10^3 mm^{-3}) that, of course, do not have bubbles bigger than their own particle size, but also do not show evidence of coalescence or growth. However, bubble growth of the golden pumice within the short-lived lava fountaining at PdF is not as significant as in the Hawaiian reticulites (Mangan and Cashman 1996) as we observed relatively high amount of isolated vesicles in the golden pumice and fluidal scoria (up to 40 vol%; Fig. 5.6b) and relatively high Nv (see also Fig. 11 in Gurioli et al. 2018). Thus, we suggest that the higher vesicularity and of the golden pumice is more representative of the magmatic conditions at fragmentation, whereas the lower vesicularity of the ash is explained by the relatively small size of the ash facilitating the gas to escape.

Crystal contents and size distributions (Fig. 5.10a) also show that microlites in the large golden pumice are slightly bigger (maximum length of 0.8 mm) than the ones in the ash fraction (maximum length of 0.5 mm). This evidence suggests that the former crystallized during a longer residence time within the lava fountains (relative slight CSD slope) than the golden/fluidal ash microlites (steeper CSD slope). Moreover, very few and relatively small

rounded vesicles are observed among all the highly deformed vesicles within the Pele's hairs and tears, which suggest relatively short time between the bubble deformation (post-fragmentation) and quenching (Cannata et al. 2019). D'Oriano et al. (2014) also suggest that the microlites cannot grow significantly after the ash emission considering reasonable quenching rates of 20 °C s^{-1} (Xu and Zang 2002) and maximum crystal growth rates of 2×10^{-5} mm s^{-1} for plg and 6×10^{-6} mm s^{-1} for cpx (cf. following paragraphs). All these latter points suggest that the golden ash fraction experienced almost immediate and efficient quenching after the fragmentation, compared to bomb-sized pyroclasts.

In accordance with Di Muro et al. (2015), Gurioli et al. (2018) and the **Chapter IV**, and regarding the crystal size, shapes and compositions, as well as the melt temperatures and H_2O contents of the different components, we suggest that the micro-phenocrysts of ol and cpx observed in the eruptive products are formed before the magma degassing by cooling-driven crystallization in the magma reservoir. On the other hand, we support that the microlites observed in the eruptive products (plg, cpx, micro-ol and oxides), are first formed by degassing-driven crystallization during the eruption (golden component) and then continued to form and grow during the progressive cooling and degassing of transitional and opaque components at very shallow levels (cf. following section). Focusing on the ash fraction, the golden/fluidal ash are characterized by an almost microlite-free (1 vol%; Fig. 5.10a) matrix. Microlite compositions show intermediate compositions (An_{65-71} for plg and Fs_{12-14} for cpx), coherent with the degassing-driven crystallization composition range recorded during previous eruptions. The average H_2O content in this melt is 0.6 wt% with an average temperature of 1124 °C, showing that this melt is not completely degassed (disequilibrium exsolution during the magmatic ascent). Moreover, unimodal VSD (Fig. 5.10c) and linear CSD (Fig. 5.10a) suggest that this magma experienced one event of bubble and crystal nucleation and growth within the eruptive dyke. According to Di Muro et al. (2014, 2016), 1 wt% of H_2O is the typical H_2O recorded within the melt inclusions at PdF for entrapment pressure of around 50 MPa (that is at the H_2O-CO_2 saturation pressure typically recorded by olivine hosted melt inclusions, which correspond to the shallow magmatic system depth, around 2 km depth). This means that around 0.4 wt% of the H_2O has been exsolved from the melt, forming the bubble nucleation and growth. Then, the integrated H_2O exsolution rate during the magma ascent in the dyke were are estimated thanks to the microlite number density H_2O exsolution rate meter of Toramaru et al. (2008), which give a mean H_2O exsolution rate of 5.5×10^{-4} wt% s^{-1} for the golden ash component. Considering this estimation, around 10 min are needed to exsolved 0.4 wt% of

H_2O. This duration is consistent with the estimated decompression rate of 0.14 MPa s^{-1} (around 4 m s^{-1}), thanks to the vesicle number density decompression rate meter of Toramaru (2006). This value is also coherent with typical decompression rates of basaltic eruptions (Ferguson et al. 2016; Shea 2017) and similar to those calculated for the initial stages of the June 2014 eruption (0.15 MPa s^{-1}), but it is higher than the initial stage of the July 2015 eruption (0.08 MPa s^{-1}) which did not produce significant golden pumice and pre-eruptive nucleation (cf. **Chapter IV**).

Focusing on the CSD shapes, and considering the CSD theory (Marsh 1988; Higgins 2000) we were able to trace back the average growth (7.8×10^{-5} and 2.6×10^{-5} mm s^{-1} for plg and cpx microlites respectively) and nucleation (1.5 and 0.9 mm^3 s^{-1} for plg and cpx microlites respectively) rates of the golden component (Fig. 5.11a; Table S5.5). These estimated values are slightly lower than found thanks to undercooling experiments (Arzilli et al. 2019b). However, our estimated rates are minimum values considering that the degassing and the micro-crystallization occurred since the beginning of the magmatic ascent within the eruptive conduit, which may not be the case. In any case, these rates associated with relatively low residence time in the conduit leads to low microlites content which maintain relatively low and typical basaltic magma viscosity of 1.4 10^2 Pa s^{-1} estimated with the three-phase viscosity model (integrating the Maron and Pierce (1956), Llewellin and Manga (2005), Giordano et al. (2008), Mader et al. (2013) and Truby et al. (2015) models). Relatively high permeability has also been measured (Fig. 5.7) within golden pumice and fluidal scoria (k_1 between 10^{-11} and 10^{-9} m^2) consistent with high gas percolation rate. APASH measurements indicate round-, vesicle- and elongated-shapes ash particles (Fig. 5.8a) which is consistent with low viscous magma, inertial fragmentation by rapid acceleration and open-vent Hawaiian-style activity (Gonnerman and Manga 2014; Cashman and Scheu 2015) all along the eruption within the vent A.

2.5.2.2 Transitional and opaque scoria/ash emission as the indicator of rapid change of the sub-surface magmatic conditions

The change of activity during the last day of the eruption is associated with a significant change of the deposit (i) grain sizes (Fig. 5.3), (ii) textures (Figs. 5.5, 5.6, 5.7 and 5.10) and (iii)

particle shape (Fig. 5.8). In this section, we try to investigate the origin of this unusual explosive dynamics of the vent B (gas or magma input, viscosity, permeability, decompression rate?) which was characterized by degassing, transient ash plume and bomb emissions (Fig. 5.4). The transitional and opaque ash emitted from the vent B during the last day of activity are very different compared to the golden/fluidal ash and are characterized by a decrease in vesicle content (between 13 and 14 vol% for the transitional ash and between 7 and 10 vol% for the opaque ash, depending on the methods used), by an increase in microlite (15 vol% and 100 vol% respectively; Fig. 5.10c) and by a differentiated matrix (Fig. 5.9) with respect to the golden/fuidal component.

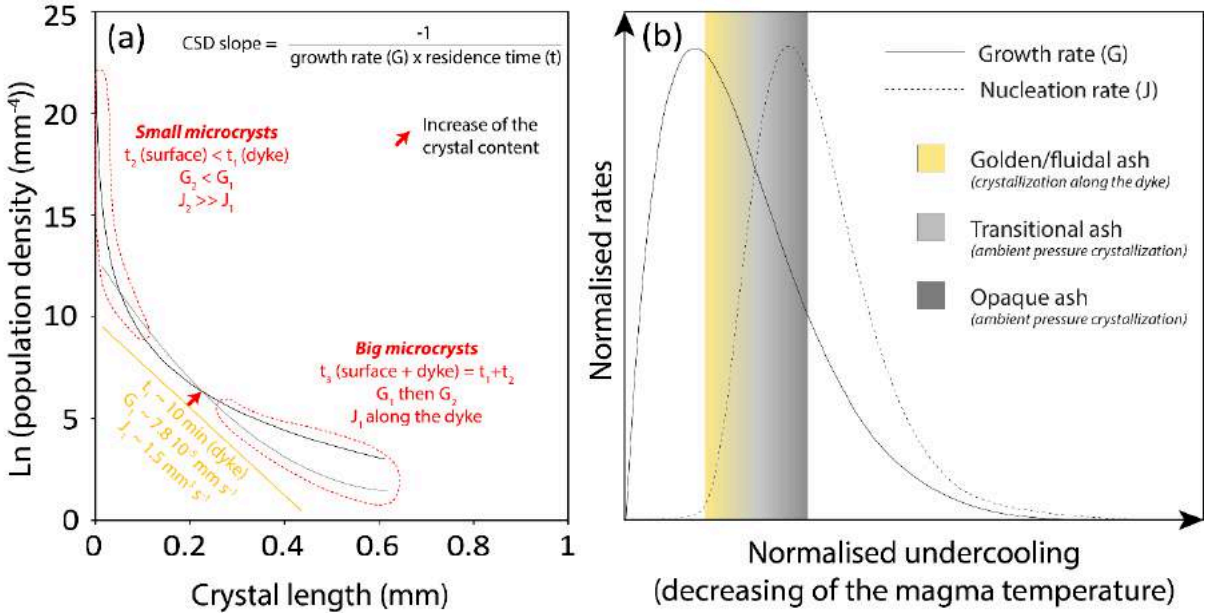

Figure 5.11 *– (a) Interpretation of the plg CSD evolution of the three different eruptive components. (b) Evolution of the crystal growth (G) and nucleation (J) rates as a function of the degree of undercooling (modified from Higgins 2000).*

The slight CSD shift between the golden/fluidal ash and the transitional and opaque ash (red arrow in Fig. 5.11a) also show that the crystal content increase (Higgins 2000) in this two latter components. The curved CSDs of the transitional and opaque components also suggest that the steeper part of the CSD slopes of the relatively small microlites, compared to the linear CSDs of the golden/fluidal component, results from newly formed microlites at sub-surface and degassed conditions associated with low time of crystallization and relatively high degree of undercooling. This is also causing the decrease of the crystal growth rates and the drastic

increase in the nucleation rates (Figs. 5.11a and 5.11b). On the other hand, we suggest that the slight more gentle CSD slopes for the biggest microlites are consistent with the progressive crystal growth (not obvious in terms of length but better visible with the width which not appears in the CSD plots) of the inherited golden/fluidal ash microlites (which form along the eruptive dyke during the magma degassing). This is permitted thanks to an increase of the total duration of crystallization of these golden/fluidal inherited microlites (Fig. 5.11a). Therefore this concave-upward shape of the CSD in the transitional and opaque fragments can be interpreted as a mixing between different microlite populations generated during a complex magmatic history in which phases of crystallization took place under distinct and variable conditions as described for other volcanic systems (e.g. Armienti et al. 1994; Higgins et al. 2002, 2006; D'Oriano et al. 2014; Pompilio et al. 2017) and with petrological experiments (e.g. Marsh 1988; Zieg and Logfren 2006; Vona and Romano 2013). The CSD interpretation is supported by the difference in composition between the cores of the largest microlites (An_{65-71} for plg and Fs_{12-14} for cpx) and the small microlites compositions (An_{56-64} for plg, Fs_{12-17} for cpx). This indeed suggests that the largest microlites are inherited from an initial crystallization within the eruptive dyke and that the small microlites formed afterwards near the surface with more sodic and ferric compositions (secondary crystallization occurring before the fragmentation). A simplified equation of the one presented (equation 13) in La Spina et al. (2015) can be used to estimate the equivalent pressure (P, in Pa) of the magmatic exsolution and crystallization for the degassed transitional component, using the dissolved H_2O content (x_d mass fraction) as well as the solubility coefficient (σ) and solubility exponent (ε): $x_d = \sigma(P)^{\epsilon}$. Using the values reported in this last study (for Stromboli magmas), and the corresponding water content of the transitional component (0.05 wt%) component, this calculations suggest that the equivalent pressure representative of transitional material is 0.1 MPa, which is coherent with the initial interpretation of the magmatic degassing and crystallization at ambient pressure.

Some melt temperatures measured from the transitional ash components are slightly higher than the golden/fluidal melt and bulk rock ones (1124-1121 °C). Regarding numerical models (La Spina et al. 2015), H_2O degassing should decrease the magma temperature. However, as shown by petrological experiments, H_2O degassing associated with the latent heat of crystallization should slightly increase the magma temperatures (Putirka 2008; **Chapter IV**).

In any case, the estimated decrease temperatures within the transitional ash (1148 to 1110 °C) support the idea of a progressive degassing and cooling-driven crystallization at the

very shallow depth until the total crystallization of the magma associated with the appearance of ol microlites (Fo_{69-78}) and Fe-Ti-rich oxides in the opaque component (< 1100 °C). Relatively low H_2O content in the melt, especially in the transitional component, shows that the explosive dynamics is not due to a gas-rich magma. Moreover, no sign of re-heating features (sign of arrival of a hotter magma) are observed in all the eruptive products. The arrival/presence of the K_2O-rich magma did not add heat to the system, but the increase in lava flux was sufficient to pressurize it. The fact that opaque material can be either K_2O-poor (initial magma) or K_2O-rich (emitted since the 16) reflects that the opaque material could start to form (by degassing and crystallization) shortly before the 16 of September, when K_2O-poor magma was still emitted and when the vent B started to decrease in terms of intensity and in which this dense opaque material could accumulate.

In parallel, the progressive decrease of N_V (3.2×10^3 and 1.1×10^3 mm^{-3} for transitional and opaque ash respectively) and V_G/V_L ratio (0.2 for both transitional and opaque ash; Fig. 5.10a), as well as the low vesicle volumes and the bimodal vesicle population within the opaque ash (Fig. 5.10b), with respect to the golden/fluidal ash, suggest that the transitional and opaque ash component result from the gas loss and bubble coalescence of the initial texture of the golden/fluidal component. Global decreases in porosity (Fig. 5.6a) and in isolated vesicle content (Fig. 5.6b) also highlight both gas loss and bubble coalescence. The absence of isolated vesicles in the opaque lapilli-sized fragments, also suggest that the opaque scoria cooled progressively, in contrast to the golden and fluidal fragments that quenched faster in the air. We suggest that the progressive cooling favor the post-fragmentation connections between the vesicles and the breaking of the solidified opaque matrix (Colombier et al. 2017b; Gurioli et al. 2018). Moreover, transitional and opaque components are less porous and less permeable than the golden/fluidal one (Fig. 5.7). Their Darcian permeabilities are measured down to 10^{-12} $m^{2,}$ showing a lower degree of gas percolation. Finally, APASH measurements show a progressive change of the ash morphology (Fig. 5.8b and 5.8c): transitional ash shape signature is approximately the same as the golden/fluidal one except that they no longer form elongated ash particles and Pele's hairs and tears, reflecting slight increase in magma viscosity (1.8×10^3 Pa s^{-1}). Opaque ash shape signature is very different from the two latter components, showing rough surfaces and reflecting drastic increase in viscosity (tends to 10^9 Pa s^{-1}) and brittle fragmentation.

As a conclusion, we suggest that the transitional and opaque textures are inherited from a progressive sub-surface cooling, inducing advanced degassing and secondary crystallization

of the magma, which may occur either by (i) recycling material within active vents as already proposed for Etna (D'Oriano et al. 2014), and/or (ii) by directly cooling of the magma at its free surface facilitated by the slight decrease in the lava flux (Figs. 5.2a and 5.2b, clogging of vent B) as already observed on Stromboli (Gurioli et al. 2014), and/or (iii) by collapse of inner parts of the vent as we observed some collapse and instabilities features within the eruptive vents (Fig. 5.3) again observed on Stromboli (Patrick et al. 2007; Capponi et al. 2016), and/or by the infiltration of external water accelerating the cooling process. In each case, this degassed, crystallized and viscous magma, represented by the transitional and mainly the opaque component, formed a relatively impermeable magmatic layer at the fragmentation level within the vent B, during its decrease in activity mainly between the 16 and 17 of September. The suggested increase of lava flux during the last day of activity may have reactivated the vent B which was at that moment clogged by this opaque layer, in contrast with the vent A, which remained active in a sustained way. The fact that we observed some mingled scoria and ash between golden/fluidal or transitional magma, coating the opaque material, confirm that the opaque material is snatched and fragmented by the ascending and pressurized magma (secondary fragmentation), represented by the transitional and golden components, the last day of the eruption within the vent B.

Looking at field observations, slight degassing on the crater rim of the vent B during the last day of the eruption, as well as the source of the opaque ash plume that also seemed to originate from the crater rim, suggest that some of the gas was able to escape. This released some pressure in the shallow system related to vent B. However, we suppose that not all the gas was able to escape, resulting in an increase in the net pressure which is equivalent to the pressure increase due to the ascending magma minus the slight decrease due to gas escape. Sudden and local pressure drops (caused by these initial overpressures that cracks the plug) would enhance further volatile exsolution and growth, promoting the magma fragmentation (La Spina et al. 2019).

2.6. Evidences of plug pressurization triggering relatively energetic fragmentation and conclusions

Compared to several small eruptions of the 2014-2015 period documented by Peltier et al. (2016), Coppola et al. (2017), Gurioli et al. (2018) and in **Chapter IV**, the September 2016 eruption was characterized by relatively high lava fluxes which were associated with sustained, long-lasting lava fountaining producing a relative high amount of golden pumice. However, a significant, drastic and uncommon change of eruptive-style was observed the last day of the eruption, only from the less active vent B, while the vent A remained sustainably active with Hawaiian fountaining-dominated activity all along the eruption.

Regarding the eruption, we suggest that the stable lava flux between the 12 and 17 of September, followed by a drastic increase of intensity during the last day of the eruption, was an important parameter evolution. Indeed, we suggest that the local magmatic flux emitted by the vent B, between the 16 and 17, was insufficient to drain continuous magmatic flow in the sub-surface eruptive conduit contrary to the vent A. This also highlights the importance of the sub-surface conduit geometry evolution that may control the magma path at shallow levels (Pioli et al. 2017). This local magmatic flux decrease allowed the magma to degas and crystallize near the fragmentation/explosion level within the vent B (Figs. 5.12a and 5.12b), forming a low-permeable and rheological plug whose fragmentation generated the opaque material. Field observations, transitions between Hawaiian/Strombolian-style activities and transient explosions as well as calculated crystal growth and nucleation rates suggest that this plug formed in approximately one or two days with averaged cooling-rates between 0.005 and 0.05 °C s^{-1} (vs. 20 °C s^{-1} for a typical ash particle in the air, D'Oriano et al. 2014). This relatively slow plug cooling could have been caused by the combination of different processes as the direct cooling of the magma free-surface, and/or tephra recycling. The progressive clogging and burying of the vent B might also been facilitate by the inner vent wall collapses (Gaudin et al. 2017).

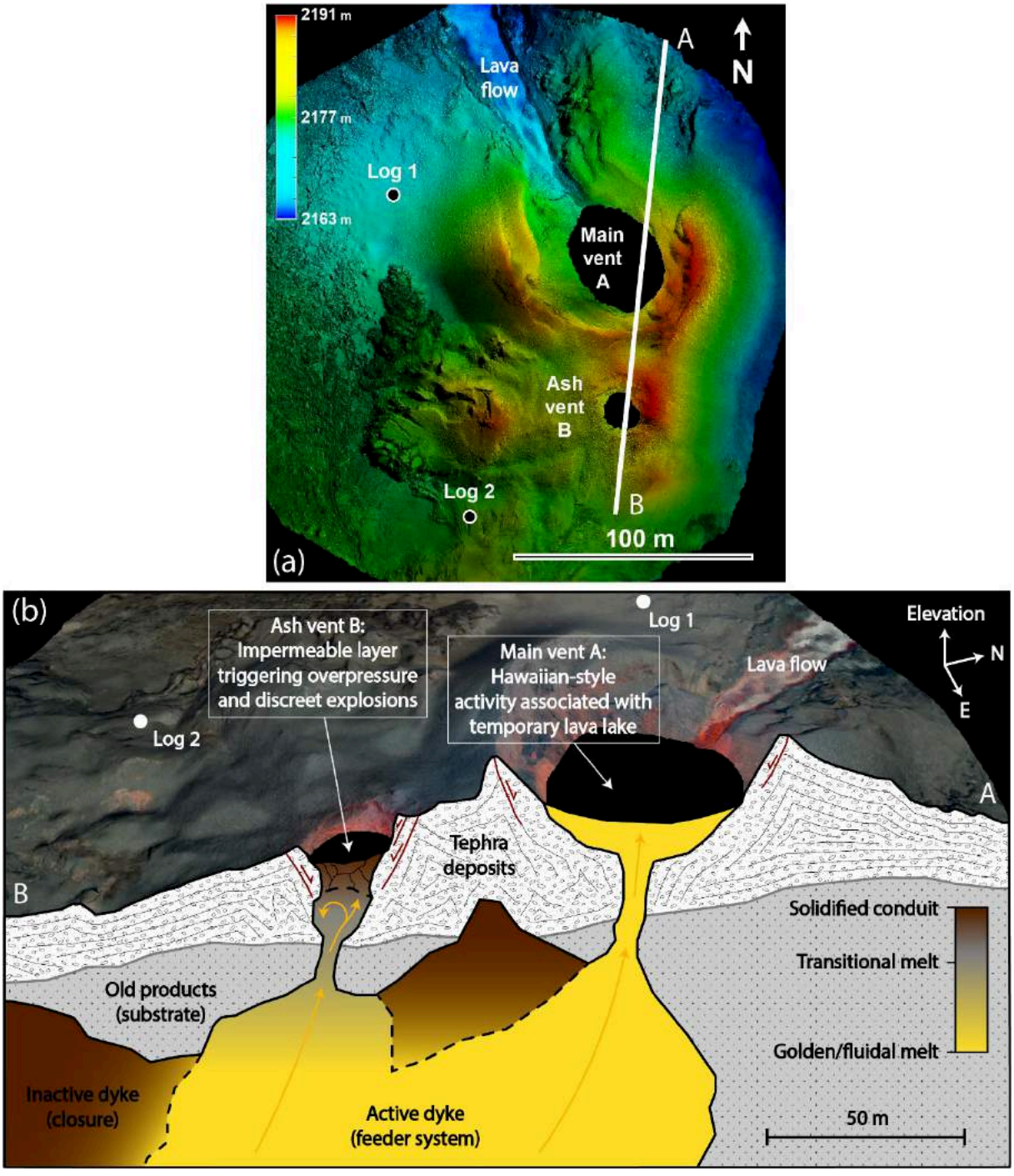

Figure 5.12 *– (a) DEM from aerial photogrammetry (15 September) of the main edifice of the eruption. (b) Schematic cross-section showing the subsurface feeding system on the 17 of September.*

Then, the late increase of the lava flux was enough to overcome the overpressure threshold to break through the plug layer and trigger the transient explosions within the vent B.

Once the overpressure threshold required to let the magmatic gas percolate into the degassed plug was reached, the partially undegassed (golden/fluidal component) magma decompressed, then fragmented and snatched some of the plug material (transitional and opaque components and mingled material). Ash morphology measurements on opaque ash, which represent the main ash emitted volume, show very different characteristics compare to the golden/fluidal ash. Opaque ash are rounded in shape but with very rough particle surface which is characteristic of snatched and fragmented particles coming from a brittle material, reflecting secondary fragmentation (Cashman and Scheu 2015; Cashman and Rust 2016). This secondary fragmentation thus represent a hazardous mechanism producing a high amount of relatively fine particles with large dispersion, while the primary fragmentation within lava fountains (inertial fragmentation by rapid acceleration) produced smaller amount of golden and transitional ash. We also prove that multi-disciplinary approaches as combining geophysical, textural and chemical measurements are critical to characterize, understand and monitor such eruptive activity. In this study we also evidenced that this kind of approach allow to constrain relatively well the pre- and syn-eruptive processes at the origin of eruption dynamics.

3. Perspectives

3.1. L'absence d'évidence de mécanismes phréatomagmatiques permet-elle de conclure sur les mécanismes de fragmentation impliqués ?

L'origine du type d'explosions transitoires observées lors de l'éruption de Septembre 2016 est parfois expliquée par l'interaction du magma avec des fluides superficiels, comme par exemple au Piton de la Fournaise (explosions sommitales de 1860, Michon et al. 2013), à l'Etna (Behncke et al. 2006), ou encore à Hawaï (Zimanowski et al. 2015). Selon le raisonnement de White et Valentine (2016), le mécanisme de fragmentation phréatomagmatique peut être relativement difficile à mettre en évidence et l'absence de preuve d'interactions entre le magma et l'eau ne nous permet pas de conclure sur les véritables mécanismes impliqués. Cependant, ces derniers auteurs ont énuméré plusieurs caractéristiques permettant de distinguer les processus magmatiques et phréatomagmatiques.

En ce qui concerne la porosité des produits juvéniles, Houghton et Wilson (1989) suggèrent que les particules produites par les interactions entre le magma et l'eau peuvent avoir une large gamme de porosité. Dans l'étude présentée dans la section précédente, les distributions de la taille des vésicules des différents produits juvéniles, ainsi que les estimations de la teneur en H_2O dissous dans les verres magmatiques, permettent de reconstituer l'historique du dégazage mais ces données ne donnent aucune indication directe sur la présence éventuelle de fluides externes dans le système. Dans le cas de l'éruption de Septembre 2016, les pyroclastes de type *transitional* et *opaque* sont relativement denses par rapport aux pyroclastes de type *golden* et *fluidal* qui proviennent d'une fragmentation purement magmatique. La formation de fragments phréatomagmatiques denses pourrait éventuellement se former dans le cas où les volatils ne pourraient pas s'exsolver ou croitre rapidement au sein du liquide magmatique, en raison d'un niveau de trempe relativement profond. Cependant l'étude texturale et pétrochimique a prouvé que les pyroclastes de type *transitional* et *opaque* représentent l'évolution progressive du magma initial peu dégazé et peu cristallisé, en un magma dégazé et relativement cristallisé.

En parallèle, Heiken (1974) suggère que les particules juvéniles émises lors d'évènements phréatomagmatiques sont généralement vitreuse, grâce à une trempe rapide

agissant au contact de l'eau. Ce type de texture n'est pas observé dans les cendres de type *opaque* et *transitional*. Cette texture vitreuse est évidemment présente dans les particules (parfois allongées) produites au sein des fontaines de lave grâce à une trempe naturelle rapide dans l'air (cf. **Chapitre VI**).

En ce qui concerne la morphologie des cendres, Walker et Croasdale (1971) ainsi que Heiken (1974) suggèrent que les particules phréatomagmatiques sont souvent caractérisées par des formes en bloc avec des bords anguleux. De manière similaire, Dellino et al. (2012) suggèrent aussi que la morphologie des cendres peut fournir d'importantes informations sur les mécanismes de fragmentations impliqués. Dans le cas de l'éruption de Septembre 2016, les cendres de type *opaque* et *transitional* ne présentent pas de signatures phréatomagmatiques, mais plutôt des surfaces très rugueuses avec des irrégularités relativement petites à l'échelle de la particule (convéxité) et des formes morphologiques relativement arrondies (solidité). Ces caractéristiques sont interprétées comme étant le résultat d'une fragmentation mécanique sèche (cf. **Chapitre VI**) par pressurisation d'une couche rhéologique imperméable.

Les processus d'agglomération des particules, étant une caractéristique bien connue des dépôts phréatomagmatiques (Gilbert et Lane, 1994), ne sont pas observés au sein des dépôts de l'éruption de Septembre 2016. Enfin, aucune particule lithique, parfois observées dans les dépôts phréatomagmatiques (cf. **Chapitre VI**), n'est observée au sein de ces dépôts.

En conclusion, le processus phréatomagmatique peut être exclut de manière confidente des mécanismes de fragmentation liés au changement de style éruptif lors de l'éruption de Septembre 2016.

3.2. Anticipation du changement de style éruptif

L'enjeu majeur qui ressort de l'étude présentée au sein de ce chapitre est l'identification et l'anticipation de la transition entre une activité hawaiienne typique vers une activité transitoire et plus explosive. En effet, à part cette éruption de Septembre 2016, ce type d'activité n'a jamais été documenté dans l'activité récente du Piton de la Fournaise, au contraire de l'Etna (D'Oriano et al ; 2014 ; Taddeucci et al. 2015 ; Polacci et al. 2019). L'émission de cendre telle

qu'observée pendant l'éruption de Septembre 2016 au Piton de la Fournaise représente donc un aléa et des risques associés non-négligeables pour les personnes approchant les sites éruptifs.

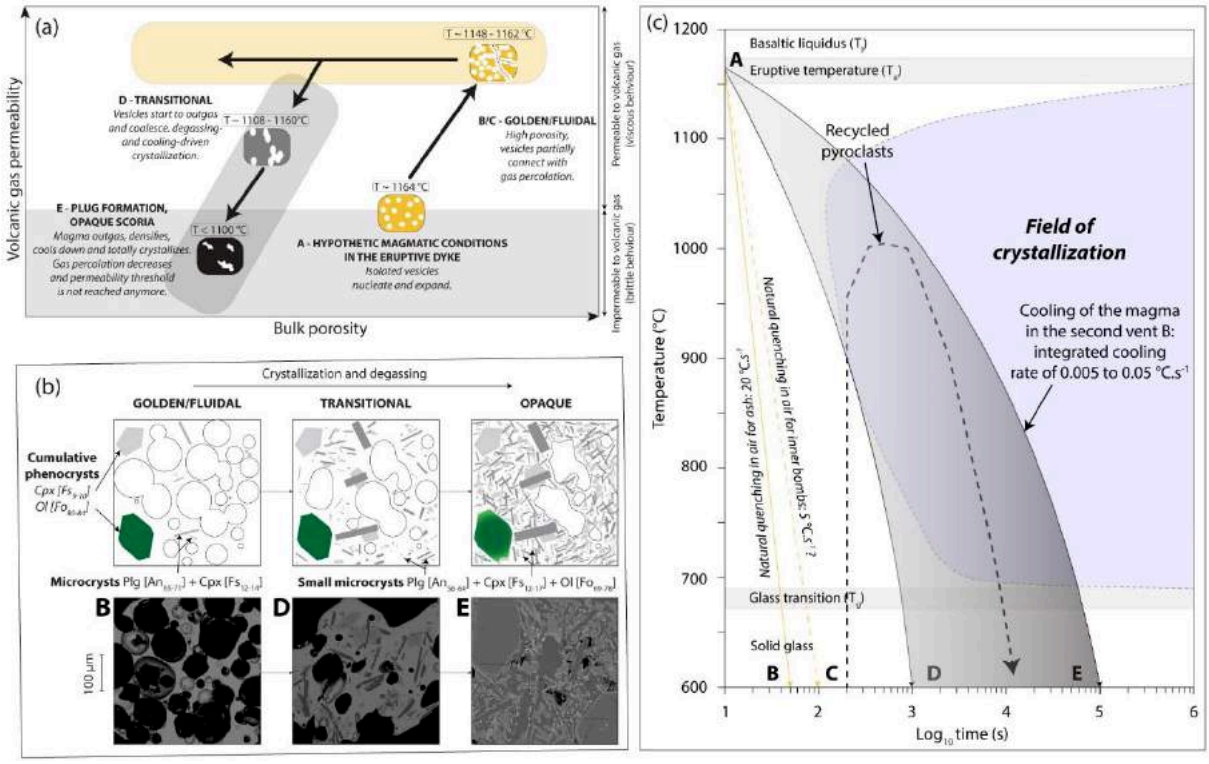

Fig. 5.13 *– Modèles conceptuels à l'origine de la formation du bouchon magmatique. (a) Evolution de la perméabilité en fonction de la porosité. (b) Evolution de la texture des pyroclastes. (c) Evolution du refroidissement du magma à la surface (modifié à partir de D'Oriano et al. 2014).*

Après avoir caractérisé et interprété l'ensemble des processus magmatiques à l'origine de ce type d'activité (Fig. 5.13), l'identification de signaux avant-coureurs demeure un problème majeur. Néanmoins, plusieurs observations et données présentées au sein de ce chapitre permettent de d'avancer plusieurs éléments de réponse.

En effet, (i) la baisse du flux magmatique local (visible à la fois sur le terrain mais aussi par télédétection ou à travers le trémor, Fig. 5.2), alimentant notamment l'évent B, a considérablement baissé lors des six premiers jours de l'éruption. Cette baisse a possiblement engendré (ii) une déstabilisation partielle de l'évent (fractures visibles autour du cratère ; Figs. 5.3 et 5.12a). Enfin, (iii) une partie des faibles projections émis par cet évent ont pu retomber

au sein-même de celui-ci (phénomène de recyclage des pyroclastes). L'enchainement de ces trois mécanismes (provoquant la formation d'une couche rhéologique), suivi d'une augmentation soudaine du flux magmatique (provoquant la surpression) sont donc potentiellement à suivre sur l'ensemble des éruptions futures pour éventuellement anticiper l'émission de cendre soudaine, comme lors de l'éruption de Septembre 2016.

Cependant, l'occurrence d'un ou plusieurs de ces mécanismes n'est pas nécessairement synonyme d'un changement majeur de l'activité éruptive. Par exemple, le flux magmatique lors de l'éruption d'Aout-Octobre 2015 a beaucoup varié (Coppola et al. 2017) et l'activité éruptive s'est même momentanément arrêtée à deux reprises pendant plusieurs heures avant de reprendre avec des flux magmatiques relativement élevés (entre 15 et 30 $m^3.s^{-1}$). Ces changements soudains du flux magmatique n'ont en effet pas impacté le style éruptif lors de la reprise de l'activité, car toutes les conditions pour former une couche rhéologique potentiellement peu perméable aux gaz volcaniques, n'était probablement pas réunies.

3.2. Optimisation de l'analyse des composants des cendres

La mesure des composants au sein des particules de cendres a été réalisé à l'œil nu et grâce à une binoculaire, en se basant sur les caractéristiques extérieures (couleurs et formes) des particules. La mise en place d'une procédure d'identification des particules en utilisant le potentiel du Morphologi G3 de Malvern (mesure de la transparence et de la forme) pourrait en effet être une solution pour gagner du temps à la fois sur l'analyse des composants et sur la mesure de la morphologie des particules (mesures conjointes). En effet, dans le cas des différents types de cendre émises lors de l'éruption de Septembre 2016, la mesure de la transparence des particules, en plus de leurs caractéristiques morphologiques, pourrait être une caractérisation relativement utile pour déterminer leur appartenance aux différents groupes de composant identifiés au sein de cette éruption (*golden*, *fluidal*, *transitional* et *opaque*). La mise en place de cette procédure nécessite néanmoins beaucoup de tests et une certaine constance dans les paramètres de mesure pour être établie.

CHAPITRE VI

ETUDE DE LA VARIABILITE DES TEPHRAS AU PITON DE LA FOURNAISE ET AU KARTHALA

1. Présentation générale

Suite au chapitre précèdent, mettant notamment en évidence l'émission de cendres lors de l'éruption de Septembre 2016 (cf. **chapitre V**), il semble important d'identifier et comprendre l'ensemble des mécanismes volcaniques pouvant être à l'origine d'émissions de cendres plus importantes. En suivant cet objectif, le troisième ensemble de résultat présenté dans cette thèse est focalisé sur l'étude d'un ensemble d'échantillons de téphras, plus ou moins riches en cendres. L'étude granulométrique, texturale, morphologique et chimique de ces dépôts permettent la caractérisation et l'interprétation des différents processus à l'origine de la fragmentation des téphras basaltiques, pouvant se produire au sein du Piton de la Fournaise, du Karthala, mais aussi dans d'autres systèmes basaltiques.

La suite de ce chapitre, présentée en anglais, correspond à un article en préparation pour *Bulletin of Volcanology.*

2. Mise en évidence des mécanismes de fragmentation basaltique au Piton de la Fournaise et au Karthala

Variability of basaltic fragmentation efficiencies at shield volcanoes revealed by ash characterization

Simon Thivet[(1)], Lucia Gurioli[(1)], Andrea Di Muro[(2)], Julia Eychenne[(1)], Pascale Besson[(3)], Jean-Marie Nedelec[(4)]

[1] Laboratoire Magmas et Volcans, Université Clermont Auvergne - CNRS - IRD, OPGC, Campus Universitaire des Cézeaux, 6 Avenue Blaise Pascal, 63178 Aubière Cedex, France

[2] Institut de Physique du Globe (IPGP), Sorbonne Paris-Cité, CNRS UMR-7154, Université Paris Diderot, Observatoire Volcanologique du Piton de la Fournaise (OVPF), Bourg Murat, France

[3] Institut de Physique du Globe (IPGP), Sorbonne Paris-Cité, CNRS UMR-7154, Université Paris Diderot, 1 rue Jussieu, 75238 Paris

[4] SIGMA Clermont, Institut de Chimie de Clermont-Ferrand, Université Clermont Auvergne, BP 10448, Clermont-Ferrand

Article in preparation for *Bulletin of Volcanology*

Acknowledgments

We thank J-L. Devidal and J-M. Hénot for their invaluable help with the EPMA and the SEM at LMV. This research was financed by ClerVolc, the French Government Laboratory of Excellence, the EUROVOLC program and the Observatoire de Physique du Globe de Clermont-Ferrand (OPGC). We also thank the members of the OVK for their hospitality.

Supplementary material (labelled Tables S in the manuscript) are available at

http://lmv.uca.fr/thivet-simon-2/

Key-words

Ash; Basaltic; Fragmentation; Karthala; Piton de la Fournaise.

Abstract

It is commonly accepted that effusive activity represents the main emitted magmatic volume in basaltic shield volcanoes, as at Piton de La Fournaise (PdF, La Réunion Island, France) and at Karthala (Ngazidja Island, Comoros). In addition, eruptive activity occurs mostly within the non-populated calderas of these two volcanoes and generally does not cause any risks to the population. However, historical observations, recent monitoring data and field work on more or less recent tephra deposits suggest that some eruptions produced unusual and unexpected explosive phases. A comprehensive sampling of tephra from some major historical and recent eruptions on these two volcanoes allowed us to perform systematic componentry, grain size, chemical and morphological analysis in order to characterize the eruptive dynamisms involved in these basaltic eruptions. This integrative approach reveals very different characteristics of the studied tephra reflecting different fragmentation efficiencies and different associated mechanisms. On one hand, various intensities of primary ductile or partially brittle fragmentation from tephra emitted during Hawaiian fountaining or mild Strombolian explosions were identified as the most common fragmentation mechanism, in particular during the 2014-2018 relatively intense eruptive sequence at PdF. On the other hand, we distinguished more energetic events, identified both at PdF (Bellecombe and Piton Chisny tephras as well as the March 1860, September 1936 and April 2007 eruptions) and at Karthala (April and November 2005 eruptions) volcanoes. Among these relatively explosive eruptions, very different fragmentation and magmatic processes were identified, as plug pressurization and brittle fragmentation enhanced by syn-eruptive crystallization, as well as magma/water interactions, high magma decompression rates and shear fragmentation producing fine-grained cataclastic lithic ash during caldera collapse.

2.1. Introduction and objectives

Basaltic edifices, especially lava shield volcanoes such as Kilauea (Hawai'i Island, USA), Piton de la Fournaise (La Réunion Island, France) and Karthala (Ngazidja Island, Comoros), are mainly composed of lava flows with relatively low slope angles (Walker 1993).

This effusive activity is often associated with low-energy explosive Hawaiian or Strombolian-style eruptions (e.g. Head and Wilson et al. 1987, 1989; Parfitt, 2004; Houghton et al. 2016; Gurioli et al. 2018; **Chapters IV and V**). If these kind of activities produce tephra, field evidences and recent syn-eruptive observations at basaltic volcanoes also highlight more explosive events capable of producing fine-grained tephra, for instance at Etna (Taddeucci et al. 2002, 2004; Andronico et al. 2008, 2009; Polacci et al. 2019; Ferlito et al. 2009; Behncke et al. 2013; Corsaro et al. 2017), Stromboli (Bertagnini et al. 1999; Carapezza et al. 2004; Ripepe et al. 2005; Polacci et al. 2009), Kilauea (e.g. Dvorak 1992; Mastin 1997; Neal et al. 2018), Piton de la Fournaise (e.g. Michon et al. 2007, 2009, 2013; Staudacher et al. 2019, 2016 ; Ort et al. 2016) and Karthala volcanoes (Bachèlery et al. 2016). Ash-forming events represent a very different hazard from the usual effusive or low-energy explosive eruptions (Connor et al. 2015 and references therein), with impacts on the ground for the communities living downwind (e.g. adverse health effects for humans and animals, damage to crops, infrastructure and networks, water contamination; Horwell and Baxter 2006; Wilson et al. 2015) and impacts in the air for the aviation (Aspinall and Blong 2015). Critically, such explosive events are highly unexpected in basaltic settings, which makes their forecasting more challenging. It is thus essential to understand (i) what are the types of event that produce ash (magmatic, phreatomagmatic, phreatic or volcano-tectonic), (ii) what are the characteristics of the associated deposits, and (iii) what are the processes triggering and controlling the occurrence of ash-forming events.

To explore these questions, we investigate here a range of basaltic fragmentation mechanisms through the comprehensive study of several tephra deposits composed of bomb (particle diameters 64 mm), lapilli (particle diameters between 64 and 2 mm) and ash (< 2 mm, with coarse ash particle diameters > 63 µm and fine ash with particle diameters smaller than 63 µm). These deposits, originated from pre-historical, historical and recent eruptions at Piton de la Fournaise (PdF) and Karthala volcanoes, and represent a wide range of eruption styles. Based on the phenomenology of the studied events as well as the grain size, componentry, texture, morphology and chemical analysis of the tephra particles, this work gives new insights into the different eruptive mechanisms that can lead to ash-generating events at shield volcanoes. Grain size analysis is used to constrain the fragmentation efficiency of the eruptions (e.g. Heiken 1974; Wohletz 1983; Parfitt 1998; Zimanowski et al. 2003; Rose and Durant 2009). Componentry analyses allow quantifying the role of juvenile magma during these eruptions, as well as identifying the textural features characterizing these different particles in order to

determine the origin of both juvenile and non-juvenile components (e.g. White and Houghton 2006; Eychenne et al. 2015; Marino et al. 2019). Morphology of the ash particles informs on the fragmentation mechanisms (e.g. Heiken 1974; Liu et al. 2015; Nurfiani and Bouvet de Maisonneuve 2018). Finally, chemical analysis provide constraints on the mineral phases of a few key samples (e.g. Gislason et al. 2011; Botto et al. 2013; Vaca et al. 2016).

2.2. Case studies and sampling

PdF and Karthala edifices are the two emerged active volcanoes of the Southwest Indian Ocean which are situated East and West of Madagascar, respectively (Fig. 6.1a). These two volcanoes share similar characteristics in terms of morphology and structure. The main volcano-tectonic structure of PdF is the Enclos Fouqué caldera (Fig. 6.1b). This horseshoe-shaped depression composed of several lobes is 250 m deep, 13 km long in the E-O axis and 6 to 8 km wide in the N-S axis (Michon and Saint-Ange 2008). Since the settling of sedentary man life within La Réunion Island (second part of the 17th century), the volcanic activity is mainly concentrated within this structure (e.g. Villeneuve and Bachèlery 2006; Staudacher et al. 2016; Peltier et al. 2018) where some rift-zones have been identified (Bachèlery 1981; Michon et al. 2009, 2016b). Older deposits originating from eruptive sources situated outside this caldera were also described (Morandi et al. 2016; Principe et al. 2016; Ort et al. 2016). At Karthala volcano, volcano-tectonic structures are also well developed with a summit complex of nested calderas and craters about 3.5 km-long and 2.8 km-wide (Fig. 6.1c). Karthala rift zones are much more developed than at PdF (Bachèlery et al. 2016) and spread outside the summit calderas area, where lava effusion and Hawaiian-style eruptions occurred, but less frequently than at PdF. However, the eruptions studied here occurred within the summit caldera of Karthala, where explosive activity has already been documented (Bachèlery et al. 2016).

Sampling of all the deposits presented in this study was performed during several field campaigns through the collaboration between the Laboratoire Magmas et Volcans (LMV), the Observatoire Physique du Globe de Clermont-Ferrand (OPGC), the Observatoire Volcanologique du Piton de la Fournaise (OVPF), the Observatoire Volcanologique du Karthala (OVK) and the Institut Physique du Globe de Paris (IPGP). All the PdF and Karthala samples studied here are localized in Figures 6.1b and 6.1c, respectively.

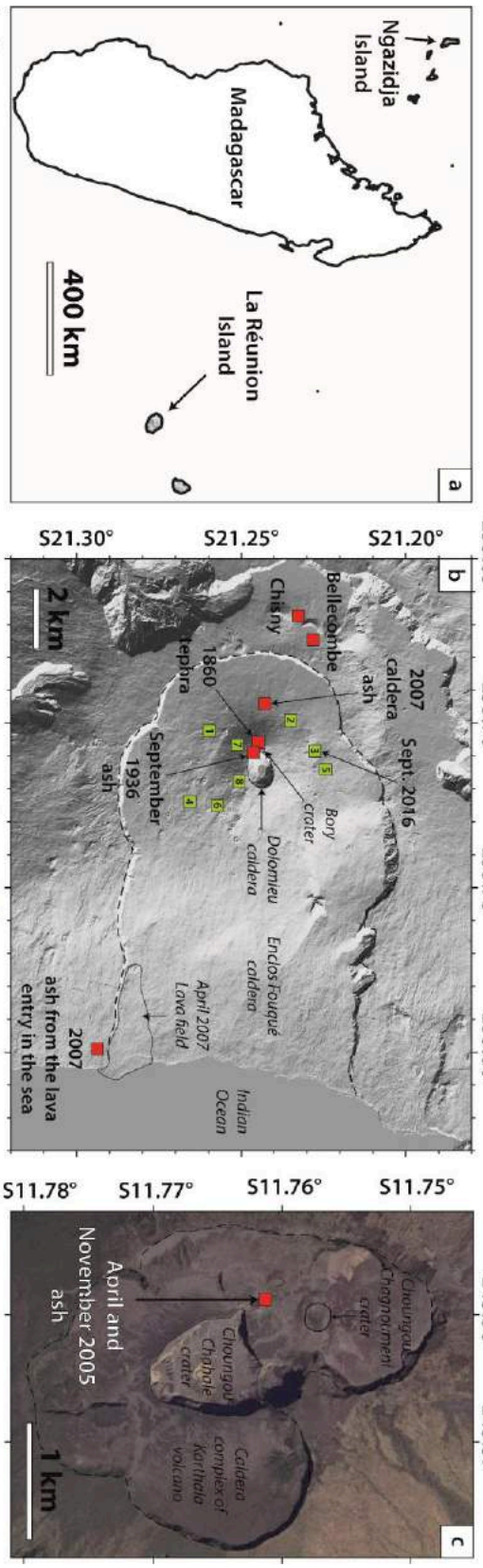

d

Volcano	Eruption	Eruptive dynamics	Sample name	Sample localisation	Distance from the source (m)	Ash fraction (<2 mm, wt%)	Fine ash fraction (<64 µm, wt%)	Juvenile ash (%)	Description
Piton de la Fournaise	September 2018	Mild Strombolian	1 REU180916_3	S21.25940° E55.70130°	50	6	0	100	- Routine samplings of recent (2018) mild Strombolian deposits.
	July 2018		2 REU180807_7	S21.23518° E55.69999°		5	0	100	This kind of eruptive activity occur at relatively low lava flux.
	September 2016	Transient explosions	3 REU161211_6	S21.22492° E55.70975°	200	97	0	100	- Transient explosions (transtonal material, REU161211_10) associated
			3 REU161211_10		100	8	0	100	with the formation of sporadic plumes (opaque ash, REU161211_6).
	September 2016	Hawaiian fountaining	3 REU161211_4	S21.22492° E55.70975°	≈ 100	10	0	100	- Routine samplings during the 2014-2016 eruptive period.
	May 2015		REU160531_5	S21.26828° E55.72406°		27	0	100	These eruptions formed flank eruptive fissures.
			4 REU160531_4			13	0	100	This kind of activity occur at relatively high lava flux compared to the mild Strombolian one.
			REU160531_3			14	0	100	
	July 2015		5 REU150731_4	S21.22108° E55.71672°		58	0	100	
	May 2015		6 REU150520_3	S21.25895° E55.72429°		13	0	100	
	February 2015		7 REU150212_13	S21.25013° E55.70597°		31	0	100	
	June 2014		8 REU141118_6	S21.25085° E55.71919°		13	0	100	
	April 2007	Transient ash emission during caldera collapse	REU070A_171	S21.24278° E55.69417°	1500	100	87	1	- 4 mm thick ash deposits collected on a clean surface after the main caldera collapse phase. Ash were emitted during the formation of the caldera.
		Ash emission during lava entry in the sea	REU070A_052	S21.24425° E55.71980°	1000	99	1	100	- 5 mm thick ash deposits collected on a clean surface after the main ash emission phase from the shoreline delimited by the newly formed April 2007 lava flow.
	September 1936	Ash emission during caldera collapse	REU14C805_5	S21.24625° E55.70895°	≈ 100	100	17	42	- Ash layer collected between an older pyroclastic layer and spatter deposits that emplaced after the ash emission.
	March 1860	Violent Strombolian	REU131112 PF_2	S21.24376° E55.70639°	≈ 500	56	1	2	- Ash collected within different layers of the stratigraphic log of *Michon et al. (2013)*.
						100	4	11	*Cf. log in supplementary material.*
	Piton Chisny	Hawaiian fountaining «Opening phase»	CH_5 CH_1	S21.23368° E55.66518°	≈ 400	6	0	100	- Ash collected within the Piton Chisny black tephra deposits.
						61	5	100	*Cf. log in supplementary material.*
	Bellecombe ash	Tephra emission associated with sliding mass movement	BE_TOP_2 BE_TOP_1 BE_BASE_2 BE_BASE_1	S21.22724° E55.67450°	≈ 500	59	2	0	- Ash collected within different layers of the stratigraphic log of *Ort et al. (2016)*.
						47	3		*Cf. log in the supplementary material.*
					≈ 3000	91	11		«BASE» samples correspond to the lower bellecombe tephra.
						85	32	0	«TOP» samples correspond to the upper bellecombe tephra.
Karthala	November 2005	Violent Strombolian	KA_TOP_2	S11.75138° E43.35892°	600 m	98	40	86	- Ash collected within the finer layers of a 110 cm thick deposit.
			KA_TOP_1			99	57	93	*Cf. log in the supplementary material.*
	April 2005		KA_BASE_2			91	33	95	«BASE» samples correspond to the April 2005 eruption.
			KA_BASE_1			97	41	67	«TOP» samples correspond to the November 2005 eruption.

Figure 6.1 *– (a) Location of La Réunion and Ngazidja Islands hosting Piton de la Fournaise and Karthala volcanoes respectively. (b) Map of Piton de la Fournaise volcano with the different studied deposits. The green numbered squares correspond to the deposits sampled*

during recent eruptive activity (2014-2018 period). The red squares represent specific deposits corresponding to pre-historical, historical and recent major eruptions. The black dashed line delimits the Enclos Fouqué caldera. (c) Map of the summit caldera complex of Karthala volcano, delimited by the black dashed line. The red square localize the sampling of the April and November 2015 deposits. (d) List and description of all the samples studied from Piton de la Fournaise and Karthala volcanoes. For each volcano, the samples are classified chronologically.

They are also listed chronologically for each volcano in Figure 6.1d in which some of the deposit characteristics are summarized. They were systematically sampled within proximal areas (between 50 to 1500 m from source) in order to work on thick deposits and visualize the entire stratigraphy representing the whole of the eruptive sequences we are interested in. Sampling of deposits from recent eruptions (part of routine sampling performed by the OVPF for each recent eruptive event, represented by green squares in Fig. 6.1b) is either done during the eruptive activity and close to the source (**Chapter IV**) or after the eruption, to be able to access strategic and very proximal deposits (Gurioli et al. 2018; **Chapter V**). Other sampling was performed on older and key deposits representative of much more explosive events at PdF (red squares in Figs. 6.1b and 6.1c).

All eruptions studied here are classified by style and phenomenology, which are inferred from observational data (recent eruptive events) and reviews of the literature (older events). The eruptions are presented in order of increasing explosivity, although some eruptions vary in intensity through time, as already well documented in general for these basaltic volcanic systems (Taddeucci et al. 2015).

2.2.1. Mild Strombolian and transient explosions at PdF

The first samples described in this study are tephra emitted during (i) mild Strombolian eruptions (e.g. July and September 2018 eruptions at PdF) and (ii) slightly more intense transient explosions (September 2016 eruption at PdF, **Chapter V**).

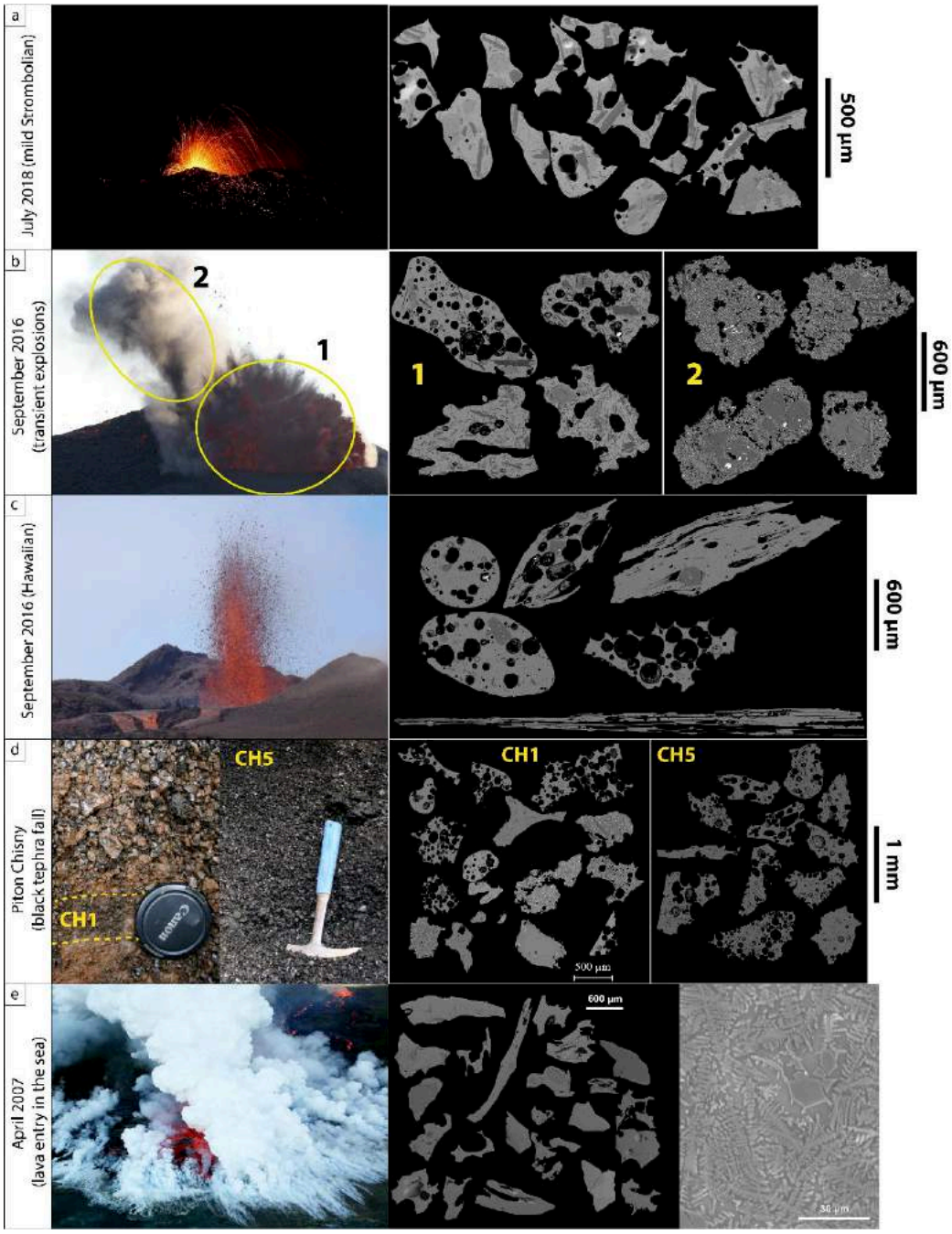

Figure 6.2 *– Eruptive phenomenology at PdF with associated ash deposits imaged in BSE. (a) Mild Strombolian activity (July 2018). (b) Transient explosions (September 2016) producing incandescent explosions (transitional pyroclasts, labelled 1) associated with discreet ash plumes (opaque pyroclasts, labelled 2). (c) Hawaiian-style activity or lava fountaining producing "golden" pyroclasts (September 2016 eruption). (d) Deposits from intense Hawaiian-style activity at Piton Chisny (Black Tephra deposits). CH1 corresponds to the initial phase and CH5 corresponds to the steady phase after the initial one. (e) Lava entry in the sea (April 2007) producing a laze and ash emission.*

(i) At PdF, mild Strombolian activity (bubble bursting at the magma free surface) is generally observed a few hours or days after the beginning of the eruptive activity, when the lava and gas fluxes are decreasing (**Chapter IV**). This mild Strombolian activity is usually formed by discrete explosions less than 10 m high (Gurioli et al. 2018) before ending with less and less energetic spattering (Hibert et al. 2015). The samples from the July (Fig. 6.2a) and September 2018 eruptions, which respectively lasted around one and 47 days, were collected just one day after each Strombolian explosion that happen after the initial lava fountaining phases of these two eruptions.

(ii) The last day of the one week long eruption of September 2016, mostly dominated by sustained lava fountaining (during the first six days), was characterized by a shift in activity (**Chapter V**): one of the active vents turned from mild projections and slight degassing to relatively more intense, transient bomb- and lapilli-dominated explosions (one explosion every 10 to 20 seconds producing both incandescent and dark projections up to 40 meters high) associated with synchronous sporadic emission of dark ash-dominated plumes (the ash particles were transported to more or less proximal areas within the plumes in favor of wind). Two months after the eruption, the whole sequence of the intense explosions and ash plumes were collected from a 1 m thick log, approximately 150 m far from the from the explosive vent (Figs. 6.1 and 6.2b).

2.2.2. Hawaiian fountaining activity at PdF

Tephra produced during mild Hawaiian fountaining activity (with maximum height to approximately 30 m) or more intense fountaining (with maximum height to approximately 200 m) are the first type of samples described in this study. For this purpose, we collected (i) recent Hawaiian deposits emplaced between 2014 and 2018 at PdF and (ii) the Piton Chisny black tephra deposit from PdF.

(i) The Figure 6.2c shows the sustained mild Hawaiian fountaining (that reached a maximum height of 40 meters) which occurred during the entire duration of the September 2016 eruption. Two months after the eruption, the whole sequence of this Hawaiian fountaining was sampled at 100 m far from the main active vent that produced these lava fountains. We also added samples from five additional eruptions that happened during the 2014-2018 period

(DynVolc 2017) and were collected from the fountaining (with plastic sheet on the ground for February, May and July 2015 eruptions) or a few months after the eruptions, when the deposits were finally accessible, like for June 2014 eruption (Gurioli et al. 2018). All these deposits were sampled approximately 100 m from the sources.

(ii) Outside the Enclos Fouqué caldera, the entire stratigraphic sequence (three meters thick) of the last Piton Chisny activity (1450 to 1630 AD) called the Black Tephra deposit (Morandi et al. 2016; Principe et al. 2016) was sampled (Fig. 6.3a). Only two samples are shown in this study (Fig. 6.2d), respectively representative of the initial phase (tephra layer named CH1, 5 to 10 cm thick) and a phase (CH5, 20 cm thick homogeneous bed of scoria lapilli within two layers of bombs) emplaced during the long-lived lava fountaining.

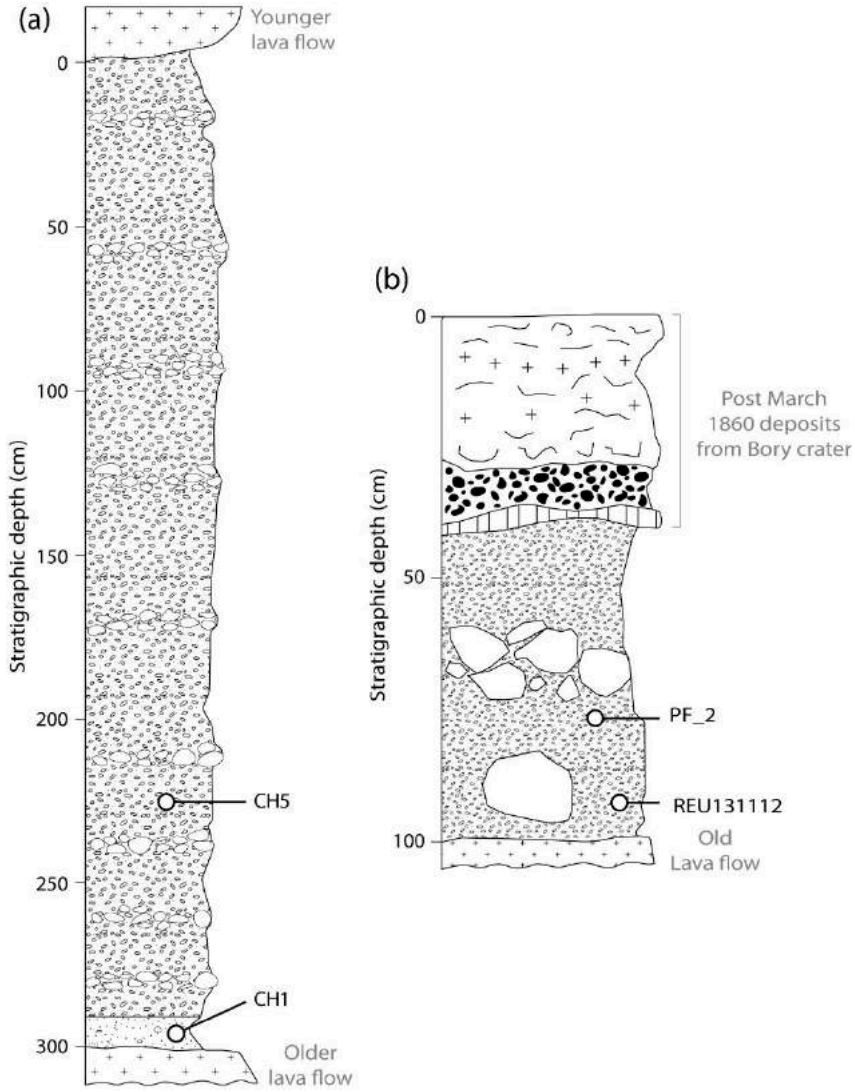

Figure 6.3 *– (a) Stratigraphic log of the Black Tephra (Piton Chisny) deposit. (b) Stratigraphic log of the proximal March 1860 deposit, modified from Michon et al. (2013).*

2.2.3. Explosions caused by lava flow entry in the sea at PdF

During the April 2007 eruption at PdF (Piton Tremblet, source of emission only 600 m above the sea level and only 3 km from the coastline; Fig. 6.1b), relatively high lava flux (maximum of 200 m^3 s^{-1}, Staudacher et al. 2009) was associated with the formation of an intense Hawaiian-style activity (lava fountain heights up to 200 m). This intense activity alimented a large lava flow that rapidly reached the ocean (Michon et al. 2007, 2011), forming a new emerged lava platform of around 5×10^5 m^2. The interaction between the seawater and the hot lava generated explosions, characterized by the emission of steam clouds and glass shards (laze) which are the third type of samples described in this study (Fig. 6.2e). The related tephra deposit was collected shortly after the emission from a 5 mm thick layer that was emplaced on a clean surface (top of a small wall, near the Tremblet village).

2.2.4. Violent Strombolian eruptions at PdF and Karthala

Three main violent Strombolian eruptions are described in this study. (i) The first one is the summit March 1860 eruption of PdF that represents one of the most explosive historic events reported (Michon et al. 2013). The two other eruptions occurred at Karthala volcano (ii) in April and November 2005. These two eruptions were the largest observed within the recent activity of Karthala volcano (Bachèlery et al. 2016).

(i) Two samples representative of the first part of the March 1860 summit violent Strombolian eruption were collected within the summit area of the volcano, and within the stratigraphic sequence (Fig. 6.3b) described by Michon et al. (2013). The drawing shown in the Figure 6.4a was realized by Velain (1878) a few years after the eruption and represents the Brûlant crater which was situated on the Eastern part of the summit area where the Dolomieu caldera is situated nowadays. After the overflow and then the emptying of an active lava lake located within the Brûlant crater (Lénat et al. 2016a and references therein), several eruptive fissures opened on the flank of the volcano in February and March 1860. Summit explosions producing ash-rich plumes and bloc ejections were observed on March 19, 1860. The Brûlant crater was partially dismantled and widened by about 300 m (Fig. 6.4a). Deposits emplaced

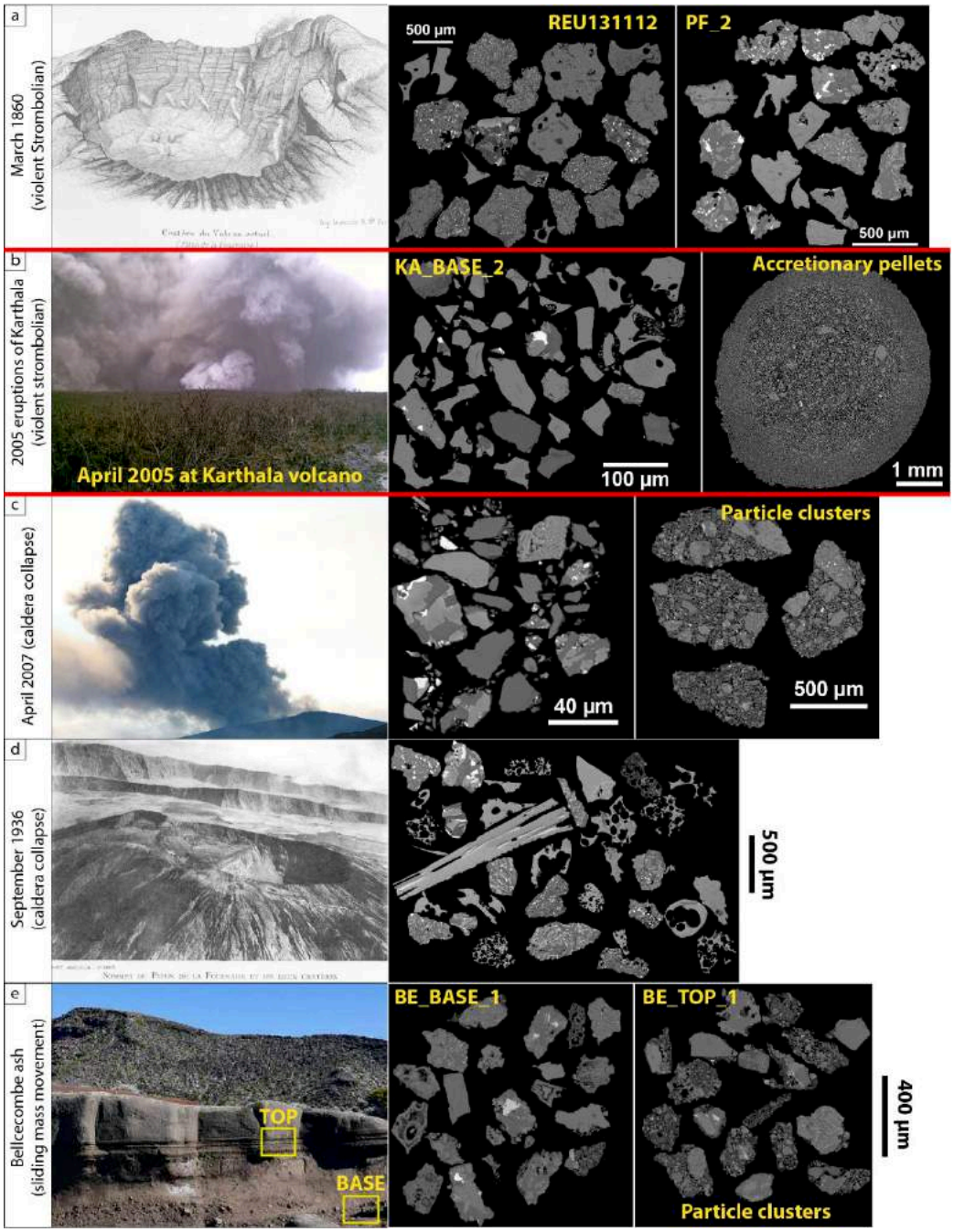

Figure 6.4 *– Eruptive phenomenology at PdF and Karthala (delimited in red) with associated ash deposits imaged in BSE. (a) Ash deposits from the March 1860 summit eruption at PdF. Sketch from Velain (1878) representing the Brûlant crater a few years after the eruption. (b) Ash emission from the April 2005 eruption at Karthala volcano. Picture taken by Daniel Hoffschir. Accretionary lapilli are zoned in term of particle size with finer particles in the rims and bigger particles in the center. (c) Ash emission enhanced by the April 2007 major caldera collapse at PdF. Particles within the particle clusters are randomly distributed. (d) Ash deposits associated with the September 1936 partial caldera collapse and an associated*

opening fissure at PdF. Picture from Lacroix (1936) taken shortly after the partial caldera collapse.. (e) Bellecombe tephra deposits at Petite Carrière outcrop. BE_BASE_1 and BE_TOP_1 correspond to the Lower and Upper Bellecombe Tephra respectively.

during this paroxysmal event were, at that time, dispersed in all the PdF massif area (Villeneuve and Bachèlery 2006). Nowadays, deposits related to this eruption are found in the summit area of the central cone of PdF (Fig. 6.1b; Michon et al. 2013). Here, we focus only on two samples representative of the relatively fine-grained-matrix (lapilli and coarse ash) of the first half of the coarse-grained (bombs, blocks and lapilli) March 1860 deposit sequence (Fig. 6.3b), collected approximately 500 m from the Brûlant crater (REU131112 at the base and PF_2 at the top).

(ii) Between 2005 and 2007, the morphology of the summit area of Karthala volcano was modified by four distinct eruptions (Fig. 6.5). Here, we focus on the two more explosive eruptions of this short but active period, namely the April and November 2005 eruptions that were described as phreatomagmatic events (Bachèlery et al. 2016). Before these two eruptions, a visible hydrothermal lake was present at the surface within the Choungou-Chahalé crater (Fig. 6.5a), where was located the source of both eruptions. This lake, which changed in color from orange to green and then blue in the period 1991-2003 (probably indicating acidity changes) disappeared after the November 2005 eruption which partially filled the Choungou-Chahalé crater with lava (Figs. 6.1c and 6.5). The April and November 2005 eruptions began with violent Strombolian and phreatomagmatic phases (Fig. 6.4b) and rapidly decreased in intensity (since the hydrothermal lake was rapidly vaporized and the lava flux decreased) forming temporary lava lake within the crater. Note that the water lake returned to the bottom of the Choungou-Chahalé crater less than one month after the end of the first eruption. Deposits emplaced during these two eruptions (corresponding to the initial and relatively intense phreatomagmatic phases) were sampled within the summit caldera complex, 600 m from the source (Figs. 1e and 6.6a). Similarly to the summit area of PdF, the November 2005 eruption emplaced lithic blocs (mainly fragments of dense lavas) near the vent (Fig. 6.5f). The stratigraphic log studied near the source includes deposits from both the 2005 eruptions (Fig. 6.6). Samples labelled KA_BASE_1 and KA_BASE_2 and collected at the base of the log can be confidently attributed to the April eruption, while KA_TOP_1 and KA_TOP_2 were sampled at the top of the sequence and are part of the November eruption. These samples were willingly collected within the tephra layers with the smallest grain sizes.

Figure 6.5 *– Evolution of the recent morphology and eruptive activity of the summit of Karthala volcano. The yellow arrows are geographical markers, showing well identifiable red ash deposits. (a) Choungou-Chahalé crater in 2003 (Bachèlery et al. 2016). (b) Ash emission from the Choungou-Chahalé crater, 17 April 2005 (picture from D. Hoffschir). (c) Aerial picture of the lava lake activity within the Choungou-Chahalé crater, 18 April 2005 (Bachèlery et al. 2016). (d) Lava lake activity within the Choungou-Chahalé crater, 26 November 2005 (Bachèlery et al. 2016). (e) Lava lake activity within the Choungou-Chahalé crater, 30 November 2005 (Bachèlery et al. 2016). (f) Choungou-Chahalé crater in October 2019.*

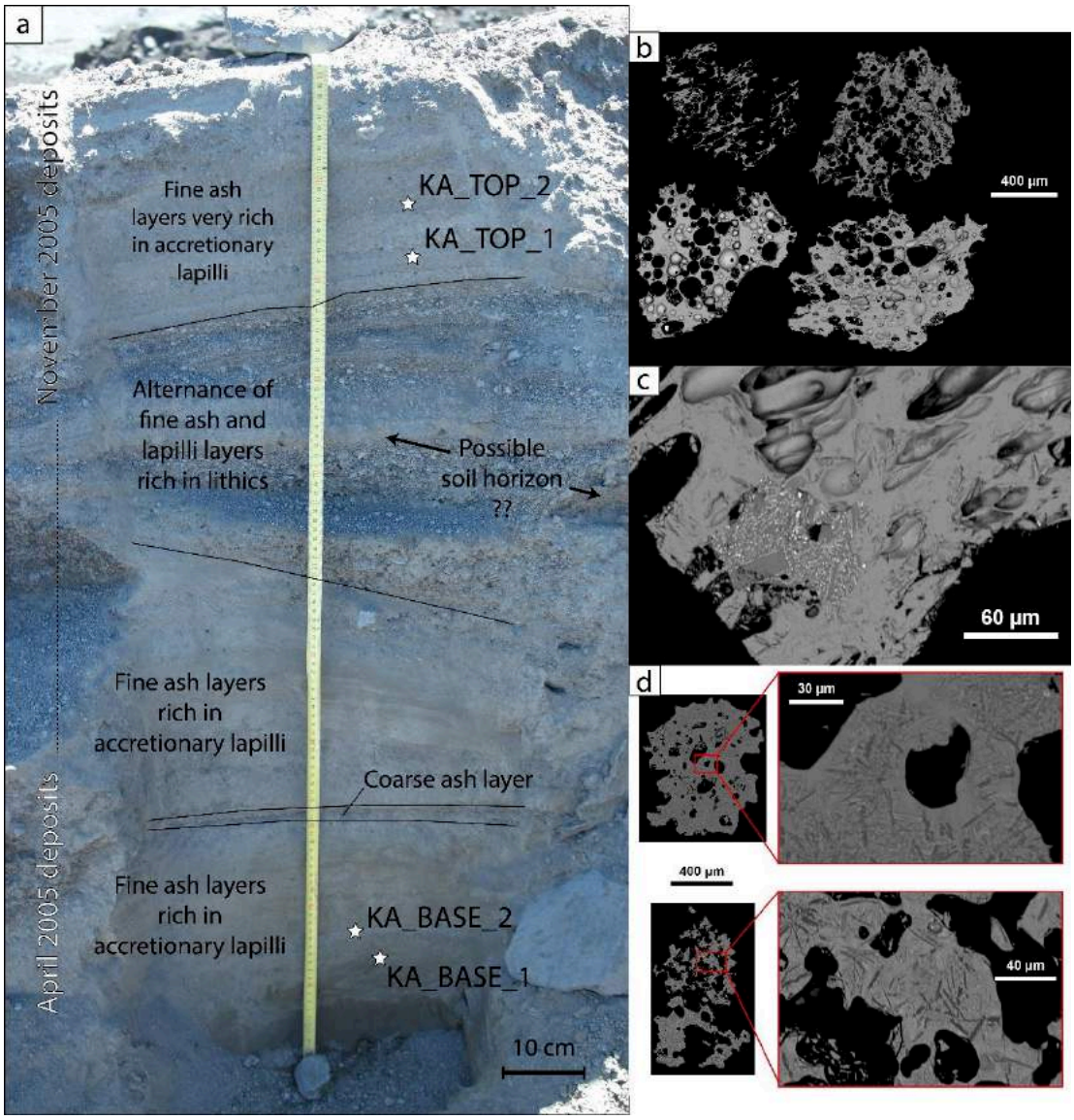

Figure 6.6 *– (a) Stratigraphic log of the 2005 eruptive deposits within the Karthala caldera complex. KA_BASE_1, KA_BASE_2, KA_TOP_1 and KA_TOP_2 are the four sampled layers described in this study. (b) Vesicular and glassy particles (golden ash), from the KA_TOP_1 sample (BSE images). (c) Mingled ash particle with a tachylite texture englobed by a vesicular and glassy matrix, from the KA_BASE_2 sample (BSE images). (d) Degassed and crystallized particles (tachylite), from the KA_BASE_2 sample (BSE images).*

2.2.5. Caldera collapses at PdF

Basaltic tephra can also be produced during caldera collapse events and generally originate from relatively explosive and paroxysmal eruptions. Tephra deposits related to two main caldera collapse events at PdF are studied here, namely (i) the April 2007 event that formed the actual Dolomieu caldera, and (ii) the September 1936 partial caldera collapse that occurred within the same summit area as the 2007 collapse.

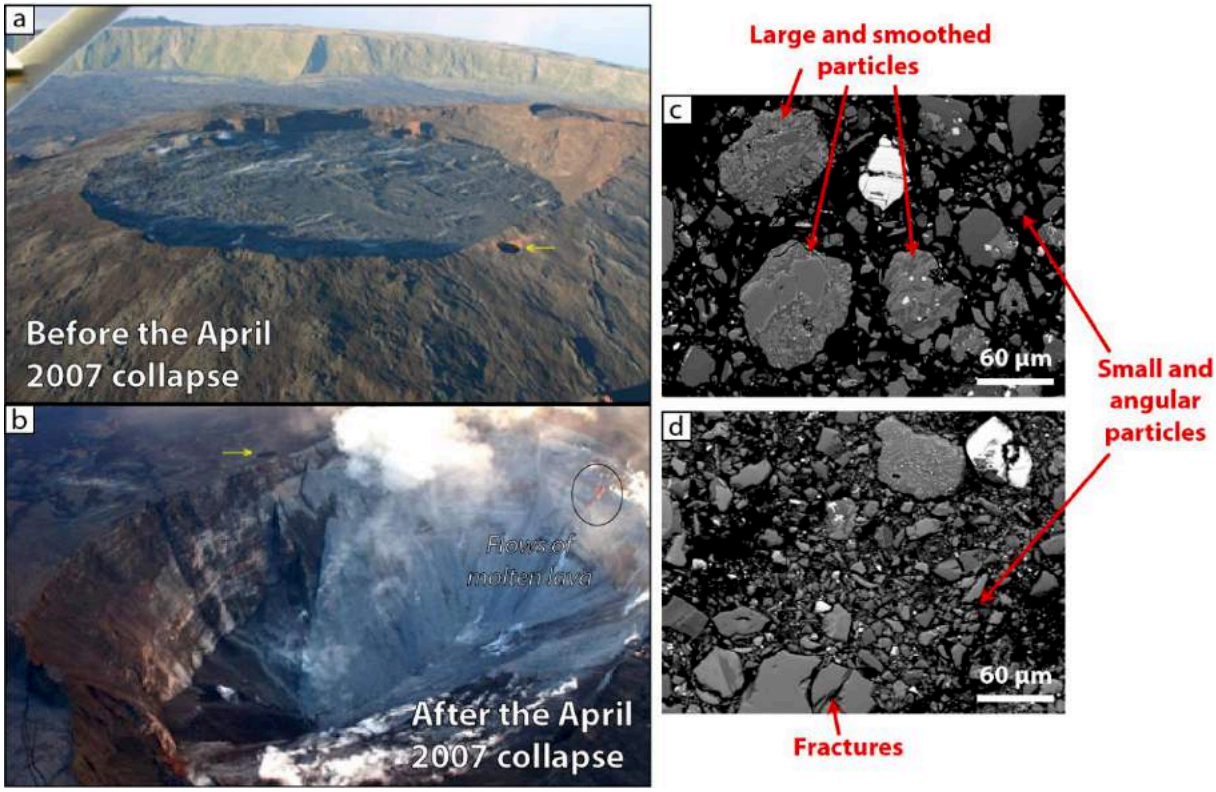

Figure 6.7 *– (a) The Dolomieu caldera of PdF before the caldera collapse. (b) The Dolomoeu caldera after the collapse with visible flows of molten lava (pictures from L. Ferlicot). The yellow arrows are geographical markers, showing La Soufrière crater. (c) and (d) SEM images of the ash particles from the REU0704_171 sample.*

(i) As already described previously, the April 2007 eruption extruded lava with a high flux. This exceptionally high intensity caused a brutal draining of the shallow magmatic system, situated around 2 km underneath the summit cone of the volcano (Peltier et al. 2008). On April 5 at, a first collapse was recorded by the OVPF seismic network. A major collapse occurred a few hours later, after which a modified summit area morphology was observed (Fig. 6.7). This

major collapse was followed by numerous but weaker collapses until the April 15 (Fontaine et al. 2014), producing a 340 m deep depression of a total volume of 96×10^6 m^3 (Urai et al. 2007). A few minutes after the main collapse associated with ash emission (Fig. 6.4c), several flows of molten lava occurred on the newly formed caldera rims (Fig. 6.7b; Staudacher et al. 2009). The emitted ash mostly dispersed within the Enclos Fouqué caldera (Staudacher et al. 2009; Michon et al. 2011, 2013) and was collected in different locations. In this study, we focus on a sample that was collected 1.5 km from the source on the Western part of the Enclos Fouqué caldera (Fig. 1b) on a clean solar panel surface of an OVPF station (named "La Dalle") in order to avoid any contamination. At the time of sampling the ash thickness was approximately 4 mm.

(ii) A second deposit related to the partial caldera collapse of September 1936 (Lénat et al. 2016a and references therein) was studied. This collapse was the largest one observed before 2007 and formed after a continuous eruptive activity between 1931 and 1936 (proximal magmatic activity to summit area of PdF was probably still active during the collapse). The aerial picture shown in Figure 3d is one of the first of the PdF and was taken shortly after the partial caldera collapse (Lacroix 1936), which is visible on the Eastern part of the summit area (on the right side of the picture). The related sample of this event was collected within the summit area of PdF (Fig. 6.1b).

2.2.6. Mass-sliding events at PdF

According to Bachèlery (1981), Morandi et al. (2016) and Ort et al. (2016), the Enclos Fouqué caldera (Fig. 6.1b) may have formed during successive mass-sliding events towards the East. These authors have related the caldera forming events with the Bellecombe tephra (4900 to 2250 BP), a thick and widespread deposit that can be found all over the PdF massif. Ort et al. (2016) divided the stratigraphic sequence of the Bellecombe tephra into two main units. The Lower Bellecombe tephra may correspond to a flank extension of Enclos Fouqué caldera that opened steeply dipping fissures tapping relatively young hydrothermal/magmatic systems located under the newly formed Enclos Fouqué caldera. Similarly, the upper Bellecombe tephra is related to a fissure opening linked with a relative more mature hydrothermal/magmatic reservoir, initially emplaced westwards within the Plaine des Sables area. Two samples were

collected within the lower unit (around 60 cm thick) and two other ones within the upper unit (around 210 cm thick, Figs. 6.4e and 6.8) in a proximal outcrop named “Petite Carrière” (Fig. 6.1b).

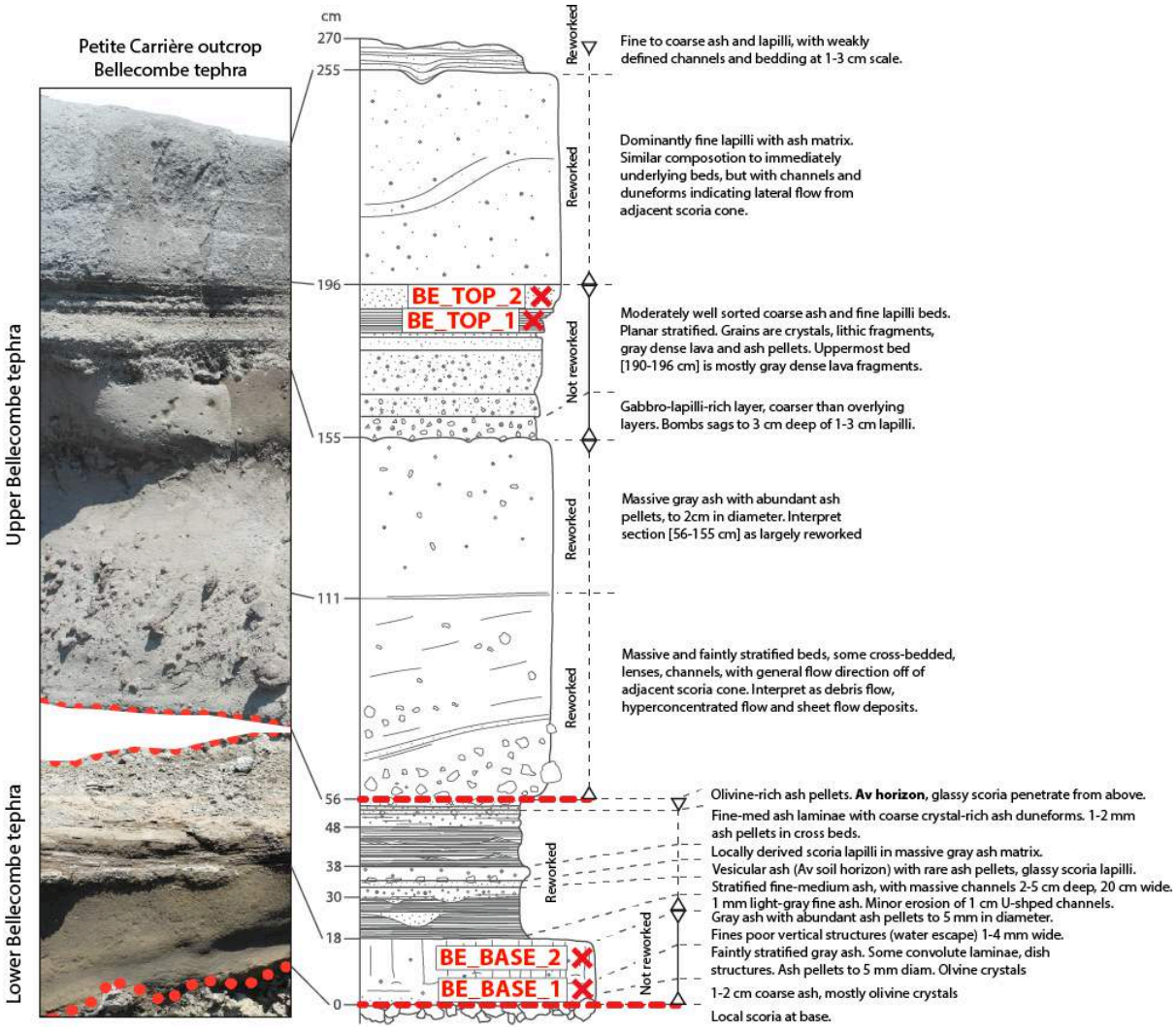

Figure 6.8 *– Stratigraphic log of the Bellecombe Tephra at PdF (modified from Ort et al. 2016). BE_BASE_1, BE_BASE_2, BE_TOP_1 and BE_TOP_2 are the four sampled layers described in this study.*

2.3. Methods

2.3.1. Grain size

Grain size analyses were performed on all the studied deposits. Beforehand, the samples were dried in the oven at 90 °C during 24 to 48 hours. Manual sieving at a ½ Φ scale between -6 Φ (64 mm, $\Phi = -\log_2$ (d in mm)) and 5 Φ (32 µm) was carried out following the adapted procedure of Gurioli et al. (2018). The Particle Size Distributions (PSD) of the fine ash-rich deposits (fine ash are particles with a diameter < 64 µm, Schmid 1981), were quantified by laser diffraction using a Mastersizer 3000 of Malvern. The laser diffraction (LDPSA for Laser Diffraction Particle Size Analyzer) technique determines the PSD of a dispersed sample in an aqueous solution through the application of the Mie theory (Riley et al. 2003). PSD of samples spanning a wide range of grain size fractions, from lapilli to fine ash, were determined by combining both techniques (sieving and LDPSA). The two datasets acquired are correlated, merged and corrected to find the total PSD of the deposits. Raw grain size data are available in the supplementary material (Table S1).

2.3.2. Componentry, texture and chemical analysis

For each sample, componentry analyses were performed on one specific grain size fraction (depending on the samples, cf. Figs 6.2 and 6.4) in order to distinguish the juvenile particles from the non-juvenile particles (White and Houghton 2006). Juvenile particles were identified based on their surface texture, porosity, crystal assemblage and degree of alteration. The identification and description of the juvenile and non-juvenile particles came from the observation of the lapilli grain fractions using binoculars, and of the ash fractions using Scanning Electron Microscopy (SEM). Only the most representative grain size fraction (PSD modes) within the ash domain (< 2 mm) of each deposit was impregnated in epoxy resin for preparation of polished sections. Internal textures of the samples were investigated by Backscattered Electron (BSE) imagery using both the JEOL JSM-5910 LV SEM and the

Cameca SxFiveTactis Electron Probe Micro Analysis (EPMA) at LMV, with an acceleration voltage of 15 kV.

Some chemical analyses were also performed on a few samples (Table S2), by in-situ glass analyses with Cameca SxFiveTactis EPMA and bulk-rock analyses with ICP-AES (Horiba Jobin-Yvon Ultima C spectrometer), following the procedure adapted from Gurioli et al. (2018). For some key ash samples, mineral phases were identified by X-ray diffraction (XRD) analysis with an Empyrean diffractometer, operated at 43 kV and 38 mA, with the use of Ka radiation from a Cu anode. Inorganic Crystal Structure (ICSD) and Crystallography Open (COD) databases were used to identify the mineral phases. The ash samples were analyzed from 2 to 50 degrees 2θ, with a step width of 0.02 degrees 2θ and two second counting time for each step.

2.3.3. Ash morphology

Ash morphology was quantified on a very large dataset following the method developed by Leibrandt and Le Pennec (2015) and adapted in **Chapter V**. Before the analysis, specific grain size fractions were selected within ¼ Φ bins from 0.75 Φ (600 µm) to 4 Φ (34 µm), depending on the deposit grain size. We performed ash morphology measurements on similar grain size fractions from one deposit to another to allow data comparison without grain size bias. On the contrary, several grain size fractions were measured within the same sample to check any effects of the grain size on the particle morphology. Apparent Projected Shape of Ash (APASH) was measured on a very high number of ash particles using the automated Morpho-Grainsizer Morphologi G3 of Malvern. The instrument disperses the ash sample on a glass slide and measures automatically several morphology and roughness parameters. In this study we focused on two roughness parameters, namely the solidity (SLD) and the convexity (CVX), which represent morphological (particle scale) and textural (smaller scale) roughness of the particles respectively (Liu et al. 2015). We also focused on one morphological parameter, namely the aspect ratio (AR) of the particles, which represent the elongation of the particles. These three parameters were used to compare morphology characteristics of the different ash samples and are defined as follow (Leibrandt and Le Pennec; 2015): SLD = A/A_{CH}, CVX = P_{CH}/P and AR = W_b/L_b where A is the particle area (μm^2), A_{CH} is the area (μm^2) of the convex-

hull (smallest convex polygon that contains all the pixels of the particle), P is the particle perimeter (µm), P_{CH} the convex-hull perimeter (µm), W_b the minor axis and L_b the major axis of the particle. SLD, CVX and AR are dimensionless parameters varying between 0 and 1. The raw data (Table S3) were filtered in case of artificial particle clusters.

2.4. Results

In this section, the samples are described in terms of ash (< 2 mm or -1 Φ) and fine ash (< 64 µm or 4 Φ) contents, componentry and texture variability (Figs. 6.2 and 6.4). PSDs and (Fig. 6.9) ash morphology features (Fig. 6.10) are also described.

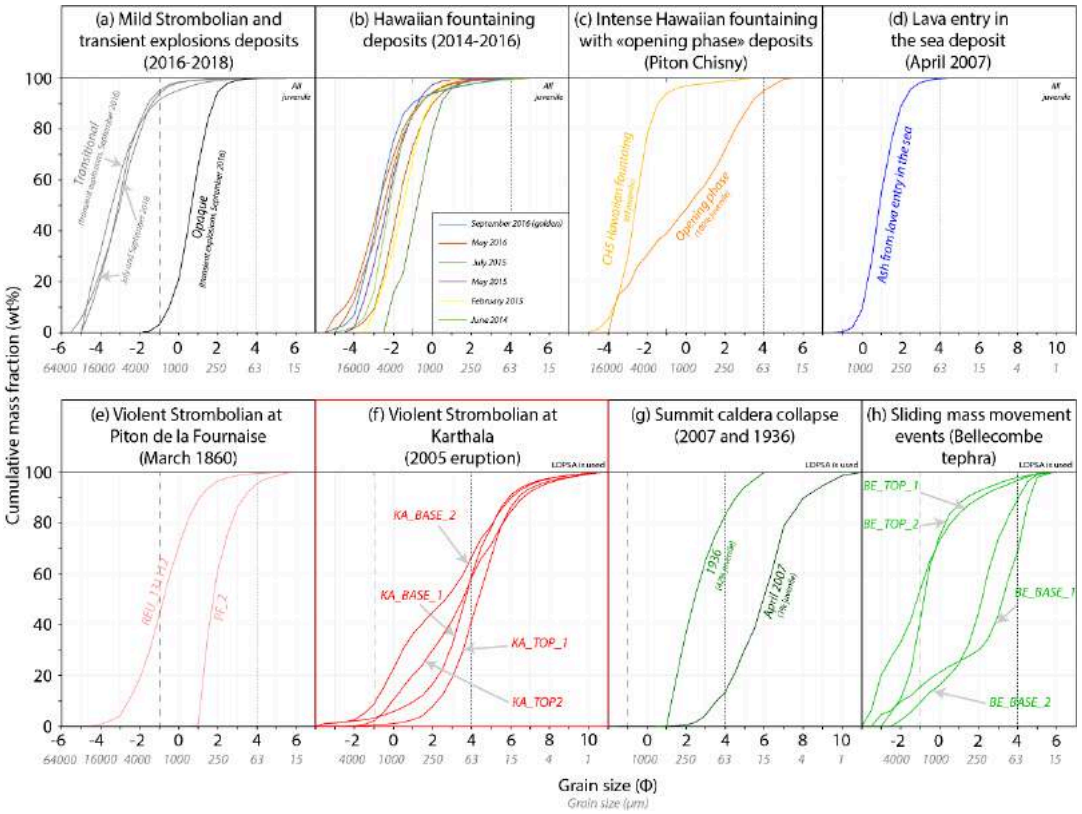

Figure 6.9 *– Particle Size Distributions (PSD) of the different studied deposits. Coarse ash boundary is represented by the black dashed line at -1 Φ (2 mm). Fine ash boundary is represented by the black dashed line at 4 Φ (64 mm). The samples are represented with a color code reflecting their associated eruptive styles. Karthala samples are delimited in red.*

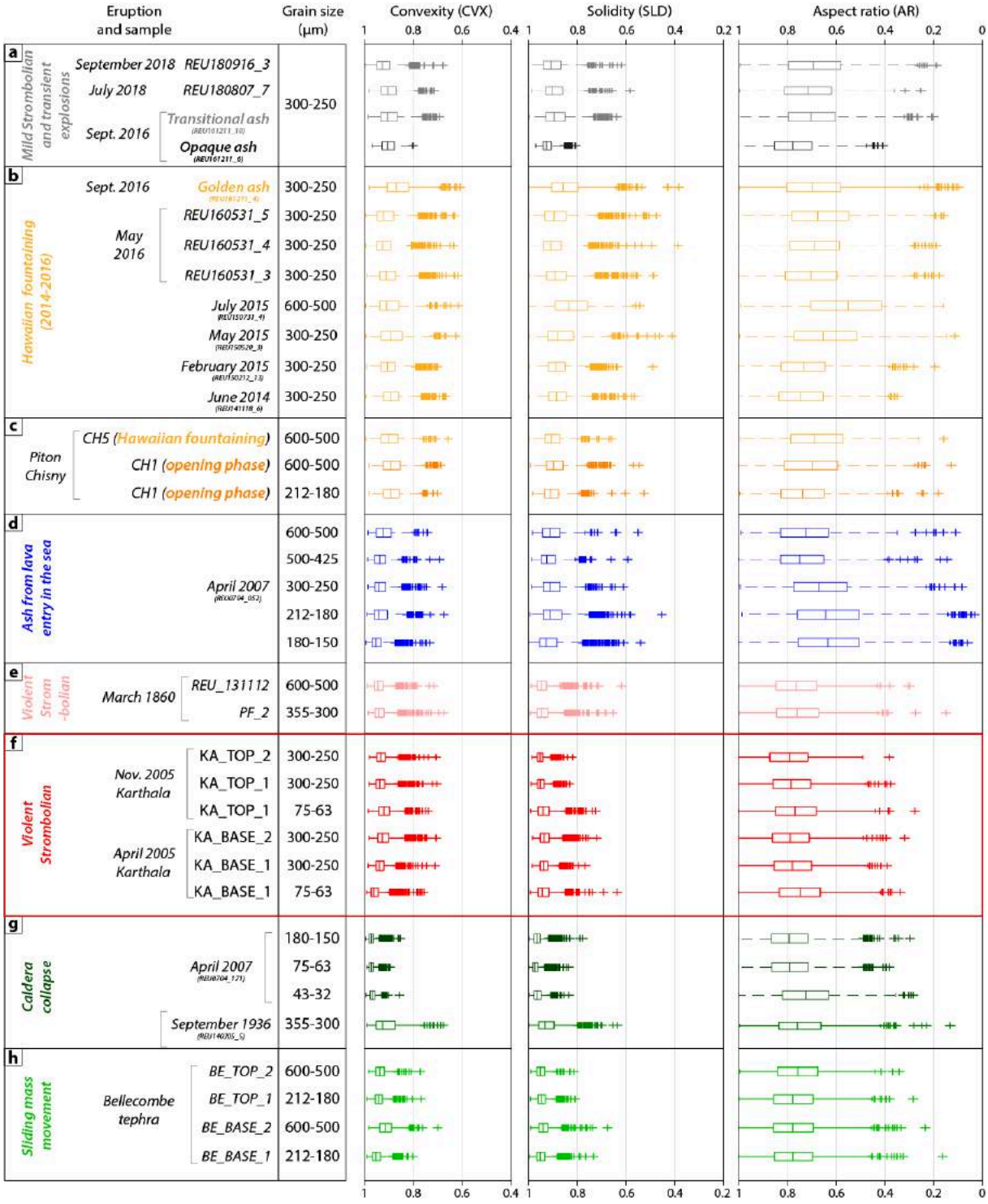

Figure 6.10 *– Apparent Projected shape of ASH (APASH) for each sample, in terms of convexity (CVX), solidity (SLD) and aspect ratio (AR). The eruptions and samples are mentioned as well as the grain size used for each measurement. Vertical line within the boxes represents the median and box boundaries represent the 25th and 75th percentiles of each dataset. Error bars represent 2.7σ of each dataset and outlier data are represented with crosses. The same color as the Figure 6.9 code is used.*

2.4.1. Tephra deposits from mild Strombolian and transient explosions at PdF

2.4.1.1. The July and September 2018 mild Strombolian activities

The deposits collected from mild Strombolian activities during the July 2018 and September 2018 (Fig. 6.2a) eruptions at PdF are mostly composed of bombs and scoria lapilli and only of 5 to 6 wt% of ash, with no detectable fine ash. All the particles of these deposits are juveniles and their PSDs are unimodal, with modes between 8 and 5.6 mm (Fig. 6.9a). Texture observations performed on the 355-200 µm grain size fraction highlights that these juvenile particles are typically characterized by intermediate contents of vesicles (around 10 to 20 vol%) and microlites (around 20 to 30 vol%) within a glassy matrix. Most of the vesicles are rounded, with no evidence of deformation features, while some vesicles appear to coalesce. Observed microlites are the plagioclase, clinopyroxene and very scarce olivine, in order of abundance. Ash morphology measurements were performed on the 300-250 µm grain size fraction and most of the particle CVXs, SLDs and ARs do not exceed respectively 0.7, 0.6 and 0.2 (Fig. 6.10a), reflecting fluidal shapes associated with spiny, rough particles. No free-crystals are observed.

2.4.1.2. The September 2016 transient explosions

Deposits from the September 2016 transient explosions contain two different type of juvenile particle components, respectively named transitional (REU161211_10, labelled 1 in Fig. 6.2b) and opaque scoria or ash (REU161211_6, labelled 2 in Fig. 6.2b), following the nomenclature of **Chapter V**. The respective textures of these two juvenile components share similar characteristics to that described in other basaltic systems: in order to use a consistent nomenclature within the next sections and for other samples, transitional and opaque components can be respectively related to the sideromelane and tachylite components, already described at Etna (e.g. Taddeucci et al. 2002; D'Oriano et al. 2014; Polacci et al. 2019).

The deposit formed by the sideromelane component is a typical coarse grained Strombolian deposit composed by only 8 wt% of ash, while the deposit related to the tachylite

component is composed of 97 wt% of coarse ash. None of these deposits contain detectable fine ash. PSD of the sideromelane deposit (Fig. 6.9a) shows a similar pattern as the mild Strombolian samples previously described, although with a coarser grain size mode between 32 and 22.6 mm. In contrast, the PSD of the fine-grained tachylite deposit is unimodal with a mode between 710 and 500 µm (Fig. 6.9a). The sideromelane ash textures have similar textures than the ones described in the Mild Strombolian section, with intermediate content of vesicles (13 vol%) and microlites (17 vol%) of plagioclase, clinopyroxene and olivine (within the 710-500 µm grain size fraction; **Chapter V**). Vesicles are sometimes deformed. XRD analyses discard the presence of any hydrothermal-induced mineral phases on these deposits.

The tachylite ash particles are characterized by a low content of vesicles (10 vol%), and a fully crystallized matrix (100 vol%) composed of normally zoned microlites of plagioclase and clinopyroxene associated with olivine microlites and Fe-Ti rich micro-oxides (within the 710-500 µm grain size fraction; **Chapter V**). Sideromelane and tachylite textures are sometimes mingled together (mingled clasts) even at microscopic scale (**Chapter V**).

Ash morphology, performed on the 300-250 µm grain size fraction (Fig. 6.10a), show that the sideromelane ash has very similar morphology signatures as the mild Strombolian samples. However, the tachylite ash does not have smooth surface anymore (CVX and SLD values < 1) and is rougher both at particle scale (SLD) and at smaller scale (CVX), than the sideromelane ash, with no evidence of significant elongation (AR values > 0.4).

2.4.2. Tephra deposits from Hawaiian fountaining activities at PdF

2.4.2.1. Recent (2014 to 2018) Hawaiian fountaining activities

Depending on the eruptions, the deposits are composed mostly of fluidal or pumiceous bombs and lapilli with a content of ash between 10 and 58 wt%, but none of them contain detectable fine ash. Their PSD (Fig. 6.9b) are unimodal with modes at 8 and 2 mm depending on the eruptions. All these Hawaiian deposits are only composed of juvenile particles, characterized by relatively vesicle-rich and crystal-poor particles, as shown by the textural analysis performed within the 710-500 µm grain size fraction, ash particles of September 2016

Hawaiian fountaining. These particles were indeed vesicle-rich (42 vol%) and microlite-poor (1 vol%) compared to the sideromelane and tachylite ash particles. In general, crystals are mainly plagioclase and scarce clinopyroxene microlites. Micro-phenocrysts of olivine (Fig. 6.2c), plagioclase or clinopyroxene can also occur depending on the eruptions. Vesicles can be either rounded and isolated within the glassy matrix or highly elongated. Regarding the morphology of these particles especially the CVX (down to 0.6), SLD (down to 0.4) and AR values (down to 0.1). These particles are indeed relatively heterogeneous in terms of shapes, which are composed of rounded droplets (CVX, SLD and AR values near 1), fluidal particles, as well as elongated ones forming Pele's hairs. Note that the July 2015 sample was measured within a different grain size fraction (between 600 and 500 µm) but no significant differences are observed in terms of shape except that elongated particles are slightly more abundant in this fraction, showing the lowest AR median (0.65) measured in this study (Fig. 6.10b).

2.4.2.2. The Black Tephra deposits of Piton Chisny (1450 to 1630 AD)

The initial phase of the sampled sequence (labelled CH1 in Fig. 6.2d), is composed of lapilli (39 %) and ash (61 wt%) among with scarce fine ash (5 wt%). These ash is either composed of golden, sideromelane-like or tachylite-like particles. This sample is multimodal (Fig. 6.9c) with two main modes between 16 and 11.3 mm (only composed of golden pumice and sideromelane-like lapilli) as well as between 250 and 180 µm (mostly composed of tachylite-like ash with scarce golden and sideromelane-like ash). Indeed, the content in tachylite-like particles within the deposit increase towards fine grain sizes, from 6 % (2.8-2 mm), to 10 % (2-1.4 mm), to 11 % (1.4-1 mm) to 19 % (710-500 µm) to finally 83 % (250-180 µm). Scarce olivine micro-phenocrysts-free particles were also observed (Fig. 6.2d). The tachylite-like particles of the CH1 sample have similar textures and shapes like the September 2016 tachylite ash (Fig. 6.2d). However this similarity does not appear in the morphology measurements (Fig. 6.10c) as these tachylite particles within the CH1 sample are diluted with sideromelane-like and golden particles.

This CH1 layer is overlain by a sequence of about 3 m thick coarser layers (separated by several bomb-rich layers) which have very similar PSD (Fig. 6.9a). The labelled sample CH5 (Fig. 6.2d) is representative of these subsequent deposits which is only composed of

juvenile, fluidal particles, with only 6 wt% content of ash. Thus, this deposit is relatively different from the opening phase and very similar to the recent Hawaiian fountaining deposits described earlier in this section, with a unimodal PSD (mode being between 8 and 5.6 mm). The ash morphologies are also quite similar to the recent Hawaiian fountaining ash (Fig. 6.10c).

2.4.3. Tephra deposits from the explosions caused by the April 2007 lava flow entry in the sea at PdF

The deposit from the April 2007 lava flow entry is only composed of juvenile coarse ash among with very scarce fine ash (1 wt%). The PSD of this deposit is unimodal, mode being between 710 and 500 µm (Fig. 6.9d). Particles are dense and glassy, characterized by relatively low vesicle content, very low microlite content (less than 10 vol%) and variable olivine phenocryst content (Fig. 6.2e), in agreement with the fragmentation of the rich olivine lava from whom they are originated (Staudacher et al. 2009; Di Muro et al. 2014). These olivines are highly fractured. Matrix of very scarce particles have a dendritic texture (Fig. 6.2e). Morphology of these particles is highly distinguishable mostly because these particles are relatively elongated with extreme AR values down to 0.05 (Fig. 6.10d), reflecting the presence of glass shards (Fig. 6.2e). In term of morphology, no significant changes are observed within the different grains size fraction measured.

2.4.4. Tephra deposits from Violent Strombolian eruptions

2.4.4.1. The March 1860 summit eruption at PdF

The sample collected at the base of the deposit (REU131112) is composed of lapilli (44 wt%) and ash (56 wt%) among with very scarce fine ash (1 %). Its PSD is unimodal with a mode between 3.8 and 1.4 mm (Fig. 6.9e). Within the 710-500 µm grain size fraction, juvenile particles represent only 2 % which are characterized by non-altered, more or less vesiculated

and glassy matrix. The non-juvenile particles (98 %) are dense, characterized by fully crystallized matrix (Fig. 6.4a). The size of the crystals of these particles vary from a few tens of microns (microlite-rich and altered or oxidized particles, thus considered as recycled non-juvenile particles) to several hundreds of microns (micro-gabbro texture, thus considered as non-juvenile intrusive fragmented material). Micro-gabbro textures are characterized by crystal bigger in lengths and widths (plagioclase, clinopyroxene and olivine) than in the juvenile or recycled particles (microlites and micro-phenocrysts sometimes associated with unaltered glass). Scarce olivine free crystals are counted within the non-juvenile particles, because they are not wetted with fresh glass. PF_2 sample is only composed of ash with the presence of little amount of fine ash (4 wt%), being its PSD unimodal with a mode between 500 and 355 µm (Fig. 6.9e). Within the 355-300 µm grain size fraction, most of the particles are non-juvenile (89 %). All the particles of this layer show the same textures as in the REU131112 sample. XRD analysis performed on the PF_2 samples suggests the presence of plagioclase, clinopyroxene, olivine (already observed with the SEM) and hematite phases. The particle morphology of the two samples representative of this eruption are very similar to each other (Fig. 6.10e): CVX and SLD medians for both samples are between 1 and 0.9 and AR values are relatively high with medians between 0.8 and 0.7, mostly reflecting gabbroic or altered particles with rough and blocky shapes.

2.4.4.2. The 2005 summit explosions at Karthala volcano

The four samples collected and representative of both April and November 2005 eruptions at Karthala volcano are mainly composed of ash (between 91 and 99 wt%) among with variable amount of fine ash (from 33 to 57 wt%). Based on the 710-500 µm grain size fraction, juvenile fraction vary from 67 % (KA_BASE_1), to 86 % (KA_TOP_2), to 93 (KA_TOP_1), to finally 95 % (KA_BASE_2). Unaltered juvenile particles (Fig. 6.4b) can be either highly vesiculated with low crystal content (golden ash, Figs. 6.6b and 6.6c) or denser with a variable crystal content (sideromelane and tachylite-like textures, Figs. 6.6c and 6.6d). These two end-member textures can also be mingled (Fig. 6.6c). Scarce crystal free particles are counted within the juvenile particles as they are sometimes coated with unaltered glass. Non-juvenile particles within these deposits are characterized by micro-gabbroic textures (Fig.

6.4b), similar to those described at PdF. Fine ash particles between 63 and 45 µm were imaged (Fig. 6.4b) and these particles are mainly composed of relatively dense juvenile fragments with scarce non-juvenile fragments of micro-gabbro and crystal free particles (mostly plagioclase and clinopyroxene). The four samples are quite rich in millimeter to centimeter rounded accretionary lapilli (following the Brown et al. 2012 nomenclature), where a particle size gradient is identifiable (coarser particles being in the middle, whereas finer particles being in the rims, Fig. 6.4b). PSDs of the KA_BASE_2 and KA_TOP_2 samples are multimodal (Fig. 6.9f). The first coarser mode of the KA_BASE_2 sample is between 1000 and 710 mm and is mainly composed of tachylite-like particles (60 %), while the second finer mode is between 90 and 16 µm and is mainly composed of golden ash (90 %). Similarly ,the first coarser mode of the KA_TOP_2 sample is between 1000 and 710 µm but is mainly composed of non-juvenile altered (20 %) and micro-gabbroic particles (40 %), while the second finer mode is between 90 and 16 µm and is mainly composed of juvenile golden or ash (90 %). PSDs of KA_BASE_1 and KA_TOP_1 are unimodal, both with modes between 90 and 16 µm and these samples are mostly composed of golden ash. Ash morphology measurements performed on 300-250 and 75-63 µm grain size fractions show very similar trends to those of the March 1860 samples. APASH signatures of these Karthala samples (Fig. 6.10f) do not represent specific shapes as they are relatively heterogeneous in terms of juvenile and non-juvenile components, but the SEM images show that the fine juvenile ash particles have blocky and fractured shapes, without any rough surfaces.

2.4.5. Tephra deposits from caldera collapse at PdF

2.4.5.1. The April 2007 caldera collapse

The studied tephra related to the ash emission during the caldera collapse of April 2007 is only composed of ash particles among with a big amount of fine ash (87 wt%). The PSD of this sample is unimodal with a mode between 15 and 8 µm (Fig. 6.9g). The main part of the particles are considered as non-juvenile (99 %), with the exception of very scarce particles considered as juvenile particles as they share similar characteristics as sideromelane or tachylite-like textures and show no evidence of significant alteration. Also note that very scarce

Pele's hairs were also observed within this deposit. These juvenile particles are only observed within the coarser grain sizes of the deposits between 500 and 125 µm. The non-juvenile particles are relatively heterogeneous, with the presence of various gabbroic textures (assemblage of plagioclase, pyroxene, olivine and oxides), as well as crystal-free particles, with no evidence of the presence of fresh magma. Particle clusters (following the Brown et al. 2012 nomenclature) are also present forming irregular-shaped aggregates, constituted of both coarse and fine grains, with no specific grains size distribution (Fig. 6.4c). The nature of the very fine ash particles (< 32 µm) is the same as the non-juvenile coarser grains and are most of the time composed of a single, fractured crystal from the gabbroic particles observed within coarser grains (Fig. 6.4c). Note that we also performed two bulk rock analyses on this deposit, picking randomly small amount of ash on the bulk sample. These two analyses suggest relatively different bulk compositions highlighting the fact that these ash particle are relatively heterogeneous. XRD analysis performed on this deposit confirmed the presence of plagioclase, clinopyroxene and olivine crystals (from the gabbro fragments) and suggest the presence of both montmorillonite (clay) and hematite phases. Ash morphology performed on this sample and on three different grain sizes (Fig. 6.10g) show very different results from the other samples: most of the CVX and SLD values range between 1 and 0.9 reflecting the presence of fine and blocky or large and rounded particles without significant rough surface features (Figs. 6.7c and 6.7d). Relatively high AR values (median between 0.8 and 0.7) also suggest that these particle are most blocky without elongation features.

2.4.5.2. The September 1936 partial caldera collapse

The studied deposit is only composed of ash among with 4 wt% of fine ash. Its PSD is unimodal with a mode between 500 and 355 µm (Fig. 6.9g). Within the 355-250 µm grain size fraction, 42 % of the particles are unaltered juvenile fragments. Juvenile particles are characterized by vesicle-rich and crystal-poor matrix, more or less deformed with rounded and fluidal shapes (golden ash). Non-juvenile particles are gabbroic rock fragments, as already described in the previous sections. Ash morphology performed on the 355-300 µm grain size fraction show very different results from the April 2007 caldera deposit as the 1936 deposit contains juvenile fragments from synchronous Hawaiian lava fountaining and the grain size

fraction is coarser. XRD analysis performed on this bulk sample highlight the presence of plagioclase, clinopyroxene and olivine as well as small amount of hematite. The CVX, SLD and AR values englobe particles coming from both the summit ash emission associated with the collapse and the eruptive fissure (Fig. 6.10g).

2.4.6. The Bellecombe tephra deposits associated to massive mass-sliding events (4900 to 2250 BP)

Samples collected within the first 20 cm (not reworked fall deposits) of the Lower Bellecombe Tephra (BE_BASE_1 and BE_BASE_2) have similar ash content (between 85 and 91 wt%), with however slightly different fine ash content (32 and 11 wt% respectively). Grain size mode of these two samples (Fig. 6.9h) are skewed toward relatively fine grain size fractions (between 63 and 31 µm for the BE_BASE_1 sample and between 250 and 180 µm for the BE_BASE_2 sample). Based on the componentry analysis performed on the 355-250 µm grain size fraction of the BE_BASE_1 sample (Fig. 6.4e), we suggest that this ash fraction is only composed of non-juvenile particles either characterized by micro-gabbro (40%), altered glassy (40%) or olivine crystal fragments (20%).

On the other hand, samples collected within the non-reworked layers of the Upper Bellecombe tephra (BE_TOP_1 and BE_TOP_2) have lower ash content than the Lower Bellecombe Tephra samples (between 47 and 59 wt%) with also lower fine ash content (between 2 and 3 wt%). Grain size mode of these two samples are skewed toward coarser grain size fraction (Fig. 6.9h) than the Lower Bellecombe tephra samples (two modes between 11.3 and 8 cm as well as between 2.8 and 1.4 cm for the BE_TOP_1 sample and one mode between 2 and 1.4 cm for the BE_TOP_2 sample). Similarly to the Lower Bellecombe tephra samples, componentry performed on the 355-250 µm grain size fraction of the BE_TOP_1 samples suggest that this ash fraction is only composed of non-juvenile particles, composed of the same types of fragments of the BE_BASE_1 sample. Irregular-shaped particle clusters are much more present than in the previous layers of the Lower Bellecombe Tephra and are characterized by heterogeneous nature and grain size organization. In addition to the plagioclase, clinopyroxene and olivine phases, XRD analysis performed on both Lower and Upper Bellecombe Tephra suggest the presence of montmorillonite and quartz.

Ash morphology measurements performed on the four Bellecombe samples show quite similar patterns (Fig. 6.10h) reflecting the presence of three different types of non-juvenile particles, namely the glassy altered ones which have fluidal to spiny shapes (especially for the Lower Tephra samples), as well as the crystal-free and micro-gabbro blocky fragments.

2.5. Discussion

2.5.1. Lapilli-dominated magmatic eruptions: ductile and partially brittle fragmentation during Hawaiian fountaining and mild Strombolian activities

In this study and regarding the deposit grain sizes, lapilli-dominated eruptions are represented by (i) the Hawaiian fountaining and (ii) the mild Strombolian explosions at PdF. Deposits coming from recent (2014-2018) lava fountaining eruptive activity, as well as the CH5 sample from the Black Tephra deposits of the Piton Chisny, have a low to intermediate ash content (between 10 to 58 wt% depending the samples) with no detectable fine ash, illustrating a moderate fragmentation efficiency of the magma. The yellow field in Figure 6.11 show that the investigated Hawaiian deposits are moderately well sorted (sorting values between 0.7 and 1.4 Φ, unimodal PSD) and with grain size median values skewed toward relatively coarse grains, between -3 and -0.5 Φ. In parallel, deposits related to mild Strombolian deposits or transient explosions (July and September 2018 eruptions, as well as the transitional tephra emitted during the September 2016 eruption at PdF) have a relatively low ash content (5 to 6 wt% without any detectable fine ash) and illustrate a slightly weaker magmatic fragmentation efficiency (the weakest of this study) producing moderately well sorted deposits (sorting values between 1 and 1.5 Φ, unimodal PSD) with relatively coarse grain size median values between -3.5 and -3 Φ (grey field in Fig. 6.11).

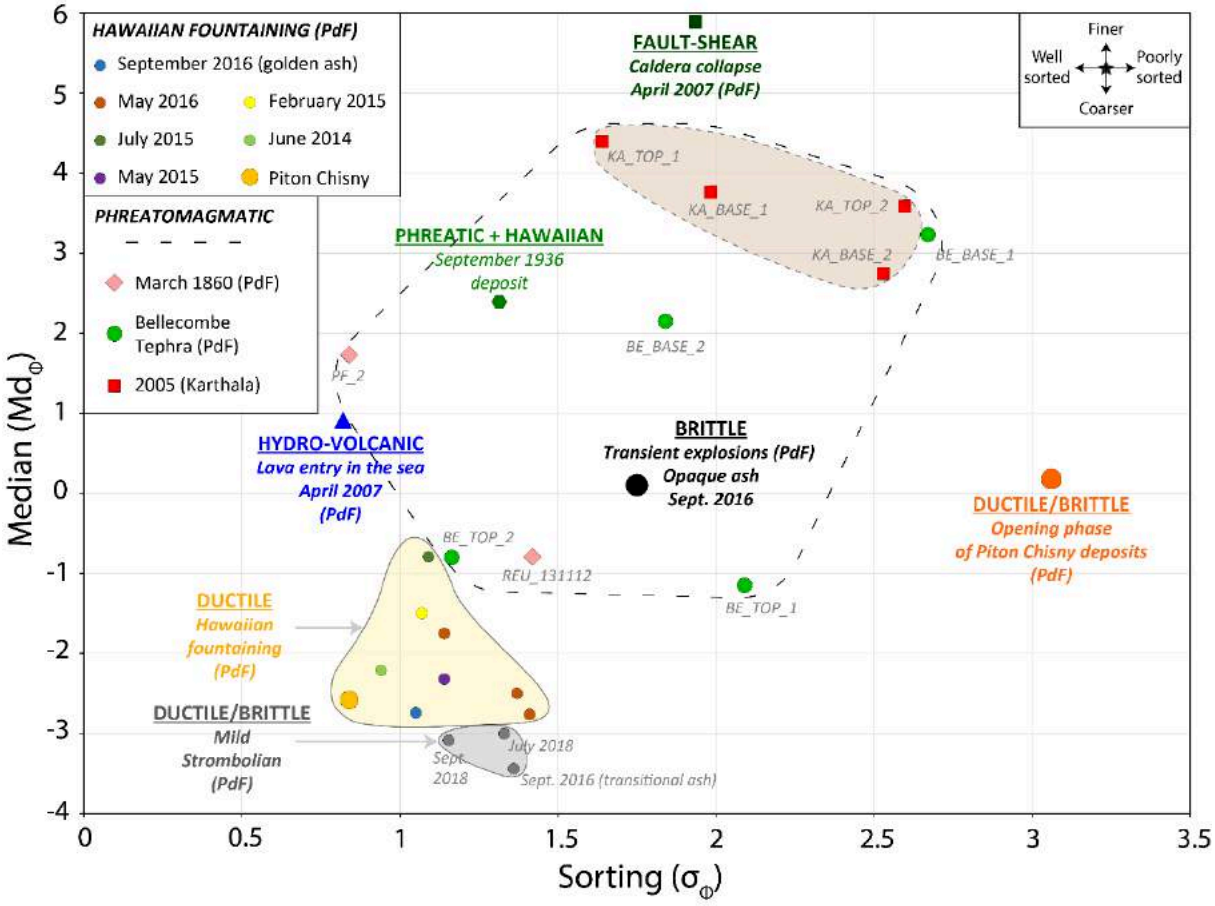

Figure 6.11 *– Median (Md_Φ) vs. sorting (σ_Φ) plot. All the studied deposits are represented with the same color code as in Figures 6.9 and 6.10.*

Deposits from these two style of activities are all juvenile. However, a decrease in porosity and an increase in crystallinity are observed from the magma emitted during the lava fountain activity (golden pumice and ash) to the one emitted during the mild Strombolian explosions (transitional or sideromelane). Relatively high vesicle number density (N_V) as well as low microlite number density (N_C) measured in the golden ash particles, for instance during the September 2016 Hawaiian fountaining (**Chapter V**), suggest that these magmas are mainly composed of relatively hot magmatic liquids that exhibited relatively high decompression rates (Toramaru 2006) associated with low to moderate syn-eruptive degassing and crystallization (Toramaru et al. 2008). This is consistent with the idea that Hawaiian fountaining is related to low-viscous and volatile-rich magmas that can produce intense bubbly flow (Cashman and Scheu 2015) or even annular flow dynamics within the volcanic conduit (e.g. Jaupart and Vergniolle 1988, 1989; Houghton and Gonnerman 2008). On the other hand, the decrease of

N_V and the increase of N_C as well as some evidence of bubble coalescence within the sideromelane ash particles suggest that mild Strombolian dynamics, typically active during slug flow within the conduits (e;g. Jaupart and Vergniolle 1988, 1989; Houghton and Gonnerman 2008; Chouet et al. 2003), is related to lower decompression rates associated with higher syn-eruptive degassing and crystallization (**Chapter IV**). At PdF, bubble explosions at the magma free surface, within generally well-constructed scoria cones, are relatively weak but close together (only a few seconds between each burst) compared to the typical Stromboli regime (e.g. Chouet 2003; Ripepe et al. 2001; Harris and Ripepe 2007).

Golden ash particle shapes that are primarily fragmented by the gas jets and by rapid acceleration within the lava fountains (Cashman and Scheu 2015; Fig. 6.2c) also reveal specific features of low-viscosity magmas (Fig. 6.10b). The presence of rounded, smooth droplets (CVX, SLD and AR values at 1) highlight the fact that liquid particles are fragmented when they are still liquid, forming liquid droplets that quenched in the air after the fragmentation. The presence of fluidal and elongated particles among with Pele's hairs (CVX, SLD and AR values respectively down to 0.6, 0.4 and 0.1) support the idea that some of the liquid particles are exposed to some deformation before to solidify and quench in the air (Cannata et al. 2019). As already stressed in **Chapter V**, ash particles easily and quickly quench in the air (around 20°C s^{-1}) after the fragmentation (Xu and Zhang 2002 ; D'Oriano et al. 2014) due to their relatively small size. However, some of the ash particles are deformed during and shortly after the fragmentation (around 20 seconds, considering a cooling rate of 20°C s^{-1}, an initial temperature of 1150 °C and glass transition temperature of 680 °C, Giordano et al. 2005). In parallel, sideromelane particle shapes from bubble explosions (Fig. 6.10a) show different results from the lava fountain activity. First, the absence of significant post-fragmentation deformation (no Pele's hairs and tears, as well as no highly deformed particles) suggest that the relatively low temperature and relatively high viscosity of the particles, compared to their Hawaiian counterparts, do not allow them to deform after the fragmentation. Moreover, the rough, sometimes spiny shapes of these particles (CVX, SLD and AR values more than 0.7, 0.6 and 0.2 respectively) without any smooth rounded one (no CVX, SLD and AR values at 1 for any particles), reflect primary but viscous and partially brittle fragmentation behavior, mostly due to lower magmatic temperatures and higher crystal contents, resulting in the increase of the viscosity (Mader et al. 2013).

Regarding all the sample features an associated eruptive styles, we can conclude that the magma emitted during Hawaiian fountaining phase has a relatively low-viscosity. Tephra

formed during this kind of activity can be related to ductile (or visco-elastic) fragmentation within the lava fountains (Fig. 6.2c), producing mostly bomb- and lapilli-sized particles with a relatively small amount of ash among with Pele's hairs. As soon as the lava flux decrease, the magma has more time to degas and crystallized within the eruptive conduit, increasing the magma viscosity. We suggest that the bubble (slug) explosions (July and September 2018 eruption at PdF) or local overpressures (September 2016 eruption at PdF) fragment the degassed and partially crystallized magma between ductile and brittle conditions (Figs. 6.2a and 6.2b), producing mostly bomb- and lapilli-sized fragments with even less amount of ash than the Hawaiian fountaining dynamic.

2.5.2. Ash-dominated eruptions

2.5.2.1. Brittle fragmentation enhanced by syn-eruptive crystallization

Significant texture variations within purely magmatic tephra of a same eruption are something well-known in a basaltic context (e.g. Pioli et al. 2014; Gurioli et al. 2014; Pompilio et al. 2017; Polacci et al. 2019). Texture evolution from golden vesicle-rich and crystal-poor particles (golden ash, cf. previous section) to vesicle-poor and crystal-rich particles (sideromelane and tachylite ash particles) are observed within three of our case studies, namely (i) the tachylite ash related to the September 2016 eruption at PdF, (ii) the initial layer (CH1) of the Back tephra deposits of the last Piton Chisny eruption at PdF, and (iii) one the sampled layers (KA_BASE_2) of the April 2005 eruption at Karthala.

The tachylite deposit (September 2016 eruption at PdF) is composed of 97 wt% of ash (without fine ash) reflecting a better fragmentation efficiency (median around 0.1 Φ) and a better sorting (around 1.7 Φ, unimodal PSD) compared to the previous discussed cases (big black circle in Fig. 6.11). In parallel, the CH1 sample (Black Tephra at PdF) is composed of 35 wt% of ash among with 5 wt% of fine ash. This last deposit is poorly sorted with a sorting value around 3.1 Φ (bimodal PSD) with a grain size median value of 0.1 Φ (orange circle point in Fig. 6.11) similar to the tachylite ash of the September 2016 eruption. The fact that the tachylite-like particles increase toward finer grains, support the idea that the viscous portions exhibit the

most intense degree of fragmentation. The larger amount of ash within the initial layer CH1 (61 wt%) in respect to the CH5 sample, as well as the presence of micro-phencoryst-free particles also highlight that significant syn-eruptive crystallization of the juvenile magma favor explosive dynamics at the surface. The KA_BASE_2 sample (April 2005 eruption at Karthala) is moderately poorly sorted with a sorting value around 2.5 Φ (bimodal PSD) with relatively high median value of 2.8 Φ (red squares in Fig. 6.11), illustrating relatively high fragmentation efficiency.

The presence of this specific degassed and crystallized juvenile particles (sideromelane and tachylite) within these three samples reflects the occurring of a significant syn-eruptive degassing and crystallization enhancing the increase of the magma viscosity (e.g. Applegarth et al. 2013, 2013; Mader et al. 2013; Pompilio et al. 2017). In this case, and as many other cases in other basaltic systems (e.g. Taddeucci et al. 2002; Sable et al. 2006; D'Oriano et al. 2014; Polacci et al. 2019) and experiments (e.g. Simakin et al. 1999; Applegarth et al. 2012, 2013; D'Oriano et al. 2014; Arzilli et al. 2015), we interpret the texture variation from the golden to the sideromelane until the tachylite as syn-eruptive degassing and crystallization processes within the eruptive conduit. Concerning the September 2016 eruption at PdF, the texture and associated features of the tachylite ash, already quantified in a previous study (**Chapter V**) highlight that these juvenile particles are totally crystallized degassed (0 wt% of dissolved H_2O, 10 vol% of vesicles). Thanks to in-situ chemical and textural analysis as well as syn-eruptive observations made at that time, these last authors suggest that the emitted ash originated from the sub-surface degassing and crystallization of the initial magma that produced, at the beginning of the eruption, the Hawaiian fountaining. The degassed/cooled magma formed a rheological and impermeable layer, which played the role a plug, within one of the two active vents. Of course, additional analyses (similar to that done in **Chapter V** for the September 2016 deposits at PdF) would be necessary to constrain the depth of this syn-eruptive crystallization of the juvenile magma concerning the CH1 (Fig. 6.2d) and Karthala KA_BASE_2 (Fig. 6.6) samples. However, as these particles are observed within the opening phase of the deposits, contrary to the September 2016 ones, we suggest that in these cases, the syn-eruptive crystallization occurred along the eruptive conduit, maybe during the magma propagation towards the surface.

In brief, the relative finer grain sizes observed in these crystal-rich particles, compared to coarser crystal-poor fragments show that the increase of the magma viscosity enhanced the magma fragmentation at the surface (Fig. 6.2d). We thus suggest that the fragmentation

efficiency drastically increase, evolving from ductile to totally brittle. The presence of both vesicle-rich (high N_V reflecting high decompression rates) and crystal-rich particles (high N_C reflecting the increase of the magmatic viscosity) within the CH1 and KA_BASE_2 samples, may even more enhance the magma fragmentation (Cimarelli et al. 2010). In the specific case of the September 2016 eruption (Fig. 6.2b), the upcoming of still partially undegassed magma fragmented the plug layer composed of tachylite magma that was snatched from the plug (**Chapter V**), thus forming a secondary, brittle fragmentation (plug pressurization mechanism). Note that, XRD analysis discard the presence of any hydrothermal-induced mineral phases that can be related to phreatomagmatic mechanisms. The brittle fragmentation is even more evidenced by the ash morphologies (Fig. 6.10). Regarding the shapes of the September 2016 opaque ash, CVX, SLD and AR values are much more skewed toward higher median values (0.9, 0.9 and 0.8 respectively) than the golden and transitional ash particles, reflecting typical tachylite textures with very rough surface with no significant particles deformation. Moreover, ash particles with CVX, SLD and AR values at 1 are not observed anymore like in the golden ash component, suggesting that the magma viscosity is too high to produce rounded droplets during the fragmentation.

2.5.2.2. The role of water and hydrothermal fluids

Many ash-dominated deposits studied here are strongly suspected to originate from hydrovolcanic, phreatomagmatic or phreatic eruptions, involving external water or hydrothermal fluids. Regarding the different eruptive styles and the associated sample signatures, different types of magma/water interactions, provoking or enhancing juvenile magmas or lithic rocks fragmentation, are identified.

Hydrovolcanic explosions producing lazes

When a lava flow is entering water masses like seawater, hydrovolcanic explosions producing laze may happen when relatively high entrance fluxes (> 4 m^3 s^{-1}) are occurring

(Mattox and Mangan 1997). This was the case during the April 2007 eruption at PdF (Fig. 6.2e), which was fed by a maximum flux of 200 $m^3 s^{-1}$. Lazes are characterized by the emission of steam clouds highly concentrated in hydrochloric acid and glass shards (Carlos et al. 2018). According to Mattox and Mangan (1997), the ideal water/magma ratio to provoke littoral explosions is around 0.15 and an open mixing of lava and seawater (when the mouth of several lava tubes or lava channels are exposed to sea waves) is the most efficient situation to produce unconsolidated deposits of glassy, dense lava fragments. The lava entry in the sea observed during the April 2007 eruption at PdF produced particles mostly composed of coarse ash (99 wt% among with 1 wt% of fine ash), with a sorting value of 0.6 Φ (unimodal PSD) and a grain size median of 0.9 Φ (blue triangle in Fig. 6.11), reflecting a quite efficient secondary fragmentation. As the magmatic particles described in Potuzak et al. (2008), the particles formed and collected during this seawater-provoked explosions are perfectly quenched and show a glassy matrix with rare microlites and more abundant phenocrysts of olivine, already present within the lava flow itself. The dendritic texture observed in very scarce particles (Fig. 6.2e) suggest that some of the fragmented material experienced not immediate but relatively fast quenching. The particles show typical fractured features on their surfaces and inside the matrix. Concentric fractures are often observed around the olivine phenocrysts (Fig. 6.2e). We suggest that the intensity of the sudden fragmentation, the almost immediate quenching as well as the thermic contraction are the main cause of these brittle features. Extreme AR values (down to 0.05) reflect the presence of typical elongated glassy shards particles (Fig. 6.10d).

Interactions between magma and fluids at shallow level provoking phreatomagmatic eruptions

(i) The two samples representative of the March 1860 summit eruption at PdF (REU131112 and PF_2 samples, pink squares in Fig. 6.11) are respectively composed of 56 wt% and 100 wt% of ash among with 1 wt% and 4 wt% of fine ash respectively. The median size of these deposits are -0.8 and 1.8 Φ with sorting values of 1.4 and 0.8 Φ (unimodal PSDs) respectively. (ii) The studied Karthala deposits (red squares in Fig. 6.11) are finer (grain size medians between 2.8 and 4.4 Φ) and less sorted (sorting values between 1.6 and 3.6 Φ). They are composed of much more fine ash (33 to 57 wt%) compared to the March 1860 PdF samples,

which highlights that the initial phases of both 2005 Karthala eruptions were relatively intense in terms of ash emission and fragmentation efficiency.

Based on the observations made at that time (Hugoulin 1860), some hypothesis emitted by Bachèlery (1981, 1999) and Michon et al. (2013) suggest that sudden arrival of hydrothermal and/or meteoritic water within the newly drained and still hot volcanic conduits and reservoirs provoked summit explosions the 19 March 1860 at PdF. This hypothesis is comforted by our results. The ubiquity of non-juvenile particles (89 to 98 % of intrusive particles with rough or blocky shapes as well as altered recycled particles) highlights the fact that the emitted material was originating from various lithic levels within the eruptive conduit. We suggest that scarce abundance of the juvenile material was not sufficient to fragment the intrusive rocks within the eruptive conduit. Moreover, these scarce juvenile particles do not show any evidence of strong explosive potential (low N_V within the juvenile ash). The contribution of external and/or hydrothermal fluids could indeed provoke the fragmentation of the wall rocks of the eruptive conduit still partially hot and partially filled with juvenile magma (2 to 11 % of observed juvenile ash). Small amount of hematite observed in these deposits may be related to acid leaching or post-depositional alteration due to the presence of hydrothermal fluids, even if further studies are needed to confirm this hypothesis.

As already discussed before, the magma of the 2005 Karthala violent Strombolian eruptions may exhibit relatively high decompression rates (high N_V) associated to significant syn-eruptive crystallization enhancing the magma viscosity. Moreover, the presence of the hydrothermal lake before each April and November 2005 eruptions highlights the presence of hydrothermal fluids in the shallow system of Karthala at that time and shows that the ground water level was near the magmatic fragmentation level. It appears that these deposits are quite rich in fine ash (35 to 60 wt%) which are mainly characterized by fragments of juvenile glassy particles (Fig. 6.4b). These particles agglomerated to form rounded accretionary pellets. Their formation was probably facilitated by the presence of vaporized water in the atmosphere, coming from the initial hydrothermal lake and their radial internal structure (Fig. 6.4b) may suggest that these particles form in the atmosphere during their emission and fallout. This hypothesis is also confirmed by the blocky shapes of the fine ash characterized by clear fracture geometries (Figs. 6.4b and 6.10f), originated from phreatomagmatic mechanisms that enhance the intensity of the magma and the lithic fragmentation. These kind of particles were not observed in the previous investigated eruptions. Regarding the textures variations of the juvenile particles and their corresponding grain sizes (viscous fragments are coarser than the

crystal-poor fragments), we suggest that the phreatomagmatism mechanism is more efficient with hot, undegassed and uncrystallized magma than degassed, cold and crystallized magma.

Contrary to the March 1860 eruption, and as already suggested by Moreland et al. (2019) for another basaltic system, we support the idea that the presence of fluids enhanced the intensity of the fragmentation but was not at the origin of April and November 2005 eruptions. Theses initial phreatomagmatic phases only lasted approximately two days for both April and November 2015 eruptions, and emplaced the investigated deposits. Once the hydrothermal lakes were totally vaporized, these initial and relatively explosive phases were indeed followed by a decrease in the explosive activity associated with the formation of a lava lake as well as moderately active lava fountains within the Choungou-Chahalé crater (Figs. 6.5c, 6.5d and 6.5e). Moreover, the two other eruptions, that occurred in May 2006 within the Choungou-Chahalé crater (which was not filled by a hydrothermal lake anymore), and in January 2007 within the Choungou-Chagnoumeni crater (with no evidence of visible fluids at the surface), did not show the same initial violent Strombolian phases as observed in 2005 eruptions, with only lava lakes and lava fountain activities (Bachèlery et al. 2016). These observations support the idea that all the 2005-2007 eruptions could have occured without the presence of any hydrothermal fluids, but their presence within the Choungou-Chahalé crater before the two eruptions of 2005 enhanced the magma fragmentation during the first explosive phases. The intensity of the phreatomagmatic explosions is also highlighted by the presence of scattered lithic blocks all around the crater (Bachèlery et al. 2016).

Sudden decompressions of hydrothermal systems provoking phreatic explosions

(i) The first case concerns the Lower Bellecombe Tephra samples composed of 85 and 91 wt% of ash among with 32 and 11 wt% of fine ash respectively. They show lower grain size medians (between -1.2 and -0.8 Φ) and slightly better sorting (between 1.2 and 2.1 Φ) compared to the Upper ones that show grain size medians between 2.1 and 3.2 Φ and sorting values between 1.8 and 2.7 Φ (Fig. 6.11). The investigated samples in term of componentry (namely BE_BASE_1 and BE_TOP_1), are considered to be only composed of non-juvenile particles, at least within 355-200 µm grain size fraction. The alteration of the main part of the particles as well as the presence of montmorillonite (clay) and quartz or cristobalite (generally formed

within high temperatures hydrothermal systems) phases highlight that these particles were fragmented during phreatic phases that implicated several hydrothermal systems. We also suggest that these phreatic (and maybe phreatomagmatic for some layers which are not studied in this paper) explosions remobilized intrusive rocks, because of the presence of gabbro fragments, similarly to the March 1860 and September 1936 deposits. The presence of particle clusters can also due to the presence of hydrothermal and/or meteoritic water.

(ii) The second case concerns the sample related to the September 1936 summit activity at PdF. This sample is moderately well sorted (sorting value of 1.3 Φ) with a grain size median around 2.4 Φ (Fig. 6.11). It only contains ash particles among with 17 wt% of fine ash. Despite its unimodal grain size distribution, this deposit is considered representative of two synchronous activities. Part of the juvenile particles share very similar characteristics with the Hawaiian fountaining deposits previously described, in terms of porosity, crystallinity, deformation and shape (Fig. 6.4d). Ductile deformation of these juvenile particles is also reflected by the measured AR down to 0.1 (Fig. 6.10g). We thus attribute these juvenile particle as derived from the synchronous opening of an eruptive fissure at the summit area of PdF, which is maybe linked with the partial drainage of the shallow magmatic system of PdF that started five year earlier (continuous activity from 1931 to 1936). This significant drainage provoked a partial summit collapse that occurred in September 1936 within the actual Dolomieu caldera area (Fig. 6.4d). We suggest that the rest of the deposit is related to the summit ash emission during the collapse. These particles are all non-juvenile and characterized by gabbroic textures suggesting that these particles were fragmented from several intrusive levels within the summit cone. We thus suggest that the ubiquity of these intrusive particles with blocky or rough shapes (quite similar to the non-juvenile particles related to the March 1860 eruption) originate from phreatic explosions enhanced by the caldera collapse and the depressurization of a shallow hydrothermal system, as already described in Hawaii (Swanson et al. 2012). Similarly to the March 1860 deposit, the presence of hematite on this ash may be due to the presence of hydrothermal fluids.

Regarding the ash morphology results of the supposed phreatic and phreatomagmatic deposits (Figs. 6.10e, 6.10f, 6.10g and 6.10h), no specific trends can be observed because the deposits are composed of different ash components. However, their APASH signatures show that the medians of the CVX and SLD medians are systematically between 1 and 0.9, reflecting the presence of blocky particles. Slightly lower AR values compared to the juvenile ash formed by ductile fragmentation, also suggest that no post-fragmentation deformation as well as no

significant ductile mechanisms, due to potential rapid quenching of the juvenile magma, are present in these phreatomagmatic deposits.

Regarding the grain size parameters, it appears that the phreatomagmatic eruptions span a wide range in terms of grain size median and sorting (black dashed line in Fig. 6.11). This range probably reflects the emission of diversified tephra in terms of components and shapes due to variation in magma-water interaction, where the Upper Bellecombe tephra and the 2005 eruptions at Karthala represent the most intense end member of this efficiency.

2.5.3. Fine ash-producing events: evidences of fault-shear fragmentation during caldera collapse

The deposit related to the April 2007 are interestingly the finest of this study (Figs. 6.9g and 6.11) with a grain size median of 5.9 Φ and a sorting value of 1.9 Φ (unimodal). It is only composed of ash particles among with 87 wt% of fine ash. This deposit is characterized by the ubiquity of non-juvenile fragments.

The very scarce non-altered juveniles may belong to recent and still partially molten magmas stored at shallow levels within the lava pile that accumulated within the Dolomieu caldera, as molten lava flows within the newly formed caldera wall were visible just after the main collapse (Fig. 6.7). These juvenile particles could also have been originated from recycled particles that were emitted during the more or less recent eruptive activity occurring within the caldera before the collapse. We also suggest that the unaltered Pele's hairs particles were not originating from the same source as the summit ash emission, but originating from the lava fountaining activity happening at that time on the Eastern flank of the volcano (Staudacher et al. 2009). Indeed, these fine, elongated particles are able to be dispersed and deposited relatively far from the source (around 10 km far from the source in this case). Moreover, some chemical analyses confirmed that these Pele's hairs have the same glass composition as the ones emitted and collected near the lava fountaining source (Villemant et al. 2009).

The coarser particles (> 125 µm) of the deposits generally show rounded or smooth shapes while the finer particles (< 63 µm) are mainly composed of blocky fragments of gabbroic crystals (Figs. 6.4c and 6.10g). Although rounded vs. blocky morphologies cannot be properly

distinguished using CVX, SLD and AR parameters (Liu et al. 2015), it is clearly visible when we look to the particles for instance with the SEM images (Figs. 6.4c and 6.7). Nevertheless, the APASH measurements performed on this deposit and on three different grain sizes, highlight very different trends from the other ash samples (Fig. 6.10). CVX, SLD and AR values are skewed towards 1 reflecting relatively regular morphologies, either smoothed for coarse particles (180-150 µm) or blocky for fine particles (75-63 and 43-32 µm). The ash emissions observed during the April 2007 incremental caldera collapse at PdF have been firstly interpreted as phreatic driven, thanks to preliminary petrologic observations (Staudacher et al. 2009). The presence of almost only non-juvenile particles, of some particle clusters, and of montmorillonite (clay) and hematite phases, is in accordance with this first interpretation. As shown by analogue experiments (Buckland et al. 2018), we suggest that coarse and fine particles are genetically linked, as the coarse and smoothed particles exhibit significant abrasion forming the fine and blocky particles. The ubiquity of gabbro fragments and the scarcity of old lava fragments also suggest that the emitted particles originate from intrusive levels of the caldera wall and the dismantled, collapsed piston. As recently suggested by Fontaine et al. (2019), the caldera collapse is mainly controlled by a potentially predictable ring fault-system. We suggest that the wall rocks abrasion and fragmentation was effective during the caldera piston collapse, forming a kind of sudden syn-collapse cataclasite as we observed very similar brittle features as within fault gauge (e.g. Engelder 1974; Marone and Sholtz 1989; Heilbronner and Keulen 2006), basal shear zones of thick lava flows (Latutrie et al. 2017), dome boundaries (Cashman et al. 2008) or conduit margins (Pallister et al. 2012). As these finely fractured rocks are propelled into the atmosphere before to be deposited, we obviously lose some of the features observed within typical fault gauge (as the microstructures and faults as well as specific organizations of the particles) but our observation support that the shapes of ash produced during the April 2007 caldera collapse are very likely to be produced by this fault-shear mechanism. The ubiquity of fine ash particles is also in accordance with this hypothesis, despite that an elutriation mechanism may occur within the ring fault system and during the collapse, preferably propelling the fine ash particles into the atmosphere.

2.6. Conclusions and risk implications

Regarding recent as well as older eruptive deposits at PdF and Karthala volcanoes, we can conclude that ash emissions are quite common during explosive basaltic eruptions (Fig. 6.11). In this study, we were able to identify some of the processes that control and/or enhance the magma and/or lithic fragmentation. We list them here with their associated hazard implications

(i) Hawaiian fountains usually produce a moderate amount of coarse ash during the ductile magmatic fragmentation. The hazard is related mostly to the formation of abundant Pele hairs that can accumulate in some areas and impact people and livestock due to their fibrous, acicular shape. In addition, preliminary studies (Duffield et al. 1977; Moune et al. 2007) have shown that the stretched vesicles of Pele's hairs can host a large number of smaller particles, including glass microsphere, and represent a surface for heterogeneous nucleation of salts from the vapor phase, and that their glass surfaces can react with the acid gases during their transport in the volcanic plume, becoming potentially even more dangerous.

(ii) Mild Strombolian explosions at PdF is the kind of activity producing the less ash content during the bubbles (or slug) explosions at the magma free surface. However, syn-eruptive degassing can enhance ash formation.

(iii) Indeed, significant syn-eruptive degassing associated with degassing-driven crystallization is identified as the main magmatic mechanism enhancing the magma fragmentation because of the increase of the viscosity, provoking brittle fragmentation. This mechanism generally results in the emission of non-negligible amounts of ash, sometimes producing relatively sudden change of the eruptive activity at the surface (i.e. September 2016 eruption at PdF). These unpredictable and sudden changes in activity can impact people who are approaching the eruptive sites.

(iv) On volcanic islands, more particularly on basaltic shield volcanoes as PdF, Karthala or Hawaii, low viscous lava flow are likely to reach the ocean, sometimes creating lazes and ash emissions. This also represents a risk to the local population because of the ash and shard fragments but also because of the gas emissions (Carlos et al. 2018).

(v) The presence of fluids at shallow levels near the magmatic systems has also been described in this study. The interaction between the magma and the water is interpreted to

provoke some eruption (i.e. March 1860 eruption at PdF). In some cases, non-juvenile lithic particle ubiquity within the investigated samples can related to phreatic phases (i.e. Bellecombe tephra as well as April 2007 and September 1936 summit ash emissions at PdF). For these products, the increase of ash associated with the presence of fine-grained cristobalite particles can have an important impact on the health respiratory (Damby et al. 2016). However, we suggest that, in some cases, the phreatomagmatism phenomenon enhanced the magma fragmentation (i.e. 2005 Karthala eruptions) but without triggering the eruptions. However, this process can sometime form relatively fine particles that have the capacity to be easily disperse in the atmosphere and impact large areas and health respiratory (Horwell 2007).

(vi) Finally, fault-shear fragmentation has been identified as the most efficient mechanism to form lithic and fine ash particles during the Dolomieu caldera collapse in April 2007. The extremely fine ash formed during event like that, even if localized, can stay longer in suspension and can affect touristic and local populations.

In conclusion, this study highlights the diversity of the basaltic fragmentation mechanisms, which are important to understand in order to anticipate the associated hazards and potential risks (Morin et al. 2016; Nave et al. 2016).

2.3. Perspectives

Lors de l'étude présentée au sein de la section précédente, plusieurs améliorations possibles apparaissent sur les différentes techniques analytiques utilisées sur l'ensemble des échantillons récoltés (notamment la mesure de la morphologie des particules, cf. perspectives du **chapitre V**), censés être représentatif de l'ensemble des mécanismes de fragmentations possibles au sein d'un système basaltique. De manière évidente, la représentativité des échantillons peut être toujours améliorée en augmentant le nombre d'échantillons et d'éruptions à étudier. Cependant, les 27 échantillons étudiés dans ce chapitre montrent déjà une variabilité relativement grande des granulométries, des composants et des textures. Cette diversité est indirectement liée à des processus de fragmentation distincts et peut être intégrée et comparée aux processus s'opérant au sein d'autres système basaltiques tels qu'au Kilauea (Hawaï), au Stromboli (Italie) ou encore à l'Etna (Italie). Cependant certaines conditions éruptives n'ont pas pu être étudiées tels que les processus sous-marins (Potuzak et al. 2008) et sub-glaciaires (Moreland et al. 2019).

Mise en place de l'ASHER

Lors de l'éruption de Mai-Avril 2018, la barrière optique du ASHER, fonctionnant de manière similaire à un disdromètre, permettant de détecter des particules entre 4 mm et 90 µm a été transporté jusqu'au site éruptif, situé sur le flanc SO du cône central du Piton de la Fournaise (Fig. 6.12). L'autre partie de l'ASHER (collecteur de cendres) n'a pas été transporté au vu des conditions d'acheminement de l'instrument sur le terrain. De plus, l'objectif de cette opération de terrain était de tester la faisabilité d'une telle démarche aux abords d'un site éruptif basaltique actif. La détection et l'échantillonnage d'éventuelles particules de cendres, associés à la mesure de certains paramètres syn-éruptifs notamment la taille et le taux d'accumulation des dépôts pourraient permettre de contraindre d'avantage les mécanismes de fragmentation magmatiques à travers des données physiques syn-éruptives.

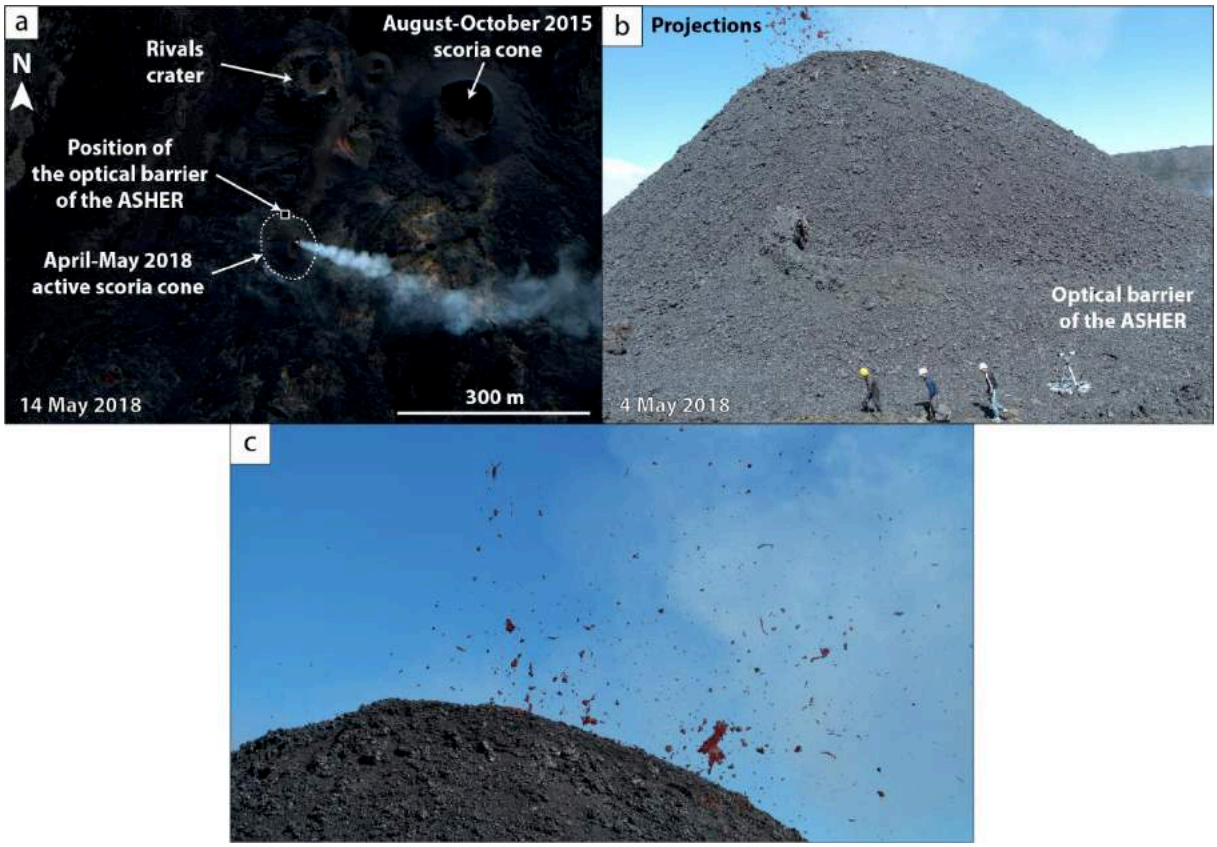

Figure 6.12 *– (a) Situation du site éruptif le 14 Mai 2018 et position de la barrière optique de l'ASHER. (b) Photo de la position de la barrière optique de l'ASHER, le 4 Mai 2018. Des projections de grandes tailles sont visibles à l'aplomb du cône de scorie. (c) Zoom sur des projections provoquées par l'explosion d'une bulle de gaz, à l'intérieur du cône de scorie.*

Cette éruption a débuté le 27 Avril 2018, formant quatre fissures éruptives au sein desquelles se forment des fontaines de laves d'une cinquantaine de mètres (flux laviques mesurées d'environ 16 $m^3.s^{-1}$, Fig. 6.13). Une chute de l'intensité de l'éruption traduit par une décroissance du trémor éruptif (stations sismiques de l'OVPF) ainsi que des flux laviques (télédétection, Fig. 6.13), est observée durant les 14 premières heures de l'éruption. A partir du 30 Avril, plusieurs fissures éruptives se referment rapidement et l'activité se focalise au sein d'un seul point d'émission majeur, formant progressivement un cône de scorie d'environ 20 mètres de hauteur (observation du 4 Mai 2018), associé à des flux laviques (environ 2 $m^3.s^{-1}$, Fig. 6.13) et une activité strombolienne (Figs. 6.12b et 6.12c) relativement faibles.

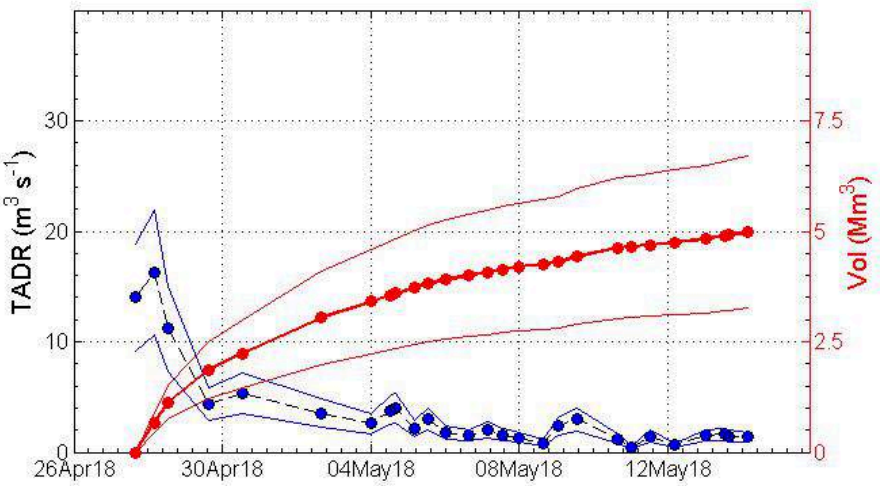

Figure 6.13 *– Evolution du flux magmatique (TADR) lors des deux premières semaines de l'éruption de Avril-Mai 2018 (données MIROVA).*

Les mesures de la barrière optique de l'ASHER, effectuées pendant environ trois heures le 4 Mai 2018, n'ont détectées aucunes particules entre 4 mm et 90 µm. Cependant, plusieurs dépôts associés à ce type d'activité ont été récoltés sur les éruptions de Juillet et Septembre 2018 (cf. section précédente). De plus, pour des raisons de sécurité et d'accessibilité, il était impossible d'installer la barrière optique de l'ASHER dans l'axe de dispersion majeur des pyroclastes (Fig. 6.12). Il est donc possible que des particules de cendre se soient formées mais cet exercice de terrain n'a pas pu confirmer leur présence pendant l'activité éruptive et n'a pas pu mesurer leurs tailles, vitesse de chute et taux d'accumulation éventuels.

En conclusion, ce test a permis de confirmer la faisabilité d'une telle procédure de terrain afin de mesurer l'émission de cendres éventuelle pendant l'activité éruptive. Cependant, plusieurs limites ont été observées et doivent être prises en compte (notamment la difficulté de la mise place expérimentale). La mise en place de l'ASHER lors d'éruptions futures et dans des conditions favorables pourra permettre de mieux contraindre certains paramètres syn-éruptifs pouvant être liés aux processus de fragmentation dominants.

CHAPITRE VII

CONCLUSIONS GENERALES ET PERSPECTIVES

1. Quantification des processus magmatiques pré-éruptifs et perspectives associées

Une des conclusions majeures de la première étude réalisée au sein de cette thèse (Gurioli et al. 2018, cf. **Annexe 2**) souligne l'importance de l'analyse texturale et pétrochimique des produits éruptifs (laves et téphras) afin de caractériser et quantifier certains processus magmatiques pré-éruptifs. De plus, l'analyse des signaux pré-éruptifs (déformation du sol, sismicité et dégazage) enregistrés par l'Observatoire Volcanologique du Piton de la Fournaise (OVPF) permet de corréler ces données aux signatures texturales et pétrochimiques enregistrées au sein du magma juvénile émis à la surface du volcan.

Cette même étude, étant spécifiquement focalisée sur la courte éruption de Juin 2014 au Piton de la Fournaise et des évènements volcano-tectoniques précurseurs à cette activité éruptive, met en évidence des processus pré-éruptifs déclencheurs relativement spécifiques. Premièrement, l'origine du magma relativement homogène en terme de composition chimique, émis lors de l'éruption de Juin 2014, est relié à la cristallisation et du dégazage progressif du dernier magma mis en place dans le système superficiel du Piton de la Fournaise en Novembre 2009 (période d'inactivité éruptive et de déflation du sol entre 2010 et 2014, cf. **Chapitre IV**). Lors des mois de Mars et d'Avril 2014, un transfert magmatique a été enregistré, notamment à travers une augmentation de la sismicité profonde et des émissions de CO_2 (Peltier et al. 2016, 2018 ; Boudoire et al. 2017). Les analyses texturales et pétrochimiques ont permis d'identifier les processus déclencheurs de l'éruption : bien qu'aucun mécanisme de mélange magmatique ne soit identifié au sein du magma de Juin 2014, l'étude menée suggère que le transfert magmatique a considérablement changé le champ de contrainte de l'édifice superficiel provoquant ainsi une nucléation secondaire brutale du magma (11 jours d'inflation du sol avant l'éruption) à l'origine de la suppression interne du réservoir superficiel et de l'éruption. L'émission de pyroclastes relativement vésiculés en début d'éruption suivis de produits laviques relativement dégazés et cristallisés (associé à une décroissance exponentielle du début magmatique mesuré tout le long de l'éruption) supporte l'hypothèse d'une vésiculation pré-éruptive d'un magma relativement différencié et cristallisé (stratification mécanique du réservoir magmatique).

De manière similaire, aucune évidence de magma profond, peu différencié et peu dégazé n'a été identifiée dans le cas de l'éruption de Septembre 2016 (cf. **Chapitre V**). De plus, des précurseurs de courte durée ainsi que l'émission de pyroclastes relativement vésiculés associée à une décroissance rapide du débit lavique en début d'éruption, suggèrent un processus pré-éruptif déclencheur semblable à celui de l'éruption de Juin 2014, le magma de Septembre 2016 étant potentiellement issu de la différenciation du magma mis en place dans le système magmatique superficiel lors de l'éruption de Août-Octobre 2015.

Parallèlement, un autre processus déclencheur majeur a été identifié, notamment lors de l'éruption de Juillet 2015 (cf. **Chapitre IV**) et implicitement lors de l'éruption d'Août-Octobre 2015 (Coppola et al. 2017). En adoptant une approche similaire, des signatures texturales, chimiques et pétrologiques suggèrent tout d'abord l'implication d'un mélange magmatique pré-éruptif (changement de la composition des micro-phénocristaux et des roches totales). Cette interprétation est cohérente avec des signaux pré-éruptifs beaucoup plus présents à moyen terme et en intensité (Peltier et al. 2016, 2018 ; Coppola et al. 2017). En effet, depuis Mars 2014, le transfert magmatique initié depuis le réservoir profond du Piton de la Fournaise vers des niveaux plus superficiels s'intensifie à partir d'Avril 2015 jusqu'en Octobre 2015 (inflation sommitale soutenue associée à des anomalies au sein des concentrations des espèces gazeuses). La mise en place progressive et l'implication directe d'un magma moins différencié au sein du système magmatique superficiel est détecté dès l'éruption de Juillet 2015. Malgré que ces implications soient restées faibles, notamment par rapport au débit lavique et à la durée de l'éruption, la contribution de ce nouveau magma, notamment l'apport de chaleur et de volatils, est interprété comme étant l'élément déclencheur majeur pour l'éruption de Juillet 2015 et de manière encore plus significative pour l'éruption d'Août-Octobre 2015.

En conclusion, les déclencheurs mis en évidence sur la période 2014-2016 au Piton de la Fournaise représentent deux processus distincts, dépendant (i) de l'activité volcano-tectonique plus ou moins profonde pouvant changer les conditions de stockage des magmas superficiels (vésiculation secondaire interne et pré-éruptive des magmas), (ii) du transfert et de la mise en place de magmas relativement profonds et peu différenciés (apport magmatique) au sein du système magmatique superficiel, source des éruptions récentes du Piton de la Fournaise.

La perspective majeure de ces travaux repose sur l'analyse systématique, rapide et conjointe des signaux pré-éruptifs enregistrés par le réseau d'observation de l'OVPF, ainsi que des signatures texturales et pétrochimiques des produits éruptifs associés. De cette façon, certaines systématiques peuvent être potentiellement identifiées, permettant de mieux

comprendre, prévoir et anticiper les débuts et les durées de chaque éruption, cette procédure pouvant être potentiellement appliquée pour d'autres systèmes volcaniques actifs. De plus, l'utilisation d'outils plus rapides et/ou complémentaires pour la quantification des textures, notamment la tomographie 3D (ex. Jerram and Higgins 2007 ; Polacci et al. 2006, 2008 ; Giachetti et al. 2011) ou encore l'analyse 2D semi-automatique (Lormand et al. 2018) pourrait contribuer à gagner du temps sur les analyses texturales.

2. Evolution des processus syn-éruptifs et influence sur les styles éruptifs et perspectives associées

Suite aux résultats de certaines analyses, l'évolution temporelle de la texture (distribution de la taille des vésicules et des microcristaux) ainsi que de la géochimie des verres magmatiques s'avèrent être des paramètres majeurs pouvant être directement liés aux différents processus s'opérant lors de la remontée des magmas vers la surface. Lors de la première étude évoquée dans la section précédente (Gurioli et al. 2018, cf. **Annexe 2**), mais plus largement au sein des **Chapitres IV et V**, les processus syn-éruptifs, en particulier l'évolution du dégazage, de la température, de la vésiculation et de la cristallisation associée des magmas, sont en effet étudiés.

Lors des courtes éruptions de Juin 2014 et Juillet 2015 (ainsi qu'aux éruptions de Février et Mai 2015) et de par les processus pré-éruptifs ainsi que les faibles volumes magmatiques impliqués, les débits laviques ont systématiquement chuté relativement rapidement jusqu'à la fin des activités éruptives en surface (Coppola et al. 2017). Ces décroissances en intensité furent associées à des changements de styles éruptifs, passant de fontaines de laves (ou activité de type hawaïenne) en début d'éruption, à des explosions relativement faibles de type stromboliennes (cf. **Chapitre IV**). Une décroissance initiale des débits laviques fut également observée lors de l'éruption de Septembre 2016 mais les débits se sont stabilisés à des niveaux intermédiaires, produisant des fontaines de laves plus ou moins soutenues. En revanche, une augmentation tardive du débit lors de cette dernière éruption provoqua la formation d'explosions transitoires, dominées par l'émission de bombes mais aussi par l'émission d'une quantité de cendres non-négligeable par rapport aux précédentes éruptions étudiées (cf. **Chapitre V**).

L'ensemble des enchainements des processus syn-éruptifs mis en évidence lors des éruptions de Juin 2014 et Juillet 2015 au Piton de la Fournaise sont représentés dans la Figure 7.1. La quantification de la densité des vésicules par unité de volume au sein de pyroclastes représentatifs des conditions de fragmentation (bombes trempées, lapilli et cendres) permettent de lier la décroissance des débits laviques à une décroissance du taux de décompression du magma et donc de la vitesse de remontée de celui-ci. L'étude de la distribution de la taille des vésicules permet de caractériser les processus de nucléation, de croissance et de coalescence des bulles lors de la remontée du magma vers la surface, qui sont relativement dépendants du

temps de résidence du magma au sein du conduit éruptif. La mise en place de géothermomètres appropriés (à la fois pour des conditions hydratées sensées reproduire les conditions de stockage magmatique superficiel et pour des conditions atmosphériques et dégazées) et la modélisation des teneurs en H_2O dissous dans les verres magmatiques ainsi que dans les roches totales, montrent que les magmas expérimentant une remontée relativement rapide et émis par des fontaines de lave ne dégazent que partiellement, au contraire des magmas expérimentant des remontées relativement lentes et émis lors d'un régime strombolien.

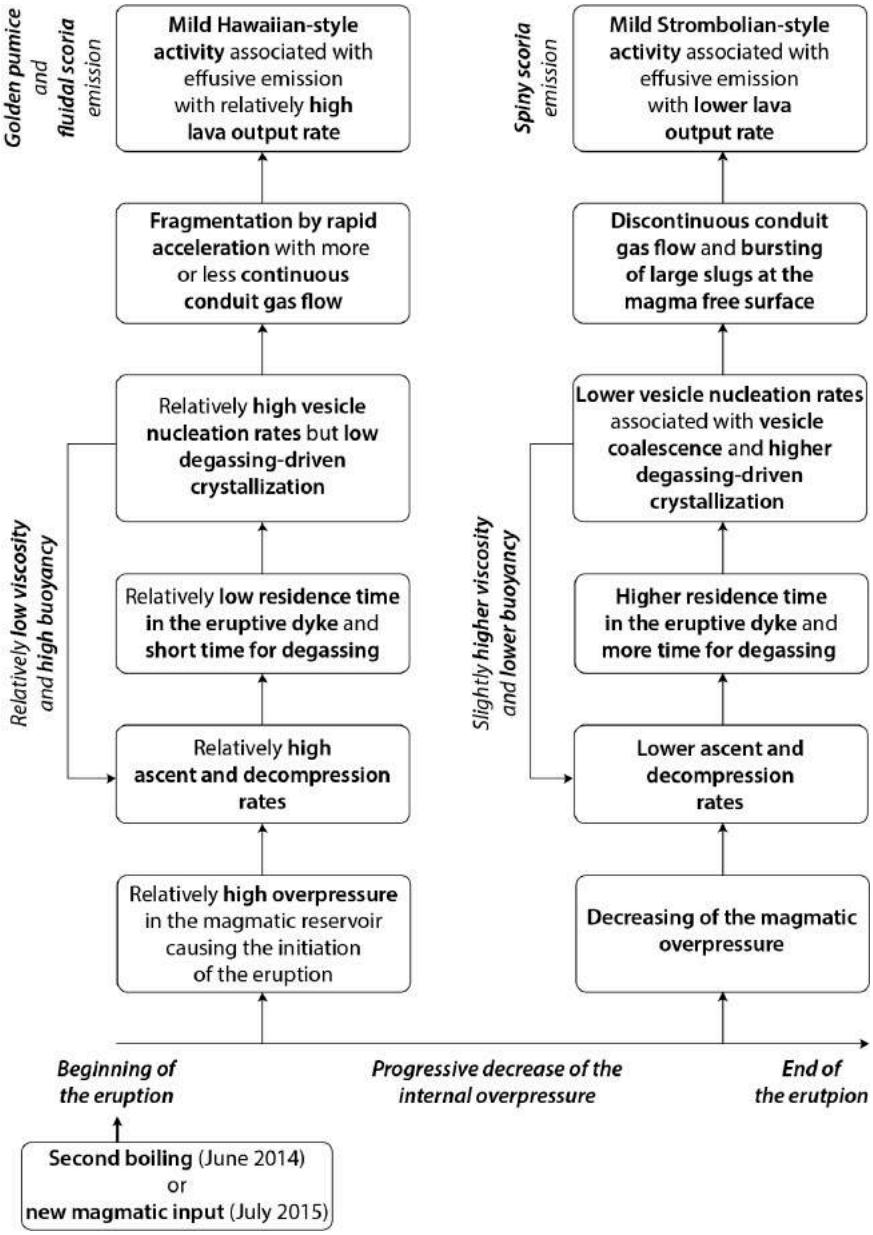

Figure 7.1 – *Schéma interprétatif des processus magmatiques pré- et syn-éruptifs contrôlant l'évolution des styles éruptifs lors des éruptions de Juin 2014 et Juillet 2015 au Piton de la Fournaise.*

Lors de ce dégazage plus ou moins efficace selon les taux de décompression, une cristallisation associée (microlites de plagioclase et de clinopyroxène) est observée. Ces phénomènes de dégazage et de cristallisation vont directement impacter l'évolution de la texture et donc de la viscosité ainsi que de la flottabilité du magma et la mise en place de régimes d'écoulements spécifiques aux types d'activités observés en surface (de type annulaire pour les fontaines de lave et de type *slug* pour les explosions stromboliennes). L'ensemble de ces paramètres influent aussi sur les mécanismes de fragmentation en surface (cf. section suivante).

Une approche similaire révèle des processus syn-éruptifs semblables pour le début de l'éruption de Septembre 2016 (Fig. 7.2), lorsque l'activité était dominée par des fontaines de laves. Cependant, une évolution différente par rapport aux éruptions précédentes est observée, reflétant des processus magmatiques syn-éruptifs également différents. En effet, l'activité éruptive s'est concentrée progressivement au sein de deux évents relativement proches, l'un restant complétement ouvert (activité plus ou moins soutenue de fontaines de lave), l'autre se refermant progressivement et évoluant différemment. Les analyses du trémor éruptif et du débit lavique corrélées aux mesures texturales et pétrochimiques des échantillons émis au sein de cet évent produisant des explosions transitoires, montrent que le magma initial (partiellement dégazé et peu cristallisé) se refroidit et dégaze relativement rapidement au niveau de la surface de fragmentation, formant ainsi une couche rhéologique, relativement imperméable aux gaz volcaniques. Sous l'influence de l'arrivée tardive d'un flux de magma assez important, cette couche nouvellement formée et agissant comme un bouchon, provoque des surpressions locales et transitoires à l'origine de l'activité explosive observée en surface.

En conclusion, l'analyse intégrée de la texture et de la chimie des échantillons ainsi que des données de terrains (photos des dynamismes et stratigraphie des dépôts), des signaux syn-éruptifs géophysiques (débit et trémor) et géochimiques (flux de SO_2), permettent d'identifier les processus clés à l'origine du changement parfois brutal et inattendu du style éruptif en surface. Deux systématiques syn-éruptives ont notamment été identifiées, (i) lors du passage d'une activité soutenue de fontaines de lave vers un dynamisme relativement faible strombolien et (ii) lors du passage d'une activité soutenue de fontaines de lave vers la coexistence entre une activité de fontaine et des explosions transitoires produisant une quantité plus élevée en cendres.

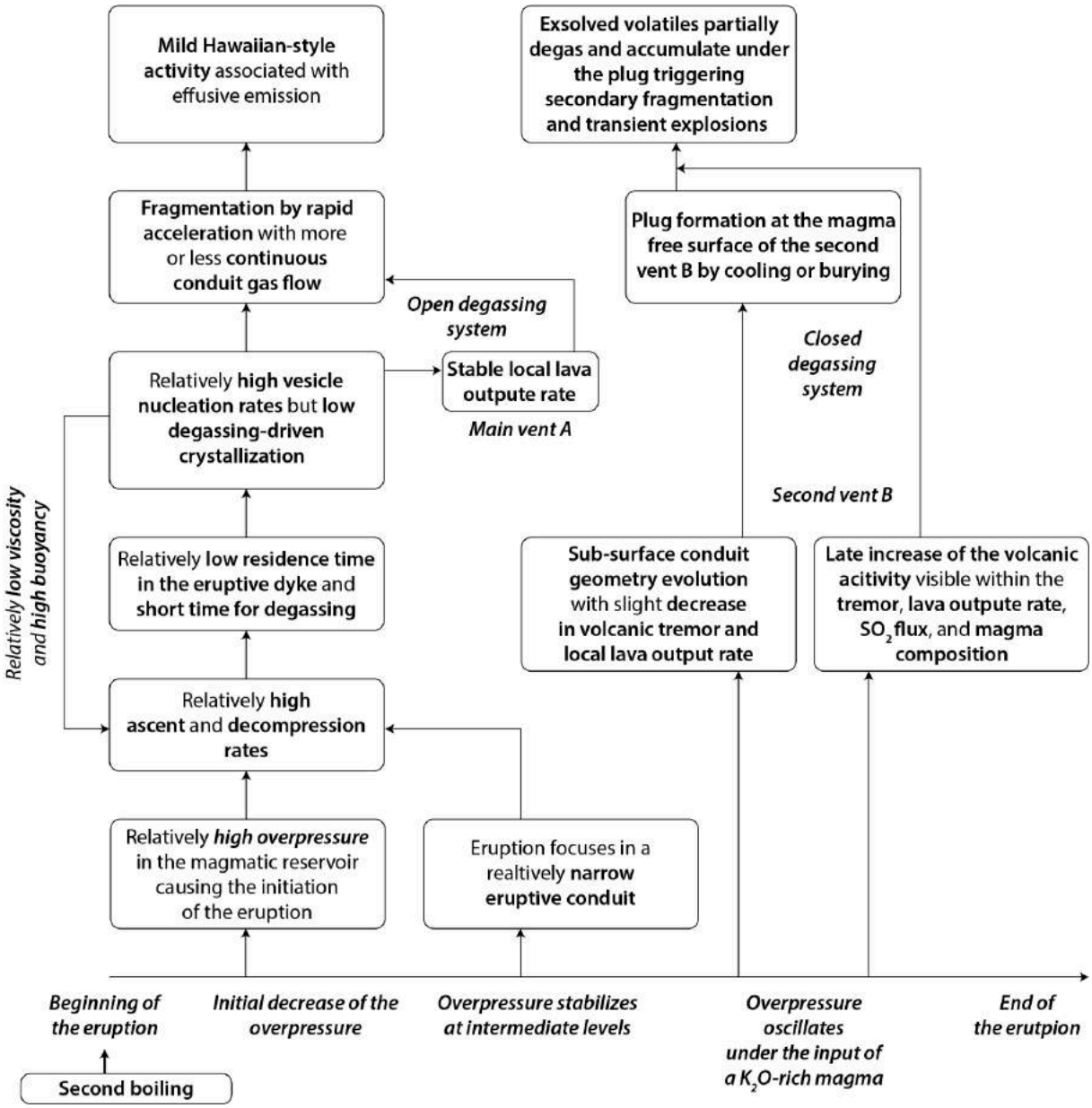

***Figure 7.2** – Schéma interprétatif des processus magmatiques pré- et syn-éruptifs contrôlant l'évolution des styles éruptifs lors de l'éruption de Septembre 2016.*

La perspective majeure ressortant de ces résultats concerne l'amélioration de la quantification de l'évolution texturale du magma lors de sa remontée vers la surface, notamment sur la nucléation et la croissance des bulles et des microcristaux (cf. **Chapitre IV**). A travers une étude spécifique sur la distribution de la taille des vésicules et des cristaux ainsi qu'à l'exploitation des théories des dynamiques de dégazage (ex. Lesne et al. 2011 ; Taddeucci et al. 2015 ; Di Muro et al ; 2016) et de cristallisation (ex. Marsh 1988 ; Higgins 2000, 2006), l'évolution temporelle (ex. au cours de la remontée du magma vers la surface) et spatiale (ex.

modèle de diffusion autour zones gazeuses au sein du conduit éruptif) de la viscosité (ex. Maron and Pierce 1956 ; Llewellin and Manga 2005 ; Giordano et al. 2008 ; Mader et al. 2013 ; Truby et al. 2015) et de la teneur en volatils du magma pourrait être mieux contraints afin d'établir un modèle dynamique global du potentiel explosif des magmas. En utilisant les estimations des teneurs en cristaux et des températures pré-éruptives, la modélisation en utilisant les algorithmes MELTS (Ghiorso et Sack 1995 ; Asimow and Ghiorso 1998) pourrait aussi contraindre numériquement l'évolution de la texture et de la chimie du magma lors de son transfert vers la surface.

3. Mise en évidence des mécanismes de fragmentation et perspectives associées

D'après les observations effectuées précédemment, les processus magmatique pré-éruptifs semblent contrôler de manière plus ou moins significative l'enchaînement des processus syn-éruptifs opérant au sein du conduit éruptif. Certains des processus opérant lors de la remontée du magma influent directement sur la diversité des styles éruptifs en surface et donc sur les mécanismes de fragmentations impliquées (cf. **Chapitre VI**). Dans un premier temps, la caractérisation des particules cendreuses juvéniles a permis de relier la variabilité des textures observées à la granulométrie des dépôts ainsi qu'aux styles éruptifs et donc aux mécanismes de fragmentation.

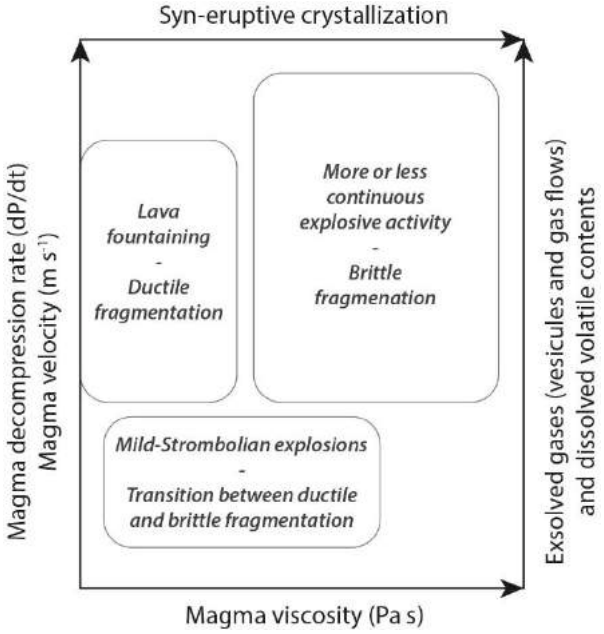

Figure 7.3 – *Influence de la quantité initiale des volatils et de la cristallisation syn-éruptive des magmas sur le style éruptif en surface et les mécanismes de fragmentation impliquées.*

En intégrant l'ensemble des données acquises, notamment la texture et la géochimie des composants, (i) la teneur initiale en volatils des magmas et leurs comportement lors de la remontée du magma vers surface est indirectement liée au taux de décompression de celui-ci et donc à sa vitesse de remontée au sein du conduit éruptif. Selon le temps de résidence et la

vitesse d'ascension du magma le long du conduit, les volatils initialement dissous vont plus ou moins s'exsolver pour former des bulles et des régimes d'écoulement gazeux distincts (cf. section précédente). (ii) Parallèlement, une cristallisation syn-éruptive plus ou moins prononcée, associée au dégazage, contrôle de manière significative l'évolution de la viscosité des magmas. En comparant les caractéristiques des magmas émis lors d'épisodes de fontaines de lave, d'explosions stromboliennes relativement faible, ou encore lors d'explosions transitoires plus violentes, une transition vers un mécanisme de fragmentation ductile du magma (fontaines de lave) vers un mécanisme de fragmentation partiellement (faibles explosions stromboliennes) ou entièrement fragile (explosions relativement plus violentes et plus ou moins transitoires) est observée (Fig. 7.3).

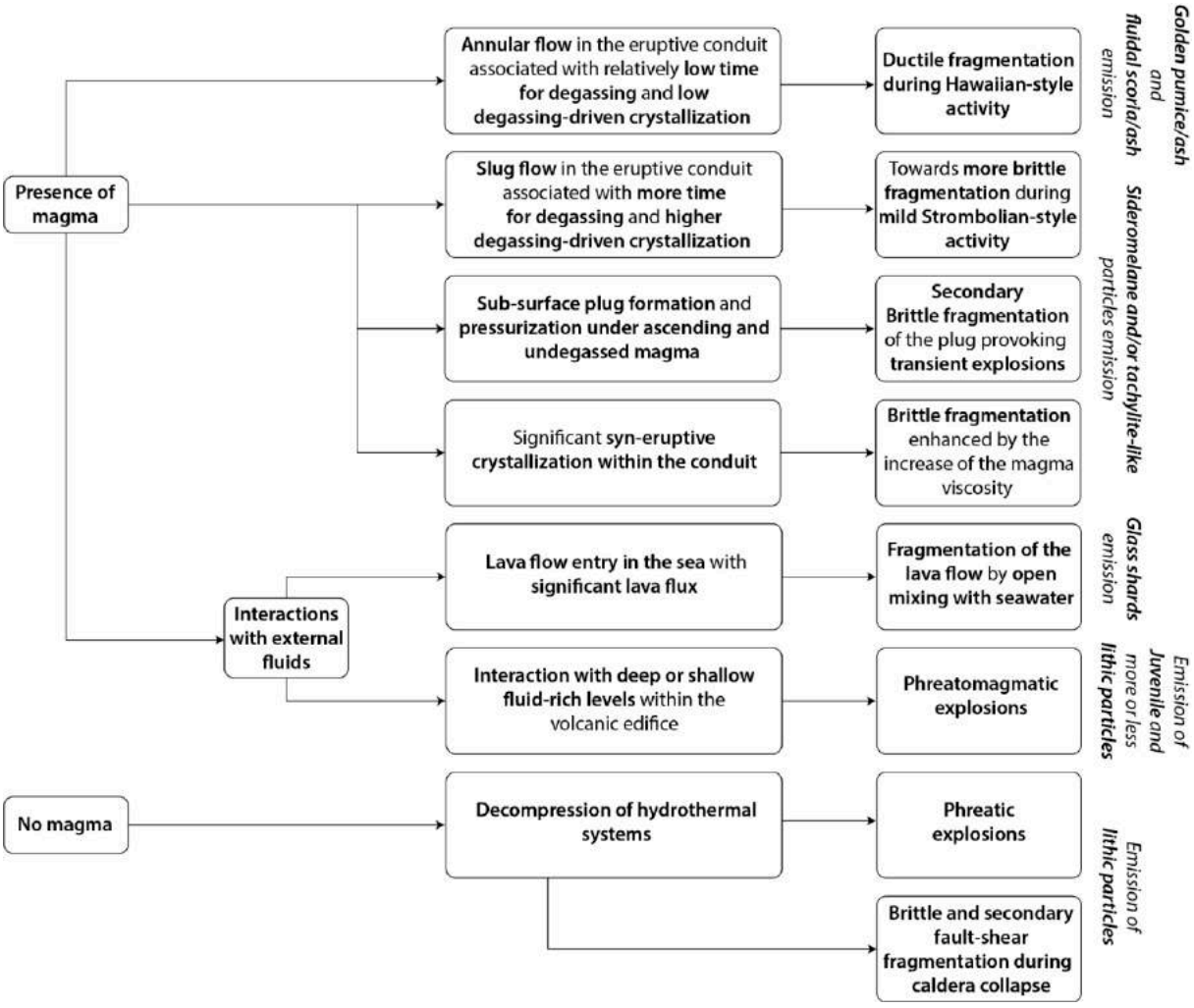

***Figure 7.4** – Schéma interprétatif des processus volcano-tectoniques à l'origine des différents mécanismes de fragmentation identifiés à travers la caractérisation des produits éruptifs explosifs.*

Dans certains cas particuliers et souvent paroxysmaux, des éléments extérieurs aux processus magmatiques viennent perturber les systèmes initiaux et accroître le potentiel explosif des magmas (Fig. 7.4). (i) Les interactions entre le magma et des fluides tels que l'eau initient (entrées de coulées de laves dans des masses d'eau) ou renforcent (explosions phréatomagmatiques au sein du système magmatique plus ou moins superficiel) l'explosivité et l'intensité de la fragmentation du magma mais aussi des roches environnantes sous l'effet de la vaporisation brutales des fluides (hydrothermaux et/ou météoritiques). (ii) La décompression brutale de systèmes hydrothermaux lors d'évènements d'effondrements, notamment de calderas sont aussi à l'origine d'explosions phréatiques, n'impliquant pas de magma juvénile. (iii) Enfin, en se focalisant sur la granulométrie et la morphologie des cendres émises lors de l'effondrement caldérique d'Avril 2007 au Piton de la Fournaise, une fragmentation secondaire par friction est mise en évidence, générant des particules cendreuses relativement fines.

La mise en place de l'ASHER au cours d'activités relativement explosives et dans des zones de retombées proximales représente la perspective majeure de ces travaux focalisés sur l'étude des dépôts cendreux (cf. **Chapitre VI**). En effet, la quantification de l'évolution de la granulométrie et des taux d'accumulation des retombées, en termes d'épaisseurs et de masses, peuvent être des informations importantes et complémentaires pour quantifier les dynamismes éruptifs. De plus l'échantillonnage en temps réel de ces dépôts pourrait permettre de corréler l'évolution pétrochimique des pyroclastes avec les données acquises en temps réel (Gurioli et al. 2016, cf. **Annexe 1**).

En conclusion, l'ensemble des études réalisées au cours de cette thèse, majoritairement appliquées au Piton de la Fournaise, montrent que l'évolution des styles éruptifs (pouvant impliquer des aléas volcaniques conséquents) sont fortement dépendant des processus volcano-tectoniques pré- et syn-éruptifs. L'analyse intégrée des échantillons représentatifs de la diversité des styles éruptifs ainsi que les observations de terrain et l'étude des signaux géophysiques et géochimiques syn-éruptifs représentent une approche constructive et essentielle pour la compréhension du fonctionnement des systèmes volcaniques et des aléas associés.

REFERENCES BIBLIOGRAPHIQUES

A

Aiuppa, A., Burton, M., Caltabiano, T., Giudice, G., Guerrieri, S., Liuzzo, M., … Salerno, G. (2010). Unusually large magmatic CO_2 gas emissions prior to a basaltic paroxysm. *Geophysical Research Letters*, *37*(17), 1–5. https://doi.org/10.1029/2010GL043837

Aki, K., & Ferrazzini, V. (2000). Seismic monitoring and modeling of an active volcano for prediction. *Journal of Geophysical Research: Solid Earth*, *105*(B7), 16617–16640. https://doi.org/10.1029/2000JB900033

Albarède, F., Luais, B., Fitton, G., Semet, M., Kaminski, E., Upton, B. G. J., … Cheminée, J. L. (1997). The geochemical regimes of piton de la Fournaise volcano (Réunion) during the last 530000 years. *Journal of Petrology*, *38*(2), 171–201. https://doi.org/10.1093/petroj/38.2.171

Albert, H., Costa, F., Di Muro, A., Herrin, J., Métrich, N., & Deloule, E. (2019). Magma interactions, crystal mush formation, timescales, and unrest during caldera collapse and lateral eruption at ocean island basaltic volcanoes (Piton de la Fournaise, La Réunion). *Earth and Planetary Science Letters*, *515*, 187–199. https://doi.org/10.1016/j.epsl.2019.02.035

Aloisi, M., Mattia, M., Ferlito, C., Palano, M., Bruno, V., & Cannavò, F. (2011). Imaging the multi-level magma reservoir at Mt. Etna volcano (Italy). *Geophysical Research Letters*, *38*(16), https://doi.org/10.1029/2011GL048488

Alparone, S., Andronico, D., Lodato, L., & Sgroi, T. (2003). Relationship between tremor and volcanic activity during the Southeast Crater eruption on Mount Etna in early 2000. *Journal of Geophysical Research: Solid Earth*, *108*(B5), 1–13. https://doi.org/10.1029/2002JB001866

Anderson, A. T. (1995). CO2 and the eruptibility of picrite and komatiite. *Lithos*, *34*(1–3), 19–25. https://doi.org/10.1016/0024-4937(95)90005-5

Andronico, D., & Corsaro, R. A. (2011). Lava fountains during the episodic eruption of South–East Crater (Mt. Etna), 2000: insights into magma-gas dynamics within the shallow volcano plumbing system. *Bulletin of Volcanology*, *73*(9), 1165–1178. https://doi.org/10.1007/s00445-011-0467-y

Andronico, D., Corsaro, R. A., Cristaldi, A., & Polacci, M. (2008). Characterizing high energy explosive eruptions at Stromboli volcano using multidisciplinary data: An example from the 9 January 2005 explosion. *Journal of Volcanology and Geothermal Research*, *176*(4), 541–550. https://doi.org/10.1016/j.jvolgeores.2008.05.011

Andronico, D., Lo Castro, M. D., Sciotto, M., & Spina, L. (2013). The 2010 ash emissions at the summit craters of Mt Etna: Relationship with seismo-acoustic signals. *Journal of Geophysical Research: Solid Earth*, *118*(1), 51–70. https://doi.org/10.1029/2012JB009895

Andronico, Daniele, Cristaldi, A., Del Carlo, P., & Taddeucci, J. (2009). Shifting styles of basaltic explosive activity during the 2002-03 eruption of Mt. Etna, Italy. *Journal of Volcanology and Geothermal Research*, *180*(2–4), 110–122. https://doi.org/10.1016/j.jvolgeores.2008.07.026

Andronico, Daniele, Scollo, S., Lo Castro, M. D., Cristaldi, A., Lodato, L., & Taddeucci, J. (2014). Eruption dynamics and tephra dispersal from the 24 November 2006 paroxysm at South-East Crater, Mt Etna, Italy. *Journal of Volcanology and Geothermal Research*, *274*(November 2006), 78–91. https://doi.org/10.1016/j.jvolgeores.2014.01.009

Applegarth, L. Jane, Tuffen, H., James, M. R., Pinkerton, H., & Cashman, K. V. (2013). Direct observations of degassing-induced crystallization in basalts. *Geology*, *41*(2), 243–246. https://doi.org/10.1130/G33641.1

Applegarth, L.J., Tuffen, H., James, M. R., & Pinkerton, H. (2013). Degassing-driven crystallisation in basalts. *Earth-Science Reviews*, *116*(1), 1–16. https://doi.org/10.1016/j.earscirev.2012.10.007

Armienti, P., Pareschi, M. T., Innocenti, F., & Pompilio, M. (1994). Effects of magma storage and ascent on the kinetics of crystal growth. *Contributions to Mineralogy and Petrology*, *115*(4), 402–414. https://doi.org/10.1007/BF00320974

Arzilli, F., La Spina, G., Burton, M., Polacci, M., Le Gall, N., Hartley, M., & Nonni, S. (2019). Magma fragmentation in highly explosive basaltic eruptions induced by rapid crystallisation. *Nature Geoscience*. https://doi.org/10.1038/s41561-019-0468-6

Arzilli, Fabio, Agostini, C., Landi, P., Fortunati, A., Mancini, L., & Carroll, M. R. (2015). Plagioclase nucleation and growth kinetics in a hydrous basaltic melt by decompression experiments. *Contributions to Mineralogy and Petrology*, *170*(5–6), 1–16. https://doi.org/10.1007/s00410-015-1205-9

Arzilli, Fabio, Morgavi, D., Petrelli, M., Polacci, M., Burton, M., Di Genova, D., … Perugini, D. (2019). The unexpected explosive sub-Plinian eruption of Calbuco volcano (22–23 April 2015; southern Chile): Triggering mechanism implications. *Journal of Volcanology and Geothermal Research*, *378*, 35–50. https://doi.org/10.1016/j.jvolgeores.2019.04.006

Arzilli, Fabio, Piochi, M., Mormone, A., Agostini, C., & Carroll, M. R. (2016). Constraining pre-eruptive magma conditions and unrest timescales during the Monte Nuovo eruption (1538 ad; Campi Flegrei, Southern Italy): integrating textural and CSD results from experimental and natural trachy-phonolites. *Bulletin of Volcanology*, *78*(10), 72. https://doi.org/10.1007/s00445-016-1062-z

Asimow, P. D., & Ghiorso, M. S. (1998). Algorithmic modifications extending MELTS to calculate subsolidus phase relations. *American Mineralogist*, *83*(9–10), 1127–1132. https://doi.org/10.2138/am-1998-9-1022

Aspinall, W., & Blong, R. (2015). *Volcanic Risk Assessment*. *The Encyclopedia of Volcanoes* (Second Edition). Elsevier Inc. https://doi.org/10.1016/b978-0-12-385938-9.00070-5

B

Bachélery, P. (1999). *Le Fonctionnement des volcans boucliers. Exemple des volcans de la Réunion et de la Grande Comore*.

Bachèlery, P., & Coudray, J. (1993). Carte volcano-tectonique (1/50000e) de la Grande Comore et notice explicative.

Bachelery, P., Lenat, J.-F., Di Muri, A., & Michon, L. (2016). *Active Volcanoes of the Southwest Indian Ocean*. (P. Bachelery, J.-F. Lenat, A. Di Muro, & L. Michon, Eds.), *Active volcanoes of the Southwest Indian Ocean: Piton de la Fournaise and Karthala*. Berlin, Heidelberg: Springer Berlin Heidelberg. https://doi.org/10.1007/978-3-642-31395-0

Bachèlery, P., & Mairine, P. (1990). Evolution volcano-structurale du Piton de la Fournaise depuis 0.53 Ma. In *Le volcanisme de la Réunion,*.

Bachèlery, Patrick. (1981). *Le Piton de la Fournaise (île de la Réunion). Etude volcanologique, structurale et pétrologique.*

Bachèlery, Patrick, & Hémond, C. (2016). Geochemical and Petrological Aspects of Karthala Volcano. In *Active Volcanoes of the Southwest Indian Ocean* (pp. 367–384). https://doi.org/10.1007/978-3-642-31395-0_23

Bachèlery, Patrick, Morin, J., Villeneuve, N., Soulé, H., Nassor, H., & Ali, A. R. (2016). Structure and Eruptive History of Karthala Volcano. In P. Bachelery, J.-F. Lenat, A. Di Muro, & L. Michon (Eds.), *Active volcanoes of the Southwest Indian Ocean: Piton de la Fournaise and Karthala* (pp. 345–366). Berlin, Heidelberg: Springer Berlin Heidelberg. https://doi.org/10.1007/978-3-642-31395-0_22

Bachmann, O., & Bergantz, G. W. (2006). Gas percolation in upper-crustal silicic crystal mushes as a mechanism for upward heat advection and rejuvenation of near-solidus magma bodies. *Journal of Volcanology and Geothermal Research*, *149*(1–2), 85–102. https://doi.org/10.1016/j.jvolgeores.2005.06.002

Bai, L., Baker, D. R., & Hill, R. J. (2010). Permeability of vesicular Stromboli basaltic glass: Lattice Boltzmann simulations and laboratory measurements. *Journal of Geophysical Research*, *115*(B7), 1–16. https://doi.org/10.1029/2009jb007047

Bai, L., Baker, D. R., Polacci, M., & Hill, R. J. (2011). In-situ degassing study on crystal-bearing Stromboli basaltic magmas: Implications for Stromboli explosions. *Geophysical Research Letters*, *38*(17), n/a-n/a. https://doi.org/10.1029/2011GL048540

Bain, A. A., Calder, E. S., Cortés, J. A., Cortés, G. P., & Loughlin, S. C. (2019). Textural and geochemical constraints on andesitic plug emplacement prior to the 2004–2010 vulcanian explosions at Galeras volcano, Colombia. *Bulletin of Volcanology*, *81*(1), 1. https://doi.org/10.1007/s00445-018-1260-y

Barruol, G., & Fontaine, F. R. (2013). Mantle flow beneath La Réunion hotspot track from SKS splitting. *Earth and Planetary Science Letters*, *362*, 108–121. https://doi.org/10.1016/j.epsl.2012.11.017

Barsotti, S., Andronico, D., Neri, A., Del Carlo, P., Baxter, P. J., Aspinall, W. P., & Hincks, T. (2010). Quantitative assessment of volcanic ash hazards for health and infrastructure at Mt. Etna (Italy) by numerical simulation. *Journal of Volcanology and Geothermal Research*, *192*(1–2), 85–96. https://doi.org/10.1016/j.jvolgeores.2010.02.011

Battaglia, J., Aki, K., & Staudacher, T. (2005). Location of tremor sources and estimation of lava output using tremor source amplitude on the Piton de la Fournaise volcano: 2. Estimation of lava output. *Journal of Volcanology and Geothermal Research*, *147*(3–4), 291–308. https://doi.org/10.1016/j.jvolgeores.2005.04.006

Battaglia, J., Brenguier, F., & Roult, G. (2016). Seismic Monitoring at Piton de la Fournaise. In *Active Volcanoes of the Southwest Indian Ocean* (pp. 223–242). https://doi.org/10.1007/978-3-642-31395-0_13

Battaglia, J., Ferrazzini, V., Staudacher, T., Aki, K., & Cheminée, J.-L. (2005). Pre-eruptive migration of earthquakes at the Piton de la Fournaise volcano (Réunion Island). *Geophysical Journal International*, *161*(2), 549–558. https://doi.org/10.1111/j.1365-246X.2005.02606.x

Behncke, B., Calvari, S., Giammanco, S., Neri, M., & Pinkerton, H. (2008). Pyroclastic density currents resulting from the interaction of basaltic magma with hydrothermally altered rock: An example from the 2006 summit eruptions of Mount Etna, Italy. *Bulletin of Volcanology*, *70*(10), 1249–1268. https://doi.org/10.1007/s00445-008-0200-7

Behncke, Boris, Branca, S., Corsaro, R. A., De Beni, E., Miraglia, L., & Proietti, C. (2014). The 2011-2012 summit activity of Mount Etna: Birth, growth and products of the new SE crater. *Journal of Volcanology and Geothermal Research*, *270*(May 1971), 10–21. https://doi.org/10.1016/j.jvolgeores.2013.11.012

Bell, A. F., & Kilburn, C. R. J. (2012). Precursors to dyke-fed eruptions at basaltic volcanoes: Insights from patterns of volcano-tectonic seismicity at Kilauea volcano, Hawaii. *Bulletin of Volcanology*, *74*(2), 325–339. https://doi.org/10.1007/s00445-011-0519-3

Belousov, A., Belousova, M., Edwards, B., Volynets, A., & Melnikov, D. (2015). Overview of the precursors and dynamics of the 2012-13 basaltic fissure eruption of Tolbachik Volcano, Kamchatka, Russia. *Journal of Volcanology and Geothermal Research*, *307*, 22–37. https://doi.org/10.1016/j.jvolgeores.2015.06.013

Bertagnini, A., Coltelli, M., Landi, P., Pompilio, M., & Rosi, M. (1999). Violent explosions yield new insights into dynamics of Stromboli volcano. *Eos, Transactions American Geophysical Union*, *80*(52), 633. https://doi.org/10.1029/99EO00415

Blackburn, E. A., Wilson, L., & Sparks, R. S. J. (1976). Mechanisms and dynamics of strombolian activity. *Journal of the Geological Society*, *132*(4), 429–440. https://doi.org/10.1144/gsjgs.132.4.0429

Blong, R. J. (1984). Hazards Produced by Volcanic Eruptions. In *Volcanic Hazards* (pp. 14–69). Elsevier. https://doi.org/10.1016/B978-0-12-107180-6.50007-X

Boivin, P., & Bachèlery, P. (2009). Petrology of 1977 to 1998 eruptions of Piton de la Fournaise, La Réunion Island. *Journal of Volcanology and Geothermal Research*, *184*(1–2), 109–125. https://doi.org/10.1016/j.jvolgeores.2009.01.012

Bonali, F. L., Corazzato, C., & Tibaldi, A. (2011). Identifying rift zones on volcanoes: An example from La Réunion island, Indian Ocean. *Bulletin of Volcanology*, *73*(3), 347–366. https://doi.org/10.1007/s00445-010-0416-1

Bonneville, A., Barriot, J. P., & Bayer, R. (1988). Evidence from geoid data of a hotspot origin for the southern Mascarene Plateau and Mascarene Island (Indian Ocean). *Journal of Geophysical Research*, *93*(B5), 4199–5212. https://doi.org/10.1029/JB093iB05p04199

Botto, I. L., Canafoglia, M. E., Gazzoli, D., & González, M. J. (2013). Spectroscopic and microscopic characterization of volcanic ash from puyehue-(Chile) eruption: Preliminary approach for the application in the arsenic removal. *Journal of Spectroscopy*, *1*(1). https://doi.org/10.1155/2013/254517

Boudoire, G., Liuzzo, M., Di Muro, A., Ferrazzini, V., Michon, L., Grassa, F., … Gurrieri, S. (2017). Investigating the deepest part of a volcano plumbing system: Evidence for an active magma path below the western flank of Piton de la Fournaise (La Réunion Island). *Journal of Volcanology and Geothermal Research*, *341*, 193–207. https://doi.org/10.1016/j.jvolgeores.2017.05.026

Boudoire, G., Rizzo, A. L., Di Muro, A., Grassa, F., & Liuzzo, M. (2018). Extensive CO 2 degassing in the upper mantle beneath oceanic basaltic volcanoes: First insights from Piton de la Fournaise volcano (La Réunion Island). *Geochimica et Cosmochimica Acta*, *235*, 376–401. https://doi.org/10.1016/j.gca.2018.06.004

Boudoire, G., Brugier, Y.-A., Di Muro, A., Wörner, G., Arienzo, I., Metrich, N., Zanon, V., Braukmüller, N., Kronz, A., Le Moigne, Y., Michon, L. (2019). Eruptive Activity on the Western Flank of Piton de la Fournaise (La Réunion Island, Indian Ocean): Insights on Magma Transfer, Storage and Evolution at an Oceanic Volcanic Island. *Journal of Petrology*. https://doi.org/10.1093/petrology/egz045

Bret, L., Fevre, Y., Join, J. L., Robineau, B., & Bachelery, P. (2003). Deposits related to degradation processes on Piton des Neiges Volcano (Reunion Island): Overview and geological hazard. *Journal of Volcanology and Geothermal Research*, *123*(1–2), 25–41. https://doi.org/10.1016/S0377-0273(03)00026-X

Brown, R. J., Bonadonna, C., & Durant, A. J. (2012). A review of volcanic ash aggregation. *Physics and Chemistry of the Earth*, *45–46*, 65–78. https://doi.org/10.1016/j.pce.2011.11.001

Brown, S. K., Jenkins, S. F., Sparks, R. S. J., Odbert, H., & Auker, M. R. (2017). Volcanic fatalities database: analysis of volcanic threat with distance and victim classification. *Journal of Applied Volcanology*, *6*(1). https://doi.org/10.1186/s13617-017-0067-4

Brugier, Y.-A. (2016). *Magmatologie du Piton de la Fournaise (Ile de la Réunion). Approche Volcanologique, Pétrologique et Expérimentale.*

Brullas, C. (2015). *Do the fossil bubbles trapped in ash, lapilli and bomb provide the same information about fragmentation? Answers from Fuego volcano, Guatemala.*

Bureau, H., Métrich, N., Pineau, F., & Semet, M. P. (1998). Magma-conduit interaction at Piton de la Fournaise volcano (Reunion Island): A melt and fluid inclusion study. *Journal of Volcanology and Geothermal Research*, *84*(1–2), 39–60. https://doi.org/10.1016/S0377-0273(98)00029-8

Bureau, H., Pineau, F., Métrich, N., Semet, M. P., & Jaboy, M. (1998). A melt and fluid inclusion study of the gas phase at Piton de la Fournaise volcano Reunion Island. *Chemical Geology*.

Burkhard, D. J. (2002). Kinetics of crystallization: example of micro-crystallization in basalt lava. *Contributions to Mineralogy and Petrology*, *142*(6), 724–737. https://doi.org/10.1007/s00410-001-0321-x

Burkhard, D. J. M. (2005). Nucleation and growth rates of pyroxene, plagioclase, and Fe-Ti oxides in basalt under atmospheric conditions. *European Journal of Mineralogy*, *17*(5), 675–686. https://doi.org/10.1127/0935-1221/2005/0017-0675

Burton, M., Allard, P., Mure, F., & La Spina, A. (2007). Magmatic Gas Composition Reveals the Source Depth of Slug-Driven Strombolian Explosive Activity. *Science*, *317*(5835), 227–230. https://doi.org/10.1126/science.1141900

Büttner, R., Dellino, P., & Zimanowski, B. (1999). Identifying magma–water interaction from the surface features of ash particles. *Nature*, *401*(6754), 688–690. https://doi.org/10.1038/44364

C

Cannata, C. B., De Rosa, R., Donato, P., Donato, S., Lanzafame, G., Mancini, L., & Houghton, B. F. (2019). First 3D imaging characterization of Pele's hair from Kilauea volcano (Hawaii). *Scientific Reports*, *9*(1), 1711. https://doi.org/10.1038/s41598-018-37983-9

Cantelli, L., Fichera, A., Guglielmino, I. D., & Pagano, A. (2006). Nonlinear dynamics of air-water mixtures in vertical pipes: Experimental trends. *International Journal of Bifurcation and Chaos*, *16*(9), 2749–2760. https://doi.org/10.1142/S0218127406016434

Capponi, A., James, M. R., & Lane, S. J. (2016). Gas slug ascent in a stratified magma: Implications of flow organisation and instability for Strombolian eruption dynamics. *Earth and Planetary Science Letters*, *435*, 159–170. https://doi.org/10.1016/j.epsl.2015.12.028

Capponi, Antonio, Taddeucci, J., Scarlato, P., & Palladino, D. M. (2016). Recycled ejecta modulating Strombolian explosions. *Bulletin of Volcanology*, *78*(2), 1–13. https://doi.org/10.1007/s00445-016-1001-z

Carapezza, M. L., Inguaggiato, S., Brusca, L., & Longo, M. (2004). Geochemical precursors of the activity of an open-conduit volcano: The Stromboli 2002-2003 eruptive events. *Geophysical Research Letters*, *31*(7), 1–4. https://doi.org/10.1029/2004GL019614

Carey, R. J., Manga, M., Degruyter, W., Swanson, D., Houghton, B., Orr, T., & Patrick, M. (2012). Externally triggered renewed bubble nucleation in basaltic magma: The 12 October 2008 eruption at Halemaumau Overlook vent, Klauea, Hawai'i, USA. *Journal of Geophysical Research B: Solid Earth*, *117*(11), 1–10. https://doi.org/10.1029/2012JB009496

Carlos, W. G., Gross, J. E., Jamil, S., Dela Cruz, C. S., Damby, D., & Tam, E. (2018). Volcanic Eruptions and Threats to Respiratory Health. *American Journal of Respiratory and Critical Care Medicine*, *197*(12), P21–P22. https://doi.org/10.1164/rccm.19712P21

Cashman, Katharine, & Rust, A. (2016). Introduction. In *Volcanic Ash* (pp. 5–22). Elsevier. https://doi.org/10.1016/B978-0-08-100405-0.00002-1

Cashman, K. V. (1988). Crystallization of Mount St. Helens 1980-1986 dacite: A quantitative textural approach. *Bulletin of Volcanology*, *50*(3), 194–209. https://doi.org/10.1007/BF01079682

Cashman, Katharine V. (1993). Relationship between plagioclase crystallization and cooling rate in basaltic melts. *Contributions to Mineralogy and Petrology*, *113*(1), 126–142. https://doi.org/10.1007/BF00320836

Cashman, Katharine V., Sparks, R. S. J., & Blundy, J. D. (2017). Vertically extensive and unstable magmatic systems: A unified view of igneous processes. *Science*, *355*(6331). https://doi.org/10.1126/science.aag3055

Cashman, Katharine V, & Scheu, B. (2015). Magmatic Fragmentation. In *The Encyclopedia of Volcanoes* (Second Edi, pp. 459–471). Elsevier. https://doi.org/10.1016/B978-0-12-385938-9.00025-0

Cassidy, M., Manga, M., Cashman, K., & Bachmann, O. (2018). Controls on explosive-effusive volcanic eruption styles. *Nature Communications*, *9*(1). https://doi.org/10.1038/s41467-018-05293-3

Catry, T. (2011). Magma Injections and Destabilization of basaltic volcanoes: a numerical study.

Charvis, P., Laesanpura, A., Gallart, J., Hirn, A., Lépine, J.-C., de Voogd, B., … Pontoise, B. (1999). Spatial distribution of hotspot material added to the lithosphere under La Réunion, from wide-angle seismic data. *Journal of Geophysical Research: Solid Earth*, *104*(B2), 2875–2893. https://doi.org/10.1029/98jb02841

Chevrel, M. O., Harris, A. J. L., James, M. R., Calabrò, L., Gurioli, L., & Pinkerton, H. (2018). The viscosity of pāhoehoe lava: In situ syn-eruptive measurements from Kilauea, Hawaii. *Earth and Planetary Science Letters*, *493*, 161–171. https://doi.org/10.1016/j.epsl.2018.04.028

Chouet, B., Dawson, P., Ohminato, T., Martini, M., Saccorotti, G., Giudicepietro, F., … Scarpa, R. (2003). Source mechanisms of explosions at Stromboli Volcano, Italy, determined from moment-tensor inversions of very-long-period data. *Journal of Geophysical Research: Solid Earth*, *108*(B1), ESE 7-1-ESE 7-25. https://doi.org/10.1029/2002jb001919

Cimarelli, C., Costa, A., Mueller, S., & Mader, H. M. (2011). Rheology of magmas with bimodal crystal size and shape distributions: Insights from analog experiments. *Geochemistry, Geophysics, Geosystems*, *12*(7), 1–14. https://doi.org/10.1029/2011GC003606

Cimarelli, C., Di Traglia, F., & Taddeucci, J. (2010). Basaltic scoria textures from a zoned conduit as precursors to violent Strombolian activity. *Geology*, *38*(5), 439–442. https://doi.org/10.1130/G30720.1

Cioni, R., D'Oriano, C., & Bertagnini, A. (2008). Fingerprinting ash deposits of small scale eruptions by their physical and textural features. *Journal of Volcanology and Geothermal Research*, *177*(1), 277–287. https://doi.org/10.1016/j.jvolgeores.2008.06.003

Cioni, R., Pistolesi, M., Bertagnini, A., Bonadonna, C., Hoskuldsson, A., & Scateni, B. (2014). Insights into the dynamics and evolution of the 2010 Eyjafjallajökull summit eruption (Iceland) provided by volcanic ash textures. *Earth and Planetary Science Letters*, *394*(May 2010), 111–123. https://doi.org/10.1016/j.epsl.2014.02.051

Class, C., & Goldstein, S. L. (1997). Plume-lithosphere interactions in the ocean basins: constraints from the source mineralogy. *Earth and Planetary Science Letters*, *150*(3–4), 245–260. https://doi.org/10.1016/S0012-821X(97)00089-7

Class, C., Goldstein, S. L., Stute, M., Kurz, M. D., & Schlosser, P. (2005). Grand Comore Island: A well-constrained "low 3He/4He" mantle plume. *Earth and Planetary Science Letters*, *233*(3–4), 391–409. https://doi.org/10.1016/j.epsl.2005.02.029

Claude-Ivanaj, C., Bourdon, B., & Allègre, C. J. (1998). Ra-Th-Sr isotope systematics in Grande Comore Island: A case study of plume-lithosphere interaction. *Earth and Planetary Science Letters*, *164*(1–2), 99–117. https://doi.org/10.1016/S0012-821X(98)00195-2

Coffin, M. F., & Rabinowitz, P. D. (1987). Reconstruction of Madagascar and Africa: Evidence from the Davie Fracture Zone and Western Somali Basin. *Journal of Geophysical Research*, *92*(B9), 9385. https://doi.org/10.1029/JB092iB09p09385

Colò, L., Ripepe, M., Baker, D. R., & Polacci, M. (2010). Magma vesiculation and infrasonic activity at Stromboli open conduit volcano. *Earth and Planetary Science Letters*, *292*(3–4), 274–280. https://doi.org/10.1016/j.epsl.2010.01.018

Colombier, M., Gurioli, L., Druitt, T. H., Shea, T., Boivin, P., Miallier, D., & Cluzel, N. (2017). Textural evolution of magma during the 9.4-ka trachytic explosive eruption at Kilian Volcano, Chaîne des Puys, France. *Bulletin of Volcanology*, *79*(2), 17. https://doi.org/10.1007/s00445-017-1099-7

Colombier, Mathieu, Wadsworth, F. B., Gurioli, L., Scheu, B., Kueppers, U., Di Muro, A., & Dingwell, D. B. (2017). The evolution of pore connectivity in volcanic rocks. *Earth and Planetary Science Letters*, *462*, 99–109. https://doi.org/10.1016/j.epsl.2017.01.011

Connor, C., Bebbington, M., & Marzocchi, W. (2015). *Probabilistic Volcanic Hazard Assessment*. *The Encyclopedia of Volcanoes* (Second Edition). Elsevier Inc. https://doi.org/10.1016/b978-0-12-385938-9.00051-1

Coppola, D., & Cigolini, C. (2013). Thermal regimes and effusive trends at Nyamuragira volcano (DRC) from MODIS infrared data. *Bulletin of Volcanology*, *75*(8), 744. https://doi.org/10.1007/s00445-013-0744-z

Coppola, D., Di Muro, A., Peltier, A., Villeneuve, N., Ferrazzini, V., Favalli, M., … Aiuppa, A. (2017). Shallow system rejuvenation and magma discharge trends at Piton de la Fournaise volcano (La Réunion Island). *Earth and Planetary Science Letters*, *463*(463), 13–24. https://doi.org/10.1016/j.epsl.2017.01.024

Coppola, D., Laiolo, M., Cigolini, C., Donne, D. D., & Ripepe, M. (2016). Enhanced volcanic hot-spot detection using MODIS IR data: results from the MIROVA system. *Geological Society, London, Special Publications*, *426*(1), 181–205. https://doi.org/10.1144/SP426.5

Coppola, D., Piscopo, D., Staudacher, T., & Cigolini, C. (2009). Lava discharge rate and effusive pattern at Piton de la Fournaise from MODIS data. *Journal of Volcanology and Geothermal Research*, *184*(1–2), 174–192. https://doi.org/10.1016/j.jvolgeores.2008.11.031

Corsaro, R.A., Andronico, D., Behncke, B., Branca, S., Caltabiano, T., Ciancitto, F., … Spata, G. (2017). Monitoring the December 2015 summit eruptions of Mt. Etna (Italy): Implications on eruptive dynamics. *Journal of Volcanology and Geothermal Research*, *341*(December 2015), 53–69. https://doi.org/10.1016/j.jvolgeores.2017.04.018

Corsaro, Rosa Anna, & Pompilio, M. (2004). Buoyancy-controlled eruption of magmas at Mt Etna. *Terra Nova*, *16*(1), 16–22. https://doi.org/10.1046/j.1365-3121.2003.00520.x

Costantini, L., Houghton, B. F., & Bonadonna, C. (2010). Constraints on eruption dynamics of basaltic explosive activity derived from chemical and microtextural study: The example of the Fontana Lapilli Plinian eruption, Nicaragua. *Journal of Volcanology and Geothermal Research*, *189*(3–4), 207–224. https://doi.org/10.1016/j.jvolgeores.2009.11.008

Courtillot, V., Besse, J., Vandamme, D., Montigny, R., Jaeger, J. J., & Cappetta, H. (1986). Deccan flood basalts at the Cretaceous/Tertiary boundary? *Earth and Planetary Science Letters*, *80*(3–4), 361–374. https://doi.org/10.1016/0012-821X(86)90118-4

Courtillot, V., Davaille, A., Besse, J., & Stock, J. (2003). Three distinct types of hotspots in the Earth's mantle. *Earth and Planetary Science Letters*, *205*(3–4), 295–308. https://doi.org/10.1016/S0012-821X(02)01048-8

D

D'Oriano, C., Bertagnini, A., Cioni, R., & Pompilio, M. (2015). Identifying recycled ash in basaltic eruptions. *Scientific Reports*, *4*(1), 5851. https://doi.org/10.1038/srep05851

D'Oriano, C., Bertagnini, A., & Pompilio, M. (2011). Ash erupted during normal activity at Stromboli (Aeolian Islands, Italy) raises questions on how the feeding system works. *Bulletin of Volcanology*, *73*(5), 471–477. https://doi.org/10.1007/s00445-010-0425-0

Damby, D. E., Murphy, F. A., Horwell, C. J., Raftis, J., & Donaldson, K. (2016). The in vitro respiratory toxicity of cristobalite-bearing volcanic ash. *Environmental Research*, *145*, 74–84. https://doi.org/10.1016/j.envres.2015.11.020

De Voogd, B., Palomé, S. P., Hirn, A., Charvis, P., Gallart, J., Rousset, D., … Perroud, H. (1999). Vertical movements and material transport during hotspot activity: Seismic reflection profiling offshore La Réunion. *Journal of Geophysical Research: Solid Earth*, *104*(B2), 2855–2874. https://doi.org/10.1029/98JB02842

Debeuf, D. (2004). *Étude de l'évolution volcano-structurale et magmatique de Mayotte (archipel des Comores, océan Indien).*

Del Bello, E., Lane, S. J., James, M. R., Llewellin, E. W., Taddeucci, J., Scarlato, P., & Capponi, A. (2015). Viscous plugging can enhance and modulate explosivity of strombolian eruptions. *Earth and Planetary Science Letters*, *423*, 210–218. https://doi.org/10.1016/j.epsl.2015.04.034

Dellino, P., Gudmundsson, M. T., Larsen, G., Mele, D., Stevenson, J. A., Thordarson, T., & Zimanowski, B. (2012). Ash from the Eyjafjallajökull eruption (Iceland): Fragmentation processes and aerodynamic behavior. *Journal of Geophysical Research: Solid Earth*, *117*(B9), 1–10. https://doi.org/10.1029/2011JB008726

Di Muro, A., Metrich, N., Vergani, D., Rosi, M., Armienti, P., Fougeroux, T., … Civetta, L. (2014). The Shallow Plumbing System of Piton de la Fournaise Volcano (La Reunion Island, Indian Ocean) Revealed by the Major 2007 Caldera-Forming Eruption. *Journal of Petrology*, *55*(7), 1287–1315. https://doi.org/10.1093/petrology/egu025

Di Muro, Andrea, Métrich, N., Allard, P., Aiuppa, A., Burton, M., Galle, B., & Staudacher, T. (2016). Magma Degassing at Piton de la Fournaise Volcano. In *Active Volcanoes of the Southwest Indian Ocean. Active Volcanoes of the World.* (pp. 203–222). https://doi.org/10.1007/978-3-642-31395-0_12

Di Muro, Andrea, Staudacher, T., Ferrazzini, V., Métrich, N., Besson, P., Garofalo, C., & Villemant, B. (2015). Shallow Magma Storage at Piton de la Fournaise Volcano After 2007 Summit Caldera Collapse Tracked in Pele's Hairs. In *American Geophysical Union Monograph* (Vol. 208, pp. 189–212). https://doi.org/10.1002/9781118872079.ch9

Di Traglia, F., Cimarelli, C., de Rita, D., & Gimeno Torrente, D. (2009). Changing eruptive styles in basaltic explosive volcanism: Examples from Croscat complex scoria cone, Garrotxa Volcanic Field (NE Iberian Peninsula). *Journal of Volcanology and Geothermal Research*, *180*(2–4), 89–109. https://doi.org/10.1016/j.jvolgeores.2008.10.020

Duffield, W. A., Gibson, E. K., & Heiken, G. (1977). Some characteristics of Pele's hair. In *J. Res. US Geol. Surv* (pp. 93–101).

Duncan, R. A. (1990). The Volanic record of the Reunion Hotspot. *Proc., Scientific Results, ODP, Leg 115, Mascarene Plateau*, *115*, 3–10.

Duncan, R. A., Backman, J., Peterson, L., & The Shipboard Scientific Party. (1989). Reunion hotspot activitity through tertiary time: Initial results from the ocean drilling program, leg 115. *Journal of Volcanology and Geothermal Research*, *36*(1–3), 193–198. https://doi.org/10.1016/0377-0273(89)90013-9

Dvorak, J. J. (1992). Mechanism of explosive eruptions of Kilauea Volcano, Hawaii. *Bulletin of Volcanology*, *54*(8), 638–645. https://doi.org/10.1007/BF00430777

E

Edwards, M.J., & Pioli, L. (2019). Magma and tephra characteristics for the 17–25 May 2016 Mt Etna eruption. *Data in Brief*, *22*, 65–71. https://doi.org/10.1016/j.dib.2018.11.093

Edwards, Matthew John, Pioli, L., Andronico, D., Scollo, S., Ferrari, F., & Cristaldi, A. (2018). Shallow factors controlling the explosivity of basaltic magmas: The 17–25 May 2016 eruption of Etna Volcano (Italy). *Journal of Volcanology and Geothermal Research*, *357*, 425–436. https://doi.org/10.1016/j.jvolgeores.2018.05.015

Emerick, C. M. (1985). Age progressive volcanism in the Comores Archipelago and northern Madagascar.

Emerick, C. M., & Duncan, R. A. (1982). Age progressive volcanism in the Comores Archipelago, western Indian Ocean and implications for Somali plate tectonics. *Earth and Planetary Science Letters*, *60*(3), 415–428. https://doi.org/10.1016/0012-821X(82)90077-2

Engelder, J. (1974). Cataclasis and the Generation of Fault Gouge. *Geological Society of America Bulletin*, *85*(10), 1515. https://doi.org/10.1130/0016-7606(1974)85<1515:CATGOF>2.0.CO;2

Eshel, G., Levy, G. J., Mingelgrin, U., & Singer, M. J. (2004). Critical evaluation of the use of laser diffraction for particle-size distribution analysis. *Soil Science Society of America Journal*, *68*(3), 736–743. https://doi.org/10.2136/sssaj2004.7360

Eychenne, J., Houghton, B. F., Swanson, D. A., Carey, R. J., & Swavely, L. (2015). Dynamics of an open basaltic magma system: The 2008 activity of the Halema'uma'u Overlook vent, Kīlauea Caldera. *Earth and Planetary Science Letters*, *409*, 49–60. https://doi.org/10.1016/j.epsl.2014.10.045

Eychenne, J., & Le Pennec, J.-L. (2012). Sigmoidal particle density distribution in a subplinian scoria fall deposit. *Bulletin of Volcanology*, *74*(10), 2243–2249. https://doi.org/10.1007/s00445-012-0671-4

F

Famin, V., Welsch, B., Okumura, S., Bachèlery, P., & Nakashima, S. (2009). Three differentiation stages of a single magma at Piton de la Fournaise volcano (Reunion hot spot). *Geochemistry, Geophysics, Geosystems*, *10*(1), 1–18. https://doi.org/10.1029/2008GC002015

Fenner, C. (1929). The crystallization of basalts.

Ferguson, D. J., Gonnermann, H. M., Ruprecht, P., Plank, T., Hauri, E. H., Houghton, B. F., & Swanson, D. A. (2016). Magma decompression rates during explosive eruptions of Kīlauea volcano, Hawaii, recorded by melt embayments. *Bulletin of Volcanology*, *78*(10). https://doi.org/10.1007/s00445-016-1064-x

Ferlito, C., Viccaro, M., & Cristofolini, R. (2009). Volatile-rich magma injection into the feeding system during the 2001 eruption of Mt. Etna (Italy): Its role on explosive activity and change in rheology of lavas. *Bulletin of Volcanology*, *71*(10), 1149–1158. https://doi.org/10.1007/s00445-009-0290-x

Fevre, Y. (2013). *Mécanismes et vitesses d'érosion à l'échelle géologique sur une île volcanique jeune à relief élevé - La Réunion (Océan Indien).*

Fisk, M. R., Duncan, R. A., Baxter, A. N., Greenough, J. D., Hargraves, R. B., & Tatsumi, Y. (1989). Reunion hotspot magma chemistry over the past 65 my: results from Leg 115 of the Ocean Drilling Program. *Geology*, *17*(10), 934–937. https://doi.org/10.1130/0091-7613(1989)017<0934:RHMCOT>2.3.CO;2

Fisk, M. R., Upton, B. G. J., Ford, C. E., & White, W. M. (1988). Geochemical and experimental study of the genesis of magmas of Reunion Island, Indian Ocean. *Journal of Geophysical Research: Solid Earth*, *93*(B5), 4933–4950. https://doi.org/10.1029/JB093iB05p04933

Flower, M. F. J., & Strong, D. F. (1969). The significance of sandstone inclusions in lavas of the comores archipelago. *Earth and Planetary Science Letters*, *7*(1), 47–50. https://doi.org/10.1016/0012-821X(69)90010-7

Fontaine, F. R., Roult, G., Hejrani, B., Michon, L., Ferrazzini, V., Barruol, G., … Massin, F. (2019). Very- and ultra-long-period seismic signals prior to and during caldera formation on La Réunion Island. *Scientific Reports*, *9*(1), 8068. https://doi.org/10.1038/s41598-019-44439-1

Fontaine, Fabrice R., Barruol, G., Tkalčić, H., Wölbern, I., Rümpker, G., Bodin, T., & Haugmard, M. (2015). Crustal and uppermost mantle structure variation beneath La Réunion hotspot track. *Geophysical Journal International*, *203*(1), 107–126. https://doi.org/10.1093/gji/ggv279

Fontaine, Fabrice R., Roult, G., Michon, L., Barruol, G., & Muro, A. Di. (2014). The 2007 eruptions and caldera collapse of the Piton de la Fournaise volcano (La Réunion Island) from tilt analysis at a single very broadband seismic station. *Geophysical Research Letters*, *41*(8), 2803–2811. https://doi.org/10.1002/2014GL059691

Formenti, Y., & Druitt, T. . (2003). Vesicle connectivity in pyroclasts and implications for the fluidisation of fountain-collapse pyroclastic flows, Montserrat (West Indies). *Earth and Planetary Science Letters*, *214*(3–4), 561–574. https://doi.org/10.1016/S0012-821X(03)00386-8

Freret-lorgeril, V. (2019). *Le terme source des panaches de téphras : applications radars aux volcans Etna et Stromboli (Italie)*.

Froger, J. L., Famin, V., Cayol, V., Augier, A., Michon, L., & Lénat, J. F. (2015). Time-dependent displacements during and after the April 2007 eruption of Piton de la Fournaise, revealed by interferometric data. *Journal of Volcanology and Geothermal Research*, *296*(April 2007), 55–68. https://doi.org/10.1016/j.jvolgeores.2015.02.014

Fukushima, Y., Cayol, V., Durand, P., & Massonnet, D. (2010). Evolution of magma conduits during the 1998-2000 eruptions of Piton de la Fournaise volcano, Réunion Island. *Journal of Geophysical Research: Solid Earth*, *115*(10), 1–21. https://doi.org/10.1029/2009JB007023

G

Gailler, L. S., & Lénat, J. F. (2010). Three-dimensional structure of the submarine flanks of La Réunion inferred from geophysical data. *Journal of Geophysical Research: Solid Earth*, *115*(12), 1–27. https://doi.org/10.1029/2009JB007193

Gailler, L. S., & Lénat, J. F. (2012). Internal architecture of La Réunion (Indian Ocean) inferred from geophysical data. *Journal of Volcanology and Geothermal Research*, *221–222*, 83–98. https://doi.org/10.1016/j.jvolgeores.2012.01.015

Gailler, L. S., Lénat, J. F., Lambert, M., Levieux, G., Villeneuve, N., & Froger, J. L. (2009). Gravity structure of Piton de la Fournaise volcano and inferred mass transfer during the 2007 crisis. *Journal of Volcanology and Geothermal Research*, *184*(1–2), 31–48. https://doi.org/10.1016/j.jvolgeores.2009.01.024

Gallart, J., Driad, L., Charvis, P., Sapin, M., Hirn, A., Diaz, J., … Sachpazi, M. (1999). Perturbation to the lithosphere along the hotspot track of La Réunion from an offshore-onshore seismic transect. *Journal of Geophysical Research: Solid Earth*, *104*(B2), 2895–2908. https://doi.org/10.1029/98JB02840

Galle, B., Johansson, M., Rivera, C., Zhang, Y., Kihlman, M., Kern, C., … Hidalgo, S. (2010). Network for Observation of Volcanic and Atmospheric Change (NOVAC)—A global network for volcanic gas monitoring: Network layout and instrument description. *Journal of Geophysical Research*, *115*(D5), D05304. https://doi.org/10.1029/2009JD011823

Gardner, J. E., Thomas, R. M. E., Jaupart, C., & Tait, S. (1996). Fragmentation of magma during Plinian volcanic eruptions. *Bulletin of Volcanology*, *58*(2–3), 144–162. https://doi.org/10.1007/s004450050132

Gaudin, D., Taddeucci, J., Scarlato, P., del Bello, E., Ricci, T., Orr, T., … Bucci, A. (2017). Integrating puffing and explosions in a general scheme for Strombolian-style activity. *Journal of Geophysical Research: Solid Earth*, *122*(3), 1860–1875. https://doi.org/10.1002/2016JB013707

Genareau, K., Wallace, K. L., Gharghabi, P., & Gafford, J. (2019). Lightning Effects on the Grain Size Distribution of Volcanic Ash. *Geophysical Research Letters*, *46*(6), 3133–3141. https://doi.org/10.1029/2018GL081298

Gerlach, T. M. (1986). Exsolution of H2O, CO2 , and S during eruptive episodes at Kilauea Volcano, Hawaii. *Journal of Geophysical Research: Solid Earth*, *91*(B12), 12177–12185. https://doi.org/10.1029/JB091iB12p12177

Ghiorso, M. S., & Sack, R. O. (1995). Chemical mass transfer in magmatic processes IV. A revised and internally consistent thermodynamic model for the interpolation and extrapolation of liquid-solid equilibria in magmatic systems at elevated temperatures and pressures. *Contributions to Mineralogy and Petrology*, *119*(2–3), 197–212. https://doi.org/10.1007/BF00307281

Giachetti, T., Burgisser, A., Arbaret, L., Druitt, T. H., & Kelfoun, K. (2011). Quantitative textural analysis of Vulcanian pyroclasts (Montserrat) using multi-scale X-ray computed microtomography: Comparison with results from 2D image analysis. *Bulletin of Volcanology*, *73*(9), 1295–1309. https://doi.org/10.1007/s00445-011-0472-1

Gilbert, J. S., & Lane, S. J. (1994). The origin of accretionary lapilli. *Bulletin of Volcanology*, *56*(5), 398–411. https://doi.org/10.1007/BF00326465

Gillot, P. Y., & Nativel, P. (1989). Eruptive history of the Piton de la Fournaise volcano, Reunion Island, Indian Ocean. *Journal of Volcanology and Geothermal Research*, *36*(1–3), 53–65. https://doi.org/10.1016/0377-0273(89)90005-X

Gillot, Pierre Yves, Lefèvre, J. C., & Nativel, P. E. (1994). Model for the structural evolution of the volcanoes of Réunion Island. *Earth and Planetary Science Letters*, *122*(3–4), 291–302. https://doi.org/10.1016/0012-821X(94)90003-5

Giordano, D., Nichols, A. R. L., & Dingwell, D. B. (2005). Glass transition temperatures of natural hydrous melts: A relationship with shear viscosity and implications for the welding process. *Journal of Volcanology and Geothermal Research*, *142*(1-2 SPEC. ISS.), 105–118. https://doi.org/10.1016/j.jvolgeores.2004.10.015

Giordano, Daniele, Russell, J. K., & Dingwell, D. B. (2008). Viscosity of magmatic liquids: A model. *Earth and Planetary Science Letters*, *271*(1–4), 123–134. https://doi.org/10.1016/j.epsl.2008.03.038

Gislason, S. R., Hassenkam, T., Nedel, S., Bovet, N., Eiriksdottir, E. S., Alfredsson, H. A., … Stipp, S. L. S. (2011). Characterization of Eyjafjallajökull volcanic ash particles and a protocol for rapid risk assessment. *Proceedings of the National Academy of Sciences of the United States of America*, *108*(18), 7307–7312. https://doi.org/10.1073/pnas.1015053108

Gonnermann, H. M., & Manga, M. (2003). Explosive volcanism may not be an inevitable consequence of magma fragmentation. *Nature*, *426*(6965), 432–435. https://doi.org/10.1038/nature02138

Gonnermann, H. M., Manga, M., & Fagents, S. A. (2014). Dynamics of magma ascent in the volcanic conduit. In T. K. P. Gregg & R. M. C. Lopes (Eds.), *Modeling Volcanic Processes* (Vol. 99, pp. 55–84). Cambridge: Cambridge University Press. https://doi.org/10.1017/CBO9781139021562.004

Gouhier, M, Guéhenneux, Y., Labazuy, P., Cacault, P., Decriem, J., & Rivet, S. (2016). HOTVOLC: a web-based monitoring system for volcanic hot spots. *Geological Society, London, Special Publications*, *426*(1), 223–241. https://doi.org/10.1144/SP426.31

Gouhier, Mathieu, Harris, A., Calvari, S., Labazuy, P., Guéhenneux, Y., Donnadieu, F., & Valade, S. (2012). Lava discharge during Etna's January 2011 fire fountain tracked using MSG-SEVIRI. *Bulletin of Volcanology*, *74*(4), 787–793. https://doi.org/10.1007/s00445-011-0572-y

Graham, D., Lupton, J., Albarède, F., & Condomines, M. (1990). Extreme temporal homogeneity of helium isotopes at Piton de la Fournaise, Réunion Island. *Nature*, *347*(6293), 545–548. https://doi.org/10.1038/347545a0

Guéhenneux, Y., Gouhier, M., & Labazuy, P. (2015). Improved space borne detection of volcanic ash for real-time monitoring using 3-Band method. *Journal of Volcanology and Geothermal Research*, *293*, 25–45. https://doi.org/10.1016/j.jvolgeores.2015.01.005

Gurioli, L., Andronico, D., Bachelery, P., Balcone-Boissard, H., Battaglia, J., Boudon, G., … Thordarson, T. (2015). MeMoVolc consensual document: a review of cross-disciplinary approaches to characterizing small explosive magmatic eruptions. *Bulletin of Volcanology*, *77*(6), 49. https://doi.org/10.1007/s00445-015-0935-x

Gurioli, L., Colo', L., Bollasina, A. J., Harris, A. J. L., Whittington, A., & Ripepe, M. (2014). Dynamics of Strombolian explosions: Inferences from field and laboratory studies of erupted bombs from Stromboli volcano. *Journal of Geophysical Research: Solid Earth*, *119*(1), 319–345. https://doi.org/10.1002/2013JB010355

Gurioli, L., Di Muro, A., Vlastelic, I., Bachèlery, P., Harris, A. J. L., Thivet, S., … Delage, E. (2016). Les apports d'une vision intégrée des données volcanologiques (DynVolc). In *Des Volcans aux Nuages, Revue d'Auvergne*.

Gurioli, L., Harris, A. J. L., Colò, L., Bernard, J., Favalli, M., Ripepe, M., & Andronico, D. (2013). Classification, landing distribution, and associated flight parameters for a bomb field emplaced during a single major explosion at Stromboli, Italy. *Geology*, *41*(5), 559–562. https://doi.org/10.1130/G33967.1

Gurioli, L., Harris, A. J. L., Houghton, B. F., Polacci, M., & Ripepe, M. (2008). Textural and geophysical characterization of explosive basaltic activity at Villarrica volcano. *Journal of Geophysical Research: Solid Earth*, *113*(8), 1–16. https://doi.org/10.1029/2007JB005328

Gurioli, L. (2017). DynVolc Database. https://doi.org/http://dx.doi.org/10.25519/DYNVOLC-Database

Gurioli, Lucia, Di Muro, A., Vlastélic, I., Moune, S., Thivet, S., Valer, M., … Hénot, J.-M. (2018). Integrating field, textural, and geochemical monitoring to track eruption triggers and dynamics: a case study from Piton de la Fournaise. *Solid Earth*, *9*(2), 431–455. https://doi.org/10.5194/se-9-431-2018

H

Harris, A., Chevrel, M., Coppola, D., Ramsey, M., Hrysiewicz, A., Thivet, S., … Gurioli, L. (2019). Validation of an integrated satellite-data-driven response to an effusive crisis: the April–May 2018 eruption of Piton de la Fournaise. *Annals of GeophysicsAnnals of Geophysics*, *61*(Vol 61 (2018)). https://doi.org/10.4401/ag-7972

Harris, A. J. L., Villeneuve, N., Di Muro, A., Ferrazzini, V., Peltier, A., Coppola, D., … Arellano, S. (2017). Effusive crises at Piton de la Fournaise 2014–2015: a review of a multi-national response model. *Journal of Applied Volcanology*, *6*(1), 11. https://doi.org/10.1186/s13617-017-0062-9

Harris, A., & Ripepe, M. (2007). Synergy of multiple geophysical approaches to unravel explosive eruption conduit and source dynamics – A case study from Stromboli. *Geochemistry*, *67*(1), 1–35. https://doi.org/10.1016/j.chemer.2007.01.003

Harris, Andrew J. L., Dehn, J., & Calvari, S. (2007). Lava effusion rate definition and measurement: a review. *Bulletin of Volcanology*, *70*(1), 1–22. https://doi.org/10.1007/s00445-007-0120-y

Harris, Andrew J.L., & Rowland, S. K. (2015). *Lava Flows and Rheology*. *The Encyclopedia of Volcanoes* (Second Edition). Elsevier Inc. https://doi.org/10.1016/b978-0-12-385938-9.00017-1

Head, J. W., & Wilson, L. (1987). Lava fountain heights at Pu'u 'O'o, Kilauea, Hawaii: Indicators of amount and variations of exsolved magma volatiles. *Journal of Geophysical Research: Solid Earth*, *92*(B13), 13715–13719. https://doi.org/10.1029/JB092iB13p13715

Head, J. W., & Wilson, L. (1989). Basaltic pyroclastic eruptions: Influence of gas-release patterns and volume fluxes on fountain structure, and the formation of cinder cones, spatter cones, rootless flows, lava ponds and lava flows. *Journal of Volcanology and Geothermal Research*, *37*(3–4), 261–271. https://doi.org/10.1016/0377-0273(89)90083-8

Heiken, G. (1974). Atlas of Volcanic Ash. *Smithsonian Contributions to the Earth Sciences*, *no. 12*(12), 1–101. https://doi.org/10.5479/si.00810274.12.1

Heilbronner, R., & Keulen, N. (2006). Grain size and grain shape analysis of fault rocks. *Tectonophysics*, *427*(1–4), 199–216. https://doi.org/10.1016/j.tecto.2006.05.020

Helz, R. T., & Thornber, C. R. (1987). Geothermometry of Kilauea Iki lava lake, Hawaii. *Bulletin of Volcanology*, *49*(5), 651–668. https://doi.org/10.1007/BF01080357

Hibert, C., Mangeney, A., Polacci, M., Muro, A. Di, Vergniolle, S., Ferrazzini, V., … Lauret, F. (2015). Toward continuous quantification of lava extrusion rate: Results from the multidisciplinary analysis of the 2 January 2010 eruption of Piton de la Fournaise volcano, La Réunion. *Journal of Geophysical Research: Solid Earth*, *120*(5), 3026–3047. https://doi.org/10.1002/2014JB011769

Higgins, Michael D. (2000). Measurement of crystal size distributions. *American Mineralogist*, *85*(9), 1105–1116. https://doi.org/10.2138/am-2000-8-901

Higgins, Michael D. (2002). Closure in crystal size distributions (CSD), verification of CSD calculations, and the significance of CSD fans. *American Mineralogist*, *87*(1), 171–175. https://doi.org/10.2138/am-2002-0118

Higgins, Michael Denis. (2006). *Quantitative Textural Measurements in Igneous and Metamorphic Petrology*. Cambridge: Cambridge University Press. https://doi.org/10.1017/CBO9780511535574

Holt, S. J., Carey, R. J., Houghton, B. F., Orr, T., McPhie, J., & Feig, S. (2019). Eruption and fountaining dynamics of selected 1985–1986 high fountaining episodes at Kīlauea volcano, Hawai'i, from quantitative vesicle microtexture analysis. *Journal of Volcanology and Geothermal Research*, *369*, 21–34. https://doi.org/10.1016/j.jvolgeores.2018.11.011

Horwell, C. J. (2007). Grain-size analysis of volcanic ash for the rapid assessment of respiratory health hazard. *Journal of Environmental Monitoring*, *9*(10), 1107–1115. https://doi.org/10.1039/b710583p

Horwell, C. J., & Baxter, P. J. (2006). The respiratory health hazards of volcanic ash: A review for volcanic risk mitigation. *Bulletin of Volcanology*, *69*(1), 1–24. https://doi.org/10.1007/s00445-006-0052-y

Houghton, B. (2015). *Part IV Explosive Volcanism*. *The Encyclopedia of Volcanoes* (Second Edition). Elsevier Inc. https://doi.org/10.1016/b978-0-12-385938-9.02006-x

Houghton, B. F., & Gonnermann, H. M. (2008). Basaltic explosive volcanism: Constraints from deposits and models. *Geochemistry*, *68*(2), 117–140. https://doi.org/10.1016/j.chemer.2008.04.002

Houghton, B. F., Taddeucci, J., Andronico, D., Gonnermann, H. M., Pistolesi, M., Patrick, M. R., … Scarlato, P. (2016). Stronger or longer: Discriminating between Hawaiian and Strombolian eruption styles. *Geology*, *44*(2), 163–166. https://doi.org/10.1130/G37423.1

Houghton, B. F., & Wilson, C. J. N. (1989). A vesicularity index for pyroclastic deposits. *Bulletin of Volcanology*, *51*(6), 451–462. https://doi.org/10.1007/BF01078811

Houghton, B. F., Wilson, C. J. N., Del Carlo, P., Coltelli, M., Sable, J. E., & Carey, R. (2004). The influence of conduit processes on changes in style of basaltic Plinian eruptions: Tarawera 1886 and Etna 122 BC. *Journal of Volcanology and Geothermal Research*, *137*(1–3), 1–14. https://doi.org/10.1016/j.jvolgeores.2004.05.009

Hugoulin, F. (1860). Dernière éruption du volcan de l'île de la Réunion (19 mars 1860), 483–487.

J

James, M. R., Lane, S. J., Chouet, B., & Gilbert, J. S. (2004). Pressure changes associated with the ascent and bursting of gas slugs in liquid-filled vertical and inclined conduits. *Journal of Volcanology and Geothermal Research*, *129*(1–3), 61–82. https://doi.org/10.1016/S0377-0273(03)00232-4

Jaupart, C., & Vergniolle, S. (1988). Laboratory models of Hawaiian and Strombolian eruptions. *Nature*, *331*(6151), 58–60. https://doi.org/10.1038/331058a0

Jaupart, C., & Vergniolle, S. (1989). *The generation and collapse of a foam layer at the roof of a basaltic magma chamber*. *Journal of Fluid Mechanics* (Vol. 203). https://doi.org/10.1017/S0022112089001497

Jerram, D. A., & Higgins, M. D. (2007). 3D Analysis of Rock Textures: Quantifying Igneous Microstructures. *Elements*, *3*(4), 239–245. https://doi.org/10.2113/gselements.3.4.239

Jha, B., Cueto-Felgueroso, L., & Juanes, R. (2011). Fluid mixing from viscous fingering. *Physical Review Letters*, *106*(19), 1–4. https://doi.org/10.1103/PhysRevLett.106.194502

Jones, T. J., Houghton, B. F., Llewellin, E. W., Parcheta, C. E., & Höltgen, L. (2018). Spatter matters – distinguishing primary (eruptive) and secondary (non-eruptive) spatter deposits. *Scientific Reports*, *8*(1), 9179. https://doi.org/10.1038/s41598-018-27065-1

K

Kawabata, E., Cronin, S. J., Bebbington, M. S., Moufti, M. R. H., El-Masry, N., & Wang, T. (2015). Identifying multiple eruption phases from a compound tephra blanket: an example of the AD1256 Al-Madinah eruption, Saudi Arabia. *Bulletin of Volcanology*, *77*(1), 6. https://doi.org/10.1007/s00445-014-0890-y

Kolzenburg, S., Giordano, D., Giordano, D., Di Muro, A., Di Muro, A., Dingwell, D., & Dingwell, D. (2018). Equilibrium Viscosity and Disequilibrium Rheology of a high Magnesium Basalt from Piton De La Fournaise volcano, La Reunion, Indian Ocean, France. *Annals of Geophysics*, *61*(Vol 61 (2018)). https://doi.org/10.4401/ag-7839

Krumbein, W.C. (1934). Size Frequency Distributions of Sediments. *SEPM Journal of Sedimentary Research*, *Vol. 4*(2). https://doi.org/10.1306/D4268EB9-2B26-11D7-8648000102C1865D

Krumbein, W.C. (1938). Size Frequency Distributions of Sediments and the Normal Phi Curve. *SEPM Journal of Sedimentary Research*, *Vol. 8*(3), 84–90. https://doi.org/10.1306/D4269008-2B26-11D7-8648000102C1865D

Kuo, L. C., & Kirkpatrick, R. J. (1982). Pre-eruption history of phyric basalts from DSDP legs 45 and 46: Evidence from morphology and zoning patterns in plagioclase. *Contributions to Mineralogy and Petrology*, *79*(1), 13–27. https://doi.org/10.1007/BF00376957

L

La Spina, G., Burton, M., & de' Michieli Vitturi, M. (2015). Temperature evolution during magma ascent in basaltic effusive eruptions: A numerical application to Stromboli volcano. *Earth and Planetary Science Letters*, *426*, 89–100. https://doi.org/10.1016/j.epsl.2015.06.015

La Spina, G., Clarke, A. B., de' Michieli Vitturi, M., Burton, M., Allison, C. M., Roggensack, K., & Alfano, F. (2019). Conduit dynamics of highly explosive basaltic eruptions: The 1085 CE Sunset Crater sub-Plinian events. *Journal of Volcanology and Geothermal Research*, *387*, 106658. https://doi.org/10.1016/j.jvolgeores.2019.08.001

Labazuy, P. (1996). Recurrent landslides events on the submarine flank of Piton de la Fournaise volcano (Reunion Island). *Geological Society Special Publication*, *110*(110), 295–306. https://doi.org/10.1144/GSL.SP.1996.110.01.23

Lacroix, A. (1936). *Le Volcan actif de l'île de la Réunion et ses produits*.

Lange, R. A., Frey, H. M., & Hector, J. (2009). A thermodynamic model for the plagioclase-liquid hygrometer/thermometer. *American Mineralogist*, *94*(4), 494–506. https://doi.org/10.2138/am.2009.3011

Latutrie, B., Harris, A., Médard, E., & Gurioli, L. (2017). Eruption and emplacement dynamics of a thick trachytic lava flow of the Sancy volcano (France). *Bulletin of Volcanology*, *79*(1), 4. https://doi.org/10.1007/s00445-016-1084-6

Lautze, N. C., & Houghton, B. F. (2005). Physical mingling of magma and complex eruption dynamics in the shallow conduit at Stromboli volcano, Italy. *Geology*, *33*(5), 425–428. https://doi.org/10.1130/G21325.1

Lautze, N. C., Taddeucci, J., Andronico, D., Cannata, C., Tornetta, L., Scarlato, P., … Lo Castro, M. D. (2012). SEM-based methods for the analysis of basaltic ash from weak explosive activity at Etna in 2006 and the 2007 eruptive crisis at Stromboli. *Physics and Chemistry of the Earth*, *45–46*, 113–127. https://doi.org/10.1016/j.pce.2011.02.001

Lautze, N., Taddeucci, J., Andronico, D., Houghton, B., Niemeijer, A., & Scarlato, P. (2013). Insights into explosion dynamics and the production of ash at Stromboli from samples collected in real-time, October 2009. *Special Paper of the Geological Society of America*, *498*(October 2009), 125–139. https://doi.org/10.1130/2013.2498(08)

Leclaire, L., Bassias, Y., Clocchiatti, M., & Segoufin, J. (1989). The Davie Ridge in the Mozambique channel: a stratigraphic and geodynamic approach. *Comptes Rendus - Academie Des Sciences, Serie II*, *308*(12), 1077–1082.

Leduc, L., Gurioli, L., Harris, A., Colò, L., & Rose-Koga, E. F. (2015). Types and mechanisms of strombolian explosions: characterization of a gas-dominated explosion at Stromboli. *Bulletin of Volcanology*, *77*(1), 8. https://doi.org/10.1007/s00445-014-0888-5

Leibrandt, S., & Le Pennec, J.-L. (2015). Towards fast and routine analyses of volcanic ash morphometry for eruption surveillance applications. *Journal of Volcanology and Geothermal Research*, *297*, 11–27. https://doi.org/10.1016/j.jvolgeores.2015.03.014

Lemoine, A., Bertil, D., Roullé, A., & Briole, P. (2019). The volcano-tectonic crisis of 2018 east of Mayotte, Comoros islands. *Geophys. J. Int*, 1–33.

Lénat, J.-F. (2016). A Brief History of the Observation of the Central Area of Piton de la Fournaise. In *Active volcanoes of the Southwest Indian Ocean: Piton de la Fournaise and Karthala* (pp. 3–21). https://doi.org/10.1007/978-3-642-31395-0_1

Lénat, J.-F., Gibert-Malengreau, B., & Galdéano, A. (2001). A new model for the evolution of the volcanic island of Réunion (Indian Ocean). *Journal of Geophysical Research: Solid Earth*, *106*(B5), 8645–8663. https://doi.org/10.1029/2000JB900448

Lénat, J. F., & Bachèlery, P. (1990). Structure and dynamics of the central zone of Piton de la Fournaise volcano. *Le Volcanisme de La Réunion*, (January), 257–296.

Lénat, J. F., & Labazuy, P. (1990). Morphologies et structures sous-marines de la Réunion. In *Le volcanisme de la Réunion. Monographie.* (pp. 43–74).

Lénat, Jean François, Bachèlery, P., & Peltier, A. (2012). The interplay between collapse structures, hydrothermal systems, and magma intrusions: The case of the central area of Piton de la Fournaise volcano. *Bulletin of Volcanology*, *74*(2), 407–421. https://doi.org/10.1007/s00445-011-0535-3

Lénat, Jean François, Merle, O., & Lespagnol, L. (2009). La réunion: An example of channeled hot spot plume. *Journal of Volcanology and Geothermal Research*, *184*(1–2), 1–13. https://doi.org/10.1016/j.jvolgeores.2008.12.001

Lénat, Jean François, Vincent, P., & Bachélery, P. (1989). The off-shore continuation of an active basaltic volcano: Piton de la Fournaise (Réunion Island, Indian Ocean); structural and geomorphological interpretation from sea beam mapping. *Journal of Volcanology and Geothermal Research*, *36*(1–3). https://doi.org/10.1016/0377-0273(89)90003-6

Lengliné, O., Duputel, Z., & Ferrazzini, V. (2016). Uncovering the hidden signature of a magmatic recharge at Piton de la Fournaise volcano using small earthquakes. *Geophysical Research Letters*, *43*(9), 4255–4262. https://doi.org/10.1002/2016GL068383

Lesne, P., Scaillet, B., Pichavant, M., & Beny, J.-M. (2011). The carbon dioxide solubility in alkali basalts: an experimental study. *Contributions to Mineralogy and Petrology*, *162*(1), 153–168. https://doi.org/10.1007/s00410-010-0585-0

Lindoo, A., Larsen, J. F., Cashman, K. V., Dunn, A. L., & Neill, O. K. (2016). An experimental study of permeability development as a function of crystal-free melt viscosity. *Earth and Planetary Science Letters*, *435*, 45–54. https://doi.org/10.1016/j.epsl.2015.11.035

Lindoo, A., Larsen, J. F., Cashman, K. V., & Oppenheimer, J. (2017). Crystal controls on permeability development and degassing in basaltic andesite magma. *Geology*, *45*(9), 831–834. https://doi.org/10.1130/G39157.1

Liu, E. J., Cashman, K. V., & Rust, A. C. (2015). Optimising shape analysis to quantify volcanic ash morphology. *GeoResJ*, *8*, 14–30. https://doi.org/10.1016/j.grj.2015.09.001

Llewellin, E. W., & Manga, M. (2005). Bubble suspension rheology and implications for conduit flow. *Journal of Volcanology and Geothermal Research*, *143*(1–3), 205–217. https://doi.org/10.1016/j.jvolgeores.2004.09.018

Longpré, M. A., Staudacher, T., & Stix, J. (2007). The November 2002 eruption at Piton de la Fournaise volcano, La Réunion Island: Ground deformation, seismicity, and pit crater collapse. *Bulletin of Volcanology*, *69*(5), 511–525. https://doi.org/10.1007/s00445-006-0087-0

Lormand, C., Zellmer, G. F., Németh, K., Kilgour, G., Mead, S., Palmer, A. S., … Moebis, A. (2018). Weka trainable segmentation plugin in ImageJ: A semi-automatic tool applied to crystal size distributions of microlites in volcanic rocks. *Microscopy and Microanalysis*, *24*(6), 667–675. https://doi.org/10.1017/S1431927618015428

Ludden, J. N. (1978). Magmatic evolution of the basaltic shield volcanoes of Reunion Island. *Journal of Volcanology and Geothermal Research*, *4*(1–2), 171–198. https://doi.org/10.1016/0377-0273(78)90035-5

M

Mader, H. M., Llewellin, E. W., & Mueller, S. P. (2013). The rheology of two-phase magmas: A review and analysis. *Journal of Volcanology and Geothermal Research*, *257*, 135–158. https://doi.org/10.1016/j.jvolgeores.2013.02.014

Maillard, L. (1862). Notes sur l'île dela Réunion (Bourbon).

Malengreau, B., Lénat, J. F., & Froger, J. L. (1999). Structure of Reunion Island (Indian Ocean) inferred from the interpretation of gravity anomalies. *Journal of Volcanology and Geothermal Research*, *88*(3), 131–146. https://doi.org/10.1016/S0377-0273(98)00114-0

Mangan, M., Mastin, L., & Sisson, T. (2004). Gas evolution in eruptive conduits: Combining insights from high temperature and pressure decompression experiments with steady-state flow modeling. *Journal of Volcanology and Geothermal Research*, *129*(1–3), 23–36. https://doi.org/10.1016/S0377-0273(03)00230-0

Mangan, M. T., Cashman, K. V., & Newman, S. (1993). Vesiculation of basaltic magma during eruption. *Geology*, *21*(2), 157–160. https://doi.org/10.1130/0091-7613(1993)021<0157:VOBMDE>2.3.CO;2

Mangan, Margaret T, & Cashman, K. V. (1996). The structure of basaltic scoria and reticulite and inferences for vesiculation, foam formation, and fragmentation in lava fountains. *Journal of Volcanology and Geothermal Research*, *73*(1–2), 1–18. https://doi.org/10.1016/0377-0273(96)00018-2

Maria, A., & Carey, S. (2007). Quantitative discrimination of magma fragmentation and pyroclastic transport processes using the fractal spectrum technique. *Journal of Volcanology and Geothermal Research*, *161*(3), 234–246. https://doi.org/10.1016/j.jvolgeores.2006.12.006

Maron, S. H., & Pierce, P. E. (1956). Application of ree-eyring generalized flow theory to suspensions of spherical particles. *Journal of Colloid Science*, *11*(1), 80–95. https://doi.org/10.1016/0095-8522(56)90023-X

Marone, C., & Scholz, C. H. (1989). Particle-size distribution and microstructures within simulated fault gouge. *Journal of Structural Geology*, *11*(7), 799–814. https://doi.org/10.1016/0191-8141(89)90099-0

Marsh, B. D. (1989). Magma chambers. *Annual Review of Earth and Planetary Sciences. Vol. 17*, (May 1989), 439–474. https://doi.org/10.1146/annurev.earth.17.1.439

Marsh, Bruce D. (2015). *Chapter 8 – Magma Chambers*. *The Encyclopedia of Volcanoes* (Second Edition). Elsevier Inc. https://doi.org/10.1016/B978-0-12-385938-9.00008-0

Marsh, Bruce D. (1988). Crystal size distribution (CSD) in rocks and the kinetics and dynamics of crystallization. *Contributions to Mineralogy and Petrology*, *99*(3), 277–291. https://doi.org/10.1007/BF00375362

Massin, F., Ferrazzini, V., Bachèlery, P., Nercessian, A., Duputel, Z., & Staudacher, T. (2011). Structures and evolution of the plumbing system of Piton de la Fournaise volcano inferred from clustering of 2007 eruptive cycle seismicity. *Journal of Volcanology and Geothermal Research*, *202*(1–2), 96–106. https://doi.org/10.1016/j.jvolgeores.2011.01.008

Massol, H., & Koyaguchi, T. (2005). The effect of magma flow on nucleation of gas bubbles in a volcanic conduit. *Journal of Volcanology and Geothermal Research*, *143*(1–3), 69–88. https://doi.org/10.1016/j.jvolgeores.2004.09.011

Mastin, L. G. (1997). Evidence for water influx from a caldera lake during the explosive hydromagmatic eruption of 1790, Kilauea volcano, Hawaii. *Journal of Geophysical Research: Solid Earth*, *102*(B9), 20093–20109. https://doi.org/10.1029/97JB01426

Mattox, T. N., & Mangan, M. T. (1997). Littoral hydrovolcanic explosions: A case study of lava-seawater interaction at Kilauea Volcano. *Journal of Volcanology and Geothermal Research*, *75*(1–2), 1–17. https://doi.org/10.1016/S0377-0273(96)00048-0

McBirney, A. R., & Murase, T. (1984). Rheological properties of magmas. *Annual Review of Earth and Planetary Sciences. Vol. 12*, 337–358. https://doi.org/10.1146/annurev.earth.12.1.337

Merle, O., & Lénat, J.-F. (2003). Hybrid collapse mechanism at Piton de la Fournaise volcano, Reunion Island, Indian Ocean. *Journal of Geophysical Research: Solid Earth*, *108*(B3), 1–11. https://doi.org/10.1029/2002jb002014

Michon, L. (2016). The Volcanism of the Comoros Archipelago Integrated at a Regional Scale (pp. 333–344). https://doi.org/10.1007/978-3-642-31395-0_21

Michon, L., Di Muro, A., Villeneuve, N., Saint-Marc, C., Fadda, P., & Manta, F. (2013). Explosive activity of the summit cone of Piton de la Fournaise volcano (La Réunion island): A historical and geological review. *Journal of Volcanology and Geothermal Research*, *264*, 117–133. https://doi.org/10.1016/j.jvolgeores.2013.06.012

Michon, L., Ferrazzini, V., & Di Muro, A. (2016). Magma Paths at Piton de la Fournaise Volcano. *Active Volcanoes of the Southwest Indian Ocean*, 91–106. https://doi.org/10.1007/978-3-642-31395-0

Michon, L., Ferrazzini, V., Di Muro, A., Villeneuve, N., & Famin, V. (2015). Rift zones and magma plumbing system of Piton de la Fournaise volcano: How do they differ from Hawaii and Etna? *Journal of Volcanology and Geothermal Research*, *303*, 112–129. https://doi.org/10.1016/j.jvolgeores.2015.07.031

Michon, L., Massin, F., Famin, V., Ferrazzini, V., & Roult, G. (2011). Basaltic calderas: Collapse dynamics, edifice deformation, and variations of magma withdrawal. *Journal of Geophysical Research*, *116*(B3), B03209. https://doi.org/10.1029/2010JB007636

Michon, L., & Saint-Ange, F. (2008). Morphology of Piton de la Fournaise basaltic shield volcano (La Réunion Island): Characterization and implication in the volcano evolution. *Journal of Geophysical Research: Solid Earth*, *113*(3), 1–19. https://doi.org/10.1029/2005JB004118

Michon, L., Staudacher, T., Ferrazzini, V., Bachèlery, P., & Marti, J. (2007). April 2007 collapse of Piton de la Fournaise: A new example of caldera formation. *Geophysical Research Letters*, *34*(21), 1–6. https://doi.org/10.1029/2007GL031248

Michon, L., Villeneuve, N., Catry, T., & Merle, O. (2009). How summit calderas collapse on basaltic volcanoes: New insights from the April 2007 caldera collapse of Piton de la Fournaise volcano. *Journal of Volcanology and Geothermal Research*, *184*(1–2), 138–151. https://doi.org/10.1016/j.jvolgeores.2008.11.003

Miwa, T., & Toramaru, A. (2013). Conduit process in vulcanian eruptions at Sakurajima volcano, Japan: Inference from comparison of volcanic ash with pressure wave and seismic data. *Bulletin of Volcanology*, *75*(1), 1–13. https://doi.org/10.1007/s00445-012-0685-y

Miwa, T., Toramaru, A., & Iguchi, M. (2009). Correlations of volcanic ash texture with explosion earthquakes from vulcanian eruptions at Sakurajima volcano, Japan. *Journal of Volcanology and Geothermal Research*, *184*(3–4), 473–486. https://doi.org/10.1016/j.jvolgeores.2009.05.012

Moitra, P., Gonnermann, H. M., Houghton, B. F., & Giachetti, T. (2013). Relating vesicle shapes in pyroclasts to eruption styles. *Bulletin of Volcanology*, *75*(2), 691. https://doi.org/10.1007/s00445-013-0691-8

Moitra, P., Gonnermann, H. M., Houghton, B. F., & Tiwary, C. S. (2018). Fragmentation and Plinian eruption of crystallizing basaltic magma. *Earth and Planetary Science Letters*, *500*, 97–104. https://doi.org/10.1016/j.epsl.2018.08.003

Mollo, S., Giacomoni, P. P., Coltorti, M., Ferlito, C., Iezzi, G., & Scarlato, P. (2015). Reconstruction of magmatic variables governing recent Etnean eruptions: Constraints from mineral chemistry and P–T–fO2–H2O modeling. *Lithos*, *212–215*, 311–320. https://doi.org/10.1016/j.lithos.2014.11.020

Montierth, C., Johnston, A. D., & Cashman, K. V. (1995). An empirical glass-composition-based geothermometer for Mauna Loa Lavas. In *Mauna Loa Revealed: Structure, Composition, Hisotry and Hazards* (pp. 207–217). https://doi.org/10.1029/GM092p0207

Morandi, A., Di Muro, A., Principe, C., Michon, L., Leroi, G., Norelli, F., & Bachèlery, P. (2016). Pre-historic (<5 kiloyear) Explosive Activity at Piton de la Fournaise Volcano. In *Active Volcanoes of the Southwest Indian Ocean. Active Volcanoes of the World.* (pp. 107–138). https://doi.org/10.1007/978-3-642-31395-0_8

Moreland, W., Thordarson, T., Houghton, B., & Larsen, G. (2019). Driving mechanisms of subaerial and subglacial explosive episodes during the 10th century Eldgjá fissure eruption, southern Iceland. *Volcanica*, *2*(2), 129–150. https://doi.org/10.30909/vol.02.02.129150

Morgan, D. J., & Jerram, D. A. (2006). On estimating crystal shape for crystal size distribution analysis. *Journal of Volcanology and Geothermal Research*, *154*(1–2), 1–7. https://doi.org/10.1016/j.jvolgeores.2005.09.016

Morin, J., Bachèlery, P., Soulé, H., & Nassor, H. (2016). Volcanic Risk and Crisis Management on Grande Comore Island. In *Active Volcanoes of the Southwest Indian Ocean. Active Volcanoes of the World.* (Vol. 4, pp. 403–422). https://doi.org/10.1007/978-3-642-31395-0_25

Moune, S., Faure, F., Gauthier, P.-J., & Sims, K. W. W. (2007). Pele's hairs and tears: Natural probe of volcanic plume. *Journal of Volcanology and Geothermal Research*, *164*(4), 244–253. https://doi.org/10.1016/j.jvolgeores.2007.05.007

N

Nave, R., Ricci, T., & Pacilli, M. G. (2016). Perception of Risk for Volcanic Hazard in Indian Ocean: La Réunion Island Case Study. In *Active Volcanoes of the Southwest Indian Ocean. Active Volcanoes of the World.* (pp. 315–326). https://doi.org/10.1007/978-3-642-31395-0_19

Neal, C. A., Brantley, S. R., Antolik, L., Babb, J. L., Burgess, M., Calles, K., … Damby, D. (2019). The 2018 rift eruption and summit collapse of Kīlauea Volcano. *Science*, *363*(6425), 367–374. https://doi.org/10.1126/science.aav7046

Nercessian, A., Him, A., Tipine, J.-C., & Sapin, M. (1996). Internal structure of Piton de la Foumaise volcano from seismic wave propagation and earthquake distribution. *Journal of Volcanology and Geothermal Research*, *70*(996), 123–143. https://doi.org/10.1016/0377-0273(95)00042-9

Nougier, J., Cantagrel, J. M., & Karche, J. P. (1986). The Comores archipelago in the western Indian Ocean: volcanology, geochronology and geodynamic setting. *Journal of African Earth Sciences (1983)*, *5*(2), 135–145. https://doi.org/10.1016/0899-5362(86)90003-5

Nurfiani, D., & Bouvet de Maisonneuve, C. (2018). Furthering the investigation of eruption styles through quantitative shape analyses of volcanic ash particles. *Journal of Volcanology and Geothermal Research*, *354*, 102–114. https://doi.org/10.1016/j.jvolgeores.2017.12.001

O

Oehler, J. F., Labazuy, P., & Lénat, J. F. (2004). Recurrence of major flank landslides during the last 2-Ma-history of Reunion Island. *Bulletin of Volcanology*, *66*(7), 585–598. https://doi.org/10.1007/s00445-004-0341-2

Oehler, J. F., Lénat, J. F., & Labazuy, P. (2008). Growth and collapse of the Reunion Island volcanoes. *Bulletin of Volcanology*, *70*(6), 717–742. https://doi.org/10.1007/s00445-007-0163-0

Ort, M. H., Di Muro, A., Michon, L., & Bachèlery, P. (2016). Explosive eruptions from the interaction of magmatic and hydrothermal systems during flank extension: the Bellecombe Tephra of Piton de La Fournaise (La Réunion Island). *Bulletin of Volcanology*, *78*(1), 5. https://doi.org/10.1007/s00445-015-0998-8

P

Pallister, J. S., Cashman, K. V., Hagstrum, J. T., Beeler, N. M., Moran, S. C., & Denlinger, R. P. (2013). Faulting within the Mount St. Helens conduit and implications for volcanic earthquakes. *Geological Society of America Bulletin*, *125*(3–4), 359–376. https://doi.org/10.1130/B30716.1

Papale, P. (2017). Rational volcanic hazard forecasts and the use of volcanic alert levels. *Journal of Applied Volcanology*, *6*(1). https://doi.org/10.1186/s13617-017-0064-7

Parcheta, C. E., Houghton, B. F., & Swanson, D. A. (2013). Contrasting patterns of vesiculation in low, intermediate, and high Hawaiian fountains: A case study of the 1969 Mauna Ulu eruption. *Journal of Volcanology and Geothermal Research*, *255*, 79–89. https://doi.org/10.1016/j.jvolgeores.2013.01.016

Paredes-Mariño, J., Scheu, B., Montanaro, C., Arciniega-Ceballos, A., Dingwell, D. B., & Perugini, D. (2019). Volcanic ash generation: Effects of componentry, particle size and conduit geometry on size-reduction processes. *Earth and Planetary Science Letters*, *514*, 13–27. https://doi.org/10.1016/j.epsl.2019.02.028

Parfitt, E. A., & Wilson, L. (1995). Explosive volcanic eruptions-IX. The transition between Hawaiian-style lava fountaining and Strombolian explosive activity. *Geophysical Journal International*, *121*(1), 226–232. https://doi.org/10.1111/j.1365-246X.1995.tb03523.x

Parfitt, E. A., Wilson, L., & Head, J. W. (1993). Basaltic magma reservoirs: factors controlling their rupture characteristics and evolution. *Journal of Volcanology and Geothermal Research*, *55*(1–2), 1–14. https://doi.org/10.1016/0377-0273(93)90086-7

Parfitt, Elisabeth A. (1998). A study of clast size distribution, ash deposition and fragmentation in a Hawaiian-style volcanic eruption. *Journal of Volcanology and Geothermal Research*, *84*(3–4), 197–208. https://doi.org/10.1016/S0377-0273(98)00042-0

Parfitt, Elisabeth A. (2004). A discussion of the mechanisms of explosive basaltic eruptions. *Journal of Volcanology and Geothermal Research*, *134*(1–2), 77–107. https://doi.org/10.1016/j.jvolgeores.2004.01.002

Patanè, D., Di Grazia, G., Cannata, A., Montalto, P., & Boschi, E. (2008). Shallow magma pathway geometry at Mt. Etna volcano. *Geochemistry, Geophysics, Geosystems*, *9*(12), n/a-n/a. https://doi.org/10.1029/2008GC002131

Patrick, M. R., Harris, A. J. L., Ripepe, M., Dehn, J., Rothery, D. A., & Calvari, S. (2007). Strombolian explosive styles and source conditions: insights from thermal (FLIR) video. *Bulletin of Volcanology*, *69*(7), 769–784. https://doi.org/10.1007/s00445-006-0107-0

Peltier, A., Ferrazzini, V., Staudacher, T., & Bachèlery, P. (2005). Imaging the dynamics of dyke propagation prior to the 2000-2003 flank eruptions at Piton de La Fournaise, Reunion Island. *Geophysical Research Letters*, *32*(22), n/a-n/a. https://doi.org/10.1029/2005GL023720

Peltier, Aline, Beauducel, F., Villeneuve, N., Ferrazzini, V., Di Muro, A., Aiuppa, A., … Taisne, B. (2016). Deep fluid transfer evidenced by surface deformation during the 2014–2015 unrest at Piton de la Fournaise volcano. *Journal of Volcanology and Geothermal Research*, *321*, 140–148. https://doi.org/10.1016/j.jvolgeores.2016.04.031

Peltier, Aline, Famin, V., Bachèlery, P., Cayol, V., Fukushima, Y., & Staudacher, T. (2008). Cyclic magma storages and transfers at Piton de La Fournaise volcano (La Réunion hotspot) inferred from deformation and geochemical data. *Earth and Planetary Science Letters*, *270*(3–4), 180–188. https://doi.org/10.1016/j.epsl.2008.02.042

Peltier, Aline, Massin, F., Bachèlery, P., & Finizola, A. (2012). Internal structure and building of basaltic shield volcanoes: The example of the Piton de La Fournaise terminal cone (La Réunion). *Bulletin of Volcanology*, *74*(8), 1881–1897. https://doi.org/10.1007/s00445-012-0636-7

Peltier, Aline, Poland, M. P., & Staudacher, T. (2015a). Are Piton de la Fournaise (La Réunion) and Kīlauea (Hawai'i) Really "Analog Volcanoes"? In *Hawaiian Volcanoes* (pp. 507–531). https://doi.org/10.1002/9781118872079.ch23

Peltier, Aline, Poland, M. P., & Staudacher, T. (2015b). Are Piton de la Fournaise (La Réunion) and Kīlauea (Hawai'i) Really "Analog Volcanoes"? (pp. 507–531). https://doi.org/10.1002/9781118872079.ch23

Peltier, Aline, Staudacher, T., Bachèlery, P., & Cayol, V. (2009). Formation of the April 2007 caldera collapse at Piton de La Fournaise volcano: Insights from GPS data. *Journal of Volcanology and Geothermal Research*, *184*(1–2), 152–163. https://doi.org/10.1016/j.jvolgeores.2008.09.009

Peltier, Aline, Villeneuve, N., Ferrazzini, V., Testud, S., Hassen Ali, T., Boissier, P., & Catherine, P. (2018). Changes in the Long-Term Geophysical Eruptive Precursors at Piton de la Fournaise: Implications for the Response Management. *Frontiers in Earth Science*, *6*(July), 1–10. https://doi.org/10.3389/feart.2018.00104

Pering, T. D., McGonigle, A. J. S., James, M. R., Capponi, A., Lane, S. J., Tamburello, G., & Aiuppa, A. (2017). The dynamics of slug trains in volcanic conduits: Evidence for expansion driven slug coalescence. *Journal of Volcanology and Geothermal Research*, *348*, 26–35. https://doi.org/10.1016/j.jvolgeores.2017.10.009

Peters, B. J., Carlson, R. W., Day, J. M. D., & Horan, M. F. (2018). Hadean silicate differentiation preserved by anomalous 142Nd/144Nd ratios in the Réunion hotspot source. *Nature*, *555*(7694), 89–93. https://doi.org/10.1038/nature25754

Pétrologie, M. S. (2012). *élémentaire et isotopique (Sr , Nd , Hf , Pb) de laves anciennes de la Réunion : Implications sur la construction de l'édifice volcanique Magali Smietana To cite this version : HAL Id : tel-00716829 Magali SMIETANA pour l ' obtention du titre de Docte*.

Pichavant, M., Brugier, Y., & Di Muro, A. (2016). Petrological and Experimental Constraints on the Evolution of Piton de la Fournaise Magmas. In *Active Volcanoes of the Southwest Indian Ocean. Active Volcanoes of the World.* (pp. 171–184). https://doi.org/10.1007/978-3-642-31395-0_10

Pioli, L., Azzopardi, B. J., Bonadonna, C., Brunet, M., & Kurokawa, A. K. (2017). Outgassing and eruption of basaltic magmas: The effect of conduit geometry. *Geology*, *45*(8), G38787.1. https://doi.org/10.1130/G38787.1

Pioli, L., Bonadonna, C., Azzopardi, B. J., Phillips, J. C., & Ripepe, M. (2012). Experimental constraints on the outgassing dynamics of basaltic magmas. *Journal of Geophysical Research: Solid Earth*, *117*(B3). https://doi.org/10.1029/2011JB008392

Pioli, L., Erlund, E., Johnson, E., Cashman, K., Wallace, P., Rosi, M., & Delgado Granados, H. (2008). Explosive dynamics of violent Strombolian eruptions: The eruption of Parícutin Volcano 1943-1952 (Mexico). *Earth and Planetary Science Letters*, *271*(1–4), 359–368. https://doi.org/10.1016/j.epsl.2008.04.026

Pioli, L., Pistolesi, M., & Rosi, M. (2014). Transient explosions at open-vent volcanoes: The case of Stromboli (Italy). *Geology*, *42*(10), 863–866. https://doi.org/10.1130/G35844.1

Pistolesi, M., Donne, D. D., Pioli, L., Rosi, M., & Ripepe, M. (2011). The 15 March 2007 explosive crisis at Stromboli volcano, Italy: Assessing physical parameters through a multidisciplinary approach. *Journal of Geophysical Research: Solid Earth*, *116*(12), 1–18. https://doi.org/10.1029/2011JB008527

Polacci, M., Andronico, D., de' Michieli Vitturi, M., Taddeucci, J., & Cristaldi, A. (2019). Mechanisms of Ash Generation at Basaltic Volcanoes: The Case of Mount Etna, Italy. *Frontiers in Earth Science*, *7*(August). https://doi.org/10.3389/feart.2019.00193

Polacci, M., Baker, D. R., Bai, L., & Mancini, L. (2008). Large vesicles record pathways of degassing at basaltic volcanoes. *Bulletin of Volcanology*, *70*(9), 1023–1029. https://doi.org/10.1007/s00445-007-0184-8

Polacci, M., Baker, D. R., La Rue, A., Mancini, L., & Allard, P. (2012). Degassing behaviour of vesiculated basaltic magmas: an example from Ambrym volcano, Vanuatu Arc. *Journal of Volcanology and Geothermal Research*, *233–234*, 55–64. https://doi.org/10.1016/j.jvolgeores.2012.04.019

Polacci, M., Baker, D. R., Mancini, L., Tromba, G., & Zanini, F. (2006). Three-dimensional investigation of volcanic textures by X-ray microtomography and implications for conduit processes. *Geophysical Research Letters*, *33*(13). https://doi.org/10.1029/2006GL026241

Polacci, M., Burton, M. R., La Spina, A., Murè, F., Favretto, S., & Zanini, F. (2009). The role of syn-eruptive vesiculation on explosive basaltic activity at Mt. Etna, Italy. *Journal of Volcanology and Geothermal Research*, *179*(3–4), 265–269. https://doi.org/10.1016/j.jvolgeores.2008.11.026

Polacci, M., Corsaro, R. A., & Andronico, D. (2006). Coupled textural and compositional characterization of basaltic scoria: Insights into the transition from Strombolian to fire fountain activity at Mount Etna, Italy. *Geology*, *34*(3), 201. https://doi.org/10.1130/G22318.1

Pompilio, M., Bertagnini, A., Del Carlo, P., & Di Roberto, A. (2017). Magma dynamics within a basaltic conduit revealed by textural and compositional features of erupted ash: the December 2015 Mt. Etna paroxysms. *Scientific Reports*, *7*(1), 4805. https://doi.org/10.1038/s41598-017-05065-x

Poppe, S. (2012). *Caldera collapse on basaltic shield volcanoes : analogue models compared to the Karthala caldera complex, Grande Comore*.

Porritt, L. A., Russell, J. K., & Quane, S. L. (2012). Pele's tears and spheres: Examples from Kilauea Iki. *Earth and Planetary Science Letters*, *333–334*, 171–180. https://doi.org/10.1016/j.epsl.2012.03.031

Potuzak, M., Nichols, A. R. L., Dingwell, D. B., & Clague, D. A. (2008). Hyperquenched volcanic glass from Loihi Seamount, Hawaii. *Earth and Planetary Science Letters*, *270*(1–2), 54–62. https://doi.org/10.1016/j.epsl.2008.03.018

Principe, C., Morandi, A., Di Muro, A., & Michon, L. (2016). Volcanological Map of the Plaine des Sables, Piton de la Fournaise. In *Active Volcanoes of the Southwest Indian Ocean. Active Volcanoes of the World.* (pp. 327–330). https://doi.org/10.1007/978-3-642-31395-0_20

Prôno, E., Battaglia, J., Monteiller, V., Got, J.-L., & Ferrazzini, V. (2009). P-wave velocity structure of Piton de la Fournaise volcano deduced from seismic data recorded between 1996 and 1999. *Journal of Volcanology and Geothermal Research*, *184*(1–2), 49–62. https://doi.org/10.1016/j.jvolgeores.2008.12.009

Putirka, K. D. (2008). Thermometers and Barometers for Volcanic Systems. *Reviews in Mineralogy and Geochemistry*, *69*(1), 61–120. https://doi.org/10.2138/rmg.2008.69.3

R

Rae, A. S. P., Edmonds, M., Maclennan, J., Morgan, D., Houghton, B., Hartley, M. E., & Sides, I. (2016). Time scales of magma transport and mixing at Kīlauea Volcano, Hawai'i. *Geology*, *44*(6), 463–466. https://doi.org/10.1130/G37800.1

Reed, S. J. B. (2005). *Electron Microprobe Analysis and Scanning Electron Microscopy in Geology*.

Rhéty, M., Harris, A. J. L., Villeneuve, N., Gurioli, L., Médard, E., Chevrel, M. O., & Bachèlery, P. (2017). A comparison of cooling-limited and volume-limited flow systems: Examples from channels in the Piton de la Fournaise April 2007 lava-flow field. *Geochemistry, Geophysics, Geosystems*, *18*(9), 3270–3291. https://doi.org/10.1002/2017GC006839

Richards, M. A., Duncan, R. A., & Courtillot, V. E. (1989). Flood basalts and hot-spot tracks: Plume heads and tails. *Science*, *246*(4926), 103–107. https://doi.org/10.1126/science.246.4926.103

Riley, C. M., Rose, W. I., & Bluth, G. J. S. (2003). Quantitative shape measurements of distal volcanic ash. *Journal of Geophysical Research: Solid Earth*, *108*(B10), 1–15. https://doi.org/10.1029/2001jb000818

Ripepe, M., Ciliberto, S., & Della Schiava, M. (2001). Time constraints for modeling source dynamics of volcanic explosions at Stromboli. *Journal of Geophysical Research: Solid Earth*, *106*(B5), 8713–8727. https://doi.org/10.1029/2000JB900374

Ripepe, M., Marchetti, E., Ulivieri, G., Harris, A., Dehn, J., Burton, M., … Salerno, G. (2005). Effusive to explosive transition during the 2003 eruption of Stromboli volcano. *Geology*, *33*(5), 341–344. https://doi.org/10.1130/G21173.1

Roeder, P. L., & Emslie, R. F. (1970). Olivine-liquid equilibrium. *Contributions to Mineralogy and Petrology*, *29*(4), 275–289. https://doi.org/10.1007/BF00371276

Roeder, P. L., Gofton, E., & Thornber, C. (2006). Cotectic Proportions of Olivine and Spinel in Olivine-Tholeiitic Basalt and Evaluation of Pre-Eruptive Processes. *Journal of Petrology*, *47*(5), 883–900. https://doi.org/10.1093/petrology/egi099

Rogers, N. (2015). *The Composition and Origin of Magmas*. *The Encyclopedia of Volcanoes* (Second Edition). Elsevier Inc. https://doi.org/10.1016/b978-0-12-385938-9.00004-3

Romero, J. E., Vera, F., Polacci, M., Morgavi, D., Arzilli, F., Alam, M. A., … Keller, W. (2018). Tephra From the 3 March 2015 Sustained Column Related to Explosive Lava Fountain Activity at Volcán Villarrica (Chile). *Frontiers in Earth Science*, *6*(March 2015). https://doi.org/10.3389/feart.2018.00098

Rose, W. I., & Durant, A. J. (2009). Fine ash content of explosive eruptions. *Journal of Volcanology and Geothermal Research*, *186*(1–2), 32–39. https://doi.org/10.1016/j.jvolgeores.2009.01.010

Rosseel, J. B., White, J. D. L., & Houghton, B. F. (2006). Complex bombs of phreatomagmatic eruptions: Role of agglomeration and welding in vents of the 1886 Rotomahana eruption, Tarawera, New Zealand. *Journal of Geophysical Research: Solid Earth*, *111*(12), 1–24. https://doi.org/10.1029/2005JB004073

Roult, G., Peltier, A., Taisne, B., Staudacher, T., Ferrazzini, V., & Di Muro, A. (2012). A new comprehensive classification of the Piton de la Fournaise activity spanning the 1985–2010 period. Search and analysis of short-term precursors from a broad-band seismological station. *Journal of Volcanology and Geothermal Research*, *241–242*, 78–104. https://doi.org/10.1016/j.jvolgeores.2012.06.012

Rust, A. C., & Cashman, K. V. (2004). Permeability of vesicular silicic magma: inertial and hysteresis effects. *Earth and Planetary Science Letters*, *228*(1–2), 93–107. https://doi.org/10.1016/j.epsl.2004.09.025

Rust, A. C., & Cashman, K. V. (2011). Permeability controls on expansion and size distributions of pyroclasts. *Journal of Geophysical Research: Solid Earth*, *116*(B11), n/a-n/a. https://doi.org/10.1029/2011JB008494

S

Sable, J. E., Houghton, B. F., Del Carlo, P., & Coltelli, M. (2006). Changing conditions of magma ascent and fragmentation during the Etna 122 BC basaltic Plinian eruption: Evidence from clast microtextures. *Journal of Volcanology and Geothermal Research*, *158*(3–4), 333–354. https://doi.org/10.1016/j.jvolgeores.2006.07.006

Sahagian, D. L., & Proussevitch, A. A. (1998). 3D particle size distributions from 2D observations: Stereology for natural applications. *Journal of Volcanology and Geothermal Research*, *84*(3–4), 173–196. https://doi.org/10.1016/S0377-0273(98)00043-2

Saint-Ange, F. (2009). *La sédimentation volcanoclastique en contexte de point chaud (île de La Réunion, Océan Indien)*.

Salaün, A., Villemant, B., Semet, M. P., & Staudacher, T. (2010). Cannibalism of olivine-rich cumulate xenoliths during the 1998 eruption of Piton de la Fournaise (La Réunion hotspot): Implications for the generation of magma diversity. *Journal of Volcanology and Geothermal Research*, *198*(1–2), 187–204. https://doi.org/10.1016/j.jvolgeores.2010.08.022

Salvany, T., Lahitte, P., Nativel, P., & Gillot, P.-Y. (2012). Geomorphic evolution of the Piton des Neiges volcano (Réunion Island, Indian Ocean): Competition between volcanic construction and erosion since 1.4Ma. *Geomorphology*, *136*(1), 132–147. https://doi.org/10.1016/j.geomorph.2011.06.009

Sato, M. (1978). Oxygen fugacity of basaltic magmas and the role of gas-forming elements. *Geophysical Research Letters*, *5*(6), 447–449. https://doi.org/10.1029/GL005i006p00447

Scarpa, R., Tilling, R. I., & Blong, R. J. (2011). Volcanic Hazards Risk Assessment. *Monitoring and Mitigation of Volcano Hazards*, 675–698. https://doi.org/10.1007/978-3-642-80087-0_20

Schmid, R. (1981). Descriptive nomenclature and classification of pyroclastic deposits and fragments. *Geologische Rundschau*, *70*(2), 794–799. https://doi.org/10.1007/BF01822152

Schmith, J., Höskuldsson, Á., & Holm, P. M. (2017). Grain shape of basaltic ash populations: implications for fragmentation. *Bulletin of Volcanology*, *79*(2), 14. https://doi.org/10.1007/s00445-016-1093-5

Scollo, S., Coltelli, M., Bonadonna, C., & Del Carlo, P. (2013). Tephra hazard assessment at Mt. Etna (Italy). *Natural Hazards and Earth System Sciences*, *13*(12), 3221–3233. https://doi.org/10.5194/nhess-13-3221-2013

Seth, H. C. (2005). From Deccan to rèunion: No trace of a mantle plume. *Special Paper of the Geological Society of America*, *388*(January 2005), 477–501. https://doi.org/10.1130/0-8137-2388-4.477

Shea, T. (2017). Bubble nucleation in magmas: A dominantly heterogeneous process? *Journal of Volcanology and Geothermal Research*, *343*, 155–170. https://doi.org/10.1016/j.jvolgeores.2017.06.025

Shea, T., Houghton, B. F., Gurioli, L., Cashman, K. V., Hammer, J. E., & Hobden, B. J. (2010). Textural studies of vesicles in volcanic rocks: An integrated methodology. *Journal of Volcanology and Geothermal Research*, *190*(3–4), 271–289. https://doi.org/10.1016/j.jvolgeores.2009.12.003

Sheridan, M. F., & Marshall, J. R. (1983). Interpretation of pyroclast surface features using sem images. *Journal of Volcanology and Geothermal Research*, *16*(1–2), 153–159. https://doi.org/10.1016/0377-0273(83)90088-4

Sigmarsson, O., Condomines, M., & Bachèlery, P. (2005). Magma residence time beneath the Piton de la Fournaise Volcano, Reunion Island, from U-series disequilibria. *Earth and Planetary Science Letters*, *234*(1–2), 223–234. https://doi.org/10.1016/j.epsl.2005.02.015

Sigmundsson, F., Durand, P., & Massonnet, D. (1999). Opening of an eruptive fissure and seaward displacement at Piton De La Fournaise Volcano measured by RADARSAT satellite radar interferometry. *Geophysical Research Letters*, *26*(5), 533–536. https://doi.org/10.1029/1999GL900055

Simakin, A. G., Armienti, P., & Epel'baum, M. B. (1999). Coupled degassing and crystallization: Experimental study at continuous pressure drop, with application to volcanic bombs. *Bulletin of Volcanology*, *61*(5), 275–287. https://doi.org/10.1007/s004450050297

Sleep, N. H. (1990). Hotspots and mantle plumes: Some phenomenology. *Journal of Geophysical Research*, *95*(B5), 6715. https://doi.org/10.1029/JB095iB05p06715

Smietana, M. (2007). *Etude pétrologique et volcanologique des dépôts des quatre dernières éruptions du Karthala.*

Smittarello, D., Cayol, V., Pinel, V., Peltier, A., Froger, J. L., & Ferrazzini, V. (2019). Magma Propagation at Piton de la Fournaise From Joint Inversion of InSAR and GNSS. *Journal of Geophysical Research: Solid Earth*, *124*(2), 1361–1387. https://doi.org/10.1029/2018JB016856

Soldati, A., Harris, A. J. L., Gurioli, L., Villeneuve, N., Rhéty, M., Gomez, F., & Whittington, A. (2018). Textural, thermal, and topographic constraints on lava flow system structure: the December 2010 eruption of Piton de la Fournaise. *Bulletin of Volcanology*, *80*(10), 74. https://doi.org/10.1007/s00445-018-1246-9

Sparks, R. S.J. (1997). Causes and consequences of pressurisation in lava dome eruptions. *Earth and Planetary Science Letters*, *150*(3–4), 177–189. https://doi.org/10.1016/s0012-821x(97)00109-x

Sparks, R. Stephen J., & Huppert, H. E. (1984). Density changes during the fractional crystallization of basaltic magmas: fluid dynamic implications. *Contributions to Mineralogy and Petrology*, *85*(3), 300–309. https://doi.org/10.1007/BF00378108

Sparks, R.S.J. (1978). The dynamics of bubble formation and growth in magmas: A review and analysis. *Journal of Volcanology and Geothermal Research*, *3*(1–2), 1–37. https://doi.org/10.1016/0377-0273(78)90002-1

Staudacher, T. (2010). Field observations of the 2008 summit eruption at Piton de la Fournaise (Ile de La Réunion) and implications for the 2007 Dolomieu collapse. *Journal of Volcanology and Geothermal Research*, *191*(1–2), 60–68. https://doi.org/10.1016/j.jvolgeores.2010.01.012

Staudacher, T., Ferrazzini, V., Peltier, A., Kowalski, P., Boissier, P., Catherine, P., … Massin, F. (2009). The April 2007 eruption and the Dolomieu crater collapse, two major events at Piton de la Fournaise (La Réunion Island, Indian Ocean). *Journal of Volcanology and Geothermal Research*, *184*(1–2), 126–137. https://doi.org/10.1016/j.jvolgeores.2008.11.005

Staudacher, T., & Peltier, A. (2016). Ground Deformation at Piton de la Fournaise, a Review From 20 Years of GNSS Monitoring. In *Active Volcanoes of the Southwest Indian Ocean* (pp. 251–269). https://doi.org/10.1007/978-3-642-31395-0_15

Staudacher, T., Peltier, A., Ferrazzini, V., Di Muro, A., Boissier, P., Catherine, P., … Lebreton, J. (2016). Fifteen Years of Intense Eruptive Activity (1998–2013) at Piton de la Fournaise Volcano: A Review. In *Active Volcanoes of the Southwest Indian Ocean* (pp. 139–170). https://doi.org/10.1007/978-3-642-31395-0_9

Staudacher, T., Sarda, P., & Allègre, C. J. (1990). Noble gas systematics of Réunion Island, Indian Ocean. *Chemical Geology*, *89*(1–2), 1–17. https://doi.org/10.1016/0009-2541(90)90057-E

Stix, J. (2015). *Part III Effusive Volcanism*. *The Encyclopedia of Volcanoes* (Second Edition). Elsevier Inc. https://doi.org/10.1016/b978-0-12-385938-9.02005-8

Stovall, W. K., Houghton, B. F., Gonnermann, H., Fagents, S. A., & Swanson, D. A. (2011). Eruption dynamics of Hawaiian-style fountains: the case study of episode 1 of the Kīlauea Iki 1959 eruption. *Bulletin of Volcanology*, *73*(5), 511–529. https://doi.org/10.1007/s00445-010-0426-z

Stovall, W. K., Houghton, B. F., Hammer, J. E., Fagents, S. A., & Swanson, D. A. (2012). Vesiculation of high fountaining Hawaiian eruptions: episodes 15 and 16 of 1959 Kīlauea Iki. *Bulletin of Volcanology*, *74*(2), 441–455. https://doi.org/10.1007/s00445-011-0531-7

Swanson, D. A., Rose, T. R., Fiske, R. S., & McGeehin, J. P. (2012). Keanakāko'i Tephra produced by 300years of explosive eruptions following collapse of Kīlauea's caldera in about 1500CE. *Journal of Volcanology and Geothermal Research*, *215–216*, 8–25. https://doi.org/10.1016/j.jvolgeores.2011.11.009

T

Taddeucci, J., Pompilio, M., & Scarlato, P. (2004). Conduit processes during the July–August 2001 explosive activity of Mt. Etna (Italy): inferences from glass chemistry and crystal size distribution of ash particles. *Journal of Volcanology and Geothermal Research*, *137*(1–3), 33–54. https://doi.org/10.1016/j.jvolgeores.2004.05.011

Taddeucci, J., Scarlato, P., Capponi, A., Del Bello, E., Cimarelli, C., Palladino, D. M., & Kueppers, U. (2012). High-speed imaging of Strombolian explosions: The ejection velocity of pyroclasts. *Geophysical Research Letters*, *39*(2), 1–6. https://doi.org/10.1029/2011GL050404

Taddeucci, Jacopo, Edmonds, M., Houghton, B., James, M. R., & Vergniolle, S. (2015). *Hawaiian and Strombolian Eruptions*. *The Encyclopedia of Volcanoes* (Second Edi). Elsevier Inc. https://doi.org/10.1016/b978-0-12-385938-9.00027-4

Taddeucci, Jacopo, Pompilio, M., & Scarlato, P. (2002). Monitoring the explosive activity of the July-August 2001 eruption of Mt. Etna (Italy) by ash characterization. *Geophysical Research Letters*, *29*(8), 71-1-71–74. https://doi.org/10.1029/2001GL014372

Tait, S., Jaupart, C., & Vergniolle, S. (1989). Pressure, gas content and eruption periodicity of a shallow, crystallising magma chamber. *Earth and Planetary Science Letters*, *92*(1), 107–123. https://doi.org/10.1016/0012-821X(89)90025-3

Takeuchi, S. (2005). Experimental constraints on the low gas permeability of vesicular magma during decompression. *Geophysical Research Letters*, *32*(10), L10312. https://doi.org/10.1029/2005GL022491

Toramaru, A. (2006). BND (bubble number density) decompression rate meter for explosive volcanic eruptions. *Journal of Volcanology and Geothermal Research*, *154*(3–4), 303–316. https://doi.org/10.1016/j.jvolgeores.2006.03.027

Toramaru, A., Noguchi, S., Oyoshihara, S., & Tsune, A. (2008). MND(microlite number density) water exsolution rate meter. *Journal of Volcanology and Geothermal Research*, *175*(1–2), 156–167. https://doi.org/10.1016/j.jvolgeores.2008.03.035

Toramaru, Atsushi. (1989). Vesiculation process and bubble size distributions in ascending magmas with constant velocities. *Journal of Geophysical Research*, *94*(B12), 17523. https://doi.org/10.1029/JB094iB12p17523

Truby, J. M., Mueller, S. P., Llewellin, E. W., & Mader, H. M. (2015). The rheology of three-phase suspensions at low bubble capillary number. *Proceedings of the Royal Society A: Mathematical, Physical and Engineering Sciences*, *471*(2173), 20140557. https://doi.org/10.1098/rspa.2014.0557

Tulet, P., Di Muro, A., Colomb, A., Denjean, C., Duflot, V., Arellano, S., … Villeneuve, N. (2017). First results of the Piton de la Fournaise STRAP 2015 experiment: multidisciplinary tracking of a volcanic gas and aerosol plume. *Atmospheric Chemistry and Physics*, *17*(8), 5355–5378. https://doi.org/10.5194/acp-17-5355-2017

U

Underwood, E. E. (1972). The stereology of projected images. *Journal of Microscopy*, *95*(1), 25–44. https://doi.org/10.1111/j.1365-2818.1972.tb03709.x

Urai, M., Geshi, N., & Staudacher, T. (2007). Size and volume evaluation of the caldera collapse on Piton de la Fournaise volcano during the April 2007 eruption using ASTER stereo imagery. *Geophysical Research Letters*, *34*(22), 1–7. https://doi.org/10.1029/2007GL031551

V

Vaca, A. V., Arroyo, C. R., Debut, A., Toulkeridis, T., Cumbal, L., Mato, F., … Aguilera, E. (2016). Characterization of fine-grained material ejected by the cotopaxi volcano employing X-ray diffraction and electron diffraction scattering techniques. *Biology and Medicine*, *8*(3). https://doi.org/10.4172/0974-8369.1000280

Valer, M. (2016). *Origine et évolution des magmas de l'île de La Réunion : Apports de la pétro-géochimie et des inclusions magmatiques*.

Vandamme, D., & Courtillot, V. (1990). Latitudinal evolution of the réunion hotspot deduced from paleomagnetic results of leg 115. *Geophysical Research Letters*, *17*(8), 1105–1108.

Vélain, C. (1878). *Description géologique de la presqu'île d'Aden, de l'île de La Réunion, des îles Saint-Paul et Amsterdam.*

Vergniolle, S., & Brandeis, G. (1996). Strombolian explosions: 1. A large bubble breaking at the surface of a lava column as a source of sound. *Journal of Geophysical Research: Solid Earth*, *101*(B9), 20433–20447. https://doi.org/10.1029/96jb01178

Vergniolle, S., Brandeis, G., & Mareschal, J.-C. (1996). Strombolian explosions: 2. Eruption dynamics determined from acoustic measurements. *Journal of Geophysical Research: Solid Earth*, *101*(B9), 20449–20466. https://doi.org/10.1029/96JB01925

Vergniolle, Sylvie, & Jaupart, C. (1990). Dynamics of degassing at Kilauea Volcano, Hawaii. *Journal of Geophysical Research*, *95*(B3), 2793. https://doi.org/10.1029/JB095iB03p02793

Villemant, B., Salaün, A., & Staudacher, T. (2009). Evidence for a homogeneous primary magma at Piton de la Fournaise (La Réunion): A geochemical study of matrix glass, melt inclusions and Pélé's hairs of the 1998-2008 eruptive activity. *Journal of Volcanology and Geothermal Research*, *184*(1–2), 79–92. https://doi.org/10.1016/j.jvolgeores.2009.03.015

Villeneuve, N., & Bachelery, P. (2006). Revue de la typologie des éruptions au Piton de la Fournaise, processus et risques volcaniques associés. *CyberGeo*, *2006*(January 2016), 1–25.

Villeneuve, N., Neuville, D. R., Boivin, P., Bachèlery, P., & Richet, P. (2008). Magma crystallization and viscosity: A study of molten basalts from the Piton de la Fournaise volcano (La Réunion island). *Chemical Geology*, *256*(3–4), 242–251. https://doi.org/10.1016/j.chemgeo.2008.06.039

Vlastélic, I., Di Muro, A., Bachèlery, P., Gurioli, L., Auclair, D., & Gannoun, A. (2018). Control of source fertility on the eruptive activity of Piton de la Fournaise volcano, La Réunion. *Scientific Reports*, *8*(1), 1–7. https://doi.org/10.1038/s41598-018-32809-0

Vlastélic, I., Gannoun, A., Di Muro, A., Gurioli, L., Bachèlery, P., & Henot, J. M. (2016). Origin and fate of sulfide liquids in hotspot volcanism (La Réunion): Pb isotope constraints from residual Fe–Cu oxides. *Geochimica et Cosmochimica Acta*, *194*, 179–192. https://doi.org/10.1016/j.gca.2016.08.036

Vlastélic, I., Staudacher, T., Bachèlery, P., Télouk, P., Neuville, D., & Benbakkar, M. (2011). Lithium isotope fractionation during magma degassing: Constraints from silicic differentiates and natural gas condensates from Piton de la Fournaise volcano (Réunion Island). *Chemical Geology*, *284*(1–2), 26–34. https://doi.org/10.1016/j.chemgeo.2011.02.002

Vlastélic, Ivan, Lewin, E., & Staudacher, T. (2006). Th/U and other geochemical evidence for the Réunion plume sampling a less differentiated mantle domain. *Earth and Planetary Science Letters*, *248*(1–2), 379–393. https://doi.org/10.1016/j.epsl.2006.06.003

Vlastélic, Ivan, Staudacher, T., & Semet, M. (2005). Rapid change of lava composition from 1998 to 2002 at Piton de la Fournaise (Réunion) inferred from Pb isotopes and trace elements: Evidence for variable crustal contamination. *Journal of Petrology*, *46*(1), 79–107. https://doi.org/10.1093/petrology/egh062

Vona, A., & Romano, C. (2013). The effects of undercooling and deformation rates on the crystallization kinetics of Stromboli and Etna basalts. *Contributions to Mineralogy and Petrology*, *166*(2), 491–509. https://doi.org/10.1007/s00410-013-0887-0

W

Walker, G. P. L., & Croasdale, R. (1971). Characteristics of some basaltic pyroclastics. *Bulletin Volcanologique*, *35*(2), 303–317. https://doi.org/10.1007/BF02596957

Walker, George P. L. (1971). Grain-Size Characteristics of Pyroclastic Deposits. *The Journal of Geology*, *79*(6), 696–714. https://doi.org/10.1086/627699

Walker, George P. L. (1993). Basaltic-volcano systems. *Geological Society, London, Special Publications*, *76*(1), 3–38. https://doi.org/10.1144/GSL.SP.1993.076.01.01

Walker, George P.L. (1973). Explosive volcanic eruptions - a new classification scheme. *Geologische Rundschau*, *62*(2), 431–446. https://doi.org/10.1007/BF01840108

Wallace, P. J., & Anderson Jr., A. T. (1998). Effects of eruption and lava drainback on the H 2 O contents of basaltic magmas at Kilauea Volcano. *Bulletin of Volcanology*, *59*(5), 327–344. https://doi.org/10.1007/s004450050195

Wallis, G. B. (1969). One-Dimensional Two-Phase Flow. *McGraw-Hill, New York, 243*.

Watts, A. B., Ten Brink, U. S., Buhl, P., & Brocher, T. M. (1985). A multichannel seismic study of lithospheric flexure across the Hawaiian-Emperor seamount chain. *Nature*, *315*(6015), 105–111. https://doi.org/10.1038/315105a0

Welsch, B. (2000). *Signification des Océanites dans le fonctionnement du Piton de la Fournaise, Île de La Réunion*.

Wentworth, C. K. (1922). A Scale of Grade and Class Terms for Clastic Sediments. *The Journal of Geology*, *30*(5), 377–392. https://doi.org/10.1086/622910

White, J.D.L., & Houghton, B. F. (2006). Primary volcaniclastic rocks. *Geology*, *34*(8), 677. https://doi.org/10.1130/G22346.1

White, James D.L., & Valentine, G. A. (2016). Magmatic versus phreatomagmatic fragmentation: Absence of evidence is not evidence of absence. *Geosphere*, *12*(5), 1478–1488. https://doi.org/10.1130/GES01337.1

Wilson, T. M., Jenkins, S., & Stewart, C. (2015). Impacts from Volcanic Ash Fall. In *Volcanic Hazards, Risks and Disasters* (pp. 47–86). Elsevier. https://doi.org/10.1016/B978-0-12-396453-3.00003-4

Wohletz, K. H. (1983). Mechanisms of hydrovolcanic pyroclast formation: Grain-size, scanning electron microscopy, and experimental studies. *Journal of Volcanology and Geothermal Research*, *17*(1–4), 31–63. https://doi.org/10.1016/0377-0273(83)90061-6

X

Xu, Z., & Zhang, Y. (2002). Quench rates in air, water, and liquid nitrogen, and inference of temperature in volcanic eruption columns. *Earth and Planetary Science Letters*, *200*(3–4), 315–330. https://doi.org/10.1016/S0012-821X(02)00656-8

Y

Yokoyama, T., & Takeuchi, S. (2009). Porosimetry of vesicular volcanic products by a water-expulsion method and the relationship of pore characteristics to permeability. *Journal of Geophysical Research: Solid Earth*, *114*(2). https://doi.org/10.1029/2008JB005758

Z

Zieg, M. J., & Lofgren, G. E. (2006). An experimental investigation of texture evolution during continuous cooling. *Journal of Volcanology and Geothermal Research*, *154*(1–2), 74–88. https://doi.org/10.1016/j.jvolgeores.2005.09.020

Zimanowski, B., Büttner, R., Dellino, P., White, J. D. L., & Wohletz, K. H. (2015). Magma–Water Interaction and Phreatomagmatic Fragmentation. *The Encyclopedia of Volcanoes*, 473–484. https://doi.org/10.1016/b978-0-12-385938-9.00026-2

Zimanowski, B., Wohletz, K., Dellino, P., & Büttner, R. (2003). The volcanic ash problem. *Journal of Volcanology and Geothermal Research*, *122*(1–2), 1–5. https://doi.org/10.1016/S0377-0273(02)00471-7

ANNEXES

Les apports d'une vision intégrée des données volcanologiques (DynVolc)

Lucia GURIOLI[1-2], Andrea DI MURO[3], Ivan VLASTÉLIC[1], Patrick BACHÈLERY[1], Andrew J.-L. HARRIS[1], Simon THIVET[1], Laura CALABRO[1], Sandrine RIVET[2], Emmanuel DELAGE[2]

[1]Laboratoire Magmas et Volcans, Université Clermont Auvergne, CNRS-IRD, OPGC, Aubiere, France

[2]Observatoire de Physique du Globe de Clermont-Ferrand, Université Clermont Auvergne, CNRS, Aubière, France

[3]Observatoire Volcanologique du Piton de la Fournaise, Institut de Physique du Globe de Paris, Sorbonne Paris Cité, Univ. Paris Diderot, CNRS, La Réunion, France

Résumé :

DynVolc (Dynamics of Volcanoes) est un nouveau système d'observation développé et porté par l'OPGC (Observatoire de Physique du Globe de Clermont-Ferrand et l'OVPF [Observatoire Volcanologique du Piton de La Fournaise]) dans le cadre du SNOV (Service National d'Observation en Volcanologie). Ce service d'observation propose l'intégration des données texturales, pétro-géochimiques et géophysiques afin de comprendre les mécanismes complexes causant l'ascension et la fragmentation des magmas jusqu'aux éruptions. Cette approche multidisciplinaire est aujourd'hui indispensable dans les observations et les simulations en volcanologie physique. Dans le cadre de ce service, des investissements importants ont été réalisés dans l'élaboration de stratégies novatrices concernant à la fois l'échantillonnage syn-éruptif (de produits explosifs et effusifs) et l'analyse de routine de ces échantillons. Lors des crises éruptives au Piton de La Fournaise (La Réunion, France), ce système d'observation fourni des données texturales et chimiques d'échantillons pyroclastiques et de laves afin de suivre leur évolution au cours de la crise éruptive. Les échantillons sont systématiquement envoyés par l'OVPF (Observatoire Volcanologique du Piton de La Fournaise) et sont étudiés au LMV (Laboratoire Magmas et Volcans) par un groupe d'experts dans le domaine des mesures texturales, pétrographiques, géochimiques et géophysiques.

Abstract:

DynVolc (Dynamics of Volcanoes) is a new observation system developed and carried by the OPGC (Observatory of Physics of the Globe of Clermont-Ferrand and by the OVPF [Observatoire Volcanologique du Piton de La Fournaise]) within the framework of the SNOV (National Volcanology Observation Service). This observation system proposes the integration of textural, petro-geochemical and geophysical data in order to understand the complex

mechanisms determining magma ascension, fragmentation and eruption. This multidisciplinary approach is now indispensable in monitoring active volcanoes and fundamental for understanding and forecasting volcanic eruptions. Within this system, significant investiments have been made in the development of innovative strategies for sampling explosive and effusive products during ongoing eruptions, as well as routine analysis of volcanic emissions products. During volcanic crises at Piton de La Fournaise (Reunion, France), this observation system provides textural and chemical data from pyroclastic and lavic samples to monitor their evolution during the volcanic crisis. The samples are sent systematically by the OVPF and studied and analyzed at LMV (Laboratoire Magmas et Volcans) by a group of experts in the textural, petrographical, geochemical and geophysical measurements.

*

* *

I - Introduction

Une bonne compréhension de la dynamique éruptive et des processus magmatiques est cruciale pour la surveillance des volcans actifs et fondamentale pour la prévision des éruptions volcaniques (Sparks, 2003 ; Gurioli et al., 2015a). De nombreuses études récentes suggèrent que les phénomènes éruptifs sont fortement dépendants des propriétés physiques du magma résidant dans le conduit (par exemple la température, la viscosité ou encore la perméabilité). Les données pétrographiques des laves et des pyroclastes peuvent fournir des informations fondamentales concernant la teneur en volatils, la perméabilité et la microstructure du magma (Gurioli et al., 2015a). Par conséquent, le suivi textural et chimique des fragments de lave et des pyroclastes est maintenant une procédure de routine quotidienne sur les volcans actifs tels que Kilauea, l'Etna et le Stromboli (Thornber et al., 2003 ; Swanson et al., 2009 ; Tadeucci et al., 2002 ; Lautze et al., 2012 ; Andronico et al., 2013 a ; b). À ce jour, plusieurs séries temporelles de données pétrographiques et géochimiques ont été acquises sur les produits effusifs récemment émis par le Piton de la Fournaise et ceci dans les différents groupes de recherche du Laboratoire Magmas et Volcans, LMV (Vlastélic et al., 2005 ; 2007 ; 2009 ; Schiano et al., 2011 ; Boivin et Bachèlery, 2009 ; Peltier et al., 2009 ; Lénat et al., 2012). Néanmoins, ce type d'approche n'a jamais été conçu comme outil d'observation systématique d'une tâche de service. En outre, seuls quelques articles ont été publiés sur la caractérisation des produits pyroclastiques (Villemant et al., 2009 ; Michon et al., 2013 ; Di Muro et al., 2014 ; Bachèlery et al. 2015 ; Ort et al., 2016). Pour combler cette lacune de surveillance des volcans actifs en France, en particulier pour le Piton de La Fournaise, un nouveau système d'observation, DynVolc (Dynamics of Volcanoes), a été récemment développé.

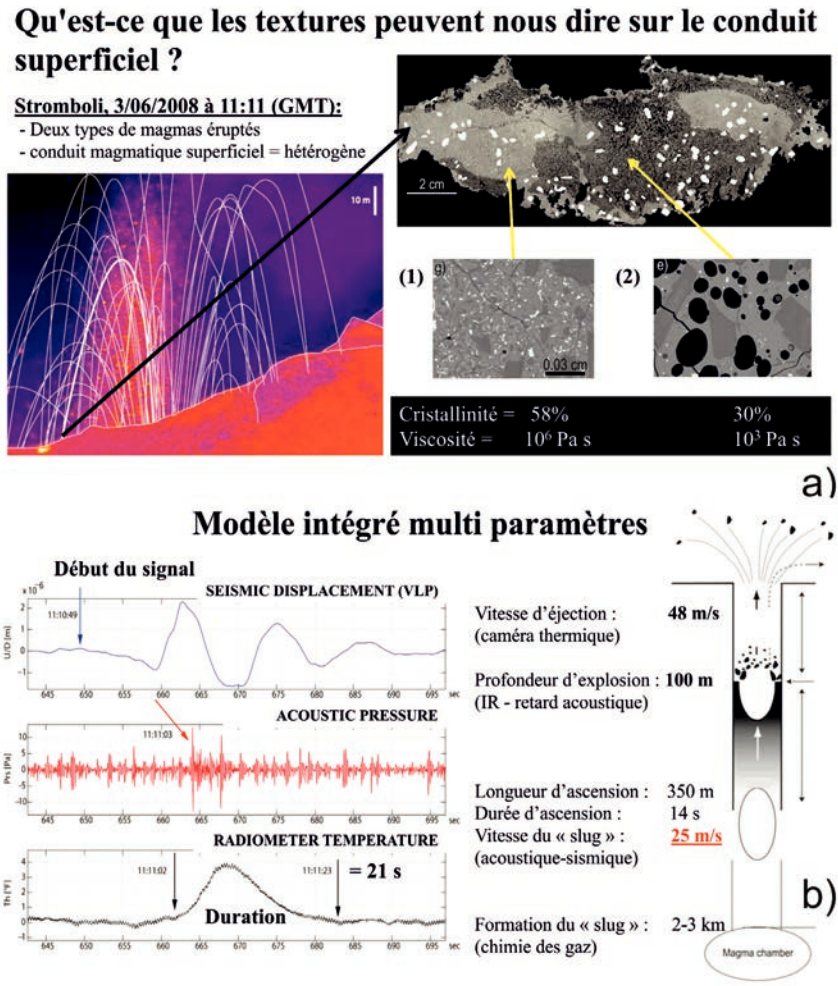

Figure 1 : Données d'observation comparées aux mesures géophysiques : a) Image thermique d'une explosion balistique normale, au Stromboli, le 3 juin 2008. La trajectoire blanche et épaisse correspond à la bombe analysée par Gurioli et al. 2014. Cette bombe est décrite en haut à droite : noir = vésicules ; blanc = phénocristaux ; zones gris claires = zones denses et riches en microlites (1) ; zones grises sombres (2) = zones vésiculées. (b) (de bas en haut) Signaux thermiques, acoustiques et sismiques acquis pour la même explosion et modèle schématique pour le système peu profond (au-dessus de 300 m) à Stromboli. La source est située à la profondeur h sous la surface et à la profondeur Δh à l'intérieur de la colonne magmatique. Le « slug » (ensemble de grosses bulles de gaz) monte la distance Δh à la vitesse U pour éclater à la surface libre à la profondeur h_C. Le nuage de fragments et de gaz monte ensuite le long du conduit non-rempli à partir de h_C à la vitesse U_{jet}, jusqu'à l'évent à la surface. Toutes les profondeurs et les vitesses sont établies en utilisant la plage typique des temps de retard thermique sismique-infrasonore (indiqués sur la figure ci-dessus) pour les capteurs situés à la distance x de l'évent, avec un intervalle de vitesse de remontée des fragments de 27 à 67m/s. Les différents faciès de texture observés dans ces bombes ont montré que le magma frais était mêlé à des zones partiellement ou complètement dégazées, oxydées, riches en cristaux, à haute viscosité et évoluées. Ces magmas se trouvaient au sommet du conduit et ne jouaient qu'un rôle passif dans le processus explosif. La portion vésiculée, fraîche, pauvre en microlite, a cependant connu une réponse à l'événement explosif, en subissant une décompression rapide. L'intégration des mesures géophysiques avec les analyses des échantillons indique que les modèles populaires d'éclatement des bulles peuvent ne pas convenir à ce cas. Nous suggérons que le magma dégazé forme un bouchon, ou couche rhéologique, au sommet du conduit, à travers lequel le magma frais éclate (d'après Gurioli et al., 2014, modifié).

II - Présentation de DynVolc

DynVolc a pour objectif de quantifier texturalement et chimiquement (i) des échantillons pyroclastiques (bombes scoriacées et / ou ponceuses, lapilli et de cendres) et (ii) des fragments de lave. Le but est de fournir, à partir des pyroclastes, les données nécessaires pour suivre l'évolution du dégazage, de la rhéologie et de la fragmentation du magma dans le temps et dans l'espace (information temporelle et spatiale), à partir du conduit jusqu'aux manifestations explosives en surface (Fig. 1a). Pour les laves (en collaboration avec A. Harris, LMV) le but est d'obtenir l'évolution temporelle et spatiale de la rhéologie d'écoulement, la dynamique, la morphologie et la chimie des laves (Fig. 2). Par conséquent, DynVolc fournit des mesures de routine systématiques, précises et reproductibles, sur les pyroclastes et les échantillons de lave pour suivre leurs variations physiques dans le temps et l'espace, en termes de :

- Texture des dépôts (taille des particules et leur distribution de taille, analyse des composants de la fraction juvénile et non-juvénile puis mesures morphologiques). Pour l'analyse morphologique des cendres, DynVolc bénéficie du soutien technique de K. Suchorski (CNRS/LMV).
- Mesures macroscopiques, sur des pyroclastes et fragments de lave (densité, porosité, connectivité et pourcentage de bulles isolées, densité du magma et perméabilité), avec le support technique de N. Cluzel (CNRS/LMV).
- Mesures texturales microscopiques (pourcentage et distribution de la taille des vésicules et des cristaux) avec le support technique de C. Constantin (LMV), pour la préparation des lames minces, et de J.-M. Hénot (CNRS/LMV) pour l'utilisation du MEB (Microscope Electronique à Balayage).
- Analyses chimiques des verres et des roches totales sur des pyroclastes juvéniles et des fragments de laves trempées avec le support technique de C. Fonquernie (LMV) pour la préparation de les échantillons, J.-L. Devidal (LMV) pour l'utilisation de la microsonde électronique, et M. Benbakkar (LMV) pour les analyses en éléments majeurs, mineurs et traces par ICP-AES (Spectrométrie d'Emission Atomique à source Plasma à Couplage Inductif).
- Analyses géochimiques des roches totales, en collaboration avec I. Vlastélic (CNRS/LMV).
- Caractérisation minéralogique des différentes phases minérales présentes, en collaboration avec P. Bachèlery (LMV).

À ce jour, ces mesures de routine sont effectuées sur des échantillons issus d'activités volcaniques passées et actuelles [par exemple Piton de La

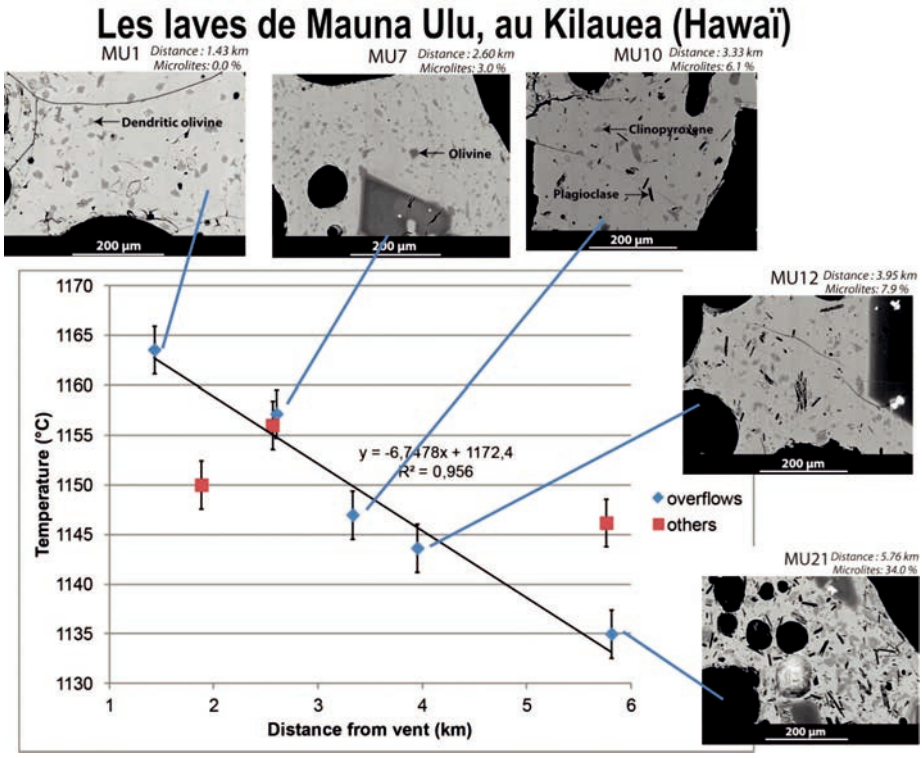

Figure 2 : Images électroniques rétrodiffusées des cinq échantillons du canal de lave de Mauna Ulu, Big Island, Etats-Unis, analysés avec la microsonde électronique, montrant l'augmentation du contenu en microlite avec la distance à l'évent et diagramme de leur température en fonction de la distance à l'évent éruptif (d'après Robert et al., 2014, modifié).

Fournaise (Réunion), Chaîne des Puys et Mont Dore (France) ; Stromboli, Etna, Vésuve, Vulcano (Italie) ; Kilauea (Hawaii, États-Unis) ; Pacaya, Fuego (Guatemala)]. Un système volcanique actif permet de combiner ces données d'observation en parallèle avec des mesures géophysiques disponibles pour mieux comprendre l'activité éruptive (Fig. 1b). Lors des crises éruptives au Piton de La Fournaise (La Réunion, France), ce système d'observation fourni des données texturales et chimiques sur des échantillons pyroclastiques et des laves pour suivre leur évolution au cours de l'éruption. Les échantillons sont envoyés systématiquement par l'Observatoire Volcanologique du Piton de La Fournaise (OVPF). En parallèle, chaque année diverses campagnes de mesures sont effectuées au Piton de la Fournaise par l'équipe du LMV en collaboration avec l'équipe de l'OVPF. Cette collaboration entre l'OPGC et l'OVPF est un réel échange scientifique et une coopération mutuelle dynamique et constructive. En fait, aujourd'hui, le système d'observation DynVolc est devenu un système d'observation mixte, dirigé par L. Gurioli (OPGC/LMV) et A. Di Muro (OVPF/IPGP).

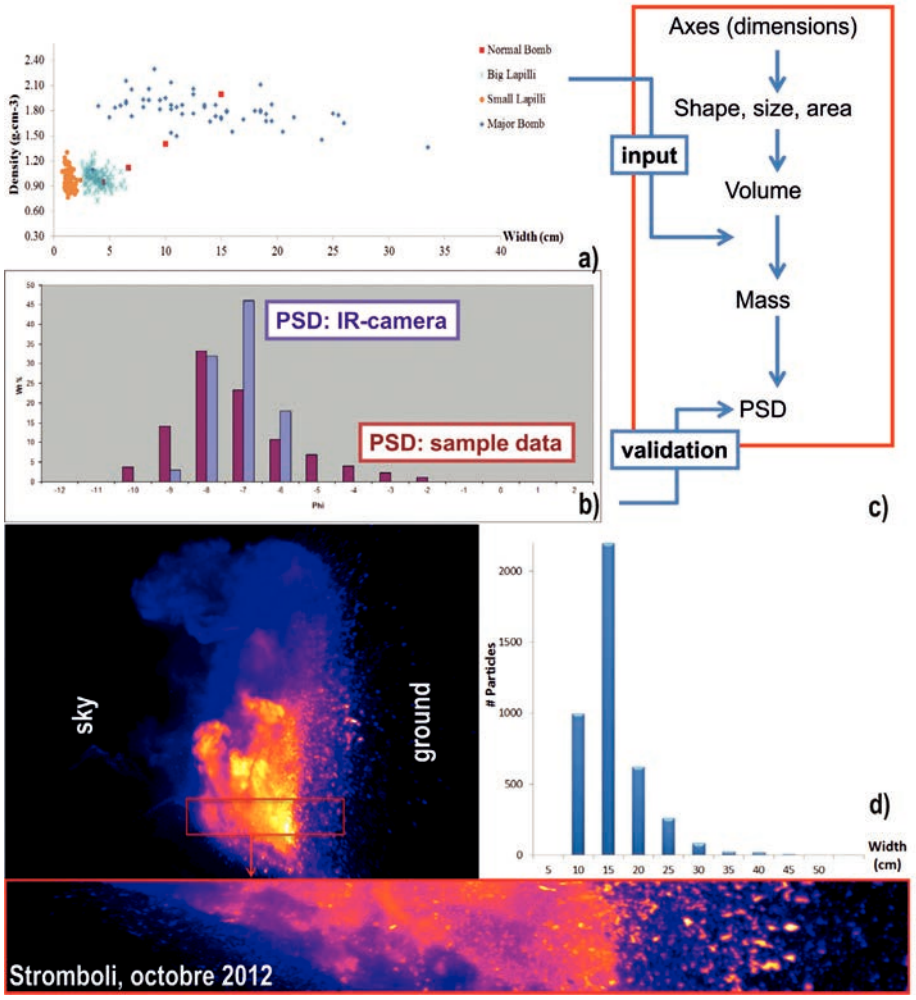

Figure 3 : Validation des données de télédétection : a) Diagramme de la densité des scories, lapilli et bombes du Stromboli, en fonction de leurs tailles ; b) Histogramme de la granulométrie d'une explosion (PSD : sample-data) et histogramme de granulométrie obtenu avec la caméra thermique (PSD : IR-camera) ; c) Schéma fonctionnel des données d'entrée et de sortie pour la validation des données granulométriques obtenues directement à partir du (d) panache avec la caméra thermique (d'après Bombrun et al., 2015, modifié).

Dans le Pôle de Télédétection, DynVolc fournit la composante des données de terrain indispensable pour la validation des données de télédétection (Lillesand et Kieffer, 1987 ; Fig. 3). Les données collectées par le déploiement de réseaux géophysiques intégrés à des systèmes en éruption permettent la caractérisation des conditions de remontée du magma et d'émission dynamique des produits associés (Fig. 1b). Les paramètres géophysiques mesurables comprennent la profondeur de la fragmentation, l'éjection et la vitesse de remontée du magma, la masse solide et gazeuse, le flux

de masse, ainsi que la variation de ces paramètres dans le conduit et intégré dans le temps (Harris et Ripepe, 2007 ; Sahetapy-Engel et Harris, 2009 ; Gouhier et Donnadieu, 2008). Les analyses texturales des pyroclastes émis pendant une éruption nous permet d'optimiser les données géophysiques, ainsi que de valider les résultats pour une meilleure caractérisation de l'événement (Gurioli et al., 2013 ; 2014 ; Harris et al., 2013 ; Leduc et al., 2015 ; Bombrun et al., 2015). En outre, les données chimiques et les conditions rhéologiques mesurées permettent de définir pleinement les conditions au niveau de la source, de la fragmentation et de l'émission du panache en surface ainsi de modéliser la mise en place des coulées de lave (Morgan et al., 2013 ; Robert et al., 2014 ; Harris et al., 2015). Dans le cas spécifique du Piton de La Fournaise, l'intégration est faite principalement entre les données DynVolc et les données visibles et thermiques obtenu par un camera infrarouge ou un appareil photo.

III - Une procédure standard

Un atelier intitulé "*Tracking and understanding volcanic emissions through cross-disciplinary integration: A textural working group*." a eut lieu à l'Université Blaise Pascal (Clermont-Ferrand, France) les 6 et 7 Novembre 2012. Cet atelier a été soutenu par l'European Science Fondation (ESF). Avec un groupe consultatif initial, l'objectif principal de l'atelier était de définir les mesures, les méthodes, les formats et les normes à appliquer dans l'intégration des données géophysiques, physiques et texturales recueillies lors des éruptions volcaniques et d'homogénéiser les procédures pour les événements passés et en cours. Le groupe de travail comprend un total de 35 scientifiques de 5 pays (France, Italie, Grande-Bretagne, Allemagne et Islande). Ce groupe de scientifiques est composé de onze conseillers du domaine de l'analyse texturale, onze spécialistes des études de dépôt, sept géochimistes et six géophysiciens. Le but de la réunion était de discuter et de définir :

- Les normes, les protocoles de précision et de mesure et mis en place de l'analyse texturale.
- Les études de terrain sur les dépôts explosifs, puis études des paramètres texturaux, chimiques et géophysiques les plus appropriés et qui peuvent être le mieux mesurés et combinés.
- Les meilleurs formats de distribution pour que les données soient facilement utilisables par chacun des groupes d'experts.
- L'échantillonnage, et les mesures de routines multidisciplinaires actuellement utilisées, et des normes de mesure appliquées par chaque communauté.

Figure 4 : Stratégie d'échantillonnage : a) prélèvements effectués quelques heures après l'événement (Gurioli et al., 2008) ; b) « échantillonnage à la main » qui implique la collecte (et la trempe) des bombes et des lapilli lorsque ces produits tombent hors du panache, dans la photo L Colo' avec la bombe de la figure 1 ; c) Stratégie de la surface propre, dans laquelle une surface préexistante est nettoyée avant l'éruption (d'après Pistolesi et al. 2011, modifié) ou d) des feuilles de plastique sont disposées près de l'évent ; e) Instrument ASHER avec f) le collecteur et g) la barrière optique.

Le groupe a convenu que l'intégration transversale à l'échelle communautaire, centrée sur la définition de ces mesures et les formats qui peuvent être les mieux combinés, est un objectif réalisable mondialement. Il y a un consensus général pour aller vers une meilleure coordination des actions avec un échange des données efficace.

Nous avons préparé un document final qui servira de base plus large à un groupe d'expert pour la bonne réalisation de cet objectif. Toutes les discussions sont présentées sur le document final du site web MeMovolc [http://www.esf.org/activities/memovolc-activities.html] et dans une revue internationale (Gurioli et al., 2015a).

Les discussions, les conclusions de la conférence et le papier ont été utilisés comme base pour la mise en place de ce système d'observation.

IV - La stratégie d'échantillonnage

La première étape de ce service d'observation consiste à collecter des échantillons représentatifs à la fois des dépôts des éruptions passées (inobservables) ou récentes (observées), pour lesquels les prélèvements sont effectués de préférence de quelques heures à quelques jours de l'événement (Gurioli et al., 2008 ; 2013 ; Fig. 4a). L'échantillonnage peut également avoir lieu au cours de l'activité éruptive avec des échantillons collectés en utilisant un dispositif d'échantillonnage placé à l'intérieur du champ de retombées. Trois méthodes d'échantillonnage simples ont été utilisées pendant des éruptions en cours : (1) la méthode de « l'échantillonnage à la main » implique la collecte (et la trempe) des bombes et lapilli lorsque ces produits tombent hors du panache mais au sein du champ de retombées actives (Lautze et Houghton, 2007 ; 2008 ; Gurioli et al., 2014, Fig. 4b) ; (2) la stratégie de la surface propre, dans laquelle des feuilles de plastique sont disposées près de l'évent ou une surface préexistante est nettoyée avant l'éruption (Figs. 4c, 4d) ; dans les deux cas, les pyroclastes tombant dans une zone connue sont collectées (Rose et al., 2008 ; Pistolesi et al., 2011 ; Eychenne et al., 2012 ; Houghton et al., 2013 ; Harris et al., 2013 ; Schipper et al. 2013) ; et (3) « la stratégie du seau », dans laquelle un grand nombre de seaux sont répartis sur une zone discrète de retombées pour une

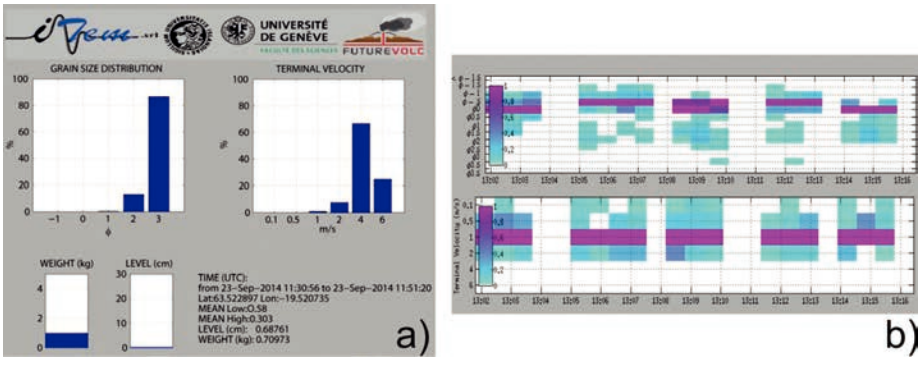

Figure 5 : Visualisation des données de l'ASHER : a) données ponctuelles sur la distribution des tailles des particules, la vitesse terminale et de collecte in situ ; b) distribution des tailles des particules et vitesse terminale en fonction du temps (d'après Marchetti et al., 2013, modifié).

certaine période de temps (Swanson et al.,2009). Lorsque cela est possible, les objectifs sont de recueillir un nombre suffisant d'échantillons pour estimer l'ampleur de l'événement à travers la charge de masse par unité de surface et pour obtenir un nombre suffisant de clastes pour la caractérisation texturale et chimique.

Récemment, un collecteur automatique de cendres a été acheté. L'instrument, ASHER (Fig. 4e), est un nouvel instrument autonome pour la collecte de cendres, capable de mesurer la distribution granulométrique (GSD), la vitesse terminale des particules (TV) et le taux d'accumulation. ASHER (Marchetti et al., 2013) a été développé dans le cadre du 7ème projet européen, FUTUREVOLC, grâce à la collaboration entre les Universités de Genève, d'Islande, et de Florence. ASHER se compose d'une unité principale d'acier inoxydable (Figs. 4f) et d'une barrière optique (Figs. 4e, 4g) d'une consommation de puissance nominale de 200 mA @ 12 Volts. L'unité principale (Fig. 4f) est une unité autonome qui comprend le collecteur et l'électronique, et permet la collecte de tephra entre 4 et 0,090 mm de diamètre, ainsi que la mesure du taux d'accumulation toutes les 30 secondes, avec des données étant disponibles en temps quasi réel. Les données brutes et traitées sont enregistrées localement dans la mémoire. Une console Web permet également le contrôle de l'unité à distance tandis que les serveurs web et ftp embarqués permettent la visualisation des données (Fig. 5), la diffusion en temps réel et le téléchargement des données. Un récepteur GPS assure une synchronisation des données et une localisation précise du site d'échantillonnage. La barrière optique (Fig. 4g) doit être connectée à l'unité centrale pour mesurer la GSD et la vitesse terminale. La vitesse terminale peut être mesurée dans la gamme de 0,1 à 6 m/s. L'instrument a été testé à Stromboli en Juillet 2016 (Fig. 4e).

V - Mesures de routine

Des mesures de routine sont effectuées sur les échantillons des éruptions passées et récentes (Figs. 6, 7, 8, 9, 10, 11). Pour les produits explosifs, notre objectif est de contraindre l'évolution temporelle du dégazage et de la rhéologie du magma. Ceci permet le suivi :

- De l'évolution des caractéristiques magmatiques lors de l'ascension du magma dans le conduit volcanique.
- Des conditions de fragmentation (en termes d'efficacité et style d'explosion).
- De la composition chimique du magma.
- De la variation de ces paramètres dans le temps.

L'ensemble des échantillons explosifs sont définis en termes de leurs caractéristiques de fragmentation :

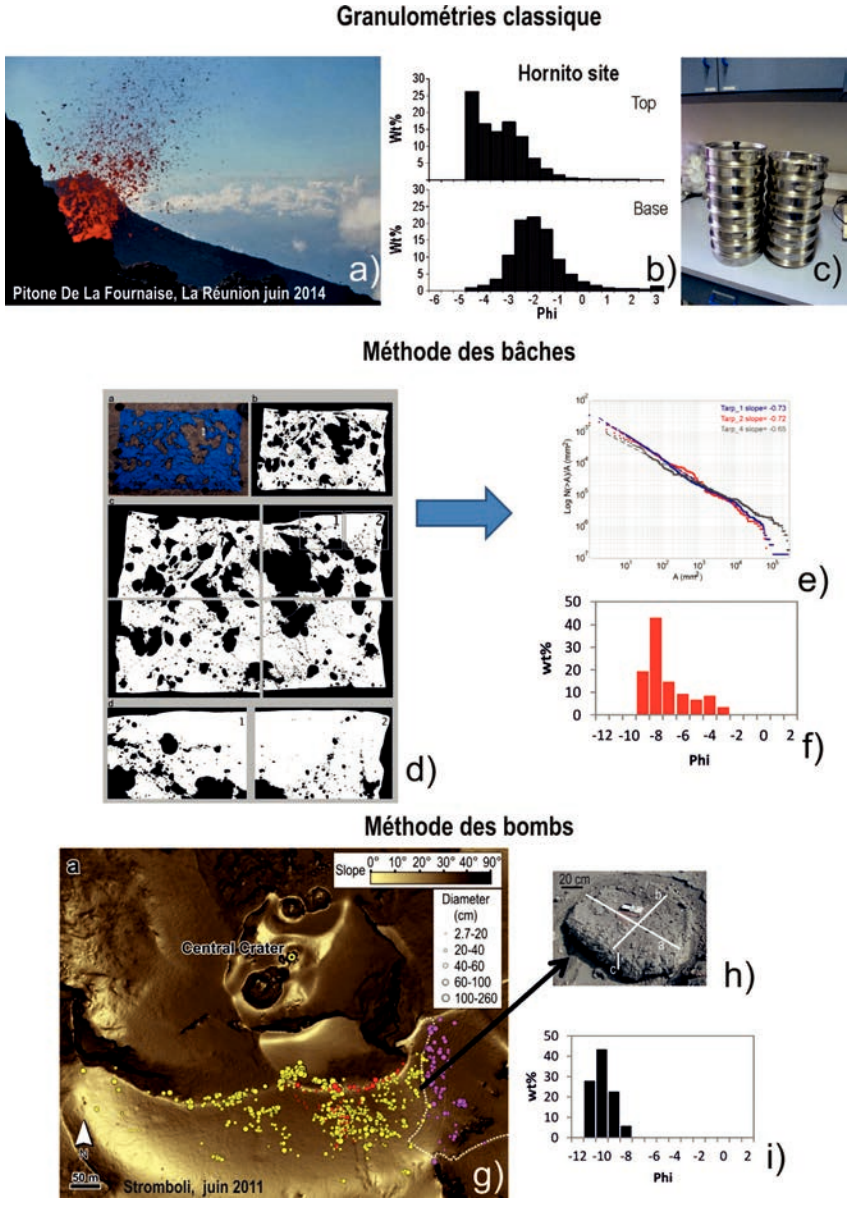

Figure 6 : Analyse granulométrique classique : a) Explosion au Piton de La Fournaise en Juin 2014 et b) distributions granulométriques de la base des dépôts (bas) jusqu'à la partie supérieure des dépôts (haut) ; c) Colonne de tamis du laboratoire textural du LMV. Méthode des bâches : d) Photo montrant la répartition des trous et images numériques, prises à des grossissements différents, traitées par un logiciel d'analyse d'image, pour réduire les images dans une échelle binaire, en noir (trous) et blanc (plastique) ; e) distribution cumulative de la taille des différentes scories ; f) distribution totale des tailles des scories résultant de la cartographie de la répartition des trous (d'après Colo' 2012, modifié). Méthode des bombes : g) Emplacements des bombes tracés par la taille sur la carte de la pente de la surface du cratère du Stromboli (la taille du cercle est fonction du diamètre de la bombe), cercles jaunes = 21 janvier 2010, cercles violets = explosion majeure du 24 novembre 2009, cercles rouges = bombes échantillonnées. La ligne rayée est la voie touristique ; h) Exemple de bombe métrique ; i) Distribution totale des tailles des bombes (d'après Gurioli et al., 2013, modifié).

- Taille des particules et distribution de la taille.
- Comptage lithologique des fractions juvéniles et non-juvéniles.
- Mesures morphologiques.

Les pyroclastes et les fragments de laves sont caractérisés en termes de :

- Densité et porosité.
- Pourcentage de vésicules connectées.
- Perméabilité.

Enfin, tous ces échantillons juvéniles sont définis par :

- Leur composition magmatique.

Les mesures sont rapides, robustes, fiables et précises grâce à l'utilisation d'instruments novateurs disponibles au laboratoire textural du LMV en combinaison avec d'autres moyens analytiques de hautes qualités accessibles au LMV.

V - 1 Analyse granulométrique

L'analyse granulométrique permet d'obtenir les caractéristiques de fragmentation de l'explosion associée (Fig. 6), l'interprétation génétique des dépôts pyroclastiques (de retombées par rapport à un écoulement) et la classification des événements volcaniques en combinaison avec la dispersion du dépôts (Walker, 1971 ; Cas et Wright, 1987 ; Wohletz et al., 1989 ; Fagents et al., 2013). L'échantillonnage doit être représentatif du dépôt et de l'explosion associée (Figs. 6a, 6b). Les analyses granulométriques classiques ont été décrites par Walker (1971). Les analyses sont faites avec un ensemble de tamis (Fig. 6c) avec des tailles de mailles espacées à des intervalles d'un ou d'un demi *phi*, où $phi = -\log_2 d$, d étant le diamètre du grain en mm et variant en taille de -6 à 4 *phi*. Les tamis sont disposés dans des diamètres de maille décroissants descendants. Les tamis sont vibrés manuellement pendant une période de temps fixe. Le poids des sédiments retenus sur chaque tamis est mesuré et converti en pourcentage et normalisé au poids total de l'échantillon. Cette méthode est rapide et suffisamment précise pour la plupart des cas. Le pourcentage des échantillons dans chaque classe peut être représenté graphiquement en diagrammes à barres ou en histogramme (Fig. 6b).

Récemment, nous avons mis au point une nouvelle stratégie d'échantillonnage pour collecter les pyroclastes pendant les explosions, en utilisant un réseau de grandes bâches de 3 × 2 m pour enregistrer les tailles, les masses et la distribution des pyroclastes qui y atterrissent (Fig. 4d). Lorsque les conditions sont favorables, les bâches peuvent être récupérées et la taille des grains peut être directement mesurée (Harris et al., 2013). Cependant, dans certaines conditions, la température élevée des pyroclastes retombant sur les bâches peut brûler le plastique, générant des trous.

Nous avons prouvé que ces trous sur la surface bâchée fournissaient une carte avec laquelle la distribution des tailles des pyroclastes pouvait être reconstruite (Colò 2012). Des photos montrant la répartition des trous et la dispersion sur chaque feuille de plastique, ont été prises avant leur extraction (Fig. 6d). Des images numériques, prises à des grossissements différents, ont été créées pour chaque feuille de plastique (Fig. 6d). Les différents grossissements ont été sélectionnés pour couvrir la répartition complète de la taille des trous. Les images des feuilles ont été traitées par un logiciel d'analyse d'image, pour réduire les images dans une échelle binaire, en noir (trous) et blanc (plastique) (Fig. 6d). Le traitement a été réalisé avec le programme Matlab FOAMS (Fast Object Acquisition and Mesurement System, Shea et al., 2010) pour obtenir la distribution cumulative de la taille des différentes scories (Fig. 6e). Cette distribution est exprimée en unité de volume et doit être transformée en poids. Une fois que les feuilles de plastique ont été retirées de la zone sommitale du volcan, les scories qui sont restées attachées à leurs trous ont été mesurées et pesées. Le tracé des mesures de surface et de masse révèle une relation linéaire entre la surface du trou et la masse, avec un coefficient de corrélation (R^2) de 0.94. Cette relation linéaire n'est valable que pour les petits fragments, ayant une surface inférieure à 2000 mm^2. Pour générer une relation pour des fragments plus grands, 53 bombes appartenant à une explosion plus intense qui s'est produite à Stromboli le 21 janvier 2010 ont été analysées (Gurioli et al., 2013, Fig. 6g). Traçant leurs poids par rapport à leurs surfaces projetées, une relation similaire a été trouvée. Ainsi, les zones de trous inférieures à 2000 mm^2 ont été multipliées par 0,94, et les surfaces supérieures à 2000 mm^2 par 0,82, suivant les coefficients de corrélation trouvés pour les deux classes de taille. Les résultats ont ensuite été convertis en pourcentage pondéral (% en poids), et la masse totale des dépôts est obtenue en additionnant les trois distributions des tailles. Les diamètres équivalents (*d*) ont été obtenus et convertis en valeurs de *phi*. On a ainsi obtenu la distribution totale des tailles qui couvre l'intervalle *phi* = -9 à -3 (équivalent à d de 512 à 8 mm, Fig. 6f).

Enfin, une autre approche nous a permis d'estimer le volume et la masse d'un champ de bombes stromboliennes (Gurioli et al., 2013). Pendant les mois de juin 2010 et juin 2011 (6 et 18 mois après l'éruption de janvier 2010 qui a mis en place les bombes), nous avons cartographié un champ de bombes qui s'étend du SE au SW du cratère central de Stromboli (Fig. 6g). À travers notre zone cartographiée, les pentes maximales étaient de 27 à 30 °, mais les bombes ont toutes été aplaties à l'impact (caractérisées par une forme d'ellipsoïde et toutes ayant une épaisseur similaire) et ont collé à la surface impactée sans se briser tout en préservant leur forme et leur position au moment de leur atterrissage. Au total, 780 bombes ont été

cartographiées. Pour chaque bombe, nous avons enregistré l'emplacement GPS et ses axes long et intermédiaire (*a* et *b*, en mm, Fig. 6h). Des photos numériques verticales ont été également prises manuellement sur 229 bombes. Ces images ont été utilisées pour dessiner le périmètre de la bombe et ainsi obtenir l'aire grâce au logiciel SPO (shape preferred orientation) de Launeau et Robin (1996). Les valeurs des aires obtenues par le logiciel ont été tracées en fonction des zones obtenues en supposant une forme elliptique de toutes les bombes (ellipse équivalente) pour rechercher une relation qui pourrait aider à calculer la surface des bombes sans s'appuyer sur des photos. La meilleure corrélation entre la surface d'une bombe ($bomb_{area}$) et *ab*, a été trouvé pour être $bomb_{area}$ = 0,7502 (*ab*) 0,9787, avec une erreur moyenne de 23 %, ce qui montre que l'hypothèse d'une forme elliptique est acceptable. Ainsi, en appliquant le coefficient de corrélation à toutes les mesures réalisées, toutes les aires ont été obtenues. Nous avons également établi une meilleure corrélation entre le volume des bombes ($bomb_{volume}$) et *ab* à partir d'une analyse de 53 bombes de masse et de densité connues (densités comprises entre 1370 à 2300 avec une moyenne 1810 kg m^{-3}) échantillonnées parallèlement et perpendiculairement à l'axe de dispersion SSE (Fig. 6g, points rouges). La meilleure corrélation est $bomb_{volume}$ = 0,2786 (*ab*) 1,3676 avec une erreur de 25 %, beaucoup plus faible que l'erreur de 150% que nous avons obtenue en estimant le volume de la bombe en multipliant l'épaisseur moyenne de la bombe (6,5 cm) par l'aire de celle-ci. Ainsi, nous avons appliqué la meilleure corrélation pour obtenir le volume pour toutes les autres bombes à travers le champ d'échantillonnage. Pour les 53 bombes échantillonnées (mentionnées précédemment), la masse a été mesurée directement en laboratoire. Pour toutes les bombes non échantillonnées, nous avons calculé la masse en multipliant le volume par la densité moyenne. Pour permettre la comparaison avec les analyses granulométriques (classiques), nous avons utilisé la dimension de l'axe *b* (Fig. 6h) pour obtenir le diamètre moyen (*d*) puis nous avons converti la valeur en *phi* et nous avons obtenu la distribution granulométrique totale (Fig. 6i, Gurioli et al., 2013).

V - 2 Comptage lithologique

Les analyses des différents composants permettent de déterminer les proportions relatives des différentes composantes dans un échantillon de pyroclastes. Les principaux composants sont habituellement des fragments juvéniles (Figs. 7a, 7b, 7e) et non-juvéniles (Figs. 7d, 7e). Les fragments juvéniles peuvent être des fragments vésiculés ou denses et des cristaux libres produits par l'explosion. Les fragments non-juvéniles sont tous les produits antérieurs à l'explosion, comme les roches encaissantes (xénolithes,

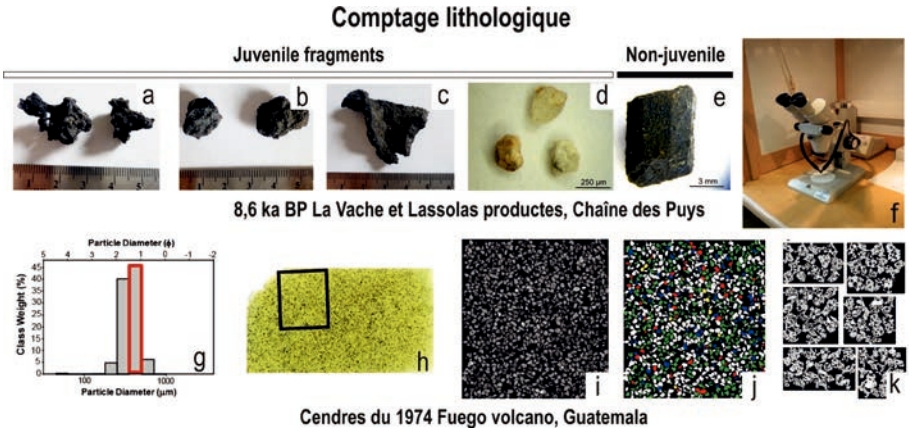

Figure 7 : Comptage lithologique : a) Images des cinq différents types de clastes dans les dépôts de La Vache et Lassolas a) clastes juvéniles vésiculés, b) clastes juvéniles arrondie, c) clastes juvéniles lamellaire, d) clastes non-juvenile granitiques et e) cristaux magmatiques (d'après Jordan et al., 2016, modifié) ; f) microscope binoculaire au laboratoire textural, LMV ; g) Histogramme de la distribution de la taille de l'échantillon de cendres de l'éruption du Fuego de 1974 ; h) Lame mince fait avec les moyennes des modes de taille des grains ; i) Acquisition d'images ESB à des grossissements x100 en utilisant la technique de la mosaïque ; j) Classification des clastes dans cinq familles (blanc = phénocristaux ; vert = vésicules ; bleu = polyèdres ; rouge = croissance sur phénocristaux ; jaune = non-juvénile) ; k) Traitement de l'image (d'après Cabré Brullas 2015, modifié).

roches profondes qui forment la chambre magmatique, fragments de l'érosion des conduits, roches altérées d'un réservoir hydrothermal situé à la profondeur du niveau de fragmentation), ou accidentelle (érodée du substratum). L'abondance et les proportions relatives de ces composants dans les différentes classes granulométriques fournissent des informations sur le type de fragmentation (magmatique ou phréatomagmatique), sur le système d'alimentation et sur les processus actifs dans le conduit (Wohletz, 1983 ; Sheridan et Marshall, 1983 ; Barberi et al., 1989 ; Taddeucci et al., 2002 ; Eycienne et al., 2015). Différentes techniques sont utilisées pour séparer les différents composants. Les classes de plus grande taille sont sélectionnées à la main. Pour les classes de taille de 2 mm à 0,5 mm, le prélèvement manuel est effectué sous un microscope binoculaire (Fig. 7f) à l'aide de pinces fines. Pour les classes les plus fines, suivant la méthode de Barberi et al. (1989), des lames minces de grains de taille similaire sont réalisées (Figs. 7g, 7h). Les grains sont comptés, à l'aide d'un comptage automatique de point au microscope optique ou compté au MEB (Figs. 7i, 7j, 7k). Au moins 750 points par lame mince sont nécessaires. En utilisant cette méthode, il est nécessaire de déterminer un facteur de conversion, afin d'obtenir un pourcentage en poids équivalent, mesurant la densité des différents grains. D'après le tableau de Van Der Plas et Tobi (1965), l'erreur est de 3,5 %.

V - 3 Analyses morphologiques

Les formes des particules enregistrent les processus responsables de leur génèse et contrôlent le comportement et l'interaction des particules (Liu et al., 2015a). Les mesures de forme fournissent des informations sur l'origine et l'évolution (Dellino et La Volpe, 1996 ; Büttner et al., 2006 ; Manga et al., 2011 ; Liu et al., 2015b), les propriétés (Duerig et al., 2012), et le comportement des particules transportées, telles que les propriétés de décantation ou de rayonnement / diffusion (Riley et al., 2003 ; Alfano et al., 2011 ; Kylling et al., 2014 ; Bagheri et al. , 2015 ; Merikallio et al., 2015). Les paramètres de forme de la particule fournissent des mesures quantitatives et reproductibles, qui minimisent la subjectivité associée à la terminologie descriptive et permettent la comparaison directe entre les particules. Alors qu'une sphère parfaite peut être décrite de manière unique par une seule propriété (son diamètre) des particules de forme irrégulière nécessitent des mesures de dimensions multiples (Blott et Pye, 2008). Les cendres volcaniques, en particulier, englobe un large éventail de formes, chacune avec des propriétés physiques et des comportements différents. La morphologie des particules de cendre joue un rôle important en terme de mécanisme de dépôt, car la forme des grains au sein du dépôt cendreux influe sur leur probabilité de se déposer ou de rester en suspension dans l'atmosphère, ce qui impact l'analyse et l'atténuation des risques liés aux cendres. Les formes des cendres juvéniles reflètent également les mécanismes de fragmentation opérant au cours d'une éruption, qui sont à leur tour contrôlés par les propriétés magmatiques (telles que la viscosité, la température et la composition) et les conditions dans lesquelles le magma monte et se fragmente (Heiken, 1972 ; Heiken et Woheletz, 1985 ; Cioni et al., 2008 ; Liu et al., 2015a, b).

L'instrument Malvern Morphologi® G3 (Fig. 8a), au LMV, a la capacité de calculer les dimensions des particules directement à partir d'images 2D, d'effectuer des analyses rapides de la taille des échantillons bien plus grandes en comparant ce qu'il était possible de réaliser par des mesures manuelles (Leibrandt et Le Pennec, 2015). Cet instrument, facile à utiliser, fournit la taille et la forme des particules de 0,5 microns à quelques millimètres par la technique de l'analyse d'image statique. La préparation des échantillons et l'analyse de forme sont réalisées suivant le protocole de Leibrandt et Le Pennec (2015). Les échantillons sont nettoyés, séchés et tamisés au quart des intervalles *phi*. Ensuite, un volume d'environ 190 mm^3 est extrait avec une cuillère de précision et introduit au centre du récipient d'échantillon qui est lui-même introduit dans la cartouche de l'unité de dispersion. L'échantillon est ensuite dispersé sur la plaque de verre du microscope par injection d'air comprimé et l'analyse automatique des particules dispersées est réalisée à un grossissement fixe (Fig. 8b). Les données brutes sont

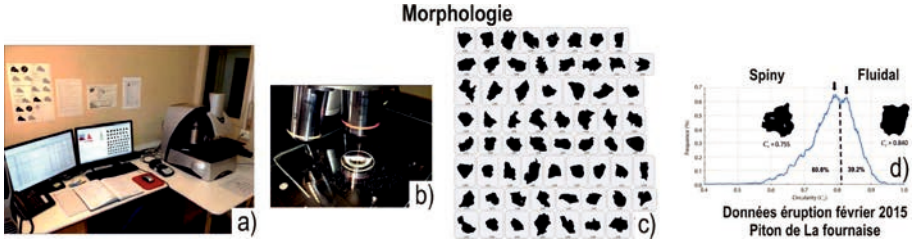

Figure 8 : Mesure de la morphologie : a) Morphologi G3 au laboratoire textural, LMV ; b) Echantillon dispersé sur la plaque de verre du microscope par injection d'air comprimé ; c) Particules de cendre de taille de 250-300 µm de l'éruption de Février 2015 ; d) Diagramme de fréquence de la circularité pour la cendre présenté dans la Figure 8c.

filtrées, d'abord par la suppression automatique de toutes les particules qui sont plus petites que l'intervalle de taille des grains de l'échantillon, afin que les poussières présentes sur la plaque de verre ne soient pas prises en compte dans la mesure. Ensuite, les données des agrégats de particules et des images de mauvaise qualité (mauvaise mise au point, seuil ou couture) sont supprimées manuellement. Cette méthode permet de mesurer une gamme de propriétés morphologiques (Figs. 8c, 8d) pour chaque particule comme : (i) les propriétés brutes (nombre, emplacement, taille, forme, transparence), (ii) les paramètres de taille (diamètre équivalent, diamètre, longueur, largeur, périmètre, volume équivalent), (iii) les paramètres de forme (rapport d'aspect, circularité, convexité, solidité, allongement), (iv) les paramètres de transparence (moyenne intensité, intensité écart-type). La force de la machine repose sur le disperseur de poudre sèche, fixé à la machine, qui disperse l'échantillon sur la plaque du microscope de manière reproductible. L'instrument enregistre des images de particules individuelles en balayant l'échantillon au-dessous de l'optique du microscope, tout en maintenant les particules dans le foyer optique (Fig. 8b).

V - 4 Les mesures de densité

Les mesures de densité sont extrêmement importantes car elles fournissent une indication de premier ordre de l'homogénéité de texture ou de l'hétérogénéité du magma au niveau de la fragmentation (Shea et al., 2010 ; 2011). De plus, les distributions de densité sont utilisées comme filtres pour sélectionner quelques clastes, représentatifs des valeurs faibles, modales élevées, de chaque sous-population observée (Gurioli et al., 2005 ; 2008). Les clastes sélectionnés sont ensuite utilisés pour la quantification texturale. Cependant, l'hypothèse selon laquelle les échantillons représentent le magma refroidi au niveau de la fragmentation a trois exigences (Gurioli et al., 2015a). Tout d'abord, le magma doit être trempé immédiatement

après la fragmentation afin d'éviter une expansion post-fragmentation qui modifiera la vésicularité du claste (Thomas et al., 1994). Deuxièmement, la densité varie en fonction de la taille des grains, donc seuls les clastes d'une taille restreintes doit être mesurés. Enfin, l'échantillon doit être représentatif de l'activité explosive considérée, en termes : (i) du temps (c'est-à-dire que nous devons échantillonner des intervalles stratigraphiques étroits dans lesquels nous pouvons supposer que les clastes représentent les parties du magma qui se sont fragmentées au moment considéré) ; (ii) de l'espace (c'est-à-dire que nous avons besoin de sélectionner plusieurs zones pour chaque événement eruptif) ; (iii) la taille des particules (c'est-à-dire si une explosion est dominée par les bombes, les lapilli ou les cendres, la méthode d'échantillonnage doit être choisie de manière appropriée) ; (iv) de la composition (c'est-à-dire si la fraction juvénile est hétérogène, l'échantillon doit refléter cette hétérogénéité). Obéir à ces règles est fondamental si l'on veut traduire l'information magmatique initiale et les propriétés du magma dans le conduit à travers les échantillons.

a. Méthode d'enveloppement des échantillons

La densité de la majorité des échantillons a été déterminée en mesurant leur masse à la fois dans l'air et dans l'eau, basé sur le principe d'Archimède (Houghton et Wilson, 1989 ; Shea et al., 2010). Cette technique a été la plus largement utilisée et a permis d'accumuler puis de comparer une large gamme de données. Pour évacuer une éventuelle présence d'eau dans les échantillons, ils sont préalablement placés dans un four à 100°C pendant une journée. Pour les échantillons de ponce ou de scories, un sous-ensemble de clastes est habituellement classé par taille décroissante et numéroté de 1 à 100 (Fig. 9a). Pour les autres spécimens, en particulier les plus gros, la roche est découpée en moitiés (Fig. 9a), une moitié étant conservée pour l'imagerie par scanner et l'autre servant pour les mesures de densité et l'imagerie microscopique. Pluieurs sous-échantillons peuvent corresprondre à des propriétés texturales différentes et sont soigneusement individualisés. Si l'échantillon est homogène, aucune autre subdivision n'est nécessaire, à condition que sa taille soit suffisante pour le peser en laboratoire.

La relation simple donnée par Houghton et Wilson (1989) nous permet en théorie de calculer la densité d'enveloppe ($\rho_{enveloppe}$) d'un objet en connaissant sa masse mesurée dans l'air (m_{air}) et dans l'eau (m_{eau}) avec l'utilisation d'une balance (Fig. 9b).

$$\rho_{envelope} = \rho \frac{m_{air}}{m_{air} - m_{eau}} \quad (1)$$

Cependant, dans le but d'imperméabiliser l'échantillon mesuré lors des pesées dans l'eau, l'application d'un parafilm autour de celui-ci est

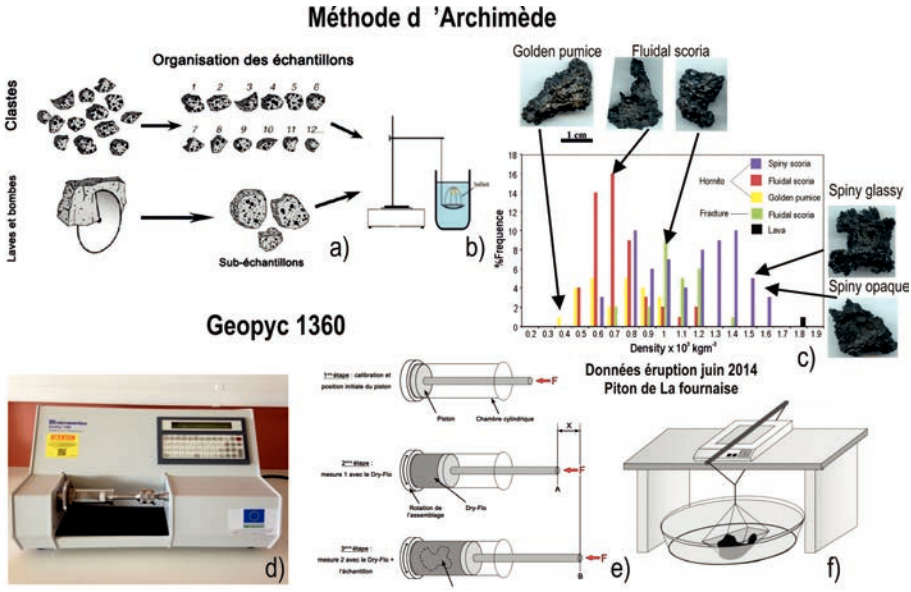

Figure 9 : Les mesures de densité : a) Mesures de densité en utilisant le principe d'Archimède : schéma illustratif la préparation d'échantillons explosifs et effusifs, d'après Shea et al. (2010), modifié ; b) Lestage avec une cage solide dans le cas où les échantillons sont moins dense que l'eau ; c) Histogramme des masses volumiques et de la porosité selon le type de claste, normalisé au nombre total d'échantillons, d'après Gurioli et al. (2015b), modifié. Les différents types de fragments sont également présentés ; d) L'analyseur de densité d'enveloppe Geopyc 1360, au laboratoire textural du LMV ; e) schéma illustratif des manipulations à suivre pour mesurer la densité des échantillons avec le Geopyc 1360. F représente la force de consolidation choisie par l'utilisateur et appliquée sur le piston, Voir le texte ci-dessous pour les explications, d'après Thivet (2016), modifié ; f) Schéma du dispositif de pesée utilisé dans l'étude des bombes du Stromboli, d'après Bernard (2011), modifié.

nécessaire. En prenant compte la masse du parafilm immergé ($m_{parafilm}$), l'équation (1) devient (Shea et al., 2010) :

$$\rho_{envelope} = \rho \frac{m_{air}}{m_{air} - m_{eau} + m_{parafilm}} \quad (2)$$

Cette méthode consiste donc à mesurer la masse de l'échantillon à la fois dans l'air ambiant et dans l'eau mais aussi de quantifier l'apport de parafilm utilisé. En appliquant la formule (2) les différentes densités sont calculées et converties en masses volumiques ($g.cm^{-3}$). Dans le cas où les échantillons sont moins dense que l'eau (< 1 $g.cm^{-3}$), une cage solide est utilisée pour les immerger totalement (Fig. 9b). L'erreur sur les pesées est faible (± 0,01 g) mais l'erreur la plus grande repose sur la détermination du volume de l'échantillon : cette méthode peut fournir parfois des densités légèrement sous-estimées dues essentiellement à l'incorporation d'air lors de la pose du parafilm. De plus l'étanchéité de l'échantillon doit être scrupuleusement respectée. La différence maximale observée sur des mesures répétées sur un seul échantillon est de 0,03 g/cm^3 (Barker et al.,

2012). En somme, les mesures sur les densités en appliquant cette méthode sont assez reproductibles et les variations dues à ces erreurs sont négligeables par rapport aux variations naturelles de densité des échantillons (Fig. 9c).

Les grosses bombes échantillonnées lors de l'éruption au Stromboli (Fig. 6g) ont été mesurées sans aucune perméabilisation (Fig. 9f). En effet, lorsque l'on plonge les échantillons dans l'eau sans préparation préalable, aucune bulle n'apparaît. Cela signifie que l'eau ne rentre pas dans les échantillons et que ces derniers sont imperméables grace à l'effet de la bordure de trempe.

b. GeoPyc 1360

Récemment, l'analyseur de densité d'enveloppe Geopyc 1360 de Micromeritics (Fig. 9d) a été installé au laboratoire textural. L'instrument mesure la densité d'enveloppe d'objets de tailles et de formes irrégulières. La taille des clastes est limitée entre 2 mm (résultats imprécis en dessous de cette valeur) et 5 cm (taille de chambre insuffisant au dessus de cette valeur). Cet instrument détermine le volume et la densité d'un objet solide par la mesure de déplacement d'un milieu solide. Ce milieu, nommé "Dry-Flo", est composé de petites sphères rigides (< 1 mm) avec un haut degré de fluidité qui peut totalement enrober les échantillons.

Après une calibration préliminaire de l'instrument (étape 1 sur la Figure 9e), la deuxième étape de l'analyse consiste à choisir une taille de chambre adéquate à l'échantillon choisi puis d'y introduire un montant suffisant de Dry-Flo pour enrober potentiellement la totalité de cet échantillon. La chambre (cylindre dont le diamètre interne est précisément connu) est insérée dans l'instrument et un piston comprime le Dry-Flo. Les forces de compression sont réglables et prédéfinies selon les tailles de chambre et donc reproductibles d'une analyse à l'autre. La position du piston est mesurée automatiquement (A sur la Figure 9e) et cette valeur établit une ligne de base uniquement avec le Dry-Flo.

La troisième étape consiste à ajouter l'échantillon dans la chambre contenant le Dry-Flo. Un processus de rotation rapide et intermittent de la chambre lors du compactage permet au Dry-Flo de bien enrober l'échantillon sur toute sa surface. La même force de compression est appliquée au mélange Dry-Flo + échantillon et la position du piston est à nouveau mesurée par l'instrument (B sur la Figure 9e).

À chaque étape, 10 cycles de mesure sont effectués pour obtenir des résultats moyennés. Une fois ces deux manipulations effectuées, l'instrument procède aux calculs. La différence de position du piston entre les deux manipulations (A-B = X sur la Figure 9e) est alors due au volume de l'échantillon. Comme la chambre est un cylindre et son diamètre interne

est connu, l'instrument calcule le volume de l'échantillon ($V_{enveloppe}$) à partir de la formule du volume du cylindre :

$$V_{envelope} = \pi r^2 X \quad (3)$$

Où *r* est le rayon interne de la chambre choisie et *X* la hauteur du cylindre correspondant à la différence de position du piston entre les deux manipulations. Ce volume est ensuite corrigé à partir d'un facteur de conversion prédéfini pour chaque taille de chambre et pour une forme de claste donnée. De plus, l'échantillon a été préalablement pesé ce qui permet de calculer la masse volumique de l'échantillon en divisant sa masse par son volume total. Pour éviter la deuxième étape de l'analyse et ainsi optimiser la vitesse de mesure, une calibration supplémentaire est effectuée : pour chaque chambre, plusieurs montants de Dry-Flo sont pesés et les positions relatives du piston mesurées. Ainsi, à chaque analyse et pour une certaine masse de Dry-Flo donnée, l'instrument peut estimer la position du piston à la deuxième étape sans passer par une mesure. Dans le cas de la présence de petits pores (< 1 mm), les particules solides que composent le Dry-Flo n'envahissent pas les cavités présentes à la surface des échantillons. En revanche, des essais montrent que sur la majorité des échantillons dont les pores sont plus gros et plus accessibles, la densité d'enveloppe est systématiquement sur-estimée car les particules que composent le Dry-Flo s'infiltrent partiellement dans les cavités. Dans ce cas, il est préférable d'imperméabiliser les échantillons avec du parafilm dont le volume reste négligeable par rapport au volume de l'échantillon. La majorité des mesures engendrent des erreurs inférieures à ± 0,02 g.cm-3. Les résultats sont donc assez reproductibles pour ce genre de mesure. Comme évoqué plus tôt, les variations dues aux erreurs sont négligeables par rapport aux variations naturelles de densité des échantillons.

c. Calculs de porosité

Les densités de tous les échantillons sont classées et la porosité est ensuite calculée grâce cette relation donnée par Houghton et Wilson (1989) :

$$P = \frac{100 * \left(\rho_{enveloppe}\right) - \left(\rho_{enveloppe}\right)}{\rho_{dense}} \quad (4)$$

où *P* est le pourcentage volumique de la porosité de l'échantillon et ρ_{dense} est la densité équivalente des produits éruptifs sans prendre en compte les bulles (densité du squelette solide). Une autre formule, donnée par Formenti et Druitt (2003), permet aussi de calculer la porosité totale des différents échantillons avec la même précision :

$$P = 1 - \frac{m_{air}}{\rho_{dense} * V_{enveloppe}} \quad (5)$$

$V_{enveloppe}$ (volume total de l'échantillon : cristaux, verre et bulles) est mesuré lors de l'utilisation du Geopyc 1360 (cf. partie V-4c) mais il peut

être aussi calculé en divisant la masse de l'échantillon par sa densité pour les échantillons uniquement mesurés avec le principe d'Archimède. La mesure de ρ_{dense} et l'utilisation de la porosité combinée à la connectivité pour calculer le pourcentage de bulles isolées sont décrites dans la partie ci-dessous (cf. partie V-5).

V - 5 Measure de connectivité

Les mesures de connectivité permettent d'obtenir le pourcentage de vésicules isolées par rapport à vésicules connectées. Ces mesures fournissent des informations de premier ordre sur la capacité de dégazage (c'est-à-dire le potentiel de perte de gaz) du magma à proximité de la fragmentation (Klug et al., 2002 ; Formenti et Druitt, 2003 ; Giachetti et al., 2010 ; Shea et al., 2011 ; 2012).

L'AccuPyc II 1340 Gas Displacement Helium Pycnometer de Micromeritics (Fig. 10a) au LMV permet de mesurer le taux de connectivité entre les vésicules, et l'abondance des vésicules isolées des échantillons (cendres, lapilli, fragments de bombes). Cet instrument est bien adapté pour ce type de mesure car l'hélium est un gaz inerte très léger qui peut s'infiltrer dans les vésicules les plus petites. Cette technique utilise le déplacement des gaz pour mesurer un volume avec précision, appliquant le principe des gaz parfaits. L'hélium est utilisé comme milieu de déplacement. Les mesures avec le pycnomètre donnent le volume des phases solides (cristaux et verre) ainsi que celui des vésicules isolées de chaque échantillon (V_{pyc}). Après avoir calibré le pycnomètre avec des objets de volumes connus et introduit l'échantillon dans une chambre étanche et appropriée (350, 100, 35 et 10 cm^3), la première valve (1 en Fig. 10b) s'ouvre et l'hélium s'écoule dans la chambre de l'échantillon (Fig. 10b, étape 1). Une fois l'équilibre de pression atteint, la valve (1 en Fig. 10b) se referme puis la pression du gaz (P_1) et la température (T_1) sont mesurées (étape 2). Ensuite, la deuxième valve (2, en Fig. 10b) s'ouvre laissant la quantité d'hélium utilisée dans la première chambre, circuler dans la seconde, de volume V_2 (étape 3) puis l'équilibre est une nouvelle fois atteint, la pression (P_2) et la température (T_2) mesurées (étape 4). La pression est ensuite évacuée (étape 5). Dans le cas de l'hélium, la loi des gaz parfaits est applicable et pour un volume molaire équivalent (pas de perte de gaz entre les deux chambres), cette loi donne :

$$PV = nRT \rightarrow \frac{P_2V_2}{P_1V_1} - \frac{T_2}{T_1} \quad (6)$$

où V_1 est le volume de la chambre de l'échantillon ($V_{chambre}$) moins (V_{pyc}). L'instrument mesure et calcule V_{pyc} ce qui donne :

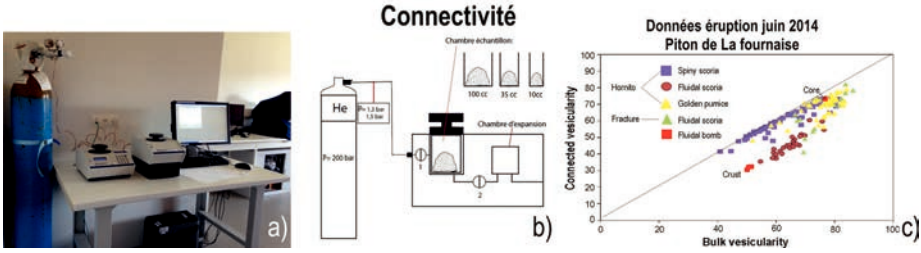

Figure 10 : Les mesures de connectivité : A) l'Accupyc II 1340 au Laboratoire textural du LMV ; b) Schéma illustratif du fonctionnement de l'Accupyc II 1340. Voir le texte ci-dessous pour les explications ; c) Taux de porosité par rapport à la vésicularité interconnectée entre les vésicules selon le type de pyroclaste. Les lignes pointillées représentent des lignes de fraction égale de vésicules isolées.

$$\frac{P_2 V_2}{P_1 * (V_{chambre} V_{pyc})} = \frac{T_2}{T_1} \leftrightarrow V_{pyc} = V_{chambre} - \frac{P_2 V_2 T_1}{T_2 P_1} \quad (7)$$

À partir de cette mesure, Formenti et Druitt (2003) donne la formule (8) ci-dessous permettant de calculer le pourcentage de la porosité interconnectée (P_c). Le degré de connexion des vésicules C est obtenu en normalisant P_c à la porosité totale P :

$$P_c = 1 - \frac{V_{pyc}}{V_{enveloppe}} \quad (8) \quad C = \frac{P_c * 100}{P}$$

Afin de mesurer ρ_{dense}, un échantillon représentatif du magma étudié a été réduit en poudre, pesé et son volume a été déterminé avec le pycnomètre dont l'utilisation s'applique à une large variété d'échantillons notamment les poudres. La densité équivalente de l'échantillon sans prendre en compte les vésicules (densité du squelette solide ρ_{dense}) est alors obtenue en divisant la masse de la poudre par son volume.

La précision sur une mesure de volume est de 0,03 % du volume de la chambre plus 0,03 % du volume de l'échantillon. Les standards de calibration permettent de vérifier la précision des mesures sur le pycnomètre. La différence Δ entre le volume mesuré lors d'une analyse et la vraie valeur du volume standard doit être inférieure à la précision. Par exemple, pour une bille de calibrage de volume connu V=51,076 cm^3 et une chambre de 100 cm^3, cette différence Δv doit être inférieure à Δv= (0,03/100)*100 + (0,03/100)*51,076 = 0,045 cm^3. Si cette condition n'est pas obtenue, il faut recalibrer le pycnomètre. Nous avons vérifié la précision avant et aprés chaque série de mesure en effectuant n analyses sur les standards jusqu'à obtenir un résultat satisfaisant, ou recalibrer l'instrument si nécessaire. Un problème majeur pour les mesures au pycnomètre concerne le volume des clastes par rapport au volume de la chambre. La majorité des clastes ont un volume inférieur à 10 % du volume de la chambre, dans ce cas la précision sur la mesure est potentiellement moins bonne.

V - 6 Mesures de permeabilité

Durant le poste de professeur invité de T. Shea (Université d'Hawaii à Manoa) à Clermont-Ferrand en mai 2013, nous avons construit un perméamètre (Figs. 11a, 11b) conçu par Takeuchi et al. (2008). L'instrument nous permet d'effectuer des mesures très reproductibles de perméabilité en utilisant des matériaux volcaniques poreux et trempés. Ces mesures sont utilisées pour comprendre le développement de la perméabilité et le dégazage des magmas vésiculés.

Le perméamètre a de larges plages de mesure de différence de pression (10^1-10^5 Pa) et débit de gaz (10^{-9}-10^{-5} m^3/s). Ces gammes nous permettent de mesurer la perméabilité visqueuse dans la gamme de 10^{-17}-10^{-9} m^2 pour des échantillons à l'échelle centimétrique, en utilisant l'équation de Forchheimer (Rust et Cashman, 2004), qui inclut l'effet d'inertie du débit de gaz passant à travers des échantillons (Voir Takeuchi et al. (2008) pour plus de détails).

Toute mesure de perméabilité nécessite une bonne préparation de nos échantillons (Fig. 11c) ainsi, elle représente une étape fondamentale dans une telle mesure. En effet, après le choix de l'échantillon approprié, un sciage est effectué sur l'échantillon en vue de l'obtention d'un parallélépipède (etape 1, Fig. 11c). La phase de sciage terminée, notre sucre en question est mis à l'étuve pendant 24 heures à 100 °C. L'échantillon est enduit d'une fine couche de résine et recouvert de parafilm (etape 2, Fig. 11c). Pour une adhésion quasi parfaite du parafilm avec les contours du sucre de roche en question, un temps de repos de près de 12 heures est observé et, après ce temps, notre sucre de roche est placé dans un tube en plastique cylindrique et colmaté à l'intérieur de ce tube cylindrique à l'aide d'un mélange de résine et de durcisseur (etape 3, Fig. 11c). Après le durcicement de la résine, nous avons obtenu un plot et avons scié puis poli les extrémités de ce plot afin de mettre à l'affleurement les faces supérieures et inférieures de l'échantillon (etape 4, Fig. 11). Ainsi, le plot obtenu est alors inséré entre deux blocs en acrylique et fixé à l'aide de deux joints toriques afin d'éviter un échappement de l'air au contact entre le plot et le bloc en acrylique (Fig. 11b). L'air pénètre à l'intérieur de l'échantillon à une pression P_i puis ressort de l'autre côté à une pression finale plus faible P_f. La différence de pression est mesurée à l'aide d'un baromètre pour différentes valeurs du débit ajustée à l'aide de deux débitmètres. (Fig. 11b). Après avoir calibré le perméamètre, les mesures de perméabilité basées sur la loi de Darcy sont effectuées :

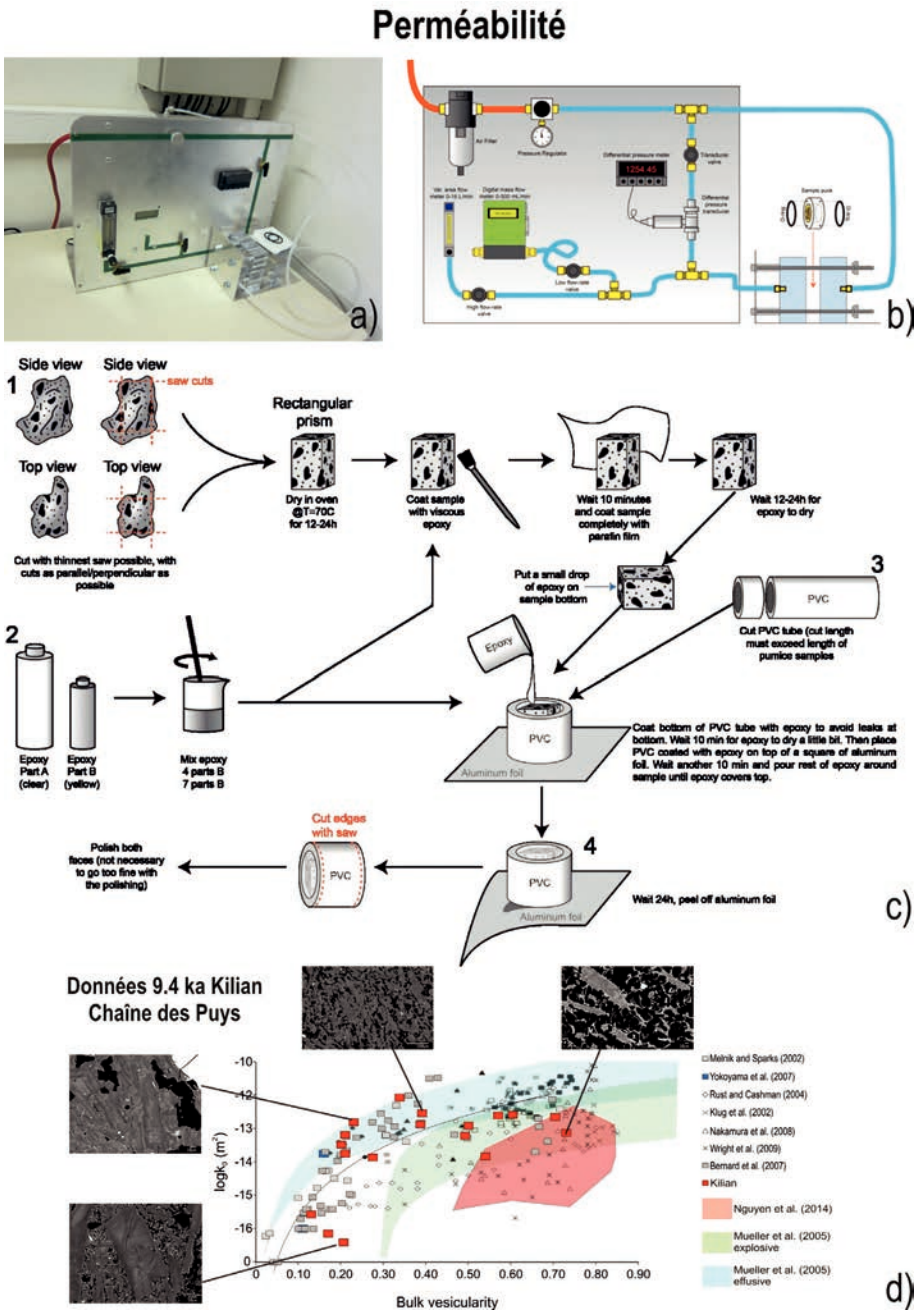

Figure 11 : a) Perméamétre au laboratoire textural, LMV ; b) dispositif de fonctionnement ; c) Préparation des échantillons d) données de perméabilité de Kilian en fonction de la vésicularité ainsi que des données d'études antérieures basées sur des mesures de perméabilité de tephras siliceux. Image BSE illustrant les diffèrents clastes (vésiculés et denses) de Kilian.

Où P est la pression, et x est la coordonnée spatiale. Par conséquent, $-dP/dx$ est le gradient de pression conduisant le flux perméable ; k_0 est la perméabilité apparente ; ν est le flux volumique, calculée à partir de la vitesse d'écoulement divisée par la surface en coupe transversale de l'échantillon et μ est la viscosité d'un fluide de travail.

L'erreur enregistrée ici est principalement liée à la variation de la pression atmosphérique qui peut potentiellment changer en fonction des conditions.

Sur la Figure 11d est représenté la variation de la perméabilité des dépôts de ponce trachytiques échantillonnés par l'éruption de Kilian, Chaîne des Puys (Colombier et al ; 2017). La présence de ponce vesiculées et perméables et des fragments plus denses et imperméables est en accord avec la présence d'un bouchon superficiel liée à une activité vulcanienne.

V-7 Analyse texturale microscopique

Les quantifications texturales des particules échantillonnées nous permettent d'obtenir des informations quantitatives à la fois sur l'ascension, la vésiculation et la fragmentation du magma. Dans le domaine textural, une ponce ou scorie est une petite fenêtre d'observation sur le conduit volcanique qui nous permet de décrire les paramètres qui seraient autrement inobservable. La quantification texturale implique une description complète de la taille, forme et distributions des vésicules et des cristaux des produits émis (Gurioli et al., 2015a).

Deux méthodes différentes sont actuellement disponibles pour extraire ces paramètres. La première consiste à convertir des données en 2-D d'une surface plane (comme une lame mince ou une photographie) en données 3-D par la stéréologie (Sahagian et Proussevitch, 1998). La seconde méthode dérive des données 3-D directement à partir de reconstructions tomographiques de rayons X et la visualisation de textures de clastes sans la nécessité de conversions stéréologiques (Song et al., 2001 ; Polacci et al. 2006 ; Degruyter et al., 2010b ; Giachetti et al., 2011 ; Baker et al., 2012), à l'aide de logiciels spécialement conçus pour des applications géo-texturales. D'autres procédés 3-D comprennent le « serial sectioning » (Bryon et al., 1995), « serial focusing » (Manga, 1998), « seria grinding » (Marschallinger, 1998) et les « digital elevation models » de grains de cendres individuels pour calculer le volume des vésicules (Proussevitch et al., 2011).

Des procédures standard pour la méthode 2-D ont été récemment publiées pour les vésicules (Shea et al., 2010 ; Gurioli et al., 2015a) et des cristaux (Higgins, 2000 ; 2006). Les techniques bidimensionnelles peuvent donner des données de haute qualité et tenir compte de la taille des vésicules et des cristaux dans l'échantillon et peuvent être appliquées à des particules allant de la taille des bombes aux cendres (Gurioli et al.,

2014 ; Leduc et al., 2015 ; Miwa et al., 2009 ; 2013 ; Miwa et Toramaru, 2013). Ces mesures sont plus utilisées notamment en présence d'une large distribution de taille à mesurer. La principale limitation de cette méthode est celle qui repose sur l'hypothèse de la forme sphérique des objets étudiés. Les corrections empiriques sont couramment utilisées pour les analyses cristallines (Higgins, 2000 ; 2006), mais pour les vésicules dont les formes sont moins uniformes, elles risquent d'introduire des erreurs systématiques et non contrôlées dans les données (Sahagian et Proussevitch, 1998). Les observations bidimensionnelles et tridimensionnelles ont des limites et un potentiel différents, et les deux méthodes deviennent complémentaires et non concurrentielles (Giachetti et al., 2011 ; Baker et al., 2012).

DynVolc fournit des mesures de texture basées sur l'approche 2-D. La méthodologie est expliquée dans Rose-Koga et al. (ce volume). Pour les applications sur des produits laviques ou plus élvolués, le lecteur peut également se référencer à Colombier et al ; (2017), Latutrie et al. (2017).

V-8 Misure petrologique, chimique et geochimique

L'analyse géochimique et pétrographique des produits pyroclastiques peut contraindre les conditions initiales, dans la chambre magmatique jusqu'à la surface, via le conduit. Combiner les études texturales avec les dépôts sur le terrain (Mattsson, 2010), les données pétrologiques (Shea et al 2009 ; 2010) et les analyses chimiques (Schipper et al., 2011 ; Shea et al.,

Figure 12 : Page web de la base des données DynVolc.

2012 ; 2014) nous permettent de livrer des images complètes d'éruptions explosives et leurs dynamiques (Gurioli et al., 2015a). Dans le service DynVolc des analyses chimiques sont réalisées à la fois in situ et en roche totale sur échantillons explosifs et effusifs. Les analyses ponctuelles sont effectuées sur les verres et les cristaux grâce à la microsonde électronique.

Les analyses en roches totales sont réalisées grâce à l'ICP-AES et permettent une caractérisation chimique préliminaire des différents magmas mis en jeu pour chaque éruption. Ces methodes sont décrites dans le papier de Rose-Koga et al ; (ce volume), excepté pour les mesures géochimiques en roche totale où le lecteur peut se référencer à Harris et al in revision.

VI - Diffusion des données

Les données décrites ci-dessus sont maintenant disponible sur le Web à (http://wwwobs.univ-bpclermont.fr/SO/televolc/dynvolc/index.php, Fig. 12), développé en collaboration avec S. Rivet. La base de données DynVolc lie des données de terrain (c'est-à-dire les résultats de la cartographie de terrain, de l'affleurement et des descriptions d'échantillons), des analyses texturales et chimiques de l'échantillon (c'est-à-dire des distributions de taille des vésicules et des cristaux) et des données géophysiques quand ils sont disponibles. La base de données couvre toute la gamme des types d'activités explosives et effusives. Les données du Piton de La Fournaise, Chaine des Puys, Mt. Dore, Stromboli, Etna, Vésuve, Villarrica, Chaitén, Pacaya et Kilauea sont déjà disponibles pour les produits explosifs et effusifs. D'autres données seront disponibles en accord avec des collaborateurs internationaux tels que l'Université de Firenze, l'INGV-Catania, l'Université de Buffalo, l'Université technologique du Michigan, l'Observatoire du volcan Hawaïen (HVO), l'Université de l'Oregon, etc.

Actuellement la base de données est en cours d'élaboration avec le support informatique de E. Delage et Y. Guehenneux pour permettre (i) l'automatisation de l'intégration des données, (ii) l'amélioration de la diffusion des données via des échanges de données standardisés, (iii) l'harmonisation des interfaces pour améliorer l'expérience de navigation web, et faciliter l'accès à information. Dans une deuxième étape le but sera de placer la base de données dans l'Observatoire Virtuel de OPGC (actuellement en phase de construction). L'observatoire virtuel (VO) est une collection d'archives de données interopérables et d'outils logiciels qui utilisent Internet pour former un environnement de recherche scientifique dans lequel des programmes de recherche peuvent être menés.

Enfin, dans le cadre du projet européen EPOS (European Plate Observing System), l'objectif est de mettre à jour la base de données dans des formats clairement définis et normalisés. Si cet objectif est atteint, la

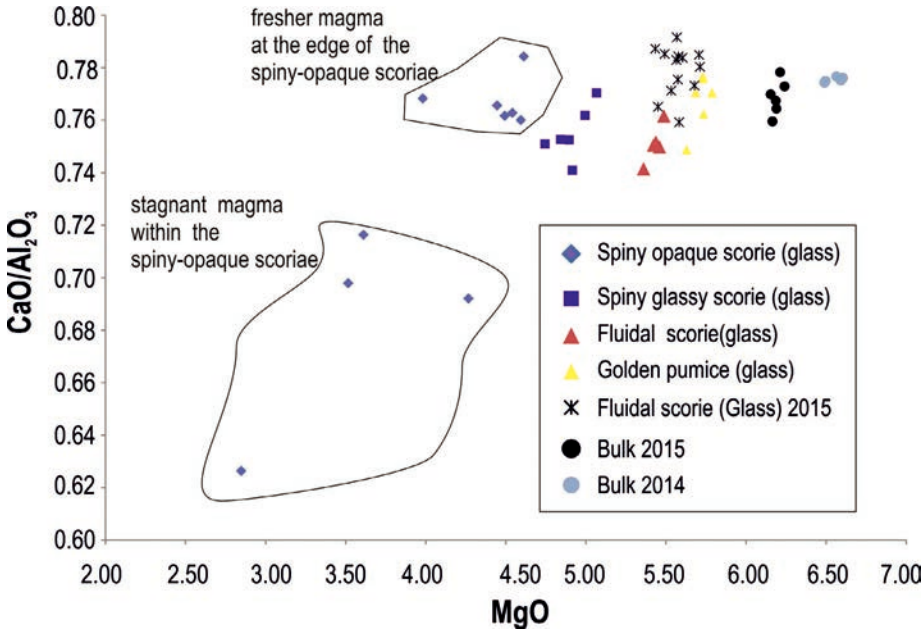

Figure 13 : Digramme CaO/Al2O3 en fonction de MgO pour les produits de l'éruption de juin 2014 et février 2015 au Piton de La Fournaise.

base de données sera comme une banque que les chercheurs peuvent utilisés pour télécharger des données ou pour insérer de nouvelles données.

VII - En conclusion : l'exemple d'étude de l'activité en cours au PdF

Depuis 2013, nous avons lancé le Service d'observation DynVolc, au Piton de La Fournaise (PdF), pour :

- caractériser l'activité en cours et passée au PdF en termes de signatures texturales, chimiques et / ou géochimiques des produits éruptifs (pyroclastes et lave),
- élucider les mécanismes déclenchant et propulsant les événements éruptifs courants, faible et peu profonds et les événements inhabituels les plus energetiques passés,
- identifier les signatures particulières qui annoncent un changement dans l'activité et utiliser les paramètres clés pour souvrir et observer l'activité en cours.

Plusieurs travaux de terrain ont été effectués pour échantillonner l'activité passée et actuelle. Cependant, au cours des crises volcaniques de juin 2014, février, mai, juillet et octobre 2015, mai 2016 et septembre 2016, plusieurs

échantillons ont été envoyés par OVPF à LMV / OPGC et plusieurs mesures ont été effectuées. Les études sur l'activité passée sont en cours sur (i) la séquence entière d'un des plus violents évènements volcaniques traduit par une activité hawaïenne et des fontaines de lave, attribués à l'activité de Chisny, (ii) toute la séquence de l'éruption violente de 1860, (iii) les petits cônes pyroclastiques à l'intérieur du cratère de Bory associé à des dépôts de projections jetés au-dessus de sa bordure occidentale, (iv) le canal de lave de courte durée mis en place en décembre 2010 et (vi) le flux de lave de 2007 riche en cristaux.

Depuis 2014, des analyses granulométriques ont été effectuées à la fois sur les dépôts cumulés (dans le temps) collectés à partir d'évents individuels (Figs. 6a, 6b) et/ou sur les explosions ponctuelles. Surtout lorsque nous ne pouvons pas observer l'activité en cours, ces analyses nous permettent de suivre le changement dans l'intensité explosive et le dynamisme éruptif dans le temps. L'activité 2014 au niveau de l'évent principal (Fig. 6a), par exemple, a été caractérisée au début (la base des dépôts, Fig. 6b) par des fontaines de lave plus violentes (la distribution granulométrique est unimodale, presque normale, Fig.6b) et vers la fin (dans la partie supérieure des dépôts, Fig. 6b) par des explosions stromboliennes moins énergiques (distribution granulometrique moins définies, asymétriques par rapport à la distribution des clastes les plus grossiers, Fig. 6b).

En termes de composition des dépôts, quatre types de clastes ont été distingués des activités de 2014 (Fig. 9c ; Gurioli et al., 2015b) à 2016: la pierre ponce dorée (golden pumice), les scories fluide, lisses (fluidal) ou rugueuses, les scories vitreuses épineuses (spiny-glassy), les scories épineuses opaques (spiny-opaque). Ces classes sont également reconnaissables dans les morphologies des cendres mesuré avec le Morphologi G3, où les clastes fluidal et golden forment un groupe distinct par rapport aux fragments épineux (Fig. 8d). Les analyses de densité (Fig. 9c) effectuées sur plus de 500 lapilli grossieres révèlent une corrélation entre porosité et morphologie, de sorte que les clastes épineux-opaques sont les plus denses (jusqu'à 1,60 x 10^3 kg m^{-3}, pour une vésicularité de 45 %) et la pierre ponce dorée, la plus légère (densité minimale de 0,4 x 10^3 kg m^{-3} pour une vésicularité allant jusqu'à 86 %, en utilisant une densité du squelette solide : 2,88 x 10^3 kg m^{-3}). L'augmentation de la vésicularité est corrélée à une augmentation du nombre de petites vésicules et une diminution des grandes vésicules issues d'un épisode de coalescence. Les données de connectivité (Fig. 10c) indiquent également que les clastes fluides et dorés (de type-hawaïens) ont plus de vésicules isolées (jusqu'à 40 %) que les clastes épineux (stromboliens) (0-5 %). La forte variation de densité est contrôlée non seulement par la vésicularité, mais aussi par la teneur en cristaux : les fragments opaques les plus denses sont les plus riches en microphénocristaux et microlites

de plagioclase, de pyroxène et d'olivine. La chimie du verre de chacun des quatre types de clastes permet de corréler la porosité et la teneur en oxydes : tandis que MgO augmente avec la porosité, FeOt diminue (de 18 à 11 %), comme exemple l'éruption de juin 2014, qui témoigne de la signature relativement moins dégazé du composant le plus léger (Fig. 13). Les fragments golden-pumice sont toujours mêlés à un magma plus frais, moins dégazé et moins riche en cristaux, en particulier microphenocristaux. Les tendances observées peuvent être expliquées par la variation du dégazage du magma et de la vitesse de remontée, les fragments fluide et doré étant le magma le plus rapide et le moins dégazé, tandis que les scories épineuses les plus denses sont vieilles, le magma dégazé lent qui a été passivement impliqué dans l'événement.

Bibliographie

Alfano F., Bonadonna C., Delmelle P., Costantini L. (2011). Insights on tephra settling velocity from morphological observations. Journal of Volcanology and Geothermal Research, 208(3-4), 86-98. doi:10.1016/j.jvolgeores.2011.09.013.

Andronico D., Lo Castro M.-D., Sciotto M., Spina L. (2013a). The 2010 ash emissions at the summit craters of Mt Etna: Relationship with seismo-acoustic signals. Journal of Geophysical Research, 118, 51–70. doi:10.1029/2012JB009895.

Andronico D., Taddeucci J., Cristaldi A., Miraglia M., Scarlato P.-G., Gaeta M. (2013b). The 15 March 2007 paroxysm of Stromboli: video-image analysis, and textural and compositional features of the erupted deposit. Bulletin of Volcanology, 75, 733-803. doi:10.1007/s00445-013-0733-2.

Bachèlery P., Lénat J.-F., Di Muro A., Michon L. (2015). Active Volcanoes of the Southwest Indian Ocean: Piton de la Fournaise and Karthala. Active Volcanoes of the World. Springer, Berlin, pp.

Baker D.-R., Mancini L., Polacci M., Higgins M.-D., Gualda G.A.R., Hill R.-J., Rivers M.-L. (2012). An introduction to the application of X-ray microtomography to the three-dimensional study of igneous rocks. Lithos, 148, 262-276.

Bagheri G.-H., Bonadonna C., Manzella I., Vonlanthen P. (2015). On the characterization of size and shape of irregular particles. Powder Technology, 270, 141-53. doi:10.1016/j.powtec.2014.10.015.

Barberi F., Cioni R., Santacroce R., Sbrana A., Vecci R. (1989). Magmatic and phreatomagmatic phases in explosive eruptions of Vesuvius as deduced by grain-size and component analysis of the pyroclastic deposits. Journal of Volcanology and Geothermal Research, 38, 287-307.

Barker S.-J., Rotella M.-D., Wilson C.J.N., Wright I.-C., Wysoczanski R.-J. (2012). Contrasting pyroclast density spectra from subaerial and submarine silicic eruptions in the Kermadec arc: implications for eruption processes and dredge sampling. Bulletin of Volcanology, 74, 1425-1443. doi:10. 1007/s00445-012-0604-2.

Bernard J. (2011). Cartographie, classification morphologique, distribution de densité et analyses texturales de bombes pyroclastiques issues d'explosions majeures récentes du Stromboli. Mémoire de Master 2 recherce, Université Blaise Pascal. 50 p.

Blott S.-J., Pye K. (2008). Particle shape: a review and new methods of characterization and classification. Sedimentology, 55(1), 31–63. doi:10.1111/j.1365-3091.2007.00892.x.

Boivin P., Bachèlery P. (2009). Petrology of 1977 to 1998 eruptions at Piton de la Fournaise, la Réunion Island. Journal of Volcanology and Geothermal Research, 184, 109-125. doi:10.1016/j.jvolgeores.2009.01.012.

Bombrun M., Harris A., Gurioli L., Battaglia J., Barra V. (2015). Anatomy of a strombolian eruption: inferences from particle data recorded with thermal video. Journal of Geophysical Research - Solid Earth, 120(4), 2367-2387. DOI.10.1002/2014BO11556.

Bryon D.-N., Atherton M.-P., Hunter R.-H.(1995). The interpretation of granitic textures from serial thin sectioning, image analysis and threedimensional reconstruction. Mineral Magazine, 59, 203-211.

Büttner R., Dellino P., Raue H., Sonder I., Zimanowski B. (2006). Stress-induced brittle fragmentation of magmatic melts: theory and experiments. Journal of Geophysical Research, 111(B8). doi:10.1029/2005jb003958.

Cabré Brullas J.-M. (2015) Are the fossil bubbles trapped in ash, lapilli and bombs capable of providing the same fragmentation imprinting? Answers from Fuego volcano, Guatemala. Mémoire de Master 2 recherce, Université Blaise Pascal. 50 p.

Cas R.A.F., Wright J.-V. (1987). Volcanic successions: modern and ancient. Allen & Unwin, London, 528 p.

Cioni R., D'Oriano C, Bertagnini A (2008). Fingerprinting ash deposits of small scale eruptions by their physical and textural features. Journal of Volcanology and Geothermal Research, 177(1), 277-87.

Colombier M., Gurioli L., Druitt T., Shea T., Boivin P., Miallier D. (2017). Textural evolution of magma during the 9.4 ka trachytic explosive eruption at Kilian Volcano, Chaîne des Puys, France. Bulletin of Volcanology 79: 17. doi:10.1007/s00445-017-1099-7.

Colò L. (2012). Study of vesiculation in basalt magma through volcanological, textural and geophysical analyses: The case study of Stromboli, PhD dissertation, Department of Earth Sciences, Univ. Firenze, Florence, Italy.

Degruyter W., Burgisser A., Bachmann O., Malaspina O. (2010b). Synchrotron X-ray microtomography and lattice Boltzmann simulations of gas flow through volcanic pumices. Geosphere, 6, 470-481.

Dellino P., LaVolpe L. (1996). Image processing analysis in reconstructing fragmentation and transportationmechanisms of pyroclastic deposits. The case of Monte Pilato-Rocche Rosse eruptions, Lipari (Aeolian Islands, Italy). Journal of Volcanology and Geothermal Research, 71(1), 13–29. doi:10.1016/0377-0273(95)00062-3.

Di Muro A., Métrich N., Vergani D., Rosi M., Armienti P., Fougeroux T., Deloule E., Arienzo I., Civetta L. (2014). The shallow plumbing system of Piton de la Fournaise Volcano (La Réunion Island, Indian Ocean) revealed by the major 2007 caldera forming eruption. Journal of Petrology 55, 1287-1315.

Duerig T., Mele D., Dellino P., Zimanowski B. (2012). Comparative analyses of glass fragments from brittle fracture experiments and volcanic ash particles. Bulletin of Volcanology, 74(3), 691–704. doi:10.1007/s00445-011-0562-0**.**

Eychenne J., Le Pennec J.-L., Troncoso L., Gouhier M., Nedelec J.-M. (2012). Causes and consequences of bimodal grain-size distribution of tephra fall deposited during the August 2006 Tungurahua eruption (Ecuador). Bulletin of Volcanology, 74, 187-205. doi:10.1007/s00445-0110517-5.

Eychenne J., Houghton B.-F., Swanson D.-A., Carey R.-J., Swavely L. (2015). Dynamics of an open basaltic magma system: the 2008 activity of the Halema'uma'u Overlookvent, Kīlauea Caldera. Earth Planetary Science Letters, 409, 49-60.

Fagents S.-A., Gregg T.K.P., Lopes R.M.C. (2013). Modeling volcanic processes. The physics and mathematics of volcanism. Cambridge University Press, Cambridge. Cambridge Books Online.

Formenti Y., Druitt T.-H. (2003). Vesicle connectivity in pyroclasts and implications for the fluidisation of fountaincollapse pyroclastic flows, Montserrat (West Indies). Earth Planetary Science Letters, 214(3), 561-574.

Giachetti T., Druitt T.-H., Burgisser A., Arbaret L., Galven C. (2010). Bubble nucleation, growth and coalescence during the 1997 Vulcanian explosions of Soufrière Hills Volcano, Montserrat. Journal Volcanology and Geothermal Research, 193(3), 215-231.

Giachetti T., Burgisser A., Arbaret L., Druitt T.-H., Kelfoun K. (2011). Quantitative textural analysis of Vulcanian pyroclasts (Montserrat) using multi-scale X-ray computed microtomography: comparison with results from 2D image analysis. Bulletin of Volcanology, 73(9), 1295-1309. doi:10.1007/s00445-011-0472-1.

Gouhier M., Donnadieu F. (2008). Mass estimations of ejecta from Strombolian explosions by inversion of Doppler radar measurements. Journal of Geophysical Researcher, 113, B10202.

Gurioli L., Houghton B., Cashman K., Cioni R. (2005). Complex changes in eruption dynamics and the transition between Plinian and phreatomagmatic activity during the 79AD eruption of Vesuvius. Bulletin of Volcanology, 67, 144-159. doi:10.1007/s00445-004-0368-4.

Gurioli L., Harris A.J.L., Houghton B.-F., Polacci M., Ripepe M. (2008). Textural and geophysical characterization of explosive basaltic activity at Villarrica volcano. Journal of Geophysical Researcher, 113, B08206. doi:10. 1029/2007JB005328.

Gurioli L., Harris A.J.L., Colo L., Bernard J., Favalli M., Ripepe M., Andronico D. (2013). Classification, landing distribution and associated flight parameters for a bomb field emplaced during a single major explosion at Stromboli, Italy. Geology, 41, 559-562. DOI 10.1130/G33967.1.

Gurioli L., Colo' L., Bollasina A.-J., Harris A.J.L., Whittington A., Ripepe M. (2014). Dynamics of strombolian explosions: inferences from inferences from field and laboratory studies of erupted bombs from Stromboli volcano. Journal of Geophysical Research, 119(1), DOI:10.1002/2013JB010355.

Gurioli L., Andronico D., Bachèlery P., Balcone-Boissard H., Battaglia J., Boudon G., Burgisser A., Burton M.-R., Cashman K., Cichy S.-B., Cioni R., Di Muro A., Dominguez L., D'Oriano C., Druitt T., Harris A.J.L., Hort M., Kelfoun K., Komorowski J.-C., Kueppers U., Le Pennec J.-L., Menand T., Paris R., Pioli L., Pistolesi M., Polacci M., Pompilio M., Ripepe M., Roche O., Rose-Koga E., Rust A., Scharff L., Schiavi F., Sulpizio R., Taddeucci J., Thordarson T. (2015). MeMoVolc consensual document: a review of cross-disciplinary approaches to characterizing small explosive magmatic eruptions. Bulletin of Volcanology, 77, 49. DOI: 10.1007/s00445-015-0935-x.

Gurioli L., Vlastelic I., Di Muro A., Boudoire G., Moune S., Bachèlery P., Villeneuve N. (2015b). The June 2014 eruption of Piton de la Fournaise: Insights from field, textural and geochemical data. Vol. 17, EGU2015-345, EGU General Assembly 2015.

Harris A.J.L., Ripepe M. (2007). Synergy of multiple geophysical approaches to unravel explovie eruption conduit and source dynamics - A case study from Stromboli. Chemie der Erde, 67, 1-35.

Harris A.J.L., Battaglia J., Donnadieu F., Gurioli L., Kelfoun K., Labazuy P., Sawyer G., Valade S., Bombun M., Barra V., Delle Donne D., Lacanna G. (2013). Full bandwidth remote sensing for total parameterization of volcanic plumes. EOS, 94, 37, 321-322.

Harris J.L.A., Rhéty M., Gurioli L., Villeneuve N., Paris R. (2015). Simulating the thermo-rheological evolution of channel-contained lava: FLOWGO and its implementation in EXCEL" From: Harris AJL, De Groeve T, Garel F, Carn SA (eds) Detecting, Modelling and Responding to Effusive Eruptions. Geological Society, London, Special Publications, 426, http://doi.org/10.1144/SP426.9.

Harris A.J.L., Villeneuve N., Di Muro A., Ferrazzini V., Peltier A., Coppola D., Favalli M., Bachèlery P., Gurioli L., Moune S., Vlastélic I., Galle B., Arellano S. (in revision) Effusive Crises at Piton de la Fournaise 2014-2015: A Multi-National Response Model. Applied Volcanology

Heiken G. (1972). Morphology and petrography of volcanic ashes. Geological Society American Bulletin, 83(7), 1961-88.

Heiken G., Wohletz K. (1985). Volcanic ash. Chicago, Harvard & MIT: University Presses of California; 1985.

Higgins M.-D. (2000). Measurement of crystal size distributions. American Mineralogist, 85, 1105-1116.

Higgins M.-D. (2006). Quantitative textural measurements in igneous and metamorphic petrology. Cambridge University Press, Cambridge.

Houghton B.-F., Wilson C.J.N. (1989). A vesicularity index for pyroclastic deposits. Bulletin of Volcanology, 51(6), 451-462.

Houghton B.-F., Swanson D.-A., Rausch J., Carey R.-J., Fagents S.-A., Orr T.-R. (2013). Pushing the volcanic explosivity index to its limit and beyond: constraints from exceptionally weak explosive eruptions at Kılauea in 2008. Geology, 41(6), 627-630.

Klug C., Cashman K.-V., Bacon C.-R. (2002). Structure and physical characteristics of pumice from the climatic eruption of Mount Mazama (Crater Lake), Oregon. Bulletin of Volcanology, 64, 486-501.

Kylling A., Kahnert M., Lindqvist H., Nousiainen T. (2014). Volcanic ash infrared signature: porous non-spherical ash particle shapes compared to homogeneous sphericalash particles. Atmospheric Measurement Techniques, 7(4), 919-29. doi:10.5194/amt-7-919-2014.

Latutrie B., Harris A., Médard E., Gurioli L. (2017). Emplacement and eruptive dynamics of a thick trachytic lava flow of the Sancy Volcano (France). Bulletin of Volcanology 79:4. DOI 10.1007/s00445-016-1084-6.

Launeau P., Robin P.-Y. (1996). Fabric analysis using the intercept method. Tectonophysics, 267, pp. 91- 119. Logiciel SPO, remis à jour continuellement, www.sciences.univ-nantes.fr/geol/UMR6112/SPO (2009).

Lautze N.-C., Houghton B.-F. (2007). Linking variable explosion style and magma textures during 2002 at Stromboli volcano, Italy. Bulletin of Volcanology, 69, 445-460.

Lautze N.-C., Houghton B.-F. (2008). Single explosions at Stromboli in 2002: use of clast microtextures to map physical diversity across a fragmentation zone. Journal of Volcanology and Geothermal Research, 170, 262-268.

Lautze N.-C., Taddeucci J., Andronico D., Cannata C., Tornetta L., Scarlato P., Houghton B., Lo Castro M.-D. (2012). SEM-based methods for the analysis of basaltic ash fromweak explosion activity at Etna in 2006 and the 2007 eruptive crisis at Stromboli. Physics and Chemistry of the Earth, 45-46, 113-127.

Leduc L., Gurioli L., Harris A.J.L., Colo' L., Rose-Koga E. (2015). Types and mechanisms of strombolian explosions: characterization of a gas-dominated explosion at Stromboli. Bulletin of Volcanology, 77, 8. DOI: 10.1007/s00445-014-0888-5.

Leibrandt S., Le Pennec J.-L. (2015). Towards fast and routine analyses of volcanic ash morphometry for eruption surveillance applications. Journal of Volcanology and Geothermal Research 297, 11-27. doi: 10.1016/j.jvolgeores.2015.03.014.

Lénat J.-F., Bachèlery P., Merle O. (2012). Anatomy of Piton de la Fournaise volcano (La Réunion, Indian Ocean). Bulletin of Volcanology. doi:10.1007/s00445-012-0640-y.

Lillesand T.-M., Kiefer R.-W. (1987). Remote sensing and image interpretation. Second Edition. John Wiley & Sons (New York): 721 p.

Liu E.-J., Cashman K.-V., Rust A.-C. (2015a). Optimising shape analysis to quantify volcanic ash morphology. GeoResJ 8:14-30.

Liu E.-J., Cashman K.-V., Rust A.-C., Gislason S.-R. (2015b). The role of bubbles in generating fine ash during hydromagmatic eruptions. Geology, 43(3), 239-42. doi:10.1130/g36336.1.

Manga M. (1998). Orientation distribution of microlites in obsidian. Journal of Volcanology and Geothermal Research, 86, 107-115.

Manga M., Patel A., Dufek J. (2011). Rounding of pumice clasts during transport: field measurements and laboratory studies. Bulletin of Volcanology, 73(3), 321–33. doi:10.1007/s00445-010-0411-6.

Marchetti E., Poggi P., Bonadonna C., Pistolesi M., Hoskuldsson A. (2014). Towards real-time measurements of tephra fallout grain-size distribution. MeMoVolc Meeting, Geneve Switzerland, Jannuary 2014.

Mattsson H.-B. (2010). Textural variation in juvenile pyroclasts from an emergent, Surteyan-type, volcanic eruption: the Capelas tuff cone, São Miguel (Azores). Journal of Volcanology and Geothermal Research, 189, 81-91.

Merikallio S., Muñoz O., Sundström A.-M., Virtanen T.-H., Horttanainen M, Leeuw GD, et al. (2015). Optical modeling of volcanic ash particles using Ellipsoids. Journal of Geophysical Research Atmosphere, 120. doi:10.1002/2014JD022792.

Michon L., Di Muro A., Villeneuve N., Fadda P., Manta F., Saint-Marc C. (2013). Explosive activity of the summit cone of Piton de la Fournaise volcano: a historical and geological review. Journal of Volcanology and Geothermal Research, 263, 117-133.

Miwa T., Toramaru A. (2013). Conduit process in vulcanian eruptions at Sakurajima volcano, Japan: inference from comparison of volcanic ash with pressure wave and seismic data. Bulletin of Volcanology, 75(1), 1-13.

Miwa T., Toramaru A., Iguchi M. (2009). Correlations of volcanic ash texture with explosion earthquakes from vulcanian eruptions at Sakurajima volcano, Japan. Journal of Volcanology and Geothermal Research, 184(3-4), 473-486.

Miwa T., Geshi N., Shinohara H. (2013). Temporal variation in volcanic ash texture during a vulcanian eruption at the Sakurajima volcano, Japan. Journal of Volcanology and Geothermal Research, 260, 80-89.

Morgan A.-H., Harris A.J.L., Gurioli L. (2013). Lava discharge rate estimates from thermal infrared satellite data for Pacaya Volcano during 2004-2010. Journal of Volcanology and Geothermal Research, 264, 1-11, doi: 10.1016/j.jvolgeores.2013.07.008.

Ort M.-H., Di Muro A., Michon L., Bachèlery P (2016). Explosive eruptions from the interaction of magmatic and hydrothermal systems during flank extension: the Bellecombe Tephra of Piton de La Fournaise (La Réunion Island). Bulletin of Volcanology, 78, 5. doi:10.1007/s00445-015-0998-8.

Peltier A., Bachèlery P., Staudacher T. (2009). Magma transport and storage at Piton de La Fournaise (La Réunion) between 1972 and 2007: a review of geophysical and geochemical data. Journal of Volcanology and Geothermal Research, 184(1-2), 93–108. doi:10.1016/j.jvolgeores.2008.12.008.

Pistolesi M., Delle Donne D., Pioli L., Rosi M., Ripepe M. (2011). The 15 March 2007 explosive crisis at Stromboli volcano, Italy: assessing physical parameters through a multidisciplinary approach. Journal Geophysical Research 116(B12). doi: 958 10.1029/2011JB008527.

Polacci M., Baker D.-R., Mancini L., Tromba G., Zanini F. (2006). Three-dimensional investigation of volcanic textures by X-ray microtomography and implications for conduit processes. Geophysical Research Letters, 33(13), L13312. doi:10.1029/2006GL026241.

Proussevitch A.-A., Mulukutla G.-K., Sahagian D.-L. (2011). A new 3D method of measuring bubble size distributions from vesicle fragments preserved on surfaces of volcanic ash particles. Geosphere, 7, 1-8.

Riley C.-M., Rose W.-I., Bluth G.J.S. (2003). Quantitative shapemeasurements of distal volcanic ash. Journal of Geophysical Research, 108(B10). doi:10.1029/2001jb000818.

Robert B., Harris A.J.L., Gurioli L., Médard E., Sehlke A., Whittington A. (2014). Textural and rheological evolution of basalt flowing down a lava channel. Bulletin of Volcanology, 76, 824, DOI: 10.1007/s00445-014-0824-8.

Rose W.-I., Self S., Murrow P.-J., Bonadonna C., Durant A.-J., Ernst G.G.J. (2008). Nature and significance of small volume fall deposits at composite volcanoes: insights from the October 14, 1974 Fuego eruption, Guatemala. Bulletin of Volcanology, 70(9), 1043-1067.

Rose-Koga E., Gurioli L., Harris A., Leduc L. (2017) L'activité volcanique du Stromboli : un laboratoire naturel de choix à la base de la classification des projections.

Rust A.-C., Cashman K.-V. (2004). Permeability of vesicular silicic magma: inertial and hysteresis effects. Earth Planetary Science Letters, 228(1-2), 93-107.

Sahagian D.-L., Proussevitch A.-A. (1998). 3D particle size distributions from 2D observations : stereology for natural applications. Journal of Volcanology and Geothermal Research, 84, 173-196.

Sahetapy-Engel S.-T., Harris A.J.L. (2009). Thermal-image-derived dynamics of vertical ash plumes at Santiaguito volcano, Guatemala. Bulletin of Volcanology, DOI 10.1007/s00445-009-0284-8.

Schiano P., K. David, I. Vlastélic, A. Gannoun, M. Klein, F. Nauret, P. Bonnand (2011). Osmium isotope systematics of historical lavas from Piton de la Fournaise (Réunion Island, Indian Ocean). Contributions to Mineralogy and Petrology, 162, 995-1009.

Schipper C.-I., White J.D.L., Houghton B.-F. (2011). Textural, geochemical, and volatile evidence for a Strombolian-like eruption sequence at Lō`ihi Seamount, Hawai`i. Journal of Volcanology and Geothermal Research, 207, 16-32.

Schipper C.-I., Castro J.-M., Tuffen H., James M.-R., How P. (2013) Shallow vent architecture during hybrid explosive-effusive activity at Cordón Caulle (Chile, 2011-12): evidence from direct observations and pyroclast textures. Journal of Volcanology and Geothermal Research, 262, 25-37.

Shea T., Larsen J.-F., Gurioli L., Hammer J.-E., Houghton B.-F., Cioni R. (2009). Leucite crystals: surviving witnesses of magmatic processes preceding the 79AD eruption at Vesuvius, Italy. Earth Planetary Science Letters, 281, 88-98.

Shea T., Houghton B.-F., Gurioli L., Cashman K.-V., Hammer J.-E., Hobden B. (2010). Textural studies of vesicles in volcanic rocks: an integrated methodology. Journal of Volcanology and Geothermal Research, 190, 271-289.

Shea T., Gurioli L., Houghton B.-F., Cashman K.-V., Cioni R. (2011). Column collapse and generation of pyroclastic density currents during the A.D.79 eruption of Vesuvius: the role of pyroclast density. Geology, 39, 695-698.

Shea T., Gurioli L., Houghton B.-F. (2012). Transitions between fall phases and pyroclastic density currents during the AD 79 eruption at Vesuvius: building a transient conduit model from the textural and volatile record. Bulletin of Volcanology, 74, 2363–2381. doi:10.1007/s00445012-0668-z.

Shea T., Hellebrand E., Gurioli L., Hugh T. (2014). Conduit- to localizedscale degassing during Plinian eruptions: insights from major element and volatile (Cl and H2O) analysis within Vesuvius AD79 pumice. Journal of Petrology, 55(2), 315-344. doi:10.1093/petrology/egt069.

Sheridan M.-F., Marshall J.-R. (1983). Interpretation of pyroclast surface features using SEM images. Journal of Volcanology and Geothermal Research, 16, 153-159.

Song S.-R., Jones K.-W., Lindquist W.-B., Dowd B.-A., Sahagian D.-L. (2001). Synchrotron X-ray computed microtomography: studies on vesiculated basaltic rocks. Bulletin of Volcanology, 63(4), 252–263. doi:10.1007/ s004450100141.

Sparks R.S.J. (2003). Forecasting volcanic eruptions. Earth Planetary Science Letters, 210, 1-15.

Swanson D.-A., Wooten K., Orr T. (2009). Buckets of ash track tephra flux from Halema'uma'u crater, Hawaii, Eos Trans. AGU, 90, 427-428, doi:10.1029/2009EO460003.

Taddeucci J., Pompilio M., Scarlato P. (2002). Monitoring the explosive activity of the July-August 2001 eruption of Mt. Etna (Italy) by ash characterization. Geophysical Research Letters, 29. doi:10.1029/2001GL014372.

Takeuchi S., Nakashima S., Akihiko Tomiya A. (2008). Permeability measurements of natural and experimental volcanic materials with a simple permeameter: toward an understanding of magmatic degassing processes. Journal of Volcanology and Geothermal Research, 177, 329-339.

Thivet S. (2016) Caractérisation magmatique du système superficiel du Piton de la Fournaise à travers l'étude texturale et chimique des produits éruptifs de 2014 et 2015. Mémoire de Master 2 recherce, Université Blaise Pascal. 50 p.

Thomas N., Jaupart C., Vergniolle S. (1994). On the vesicularity of pumice. Journal of Geophysical Research, 99, 15633-15644.

Thornber C.-R., Hon K., Heliker C., Sherrod D.-A. (2003). A Compilation of Whole-Rock and Glass Major-Element geochemistry of Kīlauea Volcano, Hawai'i, near-vent eruptive products: January 1983 through September 2001: U.S.G.S. Open File Report 03-477.

Van der Plas L., Tobi A. (1965). A chart for judging the reliability of point counting results. American Journal of Science, 263, 87-90. doi: 10.2475/ajs.263.1.87.

Villemant B., Salaün A., Staudacher T. (2009). Evidence for a homogeneous primary magma at Piton de la Fournaise (La Réunion): a geochemical study of matrix glass, melt inclusions and Pélé's hairs of the 1998-2008 eruptive activity. Journal of Volcanology and Geothermal Research, 184(1-2), 79-92.

Vlastélic I., Staudacher T., Semet M.-P. (2005). Rapid change of lava composition from 1998 to 2002 at Piton de la Fournaise (Réunion) inferred from Pb isotopes and trace elements: evidence for variable crustal contamination. Journal of Petrology, 46, 79-107.

Vlastélic I., Peltier A., Staudacher T. (2007). Short-term (1998-2006) fluctuations of Pb isotopes at Piton de la Fournaise volcano (Reunion Island): Origins and constrains on the size and shape of the magma reservoir. Chemical Geology, 244, 202-220.

Vlastélic I., Deniel C., Bosq C., Télouk P., Boivin P., Bachèlery P., Famin V., Staudacher T. (2009). Pb isotope geochemistry of Piton de la Fournaise historical lavas. Journal of Volcanology and Geothermal Researcher, 184, 63-78. doi:10.1016/j.jvolgeores.2008.08.008.

Walker G.P.L. (1971). Grain-size characteristics of pyroclastic deposits. Journal Geology, 79, 696-714.

Wohletz K. (1983). Mechanisms of hydrovolcanic pyroclast formation: grain-size, scanning electron microscopy, and experimental studies. Journal Volcanology and Geothermal Research, 17, 31-63.

Wohletz K.-H., Sheridan M.-F., Brown W.-K. (1989) Particle size distributions and the sequential fragmentation/transport theory applied to volcanic ash. Journal of Geophysical Research, 94, 15703-15721.

Solid Earth, 9, 431–455, 2018
https://doi.org/10.5194/se-9-431-2018

Solid Earth Open Access EGU

Integrating field, textural, and geochemical monitoring to track eruption triggers and dynamics: a case study from Piton de la Fournaise

Lucia Gurioli[1], Andrea Di Muro[2], Ivan Vlastélic[1], Séverine Moune[1], Simon Thivet[1], Marina Valer[1], Nicolas Villeneuve[2,3], Guillaume Boudoire[2,3], Aline Peltier[2], Patrick Bachèlery[1], Valérie Ferrazzini[2], Nicole Métrich[2], Mhammed Benbakkar[1], Nicolas Cluzel[1], Christophe Constantin[1], Jean-Luc Devidal[1], Claire Fonquernie[1], and Jean-Marc Hénot[1]

[1]Université Clermont Auvergne, CNRS, IRD, OPGC, Laboratoire Magmas et Volcans, 63000 Clermont-Ferrand, France
[2]Institut de Physique du Globe (IPGP), Sorbonne Paris-Cite, CNRS UMR-7154, Université Paris Diderot, Observatoire Volcanologique du Pitonde la Fournaise (OVPF), Bourg-Murat, France
[3]Laboratoire Géosciences Réunion, Université de La Réunion, Institut de Physique du Globe de Paris, Sorbonne Paris-Cité, UMR 7154 CNRS, 97715 Saint-Denis, France

Correspondence: Lucia Gurioli (lucia.gurioli@uca.fr)

Received: 29 August 2017 – Discussion started: 13 September 2017
Revised: 13 December 2017 – Accepted: 7 January 2018 – Published: 16 April 2018

Abstract. The 2014 eruption at Piton de la Fournaise (PdF), La Réunion, which occurred after 41 months of quiescence, began with surprisingly little precursory activity and was one of the smallest so far observed at PdF in terms of duration (less than 2 days) and volume (less than 0.4×10^6 m^3). The pyroclastic material was composed of golden basaltic pumice along with fluidal, spiny iridescent and spiny opaque basaltic scoria. Density analyses performed on 200 lapilli reveal that while the spiny opaque clasts are the densest (1600 kg m^{-3}) and most crystalline (55 vol. %), the golden pumices are the least dense (400 kg m^{-3}) and crystalline (8 vol. %). The connectivity data indicate that the fluidal and golden (Hawaiian-like) clasts have more isolated vesicles (up to 40 vol. %) than the spiny (Strombolian-like) clasts (0–5 vol. %). These textural variations are linked to primary pre-eruptive magma storage conditions. The golden and fluidal fragments track the hotter portion of the melt, in contrast to the spiny fragments and lava that mirror the cooler portion of the shallow reservoir. Exponential decay of the magma ascent and output rates through time revealed depressurization of the source during which a stratified storage system was progressively tapped. Increasing syn-eruptive degassing and melt–gas decoupling led to a decrease in the explosive intensity from early fountaining to Strombolian activity. The geochemical results confirm the absence of new input of hot magma into the 2014 reservoir and confirm the emission of a single shallow, differentiated magma source, possibly related to residual magma from the November 2009 eruption. Fast volatile exsolution and crystal–melt separation (second boiling) were triggered by deep pre-eruptive magma transfer and stress field change. Our study highlights the possibility that shallow magma pockets can be quickly reactivated by deep processes without mass or energy (heat) transfer and produce hazardous eruptions with only short-term elusive precursors.

1 Introduction

A detailed characterization and understanding of eruptive dynamics and of processes driving and modulating volcano unrest are crucial in monitoring active volcanoes and fundamental for forecasting volcanic eruptions (Sparks, 2003). Many studies suggest that eruptive phenomena are strongly dependent on the physico-chemical properties of ascending magma in the conduit (e.g. temperature, viscosity, porosity, and permeability) (e.g. Sparks, 1978; Rust and Cashman, 2011; Gonnermann and Manga, 2013; Polacci et al., 2014). Integrating petrographic, chemical, and textural data can thus provide critical information to constrain both the

pre-eruptive storage conditions and the processes related to magma ascent, degassing, and cooling (e.g. reference in Table 1 in Gurioli et al., 2015). This multidisciplinary approach is of even greater importance in the monitoring of volcanoes that emit relatively uniform magma compositions over time, like basaltic volcanoes (e.g. Di Muro et al., 2014; Gurioli et al., 2015; Coppola et al., 2017). As a result, monitoring of textures and petrochemical properties of lava fragments and pyroclasts is now routinely carried out on a daily basis at active volcanoes such as Kīlauea, Etna, and Stromboli (e.g. Taddeucci et al., 2002; Thornber et al., 2003; Polacci et al., 2006; Swanson et al., 2009; Colò et al., 2010; Houghton et al., 2011, 2013, 2016; Carey et al., 2012, 2013; Lautze et al., 2012; Andronico et al., 2013a, b, 2014; Corsaro and Miraglia, 2014; Di Muro et al., 2014; Gurioli et al., 2014; Eychenne et al., 2015; Leduc et al., 2015; Kahl et al., 2015). In the past, time series of petrographic and geochemical data have been measured for Piton de la Fournaise (PdF) basalts and particularly for effusive products. The aim of these datasets was to constrain the spatial and temporal evolution of magma for one of the most active basaltic volcanoes in the world (e.g. Albarède et al., 1997; Vlastélic et al., 2005, 2007, 2009; Boivin and Bachèlery, 2009; Peltier et al., 2009; Schiano et al., 2012; Lénat et al., 2012; Di Muro et al., 2014, 2015; Vlastèlic and Pietruszka, 2016). However, this type of approach has seldom been coupled with detailed textural studies at PdF and instead has mostly focused on crystal textures and crystal size distribution (Welsch et al., 2009, 2013; Di Muro et al., 2014, 2015). Moreover, only sporadic data exist on the textures of pyroclasts ejected by the eruptions at PdF (Villemant et al., 2009; Famin et al., 2009; Welsch et al., 2009, 2013; Michon et al., 2013; Vlastélic et al., 2013; Di Muro et al., 2015; Morandi et al., 2016; Ort et al., 2016).

Within this paper, we present a multidisciplinary textural, chemical, and petrological approach to quantify and understand the short-lived 2014 PdF eruption. This approach combines detailed study of the pyroclastic deposit (grain size and componentry) with bulk texture analysis (density, vesicularity, connectivity, permeability, morphology, vesicle distribution, and crystal content) and a petrochemical study (bulk rock, glass, minerals, melt inclusions) of the same clasts. This integrated approach has now been formalized within the French National Observation Service for Volcanology (SNOV), as routine observational systems Dynamics of Volcanoes (DynVolc, http://wwwobs.univ-bpclermont.fr/SO/televolc/dynvolc/) and Observation des gaz volcaniques, (GazVolc, http://wwwobs.univ-bpclermont.fr/SO/televolc/gazvolc) to provide data for the ongoing activity at PdF (Harris et al., 2017).

In spite of being the first of a series of eruptions, the June 2014 event was preceded by only weak inflation and by a rapid increase in the number of shallow (< 2 km below volcano summit) volcano tectonic earthquakes that happened only 11 days before the eruption (Peltier et al., 2016). The eruptive event was dominantly effusive, lasted only 20 h, and emitted a very small volume of magma (ca. 0.4×10^6 m^3; Peltier et al., 2016), which makes this event one of the smallest, in terms of duration and volume, observed at PdF up to now. In addition, the eruption started during the night and very little direct observation exists for the first few hours of the activity when the lava effusion was associated with very weak fountaining activity and Strombolian explosions.

This eruption occurred just outside the southern border of the summit Dolomieu caldera, at the top of the central cone of PdF (Fig. 1). This is a high-risk sector because of the high number of tourists. Identification of precursors of this kind of activity represents an important challenge for monitoring systems (Bachélery et al., 2016).

Therefore this eruption represents an ideal context for applying our multidisciplinary approach, with the aim of addressing the following key questions:

i. Why was such a small volume of magma erupted instead of remaining endogenic?

ii. What caused the rapid trigger and the sudden end to this small-volume eruption?

iii. Which was the source of the eruption (shallow versus deep and single versus multiple small magma batches)?

iv. What was the ascent and degassing history of the magma?

v. What was the time and space evolution of the eruptive event?

Furthermore, this eruption provides an exceptional opportunity to study processes leading to the transition from mild Hawaiian (< 20 m high fountains, following the nomenclature proposed by Stovall et al., 2011) to Strombolian activity (< 10 m high explosions), whose products are little modified by post-fragmentation processes because of the very low intensity of the activity.

2 The 2014 activity

2.1 Precursory activity

The 20 June 2014 summit eruption represents the first eruption at PdF after 41 months of quiescence. The last eruption had been on 9 December 2010, with a shallow (above sea level) intrusion on 2 February 2011 (Roult et al., 2012). From 2011, the deformation at PdF was constant with two distinct types of behaviour: (i) a summit contraction of a few centimetres every year (Fig. 1d) and (ii) a preferential displacement of the east flank at a rate of 1–3 cm per year (Brenguier et al., 2012; Staudacher and Peltier, 2015). The background microseismicity was very low (less than five shallow events per day below volcano summit) and low-temperature summit intracaldera fumaroles emitted very little sulfur (H_2S

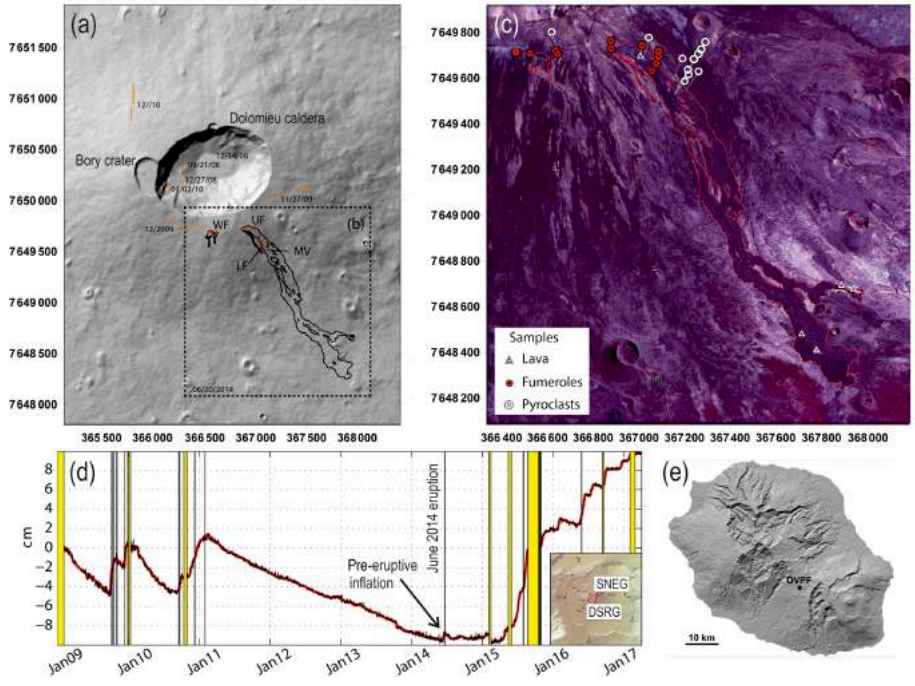

Figure 1. **(a)** Digital elevation model of the summit crater area at Piton de la Fournaise, La Réunion, France. Orange shows fractures generated by pre-2014 eruptions (reported are the dates of their activities); **(b)** red shows fractures active during the 2014 eruption: WF (western fracture), UF (upper fracture), LF (lower fracture), MV (main vent). Black shows the outline of the 2014 lava field. **(c)** Locations of sample collection points. The coordinates are in UTM, zone 40 south. **(d)** Distance change (baseline) in centimetres between two GNSS summit stations: DSRG and SNEG (see location in the inset). Increase and decrease in the signal mean a summit inflation and deflation, respectively. The yellow areas represent eruptive and intrusive periods. In **(d)**, the rapid and strong variations linked to dike injections preceding intrusions and eruptions by a few tens of minutes have been removed. **(e)** Digital elevation model of La Réunion island.

or SO_2) and carbon (CO_2) (Di Muro et al., 2016). After 41 months of rest, a new intense cycle of activity (June 2014, February 2015, May 2015, July 2015, August–October 2015, May 2016; September 2016; January 2017, and July 2017) began with surprisingly little and ambiguous precursory activity.

The 2014 summit eruption started during the night of 20–21 June, at 21:35 GMT (00:35 local time) and ended on 21 June at 17:09 GMT (21:09 local time), after less than 20 h of dominantly effusive activity. The volcano reawakening was preceded, in March and April 2014, by deep (15–20 km below sea level) eccentric seismicity and an increase in soil CO_2 flux below the western volcano flank, 15 km NW of the volcano summit (Liuzzo et al., 2015; Boudoire et al., 2017). Background microseismicity and inflation of the central cone increased progressively starting on 9 June 2014. Weak inflation recorded on both distal and summit baselines (Fig. 1d) suggests that deep (below sea level) magma uprise was pressurizing the shallow (above sea level) magma storage system (Peltier et al., 2016). On 13, 17, and 20 June, three shallow (hypocentres located above sea level) intense seismic crises occurred below the summit Dolomieu caldera (Fig. 1), with hundreds of events located in a narrow depth range between 1100 and 2100 m below the volcano summit. These seismic crises consisted of swarms of low-magnitude (M: 1–2) volcano tectonic events that increased in number from the first to the third crisis. On 20 June, seismicity increased progressively and a final seismic crisis started at 20:20 GMT, only 75 min before the eruption. This last seismic crisis was coupled with acceleration in the deformation of the summit area, which began only 60 min before the eruption. Interestingly, only slight inflation of the central cone (< 2 cm of dilatation) was detected 11 days before the 2014 eruption with a maximum of 1 and 1.6 cm enlargement at the summit and the base of the cone, respectively (Peltier et al., 2016, and Fig. 1d). A moderate increase in CO_2 and H_2S emissions from summit intracaldera fumaroles was detected starting on 2 June, but only very minor SO_2 emissions occurred before the eruption (mostly on 7 and 15 June, unpublished data). Therefore, the acceleration in both geophysical and geochemical parameters was mostly related to the late phase of dike propagation towards the surface just before the eruption. Following the end of the 20–21 June eruption, a long-term continuous inflation of the edifice began, at a moderate rate, and mostly at the base of the volcano. More than 1 year after this first eruption, the long-term deformation trends showed that the 2014 eruption marked a kink between the deflation trend, which followed the caldera-forming 2007 eruption (Staudacher et al., 2009),

and the currently ongoing continuous inflation trend (Fig. 1d and Peltier et al., 2016; Coppola et al., 2017).

2.2 Chronology of the events

We reconstructed the chronology of the events by combining a distribution map of the fissures, pyroclastic deposits, and lava flows (Fig. 1) with a review of available images and videos extracted from the observatory database, the local newspapers, and websites (Fig. 2). The 2014 eruption occurred at the summit and on the SE slopes of the Dolomieu caldera (Fig. 1a, b, and c) and evolved quickly and continuously over 20 h. The full set of fractures opened during a short period of time (minutes) and emitted short (< 1.7 km long) lava flows (Figs. 1 and 2c and d). Feeding vents were scattered along a 0.6 km long fissure set (Fig. 1a) and produced very weak (low) Hawaiian to Strombolian activity (Fig. 2).

Fissures opened from west to east, initially subparallel to the southern border of Dolomieu caldera and then propagated at lower altitude (Fig. 1). The summit part of the fractures (ca. 2500 m a.s.l., western fracture, WF in Fig. 1) emitted only small volumes of lava and pyroclasts. This part of the fracture set was active only during the first few hours of the eruption, at night. The eastern part of the fractures (upper fracture, UF in Fig. 1) descended to lower altitude (between 2400 and 2300 m a.s.l., middle fracture, Fig. 1) along the SE flank of the summit cone and emitted most of the erupted volume. As often observed in PdF eruptions, the activity progressively focused on a narrow portion of the fractures at low altitude and finally on a single vent located at the lower tip of the fracture system (main vent, at 2336 m a.s.l., MV in Figs. 1, 2). The first in situ observations in the morning of 21 June (ca. 04:00 GMT) showed that weak Strombolian activity (Fig. 2a and b) was focused on a narrow segment of the lower fractures and that aa lavas had already attained the elevation of 1983 m a.s.l. (0.2 km before maximum runout, Fig. 2c). A small, weak gas plume was also blowing northwards. A single sample of partially molten lava was collected from the still active lava front and partially water quenched (REU140621-1; Table S1 in the Supplement, Fig. 2d). During most of 21 June, the activity consisted of lava effusion in three parallel lava streams (Fig. 2c) merging in a single lava flow (Fig. 2e) and weak Strombolian explosions at several closely spaced spots along the lower part of the feeding fracture. At 13:00 (GMT), only weak explosions were observed within a single small spatter cone (Fig. 2f and g). Most of the lava field was formed of open channel aa lavas. The total volume of lava was estimated by the MIROVA service (https://www.sites.google.com/site/mirovaweb/home), with the use of MODIS images and the analyses of the flux from the spectral properties, to be within $0.34 \pm 0.12 \times 10^6$ m^3 (Coppola et al., 2017). Satellite-derived volume estimates are consistent with independent photogrammetric estimates ($0.4 \pm 0.2 \times 10^6$ m^3; Peltier et al., 2016) and rank the 2014 eruption at

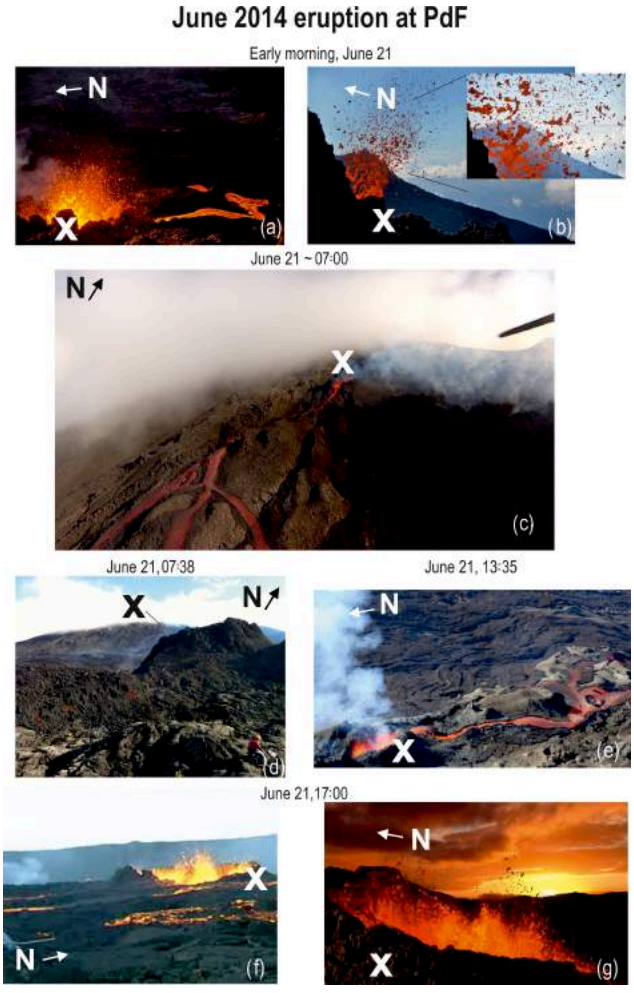

Figure 2. Photo collection from the 2014 eruption at the MV, highlighted with a white cross (see location in Fig. 1). From **(a)** to **(g)**: evolution of the Strombolian activity from early morning to evening 21 June showing a decline in the activity with time. Unfortunately, the relatively more energetic Hawaiian fountaining events that happened during the night were not documented. **(a)** Strombolian activity at the MV and associated lava flow; **(b)** enlarged view of the Strombolian activity at the MV. The images in **(a)**, **(b)**, and the inset in **(b)** are from Laurent Perrier; **(c)** aerial view of the SE flank of PdF, taken by the OVPF team from the helicopter of the gendarmerie of La Réunion; **(d)** eastern front of the lava where the OVPF team collected a quenched lava sample; **(e)** low Strombolian activity at the MV and the associated lava flow; photo from http://www.ipreunion.com/volcan/reportage/2014/06/21/eruption-du-piton-de-la-fournaise-actualise-a-17h-la-lave-coule-sur-1-5- kilometre,26023.html. Panels **(f)** and **(g)** show the decline of the Strombolian activity at the MV. The photo in **(e)** is from http://www.zinfos974.com/L-eruption-du-Piton-de-la-Fournaise-Le-point-de17h_a72981.html and the photo in **(f)** is from **(f)** http://nancyroc.com/eruption-a-la-reunion.

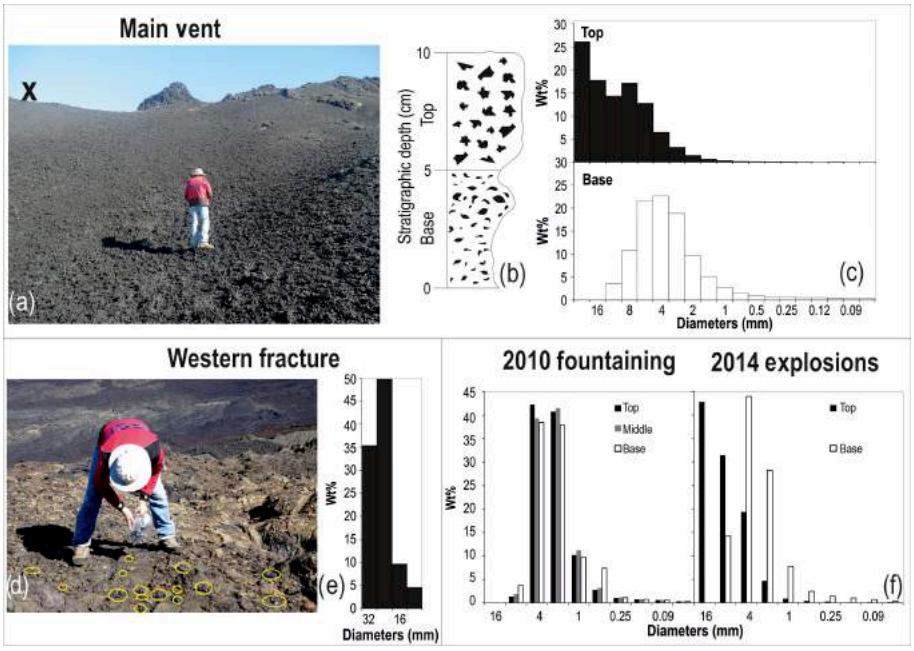

Figure 3. **(a)** Continuous blanket of scoria fallout deposit emitted from the MV (Fig. 1 for location) during the June 2014 eruption at PdF. The black cross locates the position of the MV (see Fig. 1 for the location). **(b)** Schematic stratigraphic log of the scoria fallout deposit emplaced during the June 2014 eruption at the MV. **(c)** Grain size histograms of the base and the top of the deposit of the MV; the particle diameters are at half phi. **(d)** Scattered scoria (outlined in yellow) from the WF (see Fig. 1 for the location). **(e)** Grain size histogram of the scoria deposit at the WF; the particle diameters are at half phi. **(f)** Comparison between the grain size histograms for the 2010 Hawaiian fountaining and the 2014 MV activity; both the particle axes are reported in full phi for comparison.

the lower end of the volume range typically emitted by PdF (Roult et al., 2012).

3 Methodology

3.1 Sampling strategy

Apart from the sample from the front of the still active lava flow (Fig. 2d), all other samples were collected in two phases: 3 days (pyroclasts on 24 June, Fig. 3a and Table S1) and 11 days after the eruption (lavas on 2 July, Table S1), and 3 months later (pyroclasts from the MV, Fig. 1, on 18 November and Table S1). The 24 June samples were collected from the main fractures (WF and UF, Fig. 1a), the MV, and the active lava flow (Fig. 1 and Table S1). We collected 25 scoriaceous bombs and lapilli (REU140624-9a-1 to REU140624-9a and REU140624-9b-6 to REU140624-9b-25, in Table S3) from the discontinuous deposit (Fig. 3d) emplaced at the WF site (Fig. 1a), active only at the beginning of the eruptive event. Because of the short duration of the activity at the WF, the scoria fragments on the ground were scarce (Fig. 3d). The strategy was to collect a sample that was formed by the largest available number of clasts that was representative of this discrete deposit (REU140624-9 in Table S1). From the UF (Fig. 1a) only one big scoria was collected (REU140624-13, Table S1) that broke in five parts, allowing us to measure its vesiculated core and the dense quenched external part (REU140624-13-a to REU140624-13-e, in Table S3). In contrast, the sustained and slightly more energetic activity at the lower tip of the fractures, at the MV site, built a small spatter cone (Fig. 2) and accumulated a continuous, small-volume deposit (Fig. 3a) of inversely graded scoria fallout (Fig. 3b and c). This deposit is 10 cm thick at 2 m from the vent and covers an area of about $\sim 1000\,m^2$. For this fall deposit we collected two bulk samples, one from the base (within the lower 5 cm, REU141118-6 in Table S1) and the other from the top (within the upper 5 cm, REU140624-3, in Table S1), for the grain size (Fig. 3c) and componentry analyses. The sample at the base was collected in November because on 24 June the loose proximal lapilli blanket was still very hot (405 °C; thermocouple measurement) and fumaroles with outlet temperatures in the range of 305–60 °C were sampled all along the fractures several weeks after the eruption (Fig. 1b and Table S1). These latter geochemical data are not presented in this paper. We selected 103 fragments from the coarsely grained bulk deposit within the upper 5 cm of the scoria fallout deposit (Fig. 3b) at MV (REU140624-3-1 to REU140624-3-103, in Table S3) for density, connectivity, permeability, petrological, and geochemical analysis. In addition, in November 2014, more than 200 clasts (comprising the REU141118-1 to REU141118-5 samples, Table S1) of similar size were collected, both close to the MV and in

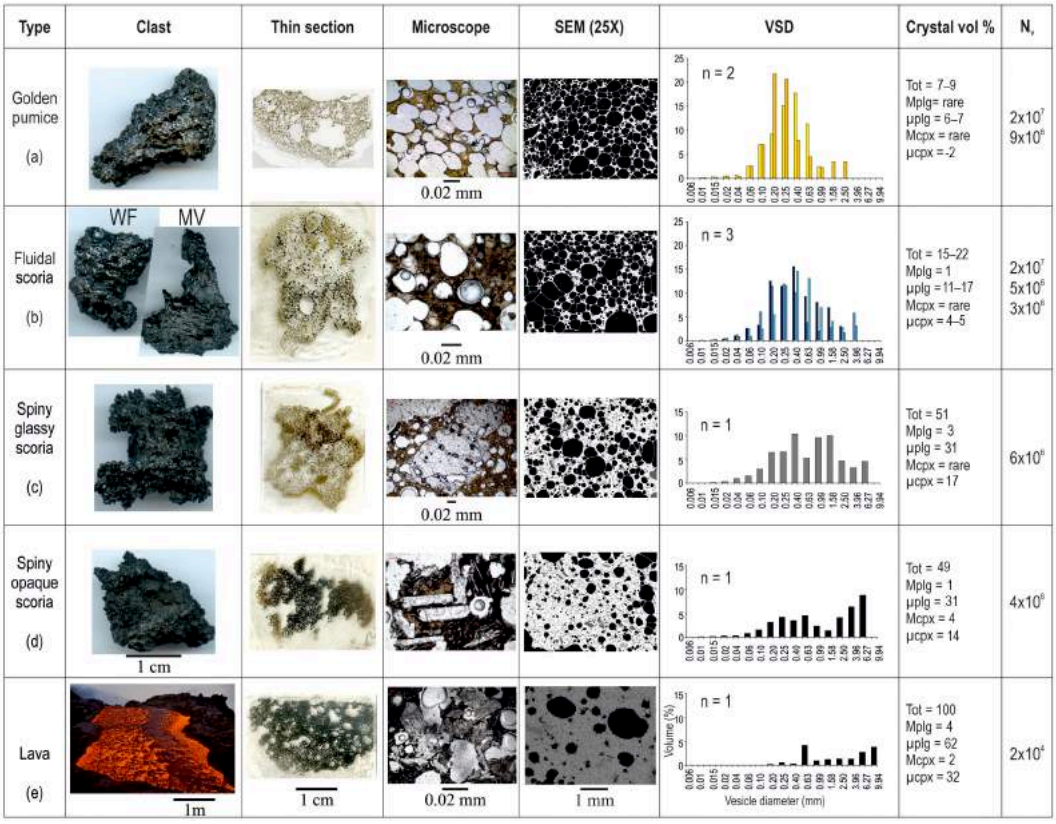

Figure 4. Textural features of June 2014 pyroclasts and lava. Clast shows a photo of the different types of juvenile pyroclasts and lava channel. The photo of the lava channel is from Laurent Perrier. WF: western fracture (smooth fluidal scoria); MV: main vent (fluidal scoria, less smooth than the ones at the WF). Thin section is the thin section imaged with a desktop scanner. Microscope is the picture taken with an optical microscope using natural light. SEM (25X) is the image captured using scanning electron microscopy (SEM) in BSE mode at 25x magnification: black is vesicles, white is glass, grey is crystals. VSD is the vesicle size distribution histograms, where the diameter, in millimetres, is plotted versus the volume percentage. n: number of measured clasts; crystal vol. %. Tot: total percentage of crystals corrected for the vesicularity; Mplg: percentage of mesocrysts of plagioclase; μplg: percentage of microcrysts of plagioclase; Mcpx: percentage of mesocrysts of pyroxene; μcpx: percentage of microcrysts of pyroxene; N_V: number density corrected for the vesicularity.

the distal area (30 m away from the MV site) to complete the particle bulk texture analyses and the chemical analyses.

3.2 Grain size and componentry

We performed grain size analyses on the two bulk samples collected from the MV, following the procedure of Jordan et al. (2016) (Table S2). The samples were dried in the oven at 90 °C and sieved at 1/2 phi intervals in the range of -5ϕ to 4ϕ (Fig. 3c); the data are also shown in full phi for comparison with the deposits of the 2010 PdF fountaining episode (Hibert et al., 2015; Fig. 3f). Sieving was carried out by hand and for not longer than 3 min to avoid breaking and abrasion of the very vesicular and fragile clasts. For the scattered scoria sampled from the WF (Figs. 1, 3d and e), we followed the grain size strategy proposed in Gurioli et al. (2013). Within this procedure we sampled each fragment and we recorded the weight and the three main axes (a being the largest, b, and c). To allow comparison with the sieving grain size analyses (Inman, 1952), we used the intermediate b axis dimension to obtain $\phi = -\log_2 b$.

Following the nomenclature of White and Houghton (2006) the componentry analysis is the subdivision of the sample into three broad components: (i) juvenile, (ii) non-juvenile particles, and (iii) composite clasts. The juvenile components are vesicular or dense fragments, as well as crystals, that represent the primary magma involved in the eruption; non-juvenile material includes accessory and accidental fragments, as well as crystals that predate the eruption from which they are deposited. Finally, the composite clasts are mechanical mixtures of juvenile and non-juvenile (and/or recycled juvenile) clasts. In these mild basaltic explosions, the non-juvenile component is very scarce, so we focused on the juvenile component that is characterized by three groups of scoria: (i) spiny opaque, (ii) spiny glassy, and (iii) fluidal, along with golden pumice (Fig. 4). The componentry quantification was performed for each grain size fraction between -5ϕ and 0.5ϕ (Fig. 5a

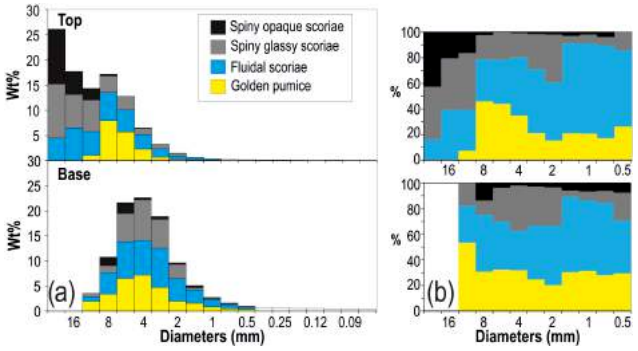

Figure 5. Proportion of each type of clast measured from the base to the top of the 10 cm thick deposit emplaced during the eruption, at the MV site. The deposit is dominated by Hawaiian-like lapilli fragments at the base (golden pumice and fluidal scoria) and Strombolian-like bombs and lapilli at the top (spiny scoria): **(a)** componentry within the different grain size classes; **(b)** normalized componentry composition from the base to the top of the deposit.

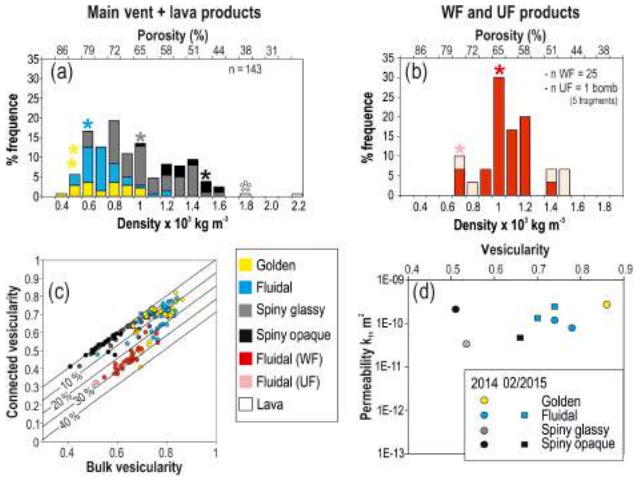

Figure 6. Density, connectivity, and permeability data of June 2014 pyroclast and lava fragments: **(a)** density distribution histogram for all the pyroclast fragments measured at the MV + two lava fragments collected from the eastern front of the lava flow (see Fig. 1 for location). n is the number of measured clasts; **(b)** density distribution histogram for the pyroclasts sampled at the WF and the bomb sampled at the UF. The bomb broke in five fragments (two fragments from the core, the least dense, and three fragments from the quenched edges, the densest). In both the density histograms the stars represent the density intervals from which we picked the clasts for the textural measurements; **(c)** graph of the connected vesicularity versus total vesicularity. The diagonal line represents equality between the connectivity and vesicularity; beneath this line the samples have isolated vesicles and the straight lines represent lines of equal fraction of isolated vesicles. Note that the bomb from the UF has the high vesicular core with less than 5 % of isolated vesicles, while the three low vesicular fragments from the quenched edge have more than 25 % of isolated vesicles (see pink spots); **(d)** Darcian viscous permeability (k_1) versus vesicularity fraction for the four typologies of clasts collected at the MV. For comparison, two fluidal fragments and one spiny opaque fragment from the February 2015 eruption are reported.

and b), and a binocular microscope was used for the identification of grains smaller than −1 (Table S2).

In the following, we will use the crystal nomenclature of Welsch et al. (2009), with the strictly descriptive terms of macrocrysts (> 3 mm in diameter) mesocrysts (from 0.3 to 3 mm in diameter), and microcrysts (< 0.3 mm in diameter). Regarding the June 2014 products, these ranges of size may however change in comparison to the December 2005 products studied by Welsch et al. (2009).

3.3 Particle bulk texture (density, porosity, connectivity, permeability) and micro-texture

For each sample site (WF, UF, and MV; Fig. 1a), we selected all the available particles within the 8–32 mm fraction for density–porosity, connectivity, and permeability measurements (Table S3). This is the smallest granulometric fraction assumed to be still representative of the larger size class in terms of density (Houghton and Wilson, 1989; Gurioli et al., 2015) and has been used in previous textural studies (e.g. Shea et al., 2010). In addition, this size range is ideal for vesicle connectivity measurements (e.g. Formenti and Druitt, 2003; Giachetti et al., 2010; Shea et al., 2012; Colombier et al., 2017a, b). Density of juvenile particles was measured using the water-immersion technique of Houghton and Wilson (1989), which is based on Archimedes' principle. A mean value for the vesicle-free rock density was determined by powdering clasts of varying bulk densities, measuring the volumes of known masses using an AccuPyc II 1340 helium pycnometer, and then averaging. The same pycnometer was also used to measure vesicle interconnectivity for each clast using the method of Formenti and Druitt (2003) and Colombier et al. (2017a). Permeability measurements were performed on five clasts: two golden pumices, one fluidal, one spiny glassy, and one opaque scoria, all collected from the MV (Table S3). Following Colombier et al. (2017a), the clasts were cut into rectangular prisms to enable precise calculation of the cross-sectional area, which is required to calculate permeability. These prisms were then embedded in a viscous resin, which was left to harden for 24 h. The sample surface had been previously coated with a more viscous resin and then wrapped with Parafilm to avoid intrusion of the less viscous resin inside the pores. The coated samples were placed with a sample holder connected to a permeameter built at Laboratoire Magmas et Volcans (LMV, France) following Takeuchi et al. (2008). The measurements were performed at atmospheric pressure (i.e. without confining pressure) and the samples were measured at a range of gas flow rates and upstream air pressures to create a curve that could be fitted using a modified version of Darcy's law (the Forchheimer equation) to solve for viscous (k_1) and in-

ertial permeabilities (k_2) (Rust and Cashman, 2011; Lindoo et al., 2016; Colombier et al., 2017a, b).

Vesicle size distribution was performed following the method of Shea et al. (2010) and Leduc et al. (2015), while the total crystallinity, the percentages for both crystal phases (plagioclase and clinopyroxene), and size populations (meso- and microcrysts) were calculated using the raw data from the FOAMS program (Shea et al., 2010), the CSD corrections program of Higgins (2000), and the CSDslice database (Morgan and Jerram, 2006) to have the percentage of crystals in 3-D with the corrected assumption for shape. We performed these analyses on eight clasts picked up from each component and density distributions (stars in Fig. 6a and b). The choice of the clasts was made mostly on the typologies, rather than on each density distribution, in order to avoid the analysis of clasts with transitional characteristics. For example, two golden pumice fragments were selected from the largest clasts that were less dense and did not break, even if the values in vesicularity were similar. A larger number of fluidal fragments were chosen (even if the density distribution was unimodal) because this typology of clasts was the most abundant and was emitted all along the active fracture; thus we did our best in order to study products representative of the WF, the UF, and the MV activities. Only one spiny glassy and one spiny opaque were selected because they were emitted only at the MV. A full description of the textural measurements all performed at LMV and the raw data of these measurements are available in the DynVolc database (2017).

3.4 Bulk geochemistry

For the determination of the bulk chemistry (Table S4 and Fig. 7) of the different pyroclasts we selected the largest pyroclasts of golden pumice and the largest fluidal, spiny glassy and spiny opaque scoriae (Table S4). We also analysed two fragments of lava, from the beginning and the end of the eruption (Table S4). Samples were crushed into coarse chips using a steel jaw crusher and powdered with an agate mortar. Major and trace element compositions were analysed using powder (whole-rock composition). In addition, for a subset of pyroclasts, glass chips (2–5 mm in size) were hand-picked under a binocular microscope and analysed separately for trace elements. For major element analysis, powdered samples were mixed with LiBO2, placed in a graphite crucible, and melted in an induction oven at 1050 °C for 4.5 min, resulting in a homogeneous glass bead. The glass was then dissolved in a solution of deionized water and nitric acid (HNO_3) and finally diluted by a factor of 2000. The final solutions were analysed using inductively coupled plasma atomic emission spectroscopy. Trace element concentrations were analysed following a method modified from Vlastélic et al. (2013). About 100 mg of sample (powder and chip) was dissolved in 2 mL of 28 M and 1 mL of 14 M HNO_3 in a Teflon beaker for 36 h at 70 °C. Solutions

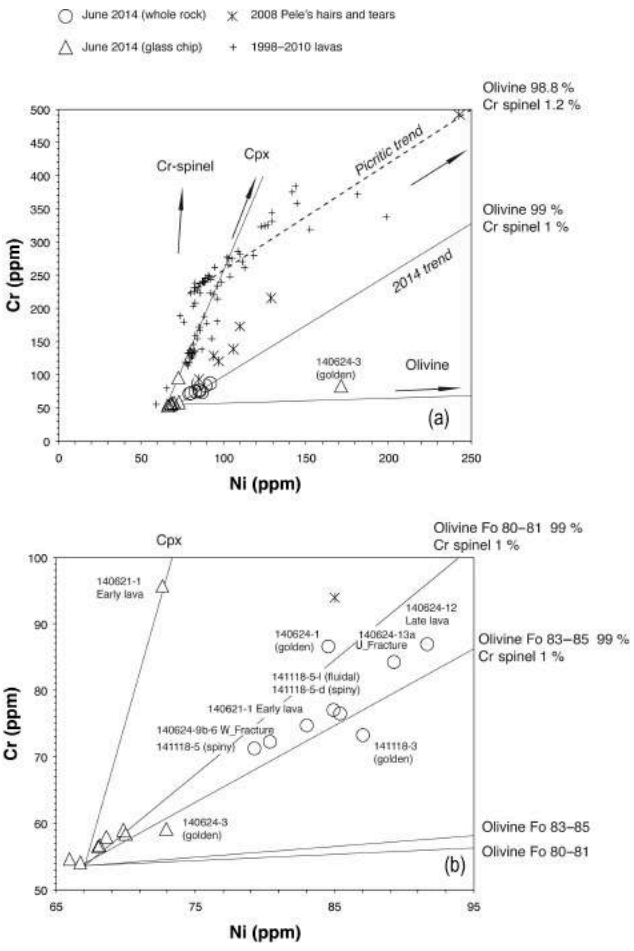

Figure 7. Ni-Cr concentration plot. **(a)** Ni-Cr signature of the June 2014 lavas compared to that of recent eruptions (Di Muro et al., 2015, and unpublished data). Whole-rock (circles) and glass (triangles) compositions are shown for the June 2014 eruption. Olivine controlled lines are indicated for olivine hosting 1.2 and 0.6 wt % Cr spinel. Compositions used for olivine (Ni = 1900 ppm, Cr = 300 ppm), clinopyroxene (Ni = 970 ppm, Cr = 4800 ppm), and Cr spinel (Ni = 1500 ppm, Cr = 25 %) are inferred from Welsch et al. (2009), Salaün et al. (2010), and Di Muro et al. (2015). **(b)** Enlargement of the Ni-Cr relationship between glass (triangles) and whole-rock (circles) samples from the June 2014 eruption. Fracture I: western fracture; Fracture II: upper fracture. Careful sample selection has permitted us to obtain a set of fragments virtually free of olivine-cpx crystals. Any addition of mafic crystals translates into enrichment in Ni-Cr; those samples that contain a few percent of crystals (consistent with textural and petrological observation) are slightly enriched in compatible elements.

were evaporated to dryness at 70 °C. The fluoride residues were reduced by repeatedly adding and evaporating a few drops of concentrated HNO_3 before being fully dissolved in ca. 20 mL of 7 M HNO_3. These solutions were diluted by a factor of 15 with 0.05 M HF (to reach rock dilution factor of ca. 4000) and trace element abundances were determined with quadrupole inductively coupled plasma mass spectrom-

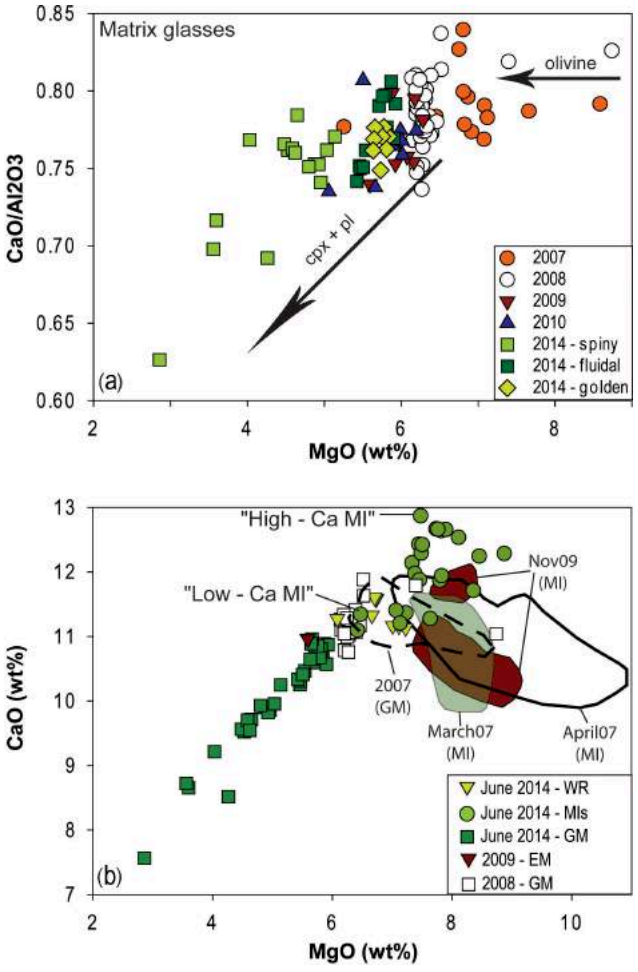

Figure 8. (a) Evolution of CaO/Al_2O_3 ratio in the matrix glasses of recent eruptions at Piton de la Fournaise as a function of MgO content (directly proportional to melt temperature). MI is the melt inclusions (grey area for the 2014 samples). **(b)** CaO versus MgO content for Piton de la Fournaise products. WR: whole rock; GM: ground mass; MI: melt inclusion; EM: embayment glass.

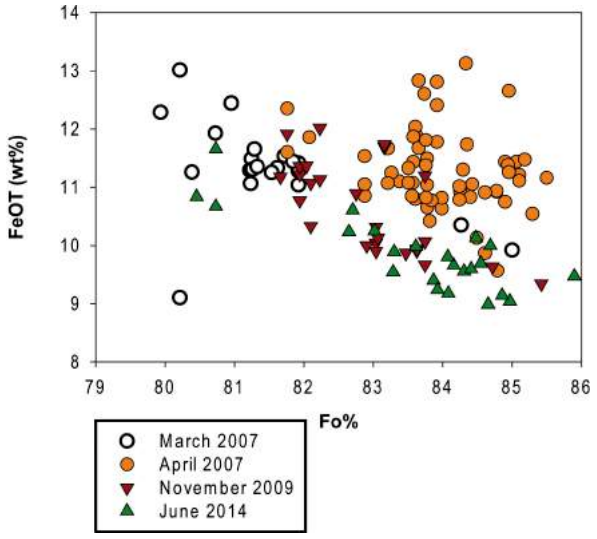

Figure 9. FeO_T in melt inclusions as a function of forsterite (Fo) content of the olivine host for recent eruptions at Piton de la Fournaise.

3.5 Glass and crystal chemistry

Spot analyses of matrix glass and crystal composition (Table S5) were carried out using a Cameca SX100 electron microprobe (LMV), with a 15 kV acceleration voltage of a 4 nA beam current with a 15 kV acceleration voltage and a beam of 5 µm diameter for glass analyses. However, for the spiny opaque scoria, characterized by abundant crystals with rapid growth textures, an 8 nA beam current and a beam of 10 µm diameter were used. For this latter sample, 10 analyses per sample were performed due to the heterogeneity within the highly crystallized glass (Fig. 8a), while for the other samples six analyses per sample were enough to characterize the clean homogeneous glass. For crystal analysis, a focused beam was used. For the characterization of the meso- and microcrysts, due to their small size, only two to three measurements were performed, one at the edge, one in the middle and one at the core of the crystals, to check for possible zonation.

3.6 Melt inclusions

Melt inclusions (MIs; Table S6, Figs. 8b and 9) were characterized in the olivine mesocrysts from the three groups of scoriae (fluidal, spiny glassy and spiny opaque) but not in the pumice group because crystals were too rare and small to be studied for MIs.

Olivine crystals were handpicked under a binocular microscope from the 100–250 and 250–600 µm grain size fractions of crushed tephra. Crystals with MIs were washed with acetone, embedded in epoxy and polished individually to generate adequate exposure of the MIs for in situ electron probe microanalysis. The MIs are spherical to oblate in shape and range in size from 10 to 200 µm. Some of the MIs contain

etry (Agilent 7500). The analyses were performed in plasma robust mode (1550 W). The reaction cell (He mode) was used to reduce interference on masses ranging from 45 (Sc) to 75 (As). The signal was calibrated externally (every four samples) with a reference basaltic standard (USGS BHVO-2) dissolved as for the samples and using the GeoReM recommended values (http://georem.mpch-mainz.gwdg.de/). For elements that are not well characterized in literature (As, Bi, Tl), or which show evident heterogeneity (e.g. Pb) in BHVO-2 powder, the signal was calibrated using the certified concentrations of a synthetic standard, which was also repeatedly measured. The external reproducibility (2σ error) of the method is 6 % or less for lithophile elements and 15 % or less for chalcophile elements.

shrinkage bubbles but all of those studied are totally deprived of daughter minerals. Major elements were measured on a Cameca SX100 microprobe at LMV (Table S6). For major elements, the larger MIs were analysed with a spot diameter of 10–20 µm and sample current of 8 nA, whereas the smaller MIs were analysed with a beam of 5 µm and a sample current of 4 nA. The results are given in Table S6, and analytical details and uncertainties are listed in Óladóttir et al. (2011) and Moune et al. (2012).

4 Results

4.1 Deposit texture (grain size, componentry, morphology) and petrological description of the samples

The pyroclastic deposits at the WF and UF sites (Fig. 1a) are formed by scattered homogeneous smooth fluidal (Fig. 3d) bombs and lapilli scoria. The average dimension of the fragments is around 4 cm (maximum axis) with bombs up to 10 cm and scoria lapilli up to 2 cm in size (Fig. 3e).

At the MV, the reversely graded deposit (Fig. 3b) is made up of lapilli and bombs, with only minor coarse ash (Fig. 3c). The lower 5 cm at the base is very well sorted and characterized by a perfect Gaussian distribution with a mode at 4 mm (Fig. 3c). In contrast, the grain size distribution of the upper 5 cm is asymmetrical with a main mode coarser than 22 cm and a second mode at 8 mm (Fig. 3c). This upper deposit is negatively skewed due to the abundance of coarse clasts. The dataset shows a similarity between the grain size distributions of the basal tephra ejected from the 2014 MV and the ones for the lava fountaining of the 2010 summit event (Fig. 3f and Hibert et al., 2015). Conversely, the top of the 2014 fall differs from fountain deposits, being coarser and polymodal, and it is ascribed to dominantly Strombolian activity (Fig. 3f).

In terms of componentry of the deposits, four types of clasts were distinguished (Fig. 4): (i) golden pumice, (ii) smooth or rough fluidal scoriae, (iii) spiny glassy scoria, (iv) spiny opaque scoria. The pumices are vesicular, low-density fragments, characterized by a golden to light brown colour, sometimes with a shiny outer surface (Fig. 4a). They are usually rounded in shape. Golden clasts studied for textures contain a few microcrysts of plagioclase (up to 0.1 mm in diameter), clinopyroxene up to 0.05–0.06 mm in diameter and small olivine up to 0.03 mm in diameter (Fig. 4), together with large areas of clean, light brown glass. The fluidal scoria fragments have dark, smooth or rough shiny surfaces (Fig. 4b). They can be more or less elongated in shape and have spindle as well as flattened shapes. The fluidal fragments are characterized by rare mesocrysts of plagioclase and clinopyroxene and microcrysts of plagioclase, clinopyroxene and olivine (Fig. 4b). The spiny glassy fragments are dark, spiny scoria that range in shape from subrounded to angular (Fig. 4c). These fragments contain abundant glassy areas, while the spiny opaque fragments lack a glassy, iridescent surface. Both groups of spiny clasts are characterized by the presence of dark and light brown glass. The spiny opaque fragments are the densest fragments and have the largest number of crystals. They contain, as the most abundant phase, relatively large meso- and microcrysts of plagioclase, up to 3 mm long, together with meso- and microcrysts of clinopyroxene and olivine (Fig. 4c and d). In the dark portions of their matrix, tiny fibrous microcrysts of olivine + clinopyroxene + plagioclase + Fe-Ti oxides occur. The spiny glassy fragments have the same crystal populations as the spiny opaque ones, but their plagioclases are much smaller and attain a maximum length of only 0.3 mm. Clusters of plagioclase and clinopyroxene and rare macrocrysts of olivine are present in both the spiny opaque and spiny glassy fragments. The olivine macrocrysts exhibit the typical compositional ($Fo_{84.2}$) and petrographic features of olivine phenocrysts described in previous studies (Clocchiatti et al., 1979; Albaréde and Tamagnan, 1988; Bureau et al., 1998a, b; Famin et al., 2009; Welsch et al., 2013). They are automorphic, fractured with oxides (mostly chromite) and MIs (Fig. 4c). Fluidal and pumice fragments studied for textures contain rare macrocrysts and mesocrysts of olivine, and the crystals are essentially microcrysts. The pumice and some fluidal fragments have lower contents of microcrysts than some fluidal and spiny fragments, with the latter having the highest microcryst content (Table S4). For comparison, two fragments of lava have been analysed as well (Table S3). The lava fragments are poorly vesiculated and completely crystalline (Fig. 4e). The lava contains the same paragenesis of crystals described in the spiny opaque fragments, with the main difference being that its matrix is completely crystallized and constituted mostly by well-formed plagioclase up to 800 µm and clinopyroxene up to 500 µm. Scarce smaller olivines are also present. Ubiquitous tiny rounded Fe-Ti oxides provide evidence of post-emplacement crystallization.

The componentry results are reported in Fig. 5 only for the MV deposits because the deposits from the WF and UF are characterized exclusively by fluidal clasts (Fig. 3). At the base of the MV deposit, the coarse fraction of the deposit is rich in golden and fluidal components that represent more than 60–70 vol. % (Fig. 5a and b). The proportion of the two groups is similar. In contrast, in the upper coarsely grained fall deposit, the clasts bigger than 8 mm are dominated by the spiny scoria fragments, while the fraction of clasts smaller than 8 mm show a dramatic increase in the golden and fluidal fragments, with the fluidal ones always more abundant than the golden ones (Fig. 5a and b). Abundant low-density golden, coarse lapilli pumice and bombs have been found scattered laterally up to 30 m from the main axis and were not found in the proximal deposit. On the basis of the high amount of pumice in the lower part of the deposit, we correlate the large, low-density clasts with the base of the proxi-

mal deposit, and consequently we interpret them as material emitted at the beginning of the June 2014 eruptive event.

4.2 Particle density, porosity, connectivity, permeability, and micro-texture

Density analyses performed on 200 coarse lapilli reveal a large variation in density values from 390 to 1700 kg m^{-3} with a median value at 870 kg m^{-3} (Table S3). The fragments collected from the MV have a bimodal density distribution, with a main population of low-density fragments with a mode at 800 kg m^{-3} and a second and denser population centred at 1400 kg m^{-3} (Fig. 6a). The golden and fluidal fragments form the lower-density population and the spiny fragments are dominant in the denser population (Fig. 6a). For these samples there is a marked correlation between porosity and morphology, so that the spiny opaque clasts are the densest (up to 1600 kg m^{-3}, with a vesicularity of 45 vol. %) and the golden pumice are the least dense (minimum density of 390 kg m^{-3} with a vesicularity of up to 86 vol. %; with a dense-rock equivalent density of 2880 kg m^{-3}). The fluidal fragments collected at the WF (Fig. 1b) have a density range from 700 to 1400 kg m^{-3} and a mode at 1000 kg m^{-3} (Fig. 6b). The five fragments from the only bomb collected at the UF are characterized by two distinct density values: the low-density one (700–800 kg m^{-3}) refers to the core of the sample, while the high-density one (1400–1500 kg m^{-3}) represents the quenched external rim of the bomb. Finally, the two fragments of lava show the highest-density values at 1800 and 2150 kg m^{-3}. This last value is one of the highest found in the lava collected from 2014 up to 2017 (see Fig. 13 in Harris et al., 2017, and DynVolc, 2017).

In all these samples, the increase in vesicularity correlates with an increase in the number of small (0.1 mm), medium (0.5–1 mm) and large (up to 4 mm) vesicles. In the fluidal clasts, these vesicles have a regular rounded or elliptical shape and are scattered throughout the sample. The low-density pumices are often characterized by the presence of a single, large central vesicle (10–15 mm) with the little vesicles and a few medium vesicles distributed all around it (Fig. 4). The spiny glass texture is characterized by a lower number of small vesicles than in the pumice and by the presence of mostly medium-sized vesicles, while the spiny opaque has more irregular shaped and very large (up to 10 mm) vesicles with a small- and a medium-sized vesicle population. In the spiny glass samples, the glass is more or less brown, with the dark brown portions being the ones with the lowest vesicle content and the highest microcryst content. The opaque samples have a central, very dark glass portion, with low vesicle content, and a more vesicular glassy portion at the outer edges (Fig. 4). The two fragments of lava are poorly vesiculated (Fig. 6a) and characterized by large, irregular vesicles (up to 5 mm in diameter). Clusters of small vesicles (up to 0.1 mm) are scattered between the large ones.

The vesicle size distribution (VSD in Fig. 4) histograms are characterized by a decrease in percentage of vesicles from the golden pumice to the lava as well as an increase in coalescence and or expansion signatures in the spiny fragments, marked by the increase in the large-vesicle population (Fig. 4c and d). This trend is also marked by the decrease in number of vesicles per unit of volume (N_v, Fig. 4) from the golden pumice to the lava. Finally, the trend is also mirrored by the total percentage of crystals (calculated in 3-D; Fig. 4 and reported for each sample in Table S3) that increases with the increase in density of the clasts, from a minimum of 7 vol. % for the golden pumice up to 49 vol. % for the spiny opaque scoria and 100 vol. % for the lava (Fig. 4). Mesocrystals, formed mostly by plagioclase and clinopyroxenes, are absent or very scarce in the golden and fluidal fragments, while they reach their maximum values, up 5 vol. %, in the spiny opaque fragment. The population of microcrystals, mostly constituted by plagioclases, ranges from a minimum of 8 vol. % in the golden pumice, up to 45 vol. % in the spiny fragments and 94 vol. % in the lava.

The connectivity data (Fig. 6c) also indicate that the fluidal and golden clasts have a larger number of isolated vesicles (up to 40 vol. %) with respect to the spiny products. The fluidal clasts from the WF are the most homogeneous with an average percentage of isolated vesicles around 30 vol. %. In contrast, both the pumice and the fluidal fragments from the MV, characterized by higher values of porosity (> 75%), have a wide range in percentage of isolated vesicles (between 20 and a few vol. %). The fragments of the bomb collected at the UF are consistent with a vesiculated core characterized by scarce isolated vesicles and the quenched rind that has 30 vol. % of isolated vesicles. Finally, the spiny fragments have the lowest content of isolated vesicles (0–5 vol. %). Despite the presence of these isolated vesicles, all the samples shear high values of permeability, with the Darcian (viscous, K_1) permeability values ranging from 10^{-11} to 10^{-10} m^2 (Fig. 6d and Table S3). The graph of vesicularity versus K_1 shows a slight increase in permeability with vesicularity, with the golden pumice being the most permeable among the samples and the spiny glassy fragment the least permeable. The three samples collected from the February 2015 eruption fit this trend. However, the densest spiny opaque scoria of the 2014 eruption share the high permeability value of the golden pumice.

4.3 Chemistry of the products

Major and trace element concentrations of whole-rock and hand-picked glass samples are reported in Table S4. Whole-rock major element composition is very uniform (e.g. 6.5 < MgO < 6.7 wt %) and well within the range of steady-state basalts (SSBs), the most common type of basalts erupted at PdF (Albarède et al., 1997). However, compatible trace elements, such as Ni and Cr, are at the lower end of the concentration range for SSB (< 100 ppm), indicat-

ing that the June 2014 eruption sampled relatively evolved melts. Ni and Cr generally show higher concentrations in 2014 bulk rocks ($79 < Ni < 92$ ppm and $71 < Cr < 87$ ppm) compared to the 2014 glass chips ($66 < Ni < 73$ ppm and $54 < Cr < 59$ ppm for all but two chips). In the Cr vs. Ni plot (Fig. 7a), whole rocks plot to the right of the main clinopyroxene ± plagioclase-controlled melt differentiation trend. This shift reflects the addition of Ni-rich olivine (Albarède and Tamagnan, 1988). We estimate that the Ni excess results from the occurrence of a low amount (0.7 to 1.3 wt %) of cumulative olivine in whole rocks, consistent with thin section observations. The composition of olivine macrocrysts (ca. Fo_{84}) is too magnesian to be in equilibrium with the low-MgO evolved composition of the 2014 magma. Using our estimate for the amount of cumulative olivine, we recalculate the olivine-corrected MgO content of the 2014 magma at 6.2 wt %. The June 2014 melt is thus only moderately depleted in compatible elements compared to the previous eruption of December 2010 (MgO ∼ 6.6 wt %, Ni ∼ 80 ppm, Cr ∼ 120 ppm). Conversely, the June 2014 melt is significantly depleted in compatible elements compared to the earlier November 2009 eruption, which sampled relatively primitive magmas (average MgO ∼ 7.7 wt %, Ni ∼ 135 ppm, Cr ∼ 350 ppm) (Fig. 7a). The 2014 evolved composition plots at the low Ni-Cr end of the PdF historical differentiation trend (Albarède and Tamagnan, 1988), near the composition of lavas erupted on 9 March 1998 after 5.5 years of quiescence (1992–1998). Note that olivine accumulation at PdF generally occurs in melt with ca. 100 ppm Ni (Albarède and Tamagnan, 1988). Olivine accumulation in evolved melts ($Ni < 70$ ppm) seems to be a distinctive feature of many small post-2007 eruptions (e.g. this event and the three 2008 eruptions; see Di Muro et al., 2015).

A closer inspection of Ni-Cr variability in June 2014 whole-rock samples (Fig. 7b) reveals that scoria from the WF (140624-9b-6, Table S4) and early erupted lavas (1406-21-1, Table S4) have the lowest amount of olivine (< 0.9 %) whereas scoria from the UF (140624-13a) and late erupted lavas (140324-12) have a slightly higher amount of olivine (> 1.2 %). This is consistent with the general trends observed at PdF of olivine increase from the start to end of an eruption (Peltier et al., 2009).

The so-called "olivine control trend" in Ni-Cr space cannot be explained by either addition of pure olivine, which contains less than 500 ppm Cr (Welsch et al., 2009; Salaün et al., 2010; Di Muro et al., 2015), or by the addition of olivine plus pyroxene (which would require ca. 50 % pyroxene with 970 ppm Ni and 4800 ppm Cr; see Fig. 7 caption). Instead, addition of olivine hosting ca. 1 % Cr spinel (with 25 wt % Cr) accounts for data and observations and is consistent with crystallization of olivine and Cr spinel in cotectic proportions (Roeder et al., 2006). The fact that some samples (golden pumice) plot off the main well-defined array can be explained by either addition of more or less evolved olivine crystals (within the range of Fo_{80--85} measured in June 2014 samples) and/or slight variations (±0.02 %) in the proportion of Cr spinel (Fig. 7b).

The glass chemistry of the four clast types allows us to correlate porosity and oxide contents and shows an increase in MgO from the spiny opaque to fluidal and golden fragments (Fig. 8a). Consistent with petrological and textural observations, the spiny opaque is the most heterogeneous type of clast in terms of glass composition (Fig. 8). The glassy portion at the edge of the clast is similar to the spiny glass, while the interior, characterized by dark areas rich in tiny fibrous microcrysts, shows scattered glass compositions with very low MgO content as well as a decrease in CaO (Fig. 8). We attribute the significant variation in glass composition within the different components to variable degrees of microcrystallization as the bulk chemistry of all clasts is very similar and globally homogeneous.

4.4 Melt inclusions

MI analyses must be corrected for post-entrapment host crystallization at the MI–crystal interface. We used a $Kd = (FeO/MgO)_{ol}/(FeO/MgO)_{melt} = 0.306$ (Fisk et al., 1988; Brugier, 2016) and an average $Fe^{3+}/\sum Fe_{total}$ ratio of 0.11 (Bureau et al., 1998a; Di Muro et al., 2016 and references therein) defined for PdF magmas. For the June 2014 melt inclusions, the post-entrapment crystallization ranges from 2.9 to 10.5 wt %. Raw and corrected major and volatile element concentrations of MIs are reported in Table S6.

Host olivines span a large compositional range from Fo_{80} to Fo_{86}. Despite the evolved bulk composition of the magma, most olivines are quite magnesian (Fo_{83-85}) and are not in equilibrium with the evolved host magma. Conversely, Mg-poor olivines (Fo_{80-81}) can be considered as being in equilibrium with the bulk rock composition. The corrected compositions of MIs in phenocrysts from the different samples partly overlap with the evolved bulk rocks (MgO_{wr}: 6.1–7.2 wt %) and extend to higher MgO contents of up to 8.8 wt % (Table S6). MIs display a narrow range of transitional basaltic compositions ($K_2O = 0.5$–0.9 wt %) and show no significant difference between the three types of scoriae. The major element composition of MIs correlates with that of the host olivines. MIs in the high Fo olivines have the highest MgO, CaO and TiO_2 and lowest K_2O concentrations (Table S6). It is interesting to note that the June 2014 products contain two populations of magnesian ($Fo_{>83}$) olivines hosting MIs with two distinct Ca contents. Most of the magnesian olivines contain MIs with unusually high CaO contents (11.6–12.9 wt %) and high CaO/Al_2O_3 ratios (0.8–0.9), higher than those of the bulk rocks (0.8) (Fig. 8). The occurrence of olivines with high-Ca MIs has been observed in all three different types of scoriae. A few magnesian olivines and all Mg-poor olivines ($Fo_{80.5-83.6}$) host MIs with lower CaO contents (11.4 wt %). This latter composition overlaps with that of the bulk rock (Fig. 8). The high-Ca population of inclusions is also enriched in TiO_2 and Al_2O_3 and de-

pleted in MgO, FeO_T and Na_2O for a given olivine Fo content with respect to the low-Ca population. Both low- and high-Ca populations of MIs have similar K_2O contents and total alkali content increases from 3 at 12.6 wt % CaO to 3.5 at 10.8 wt % CaO. However, we remark that high-Ca MIs from the June 2014 activity record a significant scattering in K_2O contents, which range from 0.55 to 0.9 wt %. These anomalous compositions potentially track processes of crystal dissolution (e.g. pyroxene dissolution).

MIs in olivines from June 2014 can best be compared with those of other recent small-volume and short-lived eruptions that emitted basalts with low phenocryst contents, like those in March 2007 (0.6×10^6 m^3) and November 2009 (0.1×10^6 m^3) (Roult et al., 2012). March 2007 aphyric basalt has a bulk homogeneous composition with intermediate MgO content (MgO_{wr}: 7.33 wt %; K_2O: 0.67 wt %). Their olivines (Fo_{81}) are in equilibrium with the bulk rock and their composition is unimodal (Di Muro et al., 2014). November 2009 products are the most magnesian lavas emitted in the 2008–2014 period; they are slightly zoned (MgO_{wr}: 7.6–8.3 wt %; K_2O: 0.75–0.62 wt %) and contain a few percent of normally zoned olivine macrocrysts with bimodal composition (Fo_{81} and $Fo_{83.5}$; see Di Muro et al., 2016). June 2014 bulk rocks (MgO_{wr}: 6.7 wt %; K_2O: 0.75 wt %) and MIs in Fo_{80-81} olivines are quite evolved. Their composition is close to that of products emitted by summit intracaldera eruptions in 2008, ca. 1.5 years after the large 2007 caldera-forming eruption (Di Muro et al., 2015) (Fig. 8). As already reported for 2008 products, many olivine macrocrysts of 2014 are clearly too magnesian to be in equilibrium with the relatively evolved host melts. Overall, MgO content in 2007–2014 MIs tends to decrease with decreasing Fo content of the host olivines. MIs in olivines also exhibit a trend of linear decrease in MgO and increase in FeO from April 2007 to 2009–2014 products (Fig. 9). MIs in March 2007, November 2009 and June 2014 follow the same trend of FeO enrichment (Fig. 9). In the large-volume and olivine-rich April 2007 products, MIs in magnesian olivines with $Fo_{>82}$ have distinctly higher MgO and FeO and lower SiO_2 and Al_2O_3 than MIs in 2009–2014 products. The distinctive FeO enrichment of many of the MIs from the April 2007 oceanite has been interpreted by Di Muro et al. (2014) as a result of post-entrapment modification related to new magma inputs into long-lasting magma storage.

Two populations of low- and high-Ca MIs are also found in the November 2009 olivines. Low-Ca melt inclusions from the November 2009 and June 2014 eruptions indicate a single trend of chemical evolution (Fig. 8), consistent with bulk rock compositions. June 2014 products have lower MgO and CaO contents than those from November 2009. Significant scattering in K_2O content (0.6–0.9 wt %) is found in low-Ca inclusions from 2009, as observed in high-Ca inclusions from the 2014 eruption, but they share similar K_2O contents. In the 2009 and 2014 products, K_2O content of MIs is partly anti-correlated with the olivine Fo content. This observation has been attributed to moderate heterogeneity of primary melts feeding the plumbing system of PdF. Rapid temporal changes of K_2O content in PdF basalts have been reported (Boivin and Bachélery, 2009).

4.5 Mineral composition and glass – plagioclase equilibrium

All 2014 scoriae (spiny, fluidal, golden) contain the same paragenesis of olivine, clinopyroxene and plagioclase. The composition of minerals found in golden, fluidal and spiny scoriae is indistinguishable.

In olivines, average MgO content decreases from macrocrysts ($Fo_{84.1}$) to mesocrysts ($Fo_{79.6}$) to microcrysts. Olivine microcrysts (Table S5) are normally zoned. Their composition ranges from $Fo_{78.0-75.3}$ in the cores to $Fo_{74.3-70.5}$ in the rims. Overall, olivines in 2014 products span the full range of typical Fo contents of recent PdF magmas (Boivin and Bachèlery, 2009; Di Muro et al., 2014, 2015). Clinopyroxene composition (augites) ranges from $En_{53}Fs_{15}Wo_{32}$ to $En_{41}Fs_{14}Wo_{45}$. Their average composition ($En_{45}Fs_{14}Wo_{41}$) is consistent with that found in other evolved melts like those emitted by the 2008 eruptions (Di Muro et al., 2015) and more generally in recent PdF products (Boivin and Bachèlery, 2009). Clinopyroxenes are unzoned; the composition of cores and rims is very similar and close to that found in microcrysts and mesocrysts. Plagioclase composition ranges from $An_{79.5}Ab_{19.9}Or_{0.6}$ to $An_{63.1}Ab_{35.7}Or_{1.2}$ with a bimodal distribution ($An_{76.5-79.5}$ and $An_{63.1-72.9}$, Fig. 10a). Similar bimodal distributions were observed in many other products at PdF (Di Muro et al., 2015). Mesocrysts ($An_{75.5}Ab_{23.8}Or_{0.7}$ on average) are more calcic with respect to microcrysts ($An_{65.7}Ab_{33.1}Or_{1.2}$ on average). Normal zoning is found from plagioclase cores to rims (Fig. 10a). The composition and zonation of 2014 plagioclases clearly contrast with the complex and often reverse zoning patterns and intermediate composition of the 2008 PdF products that were attributed to pre-eruptive magma heating (Di Muro et al., 2015).

Plagioclase–melt equilibrium and melt composition in pyroclastic rocks and water-quenched lavas were used to estimate both temperature and water content dissolved within the melt (Fig. 10b and Table S5). Temperature estimates are based on the (dry) equation of Helz and Thornber (1987) recalibrated by Putirka (2008). Dissolved water content was calculated from the plagioclase hygrometer of Lange et al. (2009) at 50 MPa. This pressure corresponds to the average CO_2–H_2O saturation pressure (recalculated with Papale et al., 2006) typically recorded in MIs from central products at PdF (e.g. 1931 eruption in Di Muro et al., 2016, and references therein). This pressure roughly corresponds to the sea level depth, which is inferred to be the location of the potential main shallow magmatic reservoir (Peltier et al., 2009; Lengliné et al., 2016; Coppola et al., 2017). The application of the plagioclase hygrometer of Lange et al. (2009)

makes it possible to estimate the dissolved water content in the melt with a nominal uncertainty of 0.15 wt % and is only slightly dependent on pressure. Plagioclase compositions not in equilibrium with the melt (glass or bulk rock) are those of mesocryst cores with the highest ($An_{>76.5}$) anorthite content (Fig. 10a and Table S5). Such compositions are more in equilibrium with CaO-richer magnesian melts than those measured in matrix glasses and bulk rocks of the 2014 eruption and likely formed during early stages of shallow magma differentiation (Fig. 10a).

In order to determine pre-eruptive conditions, calculations were performed only on paired plagioclase rims and matrix glasses in equilibrium, using the plagioclase–melt equilibrium constant of Putirka (2008) calibrated for melts whose temperature exceeds 1050 °C ($Kd_{An\text{-}Ab} = 0.27 \pm 0.05$). Our review of published and unpublished data shows that melt temperature progressively decreases from April 2007 (1188 ± 16 °C) to January–October 2010 (1147 ± 9 °C) and positively correlates with K_2O content in melts, which increases from 0.70 to 0.96 wt % (Fig. 10b). The melts from the June 2014 eruption record the lowest temperatures in post-2007 eruptions (1131 ± 15 °C) together with the highest K_2O enrichment (K_2O: 0.90 ± 0.12 wt %). The lowest temperatures are recorded by spiny scoriae, while the temperature of golden scoriae overlaps with that of 2010 products emitted before the 2010–2014 phase of quiescence. In spite of the large variability in melt composition and temperature, average pre-eruptive water content dissolved in the melts (0.5 ± 0.2 wt %) is quite homogeneous for the whole 2008–2014 period. In 2014, the lowest estimated dissolved water content (down to 0.38 wt %) is for the golden and some fluidal scoriae, while the maximum amount (0.68 wt %) is for the spiny opaque scoriae. However, water content estimated from core–bulk rock equilibrium (0.3 ± 0.1 wt %) is slightly lower than that estimated from rim and microlite–matrix glass equilibrium (0.5 ± 0.2 wt %), but the difference broadly overlaps the nominal uncertainty related to calculations. Dissolved water contents in melts of the pyroclasts are thus intermediate between those measured in 2007 melt inclusions (H_2O: 0.8 ± 0.15 wt % and up to 1.1 wt %) and those typically found in degassed matrices of lava and Pele's hairs of 2007 (Fig. 10b; 0.2 wt %; see Di Muro et al., 2015, 2016).

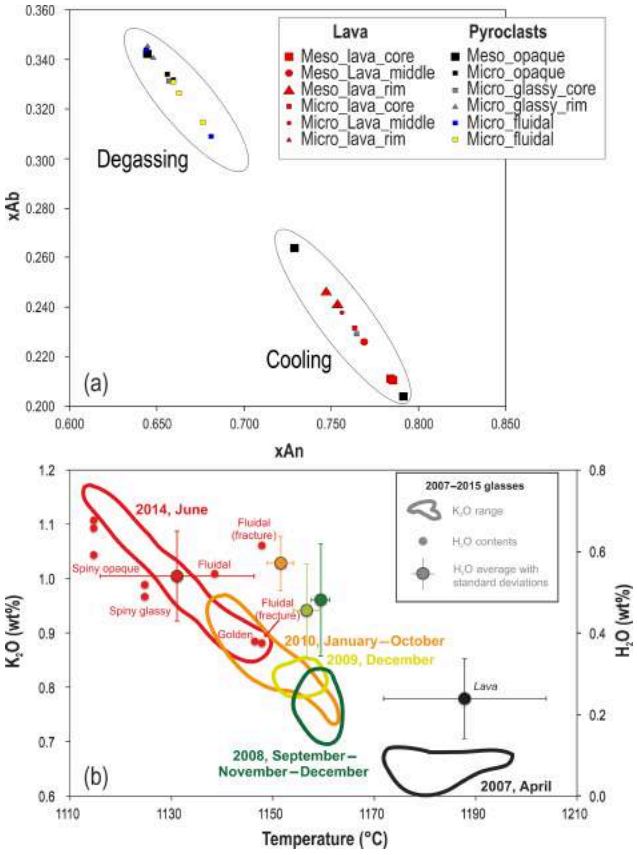

Figure 10. **(a)** Anorthite versus albite compositions for the plagioclase crystals measured for the June 2014 eruption of PdF. **(b)** Temperature, composition (K_2O), and dissolved water content (H_2O) for the evolution of 2007–2014 melts from glasses. The data have been obtained by studying the glass–plagioclase equilibrium or on the basis of matrix glass analyses. Temperature estimation based on the MgO thermometer of Helz and Thornber (1987) modified by Putirka (2008). Water content is from the plagioclase hygrometer of Lange et al. (2009). Only plagioclases in equilibrium with melts are considered, following the procedure described by Putirka (2008) for > 1050 °C melts ($Kd = 0.27 \pm 0.05$). Error bars reported in Fig. 10b correspond to the standard deviation of the plagioclase dataset, whose range is larger than the error of the method. We stress that the reported temperatures are obtained using the Helz dry model. Further uncertainty arises from the dependence of the method on dissolved water content as shown recently by Putirka (2008). In order to minimize the number of assumptions and perform a comparison between distinct eruptions, we preferred the dry model.

5 Discussions

5.1 Eruptive dynamics

The activity fed by the uppermost WF and UF (Fig. 1) was very short-lived, as shown by the presence of only scattered bombs and coarse lapilli (Fig. 3d and e). The homogeneity of these clasts, their coarsely grained nature and the fluidal smooth texture are in agreement with very short-lived fire fountaining and magma jets. Glassy outer surfaces of clasts have been interpreted as a late-stage product of fusion by hot gases streaming past the ejecta within the jet or fountain (Thordarson et al., 1996; Stovall et al., 2011). However, the occurrence of this process is not supported by the homogeneous glass composition in our fluidal clasts. Therefore, we interpret these features here just as rapid quenching and not re-melting. Vlastélic et al. (2011) documented the mobility of alkalis and other elements on PdF clasts that experienced long exposures to acid gases. In the 2014 eruption pyroclasts,

the mobility of elements was prevented by the short duration of the events.

At lower altitude and close to the MV (Fig. 1), the 5 cm layer at the base of the fall deposit is finely grained (Fig. 3b and c) and rich in fluidal and golden fragments (Fig. 5), with a perfect Gaussian grain size curve (Fig. 5), and similar to that reported from the weak 2010 fountaining event (Fig. 3f and Hibert et al., 2015). Therefore, we interpret this deposit as being due to weak Hawaiian-like fountaining (sustained, but short-lived) activity. We want to remark here that this activity happened during the night and was not observed. The top of the same deposit is coarsely grained (Fig. 3b and c), bimodal, has a lower content in coarse ash (Table S2) and is rich in spiny opaque and spiny glass fragments (Fig. 5). The reverse grain size likely records the transition from early continuous fountaining to late discrete Strombolian activity (observed and recorded on the 21 of June 2014, Fig. 2). This transition in activity is typical of many eruptions at PdF (Hibert et al., 2015). The reverse grading of the whole deposit (Fig. 3b and c) is thus not correlated with an increase in energy of the event but with two different eruptive dynamics and fragmentation processes. The decrease in coarse ash, which correlates with the decrease in energy of the event, highlights the most efficient fragmentation process within the Hawaiian fountaining with respect to the slow gas ascent and explosion of the Strombolian activity. These conclusions are consistent with (i) the continuous and progressive decrease in intensity of real-time seismic amplitude measurement recorded by the OVPF seismic network (unpublished data) and (ii) satellite-derived time-averaged lava discharge rates, which suggest continuous decay of magma output rate after an initial short-lived intense phase (Coppola et al., 2017).

5.2 Background on the texture of clasts from Hawaiian and Strombolian activities

The first micro-textural analysis of Hawaiian ejecta was performed by Cashman and Mangan (1994) and Mangan and Cashman (1996) on pyroclasts from 1984 to 1986 Pu‘u ‘Ō‘ō fountainings. The authors defined two clast types: (1) scoria consisting of closed-cell foam of $\leq 85\,\%$ vesicularity, with round, undeformed, broadly sized vesicles and (2) reticulite, an open-cell polyhedral foam with $\sim 1\,\mu m$ thick vesicle walls with $>95\,\%$ vesicularity. They stated that the scoria-to-reticulite transition is a consequence of Ostwald ripening, where larger bubbles grow at the expense of smaller bubbles due to post-fragmentation expansion of clasts within the fountain. According to this model, scoria preserves textures closer to conditions at fragmentation, whereas continued vesiculation and clast expansion in the thermally insulated core of the fountain results in reticulite. This model was confirmed at lava fountains at Etna (Polacci et al., 2006), Villarrica (Gurioli et al., 2008), Kīlauea Iki, (Stovall et al., 2011, 2012), Mauna Ulu (Parcheta et al., 2013) and Al-Madinah (Kawabata et al., 2015). These last authors also measured the connected and isolated porosity in the AD1256 Al-Madinah Hawaiian fountaining eruptions. They found that the reticulite-like textures from the central part of these very high fountains showed isolated vesicles in agreement with low shear rates and low viscosity melts, where bubbles may grow spherically and remain isolated. In contrast, at margins of the fountains, high shear may lead to stretching and mechanical coalescence of bubbles, forming the common, fluidal types of particles also seen in the deposits. They also stated that lower vesicularity and greater isolated porosity were found in some tephra, interpreted as resulting from violent Strombolian eruptive phases.

The data that we found in our study of the typical activity of PdF agree only partially with all these interpretations. The reason is that we sampled and measured products of very weak Hawaiian to Strombolian activities. If we plot the approximate durations and masses of these events on the Houghton et al. (2016) diagram, the 2014 activity of PdF falls into the two fields for transient and fountaining activity, but at the base of the diagram. We here show for the first time that short-lived and weak fountaining can preserve pyroclast textures that record magma ascent and fragmentation conditions before the explosions and also provide some information about the pre-eruptive storage conditions. The occurrence of time-variable ascent conditions is also reflected in the time evolution of eruptive dynamics, with the golden and fluidal scoriae emitted from the low Hawaiian fountaining episodes and the spiny fragments from the Strombolian-like explosions.

5.3 The four typologies of clasts and their distribution in space and in time in the 2014 eruption at PdF

Thus, as described in Sect. 5.1, longitudinal variation in eruptive style along the fracture system produces a spatial variability in the proportions of the four typologies of clasts. The uppermost fractures (WF and UF, Fig. 1a) are characterized solely by fluidal fragments (Fig. 4b); they lack both the spiny and the golden components. In addition, these fluidal clasts are the ones showing the smoothest surfaces (indicative of rapid quenching in a very hot environment), low porosity values (between 50 and 77 vol. %, Fig. 6b), the highest content in isolated vesicles (~ 30 vol. %, Fig. 4c) and low vesicle numbers (3 to 5×10^6, Fig. 4b) comparable to the spiny fragments. They have scarce mesocrysts (1 vol. %, Table S3) and a low number of microcrysts of plagioclase and clinopyroxene (11 to 12 vol. %, Table S3). These fluidal scoria fragments were emitted by short-lived jets of magma; therefore they underwent rapid quenching in a very hot environment that prevented any expansion or further vesiculation and preserved a very high number of isolated vesicles (Fig. 6d). Syn-eruptive crystallization was hindered by high ascent velocities in the dike due to the sudden release of over-pressure in the shallow magma reservoir.

The four typologies of clasts, golden pumice, fluidal scoria and the spiny fragments (Fig. 4) were only found at the MV. The relative proportions of these four typologies of clasts correlate with the eruptive dynamics. The golden lapilli and fluidal clasts were in fact dominant in the more energetic Hawaiian activity at the beginning of the eruption (during the night between 20 and 21 of June 2014). In contrast, the spiny fragments were dominant during the Strombolian activity, coinciding with the decrease in mass discharge rate (early in the morning of the 21; Fig. 2 and Coppola et al., 2017). The golden and fluidal fragments from the MV show the highest porosity (86 %, Fig. 6a), variable proportions of isolated vesicles (Fig. 6c) and high, but variable, N_v numbers (Fig. 4a). They are also characterized by a uniform vesicle size population with clear evidence of incipient expansion, especially in the fluidal fragments (Fig. 4a and b). From the connectivity graph, there is a clear decrease in isolated vesicles with the increase in vesicularity (Fig. 6c). The content in crystal, mostly formed by microcrysts of sodic plagioclase (Fig. 10a) due to magma degassing during its ascent and decompression in the conduit (Di Muro et al., 2015), is very low, especially in the golden pumice (up to 9 vol. %), and it is slightly higher for the fluidal clasts (up to 22 vol. %). We interpret the golden fragments, at the MV, to be the fastest (low number of microcrysts) and less degassed magma (high vesicularity coupled with high N_v), which experienced only a very short residence time in the magma transport system (dike + vent), followed by the fluidal fragments. In contrast the spiny fragments, characterized by a higher percentage of microcrysts and mesocrysts, by the lack of isolated vesicles, and by the presence of coalescence signature and low N_v values (Fig. 4c and d), are indicative of an extensively degassed and cooled magma. The presence of the mesocrysts (that formed in the shallow reservoir) in the spiny fragments, and their slightly cooler temperature (Fig. 10b), strongly support this interpretation. The spiny fragments likely record the slowest ascent velocity and the longest residence time in the reservoir + dike + vent system compared to the golden or fluidal counterpart. Therefore these fragments are associated with Strombolian events, and decreasing mass discharge rate, in agreement with their slower ascent that allows extensive syn-eruptive crystallization.

Among spiny fragments, the opaque ones are the densest; they lack a uniform glassy surface, and they are characterized by (i) very high microcryst content, (ii) strong coalescence signature (Fig. 4d), (iii) heterogeneous glass chemistry and (iv) mingling with hotter magma at the clast edges (Fig. 8a). All these features reveal the composite nature of these clasts. We interpret the spiny opaque as spiny glass fragments recycled inside the eruptive vent during the explosions, with the densest portion of the magma prone to falling back in the vent or fracture (Fig. 2b).

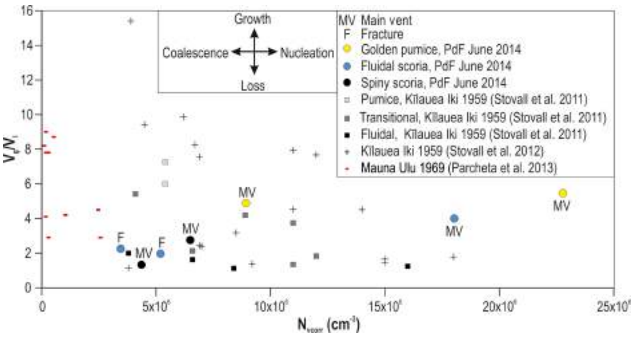

Figure 11. Volumetric ratio of vesicles to melt (V_g/V_l) versus vesicle number density.

5.4 Degassing-driven versus cooling-driven crystallization

Syn-eruptive degassing is favoured by bubble connectivity and/or permeability (Fig. 6c and d) in the ascending magma, enhanced by syn-eruptive crystallization in the conduit (especially microcrysts of plagioclase, Fig. 10a), even for magmas at low vesicularity. However, our dataset also supports the occurrence of magma stratification in the reservoir. Textural and petrological data demonstrate that the initial activity emitted a small volume of melt (represented by golden fragments and a large part of the fluidal fragments) with very scarce crystals. This crystal-poor melt was followed in time by the main volume of magma that contains a larger number of mesocrysts (spiny clasts and lava). Lava flows represent the main volume emitted in the 2014 eruption. Mesocrysts are absent in the golden, scarce in the fluidal, and more abundant in the spiny (Fig. 4b, c and d) and lava (Fig. 4e) fragments and consist in plagioclase and clinopyroxene and minor olivine. Their composition indicates that they formed in the reservoir, as shown by their different composition in respect to the microcryst counterparts that formed during melt degassing in the conduit (Fig. 10a). Most importantly, a large number of microcrysts in lava formed in the reservoir as well as during magma cooling (Fig. 10a). Thus, we have a range of crystallization conditions. The fact that the lighter plagioclase are not concentrated in the upper and early erupted portion of the reservoir can be due either to the fact that often they are locked in clusters with the clinopyroxene or that this melt was expelled from the crystal-rich portion of the reservoir (see Fig. 10b). Water exsolution from the melt can result from its extensive crystallization, which induces an increase in dissolved volatile content, up to saturation (second boiling) and can drive melt–crystal separation.

In conclusion, the crystals in the 2014 fragments do reflect the shallow reservoir conditions and the ascent degassing processes.

5.5 Textural syn-eruptive versus post-fragmentation modifications

To prove that the 2014 vesiculation of the clasts has not been modified by post-fragmentation expansion processes, following Stovall et al. (2011), we use a plot of vesicle-to-melt ratio (V_g / V_l; after Gardner et al., 1996) and vesicle number density (N_b, Fig. 11). As demonstrated by Stovall et al. (2011), the addition of small bubbles leads to an increase in N_v and only a slight increase in V_g / V_l. Bubble growth by some combination of diffusion and decompression leads to an increase in V_g / V_l at constant N_v. N_v decreases while V_g / V_l increases during bubble coalescence, whereas loss of bubbles via collapse or buoyant rise leads to a reduction in both parameters. Intermediate trends on the diagram reflect combinations of more than one of these processes. The pumice and the scoria from the MV of PdF show the highest V_g / V_l but also the highest N_v, suggesting preservation of small vesicles and growth by some combination of diffusion and decompression. The presence of the small vesicles and the lack of a strong coalescence and/or expansion signature confirm that the weak PdF activity leads to only limited post-fragmentation expansion inside the hot portions of the short-lived fountains. These data contrast with the data from the more energetic fountaining events observed at Kīlauea or elsewhere, where pre-eruptive information is basically erased because pumice textures are dominated by expansion effects due to their longer residence within the long-lived energetic fountaining. In contrast, the densest, spiny scoriae and the scoriae from the fractures activity show the lowest values of N_v and V_g / V_l due to incipient coalescence and/or loose or lack of small bubbles.

According to previous works (listed above), the golden pumice of PdF should be derived from the central part of the fountains, but they do not show the strong post-expansion signatures reported by other samples collected from more energetic Hawaiian fountainings (Fig. 11). It is interesting to note that the fluidal fragments at the MV are less smooth (Fig. 4), more vesiculated and have a lower content of isolated vesicles than the fluidal scoriae from the uppermost fractures (Fig. 6). Therefore fluidal fragments at the 2014 MV could indeed represent clasts that have been partly modified during their residence in the external part of the fountains, while the golden samples could come from the central part (Stovall et al., 2011, 2012). However, the slight differences in crystallinity and glass chemistry between the fluidal and golden fragments support the idea that each of these fragments has an imprint from the pre-fragmentation setting. In contrast, the spiny fragments from the MV and the fluidal fragments from the fractures show low N_v and low V_g / V_l in agreement with loss of vesicles and coalescence. However, the presence of large numbers of isolated vesicles within the fluidal scoriae from the fractures agrees with their provenance from a fast, hot ejection of relatively degassed magma (low N_v). In contrast, the spiny fragments, especially because of the presence of mesocrysts and an increase in syn-eruptive microcrysts, are indicative of the slowest ascent velocity and extensive degassing and cooled magma. The spiny fragments are the most degassed, densest and the most crystal-rich magma that was emitted during low-energy activity by Strombolian explosion, where recycling phenomena were also very frequent (Fig. 2f).

Our vesicle connectivity results are in full agreement with the recent review of Colombier et al. (2017b). According to these authors, connectivity values can be used as a useful tool to discriminate between the basaltic scoriae from Hawaiian (fire fountaining) and Strombolian activity. The broad range in connectivity for pumice and scoriae from fire fountaining is interpreted simply as being due to variations in the time available before quenching due to differences in location and residence time inside the fountain. The fluidal fragments from the WF are the richest in isolated vesicles because they are transported by very short-lived hot lava jets. In contrast, the higher connectivity observed in scoriae from Strombolian activity is probably related to their higher average crystallinity and more extensive degassing prior to the eruption (Colombier et al., 2017b). The spiny surface of these Strombolian fragments is due to the fact that these weak explosions emit only a small solid mass fraction and the partially quenched dense clasts land quickly after a short cooling path through the surrounding atmosphere (e.g. Bombrun et al., 2015).

All the clasts, from golden to spiny, are very permeable, independent on their vesicularity, crystal content and/or of the presence of isolated vesicles. This is in agreement with our interpretation that magma degasses during its ascent in the conduit and that promotes microlite nucleation (see the sodic plagioclase, Fig. 10a) before magma fragmentation (see also Di Muro et al., 2015, with the Pele's hair and tear samples for the three 2008 eruptions). Moreover, we always find that some of the spiny clasts (especially the opaque ones) are slightly less permeable than the golden and fluidal ones, but not with a low permeability as we would expect from their low vesicularity.

In conclusion, we can state that (i) the crystals lower the percolation threshold and stabilize permeable pathways and (ii) this is true for the syn-eruptive sodic plagioclase that favour an efficient degassing in the relatively crystal-rich magma because of their low wet angles that favour degassing over nucleation (Shea, 2017) and their aspect ratio (e.g. Spina et al., 2016). (iii) Therefore permeability develops during vesiculation through bubble coalescence, which allows efficient volatile transport through connected pathways and relieves over-pressure (Lindoo et al., 2017). Pervasive crystal networks also deform bubbles and therefore enhance outgassing (Oppenheimer et al., 2015). Based on Saar et al. (2001) crystals should start to affect the behaviour of the exsolved volatile phase when they approach 20 vol. % (Lindoo et al., 2017). In our dataset, apart from the golden and part of the fluidal fragments, all the other clasts do have mi-

crocrysts > 20 %. Our data completely support slow decompression rate allowing more time for degassing-induced crystallization, which lowers the vesicularity threshold at which bubbles start to connect.

Rapid re-annealing of pore throats between connected bubbles can happen due to short melt relaxation times (Lindoo et al., 2016). This phenomenology could explain the high number of isolated vesicles in the fountaining samples. However, vesicle distributions of the golden and fluidal fragments are almost perfect Gaussian curves, so it seems that if the relaxation process does occur then it just merged perfectly with the expected vesicle distribution. In contrast, coalescence and/or expansion (as we observe in the spiny fragments) do not fit the curves (Fig. 4). In addition, we should expect that in crystal-poor fragments, due to melt relaxing and pathway closure, the clasts became almost impermeable after quenching, as revealed by some petrological experiments performed on crystal-poor basaltic magma (Lindoo et al., 2016). In contrast, in high crystalline magmas, the presence of micro-crystals increases viscosity, thus preserving the coalesced textures (see Moitra et al., 2013). The isolated vesicle-rich fragments of the 2014 PdF eruption are highly permeable and are characterized by variable ranges of porosity and numbers of vesicles (Figs. 4 and 6d) that seem more related to the pre-eruptive conditions than to the post-relaxation of low-viscosity melts. In the 2014 crystal-poor samples, the permeability increases rapidly once the percolation threshold has been reached, and efficient degassing prevents bubble volumes from expanding past the percolation threshold (Rust and Cashman, 2011).

In conclusion, the vesicles in the 2014 fragments do also partly reflect the shallow reservoir conditions and mostly the ascent degassing processes.

5.6 Integration between the physical and textural characteristics of the products and their geochemical signature: insight into the feeding system

According to Peltier et al. (2016), the June 2014 eruption emitted magma from a shallow pressurized source located only 1.4–1.7 km below the volcano summit. Coppola et al. (2017) suggest that the 2014 event was fed by a single shallow and small-volume magma pocket stored in the uppermost part of the PdF central plumbing system. All 2014 clasts show homogeneous and evolved bulk compositions, irrespective of their textural features. June 2014 products are among the most evolved products erupted since at least 1998 and are moderately evolved with respect to those emitted in 2010, just before the 2010–2014 quiescence. Bulk rock and MI data suggest that the 2014 evolved magma can be produced by crystal fractionation during the long-lasting (4.6 yr) storage and cooling of the magma injected and partly erupted in November 2009. The different types of scoria and pumice emitted in 2014 show significant variations in glass composition (Fig. 8b) due to variable degrees of microcrystallization. In theory, microcrysts can reflect late-stage (during magma ascent and post-fragmentation) crystallization. In this case, their variable amount within, for instance, the glassy and opaque parts of the spiny scoria might reflect slower ascent velocity or longer residence time in the system (e.g. Hammer et al., 1999; Stovall et al., 2012; Gurioli et al., 2014) also in agreement with the vesicle signature. However, the four typologies of clasts also differ in terms of mesocryst content (from rare to 5 vol. % for the golden and fluidal and 14–23 vol. % for the glassy spiny and spiny opaque). Equilibrium plagioclase–melt pairs record an almost constant and moderate dissolved water content, intermediate between that expected for melts sitting in the main shallow reservoir (located close to sea level) and the degassed matrix of lavas. Dissolved water contents are thus consistent with pre-eruptive magma water degassing during its storage at a shallow level, as suggested by geophysical data, and suggest that the plagioclase mesocrysts and some of the microcrysts in the spiny scoria and in the lava grew during magma storage (Fig. 10a). Melt composition records a potential pre-eruptive thermal gradient of $\sim 30\,^{\circ}\mathrm{C}$ between the hotter (pumice and fluidal) and the cooler (spiny) magma (Fig. 10b).

Tait et al. (1989) suggest that magma evolution can lead to oversaturation of volatile species within a shallow reservoir and trigger a volcanic eruption. At PdF, the golden and the fluidal clasts might represent the portion of magma located at the top of the shallow reservoir and enriched in bubbles of water-rich fluids, released by the cooler, more crystallized and more degassed "spiny lava" magma (Fig. 10b). The small volume of magma, its constant bulk composition and the very small inflation recorded prior to the eruption (Fig. 1d) could be consistent with an internal source of over-pressure related to volatile exsolution. Larger inflation rates over a broader area are expected when shallow reservoir pressurization is related to a new magma input from a deeper source. Slight baseline extensions both on distal and proximal sites suggest that magma transfer towards shallower crustal levels started shortly before (11 days) the final magma eruption. Geochemical data do not support the occurrence of a new magma input in the degassed and cooled 2014 reservoir. We can thus speculate that stress field change related to progressive deep magma transfer has promoted volatile exsolution, melt–crystal separation and melt expansion in the shallow reservoir. Textural heterogeneity of the 2014 products partly reflects a pre-eruptive physical gradient recorded by the variability in crystal and bubble contents in the shallow reservoir feeding this eruption. The golden and fluidal fragments are the bubble-richer and hotter portion of the melt. The spiny fragments are the degassed and cooler portion of the reservoir, whose progressive tapping led to a decrease in explosive intensity (from fountaining to Strombolian activity). Our results are also consistent with processes of mechanical reservoirs and/or dike stratification, as observed by Menand

and Phillips (2007). As explained earlier, magma ascent promoted syn-eruptive degassing-induced crystallization. The spiny opaque clasts can be considered as recycled material that fell back into the system. Accumulation of olivine crystals out of equilibrium with the host magma produces minor variations in mesocryst contents as observed within the same type of clasts sampled at different times and locations during the eruption, with the scoriae from the WF and early erupted lava being the ones with the lowest amount of olivine (Table S4 and Fig. 7b). Again, this temporal variation supports an increase in large heavy crystals within the most degassed magma emitted toward the end of activity, further suggesting that it corresponds to the lower part of the reservoir.

Our dataset permits us to propose that the 2014 eruption was fed by a physically zoned magma reservoir. The low-density crystal-poor, bubble-rich magma located in the upper part of the storage system ascended first rapidly and fed the early, more energetic phase, the Hawaiian fountaining. This low-density magma is not more evolved than the spiny one (same bulk compositions) and it is not necessarily richer in dissolved volatile amounts; it is just poorer in crystal and richer in bubbles. Second boiling, possibly triggered a few days before the eruption by stress field change, is responsible for the extraction of bubble-rich melt from a crystal-rich network. This last one will represent the main volume of the erupted lava. Fast ascent of the foam hinders its crystallization and preserves a high number of vesicles, high vesicularity and it is only a little modified by post-fragmentation expansion. Decrease in initial over-pressure translates into a progressive decrease in magma ascent rate and output rate (e.g. Coppola et al., 2017, and references therein). Nucleation of microcrysts is enhanced in melt ascending with lower speed and is mostly related to syn-eruptive degassing (for the spiny fragments). The larger volume (dense lava) corresponds to crystallized and less vesiculated magma, which experiences a slow ascent in the dike and even further microcrystallization during its subaerial emplacement.

Melt inclusion results allow us to confirm the involvement of a single and only slightly heterogeneous magma source in 2014, related to cooling and fractional crystallization of an older magma batch (November 2009). Interestingly, this latter short-lived summit eruption was also characterized by the same large textural range of pyroclastic products found in 2014 in spite of its more mafic composition.

This suggests that bubble accumulation and source pressurization is highly dependent on the shallow storage depth, which facilitates rapid water exsolution (Di Muro et al., 2016), and it is not necessarily the outcome of slow magma cooling and differentiation (Tait et al., 1989).

6 Proposed model for the 2014 eruption and conclusions

In this paper we show that textural and petrochemical study of the eruptive products can be used to characterize the ongoing activity at PdF and to constrain both the trigger and the evolution of short-lived and small-volume eruptions. This approach is extremely valuable in (i) understanding processes that lead to an eruption that was preceded by short-lived and elusive precursors and (ii) in reconstructing the time evolution of eruptive dynamics in an eruption with poor direct observations.

Following the sketch in Fig. 12, we infer that residual magma from the 2009 eruption ponding at shallow levels experienced long-lasting cooling and crystallization (Fig. 12a). Between 2010 and 2014 the volcano progressively deflated (Fig. 12b), possibly because of magma degassing and cooling, facilitated by the shallow depth of the reservoir. During this phase mesocrysts and some microcrysts formed (Figs. 4e and 10a).

The occurrence of deep (> 10 km b.s.l.) lateral magma transfer since March–April 2014 has been inferred by Boudoire et al. (2017) on the basis of deep (mantle level) seismic swarms and increase in soil CO_2 emissions on the distal western volcano flank. The incipit of magma transfer towards shallower crustal levels is potentially recorded by subtle volcano inflation about 11 days before the June 2014 eruptions (Figs. 1d and 12c). We suspect that these deep processes can have progressively modified the shallow crustal stress field and favoured magma vesiculation and melt–crystal separation. Second boiling could thus have over-pressured the shallowly seated reservoir and triggered magma ascent (Fig. 12c).

Without this deep magma transfer we believe that the small reservoir activated in 2014 would have cooled down completely to form an intrusion (as suggested by the pervasive crystallization of the lava, one of the densest emitted from 2014 to 2017; Harris et al., 2017). The 2014 event represented instead the first of a long series of eruptions, whose magmas became progressively less evolved in time (Coppola et al., 2017). In this scenario the trigger mechanisms of 2014 activity are both internal and external in the sense that the small shallow reservoir hosting cooled magma permitted the creation of the conditions favourable to a second boiling (Fig. 12c, and Tait et al., 1989). The second boiling was likely triggered by an almost undetectable stress field change and was favoured by the shallow storage pressure of the magma (Fig. 12c) that promoted fast water exsolution and rapid magma response to external triggers. The second boiling possibly contributed to the inflation registered 11 days before the eruption at 1.4–1.7 km (Fig. 12c) caused by both magma expansion and transfer of hot fluids to the hydrothermal system (Lénat et al., 2011).

Our data permit the exclusion of (i) new magma input and/or fluid inputs (CO_2-rich fluids) from deep magmatic

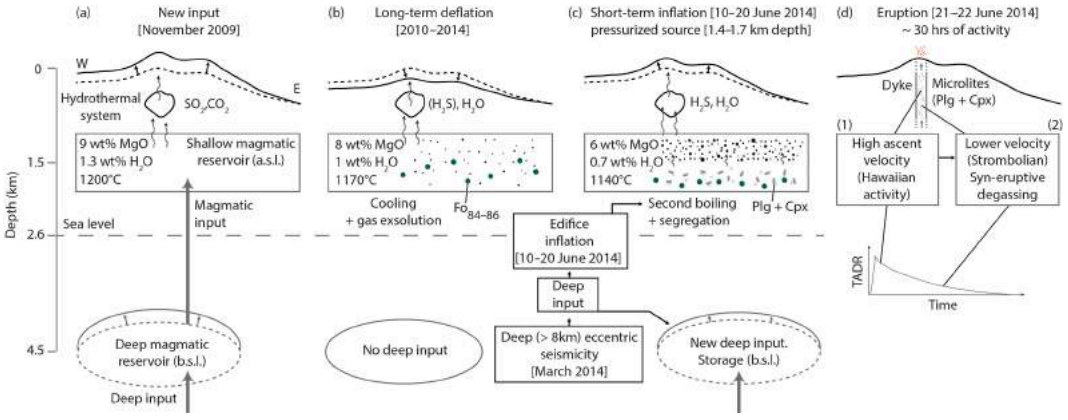

Figure 12. Schematic model of the evolution of the PdF volcanic system from the new deep magmatic input of November 2009 up to the June 2014 eruption. See explanation in the text.

levels to trigger the June 2014 eruption. We also exclude (ii) heating and enhanced convection of the shallow magma reservoir (due to heat diffusion without fluid or mass transfer) because this process is very slow. Furthermore, the 2014 minerals do not record evidence of magma heating. We can equally exclude (iii) deformation of the volcanic edifice and decompression of the magma reservoir and/or hydrothermal system due to flank sliding because geodetic data show no evidence of flank sliding able to produce stress change in the hydrothermal and magmatic system. Geophysical and geochemical data have permitted the tracking of vertical magma and fluid transfer below the volcano summit in April 2015, about 1 year after the early deep lateral magma transfer (Peltier et al., 2016). Deep processes are difficult to detect for any monitoring network.

We conclude that the over-pressure, caused by the second boiling, triggered the eruption. The occurrence of a hydrous, almost pure melt at shallow depth permitted its fast vesiculation upon ascent towards the surface. In turn, fast ascent of the foam (Fig. 12d) hindered its crystallization and preserved a high number of vesicles. Decrease in initial overpressure translated into a progressive decrease in magma ascent rate and output rate (e.g. Coppola et al., 2017, and references therein) and a temporal transition from Hawaiian activity to Strombolian activity (Fig. 12d). Nucleation of microcrysts was enhanced in melt ascending with lower speed and in turn this syn-eruptive crystallization favoured bubble connectivity and permeability in the ascending magma, even for magma at low vesicularity. The largest volume (dense lava) corresponds to highly crystallized and degassed magma already in the reservoir that experienced a slower ascent in the dike and even further micro-crystallization during its subaerial emplacement.

The texture of the products allowed us to follow the dynamic evolution of the system in space, from smooth fluidal scoriae emitted from a rapid jet of lava at the fractures, to a more stable activity at the MV, and in time. At the MV, in fact, we observed the transition from the golden and fluidal fragments emitted from Hawaiian fountaining, at the peak of the intensity of the eruption, to the spiny fragments, emitted from a declining Strombolian activity at the end of the eruption.

Therefore we here show for the first time that short-lived and weak Hawaiian fountaining and Strombolian events can preserve pyroclast textures that can be considered a valid approximation to shallow reservoir conditions and ascent degassing processes before the explosions and correlate to the eruptive dynamics as well.

To conclude, these results highlight the importance of petrological monitoring, which can provide complementary information regarding the ongoing volcanic activity to other geophysical and geochemical monitoring tools commonly used on volcanoes.

Data availability. The textural raw data and glass and bulk chemistry data are available at the DynVolc database (2017) https://doi.org/10.25519/DYNVOLC-Database, 2017. This is an open-access database. All the other data are reported in the Supplement.

The Supplement related to this article is available online at https://doi.org/10.5194/se-9-431-2018-supplement.

Competing interests. The authors declare that they have no conflict of interest.

Acknowledgements. We thank the OVPF team and T. Lecocq for monitoring and fieldwork. F. van Wyk de Vries provided an English revision for a previous version of the paper. We thank the STRAP project funded by the Agence Nationale de la Recherche (ANR-14-CE03-0004-04). This research was financed

by the French Government Laboratory of Excellence initiative no. ANR-10-LABX-0006, the Région Auvergne and the European Regional Development Fund. This is Laboratory of Excellence Clervolc contribution number 288.

Edited by: Michael Heap
Reviewed by: Amanda Lindoo, Madison Myers, and one anonymous referee

References

Albarède, F. and Tamagnan, V.: Modelling the recent geochemical evolution of the Piton de la Fournaise volcano, Réunion island, 1931–1986, J. Petrol., 29, 997–1030, 1988.

Albarède, F., Luais, B., Fitton, G., Semet, M. P., Kaminski, E., Upton, B. G. J, Bachèlery, P., and Cheminée, J. L.: The geochemical regimes of Piton de la Fournaise Volcano Réunion. during the last 530,000 years, J. Petrol., 38, 171–201, 1997.

Andronico, D., Lo Castro, M. D., Sciotto, M., and Spina, L.: The 2010 ash emissions at the summit craters of Mt Etna: relationship with seismo-acoustic signals, J. Geophys. Res., 118, 51–70, https://doi.org/10.1029/2012JB009895, 2013a.

Andronico, D., Taddeucci, J., Cristaldi, A., Miraglia, L., Scarlato, P., and Gaeta, M.: The 15 March 2007 paroxysm of Stromboli: video-image analysis, and textural and compositional features of the erupted deposit, Bull. Volcanol., 75, 733, https://doi.org/10.1007/s00445-013-0733-2, 2013b.

Andronico, D., Scollo, S., Lo Castro, M. D., Cristaldi, A., Lodato, L., and Taddeucci, J.: Eruption dynamics and tephra dispersal from the 24 November 2006 paroxysm at South-East Crater, Mt Etna, Italy, J. Volcanol. Geotherm. Res., 274, 78–91, https://doi.org/10.1016/j.jvolgeores.2014.01.009, 2014.

Bachèlery, P., Lénat, J. F., Di Muro, A., and Michon, L.: Active Volcanoes of the Southwest Indian Ocean: Piton de la Fournaise and Karthala. Active Volcanoes of the World, Springer-Verlag, Berlin and Heidelberg, 1–428, https://doi.org/10.1007/978-3-642-31395-0_12, 2016.

Boivin, P. and Bachèlery, P.: Petrology of 1977 to 1998 eruptions of Piton de la Fournaise, La Réunion Island, J. Volcanol. Geotherm. Res., 184, 109–125, 2009.

Bombrun, M., Harris, A., Gurioli, L., Battaglia, J., and Barra, V.: Anatomy of a strombolian eruption: inferences from particle data recorded with thermal video, J. Geophys. Res., 120, 2367–2387, https://doi.org/10.1002/2014JB011556, 2015.

Boudoire, G., Liuzzo, M., Di Muro, A., Ferrazzini, V., Michon, L., Grassa, F., Derrien, A., Villeneuve, N., Bourdeu, A., Brunet, C., Giudice, G., and Gurrieri, S.: Investigating the deepest part of a volcano plumbing system: evidence for an active magma path below the western flank of Piton de la Fournaise (La Réunion Island), J. Volcanol. Geotherm. Res., 341, 193–207, https://doi.org/10.1016/j.jvolgeores.2017.05.026, 2017.

Brenguier, F., Kowalski, P., Staudacher, T., Ferrazzini, V., Lauret, F., Boissier, P., Lemarchand, A., Pequegnat, C., Meric, O., Pardo, C., Peltier, A., Tait, S., Shapiro, N. M., Campillo, M., and Di Muro, A.: First Results from the UnderVolc High Resolution Seismic and GPS network deployed on Piton de la Fournaise Volcano, Seismo. Res. Lett., 83, 97–102, https://doi.org/10.1785/gssrl.83.1.97, 2012.

Brugier, Y. A.: Magmatologie du Piton de la Fournaise (Ile de la Réunion): approche volcanologique, pétrologique et expérimentale, Sciences de la Terre, Université d'Orléans, NNT: 2016ORLE2007, 251 pp., 2016.

Bureau, H., Pineau, F., Métrich, N., Semet, P. M., and Javoy, M.: A melt and fluid inclusion study of the gas phase at Piton de la Fournaise volcano (Reunion Island), Chem. Geol., 147, 115–130, 1998a.

Bureau, H., Métrich, N., Pineau, F., and Semet, M. P.: Magma-conduit interaction at Piton de la Fournaise volcano (Réunion Island): a melt and fluid inclusion study, J. Volcanol. Geotherm. Res., 84, 39–60, 1998b.

Carey, R. J., Manga, M., Degruyter, W., Swanson, D., Houghton, B., Orr, T., and Patrick, M.: Externally triggered renewed bubble nucleation in basaltic magma: the 12 October 2008 eruption at Halema'uma'u Overlook vent, Kīlauea, Hawai'i, USA, J. Geophys. Res., 117, B11202, https://doi.org/10.1029/2012JB009496, 2012.

Carey, R. J., Manga, M., Degruyter, W., Gonnermann, H., Swanson, D., Houghton, B., Orr, T., and Patrick, M.: Convection in a volcanic conduit recorded by bubbles, Geology, 41, 395–398, 2013.

Cashman, K. V. and Mangan, M. T.: Physical aspects of magmatic degassing II: constraints on vesiculation processes from textural studies of eruptive products, in: Volatiles in magmas, edited by: Carroll, M. R. and Holloway, J. R., Reviews in mineralogy, Miner. Soc. Am., Fredricksberg, 447–478, 1994.

Clocchiatti, R., Havette, A., and Nativel, P.: Relations pétrogénétiques entre les basaltes transitionnels et les océanites du Piton de la Fournaise (Ile de La Réunion, océan Indien) à partir e la composition chimique des inclusions vitreuses des olivines et des spinelles, Bull. Minér., 102, 511–525, 1979.

Colombier, M., Gurioli, L., Druitt, T. H., Shea, T., Boivin, P., Miallier, D., and Cluzel, N.: Textural evolution of magma during the 9.4-ka trachytic explosive eruption at Kilian Volcano, Chaîne des Puys, France, Bull. Volcanol., 79, 1–24, https://doi.org/10.1007/s00445-017-1099-7, 2017a.

Colombier, M., Wadsworth, F. B., Gurioli, L., Scheu, B., Kueppers, U., Di Muro, A., and Dingwel, D. B.: The evolution of pore connectivity in volcanic rocks, Earth Planet. Sci. Lett., 462, 99–109, https://doi.org/10.1016/j.epsl.2017.01.011, 2017b.

Colò, L., Ripepe, M., Baker, D. R., and Polacci, M.: Magma vesiculation and infrasonic activity at Stromboli open conduit volcano, Earth Planet. Sci. Lett., 292, 274–280, 2010.

Coppola, D., Villeneuve, N., Di Muro, A., Ferrazzini, V., Peltier, A., Favalli, M., Bachèlery, P., Gurioli, L., Harris, A., Moune, S., Vlastélic, I., Galle, B., Arellano, S., and Aiuppa, A.: A Shallow system rejuvenation and magma discharge trends at Piton de la Fournaise volcano (La Réunion Island), Earth Planet. Sci. Lett., 463, 13–24, 2017.

Corsaro, R. and Miraglia, L.: The transition from summit to flank activity at Mt. Etna, Sicily (Italy): Inferences from the petrology of products erupted in 2007–2009, J. Volcanol. Geother. Res., 275, 51–60, 2014.

Di Muro, A., Métrich, N., Vergani, D., Rosi, M., Armienti, P., Fougeroux, T., Deloule, E., Arienzo, I., and Civetta, L.: The shallow plumbing system of Piton de la Fournaise Volcano (La Réunion Island, Indian Ocean) revealed by the major 2007 caldera forming eruption, J. Petrol., 55, 1287–1315, 2014.

Di Muro, A., Staudacher, T., Ferrazzini, V., Métrich, N., Besson, P., Garofalo, C., and Villemant, B.: Shallow magma storage at Piton de la Fournaise volcano after 2007 summit caldera collapse tracked in Pele's hairs, chap 9 of Carey, R. J., edited by: Cayol, V., Poland, M. P., and Weis, D., Hawaiian Volcanoes: From Source to Surface, American Geophysical Union Monograph, 208, 189–212, https://doi.org/10.1002/9781118872079.ch9, 2015.

Di Muro, A., Métrich, N., Allard, P., Aiuppa, A., Burton, M., Galle, B., and Staudacher, T.: Magma degassing at Piton de la Fournaise volcano, Active Volcanoes of the World, series, Springer, edited by: Bachelery, P., Lenat, J. F., Di Muro, A., and Michon, L., 203–222, 2016.

DYNVOLC Database: Observatoire de Physique du Globe de Clermont-Ferrand, Aubière, France, available at: https://doi.org/10.25519/DYNVOLC-Database, 2017.

Eychenne, J., Houghton, B. F., Swanson, D. A., Carey, R. J., and Swavely, L.: Dynamics of an open basaltic magma system: the 2008 activity of the Halema'uma'u Overlook vent, Kīlauea Caldera, Earth Planet. Sci. Lett., 409, 49–60, 2015.

Famin, V., Welsch, B., Okumura, S., Bachèlery, P., and Nakashima, S.: Three differentiation stages of a single magma at Piton de la Fournaise (Réunion hotspot), Geochem. Geophys. Geosyst., 10, Q01007, https://doi.org/10.1029/2008GC002015, 2009.

Fisk, M. R., Upton, B. G. J., Ford, C. E., and White, W. M.: Geochemical and experimental study of the genesis of magmas of Reunion island, Indian Ocean, J. Geophys. Res., 93, 4933–4950, 1988.

Formenti, Y. and Druitt, T. H.:, Vesicle connectivity in pyroclasts and implications for the fluidisation of fountain-collapse pyroclastic flows, Montserrat (West Indies), Earth Planet. Sci. Lett., 214, 561–574, 2003.

Gardner, J. E., Thomas, R. M. E., Jaupart, C., and Tait, S.: Fragmentation of magma during Plinian volcanic eruptions, Bull. Volcanol., 58, 144–162, 1996.

Giachetti, T., Druitt, T. H., Burgisser, A., Arbaret, L., and Galven, C.: Bubble nucleation and growth during the 1997 Vulcanian explosions of Soufrière Hills Volcano, Montserrat, J. Volcanol. Geotherm. Res., 193, 215–231, https://doi.org/10.1016/j.jvolgeores.2010.04.001, 2010.

Gonnermann, H. M. and Manga, M.: Dynamics of magma ascent in the volcanic conduit, in: Modeling Volcanic Processes: The Physics and Mathematics of Volcanism, edited by: Fagents, S. A., Gregg, T. K. P., and Lopes, R. M. C., Cambridge University Press, Cambridge, 2013.

Gurioli, L., Harris, A. J. L., Houghton, B. F., Polacci, M., and Ripepe, M.: Textural and geophysical characterization of explosive basaltic activity at Villarrica volcano, J. Geophys. Res., 113, B08206, https://doi.org/10.1029/2007JB005328, 2008.

Gurioli, L., Harris, A. J. L., Colo, L., Bernard, J., Favalli, M., Ripepe, M., and Andronico, D.: Classification, landing distribution and associated flight parameters for a bomb field emplaced during a single major explosion at Stromboli, Italy, Geology, 41, 559–562, https://doi.org/10.1130/G33967.1, 2013.

Gurioli, L., Colo', L., Bollasina, A. J., Harris, A. J. L., Whittington, A., and Ripepe, M.: Dynamics of strombolian explosions: inferences from inferences from field and laboratory studies of erupted bombs from Stromboli volcano, J. Geophys. Res., 119, 319–345, https://doi.org/10.1002/2013JB010355, 2014.

Gurioli, L., Andronico, D., Bachelery, P., Balcone-Boissard, H., Battaglia, J., Boudon, G., Burgisser, A.,Burton, S. B. M. R., Cashman, K., Cichy, S., Cioni, R., Di Muro, A., Dominguez, L., D'Oriano, C., Druitt, T., Harris, A. J. L., Hort, M., Kelfoun, K., Komorowski, J. C., Kueppers, U., Le Pennec, J. L., Menand, T., Paris, R., Pioli, L., Pistolesi, M., Polacci, M., Pompilio, M., Ripepe, M., Roche, O., Rose-Koga, E., Rust, A., Scharff, L., Schiavi, F., Sulpizio, R., Taddeucci, J., and Thordarson, T.: MeMoVolc consensual document: a review of cross-disciplinary approaches to characterizing small explosive magmatic eruptions, Bull. Volcanol., 77, 49, https://doi.org/10.1007/s00445-015-0935-x, 2015.

Hammer, J. E., Cashman, K. V., Hoblitt, R. P., and Newman, S.: Degassing and microlite crystallization during pre-climactic events of the 1991 eruption of Mt. Pinatubo, Philippines, Bull. Volcanol., 60, 355–380, 1999.

Harris, A. J. L., Villeneuve, N., Di Muro, A., Ferrazzini, V., Peltier, A., Coppola, D., Favalli, M., Bachèlery, P., Foger, J.-L., Gurioli, L., Moune, S., Vlastélic, I., Galle, B., and Arellano, S.: Effusive Crises at Piton de la Fournaise 2014–2015: A Review of a Multi-National Response Model, Appl. Volcanol., 6, 1–29, https://doi.org/10.1186/s13617-017-0062-9, 2017.

Helz, R. T. and Thornber, C. R.: Geothermometry of Kilauea Iki lava lake, Hawaii, Bull. Volcanol., 49, 651–668, 1987.

Hibert, C., Mangeney, A., Polacci, M., Di Muro, A., Vergniolle, S., Ferrazzini, V., Taisne, B., Burton, M., Dewez, T., Grandjean, G., Dupont, A., Staudacher, T., Brenguier, F., Shapiro, N. M., Kowalski, P., Boissier, P., Catherine, P., and Lauret, F.: Multidisciplinary monitoring of the January 2010 eruption of Piton de la Fournaise volcano, La Réunion island, J. Geophys. Res., 120, 3026–3047, 2015.

Higgins, M.-D.: Measurement of crystal size distributions, Am. Mineral., 85, 1105–1116, 2000.

Houghton, B. F. and Wilson, C. J. N.: A vesicularity index for pyroclastic deposits, Bull. Volcanol., 51, 451–462, https://doi.org/10.1007/BF01078811, 1989.

Houghton, B. F., Swanson, D. A., Carey, R. J., Rausch, J., and Sutton, A. J.: Pigeonholing pyroclasts, insights from the 19 March 2008 explosive eruption of Kīlauea volcano, Geology, 39, 263–266, https://doi.org/10.1130/G31509.1, 2011.

Houghton, B. F., Swanson, D. A., Rausch, J., Carey, R. J., Fagents, S. A., and Orr, T. R.: Pushing the volcanic explosivity index to its limit and beyond: constraints from exceptionally weak explosive eruptions at Kılauea in 2008, Geology, 41, 627–630, 2013.

Houghton, B. F., Taddeucci, J., Andronico, D., Gonnermann, H. M., Pistolesi, M., Patrick, M. R., Orr, T. R., Swanson, D. A., Edmonds, M., Gaudin, D., Carey, R. J., and Scarlato, P.: Stronger or longer: Discriminating between Hawaiian and Strombolian eruption styles, Geology, 44, 163–166, https://doi.org/10.1130/G37423.1, 2016.

Inman, D. L.: Measures for describing the size distribution of sediments, J. Sed. Petrol., 22, 125–145, 1952.

Jordan, S. C., Le Pennec, J.-L., Gurioli, L., Roche, O., and Boivin, P.: Highly explosive eruption of the monogenetic 8.6 ka BP La Vache et Lassolas scoria cone complex (Chaîne des Puys, France), J. Volcanol. Geotherm. Res., 313, 15–28, 2016.

Kahl, M., Chakraborty, S., Pompilio, M., and Costa, F.: Constraints on the nature and evolution of the magma plumbing system of Mt. Etna Volcano (1991–2008) from a com-

bined thermodynamic and kinetic modelling of the compositional record of minerals, J. Petrol., 56, 2025–2068, https://doi.org/10.1093/petrology/egv063, 2015.

Kawabata, E., Cronin, S. J., Bebbington, M. S., Moufti, M. R. H., El-Masry, N., and Wang, T.: Identifying multiple eruption phases from a compound tephra blanket: an example of the AD1256 Al-Madinah eruption, Saudi Arabia, Bull. Volcanol., 77, 6, https://doi.org/10.1007/s00445-014-0890-y, 2015.

Lange, R. A., Frey, H. M., and Hector, J.: A thermodynamic model for the plagioclase-liquid hygrometer/thermometer, Am. Mineral., 94, 494–506, 2009.

Lautze, N., Taddeucci, J., Andronico, D., Cannata, C., Tornetta, L., Scarlato, P., Houghton, B., and Lo Castro, D.: SEM-based methods for the analysis of basaltic ash from weak explosive activity at Etna in 2006 and the 2007 eruptive crisis at Stromboli, Phys. Chem. Earth, 45, 113–127, https://doi.org/10.1016/j.pce.2011.02.001, 2012.

Leduc, L., Gurioli, L., Harris, A. J. L., Colo', L., and Rose-Koga, E.: Types and mechanisms of strombolian explosions: characterization of a gas-dominated explosion at Stromboli, Bull. Volcanol., 77, 8, https://doi.org/10.1007/s00445-014-0888-5, 2015.

Lénat, J.-F., Bachèlery, P., and Peltier, A.: The interplay between collapse structures, hydrothermal systems and magma intrusions: the case of the central area of Piton de la Fournaise volcano, Bull. Volc., 74, 407–421, https://doi.org/10.1007/s00445-011-0535-3, 2011.

Lénat, E. F., Bachelery, P. B., and Merle, O.: Anatomy of Piton de la Fournaise volcano (La Réunion, Indian Ocean), Bull. Volcanol., 74, 1945–1961, 2012.

Lengliné, O., Duputel, Z., and Ferrazzini, V.: Uncovering the hidden signature of a magmatic recharge at Piton de la Fournaise volcano using small earthquakes, Geophys. Res. Lett., 43, 4255–4262, https://doi.org/10.1002/2016GL068383, 2016.

Lindoo, A., Larsen, J. F., Cashman, K. V., Dunn, A. L., and Neill, O. K.: An experimental study of permeability development as a function of crystal-free melt viscosity, Earth Planet. Sci. Lett., 435, 45–54, https://doi.org/10.1016/j.epsl.2015.11.035, 2016.

Lindoo, A., Larsen, J. F., Cashman, K. V., and Oppenheimer, J.: Crystal controls on permeability development and degassing in basaltic andesite magma, Geology, 45, 831–834, 2017.

Liuzzo, M., Di Muro, A., Giudice, G., Michon, L., Ferrazzini, V., and Gurrieri, S.: New evidence of CO_2 degassing anomalies on the Piton de la Fournaise volcano and the link with volcano tectonic structures, Geochem. Geophys. Geosyst., 16, 4388–4404, https://doi.org/10.1002/2015GC006032, 2015.

Mangan, M. T. and Cashman, K. V.: The structure of basaltic scoria and reticulite and inferences for vesiculation, foam formation, and fragmentation in lava fountains, J. Volcanol. Geotherm. Res., 73, 1–18, 1996.

Menand, T. and Phillips, J. C.: Gas segregation in dykes and sills, J. Volcanol. Geother. Res., 159, 393–408, https://doi.org/10.1016/j.jvolgeores.2006.08.003, 2007.

Michon, L., Di Muro, A., Villeneuve, N., Saint-Marc, C., Fadda, P., and Manta, F.: Explosive activity of the summit cone of Piton de la Fournaise volcano (La Réunion Island): a historical and geological review, J. Volcanol. Geotherm. Res., 263, 117–133, 2013.

Moitra, P., Gonnermann, H. M., Houghton, B. F., and Giachetti, T.: Relating vesicle shapes in pyroclasts to eruption styles, Bull. Volcanol., 75, 691, https://doi.org/10.1007/s00445-013-0691-8, 2013.

Morgan D. J. and Jerram, D. A.: On estimating crystal shape for crystal size distribution analysis, J. Volc. Geotherm. Res., 154, 1–7, 2006.

Moune, S., Sigmarsson, O., Schiano, P., Thordarson, T., and Keiding, J. K.: Melt inclusion constraints on the magma source of Eyjafjallajökull 2010 flank eruption, J. Geophys. Res., 117, B00C07, https://doi.org/10.1029/2011jb008718, 2012.

Morandi, A., Principe, C., Di Muro, A., Leroi, G., Michon, L., and Bachèlery, P.: Pre-historic explosive activity at Piton de la Fournaise volcano, edited by: Bachèlery, P., Lénat, J. F., Di Muro, A., and Michon, L., in: Active Volcanoes of the Southwest Indian Ocean: Piton de la Fournaise and Karthala. Active Volcanoes of the World, Springer-Verlag, Berlin and Heidelberg, 107–138, 2016

Óladóttir, B., Sigmarsson, O., Larsen, G., and Devidal, J.-L.: Provenance of basaltic tephra from Vatnajökull subglacial volcanoes, Iceland, as determined by major- and trace-element analyses, Holocene, 21, 1037–1048, https://doi.org/10.1177/0959683611400456, 2011.

Oppenheimer, J., Rust, A. C., Cashman, K. V., and Sandnes, B.: Gas migration regimes and outgassing in particle-rich suspensions, Front. Phys., 3, 1–13, https://doi.org/10.3389/fphy.2015.00060, 2015.

Ort, M. H., Di Muro, A., Michon, L., and Bachèlery, P.: Explosive eruptions from the interaction of magmatic and hydrothermal systems during flank extension: the Bellecombe Tephra of Piton de La Fournaise (La Réunion Island), Bull. Volcanol., 78, 5, https://doi.org/10.1007/s00445-015-0998-8, 2016.

Papale, P., Moretti, R., and Barbato, D.: The compositional dependence of the saturation surface of H_2O + CO_2 fluids in silicate melts, Chem. Geol., 229, 78–95, https://doi.org/10.1016/j.chemgeo.2006.01.013, 2006.

Parcheta, C. E., Houghton, B. F., and Swanson, D. A.: Contrasting patterns of vesiculation in low, intermediate, and high Hawaiian fountains: a case study of the 1969 Mauna Ulu eruption, J. Volcanol. Geotherm. Res., 255, 79–89, 2013.

Peltier, A., Bachèlery, P., and Staudacher, T.: Magma transport and storage at Piton de la Fournaise (La Réunion) between 1972 and 2007: A review of geophysical and geochemical data, J. Volcanol. Geotherm. Res., 184, 93–108, 2009.

Peltier, A., Beauducel, F., Villeneuve, N., Ferrazzini, V., Di Muro, A., Aiuppa, A., Derrien, A., Jourde, K., and Taisne, B.: Deep fluid transfer evidenced by surface deformation during the 2014–2015 unrest at Piton de la Fournaise volcano, J. Volcanol. Geotherm. Res., 321, 140–148, https://doi.org/10.1016/j.jvolgeores.2016.04.031, 2016.

Polacci, M., Corsaro, R., and Andronico, D.: Coupled textural and compositional characterization of basaltic scoria: insights into the transition from Strombolian to fire fountain activity at Mount Etna, Italy, Geology, 34, 201–204, https://doi.org/10.1130/G22318.1, 2006.

Polacci, M., Bouvet de Maisonneuve, C., Giordano, D., Piochi, M., Mancini, L., Degruyter, W., and Bachmanng, O.: Permeability measurements of Campi Flegrei pyroclastic products: an example from the Campanian Ignimbrite and Monte Nuovo eruptions, J. Volcanol. Geotherm. Res., 272, 16–22, 2014.

Putirka, K. D.: Thermometers and barometers for volcanic systems, Rev. Mineral. Geochem., 69, 61–120, 2008.

Roeder, P., Gofton, E., and Thornber, C.: Cotectic proportions of olivine and spinel in olivine-tholeiitic basalt and evaluation of pre-eruptive processes, J. Petrol., 47, 883–900, 2006.

Roult, G., Peltier, A., Staudacher, T., Ferrazzini, V., Taisne, B., Di Muro, A., and The OVPF Team: A comprehensive classification of the Piton de la Fournaise eruptions (La Réunion Island) spanning the 1986–2010 period. Search for eruption precursors from the broad-band GEOSCOPE RER station analysis and interpretation in terms of volcanic processes, J. Volcanol. Geotherm. Res., 241, 78–104, 2012.

Rust, A. C. and Cashman, K. V.: Permeability controls on expansion and size distributions of pyroclasts, J. Geophys. Res., 116, B11202, https://doi.org/10.1029/2011JB008494, 2011.

Saar, M. O., Manga, M., Cashman, K. V., and Fremouw, S.: Numerical models of the onset of yield strength in crystal-melt suspensions, Earth Planet. Sci. Lett., 187, 367–379, https://doi.org/10.1016/S0012-821X(01)00289-8, 2001.

Salaün, A., Villemant, B., Semet, M. P., and Staudacher, T.: Cannibalism of olivine-rich cumulate xenoliths during the 1998 eruption of Piton de la Fournaise (La Réunion hotspot): Implications for the generation of magma diversity, J. Volcanol. Geother. Res., 198, 187–204, 2010.

Schiano, P., David, K., Vlastélic, I., Gannoun, A., Klein, M., Nauret, F., and Bonnand, P.: Osmium isotope systematics of historical lavas from Piton de la Fournaise (Réunion Island, Indian Ocean), Contrib. Mineral. Petrol., 162, 995–1009, https://doi.org/10.1007/s00410-012-0774-0, 2012.

Shea, T.: Bubble nucleation in magmas: a dominantly heterogeneous process?, J. Volcanol. Geotherm. Res., 343, 155–170, 2017.

Shea, T., Houghton, B. F., Gurioli, L., Cashman, K. V., Hammer, J. E., and Hobden, B.: Textural studies of vesicles in volcanic rocks: an integrated methodology, J. Volcanol. Geotherm. Res., 190, 271–289, 2010.

Shea, T., Gurioli, L., and Houghton, B. F.: Transitions between fall phases and pyroclastic density currents during the AD 79 eruption at Vesuvius: building a transient conduit model from the textural and volatile record, Bull. Volcanol., 74, 2363–2381, https://doi.org/10.1007/s00445-012-0668-z, 2012.

Sparks, R. S. J.: The dynamics of bubble formation and growth in magmas: a review and analysis, J. Volcanol. Geotherm. Res., 3, 1–37, 1978.

Sparks, R. S. J.: Forecasting volcanic eruptions, Earth Planet. Sci. Lett., 210, 1–15, 2003.

Spina, L., Cimarelli, C., Scheu, B., Di Genova, D., and Dingwell, D. B.: On the slow decompressive response of volatile- and crystal-bearing magmas: An analogue experimental investigation, Earth Planet. Sci. Lett., 433, 44–53, 2016.

Staudacher, T. and Peltier, A.: Ground deformation at Piton de la Fournaise (La Réunion Island), a review from 20 years of GNSS monitoring, edited by: Bachèlery, P., Lénat, J. F., Di Muro, A., and Michon, L., in: Active volcanoes of the Southwest Indian Ocean: Piton de la Fournaise and Karthala. Active volcanoes of the world, Springer, Berlin, 139–170, https://doi.org/10.1007/978-3-642-31395-0_9, 2015.

Staudacher, T., Ferrazzini, V., Peltier, A., Kowalski, P., Boissier, P., Catherine, P., Lauret, F., and Massin, F.: The April 2007 eruption and the Dolomieu crater collapse, two major events at Piton de la Fournaise (La Réunion Island, Indian Ocean), J. Volcanol. Geother. Res., 184, 126–137, https://doi.org/10.1016/j.jvolgeores.2008.11.005, 2009.

Stovall, W. K., Houghton, B. F., Gonnermann, H. M., Fagents, S. A., and Swanson, D. A.: Eruption dynamics of Hawaiian-style fountains: the case study of episode 1 of the Kīlauea Iki 1959 eruption, Bull. Volcanol., 73, 511–529. https://doi.org/10.1007/s00445-010-0426-z, 2011.

Stovall, W. K., Houghton, B. F., Hammer, J. E., Fagents, S. A., and Swanson, D. A.: Vesiculation of high fountaining Hawaiian eruptions: episodes 15 and 16 of 1959 Kīlauea Iki, Bull. Volcanol., 74, 441–455, https://doi.org/10.1007/s00445-011-0531-7, 2012.

Swanson, D. A., Wooten, K., and Orr, T.: Buckets of ash track tephra flux from Halema'uma'u crater, Hawai'i, Eos Trans. AGU, 90, 427–428, https://doi.org/10.1029/2009EO460003, 2009.

Taddeucci, J., Pompilio, M., and Scarlato, P.: Monitoring the explosive activity of the July–August 2001 eruption of Mt. Etna (Italy) by ash characterization, Geophys. Res. Lett., 29, 1029–1032, https://doi.org/10.1029/2001GL014372, 2002.

Tait, S., Jaupart, C., and Vergniolle, S.: Pressure, gas content and eruption periodicity of a shallow, crystallising magma chamber, Earth Planet. Sci. Lett., 92, 107–123, 1989.

Takeuchi, S., Nakashima, S., and Akihiko Tomiya, A.: Permeability measurements of natural and experimental volcanic materials with a simple permeameter: toward an understanding of magmatic degassing processes, J. Volcanol. Geotherm. Res., 177, 329–339, 2008.

Thordarson, T., Self, S., Óskarsson, N., and Hulsebosch, T.: Sulfur, chlorine and fluorine degassing and atmospheric loading by the 1783–1784 AD Laki (Skaftár Fires) eruption in Iceland, Bull. Volcanol., 58, 205–225, 1996.

Thornber, C. R., Hon, K., Heliker, C., and Sherrod, D. A.: A Compilation of Whole-Rock and Glass Major-Element geochemistry of Kīlauea Volcano, Hawai'i, near-vent eruptive products: January 1983 through September 2001: U.S.G.S. Open File Report, 03-477, 2003.

Villemant, B., Salaün, A., and Staudacher, T.: Evidence for a homogeneous primary magma at Piton de la Fournaise (La Réunion): A geochemical study of matrix glass, melt inclusions and Pélé's hairs of the 1998–2008 eruptive activity, J. Volcanol. Geotherm. Res., 184, 79–92, 2009.

Vlastélic, I. and Pietruszka, A. J.: A review of the recent geochemical evolution of Piton de la Fournaise Volcano (1927–2010), edited by: Bachèlery, P., Lénat, J. F., Di Muro, A., and Michon, L., Active Volcanoes of the Southwest Indian Ocean, in: Active Volcanoes of the World, 185–201, 2016.

Vlastélic, I., Peltier, A., and Staudacher, T.: Short-term (1998-2006) fluctuations of Pb isotopes at Piton de la Fournaise volcano (Réunion Island): origins and constraints on the size and shape of the magma reservoir, Chem. Geol., 244, 202–220, 2007.

Vlastélic, I., Deniel, C., Bosq, C., Telouk, P., Boivin, P., Bachèlery, P., Famin, V., and Staudacher, T.: Pb isotope geochemistry of Piton de la Fournaise historical lavas, J. Volcanol. Geother. Res., 184, 63–78, 2009.

Vlastélic, I., Staudacher, T., Bachèlery, P., Télouk, P., Neuville, D., and Benbakkar, M.: Lithium isotope fractionation during magma degassing: constraints from silicic differentiates and natural gas

condensates from Piton de la Fournaise volcano (Réunion Island), Chem. Geol., 284, 26–34, 2011.

Vlastélic, I., Menard, G., Gannoun, M., Piro, J.-L., Staudacher, T., and Famin, V.: Magma degassing during the April 2007 collapse of Piton de la Fournaise: the record of semi-volatile trace elements (Li, B, Cu, In, Sn, Cd, Re, Tl, Bi), J. Volcanol. Geother. Res., 254, 94–107, 2013.

Vlastélic, I., Staudacher, T., and Semet, M.: Rapid change of lava composition from 1998 to 2002 at Piton de la Fournaise (Réunion) inferred from Pb isotopes and trace elements: evidence for variable crustal contamination, J. Petrol., 46, 79–107, 2005.

Welsch, B., Faure, F., Bachèlery, P., and Famin, V.: Microcrysts record transient convection at Piton de la Fournaise volcano (La Réunion Hotspot), J. Petrol., 50, 2287–2305, 2009.

Welsch, B., Famin, V., Baronnet, A., and Bachèlery, P.: Dendritic crystallization: a single process for all textures of olivine in basalts?, J. Petrol., 54, 539–574, 2013.

White, J. D. L. and Houghton, B. F.: Primary volcaniclastic rocks, Geology, 34, 677–680, https://doi.org/10.1130/G22346.1, 2006.

ANNALS OF GEOPHYSICS, 62, 2, VO30, 2019; doi: 10.4401/ag-7972

“VALIDATION OF AN INTEGRATED SATELLITE-DATA-DRIVEN RESPONSE TO AN EFFUSIVE CRISIS: THE APRIL-MAY 2018 ERUPTION OF PITON DE LA FOURNAISE”

Andrew J.L. Harris*[,1], Magdalena Oryaëlle Chevrel[1], Diego Coppola[2], Michael S. Ramsey[3], Alexis Hrysiewicz[1], Simon Thivet[1], Nicolas Villeneuve[4], Massimiliano Favalli[5], Aline Peltier[6], Philippe Kowalski[6], Andrea Di Muro[6], Jean-Luc Froger[1], Lucia Gurioli[1]

(1) Université Clermont Auvergne, CNRS, OPGC, Laboratoire Magmas et Volcans, Clermont-Ferrand, France
(2) Dipartimento di Scienze della Terra, Università degli Studi di Torino, Torino, Italy
(3) Department of Geology and Planetary Science, University of Pittsburgh, Pittsburgh, PA, USA
(4) Laboratoire GéoSciences Réunion, Université de La Réunion, Institut de Physique du Globe de Paris, Sorbonne Paris Cité, CNRS, Saint Denis, France
(5) Istituto Nazionale di Geofisica e Vulcanologia (INGV), Pisa, Italy
(6) Observatoire Volcanologique du Piton de la Fournaise (OVPF), Institut de Physique du Globe de Paris, Sorbonne Paris Cité, Univ. Paris Diderot, CNRS, La Réunion, France

Article history
Receveid **October 11, 2018**; accepted **January 24, 2019.**
Subject classification:
xxxxxx

ABSTRACT

Satellite-based surveillance of volcanic hot spots and plumes can be coupled with modeling to allow ensemble-based approaches to crisis response. We complete benchmark tests on an effusive crisis response protocol aimed at delivering product for use in tracking lava flows. The response involves integration of four models: MIROVA for discharge rate (TADR), the ASTER urgent response protocol for delivery of high-spatial resolution satellite data, DOWNFLOW for flow path projections, and PyFLOWGO for flow run-out. We test the protocol using the data feed available during Piton de la Fournaise's April-May 2018 eruption, with product being delivered to the Observatoire du Piton de la Fournaise via Google Drive. The response was initialized by an alert at 19:50Z on 27 April 2018. Initially DOWNFLOW-FLOWGO were run using TADRs typical of Piton de la Fournaise, and revealed that flow at >120 m^3/s could reach the island belt road. The first TADR (10-20 m^3/s) was available at 09:55Z on 28 April, and gave flow run-outs of 1180-2510 m. The latency between satellite overpass and TADR provision was 105 minutes, with the model result being posted 15 minutes later. An InSAR image pair was completed six hours after the eruption began, and gave a flow length of 1.8 km; validating the run-out projection. Thereafter, run-outs were updated with each new TADR, and checked against flow lengths reported from InSAR and ASTER mapping. In all, 35 TADRs and 15 InSAR image pairs were processed during the 35-day-long eruption, and 11 ASTER images were delivered.

1. INTRODUCTION

Throughout the 1990's and 2000's methods were developed to extract lava flow discharge rates from 1 km spatial resolution satellite data collected by satellite sensors operating in the thermal infrared (e.g., Harris et al., 1997; 2007; Harris and Bologa 2009; Coppola et al., 2010). At the same time, high spatial resolution (30 m) satellite data were shown to be of value for mapping lava flow fields (e.g., Flynn et al., 1994; Wright et al., 2000; Lombardo et al., 2009), with InSAR data allowing estimation of lava flow areas, thicknesses and, hence, volumes (e.g., Zebker et al., 1996; Rowland et al., 1999; Lu et al., 2003). In parallel, a series of lava

flow models were developed to allow flow inundation areas to be simulated (e.g., Young and Wadge, 1990; Crisci et al., 2003; Vicari et al., 2007). Increasingly, the capabilities have been merged to allow an ensemble-based approach whereby satellite data from multiple wavelengths and spatial resolutions are combined to allow maximum constraint and cross-validation (e.g., Patrick et al., 2003; Rowland et al., 2003; Wright et al., 2005) and source term input into real-time lava flow emplacement models (e.g., Wright et al., 2008; Vicari et al., 2011; Ganci et al., 2016). Since 2015, just such a response model has been developed at Piton de la Fournaise (Harris et al. 2017), where we here review and validate an updated version of the protocol so as to review an ensemble approach to responding to an effusive crisis.

The response protocol is based on in situ observations and data acquisitions carried out routinely by the Observatoire du Piton de la Fournaise (OVPF) team and the integration of four models: MIROVA (Coppola et al. 2016), the ASTER (Advanced Spaceborne Thermal Emission Radiometer) urgent response protocol (Ramsey, 2016), DOWNFLOW (Favalli et al., 2005) and FLOWGO (Harris and Rowland, 2001). MIROVA is a near-real time hot spot detection system that uses MODIS data, and has been calibrated for TADR calculation at Piton de la Fournaise by Coppola et al. (2010), the ASTER urgent response protocol is a means of automatically prioritizing and targeting ASTER data acquisition during a volcanic eruption. Instead, while DOWNFLOW is a stochastic model that assesses potential flow paths based on iterative runs over a DEM with random noise added, FLOWGO can calculate the cooling-limit of flow down each path (Rowland et al., 2005; Wright et al., 2008). To estimate the maximum distance a flow can extend at a given effusion rate, FLOWGO tracks the thermal and rheological evolution of a control volume of lava as it moves down a channel, tracking the volume until the volume cools and crystallizes to such an extent that forward motion becomes rheologically impossible (Harris and Rowland 2015). FLOWGO has been initialized for and tested for lava channels at Piton de la Fournaise by Harris et al. (2016) and Rhéty et al. (2017), and - to allow improved model initialization, iteration and application - has been rewritten and rebuilt in Python as PyFLOWGO (Chevrel et al., 2018). It is this version of FLOWGO that we use here.

As described in Harris et al. (2017), the response protocol is initialized with the alert of an imminent eruption and provision of the vent location provided by the OVPF as part of their mandated monitoring and response procedures. Subsequently, it involves calling each model in sequence and passing results between each actor, and then final product to OVPF, in as timely fashion as possible. The protocol also calls in ground truth (for vent locations, effusion rates, channel dimensions, flow lengths) provided by the OVPF as well as textural and chemical data (for eruption temperatures, vesicularity, crystallinity, rheological models) produced at LMV, to improve model uncertainty and syn-response validation. We show here how the response protocol works, and define the main uncertainties, using a real-time exercise held immediately after the April-May 2018 eruption of Piton de la Fournaise. The aim of the exercise was to refine model initialization and execution for Piton de la Fournaise, reduce uncertainty, and to fully define the call-down and communication protocol. It involved first following the data feed and executing responses, in the order that they were received, followed by a validation phase in which remote sensing and model based estimates for discharge rate and flow length were compared against ground truth. In doing so, we show how an integrated multi-sensor remote sensing approach can be used to follow, document and quantify an effusive event in near-real time.

2. THE APRIL-MAY 2018 ERUPTION OF PITON DE LA FOURNAISE AND AVAILABLE DATA

The April-May 2018 eruption of Piton de la Fournaise began late on 27 April (19h50 UTC) from five north-south orientated en-echelon fissures that opened between the elevations of 2165 m and 2285 m on the southwest flank of the terminal cone (Figure 1a). Initially flow was channel-fed 'a'a which moved down the SW flank of the Dolomieu. In a short time activity reached a peak and became focused at a main vent roughly central to the fissure line at an elevation of 2200 m. Another much less active vent a few meters to the north continued to project tephra and emit flames. Around the two vents, scoria cones and tephra fields were constructed. Upon reaching the base of the Enclos Fouqué wall (between the 29 and 30 April), lava flows turned southeast to follow the base of the wall reaching a distance of 2.6 km before discharge rates

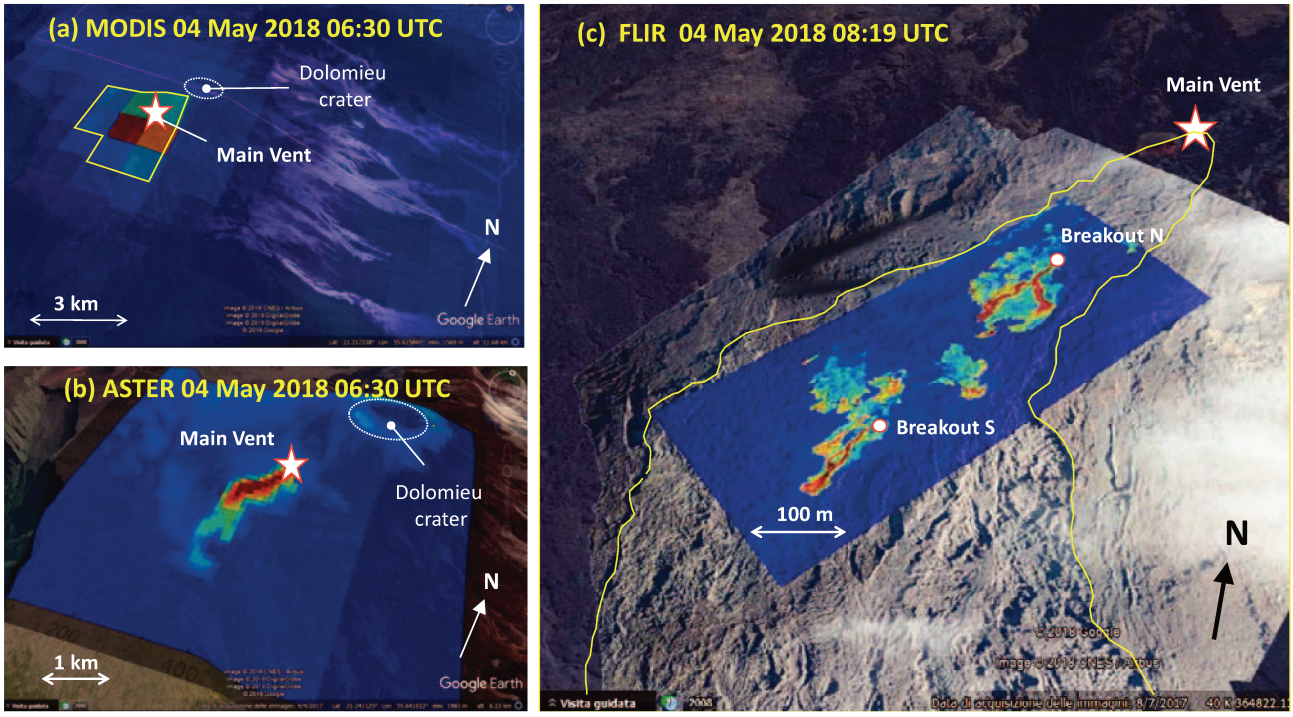

FIGURE 1. Location of the vent for the April-May 2018 eruption on the Dolomieu cone overlain on Google Earth with (a) MODIS, (b) ASTER and (c) thermal camera mosaic of the hot spots associated with active lava flow on 4 May overlain. Yellow outline in (c) gives the limit of the flow field as mapped using hand-held GPS.

declined and active flow fronts retreated to positions closer to the vent (Figure 1b). Between 4 and 7 May, flow activity was concentrated in the proximal section of the flow field with several tubes and, with two main zones of breakout being active 200 and 500 m down the tube system (Figure 1c). Breakouts from the tube system fed low-discharge rate flows which extended no more that 100-200 m. From 7 May new lava flows broke out from an ephemeral vent at the base of the Enclos Fouqué Southern wall producing local vegetation fires. Over the following days, the tube continued to extend and feed lava flows from its terminus, so that by 10 May the tube exit was around 3.2 km from the vent. This continued to feed low-discharge rate flows that extended over 1.1 km (or 4.5 km from the main vent) along the base of the Enclos Fouqué wall. Activity continued in this way until 1 June 2018 when activity died out around 14h30 (local time). During the 34.6-day-long eruption, six aerial photograph, two aerial IR image and several field observation campaigns, including GPS measurements, lava and tephra sampling, gas analysis and UAV over flights were completed by the OVPF. In addition, 35 cloud-free MODIS images, 11 ASTER images and 15 InSAR image pairs all of which were available for near-real time analysis and reporting.

3. METHODOLOGY

While implementation of MIROVA and the ASTER urgent response protocol (URP) allow near-real time collection and processing of satellite thermal data for derivation of time-averaged discharge rate and mapping of a thermal anomaly, DOWNFLOW and FLOWGO (DOWNFLOWGO) allow the flow paths and potential run out distance to be projected. These models are called in sequence, where the call-down procedure is given in Figure 2. As part of this system, output and product are shared using a standardized reporting form (as given in Appendix A) which is shared between an email distribution list involving all actors in the response chain, and to OVPF for integration into surveillance and reporting duties. With each update, the group is issued an update email, flagging the field that has been updated and giving the time and date of the update as well as the name of the person responsible for the update. The reporting form has four fields for: (i) current MIROVA-derived TADR and time series; (ii) current vent location and DOWNFLOWGO projections; (iii) current ASTER thermal distribution map, with flow field evolution time series and report; (iv) InSAR-based flow length report and coherence images (Appendix A). Another field may be added to the reporting form including relevant OVPF

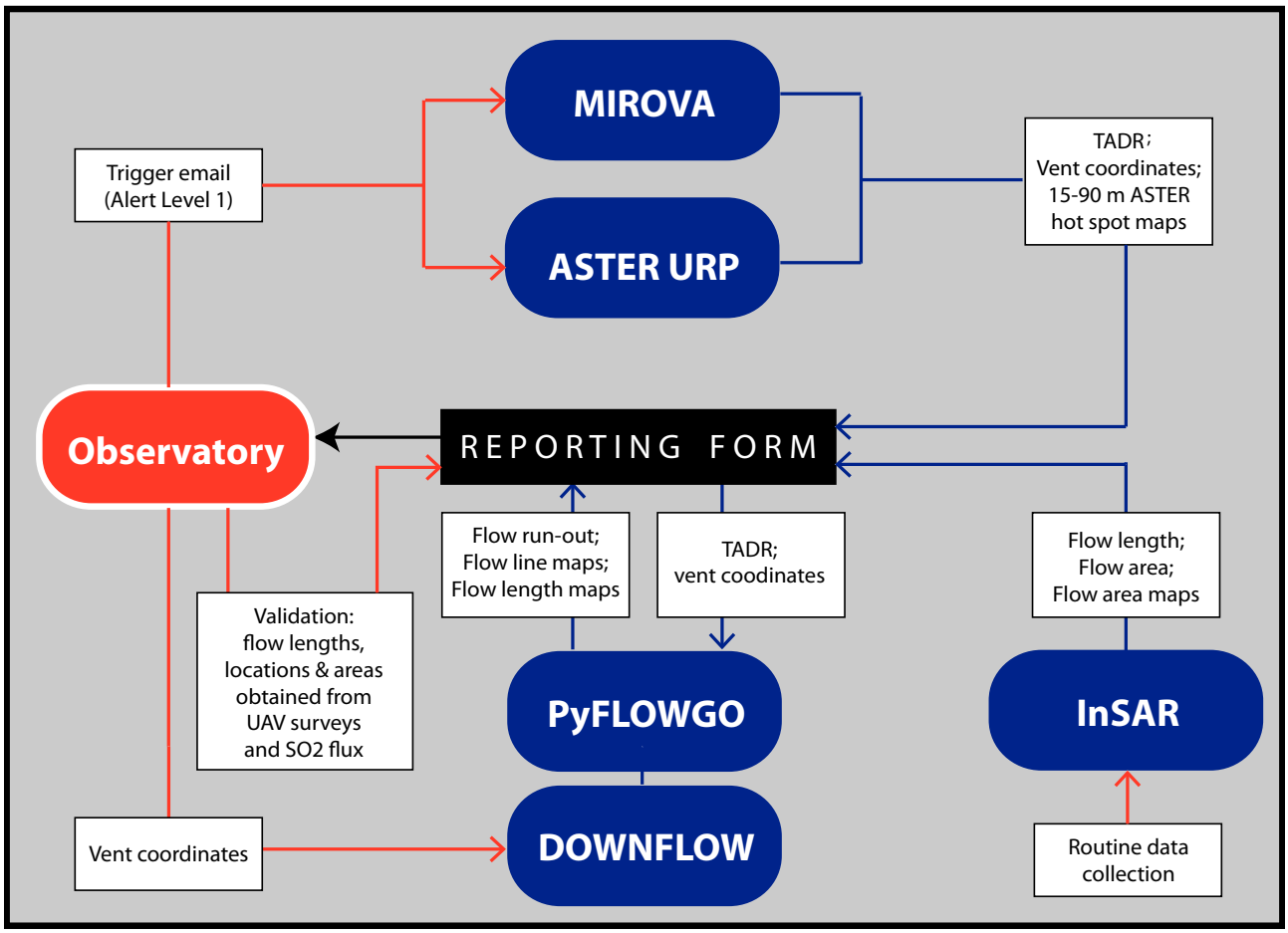

FIGURE 2. Flow chart giving the call-down and reporting procedure, as well as flow of source terms, between each model.

data collection, e.g., flow length from Structure from Motion (SfM), SO2 flux, sampling locations etc. This is left at the observatory's discretion to add depending on work loads and time commitment.

MIROVA and ASTER were called using the observatory bulletin announcing implementation of alert level 1, that is an eruption is believed (on the basis of seismic and ground deformation data) to be "imminent" (in the next minutes/hours). This causes ASTER to be targeted, and MIROVA to set up a "watch" for the first sign of a hot spot. Upon eruption onset, DOWNFLOWGO is run as soon as vent location(s) (GPS coordinates) is (are) known. The first vent location is usually provided by OVPF personnel or gendarmerie using hand-held GPS from a helicopter which is flown by the police (gendarmerie) service. Precision may vary depending on flight time available, the height of the fountains and the number of aircraft in the air space above the eruption site. Initially, to give an immediate idea of likely flow paths and inundation areas, 10000 flow lines are run to the edge of the DEM (i.e., the coast) over the most recent 5-m DEM with random noise of between ±0.8 m and ±2.5 m being added between each run. The slope from the line of steepest descent (LoSD) at ±0.001 m is then extracted (and smoothed every 10 m) and used for preliminary FLOWGO runs at various effusion rates (10, 20, 30, 40, 50, to 100 m^3/s). To do this, FLOWGO is initialized prior to the call down using typical Piton de la Fournaise thermo-rheological conditions and textural properties as given in Table 1. At the beginning of the eruption, a typical channel width of 4 m is taken (Table 1), and the model iterates on depth until the combination with calculated velocity gives the required effusion rate. Subsequently, upon derivation of a first TADR from MIROVA, the cooling-limited extent of flow down each flow line is then updated. Runs driven by the MIROVA-derived TADR are then plotted over a Piton de la Fournaise base map to give an idea of how the flow front may extend, or retreat, if TADRs increase (or decrease) over the current level. In addition, if vent location or channel width information are updated or made available, these are also modified and all models re-run.

Upon receipt of the first ASTER imagery a thermal anomaly map is produced, and flow locations and lengths

Parameter	Value	Units	Up-dated value	Source
Channel width	4	m	2 m	Updated from channel dimensions on aerial photos of 4 May
Eruption Temperature	1114	°C	1140 °C	Updated from maximum temperature data from thermal imagery of the active vent on 4 May
Phenocryst content	0.10	volume fraction	0.01 vol.%	Minimum from the 2015 lava channel
Bubble content	0.30	volume fraction	0.5 vol.%	Maximum from the 2015 lava channel
DRE Density	2970	kg/m^3		
Crust cover	100	%		
Effective Radiation Temperature	500	°C	740 °C	Mean temperature from thermal images of the south breakout channel on 4 May
Melt viscosity	Model of Villeneuve et al. (2008)	Pa s		Temperature dependent viscosity for a Piton de la Fournaise melt
Effect of crystals on mixture viscosity	Einstein Roscoe	Pa s		Valid for prolate crystal content < 0.1 (Mueller et al.2010)

TABLE 1. Key thermal, textural and rheological source terms used to initialize PyFLOWGO at Piton de la Fournaise as given by Chevrel et al. [2018)]. These are based on measurements and best-fit testing of FLOWGO on lava channels active during the December 2010 eruption of Piton de la Fournaise as described in Harris et al. [2016].

assessed on the basis of the spatial distribution of spectral radiance in 90 m ASTER band 12 (thermal infrared, 8.925-9.275 µm). In addition, vent location is checked where the intense thermal anomaly at the vent is apparent in ASTER band 3 (near-infrared, 0.807 µm) image. The 15 m-pixel size, and one pixel accuracy of the geolocation, allows the location of the vent hot spot to ±15 m. This is often better than that provided by hand-held GPS, which when run in a fast moving helicopter records a point that will lag behind the craft point by several hundred meters. If this is the case, the vent location is updated and new DOWNFLOWGO runs are produced. If tubes begin to extend from the vent, this - following Wright et al. [2000] - becomes apparent in the high spatial resolution satellite images from the distribution of spectral radiance. In such as case, the source for DOWNFLOWGO will be moved to the tube exit.

In addition, InSAR interferograms and SfM data are processed for flow thickness and length maps that both add to the information flow and allow validation of model-based flow-length projections. Although remaining largely underutilized in an operational response sense, the value of such data in producing lava flow thickness maps as long been known [e.g., Zebker et al., 1996; Rowland et al., 1999; MacKay et al., 1998; Stevens, 2002; Lu et al., 2003], as has the potential for merging with ancillary data, such as thermal-IR-derived TADRs and model-based lava flow run-outs [Rowland et al., 2003]. The InSAR method consists of computing an interferogram by subtracting the phase between two SAR images acquired for the same area at different times (for details of the method see Appendix B). These statistics which are input into a fourth field in the reporting form (Appendix A) and are also used to update the DEM used for flow path runs.

3.1 VALIDATION

On 4 May 2018 an over flight was made in an ultralight aircraft at a flight height of around 310 m above the ground surface. A thermal camera was used to collect 52 images of the lava flow field and vent system between 12:15 and 12:30 local time. The thermal camera was a FLIR Systems T650 which provides a 640 × 480 pixel image in the 8-14 μm waveband, with 0.65 mrad pixels. This, over a line-of-sight distance of 460 m (and viewing angle of 48°) gives a pixel size of 0.3 m. Images were used to obtain vent (eruption) temperatures and down channel surface temperature profiles to use in FLOWGO, as well as channel and flow dimensions plus radiative (Q_{rad}), convective (Q_{conv}) and total ($Q_{tot} = Q_{rad} + Q_{conv}$) heat fluxes to check against model output. In addition, the MODIS and ASTER images collected at 10:30 (local time) on the same day (i.e., two hours previously) were fitted to the thermal camera image mosaic to allow the heat fluxes and TADRs to be compared. TADR was extracted from the thermal camera images using $TADR = Q_{tot} / \rho (cp\Delta T + f\Lambda)$, in which ρ is the lava density, cp is specific heat capacity, ΔT is the cooling range, f is the fraction of crystals grown down flow and Λ is latent heat of crystallization. Values characteristic of recent lavas at Piton de la Fournaise were used for ρ, c_p, and f, these being 2079 kg/m^3, 1225 J/kg K and 0.1, respectively, with a cooling range of 75-250 °C [Harris et al., 2007]. At the end of the eruption, following sample analysis, the chemical, temperature, crystallinity and vesicularity sections of the initialization file for flow modeling are checked, and if necessary, updated (Table 1).

4. RESULTS

The trigger for the protocol of Figure 2 was the Bulletin released by OVPF on 27 April 2018 at 20h30 local time (16h30 UTC). The bulletin declared that a seismic crisis had begun at 20h15 local time (16h15 UTC) accompanied by rapid ground deformation indicative of "magma leaving the storage system and propagating towards the surface" [Peltier, 2018]. Consequently, an eruption was declared probable in the following minutes or hours, and the alert level was set to "Alert 1" [Peltier, 2018]. As a result, the MIROVA "watch" began at 20h30 (16h30 UTC) on 27 April, with an ASTER URP being triggered at 04h25 (00h25 UTC) on 29 April (Appendix C). In addition, on receipt of the Bulletin, DOWNFLOWGO was loaded with the most recent DEM of Piton de la Fournaise, this being the 5-m DEM generated from LiDAR data in 2010 modified by adding the largest flow fields in the area that are the October 2010 and the August 2015 using the InSAR-based thickness maps.

The eruption began at 23h50 local time (19h50 UTC) on 27 April. Initially DOWNFLOWGO was run from a vent location set on the basis of fissure location relative to pre-existing topographic features as apparent in images acquired by OVPF's web-cam monitoring network. For this case, the camera used was that of "Piton Bert" (BERC, http://www.ipgp.fr/fr/ovpf/reseau-de-cameras) which targets this sector of the volcano. Comparison of a daytime image as a background layer and an image acquired during the eruption revealed the fissure to approximately extend between two newly formed cinder cones at an elevation of 2200 m on the SW flank of the terminal cone. These cones were located at 365375 m E; 7649065 m S and 365500 m E; 7848455 m S, and DOWNFLOW was launched from a point between the two cones at 365377 m E; 7648853 m S. This showed that the flows would likely move SW down the flank of the terminal cone, and then turn SE to following the caldera wall to the coast (Figure 3). The effusion rate contour map for this case was subsequently produced and posted on the reporting form (Figure 3). This revealed that flows fed at sustained rates in excess of 120 m^3/s were capable of reaching the island belt road, to reach the coast. However, because a 4 km wide basin existed after a distance of 4 km from the vent, flows became held up at this point, with even flows at 80 m^3/s coming to a halt 4 km from the vent; and to push the model across the basin needed more than 120 m^3/s. Thus, in reality, our prediction was that either time would be needed to fill this basin, where lava needed time spread and pile up, and/or for a tube to develop across the basin - a little like the case of lava flow advance towards Etnea Zafferana in 1992 [Barberi et al., 1993].

The first cloud-free MODIS overpass occurred at 09h55 (UTC, 13h55 local time) on 28 April, i.e., around 14 hours after the eruption began. This yielded a TADR of 10-20 m^3/s (Table 2). These values were immediately input into the reporting sheet, thereby being handed onwards for input into the PyFLOWGO initialization file. The first lava flow projection map was thus also completed and posted; revealing flows were capable of extending up to 1180-2510 m under initial conditions (Figure 4a). The latency between satellite overpass and TADR provision was 105 minutes, with the model result being posted 15 minutes later. The first S1B InSAR image pair was completed around six hours after the erup-

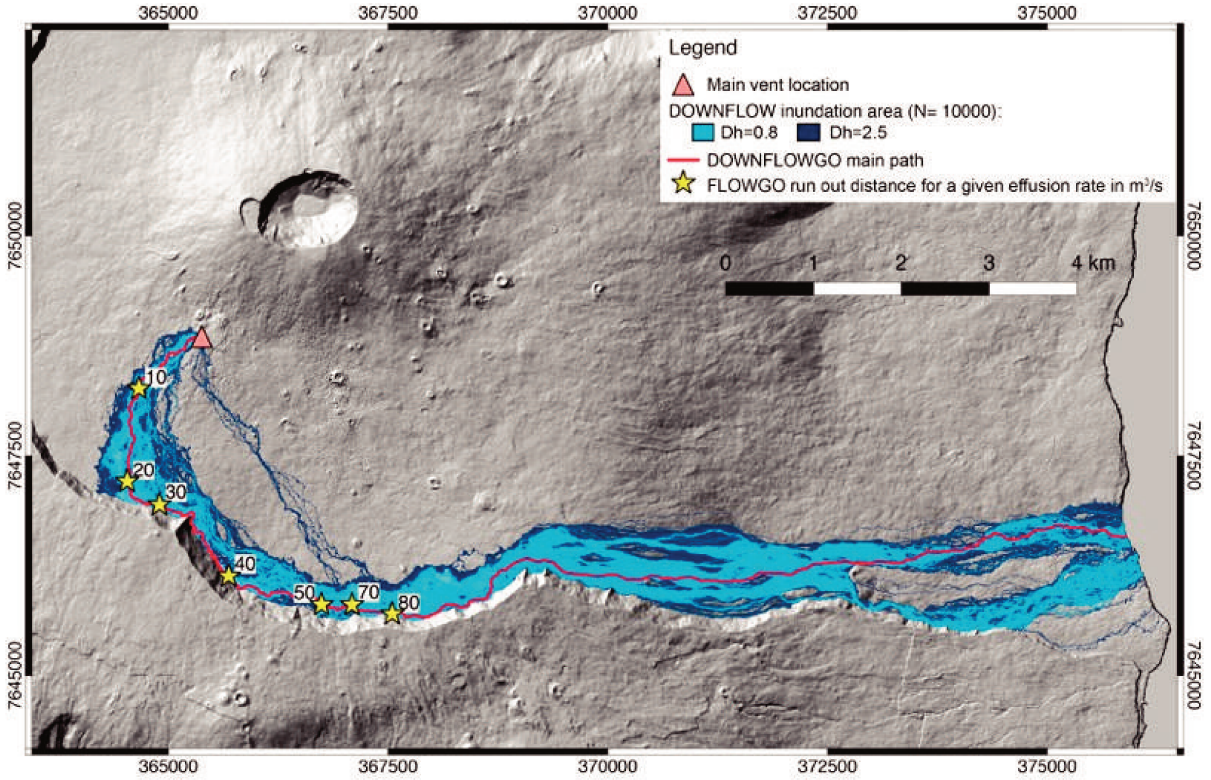

FIGURE 3. DOWNFLOW inundation area for a 10000 iterations from the initial vent location with DEM noise (Dh) of 0.8 m (light blue) and 2.5 m (dark blue), with the line of steepest descent in red. Yellow stars give the distance down the LoSD FLOWGO runs at each generic effusion rate (numbers are in m^3/s). These are the "effusion rate contours" for this eruption.

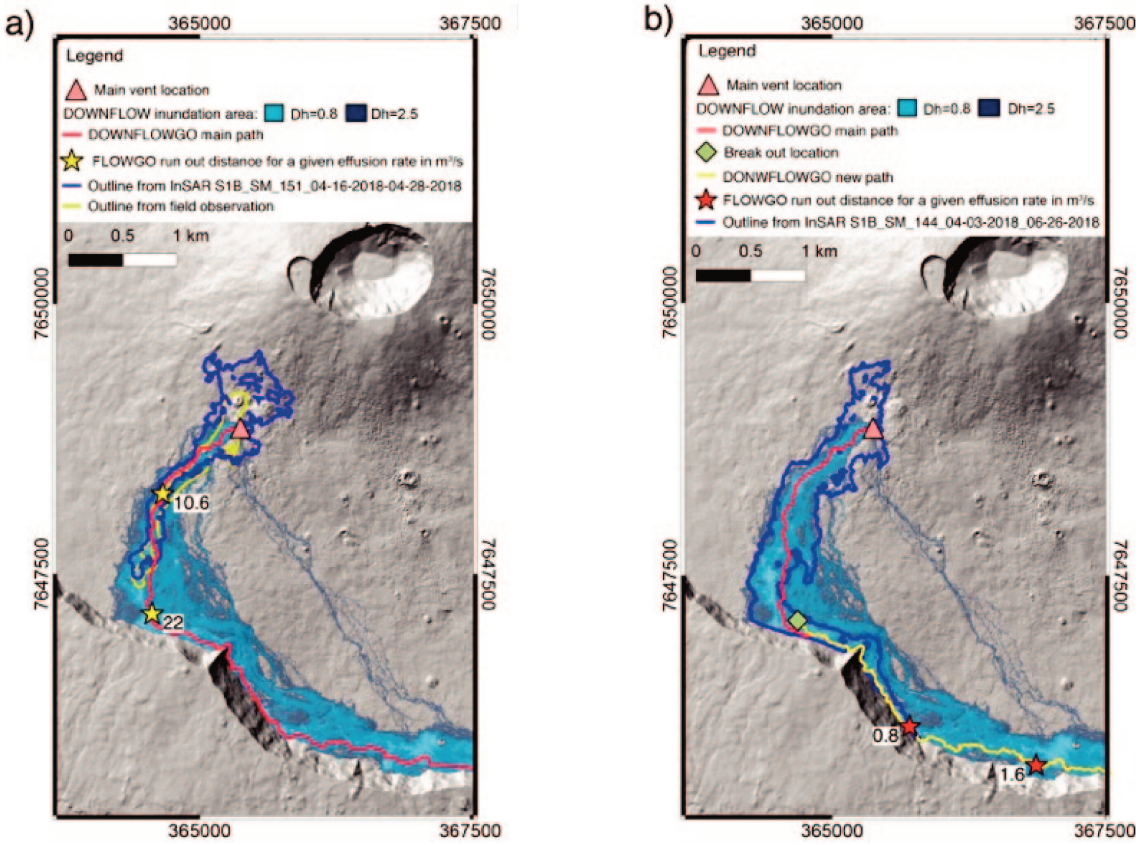

FIGURE 4. Distance down the LoSD (red line) that FLOWGO will run at the given effusion rates, these being the numbers (in m^3/s) next to each star. Runs are given from (a) the initial vent location of 28 April, and (b) the tube exit on 9 May. Overlain are the limits of the flow field defined from InSAR incoherence (blue outline) and field mapping (yellow outline) on the same dates. Background shows the DOWNFLOW inundation area.

Date & Time (UT)	Satellite	TADR (m^3/s)			Duration	Cumulative Volume ($\times 10^6$ m^3)		
(dd/mm/yyyy hh:mm)		Min.	Mid-point	Max.	(days)	Min.	Mid-point	Max.
28/04/2018 09:55	Aqua	11.4	16.3	21.2	0.51	0.47	0.66	0.86
28/04/2018 19:20	Terra	7.8	11.2	14.5	0.90	0.79	1.13	1.47
29/04/2018 21:30	Aqua	3.0	4.3	5.6	1.99	1.30	1.86	2.42
30/04/2018 19:05	Terra	3.7	5.3	6.9	2.89	1.56	2.23	2.90
02/05/2018 22:00	Aqua	2.5	3.6	4.6	5.01	2.13	3.05	3.96
04/05/2018 06:30	Terra	1.8	2.6	3.4	6.36	2.38	3.41	4.43
04/05/2018 18:40	Terra	2.7	3.8	4.9	6.87	2.48	3.55	4.61
04/05/2018 21:50	Aqua	2.8	4.0	5.2	7.00	2.51	3.59	4.67
05/05/2018 10:00	Aqua	1.5	2.1	2.8	7.51	2.61	3.72	4.84
05/05/2018 19:25	Terra	2.1	3.0	3.9	7.90	2.67	3.81	4.95
06/05/2018 06:20	Terra	1.3	1.8	2.4	8.36	2.73	3.91	5.08
06/05/2018 21:35	Aqua	1.1	1.5	2.0	8.99	2.80	4.00	5.20
07/05/2018 09:45	Aqua	1.4	2.0	2.7	9.50	2.85	4.08	5.30
07/05/2018 19:15	Terra	1.1	1.6	2.1	9.90	2.90	4.14	5.38
08/05/2018 06:10	Terra	0.9	1.3	1.7	10.35	2.94	4.19	5.45
08/05/2018 21:25	Aqua	0.6	0.9	1.1	10.99	2.98	4.25	5.53
09/05/2018 06:50	Terra	1.6	2.3	3.1	11.38	3.02	4.31	5.60
09/05/2018 19:00	Terra	2.1	3.0	3.8	11.89	3.10	4.42	5.75
10/05/2018 21:15	Aqua	0.9	1.2	1.6	12.98	3.23	4.62	6.01
11/05/2018 06:40	Terra	0.3	0.4	0.5	13.37	3.25	4.65	6.04
11/05/2018 18:50	Terra	1.0	1.5	1.9	13.88	3.28	4.69	6.10
12/05/2018 10:05	Aqua	0.4	0.6	0.8	14.51	3.32	4.75	6.17
13/05/2018 06:25	Terra	1.1	1.5	2.0	15.36	3.38	4.83	6.27
13/05/2018 18:35	Terra	1.1	1.6	2.1	15.87	3.43	4.89	6.36
13/05/2018 21:45	Aqua	1.0	1.5	1.9	16.00	3.44	4.91	6.39
14/05/2018 09:55	Aqua	1.0	1.4	1.8	16.51	3.48	4.97	6.47
14/05/2018 19:20	Terra	0.8	1.1	1.5	16.90	3.51	5.02	6.52
15/05/2018 06:15	Terra	1.4	2.0	2.6	17.35	3.55	5.08	6.60
15/05/2018 21:30	Aqua	0.9	1.3	1.7	17.99	3.62	5.17	6.72
16/05/2018 06:55	Terra	0.6	0.8	1.1	18.38	3.64	5.21	6.77
16/05/2018 19:05	Terra	0.9	1.3	1.6	18.89	3.68	5.25	6.83
17/05/2018 21:20	Aqua	0.5	0.8	1.0	19.98	3.74	5.35	6.95
19/05/2018 21:05	Aqua	0.4	0.5	0.7	21.97	3.82	5.46	7.10
22/05/2018 21:35	Aqua	0.02	0.03	0.04	24.99	3.88	5.54	7.20
24/05/2018 06:10	Terra	0.02	0.02	0.03	26.35	3.88	5.54	7.20

TABLE 2. Cloud-free MODIS images processed and TADR delivered during the April-May 2018 eruption

tion began and was also entered into the reporting sheet (Figure 5a). These revealed that the flow was already 1.8 km long and covered an area of 0.5±0.1 × 10^6 m^2(Table 3); giving an initial extension rate of around 5 m/min and coverage rate of 1400 ²/min. On the same day, at 09h00 (local time), the first SfM survey was completed and by 16h00 (local time) approximate location of the fissures and flow outline from aerial images were published by the OVPF.

At 03h33 (UTC, 07h33 local time) on 30 April, after a new aerial visit of the eruption, the center of the main fissure was precisely given at 365365 m E; 7648810 m

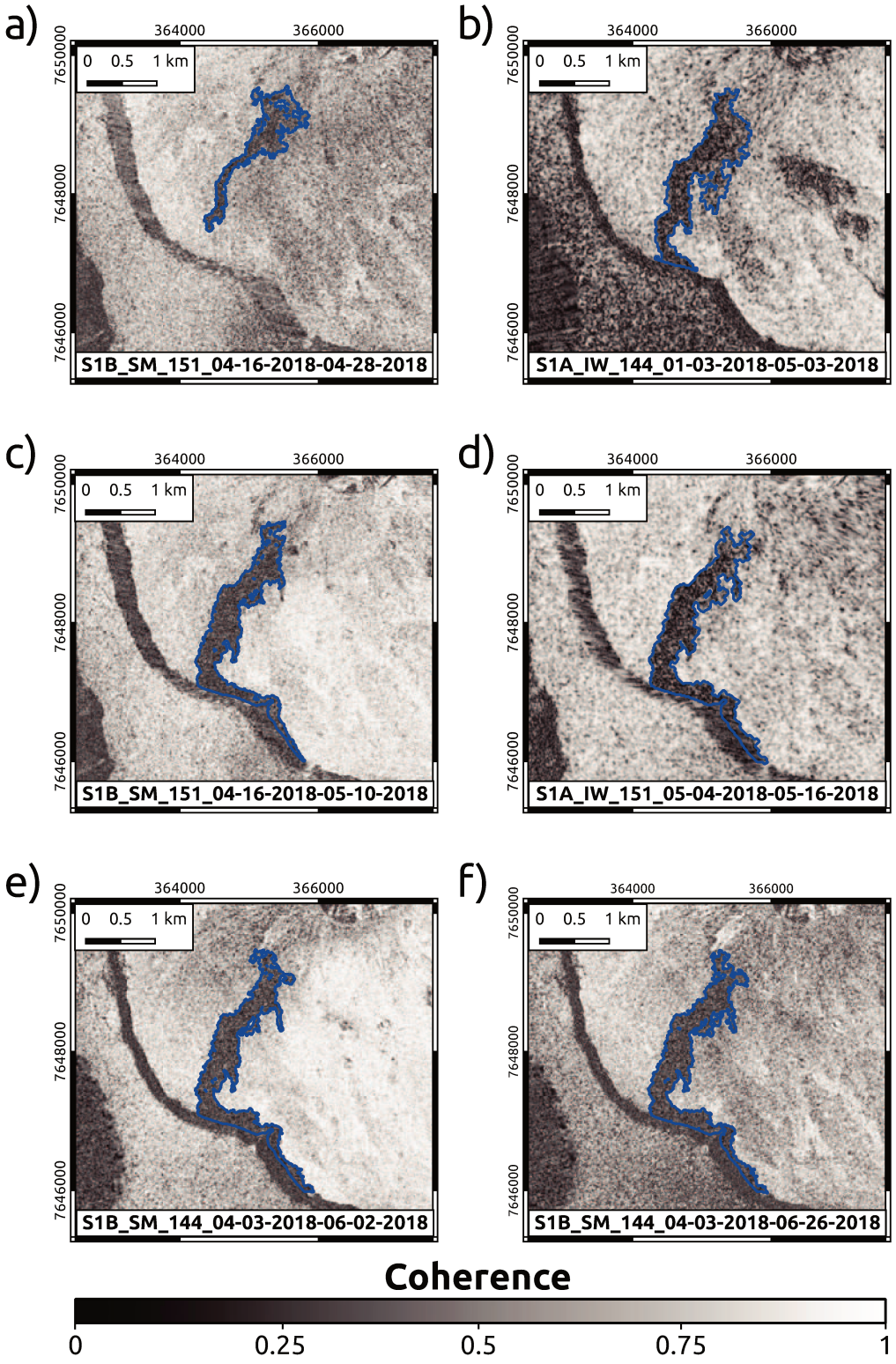

FIGURE 5. Time-series of InSAR incoherence images with lava flow field outlined in blue.

Satellite	Mode (track)	Date (dd/mm/yyyy)		Time (UT) (hh:mm:ss)	Length (km)	Area (x 10^6 m^2)	Error (x 10^6 m^2)
		Master	Slave				
S1B	**SM (151)**	**16/04/2018**	**28/04/2018**	**01:46:38**	**1.8**	**0.5**	**0.1**
S1A	**IW (144)**	**03/01/2018**	**03/05/2018**	**14:53:11**	**2.5**	**1.0**	**0.3**
S1A	IW (151)	22/04/2018	04/05/2018	01:47:32	2.6	--	--
S1B	SM (144)	27/04/2018	09/05/2018	14:52:40	3.4	1.1	0.1
S1B	**SM (151)**	**16/04/2018**	**10/05/2018**	**01:46:39**	**3.5**	**1.2**	**0.2**
S1A	IW (144)	03/01/2018	15/05/2018	14:53:12	4.0	1.2	0.2
S1A	**IW (151)**	**04/05/2018**	**16/05/2018**	**01:47:32**	**4.1**	**1.3**	**0.3**
S1B	SM (144)	27/04/2018	21/05/2018	14:52:41	4.1	--	--
S1B	SM (151)	16/04/2018	22/05/2018	01:46:39	4.1	1.3	0.1
S1A	IW (144)	03/01/2018	27/05/2018	14:53:12	4.1	1.3	0.1
S1A	IW (151)	04/05/2018	28/05/2018	01:47:33	4.1	1.3	0.1
S1B	SM (144)	27/04/2018	02/06/2018	14:52:41	--	--	--
S1B	SM (151)	16/04/2018	03/06/2018	01:46:40	--	--	--
S1A	IW (144)	03/01/2018	08/06/2018	14:53:13	4.1	--	--
S1A	IW (151)	04/05/2018	09/06/2018	01:47:34	4.1	--	--

TABLE 3. InSAR image pairs used to produce coherence maps during the April - May eruption, and the resulting flow lengths and flow field areas. The lines entered in bold are used in the reporting form (Appendix A). Track 144 for ascending pass; 151 for descending pass.

S. By this time, however, MODIS-derived TADR had declined to 3.7-6.9 m^3/s (Table 2). Updating PyFLOWGO revealed reduced run-outs of 0.7-1.0 km. The first cloud-free ASTER image was acquired on 2 May. This revealed an 11 pixel-long anomaly of saturated pixels orientated NE-SW on the south flank of the Dolomieu (Figure 6) - equivalent to a 990 m long zone of active lava (Table 4). The active vent was apparent as a single pixel hot spot in the 15-m near-infrared data and the vent location was updated to 365280 m E; 7648835 m S (Appendix D), with the TADR for this day being 3.6-4.6 m^3/s (Table 2). These details were updated in the reporting form, and the vent location for DOWNFLOWGO adjusted slightly (although this had no effect on the flow paths or LoSD). The following day (3 May), the second coherence map was produced. This revealed that the lava flow field had, at some point, reached the base of the caldera wall, turning SE to follow the base of the wall (Figure 6) having attained a length of 2.5 km (Table 3). The shorter length of the active flows implied by the size of the thermal anomaly in ASTER on 2 May, as well as the 17 pixel (1530 m) long zone of cooler pixels beyond the front of the main hot spot indicated that flow front locations had begun to retreat back up flow by this time.

The thermal camera imagery obtained from the overflight of 4 May confirmed that activity had diminished, and comprised tube-fed breakouts of channel-fed 'a'a (Figure 1c). Two main breakouts were located where the southern breakout was fed by a 2 m-wide channel which fed a 110 m pad of 'a'a. Total heat flux from the breakout was 435±50 MW, which converted to a TADR of 0.61-1.65 m^3/s. ASTER imagery revealed that, by 9 May, the tube had extended 2430 m (Figure 6) to feed lava flows of around 1.4 km in length. At the same time,

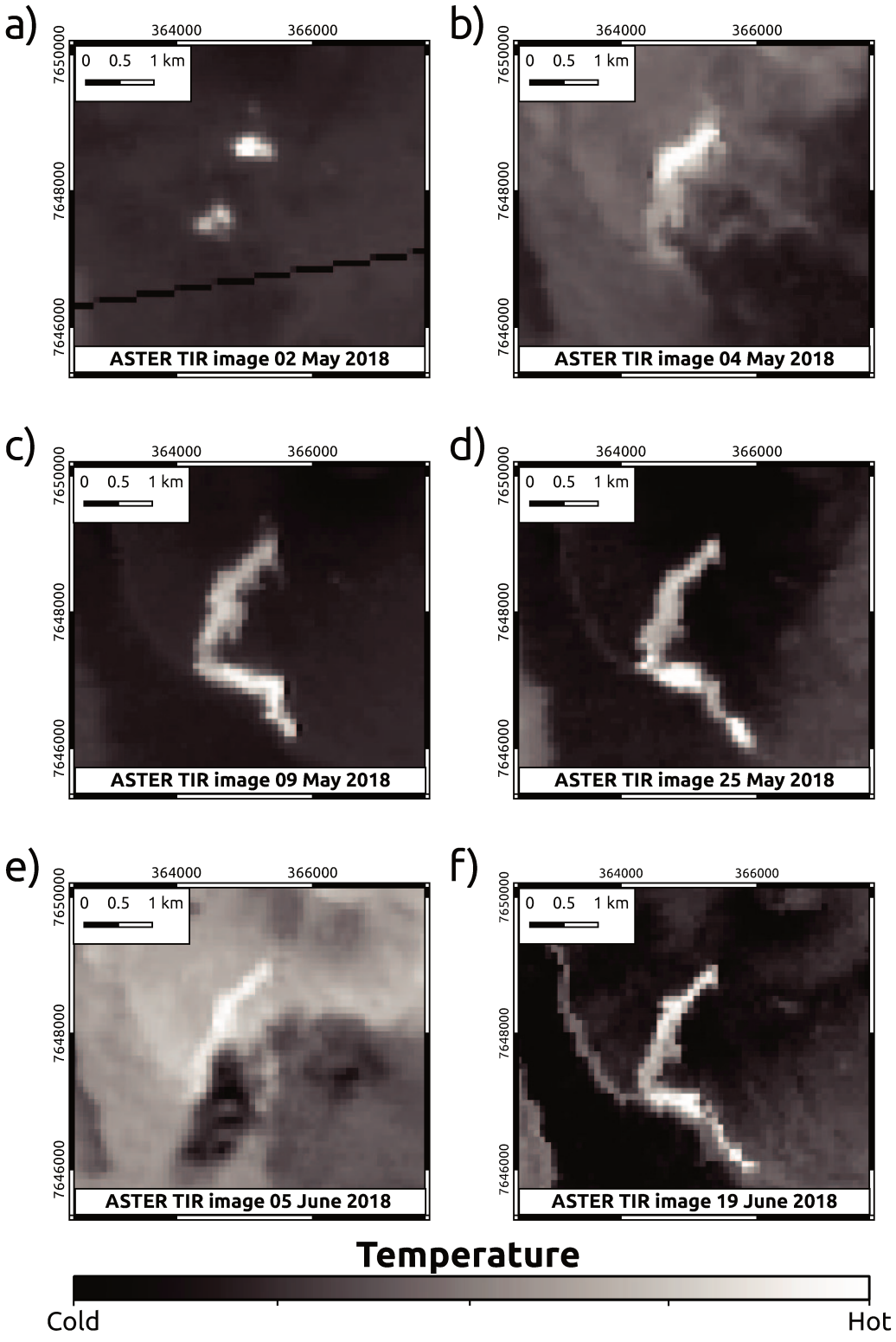

FIGURE 6. Time-series of ASTER TIR images with active flows apparent as elongate thermal anomalies (higher pixel-integrated temperatures give lighter tones: white are the hottest pixels, and black are the coldest). Note how the highest intensities in the thermal anomaly move down flow with time, and effect of lava tube extension.

MIROVA revealed continued decline in TADR (Figure 7) to between 1 and 2 m^3/s. As a result, the vent location for DOWNFLOW was moved to the tube exit, which ASTER gave as being at 364685 m E; 7647090 m S, and FLOWGO run at 1.6 and 3.8 m^3/s (Table 2) with an updated channel width and eruption temperature (Table 1). This gave flow lengths of 1-2 km beyond the end of the tube system (Figure 4b).

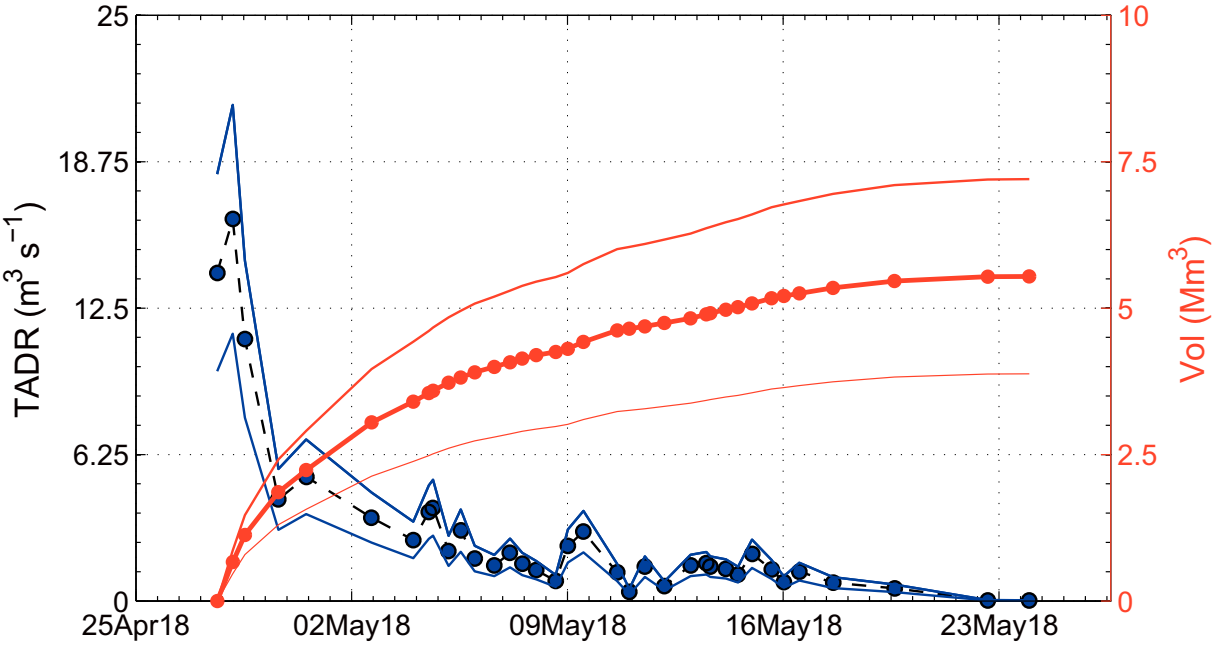

FIGURE 7. MIROVA-derived TADR and cumulative volume.

Thereafter, TADRs remained at low levels (Figure 7) and the flow field continued to build parallel with the base of the caldera wall (Figure 5). TADRs of 0.8 m^3/s characteristic of the final week of the eruption (Table 2) gave flow lengths that extended just 1 km from the end of the tube (Figure 4b). The flow field (both predicted and measured) attained a final length of 4.1 km and area of 1.3±0.1 × 10^6 m^2 (Table 3), and a volume of 5.5±1.6 x 10^6 m^2 (Table 2). In all, 35 TADR sets were processed by MIROVA (Table 2), 15 image pairs were processed for coherence analysis (Table 3), 11 ASTER images were obtained using the ASTER URP (Table 4) and DOWNFLOWGO was launched three times as TADR and vent location changed. Additionally, six aerial photograph data sets, two aerial IR image surveys and multiple field observations, including lava and tephra sampling, gas analyses, UAV over flights were completed by the OVPF. The final reporting sheet, filled out with all derived values from this data set, is given in Appendix D.

5. DISCUSSION

The aerial survey mapping of the flow field of 30 April allowed checking of the dimensions of the lava flow field derived from InSAR data; the center line length being 1.8 km (the same as that given by InSAR) and the area having excellent coincidence with the zone of incoherence obtained from the InSAR data. Likewise, dimensions of InSAR zones of incoherence, ASTER thermal anomalies and FLOWGO lengths are in excellent agreement (Figure 8). For example, the thermal anomaly in ASTER on 2 May revealed that flows had extended to a maximum distance of 2520 m in the proceeding days. This compares with the 2.5 km long zone of incoherence recorded by the InSAR pair processed the following day (3 May) and the 2510 m flow length generated by FLOWGO using the maximum TADRs obtained from MIROVA the first few days of the eruption. Closing the circle with validation of the FLOWGO run outs with good fits with dimensions of incoherence and thermal anomalies in InSAR and ASTER data gives us confidence in the source terms (including MIROVA-derived TADR) entered into the model. We next assess the uncertainty in those MIROVA-derived TADR, as well as the FLOWGO run-outs and errors due to DEM problems.

5.1 VALIDATION OF MIROVA-DERIVED TADR

The image collected on 4 May by MODIS-MIROVA indicates a total radiant power (Qrad) of 497±149 MW, corresponding to a total TADR of 2.6±0.6 m^3/s. Total radiant power is around 42 % of that measured for the south breakout on 4 May using the thermal camera (i.e., 209±20 MW). The TADR (1.13±0.52 m^3/s) obtained from the thermal image is also 43 % that of the MODIS-

Date (dd/mm/yyyy)	Time (hh:mm, UT)	Mode	Vent Location (UTM)	Tube Exit Location (UTM)	Tube length (km)	Active flow length (km)	Cooling flow length (km)
02/05/2018	18:56	Night time mode (TIR only)	0365216 m E; 7648811 m S	n/a	0	0.99	1.53
04/05/2018	06:34	Daytime full mode (both VNIR and TIR)	0365261 m E; 7648841 m S	n/a	0	0.89	1.33
09/05/2018	19:03	Night time mode (TIR only)	0365261 m E; 7648841 m S	0364927 m E; 7646953 m S	0.49	1.52	1.67
11/05/2018	6:40	Daytime off-nadir pointing mode (VNIR only)	--	--	--	--	--
13/05/2018	6:28	Daytime off-nadir pointing mode (VNIR only)	--	--	--	--	--
18/05/2018	18:57	Night time mode (TIR only)	cloudy	cloudy	cloudy	cloudy	cloudy
20/05/2018	06:34	Daytime full mode (both VNIR and TIR)	cloudy	cloudy	cloudy	cloudy	cloudy
25/05/2018	19:03	Night time mode (TIR only)	0365261 m E; 7648841 m S	0364900 m E;			
7647010 m S	2.07	0.63	1.08				
03/06/2018	18:57	Night time mode (TIR only)	cloudy	cloudy	cloudy	cloudy	cloudy
05/06/2018	06:34	Daytime full mode (both VNIR and TIR)	Post-eruption	Post-eruption	Post-eruption	Post-eruption	Post-eruption
19/06/2018	18:57	Night time mode (TIR only)	Post-eruption	Post-eruption	Post-eruption	Post-eruption	Post-eruption

TABLE 4. ASTER-URP images acquired during the eruption response. From these data, vent locations and flow field lengths were derived. Note that when the 15 m VNIR are the only data acquired because of high angle off-nadir pointing, smaller-scale features are resolved, but the dimensions of active flow features based on their thermal signature cannot be measured without the 90 m TIR data.

MIROVA, indicating confidence in the latter value and the conversion routine used. In this regard, MODIS-MIROVA uses the conversion Qrad/TADR = cRad [Coppola et al., 2010]. For Piton de la Fournaise, Coppola et al. [2010] used thermal camera data for the May-June 2003 eruption to obain cRad of 2.5±1 × 108 J m-3. The value of cRad obtained here is 2.3±1 × 108 J m-3 indicating that the conversion factor is stable, still holds and provides a TADR in good agreement with ground truth.

5.2 FLOWGO UNCERTAINTY

To test uncertainty, we take our initial run of 28 April which was initialized with a TADR of 20 m^3/s and vary the source terms of Table 1 within reasonable limits. Using the generic source terms of Table 1, the model solved for a channel depth of 4 m give a distance of 2510 m (Figure 4a).

Our first uncertainty is in eruption temperature. Thermal camera imagery of the vent on 4 May yielded max-

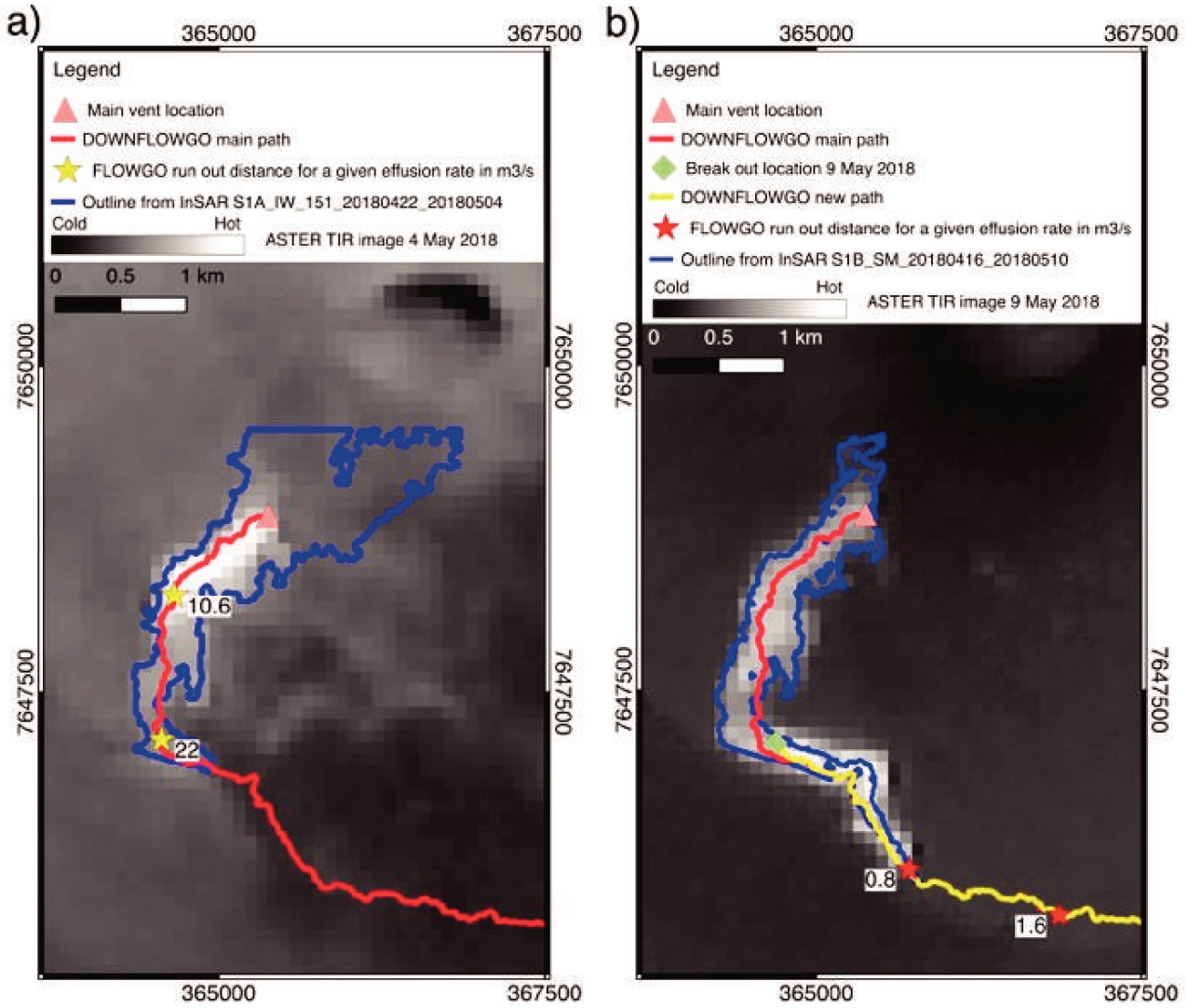

FIGURE 8. Comparison of ASTER thermal anomaly, InSAR incoherence and FLOWGO run outs for (a) 4 May (FLOWGO run from the initial vent location) and (b) 9 May (FLOWGO run from the tube exit along the new path, yellow line).

imum temperatures of up to 1210±40 °C, a value which is suspiciously high. On 10 May, similarly suspicious temperatures of 1700 °C were recorded over a small skylight at the base of the main scoria cone. These temperatures are higher than the liquidus for Piton de la Fournaise and therefore cannot correspond to lava temperatures. However, nighttime observations revealed flames over the vent, so this appears to be a flame temperature, where the presence of the flame likely explains the intense thermal anomaly in the ASTER NIR band. Flame-free maxima were 1142±35 °C, consistent with temperatures obtained from the glass chemistry. If we update the eruption from 1114 °C temperature to 1142 °C (and readjust the channel dimension to balance for similar TADR) this increases the run out by just 30 m, revealing that a 3 % uncertainty in eruption temperature results in a 1 % uncertainty in run out.

Our second uncertainty is in bubble content and crystallinity and associated rheology models. Based on our analysis of lava samples from the 2015 channel, bubble content could be as high as 50 vol.% and phenocryst content as low as 1 vol.%. Because we use a simple two phase (fluid+crystals) mixture model bubble content effects the velocity equation through its effect on density, while the lower starting crystal content reduces the viscosity of the mixture. While increasing the vesicularity to 50 vol.% decreases run-out by 120 m (11 %), decreasing the phenocryst content to 1 vol.% increases run-out by 470 m (28 %).

The third uncertainty is on surface temperature which controls heat loss and hence cooling rate. We have used the typical effective radiation temperature approximated from the data of Flynn and Mouginis-Mark [1994] for a lava channel on Kilauea to initialize the model (Table 1). The thermal imagery of the south break out channel indicates that this may be a little low,

where temperatures down the center line are 520-890 °C, with a mean and standard deviation of 740 °C and 80 °C. If we use this mean temperature for the effective radiation temperature, we have a flow length that decreases by 230 m (23 %).

Our final uncertainty is on channel width. If, for example, we reduce to a width of 2 m, depth and velocity have to increase to 1.1 m and 4.8 m/s to balance the TADR. This yields a runout of 2550 m or 46 % longer, so that an uncertainty on channel depth of 50 % yields uncertainty on runout of the same order. However, to extent uncertainties may cancel. If for example, we increase the vesicularity to 50 vol.% but decrease the phenocryst content to 1 vol.% we change the runout by just 50 m (for the same TADR). Likewise, if we decrease channel width to 2 m, but increase surface temperature to 740 °C we change the runout by 50 m. Thus, our error appears to be around 4-5 %, so that the error on a predicted runout of 3000 m, is just less than a few hundred meters.

5.3 DEM UNCERTAINTY

Until now, for the near real time response at the effusive crises at Piton de la Fournaise, DOWNFLOW was run on the SRTM DEM from 2005. When we first ran the DOWNFLOW simulation (in May), the LoSD was not south to the base of the Enclos Fouqué wall, but projected due East. It was not possible to simulate the actual flow path because post-2005 topography could not be accounted for. However, now that we have updated our flow projection by using the 5-m 2010 DEM to which lava flow fields from October 2010 and August 2015 (which were both in the southern area of the Enclos Fouqué) were added, the predicted path is south, moving around the western edge of the 2015 flow field, and to reach the wall before flowing to the east along its base. This was exactly the trajectory of the flow. Note that although the eruptive fissures were located near and onto the February 2015 flow (on the distal part) we did not update the DEM with this lava flow as it did not interfere with the ongoing flow process. To model flows on a very active volcano, where topography is constantly changing, we thus need a DEM that is updated after each eruption, so as to reduce uncertainties on predicted flow inundation area.

To obtain the inundation area, DOWNFLOW needs to be calibrated to a specific scenario, and this is achieved by tuning N and Dh [Favalli et al., 2011]. Previous simulations that were compared with real cases at Piton de la Fournaise showed that N=10000 and Dh of 2.5 m gives a good approximation of the proximal area around the Dolomieu, while a Dh of 0.8 m gives a better estimation of the lava flow distal, coastal zone. Subsequently, to obtain the LoSD, DOWNFLOW is first run with 1000 iterations at Dh=1 mm which allows pits and holes to be filled. This filled DEM is then used to obtain a second LoSD with N=1 and Dh=0.001). Down the LoSD a slope value is extracted every 10 m for use in PyFLOWGO. PyFLOWGO includes traps for cases where slope values are negative or zero, where the slope is recalculated at each step from the average of the five previous and five following positive and non-zero values down the LoSD [Chevrel et al., 2018]. This allows FLOWGO to overcome small terrain irregularities, and to project across holes and pits as well as flat zones. The value of 10 m has been chosen from several simulations and seems to be the best suited value. Although precise DEMs are always preferred, we find we have to smooth the LoSD in order to obtained results in agreement with reality.

In the present case, the changes in vent location between the first estimation and the coordinates obtained in the field or from the satellite images did not change significantly. The effect on the predicted flow path was therefore minor and limited to within 100 m of the vent area. However, knowing, and moving to, the break out location of 9 May, was essential to predict the final flow length (at the given new TADR). The protocol we are offering here, that is sharing ASTER, MODIS, and DOWNFLOWGO allow a back and forth to update the vent location and is therefore of major improvement for correct estimation of the lava flow path and runout distance. In addition this protocol is of service to OVPF to aid in monitoring needs for lava flow field evolution allowing both crisis management and appraisal of need to evacuate ground based monitoring stations falling in flow paths.

6. CONCLUSION

With the near-real time availability of data from so many satellite-based sensors, as well as the immediate availability of ground truth through upload to internet-based data hubs, the best way forward to tracking an effusive crisis is an ensemble-based approach. Such a system is open to expansion and ingestion of further data sets to improve coverage and further reduce lags between event and measurement. For example, VIIRS (Visible Infrared Imaging Radiometer Suite) can be considered as an extension to MODIS [Blackett, 2015], and

Sentinel-2 as an extension to ASTER [Cappello et al., 2018], with other sensors being incorporated as they come on-line. In this regard, technology is constantly evolving with new potential coming-on line every year where, for this case, we have begun to convolve data from sensors flown on UAVs, as well as from crowd-sourcing. Another developing avenue is small, low cost satellite networks, such as the small satellite Technology Experiment Carrier-1 (TET-1) as developed by the German Aerospace Center and dedicated to monitoring high temperature events [Zhukov et al., 2006]. Such systems offer high spatial resolution (160 m) thermal infrared imagery at a relatively high temporal resolution (3 days) and have shown to be of value in tracking effusive crises yielding TADR time series to supplement those provided by MODIS [Zakšek et al., 2005].

As shown here, merging thermal data of different resolutions allows time series generation with the best possible temporal resolution and precision; cross-validation of TADR, error and uncertainty assessment; and input into lava flow emplacement models. The next step will be the use of InSAR data to allow DEMs to be updated between eruptions so as to ensure that flow paths are correct and use the most up-to-date topography available, with the DEM evolving as the topography changes. This is a key feature, especially during a long-term eruption with changing topography and vent position. In turn, the chain can be inverted where good agreement of model-predicted flow lengths with dimensions of thermal and incoherence anomalies in high spatial resolution and thermal data suggests that the source terms input into the model are valid. Another key feature explored here is immediate delivery of a flow run out map that considers all feasible TADRs. This means that delivery of the hazard map, which can be created in a few minutes, does not have to be attendant on the first, cloud-free satellite overpass for delivery of a TADR. Instead, the map gives the hazard manager an immediate idea of possible event scenario's which can be assessed and checked when the first TADR comes in, and updated as vent locations and topographies change.

Acknowledgements. This work comes out of a three day workshop and exercise held in Clermont Ferrand in June 2018 funded by ANR-LAVA. This work was funded by the Agence National de la Recherche (ANR: www.agence-nationale-recherche.fr) through project ANR-LAVA (ANR Program: DS0902 2016; Project: ANR-16 CE39-0009, PI: A. Harris, Link: www.agence-nationale-recherche.fr/?Project=ANR-16-CE39-0009; https://sites.google.com/view/anrlava/). We would like to thank the Sentinel-1 ESA team, especially P. Potin and Y.-L. Desnos for having made possible routine Sentinel-1 StripMap acquisition on La Réunion Island. This is ANR-LAVA contribution no. 5 and IPGP contribution no. XXX.

REFERENCES

Favalli M, Pareschi MT, Neri A, Isola I (2005) Forecasting lava flow paths by a stochastic approach. Geophys Res Lett, 32(L03305). doi: 10.1029/2004GL021718.

Flynn LP, Mouginis-Mark PJ (1994) Temperature measurements of an active lava channel from spectral measurements, Kilauea Volcano, Hawaii. Bulletin of Volcanology, 56, 297-301.

Harris AJL, Rowland SK (2001) FLOWGO: a kinematic thermo-rheological model for lava flowing in a channel. Bull Volcanol, 63, 20-44. doi:10.1007/s004450000120.

Harris AJL, Baloga SM (2009) Lava discharge rates from satellite-measured heat flux. Geophys. Res. Lett., 36, L19302. doi:10.1029/2009GL039717.

Harris AJL, Rowland SK (2015) FLOWGO 2012: an updated framework for thermorheological simulations of channel-contained lava. In: Carey, R., Cayol, V., Poland, M., Weis, D. (Eds.), Hawaiian Volcanoes: from Source to Surface, Geophysical Monograph, vol. 208. American Geophysical Union, 457-481.

Harris AJL, Blake S, Rothery DA, Stevens NF (1997) A chronology of the 1991 to 1993 Etna eruption using AVHRR data: Implications for real time thermal volcano monitoring, J. Geophys. Res., 102(B4), 7985-8003. doi:10.1029/96JB03388.

Harris AJL, Dehn J, Calvari S (2007) Lava effusion rate definition and measurement: a review. Bull Volcanol, 70, 1-22.

Harris A, Rhéty M, Gurioli L, Villeneuve N, Paris R. (2016) Simulating the thermorheological evolution of channel-contained lava: FLOWGO and its implementation in EXCEL. In: Harris AJL, De Groeve T, Garel F, Carn SA, editors. Detecting, modelling and responding to effusive eruptions, vol. 426. London: Geological Society, London Special Publication, 313-36. doi:10.1144/SP426.9.

Barberi F, Carapezz ML, Valenza M, Villari L (1993) The

control of lava flow during the 1991-1992 eruption of Mt. Etna. Journal of Volcanology and Geothermal Research, 56(1-2), 1-34.

Blackett M (2015) An initial comparison of the thermal anomaly detection products of MODIS and VIIRS in their observation of Indonesian volcanic activity. Remote Sensing of Environment, 171, 75-82.

Cappello A, Ganci G, Bilotta G, Herault A, Zago V, Del Negro C (2018) Satellite-driven modeling approach for monitoring lava flow hazards during the 2017 Etna eruption. Annals of Geophysics, 61, Doi:10.4401/ag-7792.

Chevrel MO, Labroquère J, Harris AJL, Rowland SK (2018) PyFLOWGO: An open-source platform for simulation of channelized lava thermo-rheological properties. Computers and Geosciences, 111, 167-180.

Coppola D, James MR, Staudacher T, Cigolini C (2010) A comparison of field- and satellite-derived thermal flux at Piton de la Fournaise: implications for the calculation of lava discharge rate. Bull Volcanol., 72(3), 341-56. doi:10.1007/s00445-009-0320-8.

Coppola D, Laiolo M, Cigolini C, Delle Donne D, Ripepe M (2016) Enhanced volcanic hot-spot detection using MODIS IR data: results from the MIROVA system. In: Harris AJL, De Groeve T, Garel F, Carn SA, editors. Detecting, Modelling and responding to effusive eruptions, vol. 426. London: Geological Society, London, Special Publications, 181-205. http://doi.org/10.1144/SP426.5.

Crisci G, Di Gregorio S, Rongo R, Scarpelli M, Spataro W, Calvari S (2003) Revisiting the 1669 Etnean eruptive crisis using a cellular automata model and implications for volcanic hazard in the Catania area. Journal of Volcanology and Geothermal Research, 123, 211-230.

Flynn LP, Mouginis-Mark PJ, Horton KA (1994) Distribution of thermal areas on an active lava flow field: Landsat observations of Kilauea, Hawaii, July 1991. Bull. Volcanol., 56, 284-296.

Ganci G, Bilotta G, Cappello A, Herault A, Del Negro C (2016) HOTSAT: a multiplatform system for the thermal monitoring of volcanic activity using satellite data. In Harris, A. J. L., De Groeve, T., Garel, F. and Carn, S. A. (eds) 2016. Detecting, Modelling and Responding to Effusive Eruptions. Geological Society, London, Special Publications, 426, 207-221. First published online October 29, 2015, http://doi.org/10.1144/SP426.21.

Lombardo V, Harris AJL, Calvari S, Buongiono MF (2009) Spatial variations in lava flow field thermal structure and effusion rate derived from very high spatial resolution hyperspectal (MIVIS) data. J. Geophys. Res., 114, B02208. doi:10/1029.2008JB005648.

Lu Z, Fielding E, Patrick MR, Trautwein CM (2003) Estimating lava volume by precision combination of multiple baseline spaceborne and airborne interferometric synthetic aperture radar: The 1997 eruption of Okmok volcano, Alaska. IEEE Transactions on Geoscience and Remote Sensing ,41(6), I428-I436.

MacKay ME, Rowland SK, Mouginis-Mark PJ, Gareil H (1998) Thick lava flows of Karisimbi volcano, Rwanda: insights from SIR-C interferometric topography. Bull. Volcanol., 60, 239-251.

Patrick MR, Dehn J, Papp KR, Lu Z, Dean K, Moxey L, Izbekov P, Guritz R (2003) The 1997 eruption of Okmok Volcano, Alaska: a synthesis of remotely sensed imagery. J Volcanol Geotherm Res, 127, 87-105.

Peltier A (2018) Bulletin du 27 avril 2018 - 20:30 heure locale Observatoire Volcanologique du Piton de la Fournaise. Bulletin of the Observatoire Volcanologique du Piton de la Fournaise, 27 April 2018, OVPF_20180427_20h30- ISSN 2610-5101.

Ramsey M (2016) Enhanced volcanic hot-spot detection using MODIS IR data: results from the MIROVA system. In: Harris AJL, De Groeve T, Garel F, Carn SA, editors. Detecting, Modelling and responding to effusive eruptions, vol. 426. London: Geological Society, London, Special Publications, 181-205. http://doi.org/10.1144/SP426.5.

Rhéty M, Harris A, Villeneuve N, Gurioli L, Médard E, Chevrel O, Bachélery P (2017) A comparison of cooling-limited and volume-limited flow systems: Examples from channels in the Piton de la Fournaise April 2007 lava-flow field, Geochem. Geophys. Geosyst., 18, doi:10.1002/2017GC006839.

Rowland SK, MacKay ME, Garbeil H, Mouginis-Mark PJ (1999) Topographic analyses of Kilauea volcano, Hawaii, from interferometric airborne radar. Bull. Volcanol., 61, 1-14.

Rowland SK, Harris AJL, Wooster MJ, Amelung F, Garbeil H, Wilson L, Mouginis-Mark PJ (2003) Volumetric characteristics of lava flows from interferometric radar and multispectral satellite data: the 1995 Fernandina and 1998 Cerro Azul eruptions in

western Galápagos. Bull. Volcanol., 65, 311-330.
Rowland SK, Garbeil H, Harris A (2005) Lengths and hazards from channel-fed lava flows on Mauna Loa, Hawai'i, determined from thermal and downslope modeling with FLOWGO. Bull. Volcanol., 67, 634-647.
Stevens NF (2002) Emplacement of the large andesitic lava flow in the Oturere Stream valley, Tongariro Volcano, from airborne interferometric radar. New Zealand Journal of Geology and Geophysics, 45, 387-394.
Vicari A, Herault A, Del Negro C, Coltelli M, Marsella M, Proietti C (2007) Modeling of the 2001 lava flow at Etna volcano by a Cellular Automata approach. Environmental Modelling and Software, 22, 1464-1471.
Vicari A, Ganci G, Behncke B, Cappello A, Neri M, Del Negro (2011) Near-real-time forecasting of lava flow hazards during the 12-13 January 2011 Etna eruption. Geophysical Research Letters, 38, L13317. http://doi.org/10.1029/2011GL047545.
Villeneuve N, Neuville DR, Boivin P, Bachèlery P, Richet P (2008) Magma crystallization and viscosity: a study of molten basalts from the Piton de la Fournaise volcano (La Réunion island). Chemical Geology, 256, 242-251.
Wright R, Rothery DA, Blake S, Pieri DC (2000) Visualizing active volcanism with high spatial resolution satellite data: the 1991-1993 eruption of Mount Etna. Bull. Volcanol., 62, 256-265.
Wright R, Carn SA, Flynn LP (2005) A satellite chronology of the May-June 2003 eruption of Anatahan volcano. Journal of Volcanology and Geothermal Research, 146, 102-116.
Wright R, Garbeil H, Harris AJL (2008) Using infrared satellite data to drive a thermorheological/stochastic lava flow emplacement model: A method for near-real-time volcanic hazard assessment. Geophys Res Lett., 35(L19307). doi:10.1029/2008GL035228.
Zakšek K, Hort M, Lorenz E (2015) Satellite and Ground Based Thermal Observation of the 2014 Effusive Eruption at Stromboli Volcano. Remote Sens., 7, 17190-17211.
Zebker HA, Rosen P, Hensley S, Mouginis-Mark PJ (1996) Analysis of active lava flows on Kilauea volcano, Hawaii, using SIR-C radar correlation measurements. Geology, 24(6), 495-498.
Zhukov B, Lorenz E, Oertel D, Wooster M, Roberts G (2006) Spaceborne detection and characterization of fires during the bi-spectral infrared detection (BIRD) experimental small satellite mission (2001-2004). Remote Sens. Environ., 100, 29-51.
Young P, Wadge G (1990). FLOWFRONT: Simulation of a lava flow. Computers and Geosciences, 16, 1171-1191.

*CORRESPONDING AUTHOR: Andrew J.L. HARRIS,
Université Clermont Auvergne, CNRS, OPGC,
Laboratoire Magmas et Volcans,
Clermont-Ferrand, France
email: XXXXX XXXX

GEOLOGY | THE GEOLOGICAL SOCIETY OF AMERICA®

https://doi.org/10.1130/G47110.1

Manuscript received 17 May 2019
Revised manuscript received 17 October 2019
Manuscript accepted 17 October 2019

How shear helps lava to flow

A. Harris[1], S. Mannini[1]*, S. Thivet[1], M.O. Chevrel[1], L. Gurioli[1], N. Villeneuve[2,3], A. Di Muro[2,4] and A. Peltier[2,4]
[1]Université Clermont Auvergne, CNRS, IRD, OPGC, Laboratoire Magmas et Volcans, F-63000 Clermont-Ferrand, France
[2]Université de Paris, Institut de physique du globe de Paris, CNRS, F-75005 Paris, France
[3]Université de La Réunion, Laboratoire Géosciences Réunion, F-97744 Saint Denis, France
[4]Observatoire Volcanologique du Piton de la Fournaise, Institut de physique du globe de Paris, F-97418 La Plaine des Cafres, France

ABSTRACT

Understanding the thermo-rheological regime and physical character of lava while it is flowing is crucial if we are to adequately model lava flow emplacement dynamics. We present measurements from simultaneous sampling and thermal imaging across the full width of an active channel at Piton de la Fournaise (La Réunion, France). Our data set involves measurements of flow dynamics at three sites down-channel from the vent. Quantification of flow velocities, cooling rates, sample texture, and rheology allows all thermo-rheological parameters to be linked, and down- as well as cross-channel variations to be examined. Within 150 m from the vent, we recorded an unexpected velocity increase (from 0.07 to 0.1 m/s), in spite of cooling rates of 0.19–0.29 °C/m and constant slope. This change requires a switch from a Newtonian-dominated regime to a Bingham plug–dominated regime. Sample analysis revealed that the plug consists of foam-like lava, and the shear zones involve vesicle-poor (low-viscosity) lava. With distance from the vent, shear zones develop, carrying the vesicular plug between them. This causes flow to initially accelerate, helped by bubble shearing in narrow lateral shear zones, until cooling takes over as the main driver for viscosity increase and, hence, velocity decrease.

INTRODUCTION

Understanding the thermo-rheological regime of an active lava flow is fundamental if we are to adequately model its emplacement behavior (e.g., Harris and Rowland, 2001; Del Negro et al., 2005; Hidaka et al., 2005). The interrelation between physical flow properties and dynamics is a crucial link for which we are rich in heat-loss–driven models (e.g., Keszthelyi and Self, 1998) but lacking in data to allow validation of models and theory. Traditionally, lava flow rheology has been modeled as a cooling-dominated process, so that the lava steadily cools, degasses, and crystallizes down flow, increasing in viscosity from the vent to the flow front (e.g., Harris and Rowland, 2001). However, to date, only a few measurements have been performed to assess whether this assumption is valid, and these measurements have all been for active channels in Hawaii (USA), with the first measurements being made more than a kilometer or two from the vent (Lipman and Banks, 1987; Moore, 1987; Crisp et al., 1994; Cashman et al., 1999). While such a down-channel thermal and rheological regime has been borne out by analysis of inactive channels (Soule et al., 2004; Riker et al., 2009; Chevrel et al., 2013; Robert et al., 2014; Rhéty et al., 2017), thermal measurements and modeling have also indicated that down-flow cooling is inevitable and progressive, with the rate depending on degree of insulation, flow velocity, and channel dimensions (Harris and Rowland 2009). Other work has highlighted the importance of the crystallization sequence on lava viscosity and strain rate on influencing crystallization behavior and, hence, emplacement dynamics (e.g., Chevrel et al., 2013; Kolzenburg et al., 2018). The role of bubbles in lava transport properties is, however, very poorly constrained, and detailed measurements down near-vent segments of active channels are scarce, with Lipman and Banks (1987) remaining a precious resource.

Down-flow degassing will likely cause loss of volatiles and undercooling of the melt to trigger microcrystallization, both of which will increase the viscosity of the lava mixture (Sparks and Pinkerton, 1978). Down-flow evolution of bubble quantity and shape may also affect rheology, where the mixture viscosity will decrease or increase depending on whether bubbles are deformed or not (Llewellin and Manga, 2005). Down-flow degassing and loss of bubbles have also been documented in lava tubes (Cashman et al., 1994) and from the structure of inflated pāhoehoe flows (Cashman and Kauahikaua, 1997), as well as from measurements along active (Cashman et al., 1999) and solidified (Riker et al., 2009) systems. The effect of vesicles on rheology has also been inferred from *in situ* viscosity measurements on pāhoehoe lobes (Chevrel et al., 2018). However, no direct field measurements exist to constrain and link changing bubble states with flow dynamics down a lava channel.

Here, we present unique data from thermal imaging and sampling down the near-vent reach of an active lava channel at Piton de la Fournaise (Réunion Island, France) during July–August 2015. This data set allowed us to simultaneously constrain and link down- and across-flow velocity, temperature, and rheology. Surprisingly, we measured an acceleration within 150 m of the vent. At constant slope, this implies a down-flow evolution of the rheological regime, from Newtonian to Bingham. In this regard, a Newtonian fluid is one in which the shear stresses during flow linearly increase with strain rate, and the fluid will deform under an infinitesimal amount of stress applied. Instead, a Bingham fluid requires application of a finite yield stress before they begin to flow. As a result, the plot of shear stress versus shear strain does not pass through the origin for the latter, but it does for the former (e.g., Bachelor 1967). In our case, this change was caused by strain localization on the margin of a central plug. This can be supported by the difference in bubble content between lava sampled in the plug and that in the shear zones. Our current understanding of lava flow is that it can evolve from Newtonian to Bingham rheology, but bubbles are rarely taken into consideration to explain such evolution. Here, we provide a

*Current address: Department of Earth Sciences, University of Geneva, 13, Rue des Maraichers, CH-1205 Geneva, Switzerland.

CITATION: Harris, A., et al., 2020, How shear helps lava to flow: Geology, v. 48, p. , https://doi.org/10.1130/G47110.1

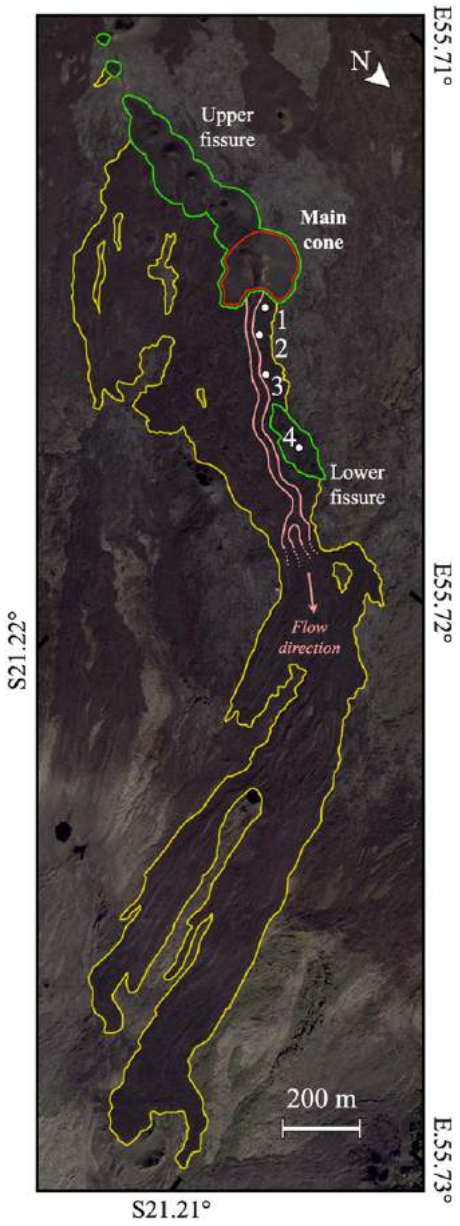

Figure 1. Map of lava flow field (yellow outline), fissures (green outline), main vent (red outline), and stable channel (pink outline) of July–August 2015 eruption of Piton de la Fournaise, La Réunion, France.

unique data set that documents this evolution and an attempt to model this with available rheological models (as detailed in the GSA Data Repository[1]), showing that bubbles play a fundamental role in determining rheology and evolving flow dynamics.

MEASUREMENTS IN AN ACTIVE LAVA CHANNEL

Channel Dimensions and Surface Velocity

Piton de la Fournaise's July–August 2015 eruption lasted 2 d (31 July–1 August) and fed a single master channel that extended 1 km (Fig. 1; Supplement DR1 in the Data Repository). Down this stable channel system, thermal image sequences were collected at four stations (30, 110, 220 and 440 m from the vent; Fig. 1) on the same day (1 August) and within 20 min of each other. Using manual particle tracking (Supplement DR2), surface velocities were measured at 0.03 ± 0.01 m/s at the channel margins and 0.07 ± 0.04 m/s at the center. The horizontal and vertical velocity profiles were best fit with a parabolic equation (Supplement DR2), indicating horizontal velocity gradients of 0.07 s^{-1} (Fig. 2) and suggesting that flow was laminar and Newtonian. Further down flow (at stations 2 and 3; Fig. 1), the channel was wider (4–5 m, instead of 2 m) and shallower (0.8 m instead of 1.8 m; Supplement DR2). A constant surface velocity was measured across a central, 3-m-wide plug at an average of 0.1 m/s at both stations, which was faster than at station 1 (Fig. 2). The central plug was flanked by two narrow, 0.5-m-wide shear zones where velocity declined to zero (Fig. 2A). These profiles revealed a plug-dominated Bingham behavior, with a velocity gradient across the shear zones of 0.2 s^{-1}, a rate three times higher than at station 1. Assuming that the plug comprised 75% of the flow by thickness (as it did by width), then the plug height was 0.47 m, for a basal shear zone height of 0.16 m, across which the velocity vertical gradient was 0.45 s^{-1} (Fig. 2B).

Heat Loss and Cooling Rate

Eruption temperature at the vent (1146 °C) was obtained from thermal images of bubbles bursting at the vent. At station 1, flow was poorly crusted, with a mean surface temperature of 704 ± 107 °C (Fig. 3). At stations 2 and 3, while the surface of the central plug was partially covered by a crust of fragmenting slabs of spiny pāhoehoe and nascent 'a'ā, the shear zones had a cover of down-flow–thickening 'a'ā. Due to the crust cover of the shear zones, surface temperatures at the channel margins were cooler than at the center, where the average surface temperature of the plug was 558 ± 38 °C, whereas it was 300 °C at the margins (Fig. 3). These surface temperature ranges converted to heat losses of 87 ± 2 kW/m^2 at station 1, and 31 ± 24 kW/m^2 and 45 ± 23 kW/m^2 at stations 2 and 3 (Fig. DR3). Cooling was then estimated between the vent and station 1 at 0.21 ± 0.07 °C/m. Lower heat losses and higher velocities at stations 2–3 resulted in cooling of 0.13 ± 0.10 °C/m and 0.12 ± 0.10 °C/m, at the two stations, respectively (Supplement DR3). Such cooling per unit distance is high in comparison to previously reported values for flow down a lava channel (typically 0.005–0.007 °C/m; Crisp et al., 1994;

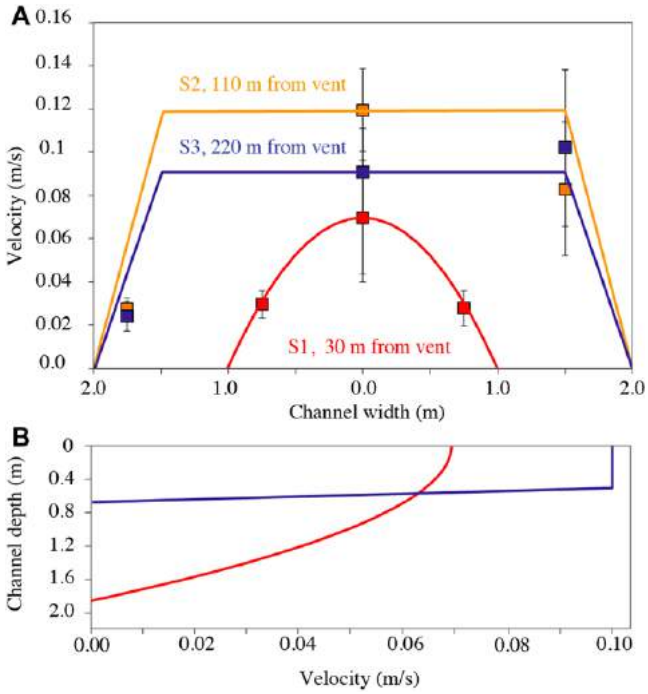

Figure 2. (A) Mean (squares) and standard deviation (given as error bars) for all velocity measurements at Piton de la Fournaise (La Réunion, France) on 1 August 2015. Lines are best-fit velocity profiles across channel width at stations 1 (red), 2 (orange), and 3 (blue) using the approach given in Supplement DR2 (see footnote 1). (B) Modeled vertical velocity profiles at stations 1 (red) and 3 (blue). For clarity, mean and standard deviation of the total data set at three stations was plotted and fitted here. Results are the same if we fit through the individual measurement sample sets that make up the population that the mean describes, where (for any one measurement set) there is always a lower velocity at station 1 than at stations 2 and 3. The full data set, for each station, is described and plotted in Supplement DR2. Note that the asymmetry of measurements at stations 2 (S2) and 3 (S3) is due to the missing far-bank shear zone, which we could not resolve from our low oblique viewing angle (see Supplement DR2).

[1]GSA Data Repository item 2020045, full description of the eruption (DR1); thermal image data collection and image details, measurements of surface velocities, modeling of velocity profiles and channel profile measurements in the field (DR2); heat loss and cooling rate calculations (DR3); sample analyses and lava viscosity calculations and results (DR4); and the full thermal image data set for all stations (DR5), is available online at http://www.geosociety.org/datarepository/2020/, or on request from editing@geosociety.org.

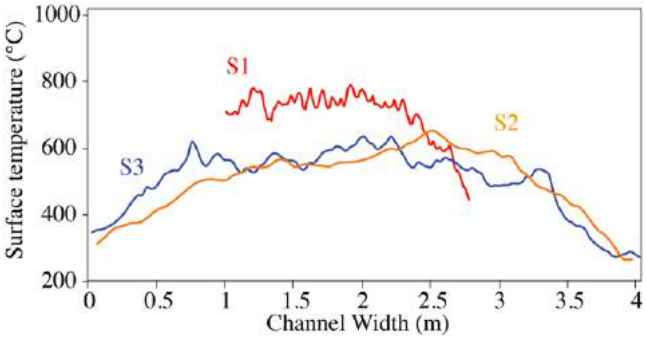

Figure 3. Surface temperature across the channel at stations 1 (red) and 3 (orange) at Piton de la Fournaise (La Réunion, France) on 1 August 2015.

Cashman et al., 1999; Soule et al., 2004; Riker et al., 2009; Robert et al., 2014; Rhéty et al., 2017). This is because, for our channel, the lava was poorly insulated, and velocities were low.

Sampling, Sample Characteristics, and Lava Viscosity

Lava was sampled on the first day near the vent and on the second day at station 2 coincident with thermal imaging (Supplement DR4). The station 2 sample was collected by inserting a metal rod laterally 50 cm into the channel, resulting in two distinct, simultaneously collected, fragments: one from the shear zone and one from the plug. Mass flux was steady during field work of day 2, during which this key (shear zone and plug) sample was collected coincident with the thermal imagery.

Lava bulk composition was basaltic with a porphyritic texture (<3 vol% phenocrysts; 15–34 vol% microlites of plagioclase and pyroxene; Supplement DR4). Near-vent samples had a bulk density of 1370 ± 280 kg/m^3, resulting in a vesicularity of 53 ± 10 vol%. Vesicles were rounded with equivalent diameters of 1 mm (Fig. 4). Temperature estimated from the glass MgO content was 1138 ± 2 °C (Supplement DR4). The two station 2 sample fragments had contrasting textural characteristics. The shear zone part was dense (2020 kg/m^3) with a vesicularity of 30 vol%, including rounded and small (0.5 mm) vesicles and a few larger (>2 mm) vesicles. Crystals showed alignment, and the calculated melt temperature was 1119 ± 1 °C. The difference between melt temperature near the vent and that of the sample from the shear zone resulted in a cooling per unit distance of 0.17 °C/m, which agrees with the theoretical calculations obtained from heat loss (Supplement DR3). Conversely, the central plug fragment had an extremely low density (500 kg/m^3), a very high vesicularity (83 vol%), and less abundant crystals (17 vol%). The vesicle population was heterogeneous, being a mixture of small-rounded (10–100 µm), larger-rounded (<0.5 mm), and irregularly shaped vesicles.

At station 1, the strain rates were relatively low (0.07 s^{-1}), and the bubble capillary number (Ca) was around 0.7 (Supplement DR4). Given a threshold Ca of 0.5, above which bubbles are able to deform (Manga et al., 1998), i.e., bubble internal forces are weaker than the surrounding fluid forces (viscosity × strain rate), the apparent viscosity of the three-phase lava (i.e., melt + crystal + bubbles) was estimated at 1.5 × 10^3 Pa·s (Supplement DR4). At station 2 within the shear zones, the vesicle-free (melt + crystal) viscosity was higher at 8.4 × 10^3 Pa·s due to lower temperature. However, because strain rates were 0.2 s^{-1} in the plug and 0.45 s^{-1} in the shear zones, we obtained Ca >> 0.5 in these locations—meaning that bubbles were highly deformable. The effect of the bubbles therefore decreased the effective viscosity to 4.7 × 10^3 Pa·s. Conversely, within the plug, although crystallinity was lower, the very high bubble concentration (>80 vol%) and very low strain rates (near 0 s^{-1}) prevented deformation of bubbles.

DISCUSSION

Given the interior flow temperature difference of 19 °C between stations 1 and 2, an average surface velocity of 0.05 m/s at station 1, and a distance between the two stations of 80 m, the time to travel to station 2 was around 1600 s. This gives cooling along the shear zones at a rate of ~0.012 °C/s, which is in line with cooling rates obtained for active flows in Hawaii (Cashman et al., 1999). Given such a decrease in temperature, we would expect a viscosity increase, and hence velocity decrease, down this vent-proximal channel length. However, the measured velocities revealed an acceleration between stations 1 and 2, after which velocity was constant until station 3. Given a constant slope between the three stations and stable effusion rate at the time of measurements, we explain this as a change in rheological behavior by strain localization on either side of a down-flow–developing central plug (i.e., within the shear zones).

We therefore propose a scenario whereby lava emitted at the vent flowed under a Newtonian

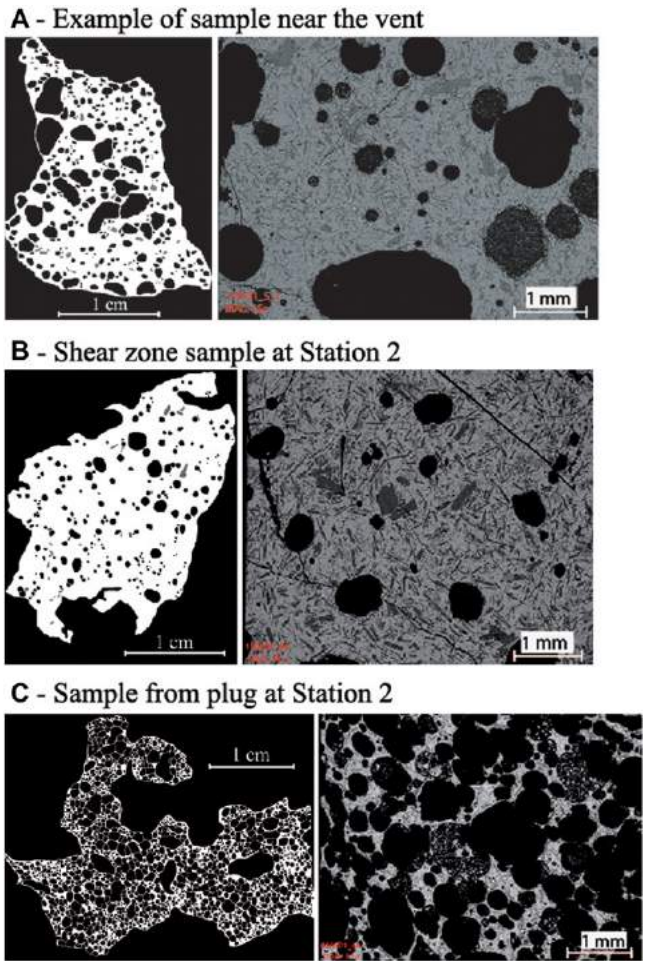

Figure 4. Binary images of thin sections and backscattered electron images for (A) near-vent sample of day 1, plus (B) shear zone, and (C) plug zone of sample taken on day 2 of the July–August 2015 eruption of Piton de la Fournaise (La Réunion, France) (white—matrix, gray—phenocrysts, and black—vesicles).

regime, as supported by the parabolic velocity profile. After 110 m (by station 2), narrow shear zones had appeared on either side of a central plug, suggesting that flow had become Bingham. In the central plug, high bubble concentration and low strain rates resulted in bubble growth and increasing capillary forces, resulting in a polyhedral foam with internal yield strength and stable bubble walls, so that the plug was not deforming. Instead, it behaved as a solid, being carried between the two marginal shear zones. At the channel margins, although temperature was lower than near the vent, strain rates were so high that bubbles were sheared. The effect of this sheared-bubble population on bulk flow rheological properties outweighed the effect of cooling, resulting in a lower viscosity. The nonsheared and bubble-rich plug was thus carried between two lateral zones of sheared lava, highlighting the effect of bubbles, which either acted as a lubricant in the shear zones or as a retardant to deformation in the plug. We note, also, that the shear zone had lower MgO than the plug (Supplement DR4). This could be due to preferential settling of larger olivine crystals in the slower-moving shear zones, further supporting the fact that the shear and plug zones were independent identities.

The lower bubble content within the shear zones could be due to more outgassing than in the plug, or shear pressing of bubbles out of the marginal shear zones and into the central plug. However, due to relaxation effects during the time between sampling and quenching (Moitra et al., 2013; Lindoo et al., 2017), the evidence of the shearing effect was lost from the vesicle signature, but it remained visible in the microlite alignment (Fig. 4B).

The change in flow regime over the proximal reach of the flow, from shear dominated with a parabolic velocity profile at the vent to plug dominated after 110 m, is reflected in the temperature profiles (Fig. 3). Temperatures were high across the entire channel close to the vent because of a highly disrupted, young crust. At stations 2 and 3, temperatures became low in the marginal shear zones, where an increasingly thick carapace of mature ʻaʻā was built (cf. Rowland and Walker, 1987), and higher across the central plug, where slabs of crust were able to form, but then broke up to expose hotter interior lava. The lower velocities of the shear zone lava also meant that lava at the channel margins had more time to cool and develop a more mature crust than at the center, as well as giving time for larger olivine crystals to preferentially settle and gas to escape.

CONCLUSION

An unexpected velocity increase and apparent viscosity decrease were recorded down a lava channel over the first 110 m of flow, in spite of stable slope, constant mass flux, and high cooling rates. This peculiar change was caused by the down-flow development of a central plug flanked by narrow shear zones in which bubbles were highly deformed, and hence where the effective viscosity was low. As in a volcanic conduit (e.g., Wright and Weinberg, 2009), the lateral shear zones lubricated the central plug. This caused the flow to initially accelerate over the proximal reach of the channel until cooling and crystallization could take over as the main drivers for viscosity increase and, hence, velocity decrease.

Our measurements represent a unique (and difficult to obtain) near-vent data set (fully described and presented in the Data Repository) in which, for the first time, we could identify and quantify a velocity increase over a relatively short distance close to the vent. Future measurements will need to focus on this near-vent part of the channel system so as to properly define and explain the complete down-channel evolution of flow dynamics.

ACKNOWLEDGMENTS

This work was funded by the Agence National de la Recherche (ANR) through project Lava Advance into Vulnerable Areas (LAVA; ANR program: DS0902 2016; project: ANR-16CE39–0009) and greatly benefited from the constructive comments of Matthew Patrick, Einat Lev, Kathy Cashman, and two anonymous reviewers. This is ANR-LAVA contribution 12.

REFERENCES CITED

Bachelor, G.K., 1967, An Introduction to Fluid Dynamics: Cambridge, UK, Cambridge University Press, Cambridge Mathematical Library Series, https://doi.org/10.1017/CBO9780511800955.

Cashman, K.V., and Kauahikaua, J.P., 1997, Reevaluation of vesicle distributions in basaltic lava flows: Geology, v. 25, p. 419–422, https://doi.org/10.1130/0091-7613(1997)025<0419:ROVDIB>2.3.CO;2.

Cashman, K.V., Mangan, M.T., and Newman, S., 1994, Surface degassing and modifications to vesicle size distributions in active basalt flows: Journal of Volcanology and Geothermal Research, v. 61, p. 45–68, https://doi.org/10.1016/0377-0273(94)00015-8.

Cashman, K.V., Thornber, C., and Kauahikaua, J.P., 1999, Cooling and crystallization of lava in open channels, and the transition of pāhoehoe lava to ʻaʻā: Bulletin of Volcanology, v. 61, p. 306–323, https://doi.org/10.1007/s004450050299.

Chevrel, M.O., Platz, T., Hauber, E., Baratoux, D., Lavallée, Y., and Dingwell, D.B., 2013, Lava flow rheology: A comparison of morphological and petrological methods: Earth and Planetary Science Letters, v. 384, p. 102–120, https://doi.org/10.1016/j.epsl.2013.09.022.

Chevrel, M.O., Harris, A.J.L., James, M.R., Calabrò, L., Gurioli, L., and Pinkerton, H., 2018, The viscosity of pāhoehoe lava: In situ syn-eruptive measurements from Kilauea, Hawaii: Earth and Planetary Science Letters, v. 493, p. 161–171, https://doi.org/10.1016/j.epsl.2018.04.028.

Crisp, J., v. Cashman, K., Bonini, J.A., Hougen, S.B., and Pieri, D.C., 1994, Crystallization history of the 1984 Mauna Loa lava flow: Journal of Geophysical Research, v. 99, no. B4, p. 7177–7198, https://doi.org/10.1029/93JB02973.

Del Negro, C., Fortuna, L., and Vicari, A., 2005, Modelling lava flows by cellular nonlinear networks (CNN): Preliminary results: Nonlinear Processes in Geophysics, v. 12, p. 505–513, https://doi.org/10.5194/npg-12-505-2005.

Harris, A.J.L., and Rowland, S.K., 2001, FLOWGO: A kinematic thermo-rheological model for lava flowing in a channel: Bulletin of Volcanology, v. 63, p. 20–44, https://doi.org/10.1007/s004450000120.

Harris, A.J.L., and Rowland, S.K., 2009, Effusion rate controls on lava flow length and the role of heat loss: A review, *in* Hoskuldsson, A., et al., eds., Studies in Volcanology: The Legacy of George Walker: International Association of Volcanology and Chemistry of the Earth's Interior Special Publication 2, p. 33–51.

Hidaka, M., Goto, A., Umino, S., and Fujita, E., 2005, VTFS Project: Development of the lava flow simulation code LavaSIM with a model for three-dimensional convection, spreading, and solidification: Geochemistry Geophysics Geosystems, v. 6, Q07008, https://doi.org/10.1029/2004GC000869.

Keszthelyi, L., and Self, S., 1998, Some physical requirements for the emplacement of long basaltic lava flows: Journal of Geophysical Research, v. 103, p. 27447–27464, https://doi.org/10.1029/98JB00606.

Kolzenburg, S., Giordano, D., Hess, K.-U., and Dingwell, D.B., 2018, Shear-rate dependent disequilibrium rheology and dynamics of basalt solidification: Geophysical Research Letters, v. 45, no. 13, p. 6466–6475, https://doi.org/10.1029/2018GL077799.

Lindoo, A., Larsen, J.F., Cashman, K.V., and Oppenheimer, J., 2017, Crystal controls on permeability development and degassing in basaltic andesite magma: Geology, v. 45, p. 831–834, https://doi.org/10.1130/G39157.1.

Lipman, P.W., and Banks, N.G., 1987, Aʻa Flow Dynamics, Mauna Loa 1984: U.S. Geological Survey Professional Paper 1350, p. 1527–1567.

Llewellin, E.W., and Manga, M., 2005, Bubble suspension rheology and implications for conduit flow: Journal of Volcanology and Geothermal Research, v. 143, p. 205–217, https://doi.org/10.1016/j.jvolgeores.2004.09.018.

Manga, M., Castro, J., Cashman, K., and Loewenberg, M., 1998, Rheology of bubble-bearing magmas: Journal of Volcanology and Geothermal Research, v. 87, p. 15–28, https://doi.org/10.1016/S0377-0273(98)00091-2.

Moitra, P., Gonnermann, H.G., Houghton, B.F., and Giachetti, T., 2013, Relating vesicle shapes in pyroclasts to eruption styles: Bulletin of Volcanology, v. 75, p. 691–698, https://doi.org/10.1007/s00445-013-0691-8.

Moore, H.J., 1987, Preliminary estimates of the rheological properties of 1984 Mauna Loa Lava, *in* Decker, R.W., Wright, T.L., and Stauffer, P.H., eds., Hawaiian Volcanism: U.S. Geological Survey Professional Paper 1350, p. 1569–1588.

Rhéty, M., Harris, A.J.L., Villeneuve, N., Gurioli, L., Médard, E., Chevrel, M.O., and Bachèlery, P., 2017, A comparison of cooling-limited and volume-limited flow systems: Examples from channels in the Piton de La Fournaise April 2007 lava-flow field: Geochemistry Geophysics Geosystems, v. 18, p. 3270–3291, https://doi.org/10.1002/2017GC006839.

Riker, J.M., Cashman, K.V., Kauahikaua, J.P., and Montierth, C.M., 2009, The length of channelised lava flows: Insight from the 1859 eruption of Mauna Loa Volcano, Hawaii: Journal of Volcanology and Geothermal Research, v. 183, p. 139–156, https://doi.org/10.1016/j.jvolgeores.2009.03.002.

Robert, B., Harris, A., Gurioli, G., Medard, E., Sehlke, A., and Whittington, A., 2014, Textural

and rheological evolution of basalt flowing down a lava channel: Bulletin of Volcanology, v. 76, p. 824, https://doi.org/10.1007/s00445-014-0824-8.

Rowland, S.K., and Walker, G.P.L., 1987, Toothpaste lava: Characteristics and origin of a lava structural type transition between pahoehoe and ʻaʻa: Bulletin of Volcanology, v. 49, p. 631–641, https://doi.org/10.1007/BF01079968.

Soule, S.A., Cashman, K.V., and Kauahikaua, J.P., 2004, Examining flow emplacement through the surface morphology of three rapidly emplaced, solidified lava flows, Kīlauea Volcano, Hawai'i: Bulletin of Volcanology, v. 66, p. 1–14, https://doi.org/10.1007/s00445-003-0291-0.

Sparks, R.S.J., and Pinkerton, H., 1978, Effect of degassing on rheology of basaltic lava: Nature, v. 276, p. 385–386, https://doi.org/10.1038/276385a0.

Wright, H.M.N., and Weinberg, R.F., 2009, Strain localization in vesicular magma: Implications for rheology and fragmentation: Geology, v. 37, p. 1023–1026, https://doi.org/10.1130/G30199A.1.

Printed in USA